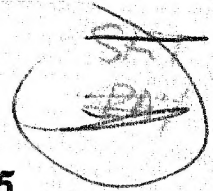
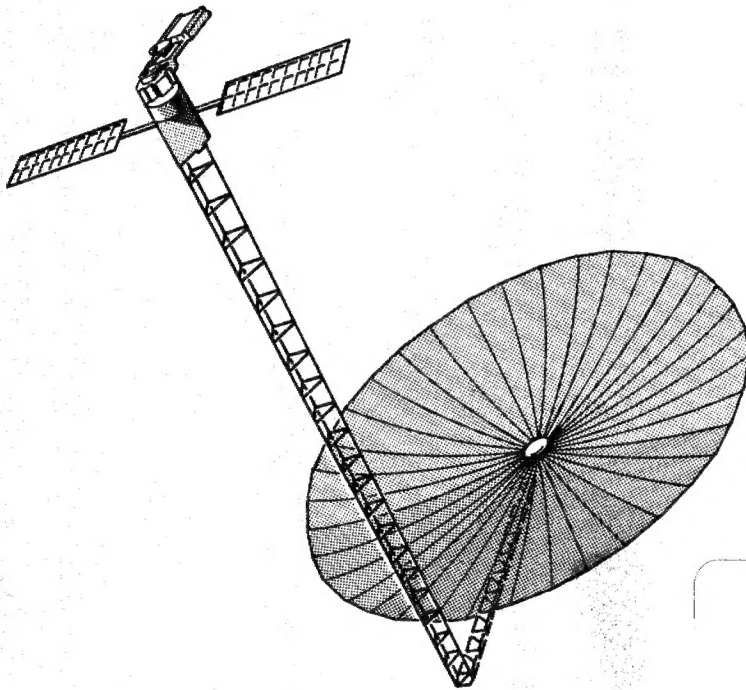


Xerox paper & the rest  
is static material



NASA Conference Publication 2245

# Research in Structural and Solid Mechanics - 1982



19960229 145

DTIC QUALITY INSPECTED 1

Research-in-progress papers  
presented at a symposium  
held at Washington, D.C.  
October 4-7, 1982



DEPARTMENT OF DEFENSE  
PLASTICS TECHNICAL EVALUATION CENTER  
WASHINGTON, D.C. 20301

NASA

PLASTIC 73560  
43569

Add 436114 + 436116

*NASA Conference Publication 2245*

# Research in Structural and Solid Mechanics - 1982

*Compiled by  
Jerrold M. Housner  
NASA Langley Research Center*

*Ahmed K. Noor  
The George Washington University  
Joint Institute for Advancement of  
Flight Sciences  
Hampton, Virginia*

Research-in-progress papers presented at  
a symposium sponsored by NASA Langley  
Research Center, Hampton, Virginia, and The  
George Washington University, Washington, D.C.,  
in cooperation with the National Science  
Foundation, the Air Force Office of Scientific  
Research, the Office of Naval Research,  
the American Society of Civil Engineers,  
and the American Society of Mechanical  
Engineers, and held at Washington, D.C.  
October 4-7, 1982

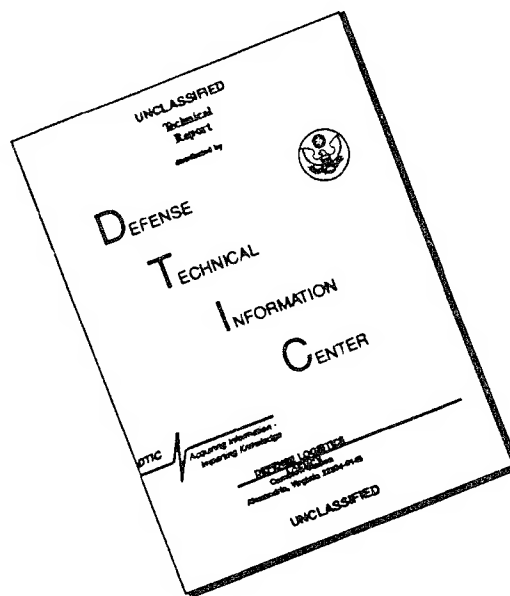


National Aeronautics  
and Space Administration

Scientific and Technical  
Information Branch

1982

# DISCLAIMER NOTICE



THIS DOCUMENT IS BEST QUALITY AVAILABLE. THE COPY FURNISHED TO DTIC CONTAINED A SIGNIFICANT NUMBER OF PAGES WHICH DO NOT REPRODUCE LEGIBLY.

## FOREWORD

This document contains a collection of papers presented at the "Symposium on Advances and Trends in Structural and Solid Mechanics," held in Washington, DC, on October 4-7, 1982. Most of the papers appearing in this document were presented in the research-in-progress sessions of the symposium. Most of the other presentations are contained in a separate conference proceedings published by Pergamon Press.\* Consequently, this document constitutes a companion to the Pergamon Press release. A supplement to NASA CP-2245 contains a synopsis of the panel discussion held at the symposium.

As indicated by the symposium title, the conference had two objectives: to present recent advances in structural and solid mechanics, including new solution procedures and new physical understanding of structural responses, and to identify the trends and future directions of the structural and solid mechanics disciplines. The first objective is accomplished by providing a forum for individuals to present their recent contributions and state-of-the-art reviews to their peers in industry, academia, and government, by providing an atmosphere for the interchange of ideas, and by compiling the symposium proceedings. However, to what extent the symposium accomplished its second objective cannot be easily measured, by either the quantity or the quality of the documents derived from the conference.

The task of discerning the trends in any existing discipline requires a comprehensive examination of the past and present states. From such information an attempt is made to extrapolate into the future. The fields of structural and solid mechanics are not short on history. Relative to structural and solid mechanics, many other engineering and scientific fields, such as those related to electronics, are newcomers. Thus, at first glance, it might appear that predicting the way structural problems will be solved in the next 10 to 20 years based on a history of many centuries would be a simple extrapolation (approximately 5 percent). However, for the purpose of establishing trends, the past 2 decades of advancement are far more significant than the last 2 centuries. Thus, 10- to 20-year trends become a 50- to 100-percent extrapolation. Indeed this makes trend predicting somewhat hazardous. Thus, the efforts of the symposium authors who tried to assess future trends are to be admired.

It is not much of an oversimplification to attribute the difficulty in assessing trends to the dependence of structural and solid mechanics, as well as nearly all engineering and scientific disciplines, on the rapidly changing electronic computer industry. The result of this dependence has been to produce rapidly growing and evolving structural and solid mechanics disciplines. This has made trend prediction difficult and, at the same time, more important. Much research could easily become useless or meaningless. To keep researchers and engineers up to date, symposiums such as this one have become increasingly important. In addition, dynamically evolving disciplines permit individuals and groups of individuals to have a greater impact on the way problems are solved. Symposiums such as the present one serve to stimulate and encourage the individuals who will play a part in setting, consciously or unconsciously, the 10- to 20-year trends mentioned earlier. Probably it is primarily in this way that the symposium fulfills its second objective.

---

\*Noor, Ahmed K.; and Housner, J. M., eds.: Advances and Trends in Structural and Solid Mechanics. Pergamon Press Ltd., 1982.



The symposium was cosponsored by the NASA Langley Research Center and the George Washington University. Cooperating organizations were the National Science Foundation, the Office of Naval Research, the Air Force Office of Scientific Research, the American Society of Civil Engineers, and the American Society of Mechanical Engineers.

The papers in this document are divided into the following topics:

1. Computational strategies for nonlinear problems
2. Material characterization
3. Advances in boundary elements and finite element technology
4. Advanced structural applications
5. Structural stability and analytical techniques
6. Structural dynamics and vehicle crashworthiness

The use of trade names or manufacturers' names does not constitute endorsement, either expressed or implied, by the National Aeronautics and Space Administration.

Jerrold M. Housner  
Ahmed K. Noor  
Compilers

# CONTENTS

FOREWORD . . . . .	iii
--------------------	-----

## COMPUTATIONAL STRATEGIES FOR NONLINEAR PROBLEMS

A SEMI-IMPLICIT DYNAMIC RELAXATION ALGORITHM FOR STATIC NONLINEAR STRUCTURAL ANALYSIS . . . . .	1
K. C. Park and C. C. Rankin	
MINIMIZATION VERSUS HOMOTOPY ALGORITHMS FOR NONLINEAR STRUCTURAL ANALYSIS . . .	11
M. P. Kamat, L. T. Watson, and V. B. Venkayya	
OPERATOR SPLIT METHODS IN THE NUMERICAL SOLUTION OF THE FINITE DEFORMATION ELASTOPLASTIC DYNAMIC PROBLEM . . . . .	25
Peter M. Pinsky, Miguel Ortiz, and Robert L. Taylor	
APPLICATION OF THE REDUCED BASIS METHOD TO NONLINEAR TRANSIENT THERMAL ANALYSIS . . . . .	49
Charles P. Shore	

## MATERIAL CHARACTERIZATION

NONLINEAR CONSTITUTIVE THEORY FOR TURBINE ENGINE STRUCTURAL ANALYSIS . . . . .	67
Robert L. Thompson	
PREDICTION OF RESIDUAL TENSILE STRENGTH OF TRANSVERSELY IMPACTED COMPOSITE LAMINATES . . . . .	43561 97
K. M. Lal	
INTERACTION OF HEAT PRODUCTION, STRAIN RATE AND STRESS POWER IN A PLASTICALLY DEFORMING BODY UNDER TENSILE TEST . . . . .	113
A. Paglietti	

## ADVANCES IN BOUNDARY ELEMENTS AND FINITE ELEMENT TECHNOLOGY

APPLICATION OF A BOUNDARY ELEMENT METHOD TO THE STUDY OF DYNAMICAL TORSION OF BEAMS . . . . .	129
Casimir Czekajski, Serge Laroze, and Daniel Gay	
A NOVEL BOUNDARY ELEMENT METHOD PROGRAM FOR HEAT TRANSFER ANALYSIS OF COMPOSITE MATERIALS . . . . .	43561 141
Kamar J. Singh	
IMPLEMENTATION OF A $C^1$ TRIANGULAR ELEMENT BASED ON THE P-VERSION OF THE FINITE ELEMENT METHOD . . . . .	153
D. W. Wang, I. N. Katz, and B. A. Szabo	

INTEGRATION OF MULTIDIMENSIONAL REGIONS WITH APPLICATIONS TO FINITE ELEMENT ANALYSIS . . . . .	171
Robert L. Mullen	
AN EMULATOR FOR MINIMIZING FINITE ELEMENT ANALYSIS IMPLEMENTATION RESOURCES . . . . .	185
Robert J. Melosh, Senol Utku, Moktar Salama, and Munir Islam	
THE FINITE ELEMENT MACHINE: AN EXPERIMENT IN PARALLEL PROCESSING . . . . .	201
O. O. Storaasli, S. W. Peebles, T. W. Crockett, J. D. Knott, and L. Adams	
A MIXED FORMULATION FINITE ELEMENT FOR LINEAR THIN SHELL ANALYSIS . . . . .	219
S. W. Lee and S. C. Wong	
AN EXACT ZOOMING METHOD FOR FINITE ELEMENT ANALYSIS . . . . .	229
Itio Hirai, Bo Ping Wang, and Walter D. Pilkey	

#### ADVANCED STRUCTURAL APPLICATIONS

DYNAMIC RESPONSE OF LINED TUNNELS BY BOUNDARY ELEMENTS . . . . .	251
G. D. Manolis	
A FINITE ELEMENT APPROACH FOR SHELLS OF REVOLUTION WITH A LOCAL DEVIATION . . . . .	265
Kye J. Han and Phillip L. Gould	
SYNTHESIS OF FRAMEWORKS UNDER MULTILEVEL PERFORMANCE CONSTRAINTS . . . . .	285
Donald E. Grierson and Thomas C. W. Chiu	
A SIMULATION LANGUAGE APPROACH TO STRUCTURAL INTERACTION PROBLEMS . . . . .	301
Malcolm A. Cutchins and James W. Purvis	
SUSCEPTIBILITY OF SYMMETRIC STRUCTURES TO NONLINEAR TORSIONAL COUPLING . . .	313
O. A. Pekau and Pradip K. Syamal	

#### STRUCTURAL STABILITY AND ANALYTICAL TECHNIQUES

ADVANCES AND TRENDS IN PLATE BUCKLING RESEARCH . . . . .	329
Arthur Leissa	
SOLUTION OF VON KÁRMÁN'S PLATE EQUATIONS WITH PERTURBATIONS AND SERIES SUMMATION . . . . .	349
L. Glen Watson and Joseph M. Chudobiak	

#### STRUCTURAL DYNAMICS AND VEHICLE CRASHWORTHINESS

CONSTRAINED MULTIBODY SYSTEM DYNAMICS - AN AUTOMATED APPROACH . . . . .	363
James W. Kamman and Ronald L. Huston	
SYSTEM IDENTIFICATION: A QUESTION OF UNIQUENESS, REVISITED . . . . .	375
Joseph E. Hardee and Vernon C. Matzen	

A COMPUTER PACKAGE FOR THE DESIGN AND EIGENPROBLEM SOLUTION OF DAMPED LINEAR MULTIDEGREE OF FREEDOM SYSTEMS . . . . .	391
Mehdi Ahmadian and Daniel J. Inman	
EXTENSIONAL COLLAPSE MODES OF STRUCTURAL MEMBERS . . . . .	405
Robert J. Hayduk and Tomasz Wierzbicki	

A SEMI-IMPLICIT DYNAMIC RELAXATION ALGORITHM  
FOR  
STATIC NONLINEAR STRUCTURAL ANALYSIS

K. C. Park and C. C. Rankin  
Applied Mechanics Laboratory  
Lockheed Palo Alto Research Laboratory  
Dept. 52-33, Building 255  
3251 Hanover Street  
Palo Alto, California 94304

SUMMARY

A semi-implicit dynamic relaxation technique is presented to solve the nonlinear structural equilibrium equation. The technique employs the same basic transient response analysis algorithm previously presented, thus enabling us to use one solution method and one software module for both static and dynamic analyses. A theoretical comparison of the present method with explicit dynamic relaxation techniques shows that the present method offers a substantially improved convergence property without ostensible computational overhead.

1. INTRODUCTION

In recent years, simplicity and program modularity in nonlinear structural analysis have been emphasized by many investigators. The overriding reasons for such emphasis have been due to the high cost of programming and of program modifications and the difficulties encountered in exchanging program modules among different analysis programs. There are three major computational complexities in nonlinear structural analysis programs: data management aspects; discrete element generations for quantities such as mass, damping, and stiffness or stresses; and the solution of the discrete equilibrium equations. This paper is concerned with the last aspect.

Traditionally, two distinct solution techniques have been implemented in a typical nonlinear structural analysis program: Newton-type techniques for solving quasistatic problems, and direct time integration (or modal synthesis) techniques for dynamics problems. Therefore, one is motivated to employ a unified family of solution techniques to both static and dynamic problems. In this regard the use of direct time integration techniques for both classes of problems offers one such possibility. When direct time integration techniques are used to solve static problems, they are called dynamic relaxation techniques in the literature (see [1] for example). Here, an increment of load is applied to the structure which is in an equilibrium state with the previous load and displacement states. The solution usually oscillates around the new equilibrium state and reaches that state through an introduction of artificial damping in the relaxation equations and/or direct time integration formulas. So far, explicit time integration techniques have been overwhelmingly preferred to implicit time techniques in dynamic relaxation techniques. This preference has been largely due to the requirements of frequent matrix generations and matrix factoring in implicit techniques, whereas in explicit techniques the solution process can be carried out by vectorized calculations.

In this paper, a semi-implicit direct time integration technique [2] is used to solve the discrete quasi-static equilibrium equations. The technique avoids matrix factorization regardless of step size changes and updated new stiffness matrices. The algorithm maintains linear (or linearized) unconditional stability and acceptable engineering solution accuracy for a broader range of step sizes. To this end, the paper is organized as follows.

Canonical first-order and second-order relaxation equations are derived from a special form of homotopy equation as applied to nonlinear structural equilibrium equations. It is shown that the relaxation equations thus derived satisfy a consistency condition in the sense that the second-order relaxation equation is in fact the correct error equation for the first-order relaxation equation, and so forth. It is also shown that certain approximations lead to various known solution techniques. For example, integration of the first-order relaxation equation by the Euler explicit integration formula with unit step size leads to Newton's method. In particular, the second-order relaxation equation, if specialized, can lead to the usual dynamic relaxation equation in the literature. This establishes a theoretical relation between the solution of equilibrium equation by Newton-like or dynamic relaxation techniques on the one hand, and direct time integration of canonical relaxation equations that are derived from the homotopy equation.

A general one-step implicit integration formula is introduced to time-discretize the relaxation equation and some approximations are introduced to several matrix operators so that the equations are practically tractable in most structural analysis programs. Normally, the canonical relaxation equations suggest that the mass matrix be the linearized stiffness matrix, and the damping matrix consist of the stiffness matrix plus the time derivative of the stiffness matrix. In this paper, the mass matrix is approximated by diagonalizing the stiffness matrix through absolute row sum and the damping matrix chosen to be proportional to both the mass and stiffness matrices. The implications of such approximations are offered in terms of computational efficiency and computer implementation.

Computer implementation of the semi-implicit dynamic relaxation algorithm is illustrated, which involves the selection of several parameters for efficiency and reliability. Finally, some numerical experiments are reported to assess the effectiveness and potential of the technique for large scale problems.

## 2. DERIVATION OF CANONICAL RELAXATION EQUATIONS

The discrete equilibrium equation for structures can be written as

$$\underline{r}(\underline{P}, \underline{u}) = \underline{P} - \underline{S}(\underline{u}) \quad (2.1)$$

where  $\underline{P}$  is the applied load vector,  $\underline{u}$  is the displacement vector,  $\underline{S}(\ )$  is the stiffness force operator that comes from the first variation of the Ritz functional of strain energy, and  $\underline{r}(\underline{P}, \underline{u})$  is the residual vector that is to be zero for equilibrium. The relaxation process for attaining the equilibrium state for (2.1) can be conceived as follows.

Suppose that there exists a unique equilibrium state  $\underline{u}^*$  for a given load  $\underline{P}$  and a solution process starts at point  $\underline{u}(0)$ . If the solution trajectory ultimately reaches the desired equilibrium state  $\underline{u}^*$  regardless of the starting point  $\underline{u}(0)$ , then the solution trajectory is called a homotopy and the equation which possesses such



property is called a homotopy equation. In mathematical terms, such an equation can be expressed as

$$\underline{r}(\underline{P}, \underline{u}) - \exp(-\underline{L}(t)) \underline{r}(\underline{P}, \underline{u}(0)) = 0 \quad (2.2)$$

provided

$$\exp(-\underline{L}(t)) \rightarrow 0 \quad \text{as } t \rightarrow \infty \quad (2.3)$$

regardless of the initial estimate  $\underline{u}(0)$ .

Note that by virtue of equation (2.3) one has from equation (2.2)

$$\underline{r}(\underline{P}, \underline{u}^*) = 0 \quad \text{as } t \rightarrow \infty \quad (2.4)$$

which is the desired equilibrium state.

Although equation (2.2) has the desirable mathematical property, it is hardly tractable by a computerized solution procedure. However, it turns out that the perturbation equations from equation (2.2) can be used as canonical forms for developing several computational solution algorithms. Differentiation of equation (2.2) once with respect to the relaxation time ( $t$ ) gives

$$-\partial \underline{S} / \partial \underline{u} \dot{\underline{u}} + \dot{\underline{L}} \exp(-\underline{L}(t)) \underline{r}(\underline{P}, \underline{u}(0)) = 0 \quad (2.5)$$

where  $\underline{P}$  is assumed to be fixed. Equation (2.5) can be rearranged to read

$$\underline{K} \dot{\underline{u}} = \dot{\underline{L}} \underline{r}(\underline{P}, \underline{u}) \quad (2.6)$$

where

$$\underline{K} = \partial \underline{S} / \partial \underline{u} \quad (2.7)$$

and equation (2.2) is used to eliminate  $\exp(-\underline{L}(t))$ . Throughout this paper equation (2.5) or (2.6) will be called a canonical first-order relaxation equation, as it will be shown that many first-order solution techniques emanate from it.

If equation (2.5) or (2.6) is differentiated once more, the following canonical second-order relaxation equation results.

$$\underline{K} \ddot{\underline{u}} + (\dot{\underline{K}} + \dot{\underline{L}} \underline{K}) \dot{\underline{u}} + \ddot{\underline{L}} \underline{S}(\underline{u}) = \ddot{\underline{L}} \underline{P} \quad (2.8)$$

Here again, equation (2.8) can be shown to be a starting form for many second-order solution techniques. Now some of the special cases of the two canonical relaxation equations will be examined.

## 2.1 Integration of First-Order Relaxation Equation

A special relaxation path for integrating the first-order relaxation equation follows if one chooses

$$\dot{\underline{L}} = \underline{I} \quad (2.9)$$

and employs the Euler explicit formula

$$\underline{u}_{n+1} = \underline{u}_n + h \dot{\underline{u}}_n \quad (2.10)$$

to solve equation (2.6), which yields

$$\underline{u}_{n+1} = \underline{u}_n + h \underline{K}^{-1} \underline{r}(\underline{p}, \underline{u}_n) \quad (2.11)$$

provided  $\underline{K}$  is nonsingular.

Note from equation (2.11) that if the step size  $h = 1$ , then (2.11) becomes Newton's method to solve the original equilibrium equation (2.1). Hence, direct integration of the specialized first-order relaxation equation (2.6) with the choice of (2.9) for  $\underline{L}$  and by the Euler explicit formula (2.10) yields the same computational method as the Newton method applied to the equilibrium equation (2.1). It should be emphasized that other Newton-like methods can be derived from (2.11) if the step size  $h$  and the Jacobian matrix  $\underline{K}$  are approximated for computational expediency. For derivations of hierarchical relaxation equations and their consistencies, the reader may consult [3].

## 2.2 Explicit Integration of Second-Order Relaxation Equation

Equation (2.8) can be specialized to

$$\underline{K} \ddot{\underline{u}} + \alpha \underline{K} \dot{\underline{u}} + \underline{S}(\underline{u}) = \underline{p} \quad (2.12)$$

if one selects

$$\ddot{\underline{L}} = \underline{I} \quad (2.13)$$

$$\dot{\underline{K}} + \dot{\underline{L}} \underline{K} \approx \alpha \underline{K} \quad (2.14)$$

One of many explicit dynamic relaxation techniques is due to Underwood [1], which approximates  $\underline{K}$  and  $\alpha$  as follows.

$$\underline{K} \approx \underline{M} = [m_i], \quad m_i = \sum_{j=1}^N |K_{ij}|, \quad j=1, N \quad (2.15)$$

$$\alpha = 2(\underline{u}^t \underline{K} \underline{u} / \underline{u}^t \underline{M} \underline{u})^{1/2} \quad (2.16)$$

When equations (2.15) and (2.16) are substituted into (2.12), one obtains

$$\ddot{\underline{u}} + \alpha \dot{\underline{u}} + \underline{S}(\underline{u}) = \underline{P} \quad (2.17)$$

Now, equation (2.17) is integrated by the central difference formula

$$\begin{aligned} \dot{\underline{u}}_{n+1/2} &= \dot{\underline{u}}_{n-1/2} + h \ddot{\underline{u}}_n \\ \underline{u}_{n+1} &= \underline{u}_n + h \dot{\underline{u}}_{n+1/2} \end{aligned}$$

Other second-order relaxation algorithms can be derived from (2.8) if  $\underline{L}$  and  $\underline{K}$  are appropriately approximated. For example, the scaling of  $\underline{S}(\underline{u})$  for a better convergence rate can be viewed from the present canonical second-order relaxation, as choosing  $\underline{L}$  other than the identity matrix.

### 3. IMPLICIT DYNAMIC RELAXATION (DR) ALGORITHM

It can be shown that if the second-order DR equation (2.8) is integrated by an implicit integration formula, the solution will converge in one step provided the step size  $h$  is large enough. This is because one must factor  $\underline{K}$  that is associated with both  $\ddot{\underline{u}}$  and  $\dot{\underline{u}}$ . The idea is then to compromise a lower convergence rate by adopting a diagonalized approximation of  $\underline{K}$  in favor of computational simplicity. Hence, as in the case of explicit DR algorithms,  $\underline{K}$  is approximated by

$$\underline{K} \approx \underline{M} = [m_i], \quad m_i = \sum_{j=1}^N |K_{ij}|, \quad j = 1, n \quad (3.1)$$

Note that the matrix  $\underline{K}$  associated with  $\ddot{\underline{u}}$  is the tangent stiffness matrix in the canonical equation (2.8), which is distinctly different from the mass matrix in structural dynamic equations. In fact, this explains why the diagonalized form as given by equation (3.1) is found to be superior in explicit DR techniques [1].

Whereas the term  $\dot{\underline{K}}$  is ignored in explicit DR techniques, it will prove essential to retain  $\dot{\underline{K}}$  in implicit DR techniques. Hence,  $\dot{\underline{K}}$  is approximated by

$$\dot{\underline{K}} \sim \beta \underline{K} \quad (3.2)$$

since one may express

$$\dot{\underline{K}} \sim ((1+\bar{\beta}) \underline{K} - \underline{K})/h \approx \beta \underline{K} \quad (3.3)$$

where  $\beta = \bar{\beta}/h$ .

With the above two approximations, equation (2.8) reduces to

$$\ddot{M} \ddot{u} + (\dot{L} K + \beta K) \dot{u} + \ddot{L} S(u) = \ddot{L} P \quad (3.4)$$

which is the desired form for the present study. However, there are still three parameters  $\beta$ ,  $L$  and  $\ddot{L}$  to be fixed before equation (3.4) can be implemented. This is dealt with next.

### 3.1 Selection of Relaxation Function $L$

It must be observed that the three undetermined parameters cannot be selected independent of the integration formula as the integration formula strongly influences the overall convergence property of any DR technique. It turns out that among one-step integration formulas, the Euler implicit formula is the most effective one. This is in contrast with the preference of the trapezoidal formula in dynamic problems for accuracy considerations. Hence, the integrator for the present study is

$$u_{n+1} = u_n + h \dot{u}_{n+1} \quad (3.5)$$

Substitution of (3.5) into (3.3) results in

$$(M + h(\dot{L} M + \beta K)) u_{n+1} + h^2 \ddot{L} S(u_{n+1}) = g_{n+1} \quad (3.6)$$

where

$$g_{n+1} = M + h(\dot{L} M + \beta K) u_n + h M \dot{u}_n + h^2 \ddot{L} P_{n+1} \quad (3.7)$$

Since  $\ddot{L}$  must exist,  $L$  can be represented in the form

$$L = (t^2/2 + b t + c) I \quad (3.8)$$

hence,

$$\ddot{L} = I \text{ and } \dot{L} = t + b \quad (3.9)$$

Now, within the time interval  $0 < t < h$ ,  $\dot{L}$  may be chosen to be

$$\dot{L} = \alpha = h + b \quad (3.10)$$

### 3.2 Convergence Property of Implicit DR Method

The convergence property of equation (3.6) can be examined by taking the linear (or linearized) case, viz.,

$$S(u_{n+1}) = K u_{n+1} \quad (3.11)$$

with the homogeneous state,  $P = 0$ . If one seeks a nontrivial solution in the form

$$u_{n+k} = \lambda^k u_n \quad (3.12)$$

the following equation results from equation (3.6)

$$(\underline{M} (\lambda - 1)^2 + h(\alpha \underline{M} + \beta \underline{K}) \lambda (\lambda - 1) + h^2 \underline{K} \lambda^2) \underline{u}_n = \underline{0} \quad (3.13)$$

As equation (3.13) can be decoupled via the transformations

$$\underline{u} = \underline{T} \underline{q}, \quad \underline{T}^t \underline{M} \underline{T} = \underline{I}, \quad \underline{T}^t \underline{K} \underline{T} = \underline{\Lambda} = [\omega^2] \quad (3.14abc)$$

equation (3.13) has a nontrivial set of solutions if and only if

$$\lambda_{1,2} = ((1 + B) + Q)/(1 + 2B + C) \quad (3.15)$$

where

$$B = h(\alpha + \beta \omega^2)/2 \quad (3.16)$$

$$C = (\omega h)^2 \quad (3.17)$$

$$Q = B^2 - C \quad (3.18)$$

The spectral radius  $\lambda$  given by equation (3.15) is to be minimized for a faster convergence. For example, if  $\lambda = 0$ , the solution converges in a single iteration step. Note that there are two solution components given by equation (3.15). For optimum convergence, one would like to have the two solution components converge with the same rate. This is achieved if one chooses

$$Q = B^2 - C = 0 \quad (3.19)$$

In practice, however, equation (3.19) can be satisfied only for two frequency components. Here, these two states are chosen to be at  $\omega_{\max}$  and  $\omega_{\min}$ , respectively. Hence, one obtains

$$(\alpha + \beta \omega_{\min}^2)^2 - 4 \omega_{\min}^2 = 0 \quad (3.20)$$

$$(\alpha + \beta \omega_{\max}^2)^2 - 4 \omega_{\max}^2 = 0 \quad (3.21)$$

Solving for  $\alpha$  and  $\beta$  from the above two equations, one obtains

$$\alpha = \frac{2 \omega_{\min} \omega_{\max}}{\omega_{\max} + \omega_{\min}} \quad (3.22)$$

$$\beta = \frac{2}{\omega_{\max} + \omega_{\min}} \quad (3.23)$$

The spectral radius  $\lambda$  now becomes from (3.15), (3.22), and (3.23),

$$\lambda = \frac{1}{1 + \omega h}, \quad \omega_{\min} < \omega < \omega_{\max} \quad (3.24)$$

### 3.3 Comparison with Explicit DR Techniques

It would be of interest to compare the spectral radii of both the present implicit DR vs. explicit DR techniques as proposed by Underwood [1] and Papadrakakis [4]. The optimum spectral radius for explicit DR techniques is given by

$$\lambda_{\text{exp}} = \frac{\omega_{\max} - \omega_{\min}}{\omega_{\max} + \omega_{\min}}, \quad \omega_{\min} < \omega < \omega_{\max} \quad (3.25)$$

while for the present implicit DR technique, it is given by (3.24).

In explicit DR technique,  $\omega_{\max}$  is often normalized to be unity while the optimum step size is found to be

$$h_{\text{opt}} = 2/(\omega_{\max}^2 + \omega_{\min}^2)^{1/2} \approx 2.0 \quad (3.26)$$

if  $\omega_{\min} \ll \omega_{\max}$ , which is often the case.

Hence, the spectral radius for the explicit DR techniques is given by

$$\lambda \approx (1 - 2\omega_{\min}), \quad \omega_{\min} < \omega < \omega_{\max} \quad (3.27)$$

whereas for the present implicit DR method it is

$$\lambda = 1/(1 + \omega h), \quad \omega_{\min} < \omega < \omega_{\max} \quad \text{and} \quad h < \infty \quad (3.28)$$

Note that for the present implicit DR method, the step size is not restricted to 2 as it does not suffer from stability loss. Even if one takes  $h = 2$  for the present method, the spectral radius is about the same at the lower eigenvalue while that of the present method approaches to 0.333 at the high eigenvalue end.

Of course, the above superior convergence property of the implicit DR method has so far sidestepped the issue of factoring the solution matrix  $(M + h(\alpha M + \beta K) + h^2 K)$ . This handicap is successfully overcome by the adoption of the semi-implicit algorithm [2] as described in the next section.

## 4. SEMI-IMPLICIT DYNAMIC RELAXATION ALGORITHM

For completeness, the second-order DR equation is written from the previous section as

$$\ddot{\underline{u}} + (\alpha \underline{M} + \beta \underline{K}) \dot{\underline{u}} + \underline{S}(\underline{u}) = \underline{P} \quad (4.1)$$



where

$$\alpha = 2 \omega_{\min} \omega_{\max} / (\omega_{\max} + \omega_{\min}) \quad (4.2)$$

$$\beta = 2 / (\omega_{\max} + \omega_{\min}) \quad (4.3)$$

and  $\omega^2$  is obtained from the eigenvalue problem

$$\omega^2 \underline{\underline{M}} \underline{\underline{x}} = \underline{\underline{K}} \underline{\underline{x}} \quad (4.4)$$

The iteration equation, when the Euler implicit formula (3.5) is used to integrate (4.1), is

$$\underline{\underline{E}} \Delta \underline{\underline{u}}_{n+1} = \underline{\underline{r}}_{n+1} / (1 + \alpha h) \quad (4.5)$$

where

$$\underline{\underline{E}} = \underline{\underline{M}} + \delta^2 \underline{\underline{K}} \quad (4.6)$$

$$\Delta \underline{\underline{u}}_{n+1} = \underline{\underline{u}}_{n+1} - \underline{\underline{u}}_n \quad (4.7)$$

$$\begin{aligned} \underline{\underline{r}}_{n+1} = & h^2 (\underline{\underline{p}}_{n+1} - \underline{\underline{S}}(\underline{\underline{u}}_{n+1}^p)) + h \underline{\underline{M}} \dot{\underline{\underline{u}}}_n \\ & - (\underline{\underline{M}} + h(\alpha \underline{\underline{M}} + \beta \underline{\underline{K}}))(\underline{\underline{u}}_{n+1}^p - \underline{\underline{u}}_n) \end{aligned} \quad (4.8)$$

$$\delta^2 = (\beta + h) h / (1 + \alpha h) \quad (4.9)$$

and  $\underline{\underline{u}}_{n+1}^p$  is a suitable predictor.

In semi-implicit method [2], the solution matrix is approximated by

$$\underline{\underline{E}} \approx \underline{\underline{M}} + \delta^2 \underline{\underline{K}} + \delta^4 \underline{\underline{C}} \quad (4.10)$$

$$\underline{\underline{E}} \approx (\underline{\underline{I}} + \delta^2 \hat{\underline{\underline{K}}}^L) \hat{\underline{\underline{M}}} (\underline{\underline{I}} + \delta^2 \hat{\underline{\underline{K}}}^U)$$

where

$$\hat{\underline{\underline{M}}} = \underline{\underline{M}} + \delta^4 \underline{\underline{m}}$$

$$\hat{\underline{\underline{K}}}^L = (\underline{\underline{K}}^L + \delta^2 \underline{\underline{k}}/2) \hat{\underline{\underline{M}}}^{-1} \quad (4.11a-d)$$

$$\hat{\underline{\underline{K}}}^U = (\hat{\underline{\underline{K}}}^L)^t, \quad \underline{\underline{K}}^U = (\underline{\underline{K}}^L)^t$$

in which  $\underline{\underline{m}}$  and  $\underline{\underline{k}}$  are diagonal matrices to be determined by requiring that

$$\underline{\underline{C}} \underline{\underline{u}}_n = 0 \quad (4.12)$$

Note that the approximate  $\tilde{E}$  as given by (4.10b) consists of two triangular and one diagonal matrices. Therefore, factoring is bypassed and only substitutions are needed to solve the relaxation iteration equation (4.5). For details on computing  $\tilde{m}$  and  $\tilde{k}$  the reader may consult [2].

#### ACKNOWLEDGMENTS

This work was supported in part by NASA Langley Research Center. The authors thank Dr. Jerrold M. Housner for his interest and encouragement in the work.

#### REFERENCES

1. Underwood, P. G.: Dynamic Relaxation - A Review. Computational Methods for Transient Analysis, T. Belytschko and T. J. R. Hughes, eds., North-Holland, 1982. (To be published.)
2. Park, K. C.: An Improved Semi-Implicit Method for Structural Dynamics Analysis. Journal of Applied Mechanics, ASME Paper No. 82-WA/APM-2, 1982. (To be published.)
3. Park, K. C.: A Family of Solution Algorithms for Nonlinear Structural Analysis Based on Relaxation Equations. International Journal for Numerical Methods in Engineering, 1982. (To be published.)
4. Papadrakakis, M.: A Method for the Automatic Evaluation of the Dynamic Relaxation Parameters. Computer Methods in Applied Mechanics and Engineering, 25, 1981, pp. 35-48.

## MINIMIZATION VERSUS HOMOTOPY ALGORITHMS

### FOR NONLINEAR STRUCTURAL ANALYSIS\*

M. P. Kamat<sup>†</sup> and L. T. Watson<sup>††</sup>

Virginia Polytechnic Institute and State University  
Blacksburg, Virginia 24061  
and

V. B. Venkayya\*\*

Flight Dynamics Laboratory  
Wright-Patterson Air Force Base, Ohio 45433

### SUMMARY

The authors assess the relative merits and demerits of the minimization techniques using globally convergent quasi-Newton algorithms on the one hand and the homotopy algorithms on the other hand for the solution of problems of nonlinear structural analysis. Like the homotopy algorithms the globally convergent quasi-Newton algorithms are equally well suited for the solution of the nonlinear equations of structural analysis directly without having to pose the problem as an equivalent minimization problem. It is only in the close neighborhood of the limit and bifurcation points, however, that quasi-Newton algorithms experience difficulties. Homotopy algorithms on the other hand are robust for practically all types of nonlinear problems but are computationally not as cost-effective since they provide an extremely accurate prediction of the response by calculating it at a large number of points. Globally convergent algorithms can perform well with very approximate Hessians, while homotopy algorithms require extremely accurate Hessians. Finally, while quasi-Newton algorithms can be very easily structured to exploit sparsity and symmetry, homotopy algorithms are not presently so structured and would require special modifications for exploitation of such features without sacrificing robustness and global convergence.

### INTRODUCTION

Newton's method or its modification is undoubtedly one of the most popular methods for the solution of problems of nonlinear structural analysis. However, in spite of its very high efficiency, because of unsuccessful convergence, or at times even divergence, researchers are increasingly recognizing the need for making these algorithms robust and globally convergent. Globally convergent algorithms using the double dogleg strategy [1] not only eliminate the convergence problems of the conventional Newton's algorithms but are also more efficient as a result of the careful, automatically controlled step length procedures.

\* This work was partially supported by NASA Grant NAG-1-139. Acknowledgement is also due to the Flight Dynamics Laboratory, WPAFB, for allowing the first author to complete this work as a Visiting Scientist there.

<sup>†</sup> Professor, Dept. of Engineering Science and Mechanics

<sup>††</sup> Associate Professor, Dept. of Computer Science

\*\* Aerospace Engineer, Structures and Dynamics Division

But even so, globally convergent quasi-Newton algorithms, in the absence of very highly specialized response parameter incrementation features [2], are ineffective in the neighborhood of limit or bifurcation points where the Jacobian of the nonlinear equations ceases to be positive definite. This is not to say that quasi-Newton algorithms cannot be used to locate limit or bifurcation points. They certainly can be, and very efficiently at that, but they cannot 'breeze' past such turning points in the absence of a proper and specialized response parameter control. It is for limit point problems that techniques like those proposed by Riks [3], Crisfield [4], and Padovan [5] have to be resorted to. The homotopy algorithm presents yet another such alternative.

In this paper we discuss in detail the globally convergent quasi-Newton minimization algorithm and the homotopy algorithms and demonstrate their effectiveness in solving certain classes of highly nonlinear problems of structural analysis. The authors believe that it is through an optimal combination of the two algorithms that a highly efficient, and at the same time robust, and globally convergent algorithm suitable for an extremely wide class of nonlinear problems can emerge.

#### GLOBALLY CONVERGENT QUASI-NEWTON ALGORITHM - The Double Dogleg Strategy

It is well known that standard Newton's method is not globally convergent; that is to say, a good starting point is essential for its convergence, and in fact it may diverge from a bad starting point if the strategy is to always take the full Newton step. For an extremely good example of such a phenomenon, consider the clamped beam of Figure 1. It can be easily verified that, depending upon the size of the load step, the conventional Newton's method can diverge by producing nonpositive definite Hessians during the iteration process. A globally convergent Newton's method using the double dogleg strategy overcomes this problem by controlling the directions and the step lengths.

The development of the double dogleg strategy as presented here is based on an excellent expose of the strategy by Dennis and Schnabel [1]. The strategy was, however, first proposed by Powell [6], although the method as proposed by Powell lacked the sophistication and the efficiency features of the present method.

#### Quadratic Model

Newton's method for unconstrained minimization essentially approximates the multivariate function  $f: \mathbb{R}^n \rightarrow \mathbb{R}$  about a point  $\underline{x}_c$  by a quadratic model of the type

$$m_c(\underline{x}_+) = m_c(\underline{x}_c + \underline{S}) = f(\underline{x}_c) + \underline{S}^T \nabla f(\underline{x}_c) + \frac{1}{2} \underline{S}^T \underline{H}_c \underline{S} \quad (1)$$

where  $\underline{S} = (\underline{x}_+ - \underline{x}_c)$  and  $\underline{H}_c$  is an approximation to the Hessian of  $f$  which is coerced to be positive definite if not already so.

To render Newton's method globally convergent, the following two conditions must be satisfied: (i) sufficiently large decreases in  $f$  values must be achieved for the step lengths taken and (ii) the rate of decrease in the direction  $\underline{S}$  at  $\underline{x}_+$  must be smaller than the rate of decrease in the direction  $\underline{S}$  at  $\underline{x}_c$ . Both these criteria can be expected to be satisfied if the following definition of acceptability of an iterate  $\underline{x}_+$  is adopted

$$f(\underline{x}_+) \leq f(\underline{x}_c) + \alpha \underline{S}^T \nabla f(\underline{x}_c) \quad (2)$$

with  $\alpha = 10^{-4}$ .

Standard backtracking along the Newton or quasi-Newton direction by retaining the same step direction but by choosing shorter step lengths can achieve convergence. These new shorter step lengths are determined by a one-dimensional quadratic or cubic model built from only function and gradient information in the quasi-Newton direction. Such a strategy, although quite successful, suffers from the fact that it fails to utilize the n-dimensional quadratic model including the model Hessian during backtracking. The double dogleg strategy on the other hand uses the n-dimensional quadratic model to choose the new step direction and the shorter step lengths.

There is a certain region within which the quadratic model  $m_c$  can be trusted to adequately approximate the function. Let  $\delta_c$  denote the radius of such a trust region around the current point  $\underline{x}_c$ . If the trust region is large enough, that is if

$$\delta_c > \| \underline{s}_c^N \|_2 \quad (3)$$

where  $\| \underline{s}_c^N \|_2$  is the distance to the Newton point from the current point  $\underline{x}_c$ , then the Newton step is taken since the Newton point is the global minimizer of  $m_c$ . In other words

$$\underline{s}_c^N = - \underline{H}_c^{-1} \underline{\nabla} f(\underline{x}_c) \quad (4-a)$$

$$\underline{x}_+ = \underline{x}_c + \underline{s}_c^N \quad (4-b)$$

The new point  $\underline{x}_+$  is checked for acceptability using Eq. (2). If the new iterate  $\underline{x}_+$  is found to be satisfactory, a new quadratic model  $m_c$  is constructed around  $\underline{x}_+$ , the trust region radius  $\delta$  is updated, and the next iteration is begun.

However, if the trust region radius  $\delta_c$  is less than the Newton step, then the direction  $\underline{s}$  is determined as being that direction that corresponds to the optimum solution of the constrained problem:

$$\text{Minimize } m_c(\underline{x}_c + \underline{s}) \quad (5)$$

$$\text{Subject to } \| \underline{s} \| \leq \delta_c \quad (6)$$

From the theory of constrained optimization, the necessary and sufficient conditions for an optimum are given by

$$\underline{s} = \underline{s}(\mu) = -(\underline{H}_c + \mu \underline{I})^{-1} \underline{\nabla} f(\underline{x}_c), \mu > 0 \quad (7-a)$$

$$\text{such that } \| \underline{s}(\mu) \| = \delta_c;$$

$$\text{or } \underline{s} = \underline{s}(0) = \underline{s}_c^N, \mu = 0 \quad (7-b)$$

$$\text{such that } \| \underline{s}(0) \| \leq \delta_c$$

Thus the curve  $\underline{s}(\mu)$  shown in Figure 2 is a curve that runs smoothly from the Newton step when  $\mu = 0$  to

$$\underline{s}(\mu) \approx -\frac{1}{\mu} \underline{\nabla} f(\underline{x}_c) \quad (7-c)$$

when  $\mu$  gets large. In other words, the solution to Eqs. (5) and (6) when  $\delta_c$  is very small is a step length  $\delta_c$  approximately in the steepest descent direction. An exact solution of Eqs. (5) and (6) to determine a direction  $\underline{S}$  requires what is known as the model trust region approach utilizing methods like the 'locally constrained optimal 'hook' step [7], requiring approximately  $O(n^3)$  operations. The double dogleg strategy provides an approximate solution of Eqs. (5) and (6) which is not much inferior to the exact solution but at a substantially reduced computational effort - approximately  $O(n^2)$  operations after  $\underline{S}_c^N$  has been calculated.

### Double Dogleg Strategy

The double dogleg is an approximation to the  $S(\mu)$  curve that must have its two properties: namely that the distance from the current point  $\underline{x}_c$  increases monotonically and the value of the quadratic model function also decreases monotonically along the double dogleg. The elbows of the double dogleg are chosen to guarantee these properties. The first elbow of the double dogleg is chosen to be the Cauchy point of the quadratic model. Thus,

$$\underline{x}_{cp} = \underline{x}_c + \underline{S}_{cp} \quad (8-a)$$

where

$$\underline{S}_{cp} = -\lambda \nabla f(\underline{x}_c) \quad (8-b)$$

$$\lambda = \frac{\|\nabla f(\underline{x}_c)\|^2}{\nabla f(\underline{x}_c)^T \underline{H}_c \nabla f(\underline{x}_c)} \quad (8-c)$$

A point  $\underline{x}_N^{\wedge}$  is then chosen along the Newton direction such that the two desired properties of the double dogleg are satisfied. The point  $\underline{x}_N^{\wedge}$  is chosen as [8]

$$\underline{x}_N^{\wedge} = \underline{x}_c + \eta \underline{S}_c^N \quad (9-a)$$

where

$$\eta = 0.8\gamma + 0.2 \quad (9-b)$$

$\gamma$  being a quantity determined from the relation

$$\|\underline{S}_{cp}\| \leq \gamma \|\underline{S}_c^N\| \leq \|\underline{S}_c^N\| \quad (9-c)$$

and is given by

$$\gamma = \frac{\|\nabla f(\underline{x}_c)\|^4}{(\nabla f(\underline{x}_c)^T \underline{H}_c \nabla f(\underline{x}_c))(\nabla f(\underline{x}_c)^T \underline{H}_c^{-1} \nabla f(\underline{x}_c))} \quad (9-d)$$

The point  $\underline{x}_N^{\wedge}$  is the second elbow of the double dogleg.

The next iterate  $\underline{x}_+$  is then given by a point along  $\underline{x}_{cp}$  and  $\underline{x}_N^{\wedge}$  such that  $\|\underline{x}_+ - \underline{x}_c\| = \delta_c$ . That is,

$$\underline{x}_+ = \underline{x}_c + \underline{S}_{cp} + \beta(\underline{S}_c^N - \underline{S}_{cp}) \quad (10-a)$$

where  $\beta$  is chosen such that

$$\|\underline{S}_{cp} + \beta(\underline{S}_c^N - \underline{S}_{cp})\| = \delta_c \quad (10-b)$$

For  $\underline{x}_+$  to be an acceptable point it has to satisfy Eq. (2). If not, the trust region



radius must be reduced. The reduction factor is determined by the quadratic backtracking strategy utilizing  $f(\underline{x}_c)$ ,  $f(\underline{x}_+)$  and the directional derivative  $\nabla f(\underline{x}_c)^T (\underline{x}_+ - \underline{x}_c)$  to fit a parabola and determine the new trust region radius corresponding to the minimum of this parabola. The new trust region radius is given by

$$\delta = -\delta_c \frac{\nabla f(\underline{x}_c)^T (\underline{x}_+ - \underline{x}_c)}{2[f(\underline{x}_+) - f(\underline{x}_c) - \nabla f(\underline{x}_c)^T (\underline{x}_+ - \underline{x}_c)]} \quad (11)$$

If  $\underline{x}_+$  passes the acceptability test, then a check is made to determine how well the quadratic approximation is modeling the function  $f$  and whether a larger step from  $\underline{x}_c$  using the current quadratic model should be attempted. When finally an acceptable  $\underline{x}_+$  has been found, the quadratic model must be redefined utilizing  $\underline{H}_+$  or an approximation to it obtained by using, say, Toint's update [9]. The new trust region radius is determined as follows:

$$\text{If } |\Delta f| \geq 0.75 |\Delta f_{\text{pred}}|, \delta_+ = 2\delta_c \quad (12-a)$$

$$\text{If } |\Delta f| < 0.1 |\Delta f_{\text{pred}}|, \delta_+ = \delta_c/2 \quad (12-b)$$

$$\text{where } \Delta f_{\text{pred}} = m_c(\underline{x}_+) - f(\underline{x}_c) \quad (12-c)$$

This in essence completes the discussion of the double dogleg strategy. Interested readers should consult reference [1] for additional details.

#### Extension for Solving Nonlinear Equations

The double dogleg strategy can be extended for developing global methods for systems of nonlinear equations such as

$$\underline{F}(\underline{x}) = 0, \quad (13)$$

the Newton step for which is given by

$$\underline{x}_+ = \underline{x}_c - \underline{J}(\underline{x}_c)^{-1} \underline{F}(\underline{x}_c), \quad (14)$$

$\underline{J}(\underline{x}_c)$  being the Jacobian of  $\underline{F}$  at  $\underline{x}_c$ . The double dogleg strategy is applied to minimize

$$f(\underline{x}) = \frac{1}{2} \underline{F}(\underline{x})^T \underline{F}(\underline{x}) \quad (15)$$

the steepest descent direction for which is given by  $\underline{S}_{\text{cd}} = -\underline{J}(\underline{x}_c)^T \underline{F}(\underline{x}_c)$  with the Newton direction  $\underline{S}_c = -\underline{J}(\underline{x}_c)^{-1} \underline{F}(\underline{x}_c)$  being a descent direction. Since this Newton direction yields a root of

$$\underline{M}_c(\underline{x}_c + \underline{S}) = \underline{F}(\underline{x}_c) + \underline{J}(\underline{x}_c)^T \underline{S} \quad (16)$$

it goes to a minimum of

$$\hat{m}_c(\underline{x}_c + \underline{S}) = \frac{1}{2} \underline{M}_c(\underline{x}_c + \underline{S})^T \underline{M}_c(\underline{x}_c + \underline{S}) \quad (17)$$

Hence, global methods for nonlinear equations can be developed by applying the double dogleg strategy to the positive definite quadratic model (17).

# HOMOTOPY METHOD [10]-[11]

The equilibrium equations have the form

$$\underline{F}(\underline{x}, \lambda) = \underline{0} \quad (18)$$

where  $\underline{x}$ ,  $\underline{F}$  are  $n$ -vectors and  $\lambda$  is a scalar. The zero set of (18) contains a smooth (assuming  $\underline{F}$  is sufficiently smooth) curve  $\gamma$  in  $(n+1)$ -dimensional  $(\underline{x}, \lambda)$  space, which in the generic case does not intersect itself nor other zeros of  $\underline{F}(\underline{x}, \lambda)$ . The exceptional cases are where  $\gamma$  intersects itself or has bifurcation points. For simplicity only the generic case will be considered here -  $\gamma$  is assumed to have no bifurcation points. The smooth curve  $\gamma$  can be parametrized by arc length  $s$ , so

$$\underline{x} = \underline{x}(s), \lambda = \lambda(s) \quad (19)$$

along  $\gamma$ . Then

$$\underline{F}(\underline{x}(s), \lambda(s)) = 0 \quad (20)$$

identically in  $s$ , and the initial value problem

$$\frac{d}{ds} \underline{F}(\underline{x}(s), \lambda(s)) = [D_{\underline{x}} \underline{F}(\underline{x}(s), \lambda(s)), D_{\lambda} \underline{F}(\underline{x}(s), \lambda(s))] \begin{Bmatrix} \frac{d\underline{x}}{ds} \\ \frac{d\lambda}{ds} \end{Bmatrix} = \underline{0} \quad (21-a)$$

$$\begin{Bmatrix} \left\| \frac{d\underline{x}}{ds} \right\| \\ \left\| \frac{d\lambda}{ds} \right\| \end{Bmatrix}_2 = 1 \quad (21-b)$$

$$\underline{x}(0) = \underline{x}_0, \lambda(0) = 0 \quad (21-c)$$

has precisely  $\gamma$  as its trajectory. The idea (referred to as a homotopy method) is to solve (18) by solving the ordinary differential equations (21a-b) with initial conditions (21-c).

This technique differs significantly from standard continuation or imbedding in that: 1) the load parameter  $\lambda$  is a dependent variable which can both increase and decrease along  $\gamma$ , and 2) no attempt is made to invert the Jacobian matrix  $D_{\underline{x}} \underline{F}(\underline{x}, \lambda)$ , thus limit points pose no special difficulty whatsoever. It differs from initial value or parameter differentiation methods also since arc length  $s$ , rather than  $\lambda$ , is the controlling parameter. The homotopy method is similar in spirit to the Riks/Wempner [3] and Crisfield [4] methods, but the implementation details are very different, and the emphasis is on ODE techniques rather than a Newton type iteration.

The calculation of  $(dx/ds, d\lambda/ds)$  in (21-a) will now be discussed. Note that (21a-b) determine the derivative  $dy/ds = (dx/ds, d\lambda/ds)$  only implicitly, and standard ODE solvers require that the problem be specified in the form

$$\frac{dy}{ds} = \underline{G}(s, \underline{y}), \underline{y}(0) = \underline{y}_0 \quad (22)$$

The generic smoothness assumption on  $\gamma$  is tantamount to the  $n \times (n+1)$  Jacobian matrix

$$\underline{DF} = [\underline{D_x F}, \underline{D_\lambda F}] \quad (23)$$

having rank  $n$ . This means that  $\underline{DF}$  has a one dimensional kernel, and thus the subspace spanned by  $\underline{dy/ds}$  is uniquely determined. Equation (21-b) fixes the length at 1 and the direction is determined by continuity (precisely, the current derivative  $\underline{dy/ds}$  must make an acute angle with the previously calculated derivative).

The calculation of the kernel of  $\underline{DF}$  is the most expensive part of the algorithm, and also the most crucial in terms of accuracy. Thus, a technique was chosen which guarantees high accuracy at a slightly greater cost than some other possibilities. Using a modification of the algorithm in [12], the equation

$$\underline{DF}(\underline{y}(s)) \left( \frac{d\underline{y}}{ds} \right) = \underline{0} \quad (24)$$

is reduced to the form

$$\underline{RZ} = \underline{0} \quad (25)$$

where  $\underline{R}$  is an  $n \times (n+1)$  upper triangular matrix, by multiplying both sides of (24) by a series of Householder reflections (see [13] and [12] for complete details). The columns of  $\underline{DF}$  are interchanged such that the diagonal elements of  $\underline{R}$  are as large as possible;  $\underline{Z}$  represents a scaled permutation of  $\underline{dy/ds}$ .  $\underline{Z}$  is calculated by setting  $Z_{n+1} = 1$  and then using back substitution in (25).  $\underline{dy/ds}$  is obtained by permuting and scaling  $\underline{Z}$ , and also reversing its direction if necessary in order to maintain continuity of the derivative.

The use of Householder reflections on (24) destroys any sparsity that  $\underline{DF}$  might have. Thus, the algorithm as described, while perfectly adequate for small dense matrices  $\underline{DF}$ , is unsuitable for very large sparse matrices  $\underline{DH}$  with, for example, a skyline structure. Note that  $\underline{DF}$  is not square and that the  $(n+1)$ st column ( $=\underline{D_\lambda F}(x, \lambda)$ ) is generally full. A sparse direct algorithm is currently under development to overcome these complications and take advantage of the typical skyline structure. Note that (24) could also be solved by an iterative method applied to the  $(n+1) \times (n+1)$  positive semidefinite matrix  $(\underline{DF})^T \underline{DF}$ .

The derivative  $\underline{dy/ds} = \underline{G}(s, \underline{y})$  for any point  $(s, \underline{y})$  is required by the ODE code used to solve (16). Since derivative evaluations are expensive, a method which needs few such evaluations is preferable. The chosen algorithm is a variable step, variable order Adams PECE method, as implemented in L. F. Shampine's subroutine STEP [14]. An Adams PECE method uses previous points, and derivatives at those points, to predict the next point on  $\lambda$  by a high order interpolating polynomial. The derivative is then evaluated at the predicted point, and another high order polynomial is constructed which corrects the prediction. If the predicted value and corrected value agree sufficiently, the corrected value is accepted and the step size and order of the formulas are adjusted to optimal values. Finally, the derivative is evaluated at the accepted point. If the prediction and correction disagree, the step size and/or order are adjusted and a step is attempted again. The rules for the step size and order adjustment are very sophisticated, and are based on both theory and computational experience (see [14]).

As a final observation, the ODE based homotopy algorithm can calculate limit points (where  $d\lambda/ds = 0$ ) very accurately and efficiently. Simply track  $\lambda$  until

$d\lambda/ds$  changes sign. The limit point then lies between the last two calculated points on  $\lambda$ , and the problem is to find  $\bar{s}$  such that  $\frac{d\lambda}{ds}(\bar{s}) = 0$ . Using the information maintained by the ODE solver,  $d\lambda/ds$  can be calculated anywhere between the last two points on  $\lambda$  with no further derivative evaluations. Thus  $s$  can be found by the secant method (applied to the zero finding problem  $d\lambda/ds = 0$ ), and no extra derivative evaluations are required.

## DISCUSSION OF RESULTS AND CONCLUSIONS

Performance evaluation of the globally convergent quasi-Newton and the homotopy algorithms is especially interesting on those problems of geometrically nonlinear structural analysis for which the standard Newton's method (SNM) does not perform well. Three such problems are illustrated in Figures 1, 3 and 4. A much more detailed evaluation of these algorithms on moderately large scale problems involving both geometric and material nonlinearities may be found in reference [15].

### Centrally Loaded Clamped Beam

The problem of Fig. 1 involves a slender clamped beam loaded by a concentrated load at its midspan. Because of symmetry only half the beam is modeled using 10 frame (3-D beam) elements leading to a model with a total of 29 degrees of freedom. The stiffening character of the model under large displacements leads to a response curve as shown in the figure. Such a response curve poses significant problems for the standard Newton's method (SNM) or the modified Newton-Raphson method (MNR) unless the load steps are small enough. However, globally convergent versions of both these methods utilizing the double dogleg strategy permits extremely large load steps. This is a definite advantage for those cases (like the two cases to be discussed next) wherein the objective of a nonlinear analysis may be primarily an accurate location of a limit or a bifurcation point.

A globally convergent Newton's method (GCNM) is defined to be one in which  $H_c$  of the quadratic model of Eq. (1) is evaluated each time the quadratic model is changed. On the other hand a globally convergent modified Newton-Raphson's method (GCMNR) is defined to be one in which  $H_c$  is evaluated only at the beginning of each load step or at the beginning of every few load steps.

The homotopy algorithm, as expected, experiences no difficulty whatsoever in predicting the response for the clamped beam of Fig. 1. In fact, since the response curve has no turning points it is an easy matter to construct a version of the algorithm that exploits the sparsity and symmetry of the Jacobian and also permits the solution of Eq. (23) by a standard  $LDL^T$  decomposition scheme. To evaluate the homotopy method in relation to GCNM and GCMNR methods it is necessary that all three methods be used in conjunction with the same load incrementation scheme. Since the homotopy method generates a large number of points along the response curve a load step of 20 lb. was used for this evaluation. Table 1 summarizes the efficiency evaluation of the different algorithms for this centrally loaded clamped beam.

A globally convergent quasi-Newton method performs a variety of checks before an iterate  $x_k$  is accepted. Many of these checks will be redundant if the load steps are small; that is to say, such checks will be redundant for those cases for which SNM and MNR work well. Hence, it is not at all surprising that in Table 1 both GCNM and GCMNR are not as cost-effective when the load steps are small. But it is because these methods are robust that they yield successful convergence for extremely large

load steps. This is the price that a robust method always must pay. In fact, the extremely high cost paid by the homotopy method is a direct consequence of the fact that the method is robust and globally convergent and hence fails to take advantage of special features in some special cases. Note that on the Cyber 74 the CPU time required by GCNM to compute the response of the 29 degree of freedom beam model for a total of 5 load steps of 400 lb. each was only 5.29 secs. The accuracy requirement on each of these load steps was  $\| \nabla f \|_2 < 10^{-10}$ . Further improvements in CPU time may be possible by resorting to updated Hessian approximations provided, for instance, by Toint's sparse updates [9] which are suitably coerced to yield positive definite Hessians. The effectiveness of this option is investigated in reference [15].

### Snap-Through of a Shallow Arch

The particular case of the shallow arch shown in Fig. 3 involves a single concentrated load at its crown. For such a case the entire response curve of the arch consisting of stable and unstable branches can be obtained by resorting to displacement incrementation [16]. Such a technique however has its obvious limitations and, in general, recourse must be made to techniques like the homotopy method to be able to track response curves involving turning points.

It was shown in Reference [17] that the BFGS algorithm along with appropriate load 'incrementation' can locate all points along the stable branches. This is the direct result of the use of positive definite inverse Hessian approximations in the BFGS algorithm. The globally convergent quasi-Newton algorithm GCMNR utilizing positive definite Hessians at the beginning of each load step has a performance identical to the BFGS algorithm for this shallow arch problem. The GCNM algorithm exhibits even a better performance if care is taken to coerce the Hessian within the load step within which snapping occurs to be positive definite. The double dogleg strategy then permits the GCNM method to converge to the distant stable equilibrium configuration. The same coercion technique, however, does not work if the strategy of taking the full Newton step is maintained as in the case of the SNM and MNR methods.

The CPU time on the Cyber 74 for the GCNM, GCMNR, and BFGS methods with 25 load steps of 400 lb. each were 16.75, 18.41 and 18.49 seconds respectively. To track the entire response curve the homotopy method required approximately 150 seconds. There is reason to believe that on larger scale problems both GCNM and GCMNR will be more cost-effective than the BFGS method not to speak of the reduced storage requirements of the globally convergent quasi-Newton methods.

The homotopy method is ideally suited for such a problem since it generates the entire response curve with no difficulty. However, GCNM, GCMNR and homotopy may all be used to determine the peak load of the arch which was estimated by GCNM at 3039.48 lb. and at 3039.78 lb. by the homotopy method [18]. If the objective is just to locate the peak loads, or for that matter the two limit points, both GCNM and GCMNR would be far superior to the homotopy method in terms of computational efficiency. The CPU time on the Cyber 74 for the GCNM, GCMNR and the homotopy methods were 22.41, 24.43, and 68.62 seconds respectively. Both GCNM and GCMNR used an initial load step of 400 lb. If even larger steps are attempted, the CPU time can be further reduced. For instance, GCNM with initial load steps of 800 lb. located the limit point to the same accuracy within 15.70 seconds of CPU time. The location of the limit or the bifurcation point in the case of the GCNM and GCMNR methods is an iterative process that involves the identification of the loss of positiveness of the

diagonal elements of the  $LDL^T$  decomposition. Once loss of positive definiteness of the Hessian is detected, the current load step is reduced by a factor of 4 and the analysis continued from the last stable equilibrium point. The homotopy method locates limit points by the root finding technique described earlier. The rather high CPU time requirements of the homotopy method are the result of its dependence on extremely accurate Jacobians. For instance both GCNM and GCMNR predict the limit point to an accuracy far in excess of that required for most engineering purposes using Hessians calculated with the forward differencing scheme of the PT strategy [20]. The homotopy method requires Jacobians evaluated using the rather costly central differencing scheme of the PT strategy. Exact Hessians or Jacobians would be preferable. With this in mind, a final example of the shallow reticulated dome of Fig. 4 will be discussed next.

### Shallow Reticulated Dome

Using the exact Hessian derived on the basis of the strain definition

$$\epsilon = \frac{L - L_0}{L_0} \quad (26)$$

with  $L_0$  and  $L$  being the undeformed and deformed lengths, respectively, of the three dimensional rod elements modeling the shallow dome of Fig. 4, its limit load is computed using the GCNM and the homotopy method. Because of symmetry (in fact, axisymmetry could have been exploited) only half the dome was modeled resulting in a total of 11 degrees of freedom. Since exact Hessians are used both methods predicted the same peak load of 233.282 lb.; an initial load step of 100 lb. GCNM required 5.78 seconds of CPU time, while the homotopy method required approximately 11.66 seconds on Cyber 74.

### REFERENCES

1. Dennis, J. E. and Schnabel, R., "Quasi-Newton Methods for Unconstrained Non-linear Problems," Short Course on Modern Computational Techniques for Nonlinear Unconstrained Optimization, 1979, Madison, Wisconsin.
2. Felippa, C. A., "Procedures for Computer Analysis of Large Nonlinear Structural Systems," Int. Symp. Large Engrg. Systems, Winnipeg, 1976, Large Engineering Systems, Ed. A. Wexler, Pergamon, Oxford, 1977.
3. Riks, E., "An Incremental Approach to the Solution of Snapping and Buckling Problems," Int. J. Solids Structures, Vol. 15, 1979, pp. 529-551.
4. Crisfield, M. A., "Incremental/Iterative Solution Procedures for Nonlinear Structural Analysis," Int. Conf. Num. Meths. Nonlinear Probls., Swansea, 1980.
5. Padovan, J., "Self-Adaptive Predictor-Corrector Algorithm for Static Nonlinear Structural Analysis," NASA CR-165410, April 1981.
6. Powell, M. J. D., "A New Algorithm for Unconstrained Optimization," Nonlinear Programming, Ed. J. Rosen, O. Mangasarian, and K. Ritter, Academic Press, New York, 1970, pp. 31-66.
7. Gay, D., "Computing Optimal Locally Constrained Steps," University of Wisconsin Report No. MRC 2013, 1980.



8. Dennis, J. E., and Mei, H. H. W., "An Unconstrained Optimization Algorithm Which Uses Function and Gradient Values," Comp. Sci. Tech., Cornell Univ., Report No. R 75-246, 1975.
9. Toint, Ph. L., "On Sparse and Symmetric Matrix Updating Subject to a Linear Equation," Mathematical Computation, Vol. 31, No. 40, 1977, pp. 954-961.
10. Watson, L. T., and Fenner, D., "Chow-Yorke Algorithm for Fixed Points or Zeros of  $C^2$  Maps", ACM Trans. Math. Software, Vol. 6, 1980, pp. 252-260.
11. Watson, L. T., "Fixed Points of  $C^2$  Maps," J. Comp. Appl. Math., Vol. 5, 1979, pp. 131-140.
12. Businger, P., and Golub, G. H., "Linear Least Squares Solutions by Householder Transformations," Numer. Math., Vol. 7, 1965, pp. 269-276.
13. Watson, L. T., "A Globally Convergent Algorithm for Computing Fixed Points of  $C^2$  Maps," Appl. Math. Comput., Vol. 5, 1979, pp. 297-311.
14. Shampine, L. F., and Gordon, M. K., Computer Solution of Ordinary Differential Equations: The Initial Value Problem, W. H. Freeman, San Francisco, 1975.
15. Vanden Brink, D. J., Kamat, M. P. and Watson, L. T., "Nonlinear Finite Element Analysis Using Globally Convergent Quasi-Newton Methods", VPI & SU Report, 1982.
16. Kamat, M. P., Watson, L. T., and Vanden Brink, D. J., "An Assessment of Quasi-Newton Sparse Update Techniques for Nonlinear Structural Analysis", J. Comp. Meths. Appl. Mech. Engrg., Vol. 26, 1981, pp. 363-375.
17. Kamat, M. P. and Hayduk, R. J., "Energy Minimization Versus Pseudo Force Technique for Nonlinear Structural Analysis", Computers and Structures, Vol. 10, 1980, pp. 403-409.
18. Kamat, M. P., "Nonlinear Transient Analysis by Energy Minimization - Theoretical Basis for the ACTION Computer Code", NASA CR-3287, July 1980.
19. Powell, M. J. D., and Toint, Ph. L., "On the Estimation of Sparse Jacobian Matrices", J. Inst. Math. Applic., Vol. 13, 1974, pp. 117-119.

Table 1. Evaluation of Algorithms - Clamped Beam, Fig. 1

Method	CYBER 74 CPU Seconds for a total load of 2 kips				
	Load Step Size				
	20 lb.	40 lb.	100 lb.	200 lb.	400 lb.
SNM	35.78	22.34	diverged	diverged	diverged
GCNM	40.85	27.68	15.23	8.28	5.29
GCMNR	52.16	-	-	17.85	-
Homotopy ( $LDL^T$ )	93.47	-	-	-	-
Homotopy (Householder Reflects.)	117.11	-	-	-	-

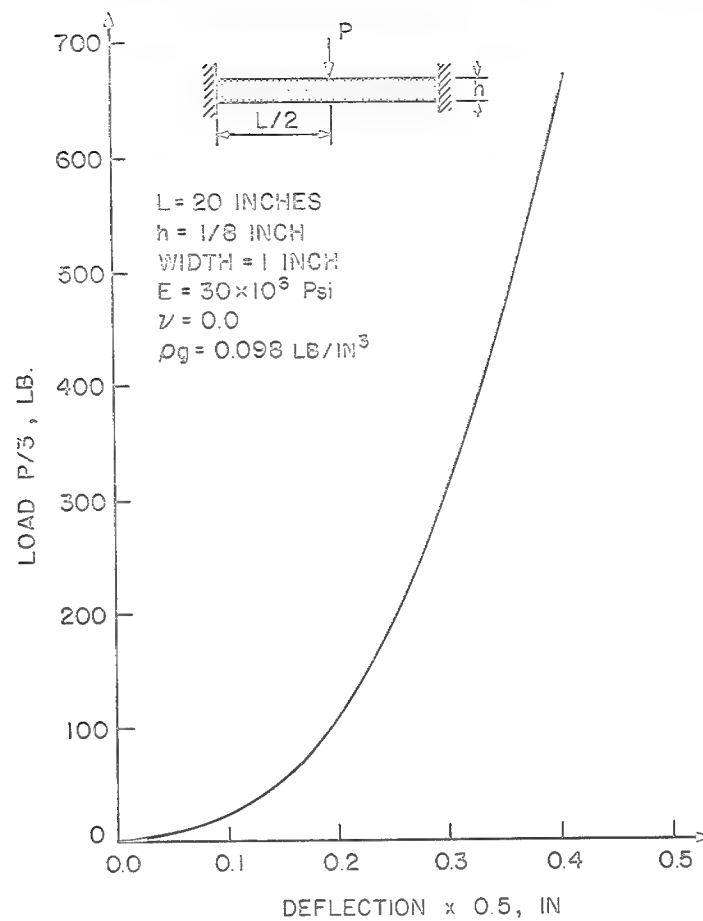


Figure 1.- Centrally loaded clamped beam.

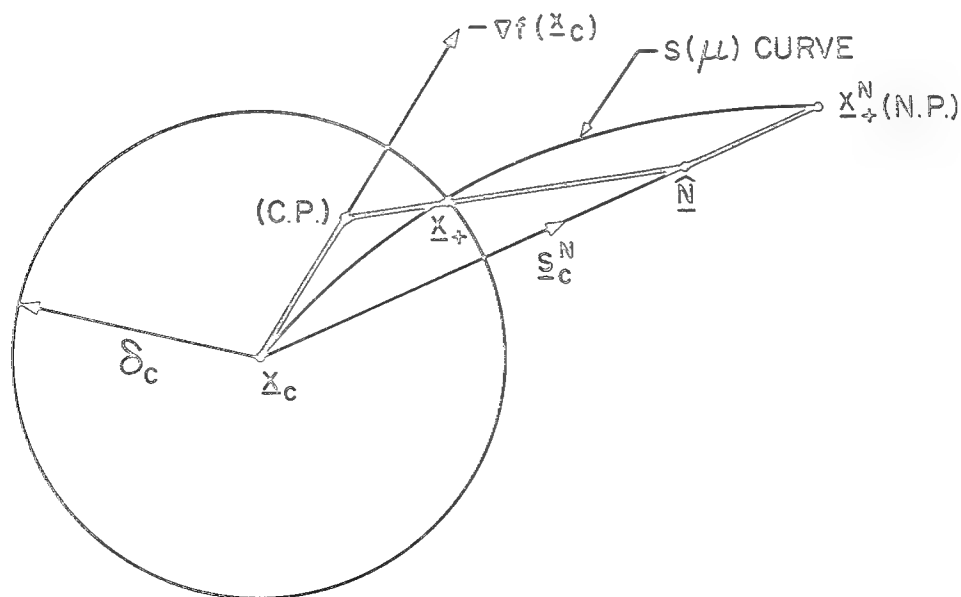


Figure 2.- The double dogleg curve,  $\underline{x}_c \rightarrow \text{C.P.} \rightarrow \hat{N} \rightarrow \underline{x}_+^N$ .

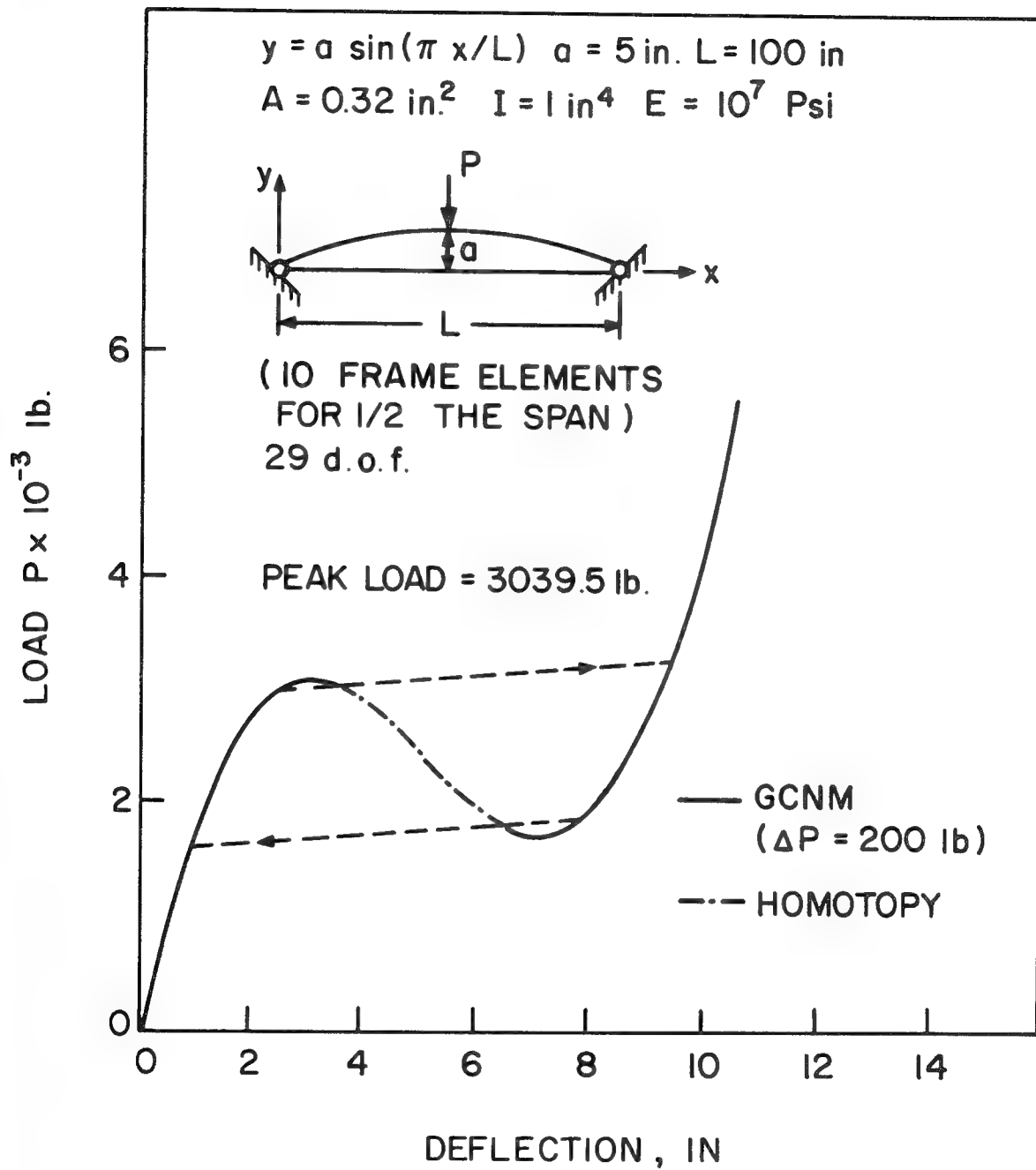
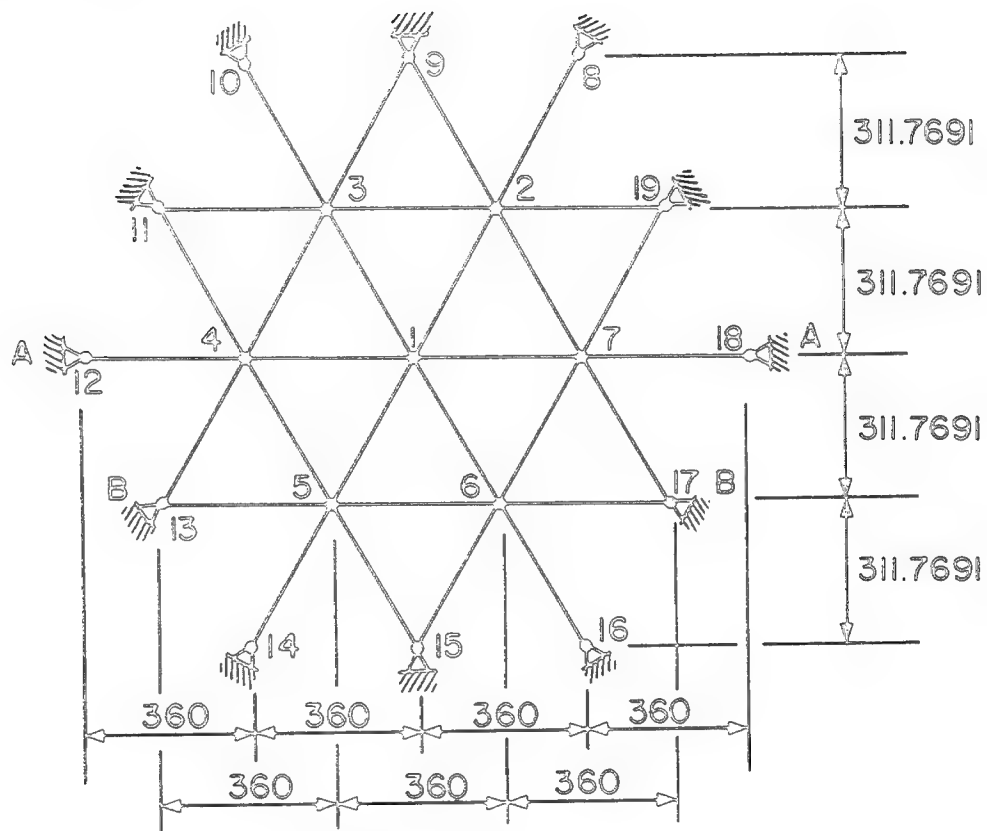


Figure 3.- Snap-through of a shallow arch.

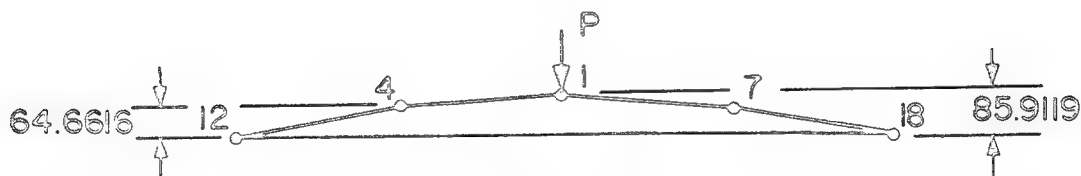
$$E = 10^7 \text{ Psi}$$

$$A_j = 0.17823 \text{ in}^2$$

$$P_{cr} = 233.28 \text{ lb.}$$



a. Plan view.



b. Section A-A.



c. Section B-B.

Figure 4.- Shallow reticulated dome under a concentrated load at the crown. (All dimensions are in inches.)

# OPERATOR SPLIT METHODS IN THE NUMERICAL SOLUTION OF THE FINITE DEFORMATION ELASTOPLASTIC DYNAMIC PROBLEM\*

*Peter M. Pinsky, Miguel Ortiz and Robert L. Taylor*

Division of Structural Engineering and Structural Mechanics  
Department of Civil Engineering  
University of California, Berkeley

## ABSTRACT

The spatial formulation of the elastoplastic dynamic problem for finite deformations is considered. A thermodynamic argument leads to an additive decomposition of the spatial rate of deformation tensor and allows an operator split of the evolutionary equations of the problem into "elastic" and "plastic" parts. This operator split is taken as the basis for the definition of a global product algorithm. In the context of finite element discretization the product algorithm entails, for every time step, the solution of a nonlinear elastodynamic problem followed by the application of plastic algorithms that operate on the stresses and internal variables at the integration points and bring in the plastic constitutive equations. Suitable plastic algorithms are discussed for the cases of perfect and hardening plasticity and viscoplasticity. The proposed formalism does not depend on any notion of smoothness of the yield surface and is applicable to arbitrary convex elastic regions, with or without corners. The stability properties of the global product algorithm are shown to be identical to those of the algorithm used for the integration of the nonlinear elastodynamic problem. Numerical examples illustrate the accuracy of the method.

## 1. Introduction

A variety of techniques have been proposed for the numerical treatment of the finite deformation elastoplastic boundary value problem [4,7,13,19]. Those based on some notion of an elastoplastic modulus tensor, such as the tangent modulus tensor method, suffer from various shortcomings. For instance, the methods are ill-suited for dealing with corners in the yield surface. Furthermore, the consistency condition of plasticity which requires that the stress trajectory be confined to the elastic domain is difficult to enforce exactly. Frequently, projection techniques have been introduced to restore consistency. In addition, these methods require elaborate schemes for making the transition from the elastic into the plastic regimes that frequently involve discarding or truncating time steps.

The limitations associated with the above methods have motivated the search for alternative methods of solution. One such alternative method makes use of the concept of a "return mapping" algorithm and was originally proposed by Mendelson [32] for the case of infinitesimal deformations. This technique consists of solving for every time step an incremental linear elastic problem followed by the application of a return mapping algorithm to the stresses to restore consistency. Clearly, this procedure automatically guarantees the satisfaction of the consistency

---

\* This work was supported by grants from the Lawrence Livermore National Laboratory and General Motors Research Laboratories.

condition. Moreover, the method results in unconditional stability [33] and reasonable accuracy [29,30,31].

In order to be convergent, numerical solution schemes have to satisfy the requirements of consistency and numerical stability. A formal study of the consistency and numerical stability properties of the global solution schemes arising from the use of return mapping algorithms is missing in the literature. At best, the existing work has only considered partial aspects of the global numerical solution scheme such as the integration of the constitutive equations [29,30,31]. It is shown in this paper how the operator split formalism provides a suitable framework in which these issues can be adequately studied.

The operator split method, briefly discussed in Section 2, has recently been applied within the context of computational mechanics and shows considerable potential as a tool for the analysis of certain classes of linear and nonlinear problems [1,2]. For instance, this technique has been recently used in connection with the heat conduction problem [2] and the structural dynamics problem [1].

In Section 3 a spatial formulation of the elastoplastic dynamic problem for finite deformations is developed. Central to the applicability of the operator split method to the elastoplastic dynamic problem is the additive decomposition of the spatial rate of deformation tensor into "elastic" and "plastic" parts. A brief discussion presenting a thermodynamic basis for such a decomposition is also presented in Section 3.

In Section 4 an operator split of the field equations into "elastic" and "plastic" parts is introduced. Product formula techniques are then applied to this additive decomposition, resulting in a step-by-step integration procedure in which a nonlinear elastodynamic problem is first solved, followed by the application of algorithms that bring in the plastic part of the field equations. The nonlinear elastodynamic problem is solved by means of a Newton-Raphson procedure based on consistent linearization of a weak form of the boundary value problem for momentum balance. The elastic rate constitutive equations are numerically integrated using an unconditionally stable and incrementally objective algorithm.

For the rate-independent case, it is shown in Section 4 that the algorithms for the integration of the plastic part of the field equations are return mapping algorithms in which the stresses corresponding to the elastic solution are projected into the elastic region by means of general return mappings. For the viscoplastic case, the plastic algorithms are shown to represent a relaxation process of the stresses towards the elastic region. In this context, the consistency and numerical stability of the resulting global solution schemes is demonstrated. The numerical stability properties of the elastoplastic product algorithm are shown to be identical to those of the algorithm employed in the integration of the elastic part of the equations of motion. Also, the return mapping technique is extended to the dynamic, viscoplastic and hardening cases.

The proposed formalism does not depend on any notion of smoothness of the yield hypersurface and is applicable to arbitrary convex elastic regions with or without corners. Under appropriate conditions, it is shown that the viscoplastic solution approximates the rate independent one in the limit of small viscosities. Finally, the accuracy of the method is demonstrated by means of numerical examples.

## 2. General Product Algorithms Based on Operator Splits of Equations of Evolution

In the present section, a collection of results is presented regarding operator split methods and product formula algorithms for general nonlinear equations of evolution. These results illustrate the point that product formulas can be advantageously applied to any set of equations of evolution where the evolutionary operator has an additive decomposition (operator split) into several, hopefully simpler, component operators. The basic idea underlying product formulas is that of treating each one of the component operators independently. In a typical integration process, one applies an algorithm to the solution vector that is consistent with the first component operator, the result of which is then operated upon with an algorithm which is

consistent with the second component operator, and so on.

Often in the numerical treatment of engineering problems one is led to consider equations of evolution of the following general form

$$\mathbf{A} \dot{\mathbf{x}} + \mathbf{B}(\mathbf{x}) = \mathbf{f} ; \quad \mathbf{x}(0) = \mathbf{x}_0 \quad (1)$$

a particular case of which is the unforced equation

$$\mathbf{A} \dot{\mathbf{x}} + \mathbf{B}(\mathbf{x}) = 0 ; \quad \mathbf{x}(0) = \mathbf{x}_0 \quad (2)$$

In the above,  $\mathbf{x}$  is an  $s$ -dimensional vector,  $\mathbf{A}$  is a positive definite symmetric matrix and  $\mathbf{B}$  is a nonlinear function from  $R^s$  into  $R^s$ .

It is useful for the subsequent discussion to endow  $R^s$  with the "energy" inner product  $\langle \mathbf{x}, \mathbf{y} \rangle = \mathbf{x}^T \mathbf{A} \mathbf{y}$  for every  $\mathbf{x}, \mathbf{y} \in R^s$ , having an associated norm  $\|\mathbf{x}\|^2 = \langle \mathbf{x}, \mathbf{x} \rangle$ .

In this context, an unconditionally stable algorithm for equation (2) is a one-parameter family of (nonlinear) functions  $\mathbf{F}(h) : R^s \rightarrow R^s$ ,  $h > 0$ , satisfying

1) Consistency:

$$\lim_{h \rightarrow 0^+} \mathbf{A} \frac{\mathbf{F}(h)\mathbf{x} - \mathbf{x}}{h} = \mathbf{B}(\mathbf{x}) \quad \text{for every } \mathbf{x} \in R^s \quad (3)$$

2) Unconditional stability:

$$\|\mathbf{F}(h)\mathbf{x} - \mathbf{F}(h)\mathbf{y}\| \leq \|\mathbf{x} - \mathbf{y}\| \quad \text{for every } \mathbf{x}, \mathbf{y} \in R^s, \quad h > 0. \quad (4)$$

In the linear case, the mapping  $\mathbf{F}(h)$  is linear in  $\mathbf{x}$  and the stability condition (4) reduces to the simpler form  $\|\mathbf{F}(h)\mathbf{x}\| \leq \|\mathbf{x}\|$  for every  $\mathbf{x} \in R^s$ . This in turn implies that the norm  $\|\mathbf{F}(h)\| \leq 1$ . Recalling the inequality  $\rho(\mathbf{F}(h)) \leq \|\mathbf{F}(h)\|$ , relating the spectral radius  $\rho(\mathbf{F}(h)) \equiv \inf_n \|\mathbf{F}(h)^n\|^{1/n}$  to the norm of  $\mathbf{F}(h)$ , it may be seen that the stability condition (4) is in general more stringent than the usual concept of stability that requires  $\rho(\mathbf{F}(h)) \leq 1$ . If  $\mathbf{F}(h)$  is a stable algorithm for (2) in the sense of (3) and (4) then convergence is guaranteed under mild conditions on  $\mathbf{B}$  [3].

In a variety of problems in mechanics the evolutionary operator  $\mathbf{B}$  and the forcing term  $\mathbf{f}$  admit an additive decomposition

$$\mathbf{B} = \sum_{i=1}^N \mathbf{B}_i ; \quad \mathbf{f} = \sum_{i=1}^N \mathbf{f}_i. \quad (5)$$

We are concerned here with the problem of constructing a class of computationally efficient algorithms that exploit the additive form of  $\mathbf{B}$  and  $\mathbf{f}$ .

Let  $\mathbf{F}_i(h)$ ,  $i = 1, 2, \dots, N$  denote stable algorithms consistent with  $\mathbf{A}$  and  $\mathbf{B}_i$ . The corresponding global product algorithm then takes the form

$$\mathbf{F}(h) = \mathbf{F}_N(h) \mathbf{F}_{N-1}(h) \cdots \mathbf{F}_1(h) \equiv \prod_{i=1}^N \mathbf{F}_i(h) \quad (6)$$

In other words, the algorithm  $\mathbf{F}(h)$  amounts to applying the individual algorithms  $\mathbf{F}_i(h)$  consecutively to the solution vector, taking the result from each one of these applications as the initial conditions for the next algorithm. The global algorithm is complete for a given time step when all the individual algorithms have been applied.

It is shown in [1] that if all the individual algorithms  $\mathbf{F}_i(h)$  are consistent with  $\mathbf{A}$  and  $\mathbf{B}_i$  in the sense of (3), then the global product algorithm  $\mathbf{F}(h)$  defined by (6) is consistent with  $\mathbf{A}$  and  $\mathbf{B}$ . It is further shown in [1] that if all the individual algorithms  $\mathbf{F}_i(h)$  are unconditionally stable in the sense of (4), then the global product algorithm  $\mathbf{F}(h)$  is also unconditionally stable. In other words the norm stability of the individual algorithms, in the sense of (4), is preserved by the product formula (6). It is interesting to note, on the other hand, that no general statements can be made about the stability of the product formula in the sense of the spectral ratio,

given that, unlike the norm, this quantity is not well-behaved with respect to matrix multiplications. A general discussion of these and other related issues can be found in [1]. Some of these results have also been discussed in [2] for the particular case of linear equations of evolution and the trapezoidal rule.

In Section 4, global product algorithms will be employed in connection with an additive decomposition of the evolutionary operator governing the finite deformation elastoplastic dynamic problem.

### 3. Field Equations for Finite Deformation Elastoplasticity.

#### 3.1. Preliminaries

In this section, definitions of tensors required for subsequent discussions are stated and connections among certain of these are established. For a complete account of the continuum basis underlying constitutive theory the interested reader is referred to [22,23].

A motion of a deformable body in the ambient space  $R^N$ , relative to a reference configuration  $B$ , is given by a time dependent mapping  $\phi_t(\mathbf{X}): B \rightarrow R^N$ ,  $t > 0$ . Here,  $\mathbf{X}$  denotes a set of material coordinates defined on the reference configuration.

The material velocity of the motion  $\phi_t$  is defined as a vector field  $\mathbf{V}$  over the reference configuration, such that  $\mathbf{V} = \frac{d}{dt}\phi_t$ . The spatial velocity field  $\mathbf{v}$  is defined by  $\mathbf{v} = \mathbf{V} \circ \phi_t^{-1}$ . Note that the spatial velocity field  $\mathbf{v}(\mathbf{x}, t)$  is dependent on a set of spatial coordinates denoted  $\mathbf{x}$ .

The deformation gradient is defined by  $\mathbf{F} = \frac{\partial \phi}{\partial \mathbf{X}}$  with components,  $F^a_A = \frac{\partial \phi^a}{\partial X^A}$ . From  $\mathbf{F}$  one can obtain the Jacobian of the motion  $J = \det \mathbf{F}$  and the right Cauchy-Green deformation tensor  $\mathbf{C}$  which is related to the deformation gradient by  $\mathbf{C} = \mathbf{F}^T \cdot \mathbf{F}$ .

The spatial velocity gradient tensor  $\mathbf{l}$  is given by  $\mathbf{l} = \nabla \mathbf{v}$ , where  $\nabla$  denotes the gradient with respect to the spatial coordinates  $\mathbf{x}$ . The symmetric part of  $\mathbf{l}$ ,  $\mathbf{d} \equiv \nabla^S \mathbf{v}$  is the spatial rate of deformation tensor, and the skewsymmetric part  $\boldsymbol{\omega} \equiv \nabla^A \mathbf{v}$  is the spin rate or vorticity tensor.

If  $\boldsymbol{\gamma}$  is a tensor field defined on the deformed configuration  $\phi_t(B)$ , the pull back of  $\boldsymbol{\gamma}$  through the motion  $\phi_t$  defines a tensor field  $\boldsymbol{\Gamma}$  on  $B$  denoted by  $\boldsymbol{\Gamma} = \phi_t^*(\boldsymbol{\gamma})$ . For example, in the case of a second order contravariant tensor the pull back operation takes the form

$$\Gamma^{AB} = (F^{-1})^A_a (F^{-1})^B_b (\gamma^{ab} \circ \phi_t).$$

This definition may be readily generalized to spatial tensor fields of any order.

Likewise, if  $\boldsymbol{\Gamma}$  is a material tensor field defined on  $B$ , the push forward of  $\boldsymbol{\Gamma}$  through the motion  $\phi_t$  defines a spatial tensor field  $\boldsymbol{\gamma}$  on  $\phi_t(B)$  denoted by  $\boldsymbol{\gamma} = \phi_{t*}(\boldsymbol{\Gamma})$ . In this case, for the example used above, the push forward operation takes the form

$$\gamma^a = F^a_A (\Gamma^A \circ \phi_t^{-1}).$$

A related concept associated with the push forward of material rates of material tensors is that of the Lie derivative of a spatial tensor with respect to the spatial velocity field. The Lie derivative entails pulling back the spatial tensor to the reference configuration, taking the material time derivative of the resulting material tensor and pushing forward the result into the current configuration. Formally, for a spatial tensor  $\boldsymbol{\gamma}$ ,

$$L_v(\boldsymbol{\gamma}) \equiv \phi_{t*} \left( \frac{d}{dt} \phi_t^*(\boldsymbol{\gamma}) \right) \quad (7)$$

This notation allows for a compact expression of many relations in continuum mechanics. For example, the Cauchy stress tensor  $\boldsymbol{\sigma}$  defined on the current configuration and the second Piola-Kirchhoff stress tensor  $\mathbf{S}$  associated with the reference configuration are related by



$$\mathbf{S} = J \phi_{t*}^*(\boldsymbol{\sigma}) \quad \text{or} \quad \boldsymbol{\sigma} = \phi_{t*}(J^{-1}\mathbf{S})$$

These relations, involving  $J$ , are called Piola transformations.

The forward Piola transformation of the material time derivative of  $\mathbf{S}$ , denoted  $\overset{\circ}{\boldsymbol{\sigma}}$ , is

$$\overset{\circ}{\boldsymbol{\sigma}} = \phi_{t*}(J^{-1}\dot{\mathbf{S}}), \quad (8)$$

the so-called Truesdell rate of Cauchy stress. For contravariant components (8) has the form

$$\overset{\circ}{\sigma} = \dot{\sigma} - \mathbf{l} \cdot \boldsymbol{\sigma} - \boldsymbol{\sigma} \cdot \mathbf{l}^T + \boldsymbol{\sigma} \operatorname{tr}(\mathbf{d})$$

where  $\dot{\boldsymbol{\sigma}}$  denotes the material time derivative of  $\boldsymbol{\sigma}$  given by  $\dot{\boldsymbol{\sigma}} = \frac{\partial \boldsymbol{\sigma}}{\partial t} + \nabla \boldsymbol{\sigma} \cdot \mathbf{v}$ . Alternatively, in terms of the Lie derivative, (8) can be written

$$\overset{\circ}{\boldsymbol{\sigma}} = J^{-1} \phi_{t*} \left( \frac{d}{dt} \phi_{t*}^*(J\boldsymbol{\sigma}) \right) = J^{-1} L_v(\boldsymbol{\tau}) \quad (9)$$

where  $\boldsymbol{\tau} \equiv (J \circ \phi_t^{-1}) \boldsymbol{\sigma}$  is the Kirchhoff stress tensor. These relations will prove to be useful in subsequent sections where their relevance is discussed in detail.

It is noted that the Truesdell rate is objective [18,22]. The principle of objectivity requires that intrinsic physical properties of a body be independent of the body's location or orientation in space. This principle is embodied in constitutive theory by requiring that constitutive equations contain only objective tensor fields. Consequently, the Truesdell rate of Cauchy stress may be considered as a candidate for use in spatial rate constitutive equations.

Many other objective rates have been proposed within the context of constitutive theory. A frequent choice is the Jaumann, or co-rotational rate of Kirchhoff stress,

$$\overset{\nabla}{\boldsymbol{\tau}} = \dot{\boldsymbol{\tau}} - \boldsymbol{\omega} \cdot \boldsymbol{\tau} + \boldsymbol{\tau} \cdot \boldsymbol{\omega}$$

The significance of the Jaumann rate as it relates to constitutive theory and its connection with the Truesdell rate has been considered in [18,28].

The local form of linear momentum balance together with traction and kinematic boundary conditions can be expressed as

$$\begin{aligned} \rho \dot{\mathbf{v}} &= \nabla \cdot \boldsymbol{\sigma} + \rho \mathbf{b} & \mathbf{x} \in \phi_t(B) \\ \boldsymbol{\sigma} \cdot \mathbf{n} &= \bar{\mathbf{t}} & \mathbf{x} \in \partial_\sigma \phi_t(B) \\ \boldsymbol{\phi} &= \bar{\boldsymbol{\phi}} & \mathbf{x} \in \partial_u \phi_t(B) \end{aligned} \quad (10)$$

where  $\rho$  is the mass density in  $\phi_t(B)$ ,  $\mathbf{b}$  is a spatial body force field, and  $\bar{\mathbf{t}}$  and  $\bar{\boldsymbol{\phi}}$  are the prescribed tractions and motion over the traction and kinematic boundaries  $\partial_\sigma \phi_t(B)$  and  $\partial_u \phi_t(B)$ , respectively.

In order to have a complete set of equations suitable constitutive equations need to be specified. The form of these equations for a limited class of elastoplastic materials is the subject of the next section.

### 3.2. Rate Constitutive Equations for Finite Deformation Elastoplasticity

In analysis of finite deformation problems the use of constitutive equations in rate form is often required. In a spatial setting, these equations express a relationship between some objective rate of a spatial stress tensor, such as the Cauchy or Kirchhoff stress tensor, and the rate of deformation.

Rate constitutive relations can be alternatively formulated in a material or a spatial setting. The former case involves rates of material tensors which are always objective. In a spatial formulation, however, material rates of objective tensors are not objective and so-called objective

stress rates, such as the Truesdell or Jaumann rates, must be introduced. This has the effect of introducing additional complexity in the development of integration algorithms for rate constitutive equations and has motivated recent research in the area [19,20,28].

The correct choice of spatial rate constitutive equations has been the subject of considerable conjecture [21,24,25,26,27], inasmuch as the principle of objectivity alone does not uniquely determine the choice of objective stress rate. It is noted, however, that the material and spatial formulations are equivalent expressions of the same physical principles and are therefore uniquely related to each other. This assertion rests on the fact that the mathematical formulation of the principles of mechanics has to be invariant with respect to the choice of reference configuration [22]. It has been shown in [28] that when this additional principle is invoked, indeterminacy in the choice of objective stress rate is removed.

The following discussion is concerned with the problem of deriving adequate spatial rate constitutive equations. The approach taken is based on a thermodynamic formulation of constitutive equations in a material setting, the spatial representation of which is then consistently derived.

The existence of a complementary free energy potential per unit mass of  $B$ , denoted  $\chi(S, Q)$ , is assumed. Here,  $S$  is the second Piola-Kirchhoff stress tensor and  $Q$  denotes a set of internal variables defined on the reference configuration  $B$ . The justification for such an assumption is discussed in [9].

From the Clausius-Duhem inequality [9,10] it can be shown that the complementary free energy is a potential for the right Cauchy-Green deformation tensor  $C$ , i.e.,

$$C = 2\rho_o \frac{\partial \chi}{\partial S} \quad (11)$$

where  $\rho_o$  denotes the reference mass density. A rate form of (11) is obtained by taking the material time derivative, resulting in

$$\dot{C} = M:\dot{S} + N \cdot \dot{Q} \quad (12)$$

where  $M$  is the material elasticity tensor, defined by  $M = 2\rho_o \frac{\partial^2 \chi}{\partial S^2}$  and  $N$  is an inelastic compliance tensor defined by  $N = 2\rho_o \frac{\partial^2 \chi}{\partial Q \partial S}$ . Since material time derivatives of material tensors are objective, constitutive equation (12) is also objective.

A spatial form of constitutive eq. (12) can be obtained as follows. Noting that  $\dot{C} = 2\phi_{,i}^*(\dot{d})$  and eq. (8), the forward Piola transformation of eq. (12) reads

$$\dot{d} = m:\overset{\circ}{\sigma} + n \cdot \overset{\circ}{q} \quad (13)$$

where  $m = \frac{1}{2}J\phi_{,i,*}(M)$  is the spatial elasticity tensor,  $n = \frac{1}{2}J\phi_{,i,*}(N)$  is a spatial inelastic compliance tensor,  $q = J\phi_{,i,*}(Q)$  are the spatial internal variables and  $\overset{\circ}{q} = \phi_{,i}^*(J^{-1}\dot{Q})$  is the Truesdell rate of  $q$ .

Equation (13) has the interpretation that the total deformation rate  $\dot{d}$  has an additive decomposition into an "elastic" part  $\dot{d}^e = m:\overset{\circ}{\sigma}$  and an "inelastic" or "plastic" part  $\dot{d}^p = n \cdot \overset{\circ}{q}$ , i.e.,

$$\dot{d} = \dot{d}^e + \dot{d}^p \quad (14)$$

This decomposition has been obtained independently of any kinematic considerations. Other theories of plasticity [11,12,14] have been based on different kinematic assumptions. By appropriate definitions of the kinematic variables these theories can be brought into correspondence with eq. (14). Eq. (14) has the alternative form

$$\overset{\circ}{\sigma} = a:(\dot{d} - \dot{d}^p) \quad (15)$$

where  $\mathbf{a} = \mathbf{m}^{-1}$  is the spatial elastic modulus tensor. Further details regarding the above discussion can be found in [18].

In order to have a complete set of constitutive equations one has to supplement eq. (15) with some constitutive relations for  $\mathbf{d}^p$  and  $\mathbf{q}$ . For the time being, it will suffice to assume that  $\mathbf{d}^p$  can be expressed as a function of the stresses and the spatial internal variables  $\mathbf{q}$ , i.e.,

$$\mathbf{d}^p = \mathbf{T}(\boldsymbol{\sigma}, \mathbf{q}) \quad (16)$$

The internal variables  $\mathbf{q}$  may for example represent the yield stress for an isotropic hardening model or the translation of the elastic domain for a kinematic hardening model. Eq. (16) is general enough to accommodate perfect and hardening viscoplasticity. Specific examples of such constitutive relations that are widely used in practice are given in Section 4.2. Also, for the purpose of the discussion on plastic algorithms that follows in Section 4.2, it proves convenient to consider inviscid plasticity as a limiting case of viscoplasticity, as the viscosity tends to 0. In this indirect way, eq. (16) also encompasses the inviscid plasticity case. It is finally assumed that the evolution of the internal variables is governed by kinetic equations of the form

$$\overset{\circ}{\mathbf{q}} = \mathbf{f}(\boldsymbol{\sigma}, \mathbf{q}) \quad (17)$$

Note that the use of the Truesdell rate in the left hand side of (17) makes these equations objective and consistent with a set of material kinetic equations [18].

The spatial rate form of the constitutive equation (15) expresses the linear dependence of the Truesdell rate of Cauchy stress  $\boldsymbol{\sigma}$  on the elastic part of the spatial deformation rate tensor  $\mathbf{d}^e$  through the spatial elasticity tensor  $\mathbf{a}$ . It can be shown by use of a Legendre transformation [18] that  $\mathbf{a}$  is a function only of the deformation and the internal variables. However, eq. (15) is expressible in terms of other stress rates if the difference between these rates and the Truesdell rate of Cauchy stress is absorbed in the definition of the elasticity tensor. In this case, the elasticity tensor will, in general, be a function of the stress tensor, the deformation and the internal variables [18].

### 3.3. Summary of Field Equations

For later reference, the field equations introduced above are summarized as follows

$$\begin{aligned} \dot{\boldsymbol{\phi}}_t &= \mathbf{v} \otimes \boldsymbol{\phi}_t & \overset{\circ}{\mathbf{q}} &= \mathbf{f}(\boldsymbol{\sigma}, \mathbf{q}) \\ \rho \dot{\mathbf{v}} &= \nabla \cdot \boldsymbol{\sigma} + \rho \mathbf{b} & \boldsymbol{\sigma} \cdot \mathbf{n} &= \bar{\mathbf{t}} \quad \mathbf{x} \in \partial_{\sigma} \boldsymbol{\phi}_t(B) \\ \overset{\circ}{\boldsymbol{\sigma}} &= \mathbf{a} : (\mathbf{d} - \mathbf{T}(\boldsymbol{\sigma}, \mathbf{q})) & \boldsymbol{\phi} &= \bar{\boldsymbol{\phi}} \quad \mathbf{x} \in \partial_u \boldsymbol{\phi}_t(B) \end{aligned} \quad (18)$$

It is demonstrated in the next section that the field eqs. (18) admit an additive decomposition into elastic and plastic parts suggesting a global solution procedure based on the product formula algorithms discussed in Section 2. The product formula algorithm applied to this decomposition results in a step-by-step integration procedure in which a nonlinear elastodynamic problem is first solved, followed by the application of algorithms that bring in the plastic part of the evolutionary equations.

### 4. The Elastoplastic Split of the Dynamic Equations of Motion and Related Product Algorithms.

The field equations (18) exhibit an additive decomposition into an elastic part

$$\begin{aligned} \dot{\boldsymbol{\phi}}_t &= \mathbf{v} \otimes \boldsymbol{\phi}_t & \overset{\circ}{\mathbf{q}} &= 0 \\ \rho \dot{\mathbf{v}} &= \nabla \cdot \boldsymbol{\sigma} + \rho \mathbf{b} & \boldsymbol{\sigma} \cdot \mathbf{n} &= \bar{\mathbf{t}} \quad \mathbf{x} \in \partial_{\sigma} \boldsymbol{\phi}_t(B) \\ \overset{\circ}{\boldsymbol{\sigma}} &= \mathbf{a} : \mathbf{d} & \boldsymbol{\phi} &= \bar{\boldsymbol{\phi}} \quad \mathbf{x} \in \partial_u \boldsymbol{\phi}_t(B) \end{aligned} \quad (19)$$

and a plastic part

$$\begin{aligned}\dot{\phi}_i &= 0 \\ \rho \dot{v} &= 0 \\ \partial \sigma / \partial t &= -a : T(\sigma, \eta) \\ \partial \tau / \partial t &= f(\sigma, \tau)\end{aligned}\quad (20)$$

This suggests the possibility of using the product formula techniques to construct efficient numerical algorithms that exploit such additive decomposition. It is noted that eqs. (19) define a finite deformation elastodynamic problem, while the second set of eqs. (20) leaves the configuration unchanged and defines a pointwise relaxation process for stresses and internal variables.

In the present context, a product algorithm relative to the elastoplastic additive decomposition of the equations of motion takes the following meaning. Consider two unconditionally stable algorithms  $F^{el}(h)$  and  $F^{pl}(h)$  consistent with the individual equations (19) and (20) according to the discussion in Section 2. Given two such algorithms, an algorithm  $F(h)$  consistent with the full equations of motion (18) can be obtained by means of the product formula

$$F(h) = F^{pl}(h) F^{el}(h) \quad (21)$$

It is recalled from Section 2 that  $F(h)$  is in fact consistent with (18) and that if the individual algorithms  $F^{el}(h)$  and  $F^{pl}(h)$  are unconditionally stable in the sense of (4) so is  $F(h)$ .

The product formula (21) simply states that a solution algorithm for the elastoplastic problem can be obtained by solving for each time step an elastic dynamic problem first, and then applying to the solution vector so obtained a plastic algorithm operating on the stresses and internal variables bringing in the effect of the plastic constitutive equations. It is interesting to note that all the boundary value aspects of the elastoplastic dynamic problem are included in the elastic eqs. (19) and are taken care of by the elastic algorithm  $F^{el}(h)$ .

In practice, the above equations are solved by means of some spatial discretization technique such as the finite element method. In this case, the plastic part of the equations of motion will correspond to a set of relaxation equations expressed at the integration points within the elements. Thus, the plastic algorithm  $F^{pl}(h)$  is applied integration point by integration point and amounts to solving eqs. (20) numerically or exactly at each one of them. In Section 4.2 several widely used plastic constitutive assumptions are considered, and the nature of the associated plastic algorithms and the resulting product formula solution schemes is re-examined for each case.

#### 4.1. Algorithm for the Elastic Dynamic Problem

This Section is concerned with the development of an algorithm  $F^{el}(h)$  for the numerical solution of the elastic dynamic boundary value problem given by eqs. (19). A weak form of this problem is expressed by

$$\int_{\phi_i(B)} [\rho (\dot{v} - b) \cdot \eta + \sigma : \nabla \eta] dv = \int_{\partial_n \phi_i(B)} \bar{t} \cdot \eta da \quad (22)$$

for all weighting functions  $\eta$  which satisfy the homogeneous boundary conditions on  $\partial_u \phi_i(B)$ . Spatial discretization is accomplished using the finite element method for which a set of global finite element interpolation functions  $N_a$ ,  $a = 1, 2, \dots, n$  is introduced. The interpolated motion and weighting functions take the form  $\phi = \phi^a N_a$  and  $\eta = \eta^a N_a$ , where the summation convention is implied and  $\phi^a$  and  $\eta^a$  denote the nodal values of  $\phi$  and  $\eta$ , respectively.

The global interpolation functions are given by the expression  $N_a = \sum_{e=1}^{N_{el}} N_a^e$  where the index  $e$  ranges over the elements and  $N_a^e$  denotes the element interpolation functions. Using the above results in (22) one obtains the following spatially discretized weak form

$$M \ddot{\phi} + P(\sigma, \tau) = F(t) \quad (23)$$

where  $\mathbf{M}$  is the mass matrix with components

$$M_{ab} = \sum_{e=1}^{Nel} \int_{\Omega^e} \rho N_a^e N_b^e d\Omega, \quad (24)$$

$\mathbf{P}(\boldsymbol{\sigma}, t)$  is the "internal force" vector with components

$$P_a = \sum_{e=1}^{Nel} \int_{\Omega^e} (\mathbf{B}_a^e)^T \cdot \boldsymbol{\sigma} d\Omega \quad (25)$$

where  $\mathbf{B}_a$  is a matrix involving spatial gradients of  $N_a$ , finally  $\mathbf{F}$  is the global force vector with components

$$F_a = \sum_{e=1}^{Nel} \left( \int_{\Omega^e} \rho \mathbf{b} N_a^e d\Omega + \int_{\partial\Omega_\sigma^e} \bar{\mathbf{t}} N_a^e d\Gamma \right). \quad (26)$$

In eqs. (24), (25) and (26)  $\Omega_e$  is a domain given by the current configuration of a finite element  $e$  such that  $\bigcup_{e=1}^{Nel} \Omega^e = \phi_t(B)$  and  $\bigcap_{e=1}^{Nel} \Omega^e = \emptyset$ .

#### 4.1.1. Temporal Integration of the Weak Form

The spatially discretized weak form (23) is integrated in time by the application of the implicit Newmark algorithm defined by

$$\mathbf{M} \cdot \dot{\mathbf{v}}_{n+1} + \mathbf{P}_{n+1}(\boldsymbol{\sigma}_{n+1}) = \mathbf{F}_{n+1} \quad (27)$$

$$\boldsymbol{\phi}_{n+1} = \boldsymbol{\phi}_n + h \mathbf{v}_n + h^2 \left[ \left( \frac{1}{2} - \beta \right) \dot{\mathbf{v}}_n + \beta \dot{\mathbf{v}}_{n+1} \right] \quad (28)$$

$$\mathbf{v}_{n+1} = \mathbf{v}_n + h \left[ (1-\gamma) \dot{\mathbf{v}}_n + \gamma \dot{\mathbf{v}}_{n+1} \right] \quad (29)$$

where subscripts  $n$  and  $n+1$  denote variables evaluated at the  $n$ th and  $n+1$ th time steps,  $h = t_{n+1} - t_n$  is the time step size and  $\beta$  and  $\gamma$  are the Newmark parameters. Substituting (28) and (29) into (27) results in

$$G(\boldsymbol{\phi}_{n+1}) \equiv \frac{1}{\beta h^2} \mathbf{M} \cdot \boldsymbol{\phi}_{n+1} + \mathbf{P}_{n+1}(\boldsymbol{\sigma}_{n+1}) - \hat{\mathbf{P}}_{n+1} = 0 \quad (30)$$

where  $\hat{\mathbf{P}}_{n+1} = \mathbf{F}_{n+1} - \mathbf{M} \cdot \left[ \left( 1 - \frac{1}{2\beta} \right) \dot{\mathbf{v}}_n - \frac{1}{\beta h} \mathbf{v}_n - \frac{1}{\beta h^2} \boldsymbol{\phi}_n \right]$ . For this formulation  $\beta \neq 0$ . It is noted that the choice of  $\beta = 0.25$  and  $\gamma = 0.5$  corresponds to the trapezoidal rule.

In order to complete eq. (30) the elastic constitutive equation (19.c) must be introduced. However, since the rate constitutive eq.(19.c) is not directly integrable it is not possible to replace  $\boldsymbol{\sigma}_{n+1}$  appearing in (30) directly in terms of the motion  $\boldsymbol{\phi}_{n+1}$ . In general eq. (30) together with (28) and (29) define a system of nonlinear equations whose solution can be obtained by consistent linearization and the application of a Newton Raphson iteration scheme. The next Section considers linearization of the weak form (30) consistent with the spatial rate constitutive equation (19.c).

#### 4.1.2. Linearization of the Discretized Weak Form of Momentum Balance

Formally, it is found that a consistent linearization procedure may be based on Taylor's formula for  $C^1$  functions [15,22]. Let  $A$  and  $B$  be Banach spaces and  $\mathbf{f}: A \rightarrow B$  be a  $C^1$  mapping and let  $\mathbf{x}' \in A$ . Then the linearization of  $\mathbf{f}$  about  $\mathbf{x}'$  is

$$L[\mathbf{f}, \mathbf{u}]_{\mathbf{x}'} = \mathbf{f}(\mathbf{x}') + \mathbf{Df}(\mathbf{x}') \cdot \mathbf{u} \quad (31)$$

for  $\mathbf{u} \in A$ . In (31)  $\mathbf{Df}(\mathbf{x}')$  is the Frechet derivative of  $\mathbf{f}$  evaluated at  $\mathbf{x}'$  and can be computed from the definition of the directional derivative

$$\mathbf{Df}(\mathbf{x}') \cdot \mathbf{u} = \frac{d}{d\epsilon} \mathbf{f}(\mathbf{x}' + \epsilon \mathbf{u})|_{\epsilon=0} \quad (32)$$

In the sequel,  $\mathbf{x}' \in \mathcal{A}$  will be interpreted as a set of spatial coordinates of the body given by the mapping  $\mathbf{x}' = \phi'_i(\mathbf{X})$  and  $\mathbf{u}: \phi'_i(B) \rightarrow \mathbb{R}^N$  will be interpreted as an infinitesimal deformation superimposed on the configuration  $\phi'_i(B)$ .

If  $\mathbb{T}$  is a tensor field defined on the reference configuration  $B$  then eq. (32) may be employed to obtain the directional derivative of  $\mathbb{T}$  in the direction of the incremental motion  $\mathbf{u}$ , resulting in

$$\mathbb{D}\mathbb{T}(\mathbf{X}, t) \cdot \mathbf{u} = \frac{d}{d\epsilon} \mathbb{T}(\phi_\epsilon^{-1}, t)|_{\epsilon=0} \quad (33)$$

where  $\phi_\epsilon = \epsilon \mathbf{u} \circ \phi'_i: B \rightarrow \mathbb{R}^N$ . Using definition (33), it can be shown [18] that the directional derivative of the second Piola-Kirchhoff stress tensor  $\mathbf{S}$  is associated with the Lie derivative of the Kirchhoff stress tensor  $\boldsymbol{\tau}$  taken with respect to the incremental motion  $\mathbf{u}$  such that

$$\mathbb{D}\mathbf{S} \cdot \mathbf{u} = \phi'_i{}^* [L_{\mathbf{u}}(\boldsymbol{\tau})] \quad (34)$$

where

$$L_{\mathbf{u}}(\boldsymbol{\tau}) = \frac{d}{d\epsilon} (\phi_\epsilon \circ \phi'^{-1})^* (\boldsymbol{\tau})|_{\epsilon=0}$$

This result is useful for the linearization of the discretized weak form (30) which is considered next.

Applying definitions (31) and (32) to eq. (30) results in

$$L[G(\phi'_{n+1})] = G(\phi'_{n+1}) + \mathbb{D}G(\phi'_{n+1}) \cdot \mathbf{u}_{n+1} = 0 \quad (35)$$

where

$$\mathbb{D}G(\phi'_{n+1}) = \frac{1}{\beta h^2} \mathbb{M} \cdot \mathbf{u}_{n+1} + \mathbb{D}\mathbf{P}_{n+1} \cdot \mathbf{u}_{n+1}. \quad (36)$$

In order to evaluate the directional derivative of  $\mathbf{P}_{n+1}$  appearing in (36) consistent with the spatial rate constitutive equation (19.c) it is convenient to return to the weak form (22) and consider the part from which  $\mathbf{P}_{n+1}$  is derived, namely

$$\sum_{e=1}^{Nel} \int_{\Omega^e} \boldsymbol{\sigma} : \nabla \boldsymbol{\eta} \, d\Omega = \int_{\phi'_i(B)} \boldsymbol{\sigma} : \nabla \boldsymbol{\eta} \, dv = \int_B \text{tr}(\mathbf{S} \cdot \mathbf{F}^T \cdot \nabla_0 \boldsymbol{\eta}_0) \, dV \quad (37)$$

where  $\boldsymbol{\eta}_0 = \boldsymbol{\eta} \circ \phi'_i$  and  $\nabla_0$  denotes the gradient with respect to the material coordinates  $\mathbf{X}$ . Using (32) and (34) it may be shown [18] that

$$\begin{aligned} \mathbb{D} \left( \int_{\phi'_i(B)} \boldsymbol{\sigma} : \nabla \boldsymbol{\eta} \, dv \right) \cdot \mathbf{u} &= \int_B \text{tr}[(\mathbb{D}\mathbf{S} \cdot \mathbf{u}) \cdot \mathbf{F}^T \cdot \nabla_0 \boldsymbol{\eta}_0 + \mathbf{S} \cdot [\nabla_0 \mathbf{u} \circ \phi'_i]^T \cdot \nabla_0 \boldsymbol{\eta}_0] \, dV \\ &= \int_{\phi'_i(B)} \text{tr}[(\boldsymbol{\sigma} \cdot \nabla \mathbf{u}^T + J^{-1} L_{\mathbf{u}}(\boldsymbol{\tau})) \cdot \nabla \boldsymbol{\eta}] \, dv. \end{aligned} \quad (38)$$

Using (9) and the hyperelastic constitutive equation (19.c), i.e.  $\overset{\circ}{\boldsymbol{\sigma}} = J^{-1} L_{\mathbf{v}}(\boldsymbol{\tau}) = \mathbf{a} : \mathbf{d}$  leads to the approximation

$$J^{-1} L_{\mathbf{u}}(\boldsymbol{\tau}) = \mathbf{a} : \nabla^S \mathbf{u}. \quad (39)$$

Substitution of (39) into (38) results in

$$\mathbb{D}\mathbf{P}_{n+1} \cdot \mathbf{u}_{n+1} = \sum_{e=1}^{Nel} \int_{\Omega^e} (\mathbf{B}_a^T \cdot (\boldsymbol{\sigma} \cdot \nabla \mathbf{u}^T + \mathbf{a} : \nabla^S \mathbf{u})|_{n+1}) \, d\Omega \quad (40)$$

It follows from (35), (36) and (40) that the linearization of (30) is given by

$$\frac{1}{\beta h^2} \mathbb{M} \cdot \mathbf{u}_{n+1}^i + \int_{\phi'_{n+1}(B)} \mathbf{B}^T \cdot (\boldsymbol{\sigma} \cdot \nabla \mathbf{u}^T + \mathbf{a} : \nabla^S \mathbf{u})|_{n+1}^i \, dv = -G(\phi'_{n+1}) \quad (41)$$

where  $\phi'_i$  in (35) has been replaced by  $\phi_{n+1}^i$  to represent an iterative solution procedure in which superscript  $i$  denotes the iteration counter. Equation (41) is linear in the incremental motion  $\mathbf{u}_{n+1}^i$ . Updating of the motion is accomplished by setting

$$\phi_{n+1}^{i+1} = \phi_{n+1}^i + \mathbf{u}_{n+1}^i. \quad (42)$$

However, updating of the stress tensor corresponding to  $\phi_{n+1}^{i+1}$  is achieved by integration of the spatial rate constitutive equation (19.c), the subject of the next section.

#### 4.1.3. Numerical Integration of Hyperelastic Rate Constitutive Equations

From a numerical point of view, an algorithm for the integration of rate constitutive equations should satisfy three requirements:

- (a) Consistency with the constitutive equations.
- (b) Numerical stability.
- (c) Incremental objectivity.

Conditions (a) and (b) are required for the convergence of the numerical integration scheme [3]. The condition of incremental objectivity is a physical requirement expressing the fact that the algorithm has to be invariant with respect to superimposed rigid body motions. This notion was first formalized in an algorithmic context in [20]. More recently, a family of computationally efficient algorithms satisfying the requirements of consistency, numerical stability and incremental objectivity has been proposed in [28]. These algorithms fit naturally into a finite element implementation of the problem since they employ quantities that are readily available in such a context. This integration scheme applies equally well for any choice of objective stress rate appearing in the constitutive equations.

The algorithmic problem can be stated as follows. It is assumed that at time  $t_n$  the configuration  $\phi_n(B)$ , denoted  $\Omega_n$ , and the stress tensor  $\sigma_n$  at each material point in  $\Omega_n$  is known. At time  $t_{n+1}$ , the continuum occupies the known configuration  $\phi_{n+1}(B)$ , denoted  $\Omega_{n+1}$ . The problem is to determine the corresponding  $\sigma_{n+1}$  at each point in  $\Omega_{n+1}$ .

In the past, some implicit numerical integration schemes applied to spatial rate constitutive equations have employed difference operations on the spatial stress components of the form  $[\sigma_{n+1}^{ij} - \sigma_n^{ij}]$ . However, such quantities are of limited value. From a mathematical point of view, the usual linear space operations such as addition and scalar multiplication can only be rigorously applied to relate tensor fields associated with a common configuration.\* These considerations lead naturally to the idea of pulling back spatial quantities to a common reference configuration in order to define difference operators to be used in numerical algorithms. Recalling that the second Piola-Kirchhoff stress tensor is the backward Piola transformation of the Cauchy stress tensor (or, alternatively, the pull back of the Kirchhoff stress), the above discussion suggests defining algorithms for the integration of the spatial rate constitutive equations based upon difference operators employing the second Piola-Kirchhoff stress tensor. For example, a generalized midpoint rule algorithm for the spatial rate constitutive equations can be introduced as follows

$$\mathbf{S}_{n+1} - \mathbf{S}_n = h \dot{\mathbf{S}}_{n+\alpha} \quad 0 \leq \alpha \leq 1 \quad (43)$$

where  $h = t_{n+1} - t_n$  and  $\dot{\mathbf{S}}_{n+\alpha}$  will be evaluated on an intermediate configuration  $\Omega_{n+\alpha}$  defined as

$$\phi_{n+\alpha} = \alpha \phi_{n+1} + (1 - \alpha) \phi_n \quad 0 \leq \alpha \leq 1 \quad (44)$$

\* The set of all configurations of a body can be shown to be a smooth manifold [17]. Each configuration of the body defines a point in this manifold. A tensor field defined on a particular configuration is a member of the tangent space associated with that configuration. Therefore, tensor fields defined on different configurations belong to different linear spaces and cannot be combined by means of the usual linear space operations such as addition and subtraction.

Using (8) and noting that  $S = J\dot{\phi}_t^*(\sigma)$ , (43) has the alternative representation

$$\dot{\phi}_{n+1}^*(J\sigma) - \dot{\phi}_n^*(J\sigma) = h \dot{\phi}_{n+\alpha}^*(J\sigma^0) \quad (45)$$

In reference to the comments above, it is noted that quantities involved in (45) are all referred to a common configuration.

To simplify (45) it is advantageous to select the reference configuration  $B$  to coincide instantaneously with  $\Omega_{n+1}$  [28], in which case (45) reduces to

$$\sigma_{n+1} - \dot{\phi}_n^*(J\sigma) = h \dot{\phi}_{n+\alpha}^*(J\sigma^0) \quad (46)$$

Defining the deformation gradients

$$\Lambda_{n+\alpha} = \left[ \frac{\partial \phi_{n+\alpha}}{\partial z_{n+1}} \right]^{-1} \quad 0 \leq \alpha \leq 1 \quad (47)$$

and Jacobians

$$J_{n+\alpha} = \det(\Lambda_{n+\alpha}) \quad 0 \leq \alpha \leq 1 \quad (48)$$

then, for contravariant components of stress, (46) has the form

$$\sigma_{n+1} - J_n^{-1} \Lambda_n \cdot \sigma_n \cdot \Lambda_n^T = h J_{n+\alpha}^{-1} \Lambda_{n+\alpha} \cdot \sigma_{n+\alpha}^0 \cdot \Lambda_{n+\alpha}^T \quad (49)$$

This equation is completed by introducing the rate constitutive equation for  $\sigma_{n+\alpha}^0$ . For example, for constitutive eq. (19.c), eq. (49) is expressed by

$$\sigma_{n+1} - J_n^{-1} \Lambda_n \cdot \sigma_n \cdot \Lambda_n^T = h J_{n+\alpha}^{-1} \Lambda_{n+\alpha} \cdot (a:d)_{n+\alpha} \cdot \Lambda_{n+\alpha}^T \quad (50)$$

This form requires the evaluation of quantities  $\Lambda_{n+\alpha}$  and  $d_{n+\alpha}$ . It is shown in [28] that  $\Lambda_{n+\alpha}$  is given by

$$\Lambda_{n+\alpha} = [(1-\alpha)I + \alpha \Lambda_n]^{-1} \cdot \Lambda_n$$

and that  $d_{n+\alpha}$  is consistently approximated by

$$d_{n+\alpha} = \frac{1}{h} \left[ \left\{ (1-\alpha)I + \alpha \Lambda_n \right\}^{-1} \left\{ \Lambda_n - I \right\} \right]^S$$

As noted above, from a numerical point of view, the proposed algorithm has to satisfy the three requirements of consistency with the spatial rate constitutive equations, numerical stability and incremental objectivity. It is shown in [28] that the above algorithm is consistent with the rate constitutive equation and that it is unconditionally stable for  $\alpha \geq 0.5$ ; moreover, it is second order accurate for  $\alpha = 0.5$ . The condition of incremental objectivity is a physical requirement expressing the fact that the algorithm has to be invariant with respect to superimposed rigid body motions occurring over the time step. It is shown in [28] that such a requirement is satisfied if and only if  $\alpha$  is restricted to the value of 0.5.

The algorithm (50) may be generalized to accommodate choices of objective stress rate other than the Truesdell rate of Cauchy stress by embedding the difference between the stress rate definitions into  $a$ . In this case (50) will, in general, become implicit in  $\sigma_{n+1}$  and may be solved by means of an iterative solution procedure [28].

A numerical example will serve to illustrate the accuracy and incremental objectivity of the algorithm. The problem considered is the homogeneous finite simple extension (i.e. with restrained Poisson effect) and simultaneous rigid rotation of a rectangular block. The constitutive equation employed to test the algorithm was taken to be  $\tau = a:d$  where  $a_{ijkl} = \lambda \delta_{ij} \delta_{kl} + \mu (\delta_{ik} \delta_{jl} + \delta_{il} \delta_{jk})$  and  $\lambda, \mu$  are constants. This constitutive equation is adopted only for the purpose of testing the integration algorithm. Referring to Fig. 1 and noting that  $\theta(t)$  represents rigid rotation of the block at time  $t$  and  $\lambda(t)$  the axial stretch ratio (in the



rotated coordinated frame), the analytical solution for two of the stress components (relative to the fixed spatial coordinate system) for a unit cube is given by [18]

$$\begin{Bmatrix} \tau_{11} \\ \tau_{22} \end{Bmatrix} = \begin{bmatrix} \cos^2 \theta & \sin^2 \theta \\ \sin^2 \theta & \cos^2 \theta \end{bmatrix} \begin{Bmatrix} 1 \\ \nu \\ 1-\nu \end{Bmatrix} \frac{E(1-\nu)}{(1+\nu)(1-2\nu)} \ln \lambda$$

The time dependence of the kinematic variables defining the problem is prescribed as

$$\theta(t) = 2\pi t \quad \text{and} \quad \lambda(t) = 1+t \quad \text{for} \quad 0 \leq t \leq 1$$

Thus, the cube is stretched to double its length and simultaneously rotated through 360 degrees. The solid curves of Fig. 1 depict the analytical solutions for this combination of  $\theta$  and  $\lambda$ .

The numerical solution was obtained by discretization of the block into four quadrilateral plane strain finite elements. The mesh is shown in Fig. 1. The analysis was performed in the fixed spatial coordinate system with the  $\theta$  and  $\lambda$  deformation states imposed by suitable prescription of the boundary node displacements. The numerical integration algorithm employed the iterative solution procedure mentioned above since it is implicit for the given constitutive equation. The stress components resulting from the analysis are shown as dots in Fig. 1. They display accuracy to within 0.1% of the analytical solution over the full range of deformation. Convergence was obtained for the problem using as few as ten equal increments of  $(\theta, \lambda)$ . This analysis tends to confirm the incremental objectivity of the numerical solution procedure.

#### 4.2. Plastic Algorithms and Associated Product Formulas for Perfect and Hardening Plasticity and Viscoplasticity.

The algorithm for the solution of the nonlinear elastodynamic problem given by eq. (19) discussed above can be expressed as

$$\mathbf{F}^{el}(h) \begin{Bmatrix} \phi_n^e \\ \sigma_{n,k}^{e,k} \end{Bmatrix} = \begin{Bmatrix} \phi_{n+1}^e \\ \sigma_{n+1,k}^{e,k} \end{Bmatrix}$$

where  $\sigma_{n+1,k}^{e,k}$  denotes the value of the solution particularized for integration point  $k$  in element  $e$ .

This section is concerned with the development of plastic algorithms  $\mathbf{F}^{pl}(h)$  for the solution of the plastic part of the field equations eqs. (20). These relaxation equations often admit closed form solutions that are readily obtained and which can be used directly in the plastic algorithm. In this case, a necessary and sufficient condition for  $\mathbf{F}^{pl}(h)$  to be unconditionally stable in the sense of (4) is that the plastic eqs. (20) be "dissipative" [34], i.e.,

$$-\sigma : \mathbf{T}(\sigma, \mathbf{q}) = \sigma : \mathbf{d}^p \geq (\mathbf{q}, \mathbf{f}(\sigma, \mathbf{q})) = (\mathbf{q}, \dot{\mathbf{q}})$$

where  $(\cdot, \cdot)$  indicates some appropriate inner product for the internal variables. This dissipativity condition is satisfied by all models of practical interest\*. Four examples of the plastic constitutive mappings appearing in (20) i.e.  $\mathbf{T}(\sigma, \mathbf{q})$  and  $\mathbf{f}(\sigma, \mathbf{q})$  are given. For simplicity of presentation, inviscid plasticity is considered as a limiting case of viscoplasticity, as the viscosity is allowed to tend to zero. A detailed mathematical discussion regarding product formula techniques for the solution of the elastoplastic and viscoplastic dynamic boundary value problems can be found in [33].

\* In fact, if the quantity  $\chi(\sigma, \mathbf{q}) = \frac{1}{2} \sigma : \mathbf{C} : \sigma + \sigma : \epsilon^p - \frac{1}{2} (\mathbf{q}, \mathbf{q})$  is taken as the complementary free energy potential, then the above dissipativity condition is simply a statement of the Clausius-Planck dissipation inequality.

#### 4.2.1. Perfect Viscoplasticity.

Consider a convex set  $C$  in stress space  $S \equiv R^6$  containing the origin. Then, given any point  $\sigma$  in  $S$ , there is always one and only one point  $P_C\sigma$  in  $C$  which is closest to  $\sigma$  [5,6]. The mapping  $P_C$  is called the closest point mapping (relative to  $C$ ). Clearly, if  $\sigma$  is a point in  $C$  then  $P_C\sigma = \sigma$ .

For a perfectly viscoplastic material, the existence of one such closed convex set  $C$  is assumed such that the plastic constitutive mapping  $T(\sigma)$  is given by

$$\dot{d}^p = \frac{\sigma - P_C\sigma}{\eta} = T(\sigma) \quad (51)$$

The parameter  $\eta$  is the viscosity of the material. Note that no internal variables are needed in this model.

It is interesting to note that  $T$  is defined regardless of the smoothness of  $C$ , given that the closest point mapping is always well-defined for every closed convex set  $C$  [5,6]. If  $\sigma$  belongs to  $C$  then  $P_C\sigma = \sigma$  and  $\dot{d}^p = 0$ . If, on the other hand,  $\sigma$  does not belong to  $C$  then  $\dot{d}^p$  is directed along the vector that joins  $\sigma$  and its closest point in  $C$  and it points outside the elastic region. The magnitude of  $\dot{d}^p$  is proportional to the distance from  $\sigma$  to  $C$ , the proportionality constant being  $\frac{1}{\eta}$ , Fig. 2.

For this specific model, the relaxation eqs. (20) at a generic integration point take the form

$$\dot{\sigma} = -a \cdot T(\sigma) = -a \cdot \frac{\sigma - P_C\sigma}{\eta} \quad (52)$$

This is a system of ordinary differential equations whose solution is

$$\begin{aligned} \sigma(t) &= \sigma_o \quad \text{if } \sigma_o \in C \\ \sigma(t) &= \exp(-a t/\eta) : \sigma_o + [1 - \exp(-a t/\eta)] : P_C\sigma_o \quad \text{otherwise} \end{aligned} \quad (53)$$

For the familiar case of isochoric plasticity in which  $C$  is a cylinder oriented along the hydrostatic axis and for isotropic elasticity, eq. (53.b) simplifies to

$$\begin{aligned} \sigma(t) &= e^{-t/\tau} \sigma_o + (1 - e^{-t/\tau}) P_C\sigma_o \\ &= p_o \mathbb{I} + e^{-t/\tau} s_o + (1 - e^{-t/\tau}) P_C s_o \end{aligned} \quad (54)$$

where  $p_o = \sigma_o : \mathbb{I}$  is the initial hydrostatic pressure and  $\tau = \eta/G$  is the relaxation time of the process, given in terms of the shear modulus of the material  $G$ .

For instance, for the von Mises yield criterion the elastic domain  $C$  is the set  $\{\sigma \in S \text{ such that } J_2 \leq k^2\}$ , where  $k$  is the shear yield stress,  $J_2 = \frac{1}{2} s : s$  and  $s$  is the deviatoric part of  $\sigma$ . In this particular instance, eq. (54) reduces to

$$\sigma(t) = p_o \mathbb{I} + e^{-t/\tau} s_o + (1 - e^{-t/\tau}) \frac{k}{r_o} s_o \quad (55)$$

where  $r_o = \sqrt{\frac{1}{2} s_o : s_o}$ .

Clearly, the simplest possible choice of plastic algorithm for this specific model consists of using the solution of the relaxation equations (53). This algorithm can be expressed

$$F^{pl}(h) \left\{ \begin{matrix} \phi_i^e \\ \sigma^{e,k} \end{matrix} \right\} = \left\{ \begin{matrix} \phi_i^e \\ \sigma^{e,k}(h) \end{matrix} \right\} \quad (56)$$

where  $\sigma^{e,k}(h)$  denotes the value of the solution (53) (or (54) and (55) when applicable) particularized for integration point  $k$  in element  $e$ , initial conditions  $\sigma_o = \sigma^{e,k}$  and  $t=h$ .

The resulting product algorithm (21) then consists of first solving an incremental elastic

problem, with time step  $h$ , ignoring the plasticity of the material. The stresses resulting from this operation are then allowed to relax at each integration point according to (53) for a period of time  $h$ , Fig. 3. Clearly, the stresses resulting from the application of the elastic algorithm that lie inside the elastic region are unaffected by this relaxation process. We finally note that the dissipativity condition discussed in Section 4.2 here reduces to  $\sigma : d^p \geq 0$  which is always satisfied provided  $C$  contains the origin. Consequently, the plastic algorithm (56) is unconditionally stable. The unconditional stability of the product algorithm then results provided the elastic algorithm is also unconditionally stable.

#### 4.2.2. Perfect Plasticity.

For a perfectly plastic material, the plastic constitutive mapping is given by

$$d^p = T(\sigma) \equiv \begin{cases} \lambda N & \text{if } \sigma \in \partial C \\ 0 & \text{if } \sigma \in \text{Int } C \end{cases} \quad (57)$$

where  $N$  denotes the normal to  $\partial C$  at  $\sigma$  and  $\lambda$  is a positive parameter but otherwise indeterminate. This definition presupposes the smoothness of the yield surface  $\partial C$ . For arbitrary elastic domains,  $\lambda N$  has to be replaced by the normal cone at  $\sigma$ , Fig. 2. In any case, it is clear that the resulting constitutive mapping  $T$  is not single valued. This situation is commonly encountered in the theory of nonlinear equations of evolution [34] and can be handled with relative ease with the aid of mathematical tools such as subdifferential calculus [33]. For simplicity, however, a simpler way around is taken below, namely that of considering perfect plasticity as a limiting case of perfect viscoplasticity as  $\eta \rightarrow 0$ . Alternatively, one may think of this limiting process as the result of allowing an infinite period of time to elapse for the relaxation of the stresses towards the elastic region. Taking this limit on the viscoplastic algorithm (56) the following plastic algorithm is obtained for the perfect plasticity case

$$F^{pl}(h) \begin{Bmatrix} \phi_i^e \\ \sigma^{e,k} \end{Bmatrix} \equiv \begin{Bmatrix} \phi_i^e \\ \sigma^{e,k(\infty)} \end{Bmatrix} = \begin{Bmatrix} \phi_i^e \\ P_{C^{e,k}} \sigma^{e,k} \end{Bmatrix} \quad (58)$$

where  $C^{e,k}$  denotes the elastic domain at integration point  $e,k$  and  $P_{C^{e,k}}$  denotes the closest point projection onto  $C^{e,k}$ . Clearly, if at some given integration point the stresses  $\sigma^{e,k}$  lie inside  $C^{e,k}$  then they remain unaffected by the plastic algorithm. Algorithm (58) applies equally well to any closed convex elastic domain, regardless of the smoothness of the yield surface. Also note the independence of (58) from  $h$  and  $\eta$ , which is a manifestation of the rate independent nature of the perfect plasticity constitutive equations. For instance, for the von Mises yield criterion one obtains from (55)

$$\sigma^{e,k(\infty)} = P_{C^{e,k}} \sigma^{e,k} = \begin{cases} \sigma^{e,k} & \text{if } r^{e,k} \leq k^{e,k} \\ p^{e,k} \mathbf{I} + \frac{k^{e,k}}{r^{e,k}} s^{e,k} & \text{otherwise} \end{cases} \quad (59)$$

where  $k^{e,k}$  denotes the shear yield stress at integration point  $e,k$ ,  $p^{e,k}$  and  $s^{e,k}$  the hydrostatic pressure and the deviatoric part of  $\sigma^{e,k}$  and  $r^{e,k} = (\frac{1}{2} s^{e,k} : s^{e,k})^{1/2}$ .

The resulting product algorithm entails, as before, the solution of an incremental elastic problem first, ignoring the plasticity of the material. The stresses resulting from this operation are then projected at each integration point onto their closest points on the elastic domain. Clearly, this projection only alters the stresses lying outside the elastic region.

Naturally, the heuristic argument that has been followed to derive (58) requires mathematical proof. This however is beyond the scope of this paper. A rigorous mathematical treatment of the viscoplastic approximation to the elastic-perfectly plastic dynamic boundary value problem can be found in [33]. It is also shown in [33] how product formulas for the

elastic-perfectly plastic problem can be treated directly without resorting to the viscoplastic limit.

It is noted that the closest point mapping in (58) can be viewed as an instance of the concept of "return mapping" discussed in [29,30,31,32] for the particular case of static problems and von Mises yield criterion. Certainly, the closest point mapping does not exhaust all the possible choices of return mapping that can be used to project stresses back to the elastic domain. A set of conditions on the return mapping have been presented in [33] that guarantee the consistency of the resulting plastic algorithm. The closest point mapping, however, stems naturally out of the geometry of the problem and has the widest possible range of applicability.

We finally recall a basic inequality regarding the closest point mapping for closed convex sets [6]

$$||P_C\sigma_1 - P_C\sigma_2|| \leq ||\sigma_1 - \sigma_2|| \quad \text{for all } \sigma_1, \sigma_2 \in S \quad (60)$$

This inequality states that the closest point mapping is contractive for any closed convex set  $C$ , and therefore the plastic algorithm (58) is always unconditionally stable, by definition (4). This also follows from the unconditional stability of the perfect viscoplasticity plastic algorithm shown in the preceding section, given that the perfectly plastic algorithm is just a limiting case of the viscoplastic one. Consequently, the product algorithm (21) is unconditionally stable, provided the elastic algorithm is also unconditionally stable.

#### 4.2.3. Hardening Viscoplasticity

In the case of hardening viscoplasticity, the elastic domain  $C(q)$  depends on the current value of the internal variables. The plastic constitutive equations then take the form

$$\begin{aligned} d^p &= \frac{\sigma - P_{C(q)}\sigma}{\eta} \equiv T(\sigma, q) \\ \dot{q} &= f(\sigma, q) \end{aligned} \quad (61)$$

where  $P_{C(q)}$  denotes the closest point mapping relative to  $C(q)$ . The relaxation equations (20) then become, for a generic integration point

$$\begin{aligned} \dot{\sigma} &= -a: \frac{\sigma - P_{C(q)}\sigma}{\eta} \\ \dot{q} &= f(\sigma, q) \end{aligned} \quad (62)$$

A specific example is furnished by the von Mises yield criterion with isotropic bilinear hardening and isotropic elasticity

$$\begin{aligned} \dot{\sigma} &= -2G d^p = \frac{-G \langle \sqrt{J_2} - k \rangle}{\eta} \frac{s}{\sqrt{J_2}} \\ \dot{k} &= 2H \left( \frac{1}{2} d^p : d^p \right)^{1/2} = H \frac{\langle \sqrt{J_2} - k \rangle}{\eta} \end{aligned} \quad (63)$$

where  $H$  denotes the shear plastic modulus. The solution of (63) is readily found to be

$$\begin{aligned} \sigma(t) &= \sigma_o, \quad k(t) = k_o, \quad \text{if } r_o \leq k_o \\ \sigma(t) &= \sigma_o - \frac{\tau}{\tau_s} (r_o - k_o) (1 - e^{-t/\tau}) \frac{s_o}{r_o} \\ k(t) &= k_o + \frac{\tau}{\tau_q} (r_o - k_o) (1 - e^{-t/\tau}) \end{aligned} \quad \text{otherwise} \quad (64)$$

where

$$\tau_s = \frac{\eta}{G}; \quad \tau_q = \frac{\eta}{H}; \quad \tau = \frac{\tau_s \tau_q}{\tau_s + \tau_q} \quad (65)$$

are relaxation times for the process. It is seen from (64) that during a relaxation process corresponding to initial stresses outside the elastic domain, the stresses steadily approach the elastic domain, which at the same time expands towards the stress point.

As in the case of perfect viscoplasticity, the closed form solution (64) can be utilized to define plastic algorithms through

$$\mathbf{F}^{pl}(h) \begin{Bmatrix} \phi_i^e \\ \sigma^{e,k} \\ \mathbf{q}^{e,k} \end{Bmatrix} = \begin{Bmatrix} \phi_i^e \\ \sigma^{e,k}(h) \\ \mathbf{q}^{e,k}(h) \end{Bmatrix} \quad (66)$$

where  $\sigma^{e,k}(h)$  and  $\mathbf{q}^{e,k}(h)$  are given by (64) particularized for integration point  $e, k$ , initial conditions  $\sigma_o = \sigma^{e,k}$ ,  $\mathbf{q}_o = \mathbf{q}^{e,k}$  and  $t=h$ . In this case, however, not only do the stresses at the integration points vary upon the application of the plastic algorithm but so do the internal variables and, as a result, the elastic domains.

Taking as inner product for the internal variables  $(\mathbf{q}_1, \mathbf{q}_2) \equiv \frac{1}{2H} k_1 k_2$ , the dissipativity condition is readily checked, which in turn implies the unconditional stability of the corresponding plastic algorithm. Therefore, once again the unconditional stability of the product algorithm (21) follows provided the elastic algorithm is unconditionally stable. The further case of kinematic hardening has also been treated in [8].

#### 4.2.4. Hardening Plasticity.

As in the case of perfect plasticity, plastic algorithms for the hardening case can be obtained from (66) by taking the limit  $\eta \rightarrow 0$ , which leads to the expression

$$\mathbf{F}^{pl}(h) \begin{Bmatrix} \phi_i^e \\ \sigma^{e,k} \\ \mathbf{q}^{e,k} \end{Bmatrix} = \begin{Bmatrix} \phi_i^e \\ \sigma^{e,k}(\infty) \\ \mathbf{q}^{e,k}(\infty) \end{Bmatrix} \quad (67)$$

Here, the asymptotic values  $\sigma^{e,k}(\infty)$  and  $\mathbf{q}^{e,k}(\infty)$  can be obtained from (64)

$$\begin{aligned} \sigma(\infty) &= \sigma_o, \quad k(\infty) = k_o \quad \text{if } r_o \leq k_o \\ \sigma(\infty) &= \sigma_o - \frac{G}{G+H} (r_o - k_o) \frac{s_o}{r_o} \\ k(\infty) &= k_o + \frac{H}{G+H} (r_o - k_o) \quad \text{otherwise} \end{aligned} \quad (68)$$

for the von Mises, isotropic hardening case. Note that these limiting values are independent of  $\eta$ .

Eq. (68) yields a suitable "return mapping" for the isotropic hardening rule. It is seen from (68) that the stress point and the yield surface meet at some intermediate point on the segment joining their initial values, the distances from these being proportional to  $G$  and  $H$ , respectively. A similar geometric interpretation can be derived for the return mapping corresponding to the kinematic hardening rule [8]. Note that the perfectly plastic case is recovered by setting  $H = 0$ .

Finally, the unconditional stability of the plastic algorithm induced by this return mapping follows from that of the corresponding viscoplastic case. Consequently, the unconditional stability of the product algorithm (21) follows also, provided the elastic algorithm is unconditionally stable.

## 5. Numerical Examples

A number of examples are presented to illustrate the effectiveness of the algorithms described above. The first example concerns the deformation of an infinitely long (plane strain) internally pressurized thick walled cylinder. The tube was discretized by means of quadrilateral elements, with 16 elements across the thickness. For perfect plasticity employing the von Mises yield criterion, Fig. 4 depicts the hoop and radial stress in the tube for an internal pressure corresponding to a plastification of 75% of the wall thickness. The three curves illustrate the rate of convergence of the method as the number of load increments taken to reach the final pressure is increased. It is observed that a small number of load increments (6) results in reasonable accuracy. For 100 load increments the solution obtained is virtually identical to the exact solution [16]. Fig. 5 shows the distribution of all stress components at various stages of the plastification of the wall which are in good agreement with the analytical solution [16].

Fig. 6 shows results corresponding to the infinitesimal deformation of an internally pressurized disk (plane stress) for the case of perfect plasticity and the Tresca yield criterion. The exact analytical solutions are compared in the same figure against the numerical solutions which for the load increment selected display an accuracy comparable to that obtained in the purely elastic solution. This example emphasizes the applicability of the proposed algorithm to the case of yield surfaces that exhibit corners.

The next example shown in Fig. 7 illustrates the effect of viscosity. Again the infinitely long thick walled tube is considered, in this case for a perfectly viscoplastic material with a von Mises yield surface. All curves correspond to an internal pressure resulting in a plastification of 50% of the wall thickness and depict the effect of varying viscosities. The figures clearly display the inviscid limit obtained by decreasing the viscosity to zero. The curves representing this limiting case are identical to those reported for perfect plasticity, Fig. 5.

The final example concerns the finite deformation of the infinitely long, internally pressurized thick walled cylinder. The material behavior was taken to be isotropic hardening plasticity with a plastic hardening modulus  $H$  corresponding to 10% of the Young's modulus, Fig. 8. As discussed in Section 4.2.4, the plastic algorithm for this problem makes use of a return mapping which simultaneously accounts for the evolution of the elastic domain. Fig. 8 depicts the hoop stress through the wall thickness for 12 prescribed inner radial displacements. The maximum load result shown in Fig. 8 (curve 12), which corresponds to a 12% increase in the internal radius of the tube, was obtained in 24 equal displacement increments with each increment requiring approximately 5 Newton-Raphson iterations as described in Section 4.1.2.

## Future Research

It is observed from Fig. 4 that the accuracy of the solution resulting from the global product algorithm deteriorates as the time step is increased. Although it has been demonstrated that the global product algorithm is consistent with the field equations in the sense of eq.(3) and has a stability condition controlled only by the stability of the nonlinear elastic algorithm, under certain conditions, the accuracy of the solution for a given time step may not be satisfactory.

On the other hand, "fully implicit" methods employing the elastoplastic tangent modulus are potentially more accurate but suffer from various shortcomings noted in Section 1. A future research effort might usefully aim to combine the accuracy of the fully implicit methods (employing the elastoplastic tangent modulus) applied to the integration of the equations of motion together with the operator split method applied to the integration of the elastoplastic constitutive equations. It is noted that methods employing the elastoplastic tangent would presumably apply only to the case where the yield hypersurface is smooth. In the case where the yield hypersurface exhibits corners the solution procedure presented in this paper will remain appropriate.

## References

1. M. Ortiz, P.M. Pinsky and R.L. Taylor, "Unconditionally Stable Element-by-Element Algorithms For Dynamic Problems," *Computer Methods in Applied Mechanics and Engineering*, (to appear).
2. T.J.R. Hughes, I. Levit and J. Winget, "Unconditionally Stable Element-by-Element Implicit Algorithms for Heat Conduction Analysis", *J. Engng. Mechs. Div. of ASCE*, (to appear).
3. G.W. Gear, **Numerical Initial Value Problems in Ordinary Differential Equations**, Prentice-Hall, 1971.
4. R.M. McMeeking and J. R. Rice, "Finite Element Formulations for Problems of Large Elastic-Plastic Deformation," *Int. J. Solids Struct.*, **11**, 601 (1975).
5. R.T. Rockafellar, *Convex Analysis*, Princeton University Press, 1970.
6. E.H. Zarantonello, "Projections on Convex Sets in Hilbert Space and Spectral Theory," in: E.H. Zarantonello (Ed.), *Symposium on Nonlinear Functional Analysis*, Academic Press, 237-424, 1971.
7. J.R. Osias and J. L. Swedlow, "Finite Elasto-Plastic Deformation - I. Theory and Numerical Examples," *Int. J. Solids Struct.*, **10**, 321 (1974).
8. M. Ortiz, P.M. Pinsky and R.L. Taylor, "Operator Split Methods for the Numerical Solution of the Elastoplastic Dynamic Problem," *Computer Methods in Applied Mechanics and Engineering*, (to appear).
9. J. Lubliner, "A Simple Theory of Plasticity," *Int. J. Solids Struct.*, **10**, 313-319 (1974).
10. B.D. Coleman and W. Noll, "The Thermodynamics of Elastic Materials with Heat Conduction and Viscosity," *Arch. Ration. Mech. Anal.*, **13**, 167-178, (1963).
11. E.H. Lee and D.T. Liu, "Finite Strain Elastic-Plastic Theory Particularly for Plane Wave Analysis," *J. Appl. Phys.*, **38**, 19-27, (1967).
12. S. Nemat-Nasser, "Decomposition of Strain Measures and Their Rates in Finite Deformation Elastoplasticity," *Int. J. Solids Struct.*, **15**, 155-166 (1979).
13. J.C. Nagtegaal and J. E. DeJong, "Some Computational Aspects of Elastic-Plastic Large Strain Analysis," *Int. J. Num. Meth. Eng.*, **17**, 15 (1981).
14. A.E. Green and P.M. Naghdi, "Some Remarks on Elastic-Plastic Deformation at Finite Strain," *Int. J. Engng. Sci.*, **9**, 1219-1229 (1971).
15. T.J.R. Hughes and K.S. Pister, "Consistent Linearization in Mechanics of Solids and Structures," *Computers and Structures*, **8**, 391-397 (1978).
16. W. Prager and P.G. Hodge, **Theory of Perfectly Plastic Solids**, John Wiley & Sons, 1963.
17. D.G. Ebin and J.E. Marsden, "Groups of Diffeomorphisms and the Motion of an Incompressible Fluid," *Ann. of Math.*, **92**, 102 (1970).
18. P.M. Pinsky, "A Numerical Formulation for the Finite Deformation Problem of Solids with Rate-Independent Constitutive Equations," *Ph.D. Dissertation*, Dept. Civil Eng., University of California, Berkeley, California, December 1981.
19. R.D. Krieg, and S. W. Key, "Implementation of a Time-Independent Plasticity Theory into Structural Computer Programs," in: J. A. Stricklin and K. J. Saczalski (Eds.), *Constitutive Equations in Viscoplasticity: Computational and Engineering Aspects*, AMD, Vol. 20, ASME, 125 (1976).
20. T.J.R. Hughes and J. Winget, "Finite Rotation Effects in Numerical Integration of Rate Constitutive Equations Arising in Large-Deformation Analysis," *Int. J. Num. Meth. Eng.*, **15**, No. 12, December 1980.

21. D. Durban and M. Baruch, "Incremental Behavior of an Elasto-Plastic Continuum," TAE Report No. 193, Dept. of Aeronautical Eng., Israel Institute of Technology, Haifa, Israel, February 1975.
22. J.E. Marsden and T.J.R. Hughes, "Topics in the Mathematical Foundations of Elasticity," in R.J. Knops (Ed.), *Nonlinear Analysis and Mechanics*, Heriot-Watt Symposium, Vol. II, Pitman Publishing Co., 1978.
23. M.E. Gurtin, *Topics in Finite Elasticity*, CBMS-NSF Regional Conference Series in Applied Mathematics, 1981.
24. C. Truesdell, "The Simplest Rate Theory of Pure Elasticity," *Comm. Pure Appl. Math.*, 8, 123-132, 1955.
25. J.G. Oldroyd, "On the Formulation of Rheological Equations of State," *Proc. Roy. Soc.*, A200, 523-541, 1950.
26. B.A. Cotter and R.S. Rivlin, "Tensors Associated with Time-Dependent Stress," *Quart. Appl. Math.*, 13, 177-182, 1955.
27. G. Jaumann, "Geschlossenes System Physikalischer und Chemischer Differentialgesetze," *Sitzungsber. Akad. Wiss. Wien (2a)*, 120, 385-530, 1911.
28. P.M. Pinsky, M. Ortiz and K.S. Pister, "Rate Constitutive Equations in Finite Deformation Analysis: Theoretical Aspects and Numerical Integration," *Computer Methods in Applied Mechanics and Engineering*, (to appear).
29. R.D. Krieg and D.B. Krieg, "Accuracies of Numerical Solution Methods for the Elastic-Perfectly Plastic Model," *ASME J. Pressure Vessel Tech.*, 99, 510-515, (1977).
30. H.L. Schreyer, R.F. Kulak and J.M. Kramer, "Accurate Numerical Solutions for Elastic-Plastic Models," *ASME J. Pressure Vessel Tech.*, 101, 226-234, (1979).
31. J.M. Santiago, "On the Accuracy of Flow Rule Approximations Used in Structural and Solid Response Computer Programs," in: *Proceedings of the 1981 Army Numerical Analysis And Computers Conference*, ARO Report 81-3, (1981).
32. A. Mendelson, *Plasticity: Theory and Application*, McMillan, 1968.
33. M. Ortiz and P.M. Pinsky, "Global Analysis Methods for the Solution of the Elastoplastic and Viscoplastic Dynamic Problems," Report No. UCB/SESM-81/08, Department of Civil Engineering, University of California, Berkeley, California, December, 1981.
34. H. Brézis, *Opérateurs Maximaux Monotones et Semi-Groupes de Contractions dans les Espaces de Hilbert*, North-Holland, 1973.



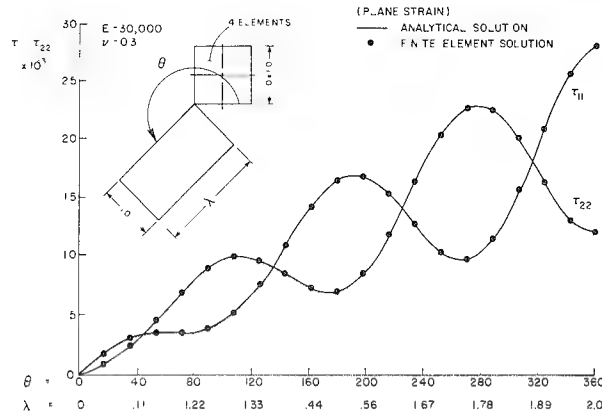


Fig. 1. Homogeneous finite simple extension and rotation. Kirchhoff stresses  $\tau_{11}$  and  $\tau_{22}$  versus axial stretch and rotation. Elastic constants  $E = 30,000$ ,  $\nu = 0.3$ .

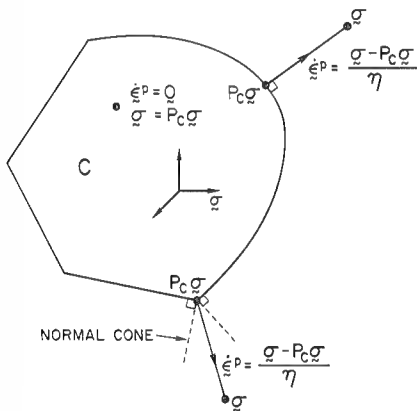


Fig. 2. Definition of viscoplastic constitutive mapping.

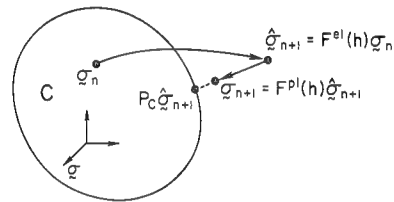


Fig. 3. Schematic representation of product algorithm.

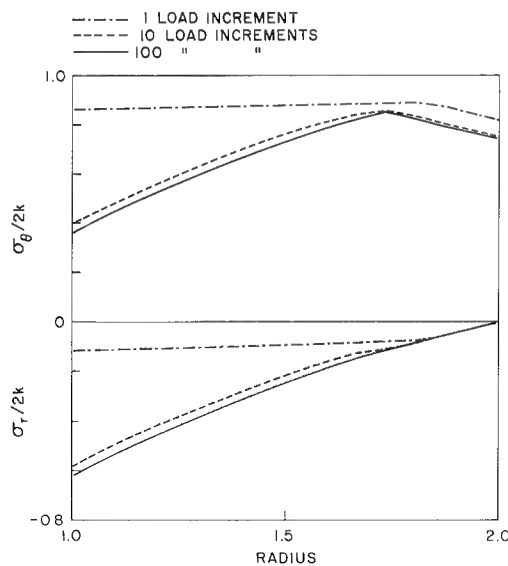


Fig. 4. Product formula solutions for an internally pressurized thick walled cylinder illustrating the rate of convergence of the algorithm. The results correspond to perfect plasticity with von Mises yield criterion and to a prescribed inner radial displacement  $2Gu/ka = 1.5$ ,  $G$  = shear modulus,  $k$  = shear yield stress,  $a$  = inner radius.

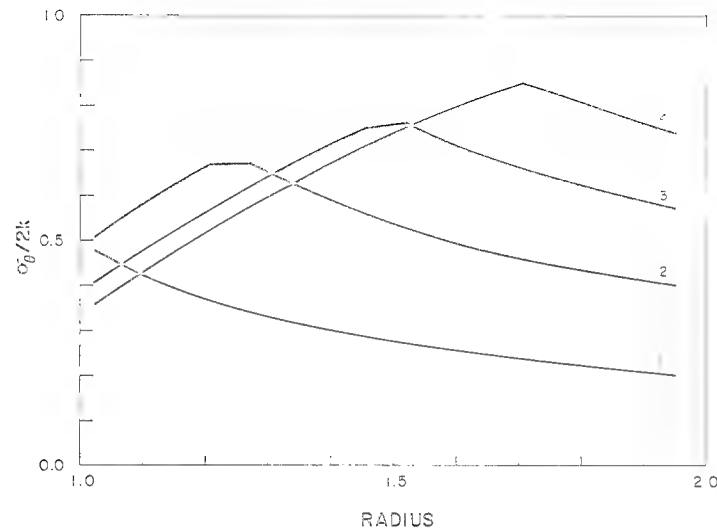


Fig. 5. Product formula solutions for an internally pressurized thick walled cylinder, with perfect plasticity and von Mises yield criterion. Curves 1-4 correspond to prescribed inner radial displacements  $2Gu/ka = 0.5, 1.0, 1.5, 2.0$ ,  $G$  = shear modulus,  $k$  = shear yield stress,  $a$  = inner radius, and 20 displacement increments from curve to curve.

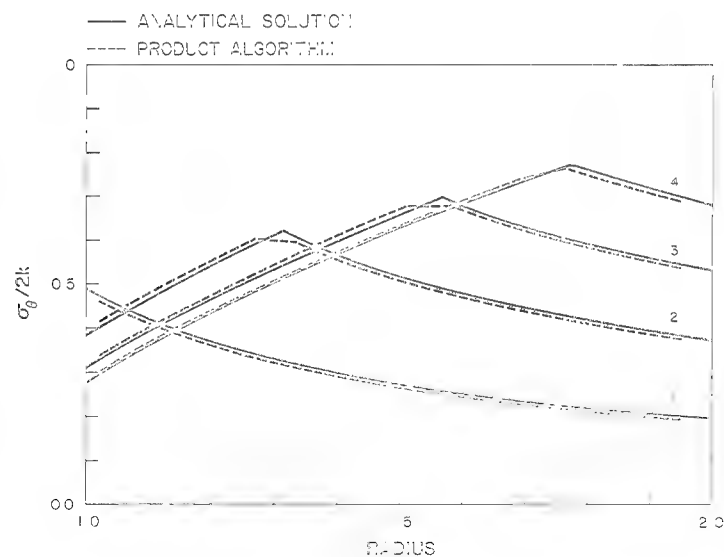


Fig. 6. Product formula solutions for an internally pressurized disk, with perfect plasticity and a Tresca yield criterion. Curves 1-4 correspond to prescribed inner radial displacements  $2Gu/ka = 0.5, 1.0, 1.5, 2.0$ ,  $G$  = shear modulus,  $k$  = shear yield stress,  $a$  = inner radius, and 20 displacement increments from curve to curve.

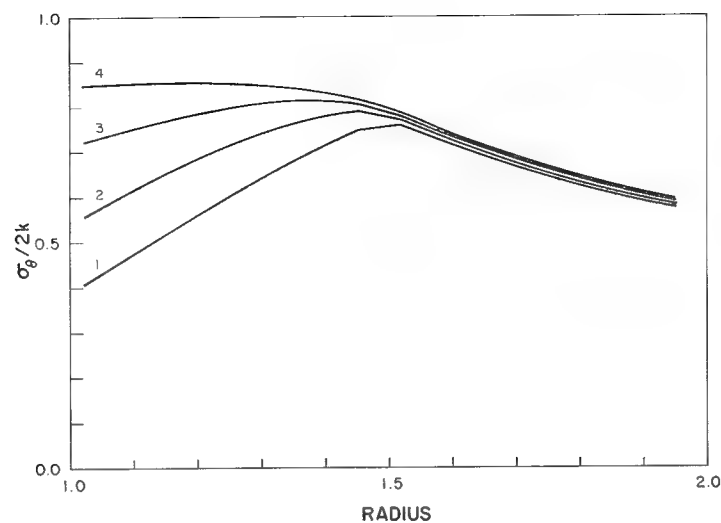


Fig. 7. Product formula solutions for an internally pressurized thick walled cylinder with perfect viscoplasticity and von Mises yield criterion. Curves 1-4 correspond to viscosities  $\eta/Gh = 0, 5, 10, 15$ ,  $G$  = shear modulus,  $h$  = time step, and a prescribed inner radial displacement  $2Gu/ka = 1.5$ . The solution was obtained in 60 time steps.

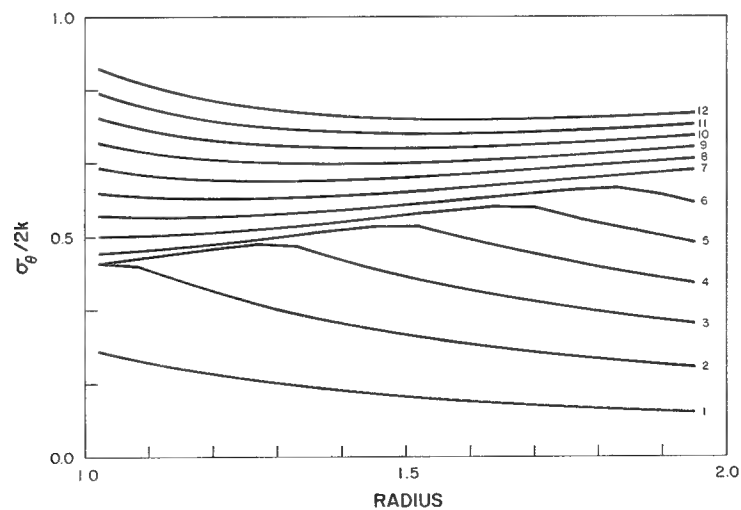


Fig. 8. Product formula solutions for an internally pressurized thick walled cylinder with isotropic hardening plasticity and von Mises yield criterion. Curves 1-12 correspond to a plastic modulus  $H/E = 0.1$ ,  $E$  = Young's modulus, prescribed inner radial displacements  $3Gu/ka = 1, 2, \dots, 12$ ,  $G$  = shear modulus,  $k$  = shear yield stress,  $a$  = inner radius, and 2 displacement increments from curve to curve. Poisson's ratio  $\nu$  was taken as 0.3.

# APPLICATION OF THE REDUCED BASIS METHOD TO NONLINEAR TRANSIENT THERMAL ANALYSIS

Charles P. Shore  
Langley Research Center  
Hampton, Virginia

## SUMMARY

An effort to apply the reduced basis method to nonlinear transient thermal analysis is described. The method combines the classical Rayleigh-Ritz and modal superposition techniques with contemporary finite-element methods to retain modeling versatility as the degrees of freedom in a problem are reduced. The essence of the method is to use a few thermal modes from eigenvalue analyses as basis vectors to represent the temperature response for a given thermal problem similar to the use of vibration modes to represent displacements in a dynamic-response problem. Approximate temperature distributions have been obtained using the reduced basis method for a small section of the Shuttle Orbiter lower wing undergoing reentry heating. Good agreement was obtained between the reduced basis method solutions and full system solutions with reductions in the degrees of freedom of up to a factor of 4. The good agreement indicates the reduced basis method has the potential for significant reduction in computing effort for thermal analysis; however, considerable work remains to determine techniques for selecting the type and number of basis vectors needed for approximate solutions to more complex transient thermal problems.

## INTRODUCTION

For some time, researchers in structural analysis have recognized that the large number of degrees of freedom frequently required for the solution of structural problems has often been the result of geometry and structural arrangement rather than complexity of the response behavior. This fact has led to considerable research into methods to reduce the degrees of freedom in structural problems and, hence, computer resources and costs. These methods have become known as reduction methods and are thoroughly reviewed in reference 1. One technique to reduce the degrees of freedom in static and dynamic problems is the reduced basis method which combines the classical Rayleigh-Ritz and modal superposition techniques with contemporary finite-element methods to retain modeling versatility as the degrees of freedom are reduced. References 1 and 2 cite several dynamic response problems where reductions in the degrees of freedom of over an order of magnitude were achieved with the reduced basis method.

Classical modal superposition techniques have also been applied to transient thermal problems in references 3 through 5. However, for nonlinear transient thermal problems, the classical techniques can require frequent updating of the thermal mode shapes and eigenvalues (decay constants, see ref. 3). Reference 6 presents a way of circumventing the updating problem using eigenvectors from two linear thermal eigenvalue problems as vectors in the reduced basis method. This method to circumvent the updating problem is based on techniques for dynamic response problems presented in reference 1. The first eigenvalue problem is based on material properties evaluated for the initial conditions of the transient problem, and the second is based on material properties evaluated for a steady-state temperature distribution corresponding to time-averaged thermal properties and time-averaged values of the transient heat load. The work described in reference 6 was restricted to one-dimensional thermal-response problems. This paper describes the status of a research effort to extend the reduced basis method using the approach from reference 6 to two-dimensional nonlinear transient thermal problems and is concerned primarily with assessing the accuracy of the method.

#### SYMBOLS

$[C], [C_r]$	capacitance matrices of full and reduced systems, respectively
$\{F\}, \{F_r\}$	internal force vectors of full and reduced systems, respectively
$\{G(Y)\}$	vector of nonlinear terms
$h$	shell thickness
$[K], [K_r]$	stiffness or conductance matrices of full and reduced systems, respectively
$[M], [M_r]$	mass matrices of full and reduced systems, respectively
$P$	applied concentrated load
$\{Q\}, \{Q_r\}$	applied load or heating vectors of full and reduced systems, respectively
$q$	applied heat flux
$r$	shell radius of curvature
$\{T\}$	vector of temperatures
$\{Y\}$	vector of displacements
$[V]$	matrix of basis vectors
$\lambda$	thermal eigenvalue (decay constant)
$\{p\}$	vector of participation coefficients for basis vectors

## DESCRIPTION OF THE REDUCED BASIS METHOD

### Application to Dynamic Response Problems

To illustrate the use of the reduced basis method for transient problems, the method of application to dynamic response problems is described in this section of the paper. The next section describes extension of the reduced basis method to transient thermal problems. The equation of motion for a nonlinear dynamic response problem neglecting damping may be written in matrix notation as:

$$[M]_{m,m} \{\ddot{X}\}_m = \{Q\}_m - \{F\}_m \quad (1)$$

$$\text{where } \{F\} = [K] \{X\} + \{G(X)\} \quad (2)$$

In equation 1,  $[M]$  represents the mass matrix,  $\{\ddot{X}\}$  is a vector of nodal accelerations and  $\{Q\}$  and  $\{F\}$  are the applied loads and internal nodal forces, respectively. The total number of degrees of freedom in the problem is denoted by  $m$ . The internal nodal forces consist of a linear portion  $[K]\{X\}$  and a vector of nonlinear displacement dependent terms  $\{G(X)\}$  as indicated in equation 2 where  $[K]$  is a stiffness matrix and  $\{X\}$  is a vector of nodal displacements. The essence of the reduction method is to use a few known modes or global basis vectors to represent the displacements in the structure. Thus,  $\{X\}$  is replaced by the following expression:

$$\{X\}_m = [r]_{m,n} \{\psi\}_n \quad (3)$$

where  $[r]$  is a matrix whose columns are the known structural mode shapes and  $\{\psi\}$  is a vector of modal participation coefficients which become the new unknowns in the problem. For practical application to dynamic response problems,  $[r]$  contains only the first few vibration modes; thus,  $n$  is much smaller than  $m$ . To reduce the equations, the expression for  $\{X\}$  (eq. 3) is substituted into equation 1 and both sides of the equation are premultiplied by the transpose of  $[r]$  to obtain:

$$[\bar{M}]_{n,n} \{\ddot{\psi}\}_n = \{\bar{Q}\}_n - \{\bar{F}\}_n \quad (4)$$

$$\text{where: } [\bar{M}]_{n,n} = [r]_{n,m}^T [M]_{m,m} [r]_{m,n}$$

$$\{\bar{Q}\}_n = [r]_{n,m}^T \{Q\}_m \quad (5)$$

$$\left. \begin{aligned} \{\bar{F}\} &= \begin{matrix} n \\ n, n \end{matrix} \begin{matrix} \bar{K} \\ n, n \end{matrix} \begin{matrix} \{\psi\} \\ n \end{matrix} + \begin{matrix} n \\ n, m \end{matrix} \begin{matrix} [r] \\ n, m \end{matrix} \begin{matrix} \{G(\psi)\} \\ m \end{matrix} \\ \begin{matrix} \bar{K} \\ n, n \end{matrix} &= \begin{matrix} n \\ n, m \end{matrix} \begin{matrix} [r] \\ n, m \end{matrix} \begin{matrix} [K] \\ m, m \end{matrix} \begin{matrix} [r] \\ m, n \end{matrix} \end{aligned} \right\} \quad (5 \text{ cont.})$$

In equation 4, the barred quantities represent the reduced matrices or vectors and are obtained by the matrix multiplications indicated in equations 5. The reduced equation of motion is now expressed in terms of the  $n$  unknown modal participation coefficients. The solution process consists of solving eigenvalue problems to obtain the basis vectors, using the basis vectors to reduce the full system equations (eq. 1) and then integrating the reduced equations (eq. 4) to obtain the modal participation coefficients. Equation 3 is then used to algebraically add the contributions of the various modes to obtain the dynamic response of the structure.

The above technique was applied to a shallow spherical cap subjected to a step load in reference 1. The problem shown in figure 1 consists of a clamped spherical cap subjected to a point load of 40 lbf at the apex applied as a step function in time. The shell is axially symmetric and the meridian was modeled by 10 shear-flexible curved elements with quintic interpolation functions for each of the displacement and rotation components (for a total of 148 nonzero displacement degrees of freedom). Two sets of basis vectors were tried. The first consisted of 10 eigenvectors from the solution of a linear eigenvalue problem based on initial conditions. The second set consisted of five vectors from the linear problem and five from the solution of a steady-state (static) nonlinear eigenvalue problem where the structural stiffness matrix was modified to contain the nonlinear stiffness terms associated with the steady-state deflections. Nondimensional motion histories for the shell apex from the full system equations (148 degrees of freedom) and the two sets of reduced equations (10 initial modes and 5 initial + 5 steady-state modes) are shown on the right of figure 1. The 10 initial or linear modes track the full system solution only for a short time and fail to duplicate the full response of the shell. The combined linear and steady-state nonlinear modes, however, do a very good job of approximating the response except for a slight shift in phase after about 200 microseconds. This good agreement for the second choice of modes led to its consideration for nonlinear transient thermal analysis as described in the next section.

#### Application To Transient Thermal Problems

Matrix equations describing heat transfer in a heated structure may be written as:

$$\begin{matrix} [K] \\ m, m \end{matrix} \begin{matrix} \{T\} \\ m \end{matrix} + \begin{matrix} [C] \\ m, m \end{matrix} \begin{matrix} \dot{\{T\}} \\ m \end{matrix} = \begin{matrix} \{Q\} \\ m \end{matrix} \quad (6)$$

where  $[K]$  is the conductance matrix,  $\{T\}$  the vector of nodal temperatures,  $[C]$  the capacitance matrix,  $\{\dot{T}\}$  the time rate of change in the nodal temperatures, and  $\{Q\}$  the applied heat load. The elements of  $[K]$  and  $[C]$  are functions of temperature. The total number of degrees of freedom is denoted by  $m$ . To reduce the equations,  $\{T\}$  is replaced by a modal representation

$$\begin{matrix} \{T\} \\ m \end{matrix} = \begin{matrix} [r] \\ m,n \end{matrix} \begin{matrix} \{\psi\} \\ n \end{matrix} \quad (7)$$

where  $[r]$  contains vectors of thermal mode shapes and  $\{\psi\}$  is a vector of unknown modal participation coefficients. The vectors in  $[r]$  may be obtained from solution of two thermal eigenvalue problems associated with the full system of equations. In the first eigenvalue problem, the elements of  $[K]$  and  $[C]$  are evaluated for thermal properties corresponding to the initial temperatures. In the second eigenvalue problem, the matrices are evaluated for thermal properties corresponding to temperatures from a quasi steady-state solution in which time-averaged thermal properties and heat load values are used. When  $\{T\}$  is replaced with the modal representation in the heat transfer equation and both sides of the equation are multiplied by the transpose of  $[r]$ , the following set of reduced equations in terms of the unknown modal participation coefficients is obtained.

$$\begin{matrix} [\bar{K}] \\ n,n \end{matrix} \begin{matrix} \{\psi\} \\ n \end{matrix} + \begin{matrix} [\bar{C}] \\ n,n \end{matrix} \begin{matrix} \dot{\psi} \\ n \end{matrix} = \begin{matrix} \{\bar{Q}\} \\ n \end{matrix} \quad (8)$$

where:

$$\left. \begin{aligned} \begin{matrix} [\bar{K}] \\ n,n \end{matrix} &= \begin{matrix} [r]^T \\ n,m \end{matrix} \begin{matrix} [K] \\ m,m \end{matrix} \begin{matrix} [r] \\ m,n \end{matrix} \\ \\ \begin{matrix} [\bar{C}] \\ n,n \end{matrix} &= \begin{matrix} [r]^T \\ n,m \end{matrix} \begin{matrix} [C] \\ m,m \end{matrix} \begin{matrix} [r] \\ m,n \end{matrix} \\ \\ \begin{matrix} \{\bar{Q}\} \\ n \end{matrix} &= \begin{matrix} [r]^T \\ n,m \end{matrix} \begin{matrix} \{Q\} \\ m \end{matrix} \end{aligned} \right\} \quad (9)$$

The barred quantities represent the reduced matrices and vectors obtained by the indicated matrix multiplications. Similar to the dynamic response problem, it is assumed that local temperatures can be represented by a few global modes or basis vectors so that  $n$  will be much smaller than  $m$ .

To implement the reduced basis method for thermal problems, the SPAR finite-element thermal analyzer (ref. 7) was used to generate conductance and capacitance matrices and heat load vectors. A standard eigenvalue extraction routine was used to solve the thermal eigenvalue problems to obtain thermal mode shapes used as basis vectors. These basis vectors were then used in a pilot computer program to reduce the full system equations (eq. 6), to integrate equation 8 using the implicit Crank-Nicholson algorithm to obtain the unknown



modal participation coefficients  $\{\psi\}$ , and to obtain the thermal response. Equation 7 was used to algebraically add the contributions from the various modes to obtain temperatures in the structure. Solution techniques used in the pilot computer program were patterned after those used in the SPAR program, i.e., the transient heat pulse was divided into intervals in which temperature and time-dependent thermal properties were evaluated at the beginning of the interval and held constant during the interval. Since the thermal properties changed from one time interval to the next, it was necessary to form and reduce the full system matrices at the beginning of each time interval. Results from the reduced basis method were evaluated by comparison with similar results from the SPAR program for the sample problems described in the next section. Time intervals and time steps used in the Crank-Nicholson integration algorithm within each time interval were the same for both the reduced basis and SPAR solutions.

### SAMPLE THERMAL PROBLEMS

Three versions of the problem shown in figure 2 were solved using the reduced basis method. The problems represent a 58 in. segment of the lower surface of the Space Shuttle wing and consist of a 119 mil thick aluminum skin covered by a 1.8 in. thick layer of Reusable Surface Insulation (RSI). The RSI, Strain Isolator Pad (SIP), and Room Temperature Vulcanizing (RTV) adhesive were modeled with two-dimensional finite elements as shown on the left of figure 2. One-dimensional elements with a quasi-linearized radiation representation were used on the RSI surface to model radiation losses, and one-dimensional conduction elements were used to model the aluminum structure. The grid shown has 84 node points and, hence, 84 degrees of freedom since the elements used to model the structure have only temperature as the nodal degrees of freedom. The lateral edges and backface were assumed to be adiabatic, and the surface was heated by heat pulses similar to that shown on the right of figure 2 which is reasonably representative of Shuttle reentry. Thermal properties of the RSI are nonlinear as indicated in figure 3 where specific heat and conductivity are shown as functions of temperature. The specific heat varies with temperature, and because the RSI is very porous, the conductivity varies with pressure as well as temperature. Thus, the nonlinear thermal properties of the RSI cause the heat transfer equation to be nonlinear. The version of the SPAR thermal analyzer used in this investigation accommodates only temperature and time-dependent properties. Consequently, the pressure dependency was converted to a time dependency by utilizing the known pressure history for a typical Shuttle reentry trajectory. Figure 4 shows the spacial and temporal heating distributions for the three cases considered in this study. The spacial distribution is shown above each model sketch and the temporal distribution below. The first problem involved uniform heating on the surface of the 1.8 in. thick RSI for a 2000 sec heat pulse. In the second problem, the heating was symmetric over the surface and the thickness of the RSI was reduced to 1 in. with a corresponding decrease in the heat pulse duration (to reduce computation

times) so that temperatures reached values comparable to those for the uniform surface heating. In the third problem, the heating was asymmetric over the RSI surface. Since the surface heating in the first problem was uniform, the problem was one-dimensional with essentially 14 degrees of freedom. Problems two and three were two-dimensional with essentially 42 and 84 degrees of freedom, respectively.

## RESULTS AND DISCUSSION

### Uniform Surface Heating

A series of temperature distributions through the depth of the model with uniform surface heating computed by a full SPAR analysis are shown in figure 5 for several discrete times during the heat pulse. These distributions indicate the type of behavior the basis vectors must approximate to be useful. Initially the entire structure is at a constant temperature of  $560^{\circ}\text{R}$ . As heating is applied, the RSI surface experiences a rapid temperature rise which gradually diffuses through the RSI and SIP to the aluminum skin. After peak heating occurs, the surface begins to cool while the interior of the RSI and the aluminum skin continue to experience a temperature increase. To be useful, the basis vectors used to reduce the degrees of freedom must characterize this nonlinear response, must give accurate solutions and must be easily and inexpensively generated. Normalized thermal mode shapes from a linear eigenvalue problem (in which matrices were evaluated at a uniform temperature of  $560^{\circ}\text{R}$ ) are shown in figure 6. Although numbered sequentially, these modes do not represent the first five modes from the eigenvalue problem associated with the two-dimensional finite-element model shown in figure 2. Because of the two-dimensional nature of the eigenvalue problem, most of the lower modes involved multiple waves in the lateral direction. A total of 84 eigenvalues were extracted, and the modes shown have only a single constant wave in the lateral direction. As a first attempt to approximate the temperature distributions for the problem with uniform surface heating, 12 modes with only a single wave in the lateral direction from the eigenvalue problem for the uniform initial temperature condition were selected as basis vectors. Additionally, to enhance the representation of the diffusion character of the temperature distribution during the first 600 sec of the heat pulse (see fig. 5), the reciprocal of the first mode shape was also used as a basis vector. Finally, to accommodate uniform temperature changes, a constant vector (all elements equal to 1) was included for a total of 14 basis vectors.

Beginning with an initial set of four vectors (constant, mode 1, reciprocal of mode 1, and mode 2), increasing numbers of vectors were used to reduce the full system of equations for the uniform surface heating problem. To illustrate the convergence of the reduced basis method, figure 7 shows the average absolute nodal error at  $t = 550$  sec as a function the number of vectors used in the solution. The error drops sharply from four to five vectors and is nearly constant after six vectors. For six vectors, the individual nodal errors ranged from  $0.1^{\circ}$  to  $1.7^{\circ}\text{R}$ . Including additional

vectors beyond six only lowered the maximum nodal error by  $0.2^{\circ}\text{R}$ . Results from the reduced basis method using six basis vectors are compared with the full system solution over the entire heat pulse in figure 8. Temperatures are shown for the surface, midpoint of the RSI, and the aluminum structure. The reduced basis temperatures agree very well with the full system results for this essentially 14 degrees of freedom problem. The temperatures indicate, that for the uniform surface heating, six mode shapes from a single eigenvalue problem based on initial temperature conditions give an excellent approximation to the full system solution.

### Symmetric Surface Heating

Since the set of eigenvectors from the eigenvalue problem based on the uniform initial temperature of  $560^{\circ}\text{R}$  proved effective for the uniform heating problem, a similar set was tried for the problem with a nonuniform but symmetric distribution of the applied heating. However, since these vectors were constant in the lateral direction they resulted in temperatures which approximated the average lateral temperature distribution from the full system solution. To obtain a closer approximation to the full system temperature solution, a set of basis vectors was generated from a second eigenvalue problem with thermal properties evaluated at temperatures from a "pseudo" steady-state problem. Time-dependent thermal properties and heat input were averaged over the heat pulse, and temperatures in the aluminum were held at a value expected during the mid-portion of the heat pulse ( $685^{\circ}\text{R}$ ) to define the steady-state problem. Only modes with a single wave in the lateral direction from the second eigenvalue problem were selected for use as basis vectors. In this instance, the single wave had a shape similar to the symmetric heating distribution. Sets of basis vectors which combined a constant vector with equal numbers of vectors from the initial temperature eigenvalue problem and the steady-state temperature eigenvalue problem were used to obtain approximate temperatures for the problem. The average absolute nodal temperature error at  $t = 300$  sec is plotted as a function of the number of vectors used in the reduction process in figure 9. The dramatic decrease in the error in going from 19 to 21 vectors indicates that some of the lower combined modes have only a small effect on the solution and could perhaps be eliminated from the solution. Obviously, other combinations of the initial and steady-state thermal modes should be tried to find the set which approximates the SPAR solution with the smallest number of vectors. Individual nodal temperature errors for the solution using 23 vectors were less than  $22^{\circ}\text{R}$  for the higher temperatures (in the RSI) and were no greater than  $2.2^{\circ}\text{R}$  in the aluminum structure. Figure 10 shows a comparison of temperatures from the 23-vector solution and the full system solution with essentially 42 degrees of freedom. Temperatures are shown for the surface, midpoint of the RSI, and the aluminum structure over the transient heat pulse. The agreement between the two solutions is very good and indicates that the reduced basis method, with about one-half the original degrees of freedom, can predict temperatures with reasonable accuracy for nonuniform symmetric heating.

## Asymmetric Surface Heating

Since the combined set of basis vectors using modes from the initial and pseudo steady-state temperature eigenvalue problems gave reasonable approximations for the problem with symmetric surface heating, similar combined sets of basis vectors were tried for the problem with asymmetric surface heating. Although several different combinations of these vectors were tried, errors in the nodal temperatures were as large as 200°R. The vectors from the pseudo steady-state problem with a single wave in the lateral direction contained large variations in the lateral direction (up to a factor of 9 compared to the variation in surface heating of 1.67). This seemed to preclude obtaining a good approximation to the full system solution. However, when a set of vectors which combined modes from the pseudo steady-state problem and edge-to-edge reflections of those modes was used a better approximation was obtained.

The average absolute nodal temperature error at  $t = 300$  sec for various numbers of vectors is shown in figure 11. The set of vectors begins with 12 vectors which included a constant vector, the reciprocal of the first mode from the initial temperature problem and five modes and their reflected images from the steady-state problem. Although the average errors are somewhat larger than those for the problem with symmetric heating, the maximum error for a single nodal temperature was less than 5 percent of the full system solution. Since the error in the temperatures seems to level out near 18 vectors, approximate temperatures were generated for the entire heat pulse using 18 vectors. Figure 12 shows a comparison of the temperatures from the reduced basis solution and temperatures from the full system solution. Temperatures are shown for the surface, midpoint of the RSI, and aluminum structure. Agreement between the reduced basis solution and the full system solution is reasonably good throughout the temperature history with the maximum error less than about 6 percent. Thus, for this 84 degrees of freedom problem, the reduced basis method gives good results with about one-quarter the original degrees of freedom.

## FUTURE WORK

Although the results presented herein for nonlinear transient thermal problems with essentially 14, 42, and 84 degrees of freedom indicate that the reduced basis method can provide reasonably accurate approximate temperature distributions with up to a factor of 4 reduction in the original degrees of freedom, considerable work will be required to realize the full potential of the method for such problems. Additional sources of basis vectors such as eigenvalue problems based on various nonlinear steady-state problems which characterize the transient problem, time derivatives of eigenvectors, and possibly one-dimensional eigenvectors (similar to the use of beam vibration modes in plate vibration problems) should be investigated. Successful implementation of the reduced basis method will also depend on development of ways for selecting the type and number of basis vectors needed for a given problem. Finally, ways of sensing and controlling the error in the reduced system of

equations will be required so that the process can be automated and cost comparisons made with full system solutions for problems with large degrees of freedom to determine the cost effectiveness of the reduced basis method for nonlinear transient thermal problems.

#### CONCLUDING REMARKS

The effort described in this paper is directed toward applying the reduced basis method to nonlinear transient thermal analysis. The method combines the classical Rayleigh-Ritz and modal superposition techniques with contemporary finite-element methods to retain modeling versatility as the degrees of freedom in the problem are reduced. The method has been used to obtain approximate solutions for the temperature history of a model of the Shuttle Orbiter wing subject to reentry heating. Results have been obtained for three heating cases: constant, symmetric, and asymmetric heating distributions applied to the outer Shuttle surface. Sets of basis vectors obtained from two thermal eigenvalue problems associated with the transient problems were used in the approximate solutions. The first eigenvalue problem was based on thermal properties evaluated at the initial temperature conditions for the transient problem. The second was based on thermal properties evaluated for a temperature distribution corresponding to a nonlinear steady-state problem with time-averaged thermal properties and heating from the transient problem. Good agreement was obtained between the reduced basis method and full system solutions for the problems with constant and symmetric applied heating distributions. For the asymmetric heating problem, the reduced basis method gave errors of about 6 percent in the nodal temperatures.

These results indicate that the method has potential for problem size reduction, but the success of the method strongly depends on the choice of basis vectors used to reduce the full system of equations. Future work will focus on the use of basis vectors from additional eigenvalue solutions based on alternate steady-state problems, time derivatives of eigenvectors, and possibly one-dimensional eigenvectors (analogous to the use of beam vibration modes in plate vibration problems). Methods for selecting the type and number of basis vectors needed for approximate solutions to more complex problems and application to transient thermal analysis of large space structures will be studied.

## REFERENCES

1. Noor, Ahmed K.: Recent Advances In Reduction Methods For Nonlinear Problems. Computers & Structures, Vol. 13, Pergammon Press Ltd., pp. 31-44, 1981.
2. Bathe, Klaus-Jürgen, and Gracewski, Sheryl: On Nonlinear Dynamic Analysis Using Substructuring and Mode Superposition. Computers & Structures, Vol. 13, Pergamon Press Ltd., pp. 699-707, 1981.
3. Rathjen, Kenneth A.: CAVE: A Computer Code for Two-Dimensional Transient Heating Analysis of Conceptual Thermal Protection Systems for Hypersonic Vehicles. NASA CR-2897, Nov. 1977.
4. Frisch, Harold P.: Thermally Induced Response of Flexible Structures: A Method for Analysis. J. Guidance and Control, Vol. 3, No. 1, Jan.-Feb. 1980.
5. Jones, G. K.; Skladany, J. T.; and Young, J. P.: Role of IAC In Large Space Systems Thermal Analysis. NASA CP 2216, Nov. 1981.
6. Shore, Charles P.: Status Report On Development of a Reduced-Basis Technique for Transient-Thermal Analysis. NASA CP 2216, Nov. 1981.
7. Marlowe, M. B.; Moore, R. A.; and Whetstone, W. D.: SPAR Thermal Analysis Processors Reference Manual, System Level 16, NASA CR-159162, 1979.

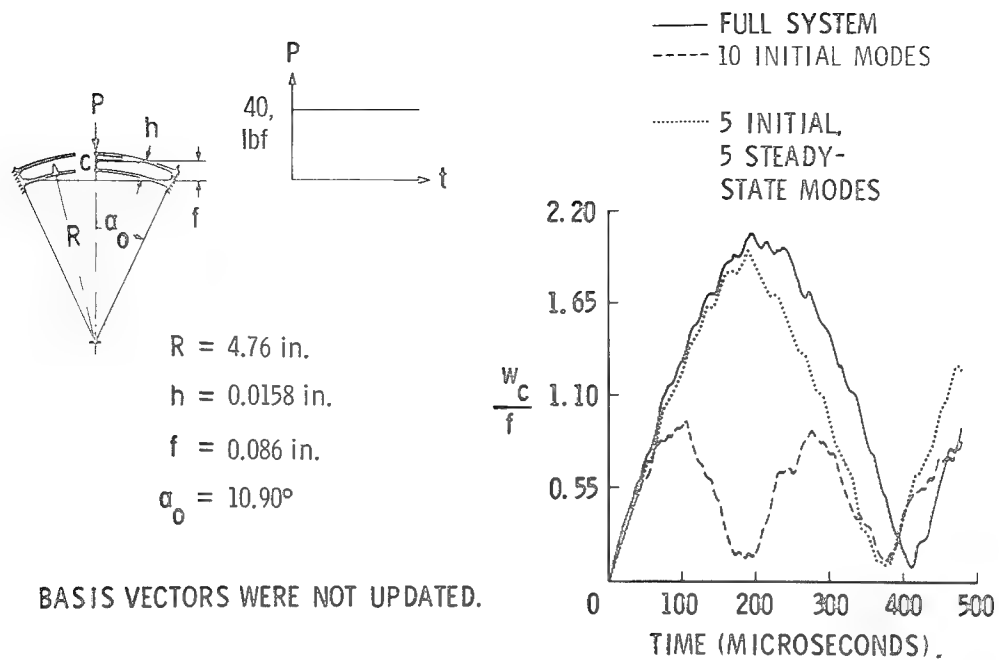


Figure 1 - Reduced basis results for transient vibrations of a clamped shallow spherical cap.

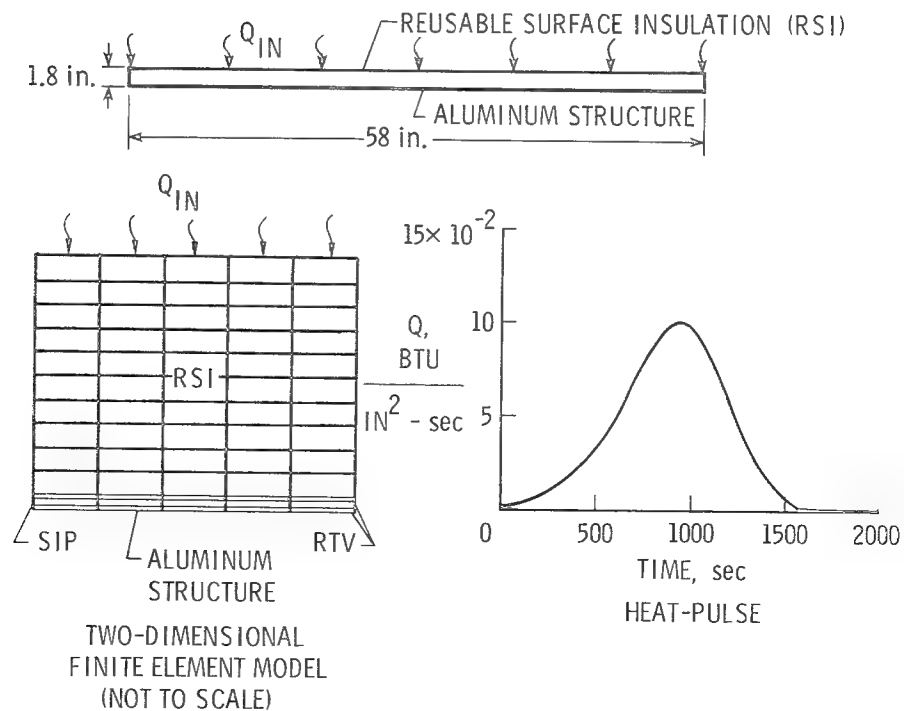


Figure 2 - Sample thermal problem.

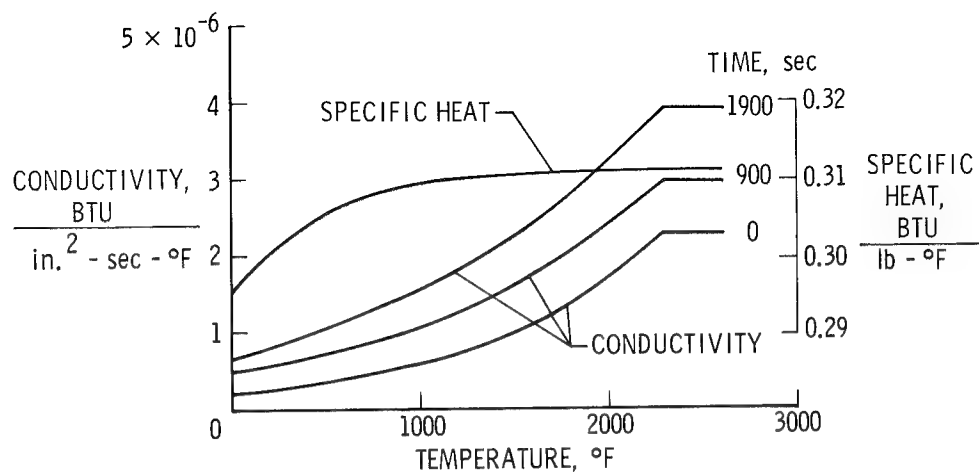


Figure 3 - Reusable Surface Insulation (RSI) thermal properties.

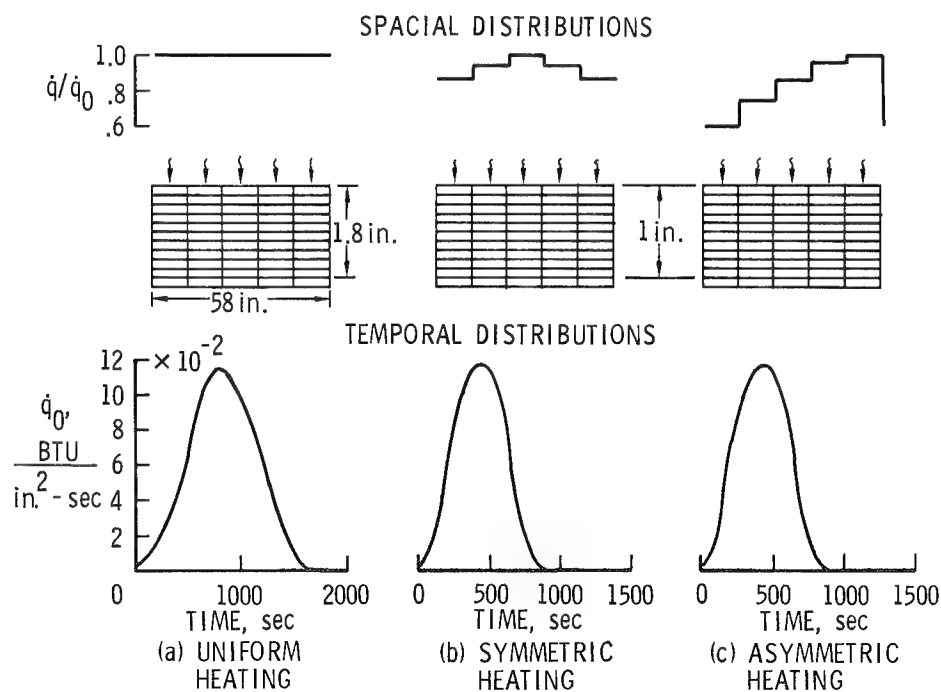


Figure 4 - Applied heating distributions for sample thermal problem.



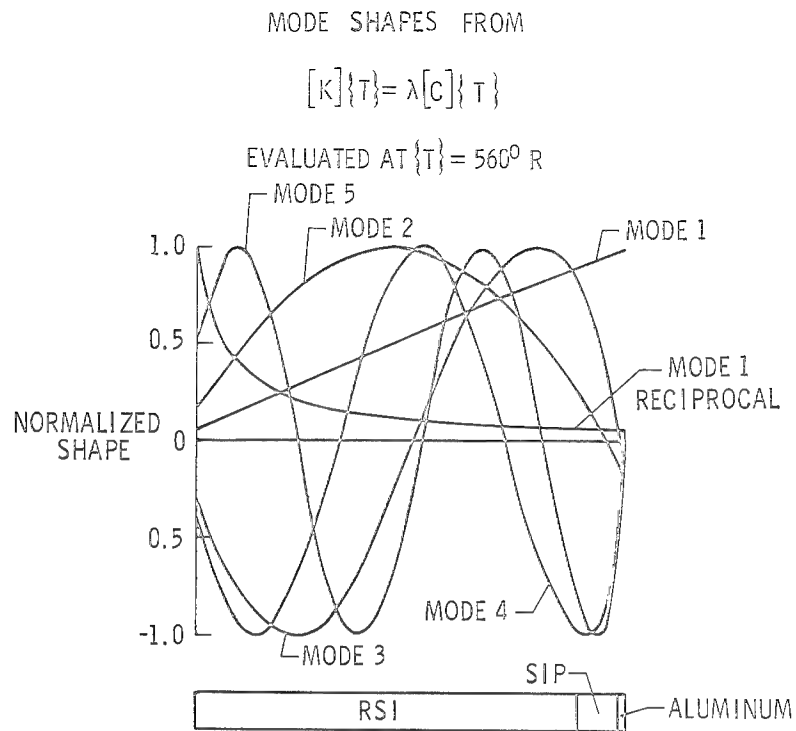


Figure 5 - Temperature profiles from full system solution for uniform heating.

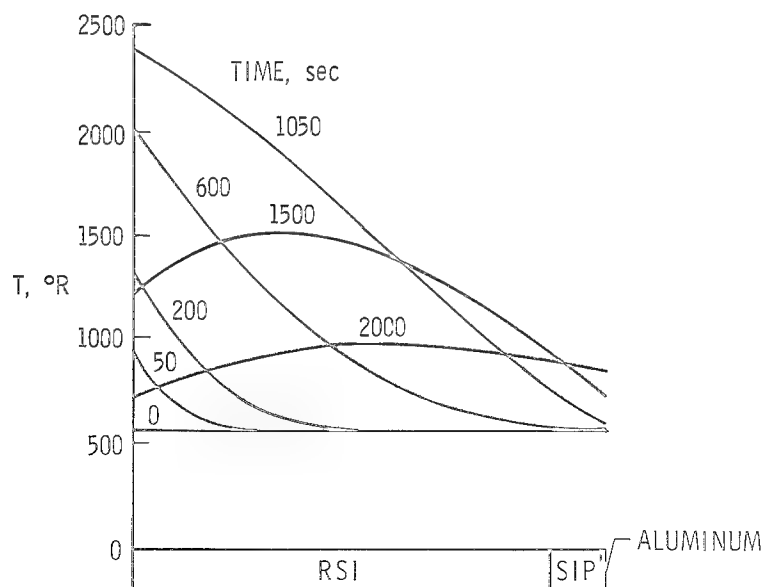


Figure 6 - Thermal mode shapes used as basis vectors for problem with uniform heating.

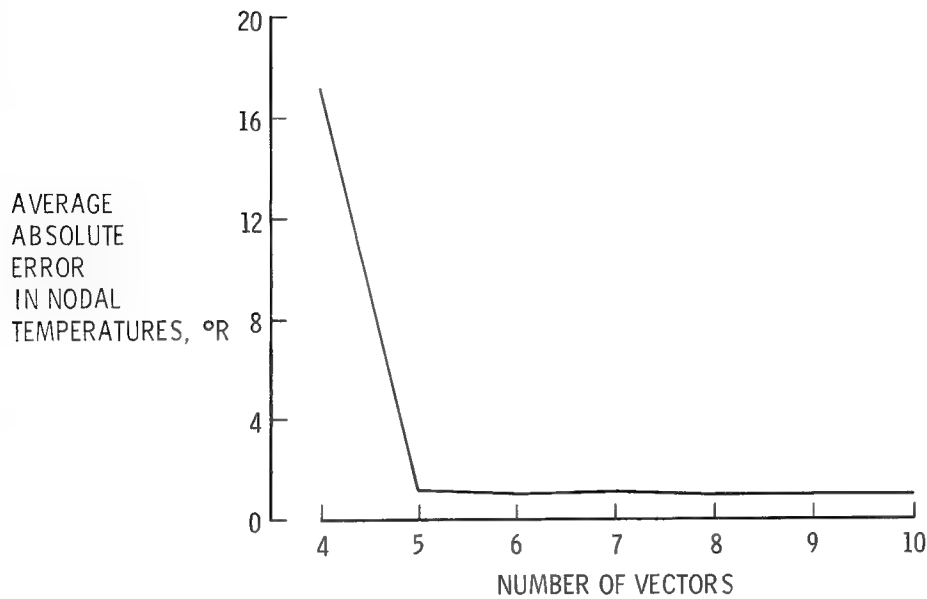


Figure 7 - Convergence of reduced basis method for problem with uniform heating at  $t = 550$  seconds.

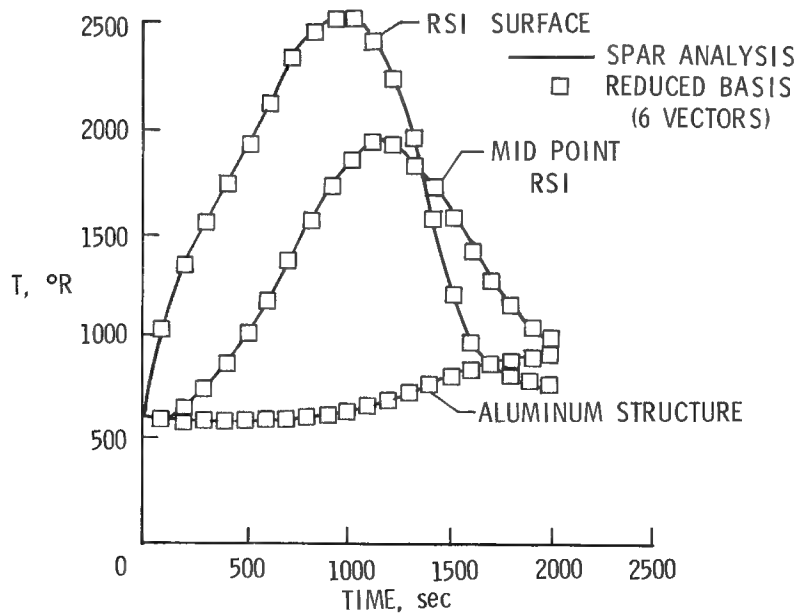


Figure 8 - Comparison of reduced basis and full system temperatures for problem with uniform heating.

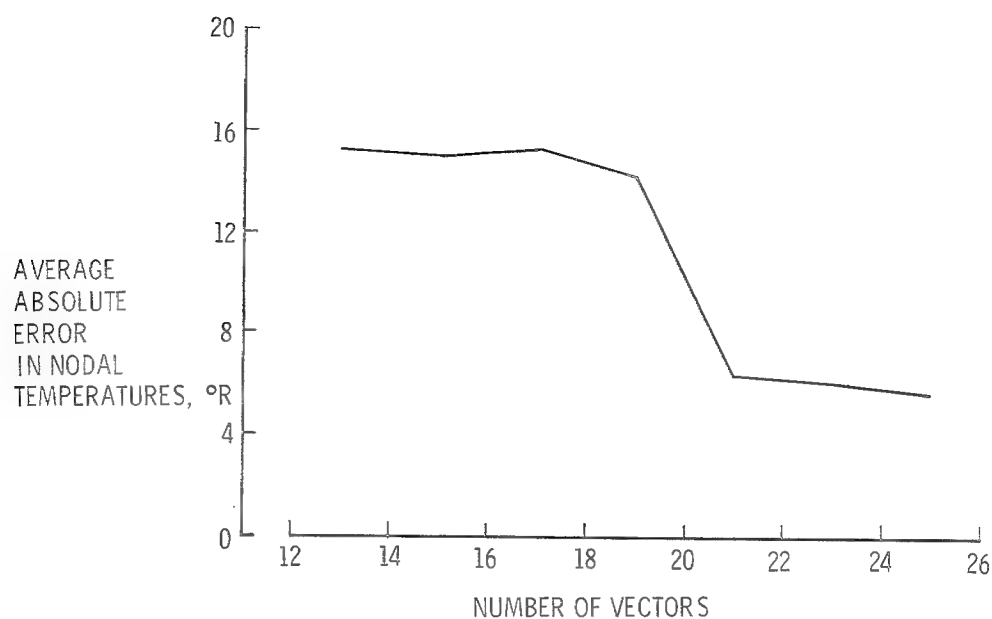


Figure 9 - Convergence of reduced basis method for problem with nonuniform symmetric heating at  $t = 300$  seconds.

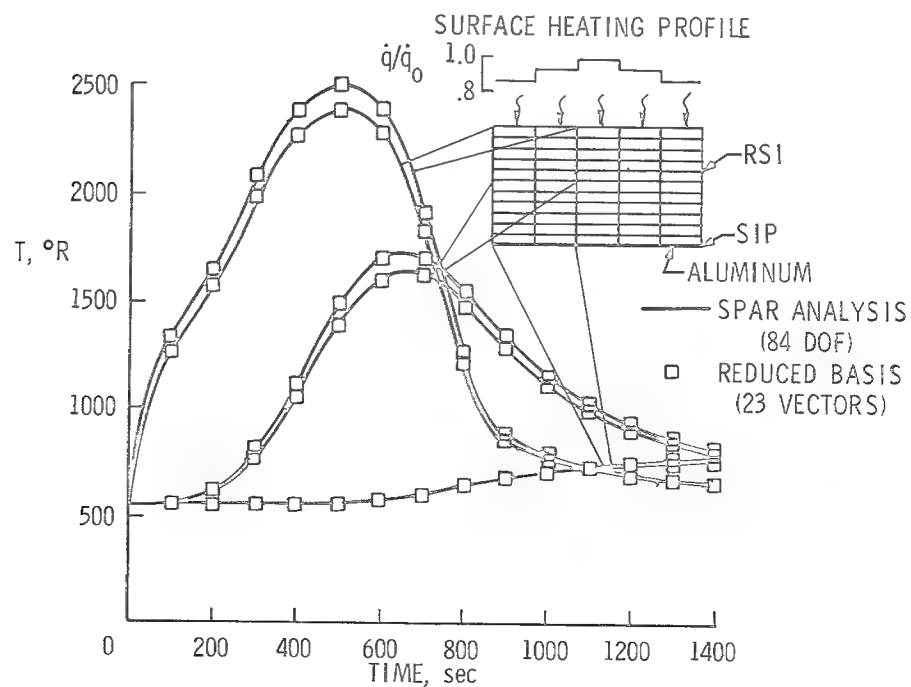


Figure 10 - Comparison of reduced basis and full system temperatures for problem with nonuniform symmetric heating.

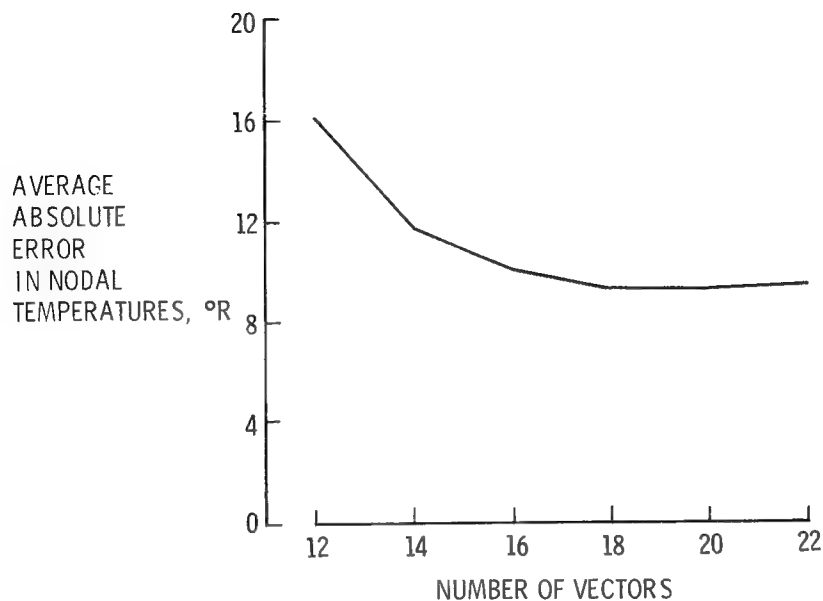


Figure 11 - Convergence of reduced basis method for problem with asymmetric heating at  $t = 300$  seconds.

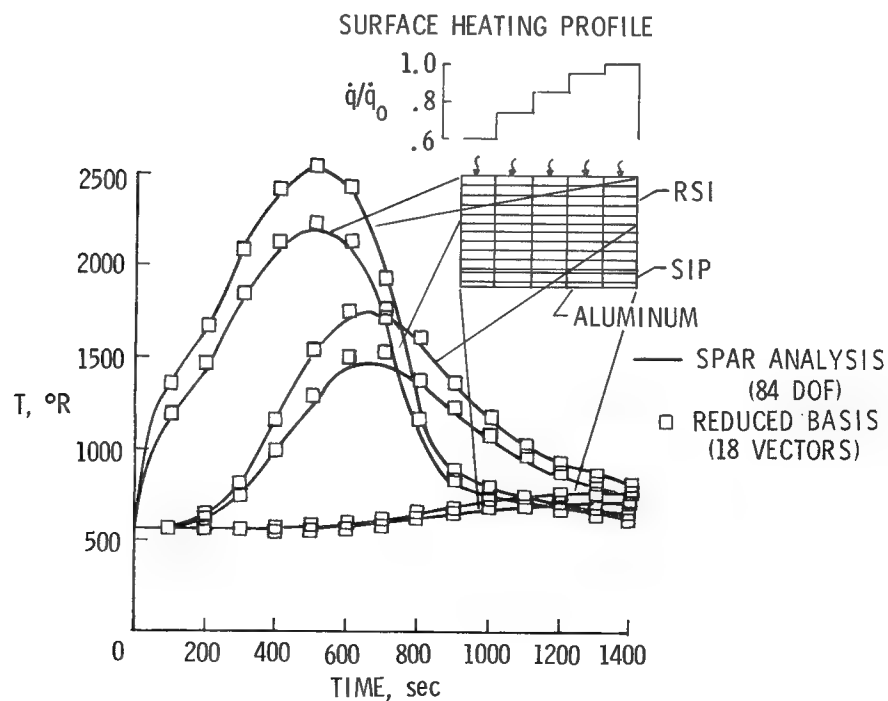


Figure 12 - Comparison of reduced basis and full system temperatures for problem with asymmetric heating.

# NONLINEAR CONSTITUTIVE THEORY FOR TURBINE ENGINE STRUCTURAL ANALYSIS

by

ROBERT L. THOMPSON  
NASA Lewis Research Center  
Cleveland, Ohio

## ABSTRACT

A number of viscoplastic constitutive theories and a conventional constitutive theory are evaluated and compared in their ability to predict nonlinear stress-strain behavior in gas turbine engine components at elevated temperatures. Specific application of these theories is directed towards the structural analysis of combustor liners undergoing transient, cyclic, thermomechanical load histories. The combustor liner material considered in this study is Hastelloy X. The material constants for each of the theories (as a function of temperature) are obtained from existing, published experimental data.

The viscoplastic theories and a conventional theory are incorporated into a general purpose, nonlinear, finite element computer program. Several numerical examples of combustor liner structural analysis using these theories are given to demonstrate their capabilities. Based on the numerical stress-strain results, the theories are evaluated and compared.

## INTRODUCTION

The development and implementation of new technology for more durable, reduced-weight, cost-effective gas turbine engine structures for the late 1980's is the objective of a recently expanded engine structures research program at the NASA Lewis Research Center. Coordinated programs involving in-house, university, and industry activities have been initiated to address difficult engine technological problems. Viscoplastic constitutive theories which model nonlinear material behavior are a part of this emerging technology which is receiving increased emphasis and use as an analytical tool for the structural analysis of turbine engine components. The severe internal thermomechanical environment in advanced turbine engines demands that these theories be used to predict cyclic stress-strain behavior. These theories are being developed because this new technology, although in its early stages of development, is inherently more suitable than the currently-used uncoupled plastic and creep

strain approach. This paper focuses on the development of this new technology as an analytical tool and the demonstration of the utility of this approach to engine structural analysis.

Specifically, this paper summarizes and evaluates the work detailed in references 1 and 2. In reference 1, an advanced three-dimensional transient heat transfer analysis code and an advanced three-dimensional nonlinear stress-strain analysis code were used to model and predict the cyclic thermal and structural responses of a simulated combustor liner specimen constructed from Hastelloy X. A conventional constitutive theory was used in the structural analysis. The information obtained from these analyses, i.e., temperatures, stresses and strains, was used in the cyclic life prediction technology evaluation for creep-fatigue interaction using existing analytical tools for crack initiation and propagation. In reference 2, the same combustor liner segment was analyzed using the same analysis procedures and codes; but instead of using a conventional constitutive theory in the structural analysis, three viscoplastic theories were used.

In this paper, both the conventional theory and viscoplastic theories used in the structural analysis of the combustor liner segment are described, including their development, determination of material constants for Hastelloy X, and implementation of the theories into the computer codes. This is followed by a brief, two-part description of the simulated combustor liner segment tested and analyzed. First, a description of how the combustor liner segment temperatures were obtained, both experimentally and analytically, is presented, since the strains in the combustor liner segment are predominately thermally induced. Second, the finite element model of the combustor liner segment and other assumptions required to perform the structural analysis are described. This is followed by a discussion of the analytical results of the structural analysis. Some additional testing required for the verification of the analyses is also discussed. Based on these analytical results, the conventional theory and the three viscoplastic theories are evaluated and assessed. Finally, future needs regarding improvements in existing structural analysis procedures and tools and the development of new ones for combustor liners are discussed.

#### CONVENTIONAL CONSTITUTIVE THEORY

In conventional theory, the total strain is additively split (decoupled) into elastic, plastic and creep components. Thus, this theory does not allow for simultaneous coupling between creep and plasticity. It also does not allow for effectively taking into account a variable strain rate. Both of these effects occur in combustor liners constructed from Hastelloy X material. Hastelloy X is highly strain rate sensitive at elevated temperature, i.e., creep and plasticity occur simultaneously. The differential heating and cooling of combustor liners produces a variable strain rate during the loading cycle. In analyzing the structural response of the combustor liner segment, procedures are developed for taking these effects into account in the conventional theory. These procedures are briefly described.

The MARC general purpose nonlinear finite element program (Ref. 3) was used to calculate the nonlinear stress-strain response of the combustor liner segment subjected to a complex cyclic thermomechanical load history. The conventional constitutive model incorporated in the MARC program was used in the structural analysis.

The time independent plasticity algorithm in MARC uses a tangent stiffness approach in which the stiffness matrix is updated and reassembled for every plastic loading increment. An iterative scheme is then used to calculate the response of the structure to each of the load increments. Convergence of this iterative scheme occurs when the strains used to estimate the stiffness matrix in the assembly phase are within a user's specified tolerance to the strains obtained in the solution phase. After convergence, stress and strain vectors are updated by adding the incremental values generated to the current values of these variables at the beginning of the increment. The program increments the next load and repeats the process. Incremental plastic deformation is based on the Prandtl-Reuss flow rule of conventional plasticity with a Von-Mises yield surface and a combined isotropic kinematic hardening rule.

The creep option in MARC allows time-dependent effects to be included by assuming the creep response equations are constitutive equations which are valid not only for constant stress histories, but also for general stress histories. The program option assumes the creep strain is independent of any prior plastic deformation. The program option also assumes that the nonlinearities due to the creep constitutive relation may be incorporated into a suitable load vector and treated by an initial strain technique.

At elevated temperature, materials such as Hastelloy X will exhibit time-dependent plastic behavior, i.e., highly strain-rate sensitive. Since the MARC plasticity algorithm has no provisions for a time-dependent plasticity theory, this phenomenon can be approximated in the MARC program by applying plasticity and creep alternately. A single cyclic plasticity model based on an estimated average strain rate was used together with a creep simulation to account for the time dependence at the lower strain rates. A brief description of the creep and plasticity program options and how they are used in this analysis are described below.

The plasticity model for the Hastelloy X material was developed and based on a trilinear representation of the monotonic tensile curves and cyclic hardening rule for a given strain rate. The monotonic stress-strain curves for temperatures between 1000°F (538°C) and 1800°F (982°C) in 200°F (93°C) increments were constructed from stabilized isothermal strain controlled test data at a strain rate of 0.008/min. This strain rate is representative of those determined from a preliminary structural analysis of the liner. The monotonic stress-strain curves were incorporated into a user subroutine in the MARC program.

A creep solution, which was activated alternatively with the plasticity solution, was included in the analysis to model the time-dependent material response of Hastelloy X at temperatures between 1300°F (704°C) and 1800°F (982°C). The simulation of the time-dependent material response at

these temperatures required that the creep tests be conducted for short time ( $< 1$  minute) high stress ( $\sigma > 0.5\sigma_{\text{yield}}$ ) conditions to obtain accurate material constants for the Hastelloy X material. These constants are needed in the creep equations. The final forms of the creep equations with the appropriate constants were incorporated into a user subroutine in MARC.

A series of isothermal tests using uniaxial Hastelloy X specimens was conducted to verify MARC stress-strain analytical predictions under monotonic and cyclic loading conditions. Some of these numerical predictions and test results are shown in Figure 1 for a temperature of 1800°F (982°C) under cyclic, strain-controlled loading between  $\pm 0.6$  percent strain. The predictions of the stress-strain loop at a strain rate of 0.008/min. are compared with test data at strain rates of 0.0024 and 0.024/min. The predicted results miss the knees of the hysteresis loops as well as the difference in the tension-compression stress levels. Because of these limitations and others discussed previously for the conventional theory, several viscoplastic constitutive theories were considered in the analysis.

## VISCOPLASTIC THEORIES

Ten viscoplastic (coupled plasticity and creep) constitutive models available in published literature were evaluated against a set of criteria (Ref. 2). Of the ten theories evaluated, three were selected for further evaluation based on their mechanisms for predicting cyclic hardening/softening and the limiting behavior of the state variables at small strain rates. Those selected were Walker's functional theory, Miller's theory, and Krieg, Swearingen and Rhode's theory, each of which is briefly described below. These theories, determined to be the most appropriate for describing material behavior of Hastelloy X at elevated temperature, were incorporated into the MARC nonlinear finite element code. The theories were calibrated against experimental data for Hastelloy X material. Finally, the most appropriate theory was applied to a three-dimensional finite element analysis of a combustor liner segment to predict its structural response.

### WALKER'S THEORY

Walker's functional theory (Ref. 2) was developed by modifying the constitutive relation for a three parameter viscoplastic solid. The two state variables in this theory, the equilibrium stress and the drag stress, account for the effects of viscoplasticity, i.e., the coupling of creep and plasticity. The equilibrium stress accounts for the Bauschinger effect by introducing nonlinear kinematic hardening into the model, while the drag stress accounts for the hardening/softening of the material by introducing isotropic hardening into the model. The growth laws for both the equilibrium and drag stresses contain dynamic work hardening and static thermal recovery terms. The theory models the cyclic hardening/softening of hysteresis loops without the use of a yield surface.

Creep, relaxation and strain-rate effects are modeled by assuming a power law for the inelastic strain rate. A limitation of this power law was noted by



Walker in that it is applicable to strain rates between  $10^{-6}$ /sec. and  $10^{-3}$ /sec. For strain rates greater than about  $10^{-2}$ /sec., the expression for the inelastic strain rate predicts stresses which are too large when compared to constant strain rate tensile test results. Walker's theory contains 14 temperature-dependent material constants. Determination of these constants requires cyclic isothermal strain-controlled uniaxial tests, as well as creep and relaxation tests.

#### MILLER'S THEORY

The formulation of Miller's theory (Ref. 4) is similar to Walker's theory. It includes the same state variables, the equilibrium stress and the drag stress state variables, which account for the Bauschinger effect and kinematic hardening, respectively. A hyperbolic sine function models the inelastic strain rate which includes the creep, relaxation and strain rate effects. Cyclic hardening/softening is modeled by the drag stress, not the equilibrium stress as in Walker's theory. The equilibrium stress contains a dynamic work hardening term and a static thermal recovery term.

To characterize the material behavior, Miller's theory requires that 12 material constants be determined from cyclic isothermal strain-controlled uniaxial tests, creep tests and relaxation tests. Of the 12 constants, nine are assumed to be independent of temperature; the other three are temperature dependent.

#### KRIEG, SWEARENGEN AND RHODE'S THEORY

This theory (Ref. 5) is also similar to Walker's theory in many respects. For example, in the formulation, a power law is used to model the inelastic strain rate, and the two state variables are the equilibrium stress and the drag stress. Cyclic hardening/softening can be modeled using the drag stress. The equilibrium stress equation contains two terms: a dynamic work hardening term and a static thermal recovery term. These terms, however, are different from those in Walker's theory. This difference results in generating hysteresis loops that have a trilinear character. Miller's theory also yields hysteresis loops that have this same character. Nine material constants are required to characterize the material behavior, all of which are assumed to be temperature dependent.

#### DIFFERENTIAL FORMS OF FUNCTIONAL THEORIES

The one-dimensional differential forms of Walker's theory, Miller's theory and Krieg, Swearngen and Rhode's theory are presented here for comparative purposes. They are derived from the three-dimensional differential forms presented in Ref. 2. The differential expressions for the equilibrium stress  $\sigma$ , drag stress  $K$ , and inelastic strain  $C$  are given below for each theory.

### Walker's Theory

$$\dot{\Omega} = (n_1 + n_2) \dot{\epsilon} - (\Omega - \dot{\Omega} - n_1 \epsilon) \left[ (n_3 + n_4 e^{-n_5 R} \frac{1}{R} + n_6 \Omega^{\frac{n-1}{2}}) \right] \quad (1)$$

$$K = K_1 - K_2 e^{-n_7 R} \quad (2)$$

$$\dot{\epsilon} = \dot{\epsilon} - \frac{\lambda + \mu}{\mu(3\lambda + 2\mu)} \dot{\sigma} = \frac{|\sigma - \Omega|^{n-1}}{K^n} (\sigma - \Omega) \quad (3)$$

The dot denotes differentiation with respect to time,  $R$  is the accumulation of inelastic strain,  $\epsilon$  is the total strain,  $\sigma$  is the stress, and  $\lambda$  and  $\mu$  are Lamé's constants. The material constants are  $\lambda$ ,  $\mu$ ,  $n$ ,  $m$ ,  $n_1$ ,  $n_2$ ,  $n_3$ ,  $n_4$ ,  $n_5$ ,  $n_6$ ,  $n_7$ ,  $K_1$ ,  $K_2$  and  $\Omega$ , all of which are temperature dependent.

### Miller's Theory

$$\dot{\Omega} = H_1 \dot{\epsilon} - H_1 B \theta' [\sinh(A_1 \Omega)]^n \frac{\Omega}{1 - \Omega} \quad (4)$$

$$\dot{K} = H_2 \dot{\epsilon} (C_2 + |\Omega| - A_2/A_1 K^3) - H_2 C_2 B \theta' [\sinh(A_2 K^3)]^n \quad (5)$$

$$\dot{\epsilon} = \dot{\epsilon} - \frac{\lambda + \mu}{\mu(3\lambda + 2\mu)} \dot{\sigma} = B \theta' [\sinh(\frac{\sigma - \Omega}{K})^{\frac{3}{2}}]^n \quad (6)$$

The  $\theta'$  that appears in the inelastic expression is calculated from the following expressions which are dependent upon the metal melting temperature,  $T_m$ .

$$\theta' = \theta + p \left[ -\frac{Q^*}{0.6 k T_m} \left( 1 + \ln \frac{0.6 T_m}{T} \right) \right] \text{ for } T < 0.6 T_m \quad (7)$$

$$\theta' = \theta + p \left( -\frac{Q^*}{k T} \right) \text{ for } T \geq 0.6 T_m \quad (8)$$

where  $T$  is the temperature in degrees Kelvin. The material constants  $n$ ,  $B$ ,  $H_1$ ,  $H_2$ ,  $A_1$ ,  $A_2$ ,  $C_2$ ,  $Q^*$  and  $k$  are independent of temperature;  $\lambda$ ,  $\mu$  and  $\theta'$  are temperature dependent. Note that  $k_0$  is the initial value of  $k$ .

### Krieg, Swearingen and Rhode's Theory

$$\dot{\Omega} = A_1 \dot{\epsilon} - A_2 \Omega |\Omega| (e^{A_3 \Omega^2} - 1) \quad (9)$$

$$\dot{K} = A_4 \dot{\epsilon} - A_5 (K - K_0)^n \quad (10)$$

$$\dot{\epsilon} = \dot{\epsilon} - \frac{\lambda + \mu}{\mu(3\lambda + 2\mu)} \dot{\sigma} = \frac{|\sigma - \Omega|^{n-1}}{K^n} (\sigma - \Omega) \quad (11)$$

The material constants  $\lambda$ ,  $\mu$ ,  $A_1$ ,  $A_2$ ,  $A_3$ ,  $A_4$ ,  $A_5$ ,  $n$  and  $K_0$  depend on temperature, where  $K_0$  is the initial value of  $K$ .

### DETERMINATION OF MATERIAL CONSTANTS

The material constants for Walker's theory, Miller's theory and Krieg, Swearingen and Rhode's theory were determined from uniaxial tests of Hastelloy X material. Test data were generated under cyclic strain-controlled

conditions for a range of temperatures from 800°F (427°C) to 1800°F (982°C) in increments of 200°F (93°C). Strain rates ranged from  $2 \times 10^{-2}$ /sec. to  $1.25 \times 10^{-6}$ /sec. for strain amplitudes of  $\pm 0.6$  and  $\pm 1.0$  percent strain. Creep and relaxation test data were also generated in order to obtain some of the material constants. Values of the material constants for each of theories are tabulated in Table I.

## COMPARISON OF THEORETICAL AND EXPERIMENTAL RESULTS

Based on the above one-dimensional differential equations with the appropriate material constants, Walker's theory, Miller's theory and Krieg, Swearengen and Rhode's theory were used to generate steady-state hysteresis loops for a range of temperatures and strain rates at a single strain amplitude. The predicted steady state hysteresis loops for Walker's theory, Miller's theory, and Krieg, Swearengen and Rhode's theory for a temperature of 1400° F (760° C) are shown in Figures 2 through 4, respectively. The corresponding experimental steady-state hysteresis loops are shown in Figure 5. The loops represent the predicted stress-strain behavior of the Hastelloy X for strain rates varying from  $3.9 \times 10^{-3}$ /sec. to  $1.2 \times 10^{-6}$ /sec. and for a strain amplitude of  $\pm 0.6$  percent strain. Both the theoretical and experimental data for a range of temperatures and strain rates are presented in Ref. 2.

Some of the salient features in the comparison of these curves are discussed. The peak stresses in the hysteresis loops predicted from Walker's theory agree with the experimental results. However, at the lower strain rates the theoretical predictions of the stress-strain behavior are too rounded at the knees, while at the higher strain rates the theoretical predictions are too square. Miller's theory, while predicting the peak stresses fairly accurately, exhibits a trilinear character of the hysteresis loops for all strain rates shown and does not predict the roundedness of the experimental loops. Krieg, Swearengen and Rhode's theory does not predict the peak stresses as accurately as Walker's theory or Miller's theory. In addition, the theoretical predictions of the hysteresis loops from this theory are too square for all the strain rates considered. The squareness of the hysteresis loop at the lower strain rates for each of the theories is attributed to two factors: (1) because the equilibrium stress saturates to a smaller value at low-strain rates due to static thermal recovery and (2) because the constants which govern the hardening rate of the equilibrium stress, e.g.,  $n_2$  in equation 1,  $H_1$  in equation 4, and  $A_1$  in equation 9, result in the equilibrium stress saturating more rapidly at low-strain rates. Most of the features discussed in this illustrative example are equally valid for temperatures between 1200° F (649° C) and 1800° F (982° C).

Both creep and relaxation tests were also conducted and the data obtained were compared with theoretical creep and relaxation predictions using the three theories. Experimental and predicted creep responses at various points on both the tension and compression loading branches are shown in Figures 6a and 6b for a temperature of 1600°F (871°C), a strain rate of  $3.7 \times 10^{-4}$ /sec., and a strain amplitude of  $\pm 0.6$  percent strain. Comparison of Walker's theory with experimental data shows good agreement. The creep response predicted by Krieg, Swearengen and Rhode's theory, although not

shown, is similar to Walker's theory. Because Miller's theory predicts the same response in tension and compression, only the results of compression creep are shown. Miller's theory predicts strains that are not as good as Walker's predictions at the lower compression stress levels, but predicts strains that are more accurate than Walker's theory at the higher compressive stress levels. Stress relaxation data were also generated and compared with theoretical results of the three theories. These comparisons are presented in Ref. 2.

### COMPUTER PROGRAM SIMULATIONS

The viscoplastic theories of Walker, Miller, and Krieg, Sweeney and Rhode were incorporated into the MARC program in their three-dimensional form by means of an initial-stress technique. In this technique, all the material nonlinearities are incorporated into an initial load vector and are treated as a pseudobody force in the finite element equilibrium equations.

The MARC nonlinear equilibrium equations governing the incremental response of the structures to an increment in load are generated from the principles of virtual work. The program assumes for a nonlinear structural problem, e.g., material nonlinearity, that the load history is divided into a number of incrementally applied load steps. Each load step is analyzed sequentially as a linear matrix problem using an appropriate stiffness matrix and load vector. At each load step, linear matrix methods are used to solve the incremental equilibrium equations, but the incremental equilibrium equations are nonlinear since the load vector depends on the displacement increment obtained in the solution of the incremental equilibrium equations. The computed displacement increment is compared with the initial displacement increment. If the computed increment is equal, within a user specified tolerance, to the initial value, the solution is assumed to have converged. Otherwise the process is repeated.

Each of the three theories was incorporated into the MARC program by means of a user-supplied subroutine. This user subroutine is called at each integration point in each element and supplies the elasticity matrix and the inelastic stress increment vector to the main program for each incrementally applied load step. However, because the constitutive theories form a "stiff" system of differential equations, the finite element load increment is split into a number of equal subincrements in the user subroutine, and the theories are integrated over the small subincrements for an accurate representation of the incremental constitutive equations. The integration of the constitutive equations for the theories is accomplished by means of an explicit Euler forward-difference method. This method is found to work efficiently and accurately provided the subincrement time steps are sufficiently small so as to avoid the numerical stability level of the Euler integration method. However, because the solution time required for a complete load increment integration depends linearly on the number of subincrements for this method, there was, and is, considerable incentive for reducing the number of subincrements required for each load increment.

Walker has developed a method for reducing the number of subincrements required within the user subroutine for his theory (see Ref. 3). The constitutive equations for Walker's theory are written in integral form and these equations are integrated over a subincrement using a recursive integration technique. This integration technique is sufficiently accurate, efficient and stable so that possibly only one subincrement per finite element load increment is needed. The method, however, requires that the input history for the load or strain and temperature, each with respect to time, be accurately modeled with piecewise constant values. Even with these restrictions, the accuracy and stability of the recursive integration scheme allow the use of large loading increments in a nonlinear structural finite element analysis, with a comparable reduction in computer-run time compared to the Euler forward-difference method.

At this point, the selection of the constitutive theories to be used in the structural analysis and their incorporation into a finite element computer program have been presented and discussed. Still to be determined before a structural analysis can be performed are the temperatures of the combustor liner segment.

#### COMBUSTOR LINER THERMAL ANALYSIS

Because very little experimental data for combustor liners are available, i.e., temperature and strain data, a well-controlled experimental program was conducted on a simulated combustor liner segment to obtain good temperature measurements (Ref. 1). Results from this program provided the accurate measured temperatures needed to compare with analytical temperature calculations, and the data to be used in the calibration, evaluation and verification of the various nonlinear constitutive theories to be analyzed. Strain measurements were not obtained because existing strain gages have a limited lifetime, perhaps less than two or three cycles, in the severe thermomechanical environment.

The selected component in the experimental program consisted of a simulated combustion chamber outer-liner segment, a stacked ring, louver configuration as shown in Figure 7. The test article was made of Hastelloy X. Cyclic engine level temperatures and temperature gradients were generated on the test article by using an induction heater in conjunction with a controlled cooling air temperature and flow rate. Induction heating, although not simulating an actual cyclic engine test with hot gases, is accurate to the extent that the metal temperatures and temperature gradients can be simulated. The test rig, procedures and data obtained are described in Ref. 1.

The test program, conducted under accelerated cyclic thermal loading with a 90-second thermal cycle, provided the temperature and structural responses, and failure data for comparison with analytical results. The representative transient and steady-state measured temperature distribution responses at several thermocouple locations on the combustor liner are shown in Figure 8. Because the experimental program did not provide sufficient temperature information for a detailed structural analysis, additional data were obtained from a transient, three-dimensional heat transfer analysis of the combustor liner specimen. The experimental data were used as input data to this analysis and to verify the analytical results.

To obtain accurate temperatures requires the discretization of a section of the liner into a series of thermal finite elements, with a higher density of thermal elements around the cooling holes and in the lip region, i.e., those critical areas where either cracking or buckling could occur. This may not be known a priori and could require an iterative solution involving refinement of the thermal mesh. Boundary conditions which are also important in any thermal analysis for accurate temperature predictions, and especially a transient analysis such as this, are the surrounding temperature, heat loads (fluxes), and heat transfer coefficients along the surface of the model. For the transient analysis, not only must the external boundary conditions (film coefficients, surrounding temperature, gas temperature, gas flow rates and internal heat generation) be specified, but the metal thermophysical properties such as thermal conductivity and specific heat must be specified as functions of temperature and time. Other variables which should be included in the thermal analysis are the emissivity, absorptivity and reflectivity of the metal surfaces. Also, depending on the complexity of the geometry, the view factor which affects the radiative heat loss should also be included in the thermal analysis. Each of these factors was accounted for in the thermal analysis of the combustor liner segment.

Based on the model discretization and boundary conditions, a thermal analysis of the combustor liner segment was performed. When the steady-state experimental surface temperatures of a louver section were compared with the theoretical results, it was found that the predicted temperatures were hotter, with the greatest differences between them being about 65°F (36°C). Since greater accuracy is required to compute stresses from the conventional and viscoplastic constitutive theories, some of the thermal variables were modified. The greatest degree of uncertainty was associated with the heat transfer coefficients. Therefore, in order to match the experimental with theoretical temperatures, modification of about 50 percent over the original heat transfer coefficients was required. For the transient analysis, the modified values of the heat transfer coefficients were held constant. This was a good assumption since the cooling air temperature and flow rate remained constant during the tests. As shown in Figure 9, comparison of predicted steady-state and transient temperature responses with measured data showed good agreement. The transient heat transfer solution was used to create transient incremental temperatures which were used as input to the structural analysis in which both the conventional and viscoplastic theories were used.

#### STRUCTURES FINITE ELEMENT MODEL

The three-dimensional finite element model of the combustor liner louver segment is shown in Figure 10. The model contains an included angle of 0.577 degree which represents the angle between planes of radial symmetry of two adjacent cooling holes. The model consists of 30, 20-node isoparametric brick elements of which 21 have reduced integration points (8 Gaussian points). The 10 remaining elements are full integration point elements (27 Gaussian points) and are used around the cooling holes since reduced integration point elements are unreliable for distorted shapes. The small model size and the reduced integration point elements were selected to minimize the computer execution time while still being adequate to verify the analysis procedures.

The finite element model was only a small portion of the complete shell structure. This required that appropriate boundary conditions be determined to simulate the effect of the complete shell structure and a series of louvers. The technique for connecting louver segments is described in Ref. 1. Basically, it permitted only radial displacements along radial edge planes of the louver segment modeled, and it required that the radial displacement on the front plane of the louver be related linearly to the radial displacements on the rear plane of the louver. An additional constraint on the front and rear planes was that the axial slopes of these planes must be equal.

The three-dimensional model used 640K double precision words of storage on the IBM 370/3033 computer system. The loading cycles required 78 MARC viscoplastic increments for the conventional theory and 121 MARC increments for the viscoplastic theory. Each loading cycle for both theories required about 45 minutes of computer-run time.

#### THERMAL INCREMENT FILE

The thermal increment file generated from the heat transfer analysis was used to impose the temperature increments in the loading sequence for the louver structural analysis. For each loading increment, the mechanical pressure load increment was applied, followed by the thermal load increment. The finite difference mesh size used for the heat transfer analysis was based on locating temperature solution points close to the finite element integration points used in the structural analysis to minimize the spatial interpolation of the temperatures. A general interpolator was used to generate the thermal increment file and to perform the required spatial interpolations between the two meshes. However, the interpolator was not successful in that temperatures at the integration points could not be obtained within 50°F (30°C) of the desired value from the heat transfer analysis. Thus, the finite difference thermal increment file required a considerable amount of manual modification of the temperature increments.

#### ANALYTICAL RESULTS - CONVENTIONAL THEORY

For the combustor liner specimen tested, the fatigue critical location occurred at the edge of the louver lip. The observed failure mode was axial cracking propagating from the edge toward the weld. Preliminary results of the structural analysis indicated that this location experiences a uniaxial stress field where the stress is circumferential (hoop stress). Although the predicted stress-strain response at each integration point was calculated and analyzed, the integration point closest to the louver lip was used to define the response since this is where the cracking occurred. First, the analytical results for the conventional theory are presented, followed by the results for the viscoplastic theories.

The finite element model of the louver liner, shown in Figure 10, was run through six thermomechanical load cycles. The predicted hoop stress/mechanical strain history at the integration point closest to the lip for these cycles is shown in Figure 11. During the heat-up portion (refer to Figure 3) the lip goes into compression, and at point B, the strain becomes



inelastic as a result of the time-independent plastic strain and the time-dependent creep strain. The letter designations on these curves are consistent with those on the temperature history plot shown in Figure 9. During the constant temperature portion of the cycle, creep strain is the predominant strain, from point C to point D. On the cooldown portion of the cycle, D to A, the lip goes into tension, and near the end of the cycle some inelastic strain occurs. Because the inelastic strains are not fully reversed, the stress range increases in each cycle causing the ratcheting of the stress-strain response. Cycles 2-5 ratchet in the negative strain direction and show progressively higher peak tensile stresses during the cooldown portion of each cycle. Also, the cyclic plasticity decreases during the cycling which results in a narrowing of the stress-strain curves. It is believed that because of the cyclic hardening model used, a number of loading cycles are required before a stabilized stress-strain response can be achieved at each location in the louver liner. As stated previously, in this analysis the strain rate sensitivity and the coupling of creep and plasticity have only been approximated. These approximations and their effect on the stress-strain curves in Figure 11 have yet to be fully determined.

Having obtained a predicted hoop stress/hoop strain loop at the end of the louver lip based on calculated temperatures, a semiempirical material model, a partial finite element model, and the other assumptions previously discussed, there is a question with regard to the accuracy of the numerical results. Of particular concern is the selection of the material model (conventional constitutive theory) which, to a large extent, determines the predicted structural response. The material modeling variables were calculated from isothermal test data for a fixed strain rate. The actual component response, however, underwent simultaneously varying strain rate and temperature conditions, which are significantly different from the assumed modeling conditions. To verify the material modeling and to improve the model calibration, uniaxial testing of a smooth cylindrical specimen under strain-controlled conditions was conducted to provide material response data under a more realistic thermomechanical load history.

From the three-dimensional structural analysis, the predicted circumferential mechanical hoop strain as a function of the temperature history at the edge of the louver lip was used to define the test specimen conditions. Applying this cyclic temperature versus mechanical strain history to a uniaxial cylindrical specimen of Hastelloy X, thermomechanical loops were generated. This test is known as a "faithful cycle" test because it faithfully represents the true thermomechanical behavior of the combustor liner configuration. Since the louver lip experiences only a uniaxial stress (hoop stress), the stress-strain response of a uniaxial test specimen can be considered to be representative of the actual hoop stress occurring at the louver lip. The faithful cycle of the sixth thermal load cycle is shown in Figure 12.

Figure 13 shows a comparison of the experimental data with the numerical results for the uniaxial test specimen. The experimental hysteresis loop stabilized after only a few cycles, whereas the predicted hysteresis loop did not stabilize after six cycles, and even after 15 cycles the predicted loop still had not stabilized. A summary of analytical results are: there was cyclic hardening occurring during the first 15 loading cycles; the



stress-strain response did not stabilize for the thermomechanical loop considered; and cyclic plasticity was decreasing during the cycling which resulted in a narrowing of the stress-strain curves. Since none of these results was observed from the tests, they may be material model dependent. The conclusion is that future modification and improvements of the material modeling using conventional theories are required to accurately reproduce the thermomechanical stress-strain response of Hastelloy X.

## EVALUATION OF VISCOPLASTIC THEORIES

An alternative to conventional theory is to use nonlinear viscoplastic theories since they do not have many of the limitations of the conventional theory, as discussed previously. Three viscoplastic theories were evaluated. The evaluation of Walker's theory, Miller's theory and Krieg, Swarengen and Rhode's theory was based on the comparison of predicted results with experimental data obtained from uniaxial tests described in the previous section. The "faithful cycle" (see Fig. 12) was used to evaluate the three viscoplastic theories. The most suitable of these theories was then used to predict the nonlinear three-dimensional structural response of the simulated louver liner.

The experimental results (shown in Figure 13) are compared with the numerical results obtained from the MARC program using the three viscoplastic theories. The uniaxial test specimen was modeled as an axisymmetric problem with four ring elements with appropriate boundary conditions. Incremental displacements which follow the mechanical strain history were given to the appropriate nodes, while each integration point of each element was given incremental temperature variations which follow the temperature history. Thermomechanical hysteresis loops were produced by integrating the theories around the faithful cycle. The loops predicted by Walker, Miller, and Krieg, Swarengen and Rhodes's theories are shown in Figures 14 through 16, respectively. From points A to B on the hysteresis loops, the loading portion of the curves, the temperature increased from 940°F (504°C) to 1750°F (954°C). From points B to C, the temperature remained constant at 1750°F (954°C). Stress relaxation occurred during this portion of the cycle. On the unloading branch, from points C to A, the temperature decreased almost linearly to 940°F (504°C).

Figure 14 shows the thermomechanical hysteresis loop predicted by Walker's theory. From points B to C, the theory predicts a relatively small amount of stress relaxation, although none is observed in the experimental response shown in Figure 13. In the tensile portion of the curve, the unloading portion C to A, the theory predicts some tensile yielding, but not at the same mechanical strain as the experimental response. In the compressive portion of the loading curve, the theory predicts some compressive yielding which is consistent with the experimental response. The cycles of the hysteresis loops show a progressive decrease in the stress relaxation at points B which result from the progressively lower stress levels at point B after each cycle. The loops stabilize as the stress relaxation decreases after about three cycles which is in agreement with experimental data.

The thermomechanical hysteresis loop predicted by Miller's theory is shown in Figure 15. Contrary to the experimental results, the theory predicts a large amount of stress relaxation at the maximum hold temperatures, points B to C. From points C to A, the tensile portion of the loop (cooldown phase), the theory predicts a linear behavior which is not observed experimentally. Experimental results show some tensile yielding in this region.

Figure 16 shows the thermomechanical loop predicted by Krieg, Swearngen and Rhode's theory. Only a relatively small amount of stress relaxation, points B to C, is predicted by the theory at the maximum hold temperature. Some tensile yielding, comparable to Walker's theory, occurs late in the tensile portion of the loading, but at a strain much different than the experimental response. There is also a slight stress dip at the top of the tensile portion of the loop which is not observed experimentally. The loop, like Miller's theory, stabilizes in one cycle.

Comparison of the experimental and theoretical hysteresis loops generated using the faithful cycle shows the theoretical predictions using Walker's theory and Krieg, Swearngen and Rhode's theory to be in reasonably good agreement with the experimental data, whereas Miller's theory does not agree. Comparing Walker's theory to Krieg, Swearngen and Rhodes's theory for constant temperature experimental hysteresis loops, together with creep predictions, Walker's theory gives better results. Although none of these theories accurately predicts the hysteresis loops below temperatures of about 1200°F (649°C), Walker's theory provides better results when compared with experimental data. Also, two phenomena occur below temperatures of about 1200°F (649°C) which are not modeled by the theories, although it is believed that Walker's theory can be modified to incorporate these effects. The first of these phenomena is that below a temperature of 1200°F (649°C) the hysteresis loops become progressively less strain-rate sensitive. A second phenomenon that occurs at temperatures near 1100°F (593°C) is the inverse strain-rate effect attributable to a strain age-hardening mechanism. This means as the strain rate decreases the peak stresses of the hysteresis loops in both tension and compression increase. Based on these considerations and in view of the favorable comparison of the experimental and theoretical results, Walker's theory was chosen to perform the structural analysis of the simulated combustor liner segment.

#### ANALYTICAL RESULTS - VISCOPLASTIC THEORY (WALKER)

A three-dimensional inelastic finite element analysis of the simulated combustor liner segment was performed using MARC. The analysis of the liner segment was identical to that conducted using the classical constitutive theory available in MARC except that Walker's functional theory was used. For example, the three-dimensional finite element model of the combustor liner specimen (Fig. 10), types of elements, boundary conditions, faithful cycle (Fig. 12) and thermal increment file used were identical to those used for the investigation of the classical constitutive theory. The results are shown only for the integration point closest to the end of the louver lip since this is the critical fatigue location, as explained previously.

Figure 17 shows the louver lip hoop stress as a function of hoop mechanical strain for two thermal load cycles. The analysis predicts a thermomechanical response which exhibits an apparent ratcheting in the negative strain direction. This ratcheting may be attributed to the more nearly elastic behavior observed in the low-temperature tensile portion of the hysteresis loop. In the experimental hysteresis loop (Fig. 13), more tensile yielding is observed. At the maximum tensile stress in the loop, a stress dip phenomenon is calculated. This phenomenon may result since the theory does not accurately predict the hysteresis loops at low temperatures. This might also explain why there is less tensile yielding occurring during the loading portion of the curve. Neither the excessive elastic behavior nor the stress dip phenomenon is observed in the experimental hysteresis loop (Fig 13). At the maximum compressive stress in the loop, there is very little relaxation occurring during the maximum hold period. This agrees with the experimental hysteresis loop where both creep and plasticity appear to be occurring simultaneously.

The predicted stress dip phenomenon that occurs in the maximum tensile portion of the loop may be attributed to two factors. First, since Walker's theory cannot produce a rate-insensitive response at the relatively low temperatures, corresponding to the maximum tension, the material may be relaxing at the small strain rates. Second, during the elastic loading portion of the loop the equilibrium stress remains essentially constant and is temperature independent. Because the equilibrium stress remains constant during this elastic excursion, when yielding does occur, the strain will grow very rapidly. This rapid growth may produce the dip in the tensile stress.

The stress dip phenomenon may be avoided with two changes to Walker's theory. First, the equation governing the growth of the equilibrium stress can be changed to incorporate a temperature rate term so that the equilibrium stress can grow with temperature during an elastic excursion. Second, the instantaneous stress response can be assumed to be inelastic rather than elastic. This could be accomplished with a growth law similar to that assumed for the equilibrium stress, with the result being a rate-insensitive response at lower temperatures.

#### SUMMARY OF RESULTS

The results of the evaluation of the conventional theory and viscoplastic theories used in the structural analysis of the combustor liner segment can be summarized as follows:

1. Comparison of the experimental data with the theoretical results indicated that neither the conventional theory nor the viscoplastic theory accurately predicted the cyclic thermomechanical response at the critical fatigue failure location. The thermomechanical loops generated with these theories exhibited continued cyclic hardening and ratcheting after many cycles. Tests of a uniaxial strain-controlled specimen cycled through a temperature-strain history as computed for the three-dimensional structural analysis showed that the response stabilized after a few cycles.

2. Viscoplastic theories can predict the rate-dependent response of Hastelloy X with adequate accuracy under uniaxial isothermal loading conditions for temperatures ranging from 1200° F (648° C) to 1800° F (982° C).

3. There was difficulty in consistently determining accurate temperatures for the structural integration points from the thermal nodes because of the different heat transfer and structural finite element meshes used.

4. For a thermomechanical load cycle, computer-run time for a three-dimensional structural analysis of the combustor liner segment using the viscoplastic theory was about the same as an analysis using the conventional theory. However, the new integration scheme developed by Walker for reducing the number of subincrements required for each load increment for a viscoplastic theory could result in a substantial reduction in computer-run time over the conventional theory approach.

#### FUTURE RESEARCH

Current structural analysis activities for the development and design of gas turbine engine hot section components are and have been limited, for the most part, to linear, one- and two-dimensional (axisymmetric), steady-state analyses. This is due to a number of factors such as availability of accurate, efficient and usable viscoplastic theories, complex geometric modeling requirements, limited interdisciplinary interactions, availability of software computer programs, computer hardware limitations and limited experimental data with which to compare, evaluate and verify analytical results.

Detailed investigations of transient, nonlinear, three-dimensional structural analyses and life prediction of combustor liners have, for the most part, not been attempted. However, because of the need to be able to analyze hot section structural components and to predict their life with some certainty, work is beginning in many of these areas, as outlined above. One of the most comprehensive investigations undertaken to date and summarized here, for the structural analysis and durability analysis of a simulated combustor liner segment, was accomplished by the programs described in references 1 and 2. Certainly one of the significant results of these programs was the identification of those areas of the analysis which are weak, and therefore need to be improved. Some of these weaknesses are described below.

Viscoplastic constitutive theories used to characterize nonlinear material behavior at high temperatures are not being used as analysis and design tools for combustor liner structural analyses as yet because they have not been fully developed. These theories could require as many as 14 material constants be determined from experimental data, and many of these constants are most likely temperature dependent. This imposes a severe burden on the test facilities if a number of materials are to be considered. Furthermore, viscoplastic theories are not easily adaptable for incorporation into nonlinear finite element programs. There are only a few nonlinear finite element programs which have provisions for incorporating these types of

theories. Even if the theories can be incorporated into computer programs, the analyst still needs to be familiar with the program and with the software programming.

The complex geometry of existing, as well as structurally advanced, combustor liners complicates the structural finite element modeling. Not only are large numbers of finite elements required for the structural analyses of existing and advanced combustor liners, or even a segment of a liner, but three-dimensional finite elements are also necessary. There is, therefore, a need to generate and analyze finite element models automatically using a self-adaptive solution strategy.

Another factor which limits the structural analysis of combustor liners is the interaction of several disciplines. Since temperatures and temperature gradients are required for the structural analysis, researchers in the heat transfer and structures disciplines must interact in order to transfer the thermal information from the heat transfer computer program to the structural analysis computer program accurately and efficiently. There must also be some interaction between the structures and life prediction disciplines since the output of the structural analysis is needed to perform the durability assessment. To a lesser degree, and not discussed previously, some interaction between the structures, and the material and aerodynamics disciplines is also required so that a totally integrated aerothermal-structural-life analysis of a combustor liner can be performed.

Nonlinear structural analyses of hot section engine components are also limited because there are but a few nonlinear finite element structural analysis codes available. The complexities of these codes limit their utility many times because of limited documentation and/or complex sets of input. Many programs are designed to be general purpose codes, and so they tend to be inefficient for component specific nonlinear structural analyses. This condition is expected to worsen, especially for very large finite element models and nonlinear material modeling required for structural analysis and assessment of advanced combustor liner structural concepts. It is possible that for the finite element models required, as well as the other analysis requirements, existing large mainframe computers could be saturated in terms of their storage capacity with as few as 100 three-dimensional 20-node brick elements.

Limited experimental data is another contributing factor which impacts and restricts the structural analysis of engine hot section components. Only limited data are available for characterizing material behavior at elevated temperatures. For the most part, the data have been obtained from isothermal, fast response time and uniaxial specimen tests. Some creep data are available, but they too are limited. There are limited data available for a wide range of temperatures and strain rates for any candidate material for a combustor liner application with the exception of Hastelloy X. Experimental data obtained from full-scale combustor liner tests, or even segment tests, are also limited, with most of the data being temperature data. No quantitative strain data have been obtained for the structural response. Multiaxial cyclic testing under isothermal and nonisothermal conditions at several strain rates needs to be done. Strain measurement data for a

combustor liner subjected to a severe cyclic thermomechanical environment have not been obtained because existing strain gages have a limited lifetime in this environment.

Following is a summary of the major needs which should be addressed in order to perform a thorough and complete heat transfer and structural analysis of a combustor liner.

1. Develop new and improve existing nonlinear constitutive theories.
2. Develop more efficient, accurate, affordable and user-friendly component-related nonlinear structural and heat transfer analysis codes.
3. Develop data communication linkages between thermal-structural-life-prediction analysis codes.
4. Establish coordinated, well-controlled experimental/analytical programs.
5. Develop durable, accurate instrumentation.
6. Perform multiaxial tests for isothermal and nonisothermal conditions at variable strain rates.

Each of these identifiable needs is being considered or addressed in NASA Lewis' Engine Structures Programs, which are broad in scope. The Hot Section Technology Systems Program ((HOST), Ref. 6), for example, currently underway at NASA Lewis, is addressing many of the needs cited above. The basic intent of this program is to integrate existing analytical methodologies and technologies which have remained segmented up to now, to extend existing analytical methodologies and technologies where appropriate, and to conduct experiments to verify analysis methodologies. Another Lewis program which complements the HOST program is the development and implementation of nonlinear constitutive theories for structural analysis of combustor liners. The intent of this program is to broaden the basic knowledge and understanding of material nonlinear behavior when subjected to complex cyclic thermomechanical load histories at elevated temperatures. Researchers from industry, universities and NASA Lewis are participating in this program. NASA Lewis' involvement will be to integrate the activities of industry and universities to develop a coordinated, mutually beneficial program, as well as to provide an independent evaluation and assessment of the theories and methodologies developed. The overall objective is the pooling of resources available from industry/universities/NASA for the purpose of developing and implementing nonlinear constitutive relations which can be used to accurately and efficiently predict the stress-strain response of hot section components. This, in turn, will have a significant impact on improving the fundamental technology of structural analysis and life prediction of engine components that will operate in a severe, complex, cyclic, thermomechanical environment.

## REFERENCES

1. Moreno, V.: Combustor Liner Durability Analysis, NASA CR-165250, February 1981.
2. Walker, K. P.: Research and Development Program for Nonlinear Structural Modeling With Advanced Time Temperature Dependent Constitutive Relationships, NASA CR-165533, November 1981.
3. MARC - General Purpose Finite Element Program, Vol 1-4, MARC Analysis Research Corp., Palo Alto, California.
4. Miller, A. K. : An Inelastic Constitutive Model for Monotonic, Cyclic and Creep Deformation: Part I - Equations Development and Analytical Procedures and Part II - Application to Type 304 Stainless Steel. ASME J. Eng. Mat. and Tech., Vol. 98, pp. 97-113, 1976.
5. Krieg, R. D., J. C. Swearingen, and Rhode, R. W.: A Physically Based Internal Variable Model for Rate-Dependent Plasticity. In: Inelastic Behavior of Pressure Vessel and Piping Components. ASME, PVP-PB-028, pp. 15-28, 1978.
6. Gauntner, D. J., and Ensign, C. R.: An Introduction to NASA's Turbine Engine Host Section Technology (HOST) Project, NASA CP 2190, May 1981.



TABLE I  
MATERIAL CONSTANTS FOR VISCOPLASTIC THEORIES

Walker's Theory

Material Constant	800° F (427° C)	1000° F (537° C)	1200° F (648° C)	1400° F (760° C)	1600° F (871° C)	1800° F (982° C)
$\lambda$	17.8E6	17.2E6	18.1E6	17.8E6	15.4E6	11.5E6
$\mu$	9.8E6	9.0E6	9.0E6	8.4E6	6.9E6	4.9E6
$k_1$	50931	75631	95631	251886	91505	59292
$n-1$	.059	.059	.079	.244	.195	.223
$m$	1.16	1.16	1.16	1.16	1.16	1.16
$n_2$	30.0E7	6.0E7	1.5E7	2.0E7	5.0E6	1.0E6
$n_3$	8000	1000	781	1179	673	312
$n_6$	0	0	0	0	8.98E-4	2.73E-3
	0	0	-2000	-2000	-1434	-1200

Note that constants  $k_2$ ,  $n_1$ ,  $n_4$ ,  $n_5$  and  $n_7$  are zero.

Miller's Theory

$k_0 = 8000$	$C_2 = 50000$
$n = 1.598$	$A_2 = 5.9425E-12$
$B = 1.0293E14$	$Q^* = 104600$
$H_1 = 1.0E7$	$T_m = 1588^\circ K$
$A_1 = 9.305E-4$	$K = 1.9859$
$H_2 = 100$	

The Lamé constants  $\lambda$  and  $\mu$  are given above under Walker's Theory.

Krieg, Swearngen and Rhode's Theory

Material Constant	800° F (427° C)	1000° F (537° C)	1200° F (648° C)	1400° F (760° C)	1600° F (871° C)	1800° F (982° C)
$k_0$	50931	75631	95631	251886	91505	59292
$n-1$	.059	.059	.079	.244	.195	.223
$A_1$	30.0E7	6.0E7	1.5E7	2.0E7	5.0E6	1.0E6
$A_2$	.59	1.79E-3	.66	1.54	14.96	243
$A_3$	1.0E-12	1.0E-12	1.0E-12	1.0E-12	1.0E-12	1.0E-12

Note that constants  $A_4$  and  $A_5$  are zero. Also, the Lamé constants are given above under Walker's Theory.



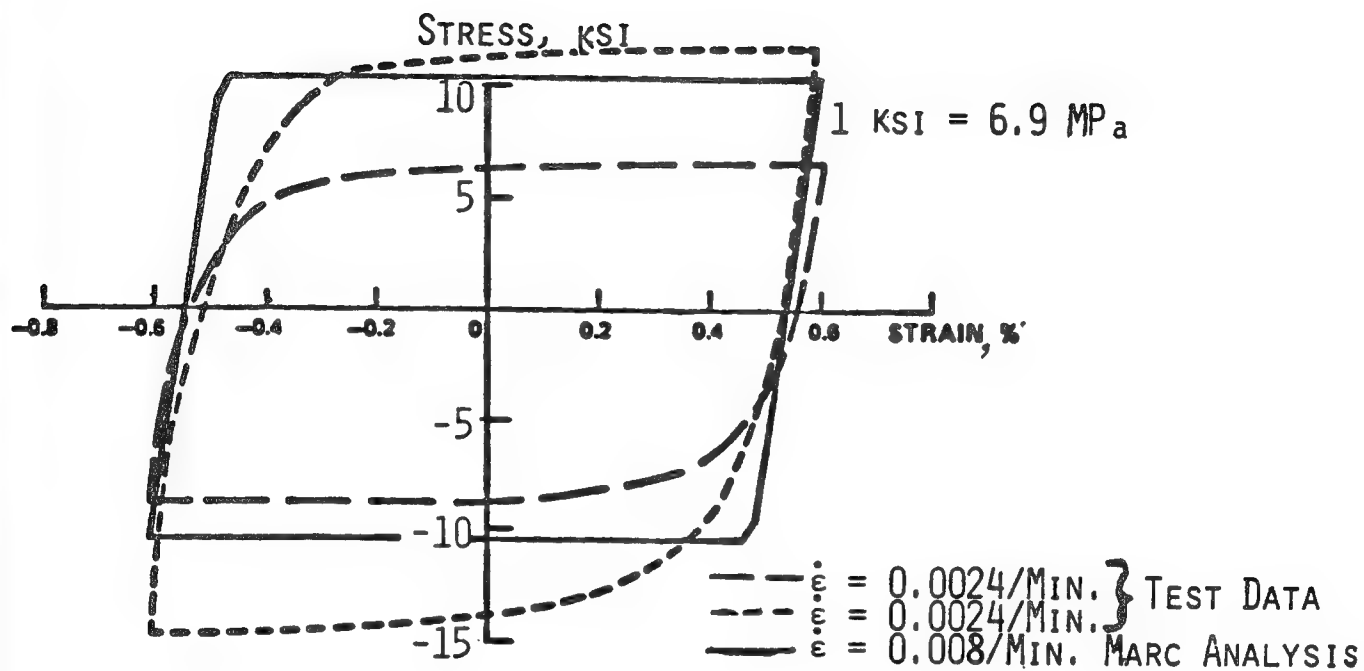


Figure 1 - Prediction of Hysteresis Loops at 1800<sup>0</sup> F (982<sup>0</sup> C)

1 ksi = 6.9 MPa

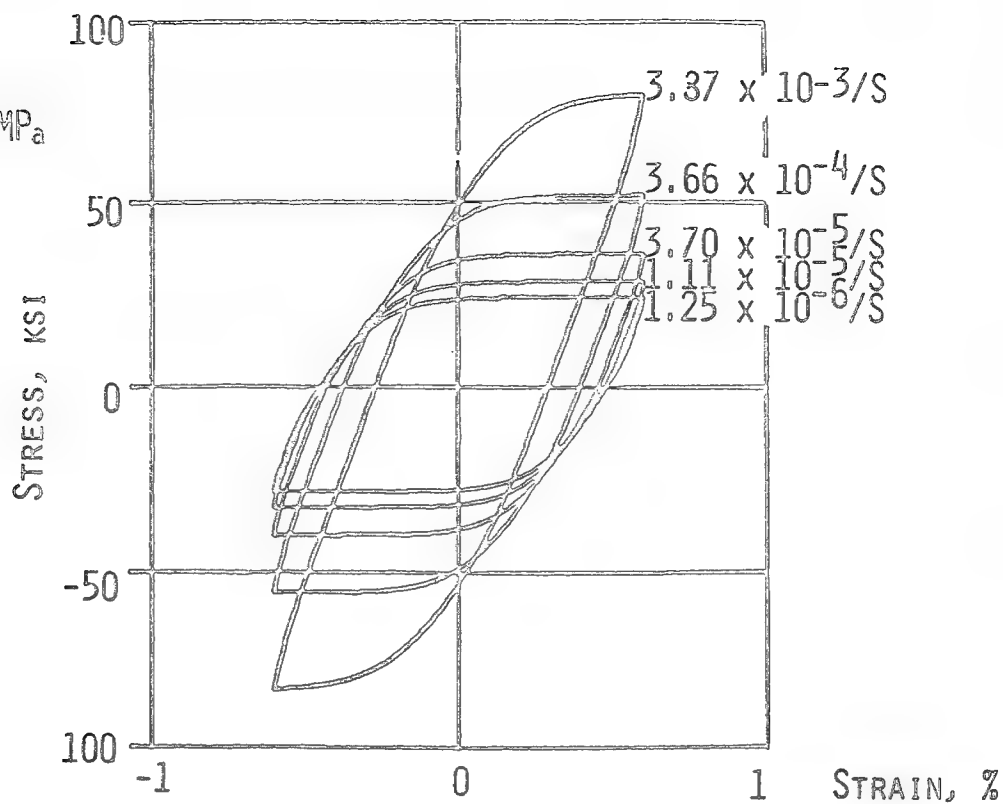


Figure 2 - Theoretical Hysteresis Loops at 1400<sup>0</sup> F (760<sup>0</sup> C) Generated With Walker's Theory

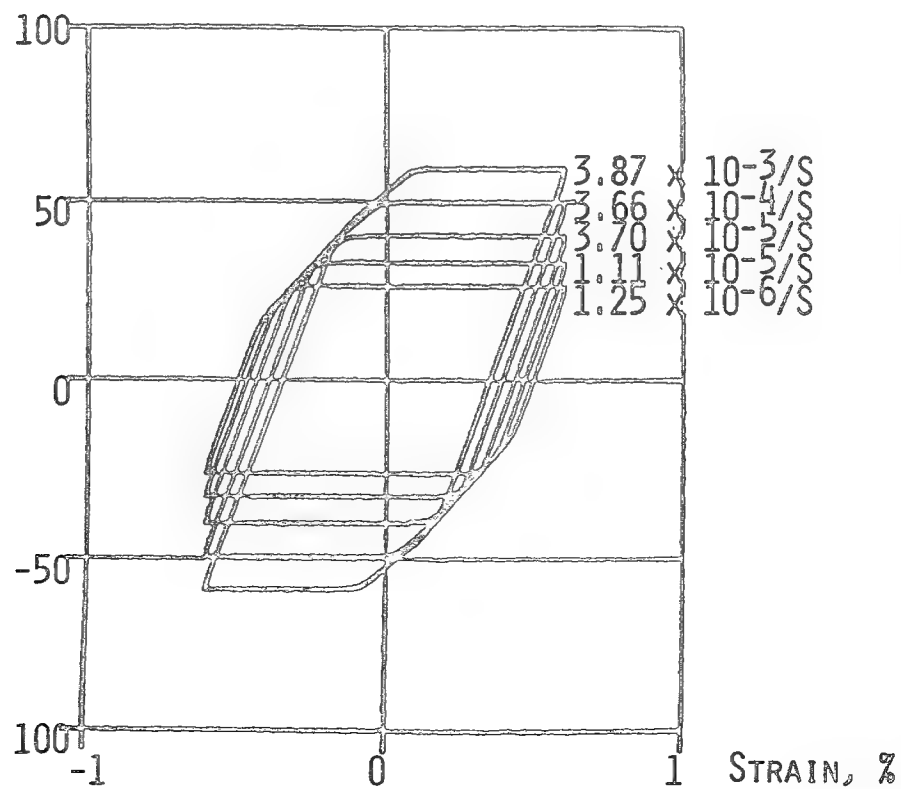


Figure 3 - Theoretical Hysteresis Loops at 1400<sup>0</sup> F (760<sup>0</sup> C) Generated With Miller's Theory

1 KSI = 6.9 MP<sub>a</sub>

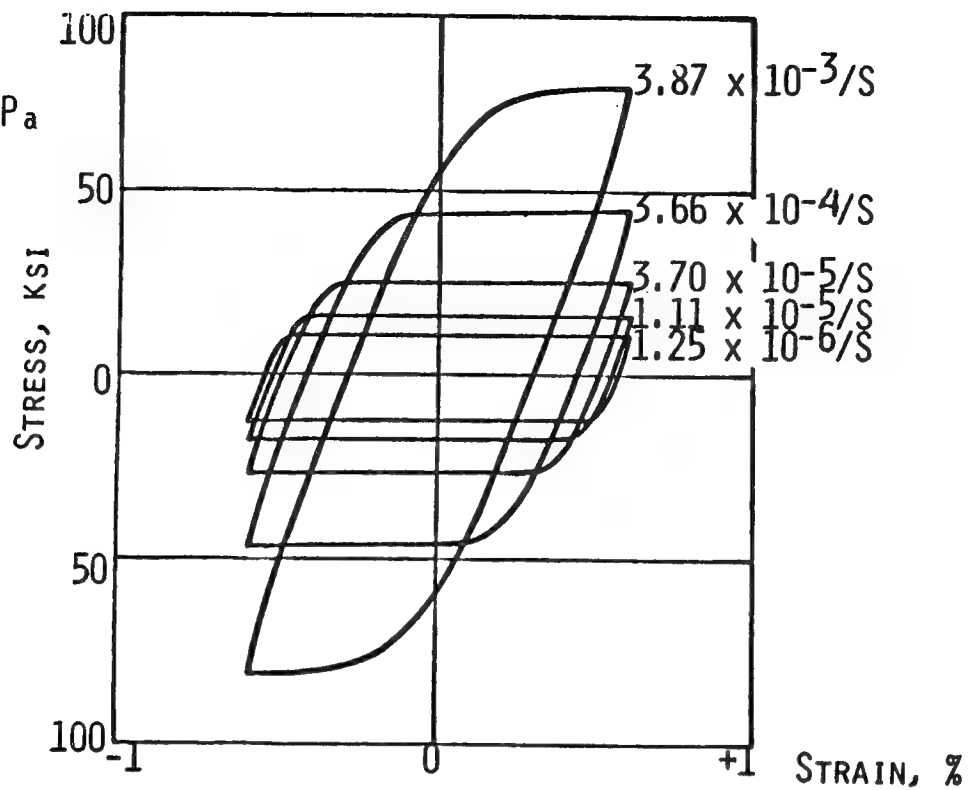


Figure 4 - Theoretical Hysteresis Loops at 1400<sup>o</sup> F (760<sup>o</sup> C) Generated With Krieg, Swearngen and Rhode's Theory

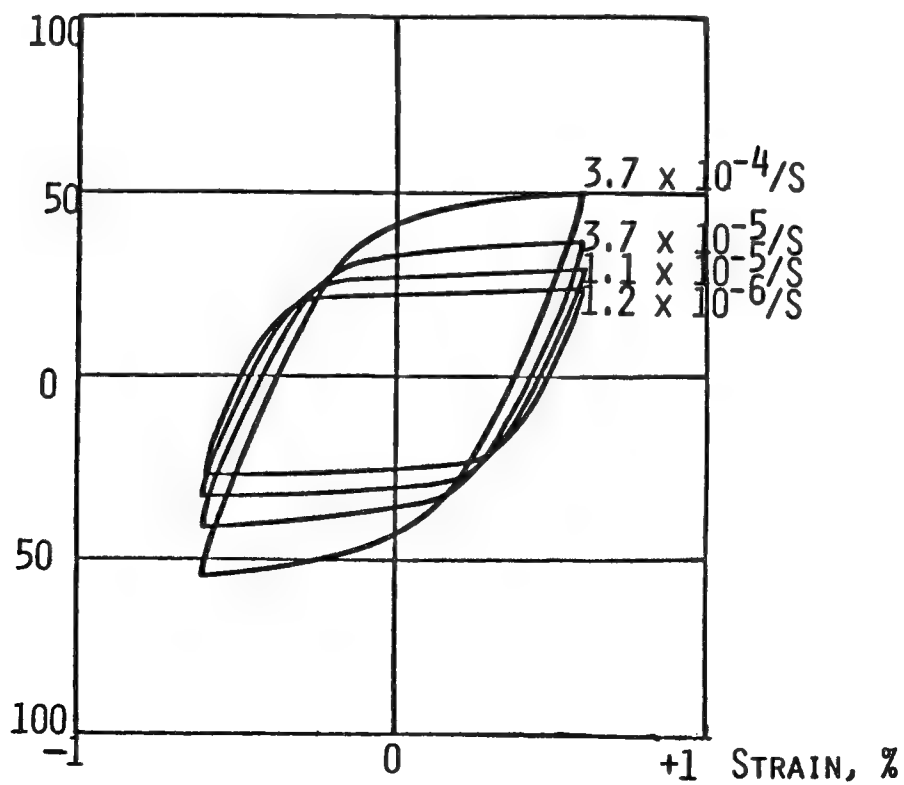


Figure 5 - Experimental Steady-State Hysteresis Loops at 1400<sup>o</sup> F (760<sup>o</sup> C)

O CALCULATION  
 - EXPERIMENT  
 1 KSI = 6.9 MPa

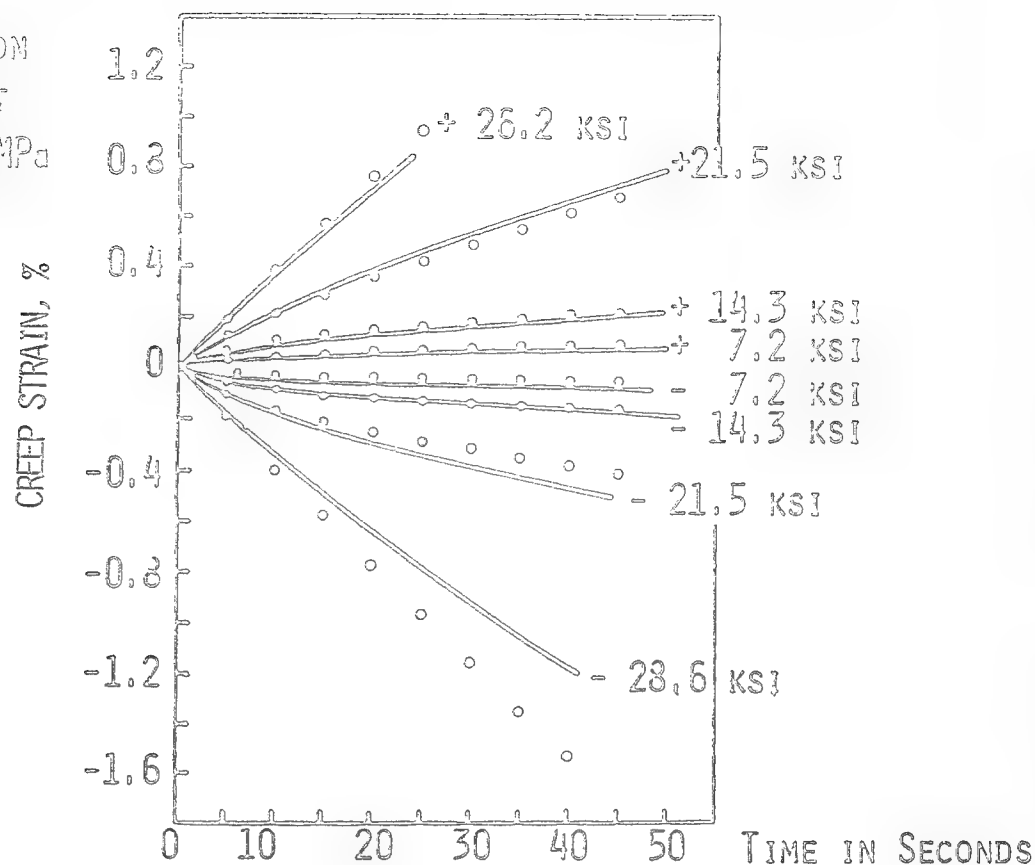


Figure 6 (a) Creep Response at 1600<sup>0</sup> F (871<sup>0</sup> C) Generated With Walker's Theory

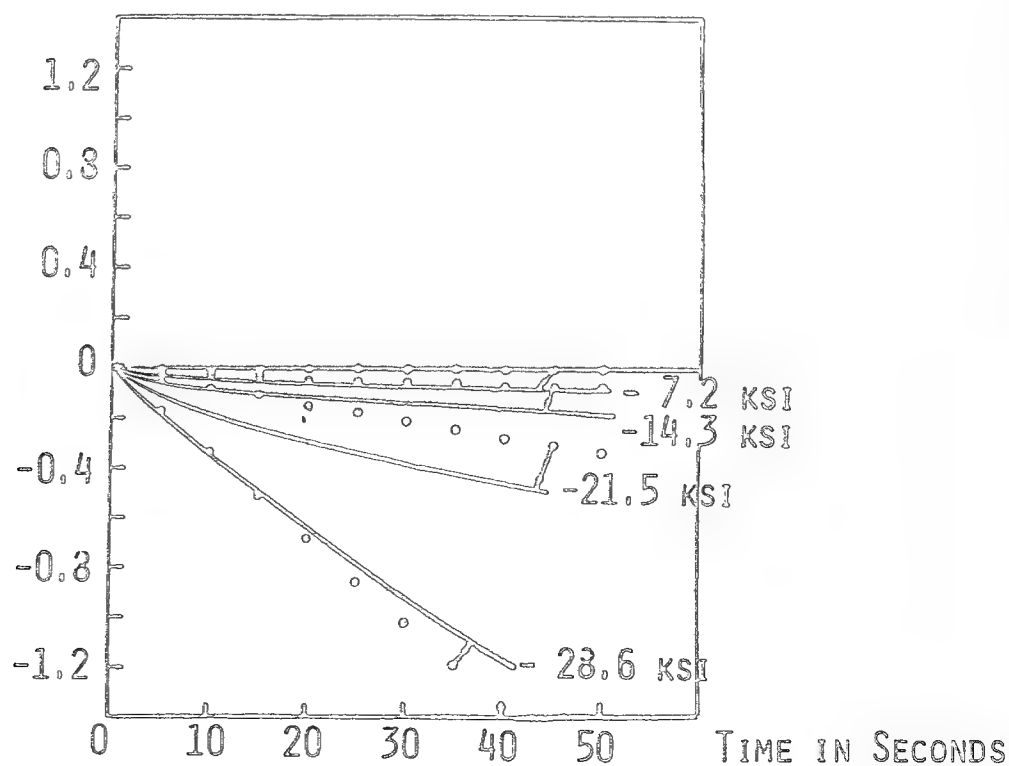


Figure 6 (b) Creep Response at 1600<sup>0</sup> F (871<sup>0</sup> C) Generated With Miller's Theory

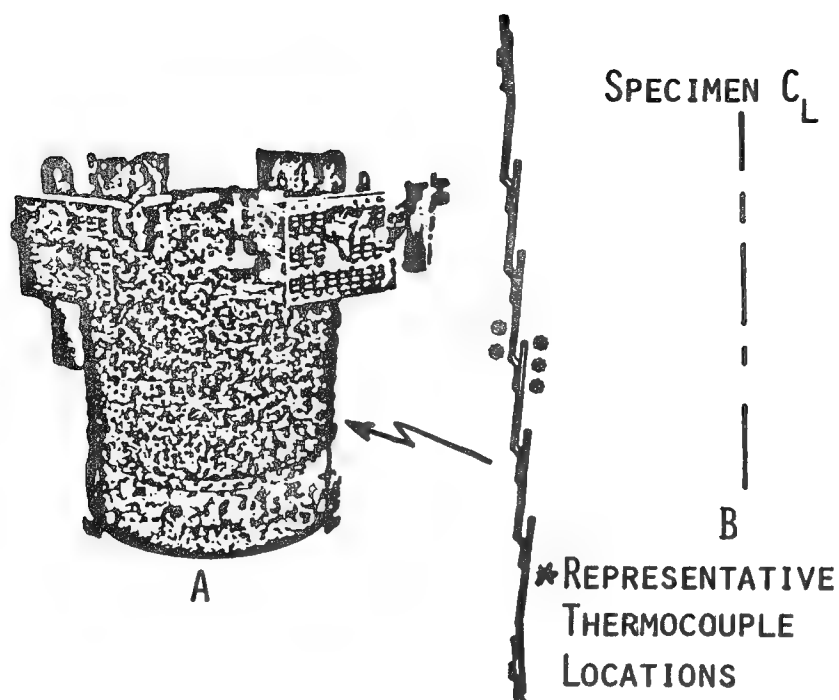


Figure 7 - Assembled Liner Test Specimen (A) and 5-Louver Test Section (B)

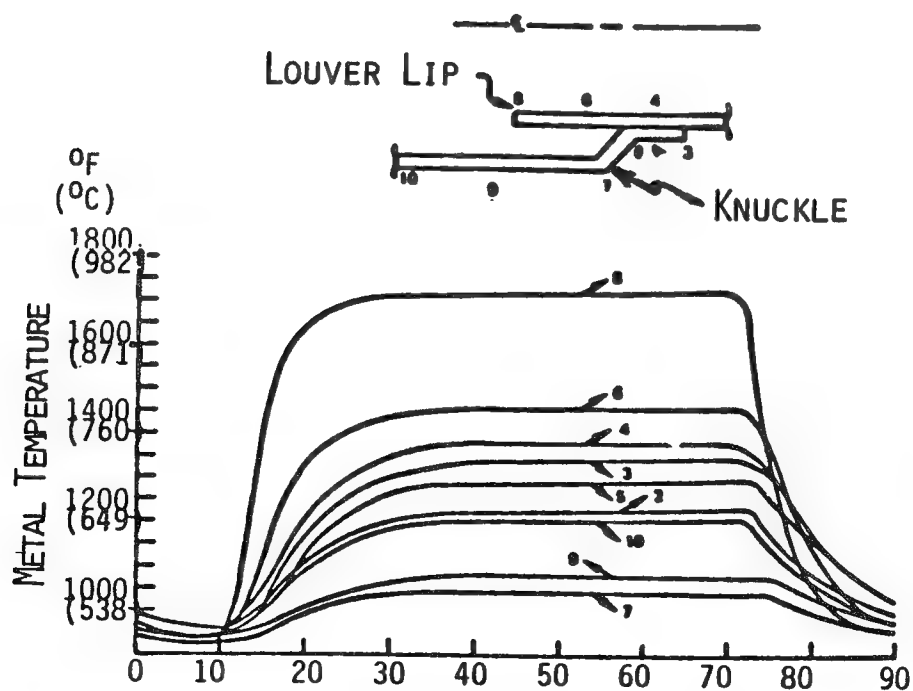


Figure 8 - Measured Thermal Response of Louver Test Section

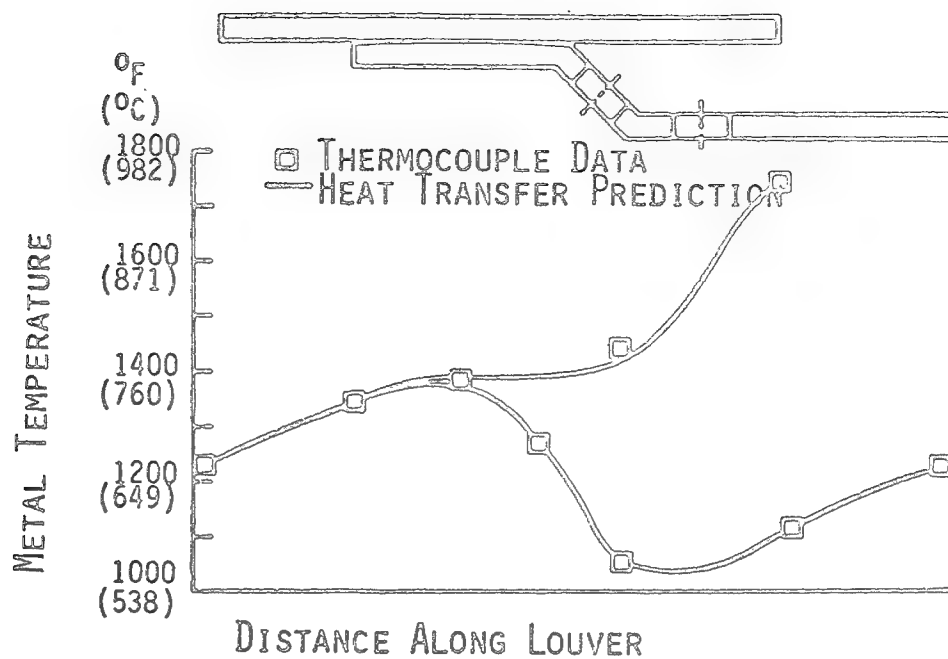


Figure 9 (a) Steady-State Temperature Distribution for Louver Test Section

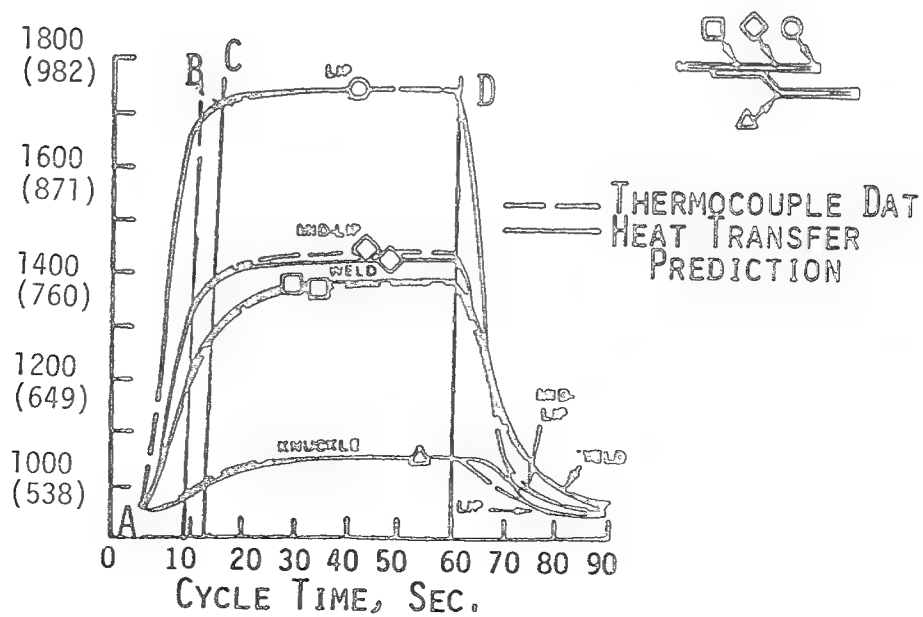


Figure 9 (b) Transient Temperature Response for Louver Test Section

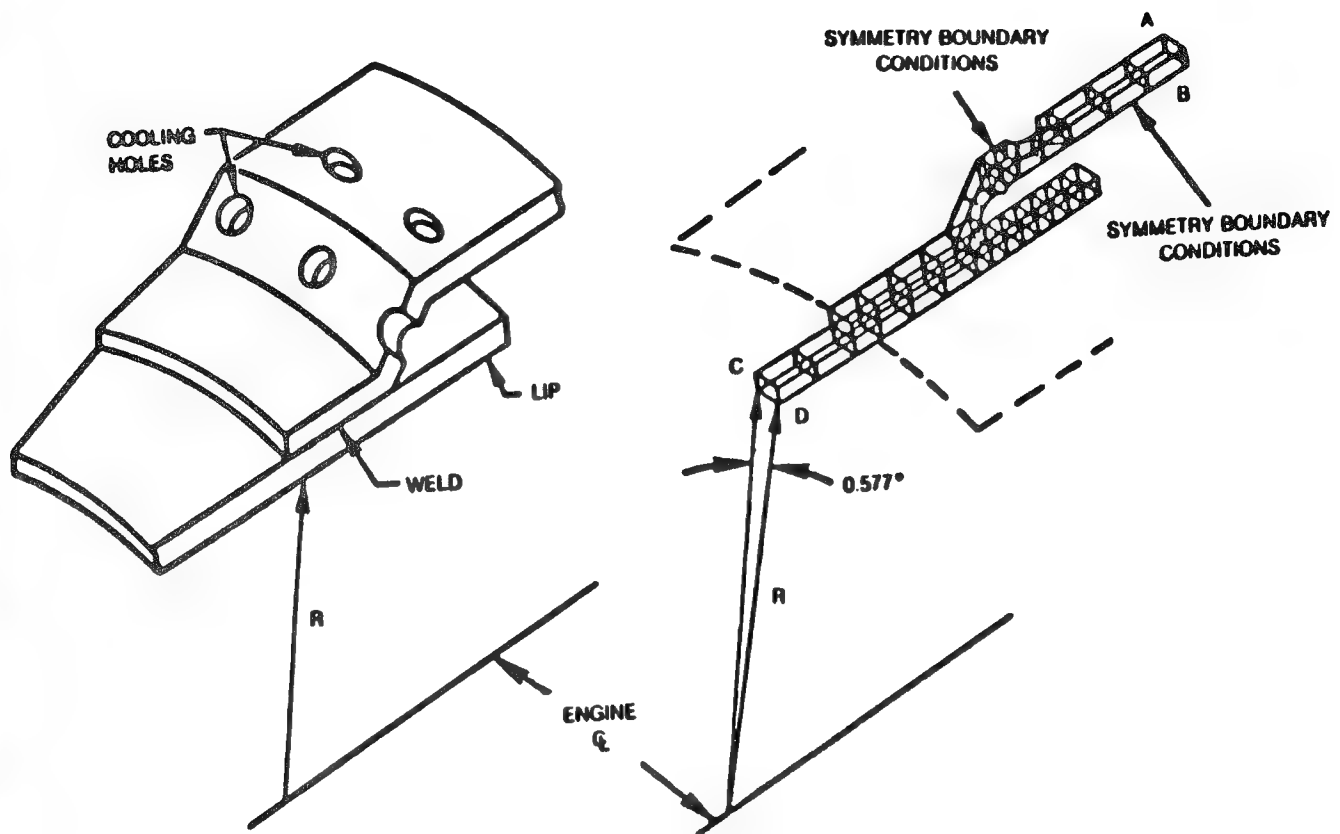


Figure 10 - Finite Element Model of Louver Test Section

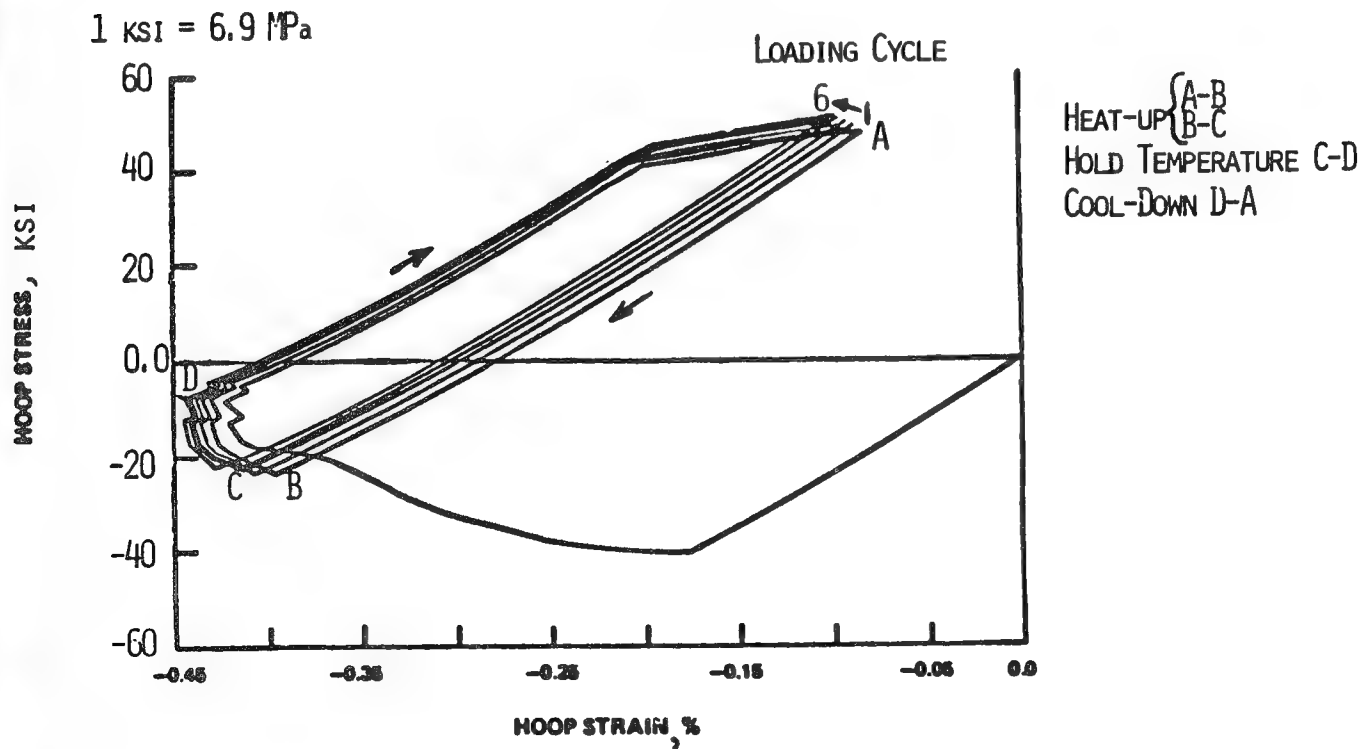


Figure 11 - Predicted Louver Lip Response for Six Loading Cycles Using Conventional Theory

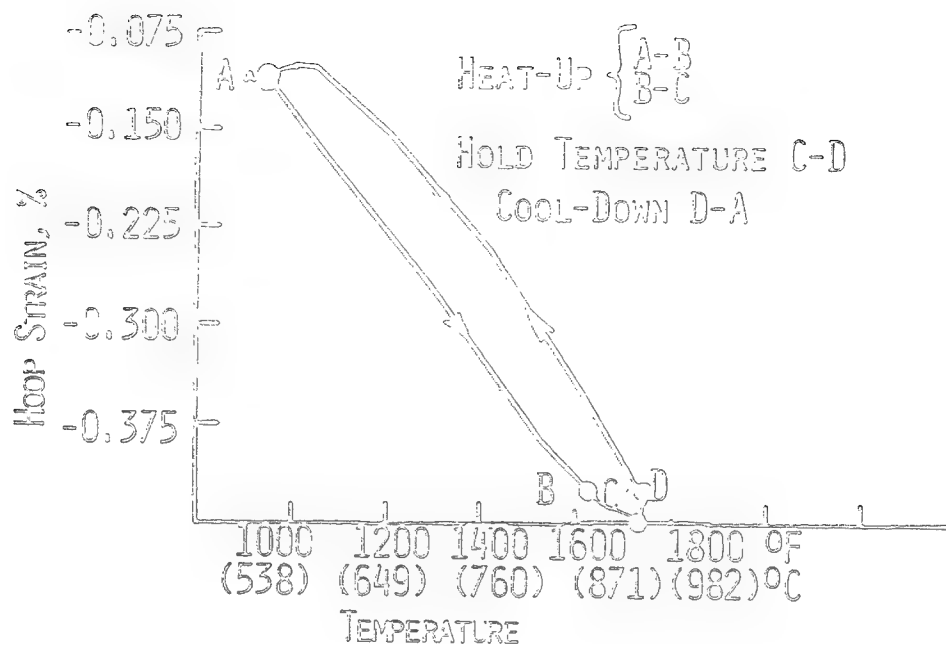


Figure 12 - Mechanical Strain-Temperature History for Sixth Cycle (Faithful Cycle)

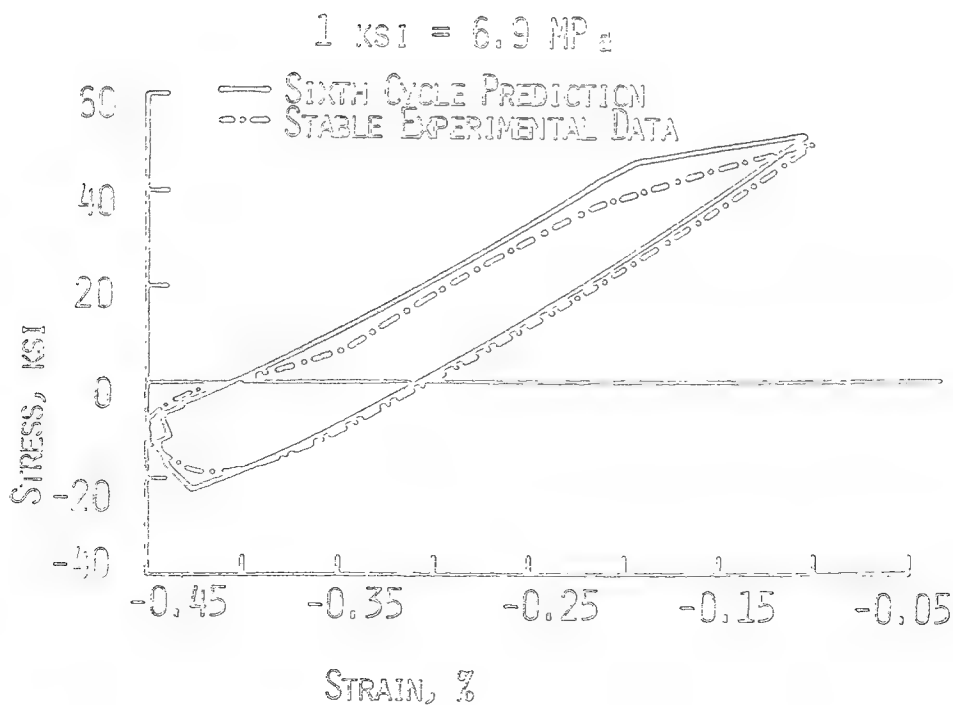


Figure 13 - Comparison of Predicted Sixth Cycle and Experimental Response



1 KSI = 6.9 MPa

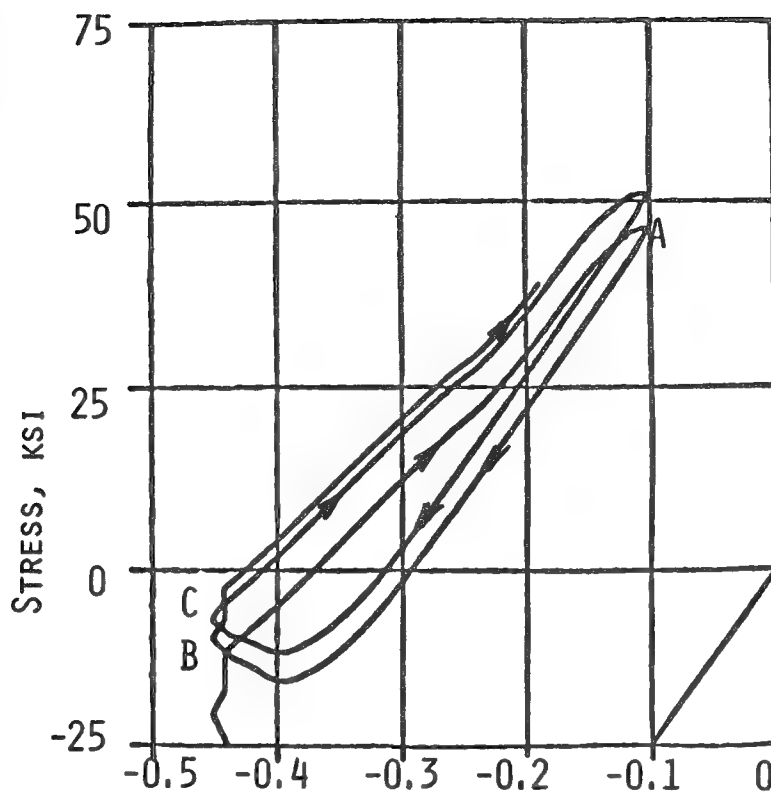


Figure 14 - Thermomechanical Loops Predicted by Walker's Theory

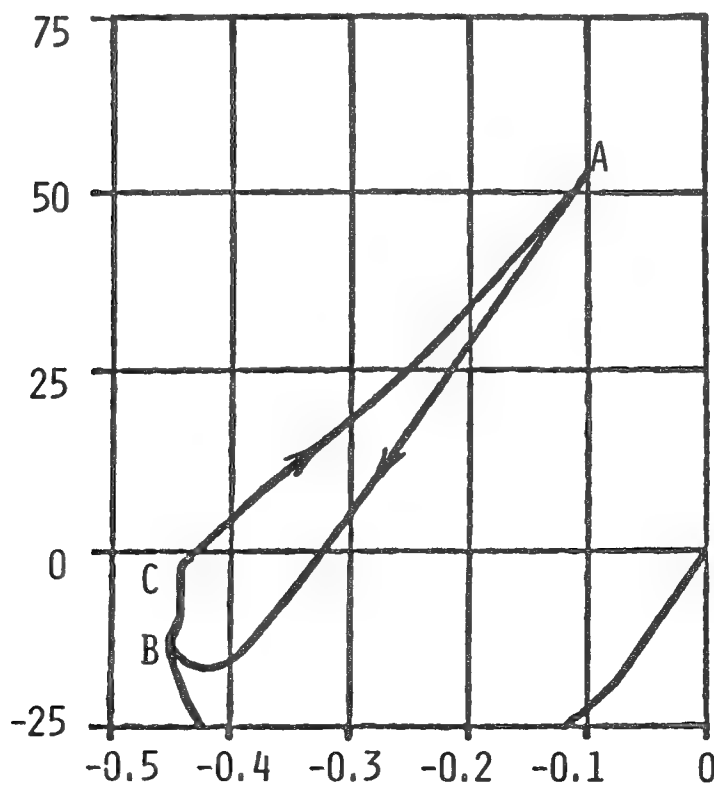


Figure 15 - Thermomechanical Loop Predicted by Miller's Theory

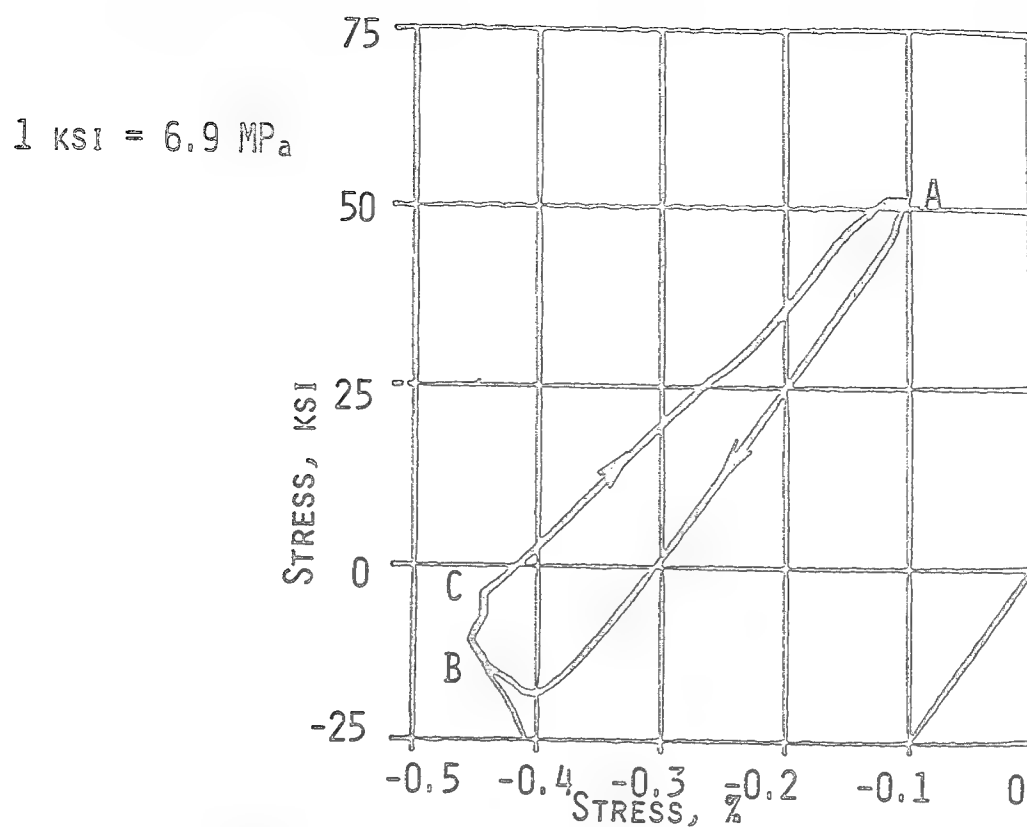


Figure 16 - Thermomechanical Loop Predicted by Krieg, Swearengen and Rhode's Theory

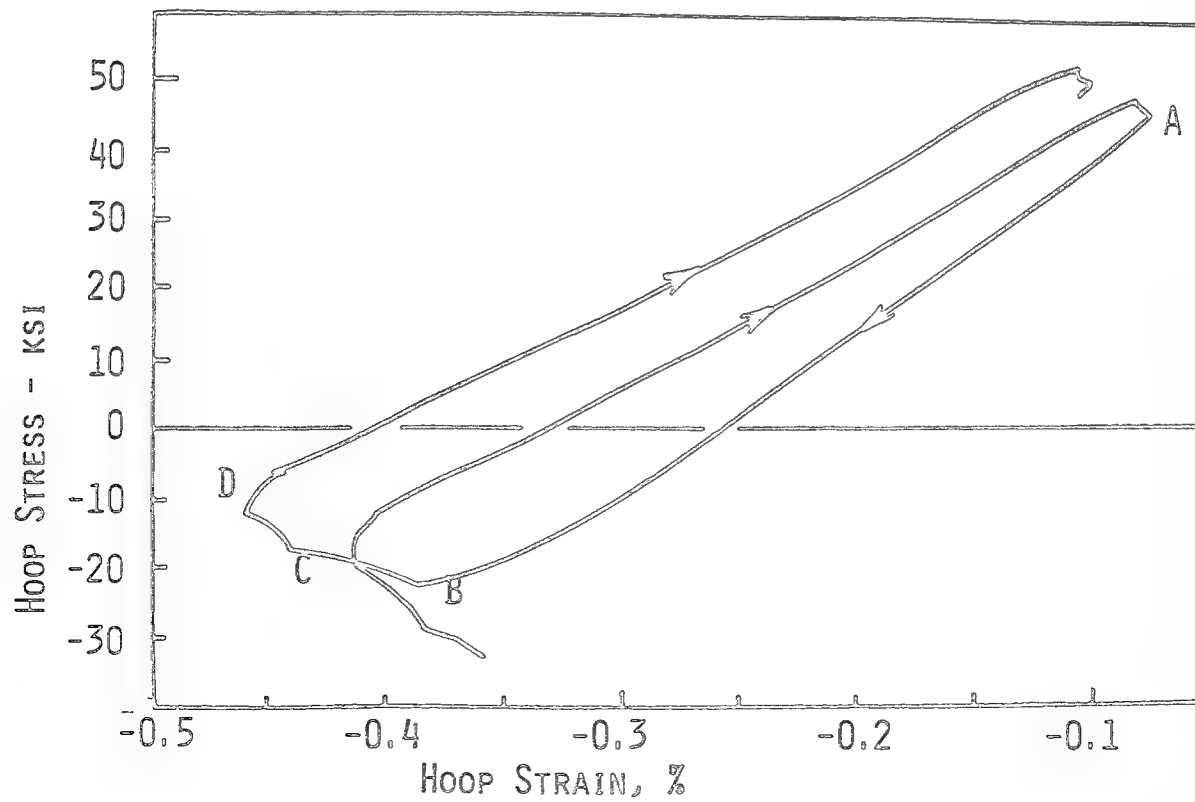


Figure 17 - Predicted Louver Lip Response for Two Loading Cycles Using Walker's Theory

PREDICTION OF RESIDUAL TENSILE STRENGTH  
OF TRANSVERSELY IMPACTED COMPOSITE LAMINATES

K. M. Lal\*  
NASA Langley Research Center  
Hampton, Virginia

SUMMARY

This paper discusses the response to low velocity impact of graphite-epoxy T300/5208 composite laminates. Steel balls of 3/8-inch, 5/8-inch, and 1-inch diameter were the projectiles. Impact energy was limited to 1.2 joules. Impacted specimens were ultrasonically C-scanned to determine the impact-damaged region. The threshold value of impact energy for impact damage was found to be approximately 0.3 joules.

A model was developed to predict the tensile residual strength of impact-damaged specimens from fracture mechanics concepts. Impacted specimens were tested in tension to provide a fracture data base. The experimental results agreed well with the predictions from fracture mechanics.

In this study, the maximum impact velocity used to simulate the low-velocity transverse impact from common objects like tool drops was 10 m/s.

INTRODUCTION

Aircraft, while in service, may be subjected to impacts from hail and bird strikes in the air, runway debris, and even ground service equipment. Such impacts can reduce the strength of the structure. In aluminum structures minor dents are usually ignored. But in graphite-epoxy composites the surface damage may appear less severe than the hidden damage. The effect of low-velocity impacts on structures in impact sensitive locations has therefore become an important consideration in assessing the suitability of composites for operational service.

Up to now most impact studies [such as references 1-7] have dealt with the description of the strength reduction due to impact on an empirical basis. The work described here represents a first step towards applying fracture mechanics concepts to correlate the damage caused by an impact with the residual strength after that damage.

Impact damage in a composite consists primarily of delaminations, ply splits, and fiber breaks. Fiber debonding and pullout may also occur, but are less significant in determining the residual strength.

At low velocities a damage threshold appears to exist, below which neither matrix nor fibers are damaged. Above the threshold initial damage may occur either in the matrix by ply splitting and delamination, or by fiber failures. At high

\*Associate Prof. of Mechanical Engineering at Old Dominion University, Norfolk, Va.  
The work conducted in this paper was supported by NASA Grant Number NAG 1196.

ballistic impact velocities a hard projectile will punch an almost clear hole in: the diameter of the projectile through the composite. At those velocities the residual tensile strength of the penetrated plate is essentially governed by the fracture mechanics for a clear hole of that diameter, which is almost the same as the residual strength for a transverse slit of length equal to the hole diameter.

Below ballistic impact velocities, the damaged area is usually larger because the impact shear or flexural waves have time to propagate towards the specimen supports. Figure 1 is a schematic of the size of the damage zone as a function of the impact velocity for a 25-mm steel projectile. The damage size is one of the parameters that influences residual strength of the component.

No data exist in the literature to define the strength reduction in impact-damaged composites over the entire impact velocity domain up to the hypervelocity impact. Figure 2 shows schematically two possible trends in the residual strength as a function of velocity. Curve (a) assumes that no strength reduction occurs up to the velocity at which damage is first observed (threshold), and that the residual strength decreases monotonically to a minimum by the hypervelocity impact. Curve (b) assumes that the strength may already be reduced at impact velocities less than the threshold of observed damage, and that the strength has a minimum coinciding with the maximum damage size. Such a minimum might be substantially below the residual strength in the hypervelocity impact case.

The data reported herein represent part of a continuing study and are limited to examining the residual strength in the low-velocity domain ( $<10$  m/s). Figure 3 shows a specimen which has been damaged by a low-velocity impact. The projectile did not penetrate, but left a damage zone of area  $A_d$  as measured by ultrasonic C-scanning.

In the model developed, friction and indentation losses were neglected. The dominant energy terms contributing to damage were the delamination energy  $I_d$  and the fiber fracture energy  $I_f$ . The measured energy loss during impact  $I_a$  and the delamination area measured by ultrasonic C-scan were used to calculate the invisible fiber damage from an energy equation.

Because fiber breakage is difficult to determine nondestructively, the energy balance model was developed in this study to first calculate the amount of fiber breakage and then to calculate a residual strength based on that damage. The purpose of such a model is to show that simple fracture mechanics offers a useful tool in the assessment of impact damage and that these tools should be systematically refined.

In the impact tests for this study, the total energy absorbed by the plates during impact was measured. The unknown friction and indentation losses were neglected, and the total energy loss was assumed to consist of two parts: the delamination energy loss,  $I_d$ , and the fiber breakage energy loss,  $I_f$ .

The delamination energy loss was first computed from an assumed delamination energy release rate and delamination area measured by ultrasonic C-scanning. The fiber fracture energy loss was then taken as the difference between the total energy loss  $I_a$  and the delamination energy loss  $I_d$ . Using the fiber fracture strain energy release rate  $G_{IC}$  from fracture tests with artificial slits, the amount of assumed fiber damage was then computed on an equivalent slit length which can be produced with the amount of energy  $I_f$ .

To test this model the measured residual strengths for the impacted plates were compared to the computed strengths for plates with the assumed equivalent slit length.

In the impact specimens not all the energy is available to fiber breakage and delamination. The computed residual strengths are therefore expected to be a lower bound on the measured values. The expectation was tested against the available data.

Also, in the impact specimens, the damage distribution is more diffused than the model assumption of an equivalent slit with 100 percent of the fibers broken. The computed slit length is therefore expected to be shorter than the observed damage size (length). This expectation is also tested against the available data.

### ANALYSIS

The classical Griffith-Irwin fracture criterion [ref. 8, 9], for fracture of orthotropic materials [ref. 10], assumes that the energy  $G_{I_c}$  required to create unit area of fracture surface is

$$G_{I_c} = K_{I_c}^2 / E_c \quad (1)$$

where  $K_{I_c}$  is the critical stress intensity and  $E_c$  is the Young's Modulus of composite laminate.

If the energy  $G_{II_c}$  is required to create a unit area of delamination by shear, the energy absorbed by delamination,  $I_d$ , will be

$$I_d = G_{II_c} A_d n \quad (2)$$

where  $A_d$  is the area of delamination detected by ultrasonic C-scan and  $n$  is number of delaminations. The assumption that all the plies in the laminate delaminate will give  $n$  equal  $N-1$ , where  $N$  is total number of plies.

The energy  $I_f$ , absorbed by fibers breaking, is then given by

$$I_f = I_a - I_d \quad (3)$$

where  $I_a$  is total energy absorbed by the laminate during impact.

The equivalent slit length can be obtained from  $I_f$  and  $G_{I_c}$ , as

$$L = I_f / 2G_{I_c} h \quad (4)$$

The fracture behavior of composite plates with transverse slits of length  $2L$  is given by

$$K_{I_c} = \sigma_c \sqrt{\pi(L+a_c)} \quad (5)$$

where  $\sigma_c$  is the failure stress and  $a_c$  is a characteristic length term introduced to describe the finite strength when  $L$  approaches zero.  $K_{Ic}$  is the critical stress intensity factor at failure in mode I. The residual strength is then determined as

$$\sigma_c = K_{Ic} / \sqrt{\pi(L+a_c)} \quad (6)$$

The fracture parameters,  $K_{Ic}$ ,  $a_c$  and  $G_{Ic}$  were determined experimentally, and  $G_{IIc}$  was taken equal to 200 joules/m<sup>2</sup> [ref.11]. The ratio of  $\sigma_c$  and  $\sigma_u$ , the ultimate strength of the laminate, gave the residual tensile strength retention factor,  $R$ .

#### Calculation of Absorbed Energy:

The energy absorbed,  $I_a$ , during impact was obtained by subtracting the rebound energy from the maximum impact energy of the projectile, and is given by

$$I_a = 1/2MV^2 - 1/2MV_R^2 \quad (7)$$

where  $V$  and  $V_R$  are maximum impact and rebound velocities, being equal to, respectively,  $\sqrt{2gH}$  and  $\sqrt{2gh}$  where  $H$  and  $h$  are drop and rebound heights of the projectile.  $M$  is the mass of the projectile. One possible loss of energy not related to impact is caused by air drag, which can be calculated by the following equation:

$$\text{percent loss in velocity} = 1 - \frac{3}{8} \frac{\rho_a}{\rho_s} C_d \frac{V^2}{gD} \quad (8)$$

where  $\rho_a$  and  $\rho_s$  are the relative mass densities of air and projectile,  $C_d$  is the drag coefficient, equal to 0.5 in low turbulent flow conditions,  $V$  and  $D$  are, respectively, the velocity and diameter of the projectile, and  $g$  is gravitational constant. The energy losses due to air drag were found to be less than 1 percent of  $g$ , the maximum kinetic energy of the projectile, for impact velocities used in this study. Therefore, the air drag losses in energy calculations were neglected.

### TEST RESULTS AND DISCUSSIONS

In order to test the model presented in this paper, impact specimens were damaged by a dropped steel ball. Impact-damaged specimens were first screened by ultrasonic C-scan to detect the damaged zone, and then tested in tension to obtain their residual tensile strength. Fracture specimens, identical to the impact specimens, were tested to obtain the toughness parameters of the material.

#### Impact Specimens:

The impact specimens were produced from T300/5208 graphite-epoxy laminate. The fiber orientation of the laminate used in this study was  $[45/0/-45/90]_s$ . The specimens were rectangular, 300 mm by 100 mm. The tensile strength and the Young's

Modulus of the laminate (loading along  $0^\circ$  fiber direction) were respectively 555 MPa and 45 GPa.

All the specimens were C-scanned before they were impacted to ensure that the specimens were free from defects like air-filled debonds and porosity. Based on the results reported in reference [12], which showed that ultrasonic attenuation of good quality graphite-epoxy composites is uniform to within 6 dB over 99 percent of its surface, all the impact specimens were C-scanned with 6-dB attenuation level.

#### Impact Tests:

The rectangular panels were fixed by a rectangular window type fixture (fig. 4) such that all four edges were clamped to provide a free area, 150 mm  $\times$  100 mm. All the specimens were clamped with uniform torque to keep mounting conditions uniform. The projectiles were 3/8-inch, 5/8-inch and 1-inch diameter. They could be dropped from the heights up to 4.5 meters. Table I lists the impact test data. The variation of energy absorbed,  $I_a$ , during the impact with impact velocity  $V$  is shown in figure 5. The absorbed energy was found increased with the size of the projectile and the impact velocity. The computed values of energies absorbed by delamination and fiber breakage are listed in Table II. The variation of absorbed energy  $I_a$  and fiber-breakage energy with maximum impact energy,  $I$ , is shown in figure 6.

#### Ultrasonic C-Scanning Results:

After impact, each specimen was inspected visually and by ultrasonic C-scanning. The magnitude of impact damage was difficult to detect visually, but the C-scanning technique defined the boundary of the impact-damage zone. The ultrasonic C-scanning technique can detect most discontinuities caused by impact damage in graphite-epoxy composites. Figure 7 shows impact-damage areas of several impact specimens detected by the C-scanning method. The length and width of the impact-damage area, as defined in figure 8, are listed in Table I for each specimen. In most cases, the shape of the damage zone was a parallelogram slightly skewed in the direction of bottom-ply. Also, the maximum length of the damage zone was along the bottom-ply fiber direction.

The variation of damage area with impact energy is shown in figure 9. The threshold value of impact energy for detectable damage by C-scanning was about 0.3 joules.

#### Fracture Tests of Impact-Damaged Specimen:

Each impact-damaged specimen was tested in tension. The load at which the specimen failed provided the residual tensile strength, defined as the load divided by the gross sectional area of the specimen. The test data for residual strength are given in the column 7 of Table I.

#### Fracture Tests of Center-Slit Specimens:

The fracture mechanics tests were conducted to obtain the residual strength,  $\sigma_c$ , of a slit specimen, inherent flaw size,  $a_c$ , and the fracture toughness,  $K_{Ic}$ , of the material.

The center-slit specimens were cut from the same lot of composite material that the impact specimens were. These specimens were also the same size as the impact specimens. Center slits of lengths 2 mm, 4 mm, 6 mm, 8 mm, 10 mm and 12 mm were ultrasonically machined into these specimens. The test data of fracture stress versus slit length for the center-slit specimens is shown in figure 10. The least-square analysis of fracture test data gave the values of material toughness,  $K_{Ic}$ , and inherent flaw size,  $a_c$ , respectively equal to 49.85 MPa $\sqrt{m}$  and .002634 m. The ultimate strength of the laminate was found to be 555 MPa.

The column 3 of the Table II gives the energy absorbed by delamination calculated from equation (2). Subtracting  $I_d$  from  $I_a$  gives the fiber-breakage energy,  $I_f$ , which is listed in column 4 of Table II. The slit lengths  $2L$ , equivalent to the impact damage, were found by using the fiber-breakage energy  $I_f$  in equation (4). The variation of equivalent slit length with maximum damage length  $D$  is shown in figure 11. As expected, the equivalent slit length is about 15 percent of the C-scan damage length  $D$ . The residual strength retention factors were then calculated by using the slit length  $2L$  and the fracture parameters in equation (6) and listed in column 6 of Table II. Figure 12 shows the variation of residual strength with the impact energy. The analysis provides a reasonable lower bound for the residual strength over the whole range of experimental impact energy.

## CONCLUSIONS

Rectangular specimens of quasi-isotropic, 8-ply, graphite-epoxy composite material were transversely impacted by steel ball projectiles. Impact damaged specimens were C-scanned and then their residual tensile strengths were obtained. An energy analysis was developed to design a damage equivalent slit-fracture specimen. The following points were concluded for this material.

1. The fracture mechanics energy model provided a reasonable lower bound for the residual strength of the impacted plates over the whole range of experimental impact energy.
2. By C-scanning, the threshold value of impact energy needed to cause damage was found to be 0.3 joules.
3. By energy calculations, the threshold value of energy absorbed was found to be 0.1 joules.
4. The length of an equivalent slit was about 15 percent of the maximum linear dimension of the impact damage zone as directed by C-scan.
5. The impact-damage zones were shaped like a parallelogram slightly skewed in the direction of bottom-ply fibers.



## REFERENCES

1. Greszczuk, L. B.: Response of Isotropic and Composite Materials to Particle Impact. Foreign Object Impact Damage to Composites, ASTM STP 568, American Society for Testing and Materials, 1975, pp. 183-211.
2. Preston, J. L., Jr.; and Cook, T. S.: Impact Response of Graphite-Epoxy Flat Laminates Using Projectiles That Simulate Aircraft Engine Encounters. Foreign Object Impact Damage to Composites, ASTM STP 568, American Society for Testing and Materials, 1975, pp. 49-71.
3. Chamis, C. C.; Hanson, M. P.; and Serafini, T. T.: Impact Resistance of Unidirectional Fiber Composites. Composite Materials-Testing and Design, ASTM STP 497, American Society for Testing and Materials, 1972, pp. 324-349.
4. Novak, R. C.; and DeCrescente, M. A.: Impact Behavior of Unidirectional Resin Matrix Composites Tested in Fiber Direction. Composite Materials-Testing and Design, ASTM STP 497, American Society for Testing and Materials, 1972, pp. 311-323.
5. Sayers, K. H.; and Harris, B.: Interlaminar Shear Strength of a Carbon Fiber Reinforced Composite Material Under Impact Conditions. Journal of Composite Materials, Vol. 7, 1973, pp. 129-133.
6. Husman, G. E.; Whitney, J. M.; and Chaplan, J. C.: Residual Strength Characterization of Laminated Composites Subjected to Impact Loading. Foreign Object Impact Damage to Composites, ASTM STP 568, American Society for Testing and Materials, 1975, pp. 92-113.
7. Suarez, J. A.; and Whiteside, J. B.: Comparison of Residual Strength of Composite and Metal Structures After Ballistic Damage. Grumman Aerospace Corp., Bethpage, N.Y., 1973.
8. Irwin, G. R.: Analysis of Stresses and Strains Near the End of a Crack Traversing a Plate. Trans. ASME, Journal of Applied Mechanics, Vol. 24, 1957, pp. 361-364.
9. Sih, G. C.; Paris, P. C.; and Irwin, G. R.: On Cracks in Rectilinearly Anisotropic Bodies. Int. Journal of Fracture Mechanics, Vol. 1, 1965, pp. 189-203.
10. Wu, E. M.: Trans. American Society of Mechanical Engineers, Series E, Vol. 34, 1967, pp. 967-982.

11. O'Brien, T. K.: Characterization of Delamination Onset and Growth in a Composite Laminate. Damage in Composites, ASTM STP 775, American Society for Testing and Materials, 1981.
12. Tideswell, N. W.; and Silvergleit, M.: Development of Ultrasonic Procedures and Calibration Standards for Determining Quality of Graphite-Epoxy Composites. Naval Sea Systems Command (NAVSEA 0 5R), Washington, D.C., June 1979.

TABLE I  
IMPACT TEST RESULTS  
(Spherical Steel Projectiles)

1		2	3	4	5	6			7
Projectile		Impact Velocity V m/s	Energy, Joules			Damage Zone			Residual Tensile Strength MPa
Diameter $\times 10^{-3}$ m	Mass kg		Maximum Kinetic, I	Rebound, $I_R$	Absorbed, $I_a$	Maximum Size, D $\times 10^{-3}$ m	Width $\times 10^{-3}$ m	Area $\times 10^{-6}$ m <sup>2</sup>	
25.4	.067	5.99	1.202	.701	.501	22.0	10.5	231	434.5
25.4	.067	5.47	1.001	.634	.367	19.0	10.0	190	473.0
25.4	.067	4.89	.803	.534	.269	13.6	9.5	130	495.0
15.9	.0164	9.15	.695	.477	.218	13.3	6.7	89	481.3
15.9	.0164	7.73	.496	.342	.154	8.9	4.5	40	529.0
15.9	.0164	6.92	.398	.284	.114	5.2	3.1	16	506.5
9.5	.00355	9.15	.148	.062	.086	0	0	0	544.5
9.5	.00355	7.73	.105	.041	.064	0	0	0	550.0

TABLE II  
COMPUTATION OF VARIOUS ENERGIES AND FACTOR, R

1	2	3	4	5	6
Impact I	Absorbed $I_a$	ENERGY, Joules		Slit Length mm	Computed Residual Strength Retention Factor, R
		Delamination $I_d$	Fiber Breakage $I_f$		
1.202	.501	.258	.243	3.64	.768
1.001	.367	.189	.178	2.66	.815
.803	.269	.137	.132	1.98	.852
.695	.218	.0936	.124	1.86	.86
.496	.154	.042	.112	1.68	.87
.398	.114	.017	.107	1.60	.875
.148	.086	0.0	.086	1.30	.898
.105	.064	0.0	.064	0.96	.92

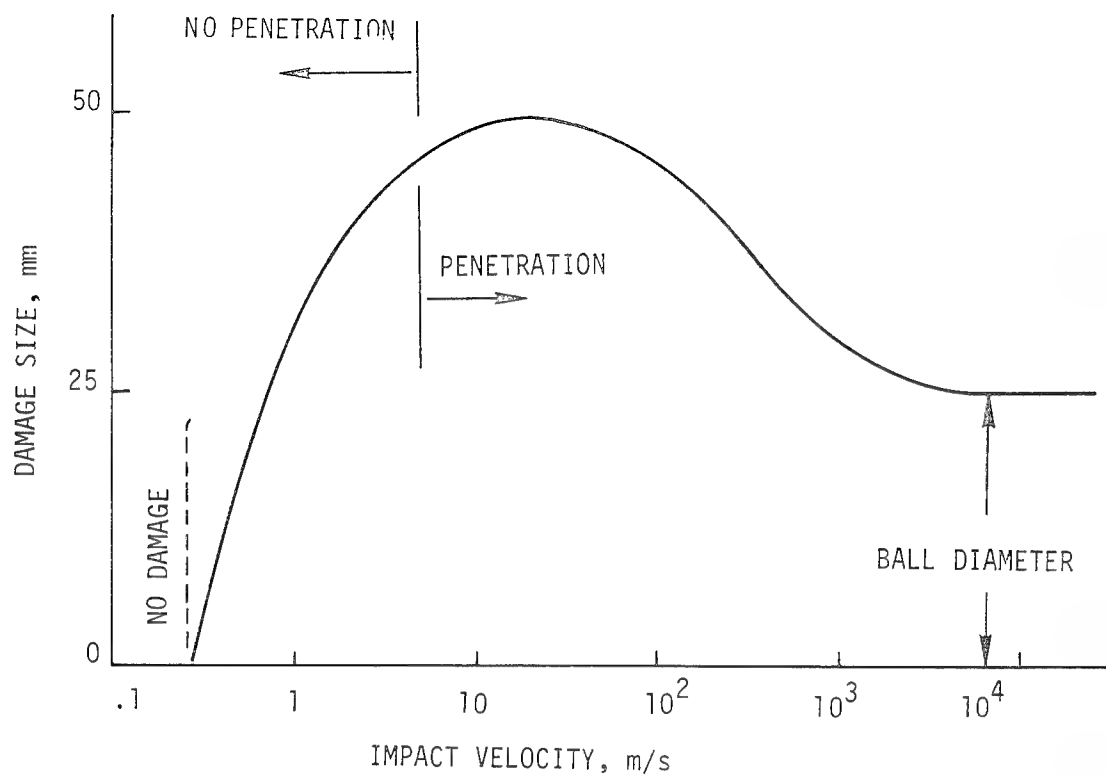


Figure 1 - Variation of damage zone size with velocity.

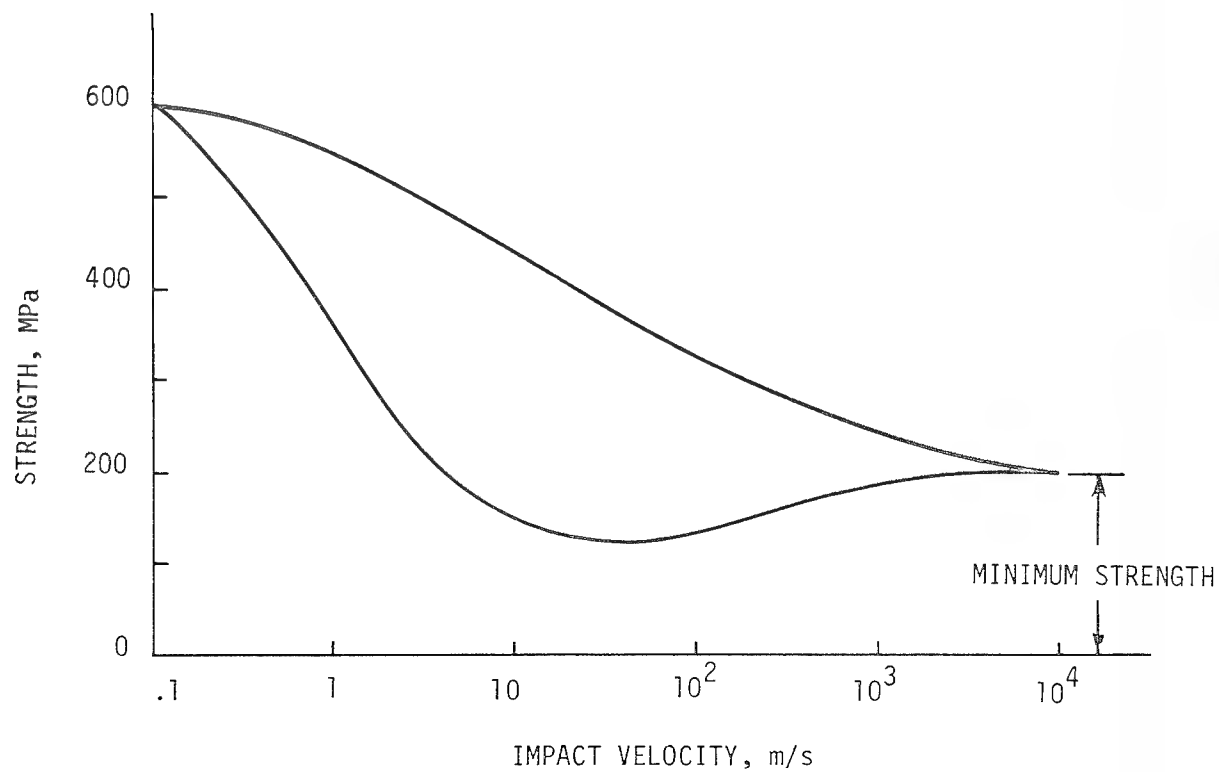


Figure 2 - Effect of velocity on the strength of impact-damaged specimen.

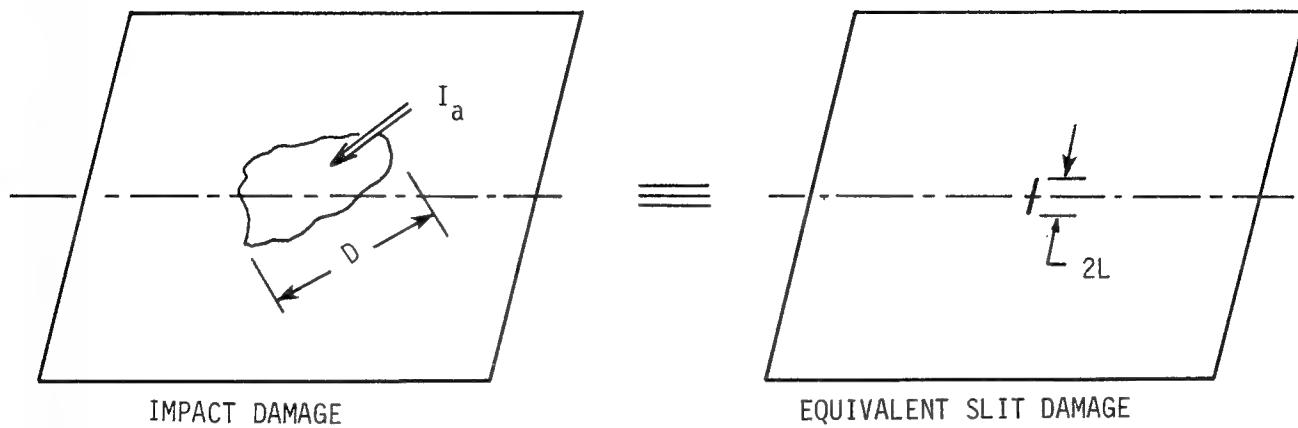


Figure 3 - Equivalence of impact damage and slit damage.

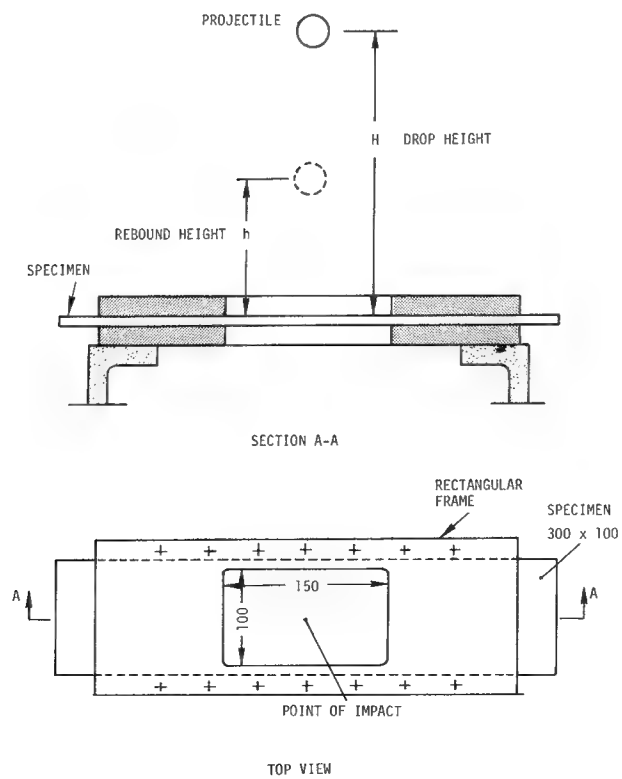


Figure 4 - Impact setup.

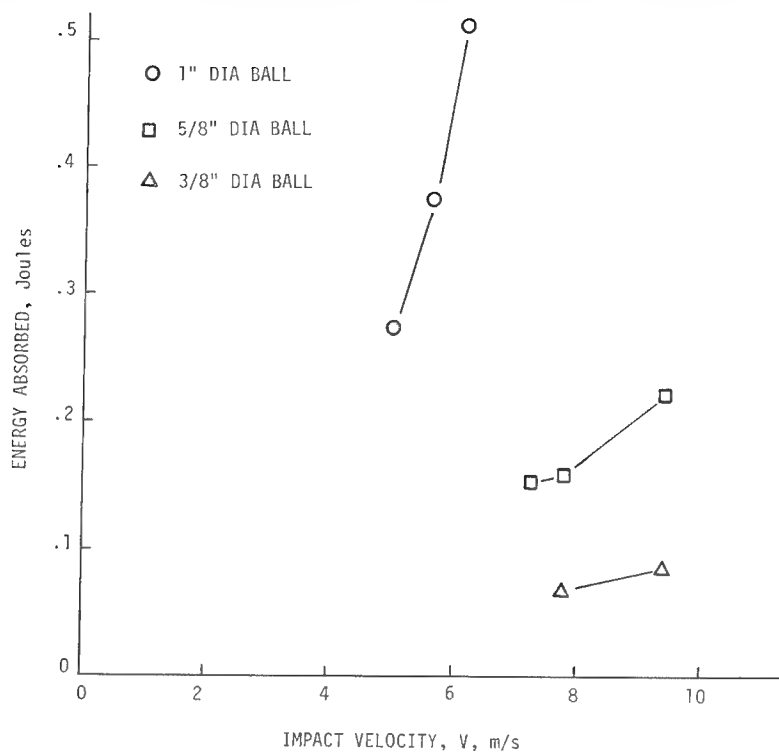


Figure 5 - Results of energy absorbed by different size projectiles at various impact velocities.

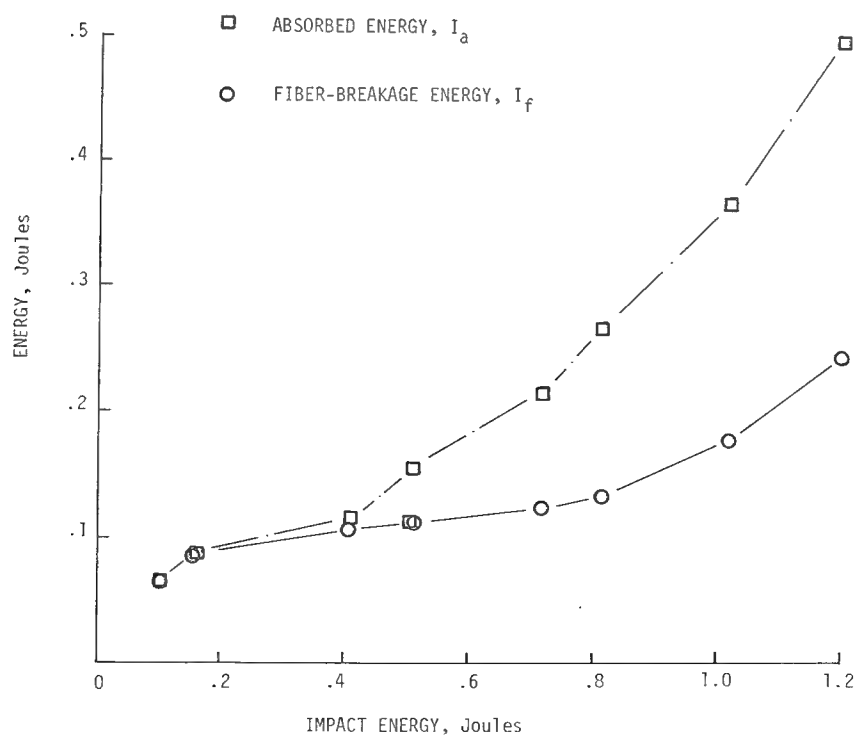


Figure 6 - Variation of absorbed and fiber-breakage energies with impact energy.

## C - SCANNING VIEWS OF IMPACTED COUPONS

GRAPHITE - EPOXY LAMINATES  $(45. 0. -45. 90)_S$

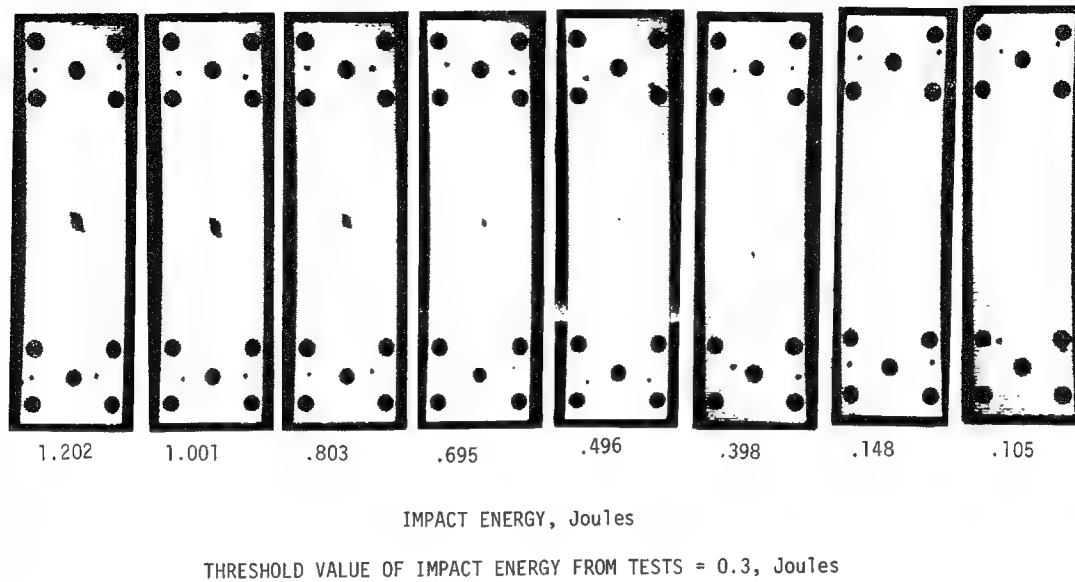


Figure 7 - Impact-damage zones by ultrasonic C-scanning (20-percent reduction).

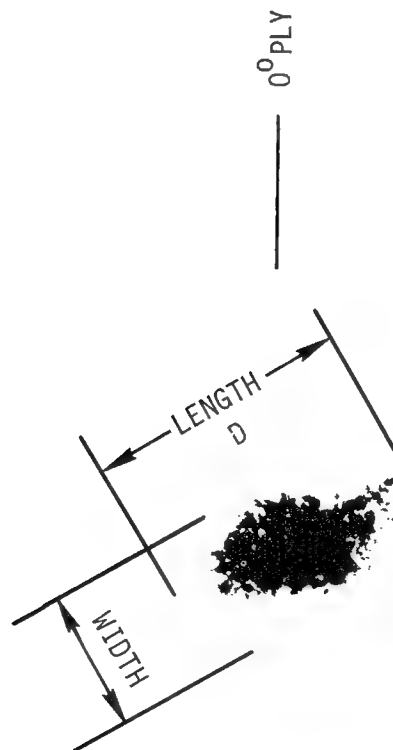


Figure 8 - Measurement of length and width of impact-damage zone obtained by C-scanning.

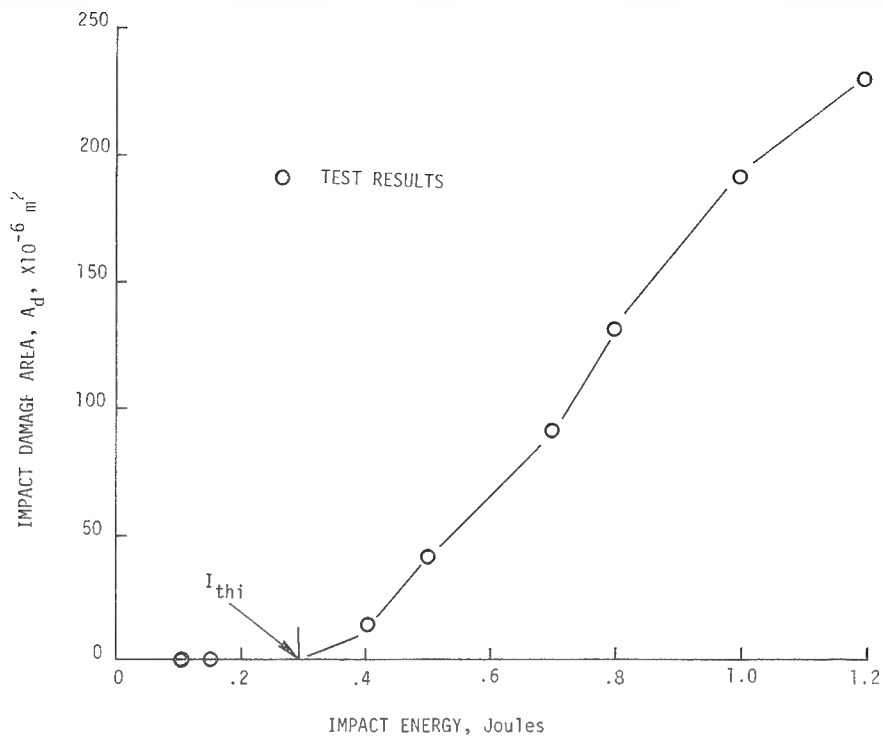


Figure 9 - Variation of impact-damage area with impact energy.

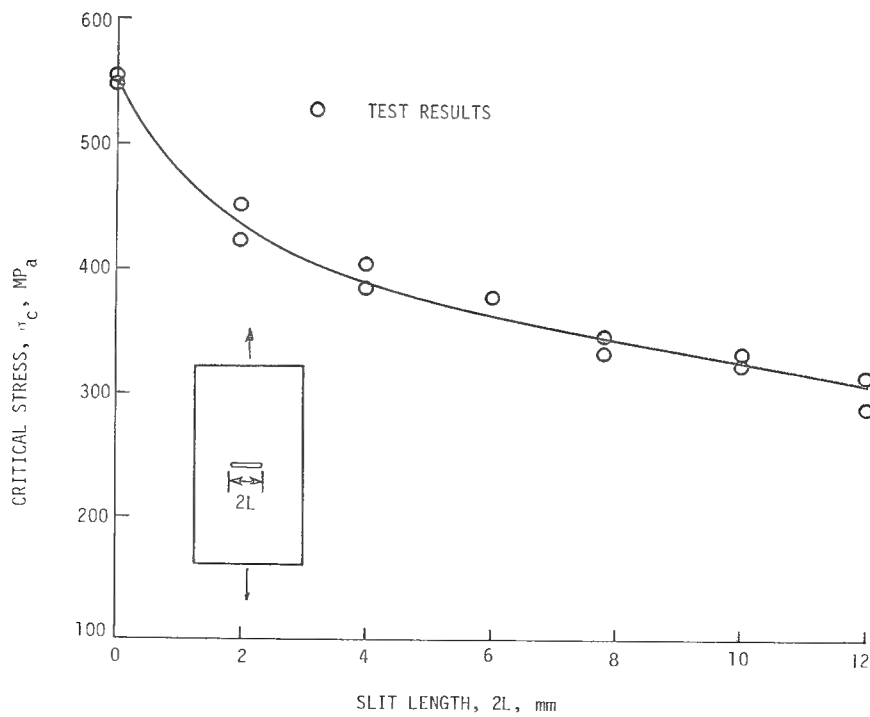


Figure 10 - Results of fracture-toughness tests.



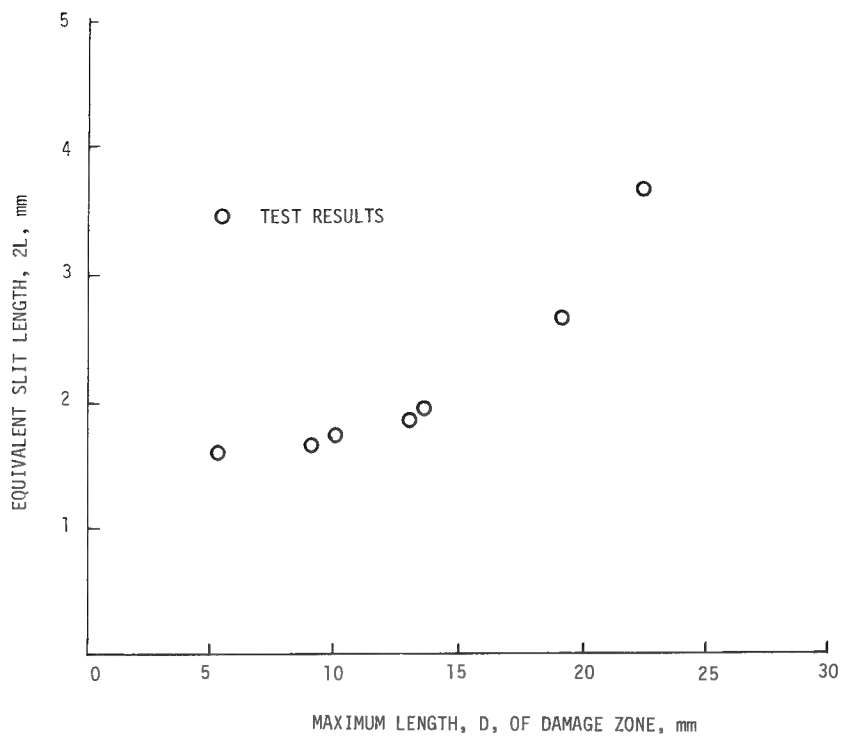


Figure 11 - Variation of equivalent slit size with impact-damage size length.

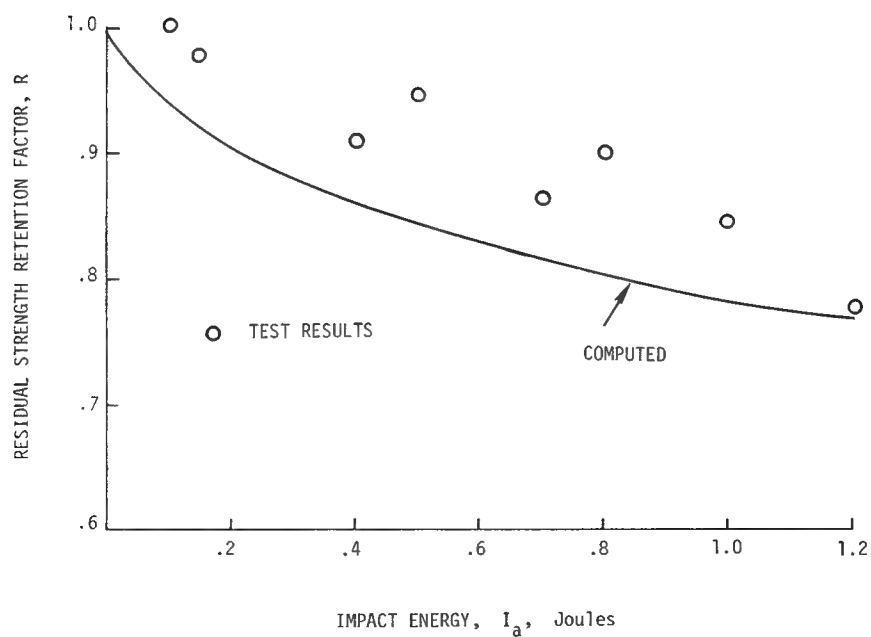


Figure 12 - Variation of tensile residual strength retention factor with impact energy.

INTERACTION OF HEAT PRODUCTION, STRAIN RATE AND STRESS POWER  
IN A PLASTICALLY DEFORMING BODY UNDER TENSILE TEST <sup>1</sup>

A. Paglietti

Istituto Scienza Costruzioni  
Università di Cagliari, 09100-CAGLIARI, Italy

SUMMARY

At high strain rates the heat produced by plastic deformation can give rise to a rate-dependent response even if the material has rate-independent constitutive equations. This effect has to be evaluated when interpreting a material test, or else it could erroneously be ascribed to viscosity. A general thermodynamic theory of tensile testing of elastic-plastic materials is given in this paper; it is valid for large strain at finite strain rates. It enables discovery of the parameters governing the thermodynamic strain-rate effect, provides a method for proper interpretation of the results of the tests of dynamic plasticity, and suggests a way of planning experiments in order to detect the real contribution of viscosity.

INTRODUCTION

Most of the mechanical work expended in producing plastic deformation of a ductile material is dissipated into heat by the material itself (ref. 1, 2). If the deformation process is slow enough and the body is not thermally insulated, the heat produced by plastic deformation can flow to the surroundings without producing any considerable variation in the temperature field of the body. For fast deformation processes as the ones considered in dynamic plasticity, however, the rate at which heat is produced may exceed the rate at which it is given off to the surroundings. The temperature of the body must, therefore, rise and eventually both its mechanical properties and its stress state are affected.

In engineering problems involving high rates of plastic deformation, the stress/strain properties of the material are usually determined by uniaxial tensile tests performed at different strain rates. The results of these tests are rate-sensitive; this fact is normally interpreted as providing evidence of visco-plastic behaviour. Accordingly, rate-dependent constitutive equations are postulated to model the behaviour of the material (see, e.g., ref. 3 and 4). The thermodynamic influence on rate-dependence should, however, be properly assessed before any rate dependence in the test response can be ascribed to rate-dependent constitutive equations. In the plastic range the thermomechanical coupling may transform the state of stress of the specimen from a uniaxial state to a tri-axial one. This may not only increase the amount of plastic work that can be dissipated in the process, but also facilitate a non-uniform production of heat within the specimen. The process may thus produce a state of stress that is far different from the uniaxial one on which the purely mechanical interpretation is based. This may provide an explanation of the discrepancies that Bell consistently observed in his extensive review (ref. 5) of the experimental results in dynamic plasticity.

Rate-independent elastic-plastic materials will be considered in this paper, and a theory to evaluate the thermodynamic rate effect during a tensile test will be

---

<sup>1</sup> Partially supported by Italian research grant CNR n. 81.0258.07, and MPI research fund for 1981/82.

proposed. The analysis enables some very general conclusions to be drawn concerning the correct interpretation of the experimental results of dynamic plasticity. It also enables design of appropriate experiments to evaluate the real contribution of viscosity. The resulting theory is valid for large deformations, and its numerical treatment is within the range of the current computational procedures. It is expected to be valid up to strain rates of about  $10^2 \text{ sec}^{-1}$ , since for higher strain rates the effect of strain wave propagation may not be negligible. The material is supposed to exhibit a rate-independent stress/strain response for quasi-static tensile tests at the standard rates of strain of  $10^{-3}$  to  $10^{-4} \text{ sec}^{-1}$ . Since strain rates above these limits will henceforth be considered, long term viscous effects such as creep are excluded. Apparently, the possibility that due to thermodynamic coupling a rate-independent elastic-plastic material can exhibit a time-dependent response was first anticipated by Drucker (ref. 6).

#### KINEMATIC DESCRIPTION

A material tensile test specimen will be regarded as a solid circular cylinder of indefinite length and external radius  $R_0$ . In its initial stress-free configuration, the specimen will be referred to a cylindrical co-ordinate system whose  $X^3$ -axis coincides with the axis of the specimen, and whose radial and angular co-ordinates are denoted by  $X^1$  and  $X^2$ . Each material particle of the specimen will thus be labelled by a triplet of material co-ordinates  $X^1, X^2, X^3$ , where  $0 \leq X^1 \leq R_0$ ,  $0 \leq X^2 < 2\pi$  and  $X^3$  may be any real number.

#### Deformation

In a tensile test the end sections of the specimen are progressively displaced from each other by a rigid translation in the direction of the specimen axis. Let this relative displacement at time  $t$  be  $\Delta L(t)$ , and let  $B = \hat{B}(t)$  denote the ratio between  $\Delta L(t)$  and the length of the specimen. If the specimen is free from lateral forces and its temperature field is axially symmetric, its deformation will for symmetry reasons be a simple extension of the form

$$\left. \begin{aligned} x^1 &= X^1 + \hat{A}(X^1, t) \\ x^2 &= X^2 \\ x^3 &= \hat{B}(t) X^3 + c \end{aligned} \right\} \quad (1)$$

Here  $x^1, x^2$  and  $x^3$  are the co-ordinates at time  $t$  of the material point of initial co-ordinates  $X^1, X^2$  and  $X^3$ ; the quantity  $A = \hat{A}(X^1, t)$  is a function of  $X^1$  and  $t$ , presently undetermined; while  $c$  is an irrelevant constant that depends on the choice of the origin of the adopted co-ordinate system. It is usually assumed that the temperature of the specimen is uniform, and thus it is concluded that  $\hat{A}(X^1, t)$  is constant. This assumption, however, is not generally true for tests at finite rate of deformation in the plastic range, owing to heat production ensuing from plastic deformation. In general, therefore, the quantity  $A$  will not be constant and, as a consequence, non-uniform stress and strain fields will be produced in the specimen. The analysis contained in this paper is then needed to relate the load/displacement data obtained from the test to the stress/strain response of the material.

#### Strain variables

For a deformation that takes a material point from its initial position  $\underline{x} \equiv (X^1, X^2, X^3)$  to the final one  $\underline{x} \equiv (x^1, x^2, x^3)$ , the total deformation gradient is defined by  $\underline{F} = \partial \underline{x} / \partial \underline{X}$ . To describe the elastic and plastic components of strain, the tensor  $\underline{F}$  will be decomposed in the form

$$\underline{F} = \underline{F}^e \underline{F}^p \quad (2)$$

as proposed by Lee and co-workers in a series of papers dating back to the late sixties (cfr. ref. 7). Here  $\underline{F}^P$  is the plastic deformation gradient relevant to an imaginary deformation process that takes the body from the initial stress-free configuration to a fictitious plastically deformed and stress-free configuration at the initial temperature, referred to as the intermediate configuration. The latter can also be reached by a rotation-free purely elastic unloading process starting from the final elastically and plastically deformed configuration. The reverse process of this purely elastic unloading process, therefore, takes the body from the intermediate configuration to the final one. It produces the elastic deformation gradient  $\underline{F}^e$  with respect to the intermediate configuration.

From eq. (1) the physical components of the total deformation gradient  $\underline{F}$  imposed by the test on the specimen can easily be obtained:

$$F_{\langle iK \rangle} = \begin{pmatrix} 1 + \partial A / \partial X^1 & 0 & 0 \\ 0 & 1 + A / X^1 & 0 \\ 0 & 0 & B \end{pmatrix} \quad (3)$$

These components form a symmetric and diagonal matrix, since the deformation does not produce any rotation in the elements of the body and since, moreover, the principal directions of strain are fixed in the body and coincide with the directions of the base vectors of the co-ordinate system. As the material is supposed to be isotropic, the matrix of the tensor  $\underline{F}^e$  must be diagonal too. In view of eq. (2) this implies that also the matrix of  $\underline{F}^P$  must be diagonal and that, therefore, in the considered system of co-ordinates the mixed components of  $\underline{F}^e$  and  $\underline{F}^P$  have the form

$$F_{\langle iK \rangle}^e = \begin{pmatrix} \lambda_i^e & 0 & 0 \\ 0 & \lambda_2^e & 0 \\ 0 & 0 & \lambda_3^e \end{pmatrix} \quad F_{\langle iK \rangle}^P = \begin{pmatrix} \lambda_1^P & 0 & 0 \\ 0 & \lambda_2^P & 0 \\ 0 & 0 & \lambda_3^P \end{pmatrix} \quad (4)$$

From eq. (2), (3) and (4) it follows that

$$F_{\langle ii \rangle} = \lambda_i^e \lambda_i^P = \lambda_i \quad (i \text{ not summed}) \quad (5)$$

Following Lee & Wierzbicki (ref.8) and Lee & McMeeking (ref.9), logarithmic strain measures will be introduced as follows:

$$\epsilon_i^e = \ln \lambda_i^e \quad (6)$$

$$\epsilon_i^P = \ln \lambda_i^P \quad (7)$$

$$\epsilon_i = \ln \lambda_i \quad (8)$$

This greatly simplifies the analysis since, as immediately follows from eq.(5), equations (6)-(8) entail additivity not only for elastic and plastic strain,

$$\epsilon_i = \epsilon_i^e + \epsilon_i^P \quad (9)$$

but also for their strain rates,

$$\dot{\epsilon}_i = \dot{\epsilon}_i^e + \dot{\epsilon}_i^P \quad (10)$$

From the component representation (3) and from the definition of  $\lambda_i$  and  $\epsilon_i$ , it

can easily be verified that  $\lambda_1, \varepsilon_1, \lambda_2$  and  $\varepsilon_2$  are all determined by the sole quantity  $A$ . This means, in particular, that  $\varepsilon_2$  can be determined once  $\varepsilon_1$  is given. The relation between them can be obtained explicitly by observing that

$$1 - \partial A / \partial X^1 = \lambda_1 = \lambda_2 + X^1 (\partial \lambda_2 / \partial X^1) \quad (11)$$

as immediately follows from the expressions of the first and the second components of  $\underline{F}$  appearing in (3). By integrating the differential equation (11), and by setting the integration constant equal to zero to prevent  $\lambda_2$  from diverging as  $X^1 \rightarrow 0$ , the relation

$$\lambda_2 = \hat{\lambda}_2(X^1, t) = \frac{1}{X^1} \int_0^{X^1} \lambda_1 \, dx^1 \quad (12)$$

is obtained. From this and from definition (8) the relation between  $\varepsilon_1$  and  $\varepsilon_2$  follows:

$$\varepsilon_2 = \hat{\varepsilon}_2(X, t) = \ln \left[ \frac{1}{X^1} \int_0^{X^1} \exp \varepsilon_1 \, dx^1 \right] \quad (13)$$

#### CONSTITUTIVE EQUATIONS

The absolute temperature  $\theta$  and the mechanical variables  $\varepsilon_i^e$  and  $\varepsilon_i^p$  are the independent field variables adopted to describe the behaviour of the elastic-plastic materials considered in this paper. Explicit constitutive equations must now be given to relate these variables to derived quantities such as specific internal energy  $u$  (per unit mass), specific entropy  $\eta$  (per unit mass), thermal energy flux vector  $\underline{e}_q$ , and (Cauchy) stress tensor  $\underline{g}$ . These quantities, however, depend on the independent variables in an involved way, since in general they are functionals (rather than ordinary functions) of  $\varepsilon_i^e, \varepsilon_i^p$  and  $\theta$ . The internal energy of the material, for instance, may be affected by the crystal lattice distortions resulting from the accumulation of plastic deformation, and hence will in general depend on the whole history of  $\varepsilon_i^p$ , rather than on their actual values. A simplification of the constitutive equations can be obtained by observing that the elastic properties of many materials are not in practice sensibly affected by plastic deformation up to values of plastic strain as high as 30%, as remarked by Lee (ref.10). It is then reasonable to assume that both  $\underline{g}$  and  $\underline{e}_q$  are unaffected by  $\varepsilon_i^p$  and that, therefore, their constitutive equations in terms of  $\varepsilon_i^e$  and  $\theta$  are those of a thermoelastic material.

On the other hand, as far as the constitutive equations of  $u$  and  $\eta$  are concerned, it should be noted that to solve an initial boundary value problem, constitutive equations are needed for the time rates  $\dot{u}$  and  $\dot{\eta}$ , and not for  $u$  and  $\eta$  themselves. In what follows, therefore, constitutive equations for  $\dot{u}$  and  $\dot{\eta}$  will be given, while the explicit expression of the functionals  $u$  and  $\eta$  will be ignored. Since the proposed equations for  $\dot{u}$  and  $\dot{\eta}$  are not integrable, they cannot give  $u$  and  $\eta$  as functions of  $\varepsilon_i^e, \varepsilon_i^p$  and  $\theta$ . The values of  $u$  and  $\eta$ , therefore, will depend on the process that the material undergoes, and hence the adopted approach amounts to introducing a functional dependence of  $u$  and  $\eta$  on  $\varepsilon_i^e, \varepsilon_i^p$  and  $\theta$ . Though not explicitly introduced and, clearly, not the most general one, this dependence is adequate and makes the analysis simpler.

#### Stress relation

As mentioned before, it is assumed that the stress tensor is related to elastic strain and absolute temperature as in a thermoelastic material (cfr. hyperelastic

materials in Sect. 82 of ref. 11). There will, therefore, be a scalar function  $\psi^e = \bar{\psi}^e(\bar{F}^e, \theta) = \bar{\psi}^e(\varepsilon_1^e, \varepsilon_2^e, \varepsilon_3^e, \theta)$  from which the tensor  $\underline{g}$  can be derived through the relation

$$\underline{g} = \rho \bar{F}^e (\partial \psi^e / \partial \bar{F}^e) \quad (14)$$

$\rho$  denoting mass density in the actual configuration. The quantity  $\psi^e$  is usually referred to as the Helmholtz free energy per unit mass. Its experimental determination is discussed in ref. 8. It is of interest here to recall that the elastic part  $u^e$  of the specific internal energy  $u$  can be defined in terms of  $\psi^e$  from the relation

$$u^e = \hat{u}^e(\bar{F}^e, \theta) = \psi^e + \theta \eta^e \quad (15)$$

where

$$\eta^e = - \partial \psi^e / \partial \theta \quad (16)$$

is the elastic specific entropy per unit mass.

By expressing  $\psi^e$  as a polynomial function of the invariants of the elastic strain tensor and of  $\theta$ , and by confining our attention to the terms up to the second degree in  $\varepsilon_i^e$  and  $\theta$ , it is not difficult to prove that in the adopted system of co-ordinates eq. (14) can be written in the explicit form:

$$(\rho_0 / \rho) \sigma_i = \lambda (\varepsilon_1^e + \varepsilon_2^e + \varepsilon_3^e) + 2 G \varepsilon_i^e - K \alpha (\theta - \theta_0) \quad (17)$$

Here  $\rho_0$  and  $\theta_0$  are the mass density and the absolute temperature of the body at the reference configuration,  $\lambda$  and  $G$  are the Lamé elastic constants, while  $K$  is the bulk modulus. In writing eq. (17) the abridged (one-index) notation

$$\sigma_i \stackrel{\text{def}}{=} \sigma_i^i \quad (i \text{ not summed}) \quad (18)$$

has been adopted. This notation is particularly convenient for the present case, as in the present reference system all non-diagonal components of  $\underline{g}$  vanish, since the base vectors are in the same direction as the principal stresses. Equations (17) differ from the classical thermoelastic constitutive equations except for the term  $\rho_0 / \rho$ , which accounts for volume changes due to finite strain (cfr. ref. 8).

For further reference the expression of the time rate of elastic entropy is recorded here, as follows from eq. (16):

$$\dot{\eta}^e = - \text{tr} [ (\partial^2 \psi^e / \partial \theta \partial \bar{F}^e)^T \dot{\bar{F}}^e ] + c_v \dot{\theta} \quad (19)$$

In this equation the quantity  $c_v$  is the material specific heat at constant volume:

$$c_v = - (\partial^2 \psi^e / \partial \theta^2) \theta \quad (20)$$

(cfr., e.g., p.31 of ref. 12). The first term in the right-hand side of eq. (19) can readily be calculated from eq. (14) and (17). However, the thermomechanical coupling that it implies is usually negligible (ref. 12, Chap. 2). This is especially so in the present case, owing to the overwhelming contribution of the thermomechanical coupling due to dissipation of the plastic work.

#### Thermal energy flux relation

It will be assumed that the constitutive equation for  $\underline{e}_q$  is given by

$$\underline{e}_q = - k_q \text{grad } \theta \quad (21)$$

where  $k_G > 0$  is the heat conduction coefficient, for simplicity assumed to be constant. While not the most general relation compatible with the present assumptions, eq. (21) has been proved to be adequate for most materials in a wide range of conditions.

#### Specific energy and specific entropy relations

The contributions  $u^P$  and  $\eta^P$  of plastic deformation to  $u$  and  $\eta$  can be evaluated on the basis of the celebrated experiments of Ferren & Taylor (ref. 1). According to these experiments the amount  $w^P$  of plastic work that is turned into heat is given by  $\gamma w^P$ , where  $\gamma$  varies slightly around the value 0.9. The remaining fraction  $(1 - \gamma)$  of plastic work is supposed to distort the crystal lattice of the material, and is thus stored in it as internal energy. On the basis of these experimental findings, it will be assumed that the same result applies locally and, therefore, that

$$\dot{u}^P = (1 - \gamma) w^P / \rho \quad (22)$$

and

$$\dot{\eta}^P = \gamma w^P / (\rho \theta) \quad (23)$$

The quantity  $w^P$  introduced in these equations is the specific plastic work per unit time (plastic power) expended on the material per unit volume of the actual configuration by the stress tensor. In the present notation it has the form

$$w^P = \text{tr} (\underline{\underline{\sigma}} \dot{\underline{\underline{F}}}^P \underline{\underline{F}}^{P-1}) = \sigma_i \dot{\epsilon}_i^P \quad (24)$$

as the tensor  $\underline{\underline{F}}^e$  is rotation-free (cfr. ref. 7 and 9). By adding the plastic components of  $\dot{u}$  and  $\dot{\eta}$  to the elastic ones, we get

$$\dot{u} = \dot{u}^e + \dot{u}^P \quad (25)$$

and

$$\dot{\eta} = \dot{\eta}^e + \dot{\eta}^P \quad (26)$$

where the quantity  $\dot{u}^e$  is readily obtained by time differentiation of eq. (15), while  $\dot{\eta}^e$  has the expression (19).

#### Yield function and plastic flow equations

According to what is experimentally observed in metal plasticity, it will be assumed that plastic deformation occurs at constant volume and that, therefore,

$$\det \underline{\underline{F}}^P = 1 \quad (27)$$

In view of eq. (2), this means that

$$\det \underline{\underline{F}} = \det \underline{\underline{F}}^e = \rho_0 / \rho \quad (28)$$

To embody requirement (27) in the theory, the yield function is usually regarded as depending on stress through the stress deviator. Rather than referring to the stress deviator of the Cauchy stress  $\underline{\underline{\sigma}}$ , the symmetric Kirchhoff deviatoric stress

$$s_i \stackrel{\text{def}}{=} s_i^1 = (\rho_0 / \rho) \left[ \sigma_i - \frac{1}{3} (\sigma_1 + \sigma_2 + \sigma_3) \right] \quad (i \text{ not summed}) \quad (29)$$

will be introduced in the formulae that follow. This was proposed by Lee (ref. 7) in order to make the yield stress depend on the factor  $\rho_0 / \rho$ , and thus avoid the contradiction of having less plastic work as the hydrostatic component of elastic strain increases by a finite extent.

For non-isothermal plasticity, an approach which is essentially due to Prager (ref. 13), and further developed by Boley & Weiner (ref. 12) and Lee (ref. 7), leads to the following expression of the constitutive equations of a work-hardening elastic-plastic material undergoing non-isothermal processes. A yield function of the form

$$f = \hat{f}(s_i, \epsilon^p_i, \theta) \quad (30)$$

regulates the plastic flow by means of the following relations:

$$\dot{\epsilon}^p_i = 0 \quad \begin{array}{l} \text{if } f < 0 \\ \text{or if } f = 0 \text{ and } \left( \frac{\partial f}{\partial s_k} \dot{s}_k + \frac{\partial f}{\partial \theta} \dot{\theta} \right) < 0 \end{array} \quad (31)$$

while

$$\dot{\epsilon}^p_i = \frac{1}{D} \frac{\partial f}{\partial s_i} \left( \frac{\partial f}{\partial s_k} \dot{s}_k + \frac{\partial f}{\partial \theta} \dot{\theta} \right) \quad \begin{array}{l} \text{if both } f = 0 \\ \text{and } \left( \frac{\partial f}{\partial s_k} \dot{s}_k + \frac{\partial f}{\partial \theta} \dot{\theta} \right) \geq 0 \end{array} \quad (32)$$

Here D is given by

$$D = - \frac{\partial f}{\partial s_r} \frac{\partial f}{\partial \epsilon^p_r} \quad (33)$$

A particular case is that of Von Mises elastic, perfectly plastic materials, for which the yield function becomes

$$f = \frac{1}{2} (s_1^2 + s_2^2 + s_3^2) - [\hat{k}(\theta)]^2 \quad (34)$$

where

$$k = \hat{k}(\theta) = \sigma^Y / \sqrt{3} \quad (35)$$

is the yield stress in simple shear at temperature  $\theta$ , and  $\sigma^Y = \hat{\sigma}^Y(\theta)$  is the yield stress in uniaxial tension at the same temperature. The plastic flow associated with eq. (34) is governed by

$$\dot{\epsilon}^p_i = 0 \quad \begin{array}{l} \text{if } f < 0 \\ \text{or if } f = 0 \text{ and } 2\mu \dot{s}_j \dot{e}_j + 2k \frac{\partial k}{\partial \theta} \dot{\theta} < 0 \end{array} \quad (36)$$

and

$$\dot{\epsilon}^p_i = \mu s_i \quad \begin{array}{l} \text{if both } f = 0 \\ \text{and } 2\mu \dot{s}_j \dot{e}_j + 2k \frac{\partial k}{\partial \theta} \dot{\theta} \geq 0 \end{array} \quad (37)$$

where

$$\mu = \frac{1}{2} s_j \dot{\epsilon}^p_j / [\hat{k}(\theta)]^2 \quad (38)$$

while

$$e_i \stackrel{\text{def}}{=} \epsilon_i - \frac{1}{3} (\epsilon_1 + \epsilon_2 + \epsilon_3) \quad (39)$$

are the components of the deviator of the total logarithmic strain tensor.

**Remark 1.** Hypothesis (23) is equivalent to assuming that the mechanical power  $\gamma w^p$  is entirely turned into thermal energy at the material element where it is expended. This may not necessarily be so for real materials, as transformations of heat into non-thermal energy may occur when the body temperature is not uniform. If this happens, it has the effect of diminishing the amount of plastic work that is actually turned



into heat at the element. Of course, somewhere else in the body the non-thermal energy thus produced must eventually be turned again into heat, if Farren & Taylor's experimental result is to be globally met. A material for which eq.(23) applies can be referred to as a perfectly dissipative elastic-plastic material.

Remark 2. Owing to the abridged notation introduced by equations (18) and (29) to express diagonal mixed tensor components by one-index symbols, the equations where these symbols appear lose their tensor character. In the orthogonal co-ordinate system adopted in this paper, however, diagonal mixed components of second order tensors coincide with their homologous physical components (ref. 14). Therefore, since the non-diagonal components of the tensors considered in this paper vanish, all the formulae in the one-index notation in fact coincide with the expressions of the correct tensor relations in physical component form. Of course the summation rule over repeated indices is assumed throughout unless otherwise stated.

Remark 3. In simple tension the hydrostatic component of the elastic strain is small since plastic yielding sets a limit to the elastic tensile strain. For many materials this limit is within the range of infinitesimal deformation. In such conditions it can reasonably be assumed that  $\rho_0 \approx \rho$ , as plastic deformation does not produce volume changes. This justifies the simplifying assumption

$$\rho_0 / \rho = 1 \quad (40)$$

which will be introduced in what follows.

#### BALANCE EQUATIONS AND INITIAL & BOUNDARY CONDITIONS

As is well-known, the local form of the 1st principle of thermodynamics is expressed by the balance equation

$$\rho \dot{u} = w_t - \text{div } \underline{e}_q \quad (41)$$

where  $w_t$  denotes the total specific power expended per unit volume by the surroundings on the volume element to which eq.(41) is referred. Generally speaking,  $w_t$  is composed of two terms (ref. 15):

$$w_t = w - p \quad (42)$$

Here  $w$  denotes the part of  $w_t$  expended through changes in the independent variables describing the state of the element, while  $p$  is the power the element supplies to the surroundings in addition to  $-w$  and to the thermal power  $\text{div } \underline{e}_q$ . For the class of materials considered in this paper,  $w$  is simply the total stress working per unit volume,  $w = \text{tr}(\underline{\sigma} \dot{\underline{F}} \underline{F}^{-1})$ . This reduces to

$$w = \sigma_1 \dot{\epsilon}_1 + \sigma_2 \dot{\epsilon}_2 + \sigma_3 \dot{\epsilon}_3 \quad (43)$$

for the deformation process defined by eq. (1). It will henceforth be assumed that there is no other supply of energy per unit volume besides that originating from  $w$  and from the thermal energy flux  $\underline{e}_q$ . In these conditions  $p$  reduces to energy production generated by the flow of heat through the element. It is expected, therefore, that  $p = 0$  when  $\text{grad } \theta = 0$ .

In the above conditions the usual approach to thermodynamics neglects  $p$  altogether. This may not be correct, as observed in ref. 15. When it is not neglected, however,

p becomes a new unknown variable and, therefore, an additional equation is needed to determine it. This is provided by the general entropy equation (ref. 16):

$$\rho \dot{\eta} = - \frac{1}{\theta} \operatorname{div} \underline{e}_q + \frac{1}{\theta^2} \underline{e}_q \cdot \operatorname{grad} \theta \quad (44)$$

While this equation can be justified in various ways, essentially it is a necessary consequence of the second principle of thermodynamics (ref.16). A complete discussion of it is well outside the scope of the present paper and has recently been reported elsewhere (ref. 16, 17). It is introduced here in order to make the present analysis consistent with the recent theory of non-equilibrium thermodynamics of ref. 15, 16 and 17. The results of this paper, however, do not suffer any substantial change if both p and eq. (44) are ignored, and one of the standard thermodynamic approaches is followed. As will be observed below, this is equivalent to neglecting a term in the final expression of the energy balance, whose contribution is expected to be small for the class of processes considered in this paper.

By observing that

$$w = w^e + w^p \quad (45)$$

and that

$$\operatorname{div} (\underline{e}_q / \theta) = (\operatorname{div} \underline{e}_q) / \theta - (\underline{e}_q \cdot \operatorname{grad} \theta) / \theta^2 \quad (46)$$

by introducing eq. (44) into eq.(41) and, finally by exploiting the adopted constitutive equations for  $\dot{u}$  and  $\dot{\eta}$ , the value of p can be determined:

$$p = - \frac{1}{\theta} \underline{e}_q \cdot \operatorname{grad} \theta \quad (47)$$

Once the entropy equation (44) is thus exploited, the quantity p can be eliminated from the energy balance equation, which therefore becomes

$$\rho \dot{u} = w + \frac{1}{\theta} \underline{e}_q \cdot \operatorname{grad} \theta - \operatorname{div} \underline{e}_q \quad (48)$$

Henceforth reference to this energy balance equation will be made. The results of the analysis which follows, however, hold true also when the term containing  $\operatorname{grad} \theta$  is dropped from it, which then reduces to the classical energy balance equation.

**Remark 4.** It is not difficult to verify that the condition  $p=0$  is compatible with the entropy equation (44) only if  $\operatorname{grad} \theta = 0$ . Hence, strictly speaking, the classical thermodynamic approach is not correct when applied to non-uniform temperature processes. It is expected, however, to provide a good approximation to the present approach, when  $\operatorname{grad} \theta$  is sufficiently small.

As far as the equilibrium equations are concerned, they reduce to

$$\operatorname{div} \underline{g} = 0 \quad (49)$$

since the effect of inertia and body forces can in the present case be neglected.

Explicit expressions of both eq. (48) and eq. (49), and their relevant initial and boundary conditions are given below for the tensile test process considered in this paper. By setting

$$x^1 = r, \quad x^2 = \phi \quad \text{and} \quad x^3 = z \quad (50)$$

and by making use of the adopted constitutive equations and of the axial-symmetry properties of the process, the energy balance equation (48) takes the explicit form:

$$\rho c_v \frac{\partial \theta}{\partial t} = \gamma w^p - k_q \frac{1}{\theta} \left( \frac{\partial \theta}{\partial r} \right)^2 + k_q \frac{\partial^2 \theta}{\partial r^2} \quad (51)$$

where  $\theta = \hat{\theta}(r, t)$ . The relevant initial condition is

$$\hat{\theta}(r, 0) = \theta_0 \quad (52)$$

while the boundary condition reads

$$\left( \frac{\partial \theta}{\partial r} \right)_{r=r_e} = [\theta(r_e, t) - \theta_0] h \quad (53)$$

where from the first part of eq. (1), we have that

$$r_e = R_e + \hat{A}(R_e, t) \quad (54)$$

The coefficient  $h$  appearing in eq. (53) depends on the specific surface heat transfer  $H$  and on the heat conduction coefficient  $k_q$  through the relation

$$h = H / k_q \quad (55)$$

(cfr. ref. 18). On the other hand, the only equilibrium equation which is not identically met is

$$\frac{\partial \sigma_1}{\partial r} + (\sigma_1 - \sigma_2)/r = 0 \quad (56)$$

Since no surface tractions are applied to the cylinder, the boundary condition associated with eq. (56) is

$$(\sigma_1)_{r=r_e} = 0 \quad (57)$$

#### DIMENSIONLESS FORMULATION

The nine relations (51), (56), (13), (17) and (31)-(32) provide sufficient conditions to determine the nine unknown fields  $\varepsilon_2, \varepsilon_3, \sigma_1, \sigma_2, \sigma_3, \varepsilon^p_1, \varepsilon^p_2, \varepsilon^p_3$  and  $\theta$ , once the test procedure is specified by assigning the test velocity [that is the function  $\varepsilon_1 = \hat{\varepsilon}_1(t)$  or, equivalently, the function  $B = \hat{B}(t)$ ] and the initial and boundary conditions, eq. (52), (53) and (57). In the case of Von Mises elastic, perfectly plastic materials, the system of governing equations depends on 12 parameters, namely  $c_v, \gamma, k_q, \lambda, G, K, \alpha, \mu, k, h, R_e$  and  $\theta_0$ . The discussion of its solutions is greatly facilitated by expressing the governing equations in dimensionless form. This is easily achieved by introducing the following dimensionless variables:

$$\left. \begin{aligned} \bar{r} &= r/R_e \\ \bar{\theta} &= \theta/\theta_0 \\ \bar{t} &= t k_q / (\rho c_v R_e^2) \\ \bar{\sigma}_i &= \sigma_i / (K \alpha \theta_0) \end{aligned} \right\} \begin{aligned} \bar{\varepsilon}_i &= \varepsilon_i / (\alpha \theta_0) \\ \bar{\varepsilon}^e_i &= \varepsilon^e_i / (\alpha \theta_0) \\ \bar{\varepsilon}^p_i &= \varepsilon^p_i / (\alpha \theta_0) \\ \bar{k} &= \tilde{k}(\bar{\theta}) = \hat{k}(\theta_0 \bar{\theta}) / (K \alpha \theta_0) \end{aligned} \quad (58)$$

The energy balance (51) and the conditions (52) and (53) then become

$$\frac{\partial \bar{\theta}}{\partial \bar{t}} = \mathcal{R} - \frac{1}{\bar{\theta}} \left( \frac{\partial \bar{\theta}}{\partial \bar{r}} \right)^2 + \frac{\partial^2 \bar{\theta}}{\partial \bar{r}^2} \quad (59)$$

$$\bar{\theta}(\bar{r}, 1) = 1 \quad (60)$$

and

$$(\partial \bar{\theta} / \partial \bar{r})_{\bar{r}=1} = [\bar{\theta}(1, \bar{t}) - 1] \mathcal{L} \quad (61)$$

Here the two dimensionless parameters  $\mathcal{R}$  and  $\mathcal{L}$  are given by

$$\mathcal{R} = \gamma w_p R_e^2 / (\theta_0 k_q) \quad (62)$$

and

$$\mathcal{L} = R_e h \quad (63)$$

The equilibrium equation (56) and the boundary condition (58) become

$$\partial \bar{\sigma}_1 / \partial \bar{r} + (\bar{\sigma}_1 - \bar{\sigma}_2) / \bar{r} = 0 \quad (64)$$

and

$$\bar{\sigma}_1(1, \bar{t}) = 0 \quad (65)$$

The elastic constitutive equations become

$$(\rho_0 / \rho) \bar{\sigma}_i = N (\bar{\epsilon}_1^e + \bar{\epsilon}_2^e + \bar{\epsilon}_3^e) + M \bar{\epsilon}_i - (\bar{\theta} - 1) \quad (66)$$

where the dimensionless constants  $M$  and  $N$  are given by

$$N = \lambda / K = 3 \nu (1 + \nu) \quad (67)$$

and

$$M = 2 G / K = 3 (1 - 2 \nu) / (1 + \nu) \quad (68)$$

and hence depend only on the Poisson ratio  $\nu$  of the material. Finally the yield function (34) becomes

$$\bar{f} = \frac{1}{2} (\bar{s}_1^2 + \bar{s}_2^2 + \bar{s}_3^2) - [\tilde{k}(\bar{\theta})] \quad (69)$$

and the plastic flow equation (37) assumes the form

$$\dot{\bar{\epsilon}}_i^p = \bar{\mu} \bar{s}_i \quad (70)$$

where

$$\bar{\mu} = K \mu \quad (71)$$

It is apparent now that, when expressed in the new variables, the problem depends only on the six dimensionless variables  $\mathcal{R}, \mathcal{L}, \nu, \bar{k}$  and  $\bar{\mu}$ . Moreover, if a given material is considered, then the constants  $\nu, \bar{k}$  and  $\bar{\mu}$  are fixed, and the characteristic parameters of the problem reduce to two,  $\mathcal{R}$  and  $\mathcal{L}$ .

Remark 5. Strictly speaking the value of  $\mathcal{R}$  depends on the point of the specimen where it is calculated, since  $w^p$  does the same. As far as an estimate of the value of  $\mathcal{R}$  is concerned, however, it is not unreasonable to assume that  $w^p$  is roughly constant throughout the specimen and that, therefore, the usual approximation of uniform stress and strain holds true. One can thus speak of a value of  $\mathcal{R}$  for the testing process. Such an approximation is justified by the fact that while the rate of strain and hence the value of  $w^p$  can vary greatly for different tests, only relatively small variations are expected for the values of  $w^p$  at different points of the specimen during the same test.

## RESULTS AND DISCUSSION

The present analysis shows that tensile tests of a given material in the plastic range of deformations are governed by only two dimensionless parameters  $\mathcal{R}$  and  $\mathcal{L}$ . This means that any dimensionless ratio between quantities relevant to the testing process cannot depend on other quantities than  $\mathcal{R}$  and  $\mathcal{L}$ . In particular, for a given value of  $\varepsilon_1$ , let  $T$  and  $T_0$  denote the traction forces that must be applied to the specimen when the test is performed at a finite strain rate  $\dot{\varepsilon}_1$  and in a quasi-static fashion, respectively. Clearly the ratio  $\tau$  between  $T$  and  $T_0$  is a measure of the strain-rate effect. Owing to the previous remark this ratio can depend on  $\mathcal{R}$  and  $\mathcal{L}$  only. That is

$$\tau = T/T_0 = \hat{\tau}(\mathcal{R}, \mathcal{L}) \quad (72)$$

This results in the following two conclusions: (a) since  $\mathcal{R}$  depends on  $w^P$  and, hence, on the rate of plastic strain, the force to be applied during a tensile test will depend on the rate of strain, even if the material is a non-viscous one; and (b) the tensile force  $T$  will in general depend on the capacity of the specimen to transfer heat to its surroundings, because  $\tau$  depends on  $\mathcal{L}$ .

One cannot exclude, of course, the sheer possibility that  $\tau$  is almost a constant function of  $\mathcal{R}$  and  $\mathcal{L}$ , and that, therefore, there is no rate effect due to thermodynamics. Experimental evidence, however, hints at excluding such a possibility. Conclusion (a) is supported by the readily available evidence that while different traction forces are needed to perform tensile tests at different strain rates, the plastic deformation to rupture the specimen is roughly rate-independent. This supports the hypothesis of rate effects of non-viscous origin and, apparently, was first noticed by Mann (cfr. pp. 326-327 of ref. 19). On the other hand, some experiments reported by Gruntfest (ref. 20) seem to lend grounds for conclusion (b). They show that different heat exchange conditions at the surface of a metal wire do in fact affect its plastic behaviour in tensile tests at non-vanishing strain rates.

The analysis of the present paper should be borne in mind when planning and interpreting experimental tests in dynamic plasticity. The rate effect exhibited by these tests is usually interpreted as viscous in origin and, accordingly, the experimental data are fed into suitable visco-plastic constitutive equations to determine the material constants. Before a rate effect can be ascribed to viscosity, however, it must first be proved that the rate effects due to thermodynamics are negligible. In view of eq. (72), this can be done by comparing at different strain rates the results of different tests having the same values of  $\mathcal{R}$  and  $\mathcal{L}$ . For all such tests the value of  $\tau$  should be the same, if viscous effects are absent. Any dependence of  $\tau$  on the rate of strain should otherwise be ascribed to viscosity.

If in the above tests the value of  $\mathcal{L}$  is kept constant (which in practice and in good approximation can be obtained by keeping the initial temperature  $\theta_0$  constant), then for any two tests, say test ' and test " , the condition

$$\mathcal{R}' = \mathcal{R}'' \quad (73)$$

is the only one that we must take care to satisfy in the tests. In view of eq. (62), condition (73) implies that

$$(w^P)'/ (w^P)'' = (R_e'')^2 / (R_e')^2 \quad (74)$$

However, within the limits of the approximation discussed in Remark 5, we can set in the plastic range

$$(w^P)' / (w^P)'' \simeq (\dot{\varepsilon}_1^P)' / (\dot{\varepsilon}_1^P)'' \simeq (\dot{\varepsilon}_1)' / (\dot{\varepsilon}_1)'' \quad (75)$$

We can conclude, therefore, that eq. (74) and hence condition (73) are satisfied provided that the tests are carried out in such a way that the relation

$$(\dot{\epsilon}_1)' / (\dot{\epsilon}_1)'' = (R_e'')^2 / (R_e')^2 \quad (76)$$

is met. In other words, to evaluate viscous effects in the plastic range from tensile tests at different strain rates, the ratio of the square of the diameters of the specimens must be equal to the inverse ratio of the rates of strain at which the specimens are tested. Otherwise the contribution of thermodynamics to the rate effect is different for different tests, and it is not possible to detect which part of the resulting rate effect is in fact due to viscosity. Such a rule appears to have been consistently ignored in the experiments to detect the viscous effect in dynamic plasticity thus far reported in literature.

#### CONCLUDING REMARKS AND SUBJECTS FOR FUTURE RESEARCH

Dissipation of mechanical energy into heat can produce a rate-dependent force/deformation response in a tensile test at non-vanishing strain rate in the plastic range. This effect can occur in rate-independent elastic-plastic materials, and should be distinguished carefully from the seemingly similar effect produced by viscosity and governed by quite different laws. Under given conditions of heat exchange with the surroundings, a material specimen exhibits a thermodynamic rate effect that depends only on one dimensionless parameter  $\mathcal{R}$ . The latter plays a role analogous to that of the Reynolds number in the theory of viscous fluids. This analogy suggests the opportunity of defining a "drag coefficient" by which the tensile force relevant to a quasi-static test should be multiplied to obtain its value at different strain rates. Such a coefficient would only depend on  $\mathcal{R}$ , for given conditions of heat exchange with the surroundings.

Further research, both numerical and experimental, is needed to determine the explicit relation between the tensile force and the parameter  $\mathcal{R}$  in a given material. Such a relation may help in finding the values of the strain rates at which the tensile force reaches a maximum or a minimum value. From the numerical standpoint, the research can be made on the basis of the equations presented in this paper. It should be remarked, moreover, that the introduction of these equations within the computational schemes treating deforming bodies should not, in principle, introduce more computational burden than the one introduced by the visco-plastic hypothesis. For materials whose rate effect is essentially thermodynamic in origin, the viscous hypothesis cannot give good approximations of general validity. In these cases a thermodynamic approach should be preferred to the standard visco-plastic one.

## REFERENCES

1. Farren, W.S.; Taylor, G.I.: The heat developed during plastic extension of metals. Proc. Royal Soc. London, vol. A 107, 1925, pp. 422-451.
2. Dillon, O.W., Jr.: An experimental study of the heat generated during torsional oscillations. J. Mech. Phys. Solids, vol. 10, 1962, pp. 235-244.
3. Bodner, S.R.: Constitutive equations for dynamic material behavior. In: Mechanical Behavior of Materials under Dynamic Loads. Lindholm, U.S. (ed.). Springer-Verlag, Berlin 1968, pp. 176-190.
4. Rice, J.R.: On the structure of stress-strain relations for time-dependent plastic deformation in metals. J. Appl. Mech., vol. 37, 1970, pp. 728-737.
5. Bell, J.F.: The experimental foundations of solid mechanics. In: Encyclopedia of Physics. Truesdell, C., (ed.). Vol. VI/1, Springer-Verlag, Berlin 1973, pp. 565-742.
6. Drucker, D.C.: Extension of the stability postulate with emphasis on temperature changes. In: Plasticity. Proc. 2nd Symp. Naval Struct. Mech.; Lee, E.H., Symonds, P.S., (eds). Pergamon Press, Oxford 1960, pp. 170-184.
7. Lee, E.H.: Elastic-plastic deformation at finite strain. J. Appl. Mech., vol. 36, 1969, pp. 1-6.
8. Lee, E.H.; Wierzbicki, T.: Analysis of the propagation of plane elastic-plastic waves at finite strain. J. Appl. Mech., vol. 34, 1967, pp. 931-936.
9. Lee, E.H.; McMeeking, R.M.: Concerning elastic and plastic components of deformation. Int. J. Solids Struct., vol. 16, 1980, pp. 715-721. Erratum ibid., vol. 17, 1981, p. 929.
10. Lee, E.H.: Some comments on elastic-plastic analysis. Int. J. Solids Struct., vol. 17, 1981, pp. 859-872.
11. Truesdell, C.; Noll, W.: The non-linear field theories of mechanics. In: Encyclopedia of Physics. Flügge, S., (ed.). Vol. III/3, Springer-Verlag 1965, pp. 1-579.
12. Boley, B.A.; Weiner, J.H.: Theory of Thermal Stresses. Wiley, New York 1960.
13. Prager, W.: Non-isothermal plastic deformation. Proc. Koninkl. Ned. Akad. Wetensch., vol. B 61, 1958, pp. 176-182.
14. Truesdell, C.: The physical components of vectors and tensors. Z. angew. Math. Mech., vol. 33, 1953, pp. 345-356.
15. Paglietti, A.: On the mathematical formulation of the first principle of thermodynamics for non-uniform temperature processes. Ann. Inst. H. Poincaré, vol. A 30, 1979, pp. 61-82.
16. Paglietti, A.: On the energy of heat flow and its implications in non-equilibrium thermodynamics. Cambridge Univ., Engineering Dept. Rep. CUED/A-Thermo/TR 13 (1980).

17. Paglietti, A.: A general equation of entropy for continuum mechanics (in Italian).  
To appear in: Atti VI Congr. Nazionale Associazione Italiana Meccanica Teorica e Applicata (AIMETA), Genova, Italy 1982.
18. Carslaw, H.S.; Jaeger, J.C.: Conduction of Heat in Solids. Clarendon Press, Oxford 1959.
19. Mann, H.C.: The relation between the tension static and dynamic tests. Proc. Am. Soc. Testing Mat., vol. 35, pt. 2, 1935, pp. 323-335.
20. Gruntfest, I.J.: A note on thermal feedback and fracture of solids. In: Fracture of Solids. Drucker, D.C., Gilman, J.J., (eds). Metallurgical Soc. Conferences, vol. 20. Wiley, New York 1963, pp. 189-193.



APPLICATION OF A BOUNDARY ELEMENT METHOD  
TO THE STUDY OF DYNAMICAL TORSION OF BEAMS

Casimir Czekajski and Serge Laroze  
National School of Aeronautics and Space

Daniel Gay  
National Institute of Applied Sciences  
Toulouse, France

SUMMARY

During dynamic torsion of beam elements, consideration of nonuniform-warping effects involves a more general technical formulation than that of Saint-Venant. Nonclassical torsion constants appear, in addition to the well-known torsional rigidity. In this paper, we describe the adaptation of the boundary integral element method to the calculation of these constants for general section shapes. The suitability of the foregoing formulation is investigated with some examples of thick- as well as thin-walled cross sections.

SYMBOLS

$x$	longitudinal axis of the beam
$y, z$	coordinates in any cross section
$\Omega$	domain occupied by the cross section
$\Gamma$	boundary of the cross section
$\theta(x, t)$	angular parameter
$\dot{\theta}(x, t)$	warping parameter
$C$	torsion torque
$B$	generalized double moment
$c$	distributed torque
$\phi(y, z)$	Saint-Venant warping function
$w(y, z)$	weighting function
$g_0(y, z)$	supplementary warping function

## TORSION FORMULATION

The static torsion theory for arbitrary cross section beams implies constant torque, and thus cannot describe the dynamic case, where both torsion torque and warping of cross sections vary along the beam's length (except for circular beams). In the same manner, variable torque and warping may occur in the static case of members with rigid connections (turbine blades, wings, structural members...).

In the particular case of shear center and centroid at the same location, we have proposed a technical theory [1] to take into account the effects connected with this nonuniform warping. Besides the classical angular parameter  $\theta(x,t)$ , the formulation considers a new degree of freedom, the so-called warping parameter  $\dot{\theta}(x,t)$  characterising the magnitude of warping of any cross section. The basic equilibrium and behavior relations are recalled as:

$$\begin{aligned} \frac{\partial C}{\partial x} + c &= \rho I \frac{\partial^2 \theta}{\partial t^2} \\ \frac{\partial B}{\partial x} + \{C - GJ \frac{\partial \theta}{\partial x}\} &= \rho I_{\phi} \frac{\partial^2 \dot{\theta}}{\partial t^2} \\ \{C - GJ \frac{\partial \theta}{\partial x}\} &= \frac{G(I-J)}{k_{\phi}} \left( \frac{\partial \theta}{\partial x} - \dot{\theta} \right) \\ B &= EI_{\phi} \frac{\partial \dot{\theta}}{\partial x} \end{aligned} \quad (1)$$

in which:

$C(x,t)$  is the torsion torque, and  $B(x,t)$  is the generalized double moment:

$$B(x,t) = \int_{\Omega} \sigma_{xx} \times \phi \, d\Omega$$

$\sigma_{xx}$  is the longitudinal stress arising from nonuniform warping, and  $\phi(y,z)$  is the classical Saint-Venant warping function defined as the solution of the potential problem in the domain  $\Omega$  occupied by the cross section:

$$\left\{ \begin{array}{l} \nabla^2 \phi = 0 \quad \text{over } \Omega \\ \partial \phi / \partial n = z n_y - y n_z \quad \text{along } \Gamma \\ \int_{\Omega} \phi \, d\Omega = 0 \end{array} \right. \quad (2)$$

We can note in relations (1) the following torsion constants:

• polar moment of inertia:  $I = \int_{\Omega} r^2 \, d\Omega$ ,  $r$  being the radius from the centroid.

• Saint-Venant torsion constant:  $J = I - \int_{\Omega} (g \vec{\text{grad}} \phi)^2 \, d\Omega \quad (3a)$

• quadratic warping moment:  $I_{\phi} = \int_{\Omega} \phi^2 \, d\Omega \quad (3b)$

•shear coefficient for nonuniform torsion:  $k_\phi$ , which is deduced from the solution  $g_0(y,z)$  of the Poisson's problem in the domain of the cross section [2]:

$$\left\{ \begin{array}{l} \nabla^2 g_0 = \frac{I-J}{I_\phi} \times \phi(y,z) \quad \text{over } \Omega \\ \partial g_0 / \partial n = 0 \quad \text{along } \Gamma \\ \int_{\Omega} g_0 d\Omega = 0 \end{array} \right. \quad (4)$$

in the form of:

$$k_\phi = - \frac{1}{I_\phi} \int_{\Omega} g_0 \phi d\Omega \quad (5)$$

The similarities between relation (1) and Timoshenko's dynamic flexure theory are found again when writing the strain and kinetic energies, and allow a simple procedure to obtain a finite element for torsion [2]. The setting up of such an element needs first the calculation of the constants noted above. In addition, longitudinal and shear stresses in every cross section can be written in the form of [1]:

$$\begin{aligned} \sigma_{xx} &= \frac{B \times \phi}{I_\phi} \\ \sigma_{xy} &= G \frac{\partial \theta}{\partial x} \left( \frac{\partial \phi}{\partial y} - z \right) + \frac{C - GJ \partial \theta / \partial x}{I - J} \times \frac{\partial g_0}{\partial y} \\ \sigma_{xz} &= G \frac{\partial \theta}{\partial x} \left( \frac{\partial \phi}{\partial z} + y \right) + \frac{C - GJ \partial \theta / \partial x}{I - J} \times \frac{\partial g_0}{\partial z} \end{aligned}$$

The torsion constants can be evaluated analytically in a few cases of section shapes with simple geometry. For any general shape, problems (2) and (4) have to be solved first. In this way, we propose the Boundary Integral Element Method (BIEM) procedure.

#### EVALUATION OF J AND $I_\phi$

The integral formulation of problem (2) is recalled as [3-4] :

$$a\phi_i = \int_{\Gamma} \frac{\partial \phi}{\partial n} w d\Gamma - \int_{\Gamma} \phi \frac{\partial w}{\partial n} d\Gamma$$

in which  $a=1, 0.5$  or zero, depending on whether  $i$  is inside the region  $\Omega$ , on the boundary  $\Gamma$  or outside the region respectively.

To find the solution of this problem, we divide the boundary into straight-line segments, and choose the nodes in their mid-points (constant elements). As a fundamental solution we take:

$$w = \frac{1}{2\pi} \text{Log } r$$

which gives the following statement:

$$2\pi a\phi_i = \sum_{j=1}^N \int_{\Gamma_j} \frac{\partial \phi}{\partial n_j} \text{Log } r_{ij} d\Gamma_j - \sum_{j=1}^N \int_{\Gamma_j} \phi_j \frac{\partial \text{Log } r_{ij}}{\partial n_j} d\Gamma_j$$

When  $i \neq j$ , we adopt the Gauss quadrature to evaluate the above integrals. When  $i = j$ , we perform the analytical calculation. Then, a system of linear equations is obtained as:

$$[A]\{X\} = \{B\}$$

in which  $\{X\}$  is the vector of unknown values of  $\partial \phi / \partial n$  and  $\phi$ , on the boundary. The solution is computed with the help of a standard subroutine.

To find the values of  $J$ , we perform the following transformation of (3-a):

$$J = I - \int_{\Omega} (\nabla \phi)^2 d\Omega$$

$$J = I - \left[ \int_{\Omega} \left( \frac{\partial}{\partial y} \left\{ \phi \frac{\partial \phi}{\partial y} \right\} + \frac{\partial}{\partial z} \left\{ \phi \frac{\partial \phi}{\partial z} \right\} \right) d\Omega - \int_{\Omega} \phi \nabla^2 \phi d\Omega \right]$$

$$J = I - \int_{\Gamma} \left( \phi \frac{\partial \phi}{\partial y} n_y + \phi \frac{\partial \phi}{\partial z} n_z \right) d\Gamma$$

which allows  $J$  to be a function of calculated boundary values  $\phi$  and  $\partial \phi / \partial n$  as follows:

$$J = I - \int_{\Gamma} \phi \frac{\partial \phi}{\partial n} d\Gamma$$

Now, we have to calculate the expression (3-b) for  $I_{\phi}$ , which needs the discretization of the domain. Usual discretization procedures employed in the Finite Element Method (FEM) need a great volume of computer memory. We have opted for a special subroutine in view of discretization of  $\Omega$ . The domain is divided into as small a number as possible of initial triangles (see figure 1). For every initial triangle, an option can be chosen, by which it is divided into  $4^n$  ( $n = 1, \dots, 6$ ) triangles without distortion in the geometry if the boundary is rectilinear. For curved boundaries, discretization is performed as shown in figure 1-A. Localization of triangles needs 20, 32, 44 or 56 memory words, according to the option chosen for subdivision of triangles (fig.2).

#### EVALUATION OF $k_{\phi}$

The integral formulation corresponding to problem (4) is:

$$ag_{0i} = \int_{\Gamma} \frac{\partial g_0}{\partial n} w \, d\Gamma - \int_{\Gamma} \frac{\partial w}{\partial n} g_0 \, d\Gamma - \frac{I-J}{I\phi} \int_{\Omega} \phi w \, d\Omega$$

Evaluation of the integral:

$$\int_{\Omega} \phi w \, d\Omega$$

needs the discretization of the domain  $\Omega$  to have been prepared already. To avoid a sharp increase in the size of the problem to be handled, and to preserve the advantage of the BIEM formulation, we have changed problem (4) into a biharmonic one, the solution of which we reach by the direct method.

Integrating by parts four times, and considering as a weighting function:

$$w = r^2 \text{Log } r$$

we have the following statement at the point  $i$  of the boundary:

$$4\pi g_{0i} = \int_{\Gamma} \{ag_0 - b \frac{\partial g_0}{\partial n} + c \nabla^2 g_0 - d \frac{\partial}{\partial n} (\nabla^2 g_0)\} d\Gamma$$

with the coefficients:

$$a = \frac{\partial}{\partial n} \{\nabla^2 (r^2 \text{Log } r)\}$$

$$b = \nabla^2 (r^2 \text{Log } r)$$

$$c = \frac{\partial}{\partial n} (r^2 \text{Log } r)$$

$$d = r^2 \text{Log } r$$

Since the values of  $\nabla^2 g_0$  and  $\frac{\partial}{\partial n} (\nabla^2 g_0)$  are known from the solution of problem (2), we obtain the formulation below for  $g_0$  on the boundary with constant elements:

$$4\pi g_{0i} = \sum_{j=1}^N g_{0j} \int_{\Gamma_j} a_{ij} \, d\Gamma - \sum_{j=1}^N \frac{\partial g_{0j}}{\partial n} \int_{\Gamma_j} b_{ij} \, d\Gamma + \sum_{j=1}^N \frac{I-J}{I\phi} \phi_j \int_{\Gamma_j} c_{ij} \, d\Gamma$$

(6)

$$- \sum_{j=1}^N \frac{I-J}{I\phi} \frac{\partial \phi}{\partial n} \int_{\Gamma_j} d_{ij} \, d\Gamma$$

When  $i \neq j$ :

$$\int_{\Gamma_j} a_{ij} d\Gamma = 4 \int_{\Gamma_j} (r_y n_y + r_z n_z) / r^2 d\Gamma$$

$$\int_{\Gamma_j} b_{ij} d\Gamma = 4 \int_{\Gamma_j} (\text{Log } r + 1) d\Gamma$$

$$\int_{\Gamma_j} c_{ij} d\Gamma = \int_{\Gamma_j} (2 \text{Log } r + 1) (r_y n_y + r_z n_z) d\Gamma$$

$$\int_{\Gamma_j} d_{ij} d\Gamma = \int_{\Gamma_j} r^2 \text{Log } r d\Gamma$$

When  $i = j$ :

$$\int_{\Gamma_j} a_{ij} d\Gamma = 4\pi - \int_{\Gamma - \Gamma_i} \frac{\partial}{\partial n} (\nabla \rho^2) d\Gamma \quad (\rho = r^2 \text{Log } r)$$

$$\int_{\Gamma_j} b_{ij} d\Gamma = 4\Gamma_i \text{Log}(\Gamma_i/2)$$

$$\int_{\Gamma_j} c_{ij} d\Gamma = 0$$

$$\int_{\Gamma_j} d_{ij} d\Gamma = \frac{1}{12} \Gamma_i^3 (\text{Log}(\Gamma_i/2) - 1/3)$$

A slightly different method to formulate Poisson's equation on the boundary only can be found in reference [5]. Such biharmonic problems can also be solved by indirect methods [6-7-8]. Due to the particular form of right-end side in problem (4), the direct formulation obtained above is more convenient for the problem on hand.

Once the values of  $g_0$  and  $\partial g_0 / \partial n$  are known on the boundary, evaluation of  $g_0$  inside the domain  $\Omega$  is straightforward following the expression (6) in which the first coefficient  $4\pi$  must be changed into  $8\pi$ . In this way, we obtain the value of integral in (5), which leads to the coefficient  $k_\phi$ .

The suitability of the method has been investigated in some cases of cross section shapes shown in figure 3. Numerical results obtained for  $I_\phi$ ,  $J$ ,  $k_\phi$  are grouped in table 1. We can note a good convergence of results when exact coefficients are known. In the case of thin-walled sections, the aforementioned constants can be obtained analytically with the help of approximate theories [8-9-10]. Experimental torsion frequencies for rectangular and I-beams have shown excellent agreement with

analytical frequencies deduced from formulation (1) associated with computed torsion coefficients. Thus, we can note the limits in the validity for the thin-walled beams approximation [11].

#### CONCLUDING REMARKS

We have developed a boundary formulation allowing the calculation of all torsion coefficients required for a dynamic torsion study. The input data consist of the description of the boundary elements only of the cross section, and a small number of initial triangles. Such a program needs only a little input data and a small memory size. Moreover, with slight modifications, all cross section shapes can be treated, including the general case where shear center and centroid differ, i.e. when flexure and torsion are coupled. In this way, we hope to improve the corresponding developments [12] with the use of higher-order boundary elements to limit the number of nodal variables.

## REFERENCES

1. Gay, D.; Boudet, R.: A Technical Theory of Dynamical Torsion for Beams of Any Cross Section Shapes. Journal of Mechanical Design. July 1980, Vol.102, pp. 627-632.
2. Potiron, A.; Gay, D.: On a Finite Element Formulation of Dynamical Torsion of Beams Including Warping Inertia and Shear Deformation Due to Nonuniform Warping. ASME, Design Engineering Technical Conference, Sept.20-23 1981, Hartford, Conn.
3. Brebbia, C.A.: The Boundary Element Method for Engineers. Pentech Press, London-Plymouth, 1978.
4. Jaswon, M.A.; Ponter, A.R.: An Integral Equation Solution of the Torsion Problem. Proc. Roy. Soc. Ser. A, 273, 1963, pp.237-246.
5. Fairweather, G.; Rizzo, F.; Shippy, D.; Wu Y.: On the Numerical Solution of Two-dimensional Potential Problems by an Improved Boundary Integral Equation Method. J. Comp. Physics, 31, 1979, pp.96-112.
6. Jaswon, M.A.; Maiti, M.: An Integral Equation Formulation of Plate Bending Problems. J. of Engineering Math., Vol.2, 1968, pp.83-93.
7. Jaswon, M.A.; Maiti, M.; Symm, G.T.: Numerical Biharmonic Analysis and Some Applications. Int. Journal of Solids and Struct., Vol.3, 1967, pp.309-322.
8. Segedin, C.M.; Brickell, D.G.: Integral Equation Method for a Corner Plate. J. Struct. Div. ASCE, Jan. 1968, pp.41-52.
9. Timoshenko, S.P.: Theory of Bending, Torsion and Buckling of Thin-Walled Members of Open Sections. Journal of the Franklin Institute. t.239, pp.215-219, 1945.
10. Vlassov, B.Z.: Pièces Longues en Voile Mince. Eyrolles, Paris, 1962.
11. Gay, D.: Influence of Secondary Effects on Free Torsional Oscillations of Thin-Walled Open Section Beams. Journal of Applied Mech. Vol 45, Sept.1978, pp.681-683.
12. Potiron, A.: Theory of Coupled Flexure and Torsion With Nonuniform Warping. Internal Report. Depart. of Mech. Nat. Inst. of Appl. Sciences, Toulouse, 1981.



TABLE 1

TORSION CONSTANTS	ANALYTICAL VALUES	CALCULATED VALUES			
		number of boundary elements / number of surface elements			

## SECTION N° 1 (fig. 3)

		40 / 6x4 <sup>2</sup>	40 / 6x4 <sup>3</sup>	80 / 6x4 <sup>3</sup>	80 / 6x4 <sup>4</sup>
J (m <sup>4</sup> )	12.64	12.76 (err:1%)	12.76 (err:1%)	12.68 (0.34%)	12.68 (0.34%)
I <sub>φ</sub> (m <sup>6</sup> )	7.634 exact values	7.546 (1%)	7.554 (1%)	7.608 (0.34%)	7.614 (0.26%)
k <sub>φ</sub>	1.281	1.267 (1%)	1.263 (1.3%)	1.276 (0.4 %)	1.274 (0.5 %)

## SECTION N° 2 (fig. 3)

		42 / 4x4	42 / 8x4	84 / 8x4	84 / 8x4 <sup>2</sup>
J (m <sup>4</sup> )	.00167 experim. Vlassov	.00246	.00246	.00161	.00161
I <sub>φ</sub> (m <sup>6</sup> )	.00129 {approxim. thin	.00455	.00451	.00461	.00463
k <sub>φ</sub>	.00281 {walled theory	1.829	1.839	1.819	1.811
	1.932				

## SECTION N° 3 (fig. 3)

		34 / 1x4 <sup>2</sup>	34 / 1x4 <sup>3</sup>	68 / 1x4 <sup>3</sup>	68 / 1x4 <sup>4</sup>
J (m <sup>4</sup> )		.02492	.02492	.02497	.02497
I <sub>φ</sub> (m <sup>6</sup> )	1.186 E-4 (exact [12])	1.169E-4 (14%)	1.179E-4 (.5%)	1.184E-4 (.2%)	1.185E-4 (0%)
k <sub>φ</sub>		2.126	2.07	2.059	2.054

## SECTION N° 4 (fig. 3)

		62 / 58x1	62 / 58x4	100 / 58x1	100 / 58x4
J (m <sup>4</sup> )	20062	19324	19324	19269	19269
I <sub>φ</sub> (m <sup>6</sup> )	158701 {approxim. thin	145817	155201	160410	162294
k <sub>φ</sub>	5.03 {walled theory	6.73	6.53	6.46	6.47

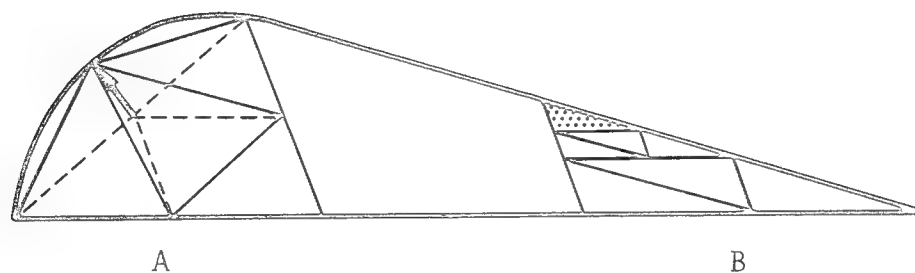


Figure 1- DISCRETIZATION OF ARBITRARY BEAM CROSS SECTIONS

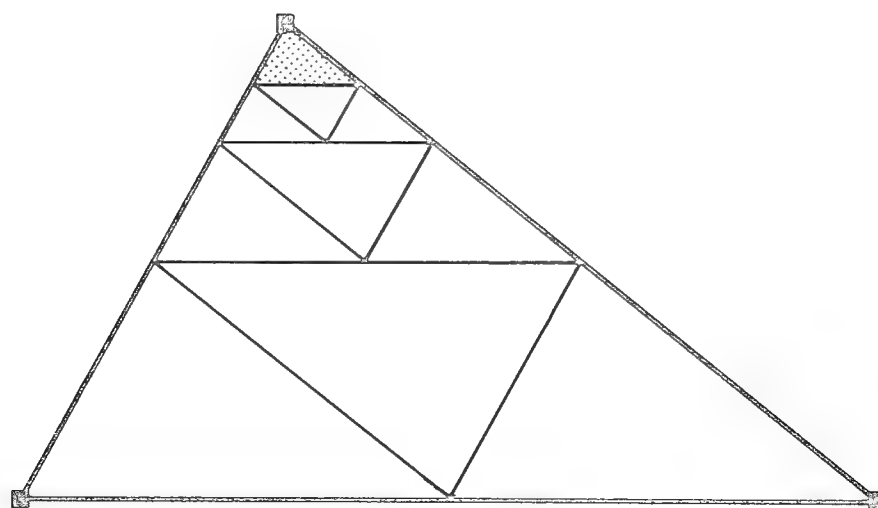


Figure 2 - DISCRETIZATION INTO  $4^3$  TRIANGLES FOR ONE INITIAL TRIANGLE NEEDS 44 MEMORY WORDS

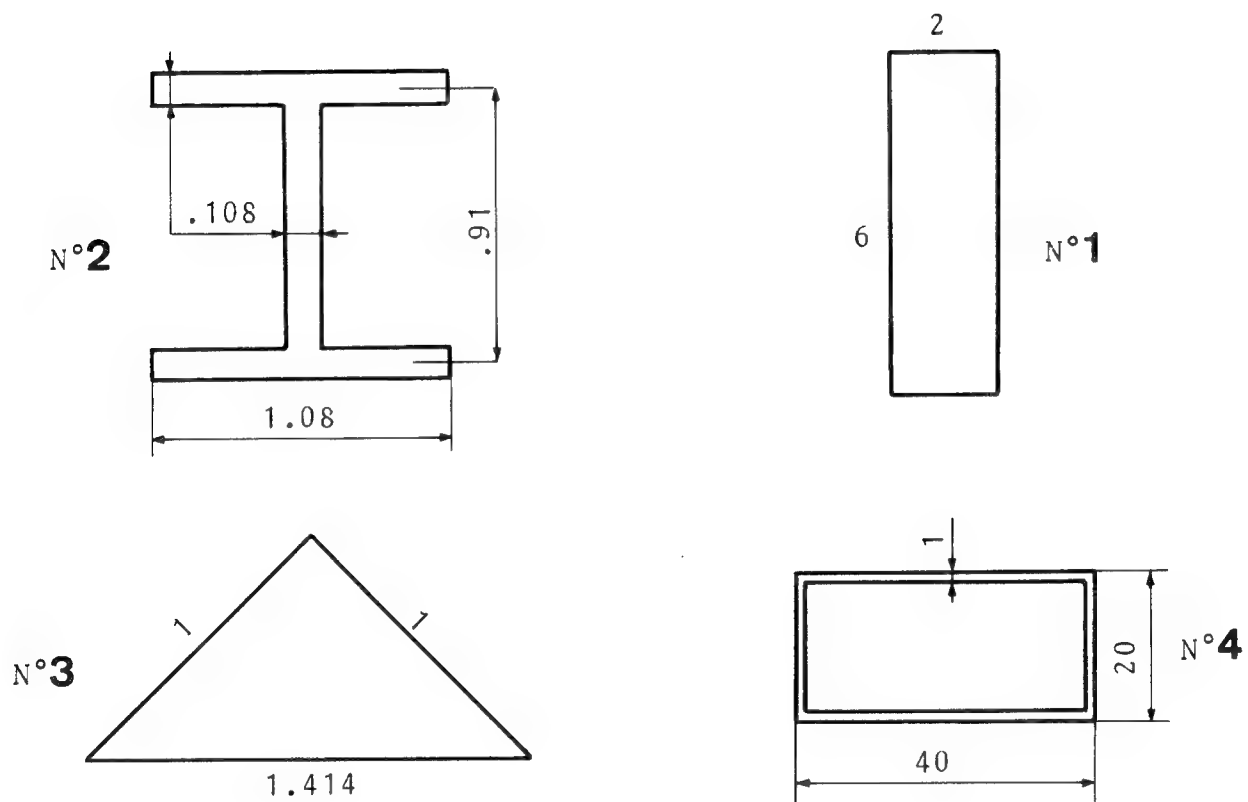


Figure 3- CROSS SECTION SHAPES

# A NOVEL BOUNDARY ELEMENT METHOD PROGRAM FOR HEAT TRANSFER ANALYSIS OF COMPOSITE MATERIALS

Kamar J. Singh  
General Electric Company  
Schenectady, New York

## SUMMARY

A Boundary Element Method Computer Program has been developed for heat transfer analysis of 2-dimensional composite structures. The program runs on a time-share mode and interacts with the user for multi-run analysis. During a run, the geometry can be modified interactively by the user as many times as desired by using various options available and the new results printed or plotted. A new concept of plotting the results for Boundary Element Method is introduced which is unique in itself. The advantage of such a program over Finite Element Method for simple design problems is quite evident.

## INTRODUCTION

For most of the heat transfer design problems, it is necessary to modify the geometry of the structure a number of times to study the effect on the temperature distribution. Such problems are usually analysed using the Finite Element Method (FEM) which is an extremely powerful analytical tool. In FEM, the whole domain is discretized into a finite number of elements as an approximation. However, because a new mesh has to be generated each time the geometry is changed even slightly, it becomes very expensive and time-consuming to go through these iterations. For example, if an insert or an opening (e.g., a cooling hole) is to be placed in a structure at an optimum location, a number of meshes or models will have to be generated for each case to study the overall response on the whole structure.

An attractive substitute to FEM for these types of problems is the Boundary Element Method (BEM) or Boundary Integral Equation Method. In this method, only the boundaries of the structure are discretized for solution of the complete domain. Though this method has its own limitations, yet for simple heat transfer or elasticity problems, the method can be utilized to its best advantage. The existing BEM computer programs have not taken the fancy of the users because of the drawbacks in their interaction with the user. If a computer program lets the user move the boundaries interactively, it becomes a very powerful method as the time spent in generating new data is almost negligible.

## THEORY

The underlying theory of BEM is well documented in the literature [1-4]. However, a brief review of the theory for potential problems is included here.

For a 2-dimensional potential problem, the Laplace equation is given by

$$\nabla^2 v = 0 \quad \text{in domain } \Omega \quad (1)$$

The boundary conditions for the problem are:

$$v = \hat{v} \quad \text{on } S_1 \quad (2)$$

and

$$v' = \hat{v}' \quad \text{on } S_2 \quad (3)$$

where  $S_1$  and  $S_2$  are complementary subsets of boundary  $S$  of  $\Omega$  and prime denotes the derivative of the function normal to the surface.

It is essential here that

$$\tilde{S} = \bigcup_{e=1}^m S_e \quad (4)$$

where  $\tilde{S}$  is the boundary element approximation of  $S$ .

$$\text{and } S_i \cap S_j = \phi \quad \text{for } i \neq j \quad (5)$$

Also  $\lim_{m \rightarrow \infty} \tilde{S} = \bar{S}$ , where superscript bar indicates closure of the quantity.

The weighted residual equation for the governing equation which satisfies Eq. (3) is:

$$\iint \nabla^2 v \cdot \bar{v} \, d\Omega = \int (v' - \hat{v}') \bar{v} \, dS \quad (6)$$

This equation identically satisfies Equation (2). However, use can be made of the Lagrangian Multiplier to include Eq. (2) in the formulation.

The functional  $F$  can then be represented as

$$\begin{aligned} F = & \frac{1}{2} \iint \left[ \left( \frac{\partial v}{\partial x} \right)^2 + \left( \frac{\partial v}{\partial y} \right)^2 \right] d\Omega + \int_{S_1} \lambda (v - \hat{v}) \, dS \\ & - \int_{S_2} \hat{v}' v \, dS \end{aligned} \quad (7)$$

Taking variation of Eq. (7) and equating it to zero:

$$\begin{aligned} & \iint \left[ \left( \frac{\partial v}{\partial x} \right) \left( \frac{\partial \delta v}{\partial x} \right) + \left( \frac{\partial v}{\partial y} \right) \left( \frac{\partial \delta v}{\partial y} \right) \right] d\Omega \\ & + \int_{S_1} \delta \lambda (v - \hat{v}) \, dS + \int_{S_1} \lambda \delta v \, dS - \int_{S_2} \hat{v}' \delta v \, dS = 0 \end{aligned} \quad (8)$$

If we choose a weighting function 'w' such that it is equal to  $\delta v$  and substitute Lagrangian multiplier as  $(-v')$ , we get by integrating first term in Eq. (8) by parts:

$$\begin{aligned} & - \iint \nabla^2 v \cdot w \, d\Omega - \int_{S_1} (v - \hat{v}) \frac{\partial w}{\partial n} \, dS \\ & - \int_{S_2} (\hat{v}' - v') w \, dS = 0 \end{aligned} \quad (9)$$

By further integrating by parts

$$\begin{aligned} & - \iint \left( \frac{\partial^2 w}{\partial x^2} + \frac{\partial^2 w}{\partial y^2} \right) v \, d\Omega - \int_{S_1} \frac{\partial v}{\partial n} w \, dS + \int_{S_1} \hat{v} \frac{\partial w}{\partial n} \, dS \\ & - \int_{S_2} \hat{v}' w \, dS + \int_{S_2} v \frac{\partial w}{\partial n} \, dS = 0 \end{aligned} \quad (10)$$

Assuming that the weighting function  $w$  satisfies the governing equation but not the boundary conditions, the fundamental solution to satisfy the Laplace equation is given by:

$$\int v \left( \nabla^2 w \right) d\Omega = -v_e \quad (11)$$

where  $v_e$  is the unknown function at point 'e'. However, at the boundary, it is equal to  $-\frac{1}{2} v_e$ . For a 2-dimensional case

$$w = \frac{1}{2\pi} \ln \left( \frac{1}{d} \right)$$

where 'd' is the distance of the node from the point under consideration.

Substituting Eq. (11) in Eq. (10), we have:

$$\begin{aligned} \frac{1}{2} v_e - \int_{S_1} v' w dS + \int_{S_1} \hat{v} w' dS - \int_{S_2} \hat{v}' w dS \\ + \int_{S_2} v w' dS = 0 \end{aligned} \quad (12)$$

The unknowns in this equation are  $v$  and  $v'$ . Eq. (12) can be written as:

$$\frac{1}{2} v_e - \int_{S_1} v' w dS - \int_{S_2} v w' dS = \int_{S_2} \hat{v}' w dS - \int_{S_1} \hat{v} w' dS \quad (13)$$

Approximating the boundary by finite number of elements  $N_1$  and  $N_2$  on surfaces  $S_1$  and  $S_2$  respectively, we have:

$$\frac{1}{2} v_e - \sum_{j=1}^{N_1} v'_j \int_{S_1} w dS - \sum_{j=1}^{N_2} v_j \int_{S_2} w' dS = \sum_{j=1}^{N_2} \hat{v}'_j \int_{S_2} w dS - \sum_{j=1}^{N_1} \hat{v}_j \int_{S_1} w' dS \quad (14)$$

In Eq. 14, the right hand side has all known quantities. This equation can be written in matrix form in a more familiar way as:

$$Ax = F$$

Where 'x' is the vector of unknown temperatures and fluxes and  $F$  a vector of known quantities.

Here  $A$  is a full positive definite matrix. The program has to store the whole matrix unlike a lesser storage required by FEM where the stiffness matrix is symmetric and banded. This is one of the drawbacks of BEM. For composite structures, the matrices for each material get coupled to form a larger matrix the size of which turns out to be the total number of elements in the whole structure.

The accuracy of the solution is dependent upon the number of elements used in the discretization process of the boundary. The more the number of elements, the better would be the accuracy, particularly near the surfaces. The inaccuracy near the boundaries becomes obvious when the results are plotted inside the domain. Quite often a few glitches will occur near the boundary. The post-processor with this program attempts to smooth out these to some extent.

### THE PROGRAM

The computer program BEMHT2 consists of linear boundary elements. The program is based on the concept of dynamic storage of vectors. The user, therefore, does not run into dimensional restrictions. It runs on time-share mode and interacts with the user on a Menu-system. Thus the user is led

through the entire analysis by the program starting from the initial data input and through any remodeling desired. The user has a choice of saving modified data created during the run. A number of analyses can be made in one run at a minimal cost and time. As many number of materials as desired can be used with the limitation that the regions should be connected in a series.

The program accepts coupled boundary conditions of conduction, convection and radiation. For convection, the user provides the heat transfer coefficient and air temperature; for radiation, the input needed is Stefan-Boltzmann constant, shape factor and source temperature. If the radiation boundary condition is used, the program goes through iterative computations until it converges.

#### A. NOMENCLATURE:

The following nomenclature is used by the program:

##### NODES:

The extremities of an element are called nodes. They describe the geometrical location of an element in the cartesian coordinate system. See Fig. 1.

##### ELEMENTS:

A surface is discretized into elements. The numbering of nodes/elements is done counter-clockwise on the external and clockwise on the internal boundaries. See Fig. 1.

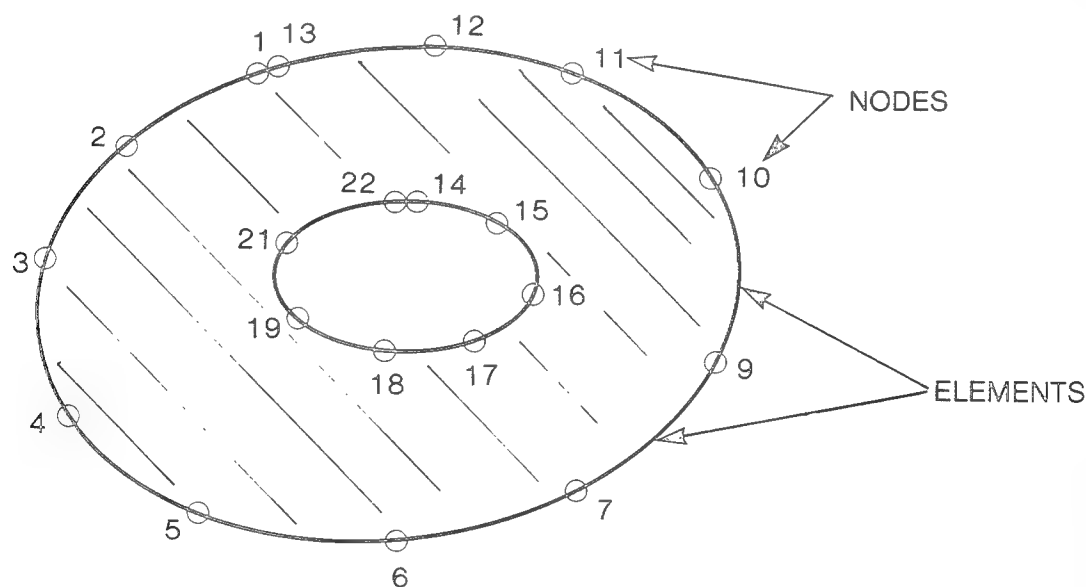


Fig. 1. Nodes and Elements

##### SURFACES:

The boundary of the structure is broken into one or more surfaces depending upon the boundary conditions and also on user's choice. A surface cannot have more than one boundary condition code but a part of the boundary with the same boundary conditions can have more than one surface. If a surface is to be modified during a sequence of runs (moving or scaling), it should be a unique surface. The end nodes of two adjoining surfaces can have the same coordinates. See Fig. 2.

##### ZONES:

Each material type has a bounded zone and the node/element numbering continues from one zone to next. The interfaces must have the same number of nodes at the same locations for compatibility of solution. See Fig 3.

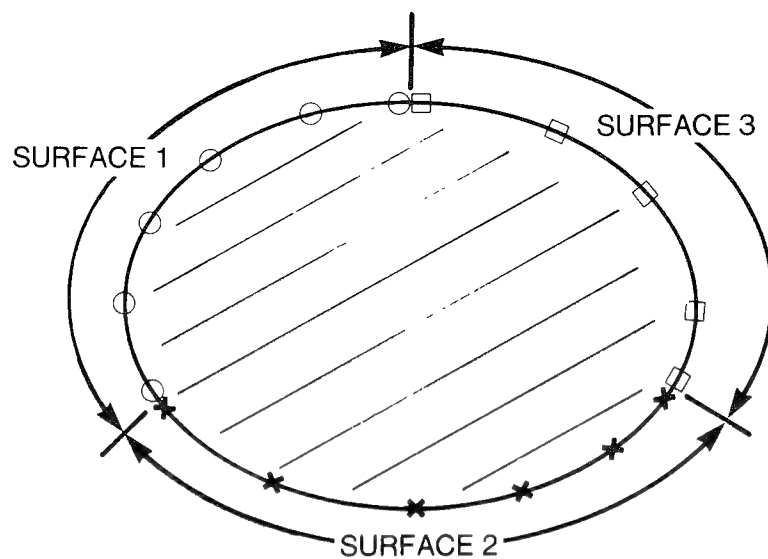


Fig. 2. Surfaces

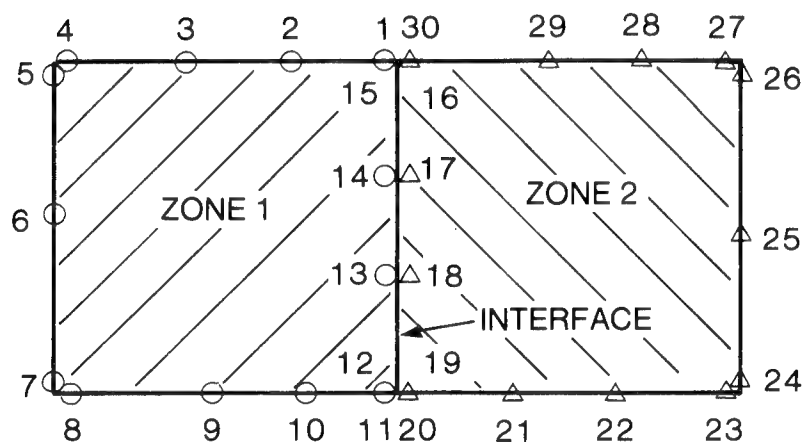


Fig. 3. Zones and Interfaces

#### BOUNDARY CONDITION CODE:

Depending upon the boundary condition on the surface, each surface is assigned a code as described below:

- Code = 0, Temperature is specified
- = 1, Flux is specified
- = 2, Convection boundary condition
- = 3, Radiation boundary condition
- = 23, Convection and radiation boundary condition
- = -1, Interface surface.

#### MOVING A SURFACE:

A surface can be moved interactively by the user when given an option to do so. The movement is limited to within the zone. See Fig. 4.



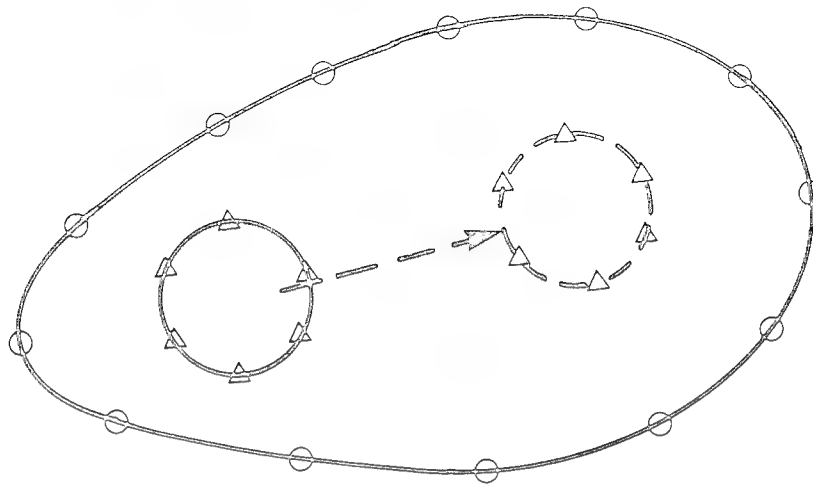


Fig. 4. Moving a Surface

#### SCALING A SURFACE:

A surface can be scaled about its geometrical center when given an option to do so. The surface can be enlarged or reduced depending upon the value of the scale factor being greater than 1.0 or less than 1.0 respectively. See Fig. 5.

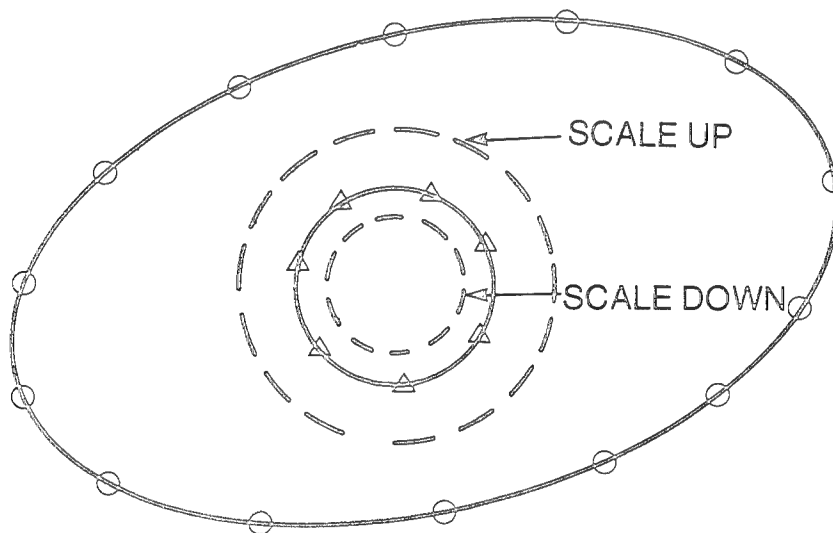


Fig. 5. Scaling a Surface

#### MOVING AND SCALING A SURFACE:

A surface can be scaled and moved in the same step within a zone. See Fig. 6.

#### MODIFYING CURVED SURFACES:

A circular curved surface can be modified in two ways. Either its radius can be changed keeping the same end points or its radius can be changed with a change in the location of the end points. See Fig. 7(a) and 7(b).

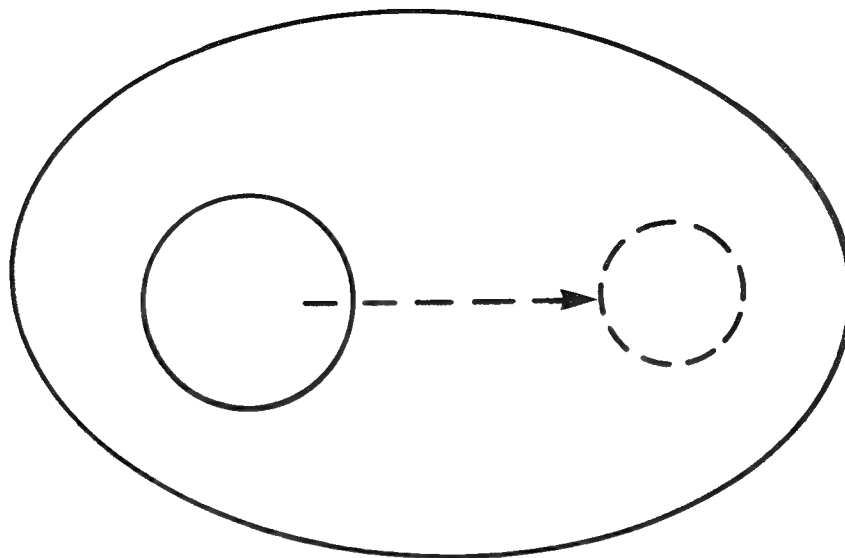


Fig. 6. Scaling and Moving a Surface

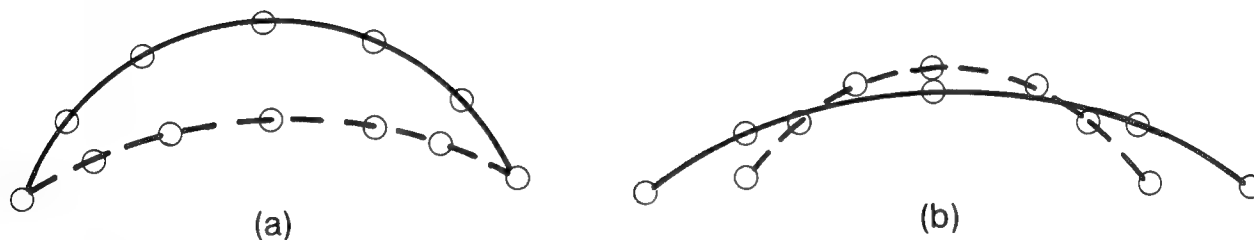


Fig. 7. Modification of a Circular Surface

#### DOUBLING NUMBER OF ELEMENTS:

The user can double the number of elements on any surface interactively. The overall numbering of elements would, therefore, change because of additional new elements. All the boundary conditions are taken care of for the new elements. Elements can be doubled on a curved surface also. See Fig. 8.

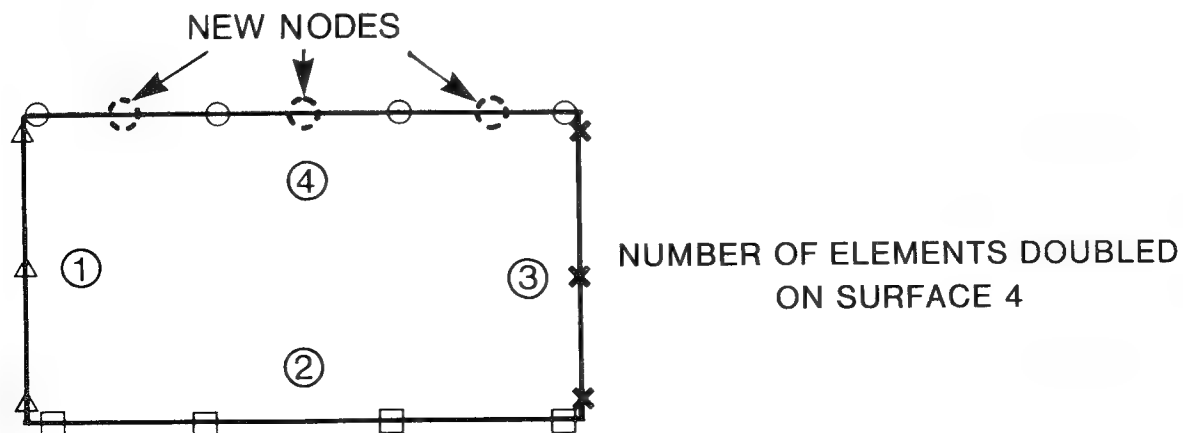


Fig. 8. Doubling Number of Elements

## B. INPUT DATA FEATURES:

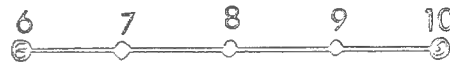
For setting up an input file, a number of data generation aids are available to reduce input effort.

### NODE INPUT:

The nodes can be linearly generated at equal intervals. If any node number is negative, the program linearly generates nodes from the previous node to this node filling up the nodes in between.

For example, from two node entries:

6, 10.0, 25.0  
-10, 14.0, 29.0



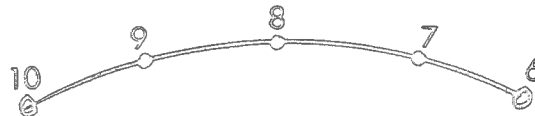
(Format being: node number, x-coordinate, y-coordinate), the resulting data is:

6, 10.0, 25.0  
7, 11.0, 26.0  
8, 12.0, 27.0  
9, 13.0, 28.0  
10, 14.0, 29.0

The user can generate nodes on a curved surface too. In that case, on the first line, one has to input 666 or 777 in place of node number for generation of nodes in anti-clockwise or clockwise direction respectively, followed by x and y coordinates of the center of the circular arc. (The choice of 666 and 777 is obvious.) On the next two lines, the user enters the node numbers and coordinates of the two extremes of the curved surface.

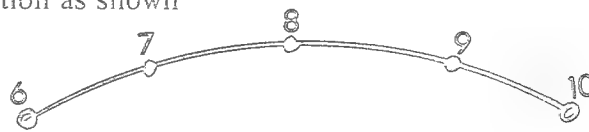
For example:

666, 2.0, 3.0  
6, 3.0, 5.0  
-10, 1.0, 5.0



will generate nodes in an anti-clockwise direction as shown  
and

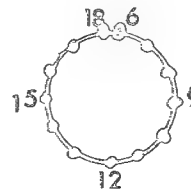
777, 2.0, 3.0  
6, 1.0, 5.0  
-10, 3.0, 5.0



will generate nodes in a clockwise direction as shown.

For a complete circle, the input would look like

777, 2.0, 3.0  
6, 2.0, 4.0  
-18, 2.0, 4.0



Nodes 6 and 18 would have the same coordinates. For anti-clockwise numbering, 666 is substituted for 777.

Nodes can also be generated in a geometric progression. If an 888 is entered in the first line, the program assumes a geometric progression. The entry following the 888 is the ratio between the length of the last element and the first element in the group. If the ratio is greater than 1.0, the size of the elements will be increasing, and if it is less than 1.0, the size would be decreasing. The third entry has to be a zero.

For example, an increasing geometric progression would be

888, 5.0, 0.0  
1, 0.0, 0.0  
-5, 10.0, 0.0



Here  $b/a = 5.0$

and a decreasing progression would be

888, 0.2, 0.0  
1, 0.0, 0.0  
-5, 10.0, 0.0



In this case,  $b/a = 0.2$

#### *BOUNDARY CONDITION INPUT:*

The boundary condition can also be generated in the same manner as nodes. The boundary condition parameters will be linearly interpolated. If the surface has boundary conditions which are all zeros, input for the nodes on these surfaces is not required.

#### *INTERNAL POINTS:*

If solution is desired for points inside the boundary, these points can be included in the input file. A number of internal points can be generated in a straight line as done for the nodes.

#### *SOME OTHER FEATURES:*

- The internal surfaces are not connected with the external surfaces. Therefore, they can be moved around within a zone
- An internal surface can be removed entirely from the analysis by an interactive command
- Two or more nodes on different surfaces can share the same coordinate

#### *C. POST-PROCESSING:*

The post-processing of results is in the form of plotting the contours of temperatures. The program plots the geometry of the structure with or without the node locations and node numbers as preferred by the user. Up to 20 contours can be plotted and these values are input by the user. The contour values can be entered in either of the two formats explained below:

- enter all the values of contours (e.g., 100, 200, 300, 400, 500)
- or enter the minimum, the maximum and the incremental value (e.g., 100, 500, 100)

The Boundary Element Method provides results at the external and internal surfaces. However, a solution at any internal point in the domain can be found from these results at the boundary. The plotting program generates a mesh of points over the whole structure. The results are computed at these mesh points and contours plotted thereafter. Any point of the mesh which falls outside the structure is ignored.

#### *D. RUNNING THE PROGRAM:*

On running the program, the first set of results is obtained. These results can be printed or plotted on a Tektronix terminal. At this stage, the program offers the following options to the user:

- number of elements on any surface(s) can be doubled
- any surface(s) can be moved

- any surface(s) can be scaled

These modifications are made by the program and the new data used in the next run. This modified data may be saved on a file if so desired. Now the next set of results is obtained and can be printed/plotted. In this manner, a number of runs are made by the user without getting out of the program.

### EXAMPLE PROBLEM

The geometry and boundary condition of the problem are shown in Fig. 9.

The center of radius  $R$  is 1.5" below the bottom surface AB.

It is required to find the temperature distribution and heat flow into different surfaces and the effect of moving the cooling hole 0.75" to the right and changing the diameter to 0.4". The discretization of the structure is shown in Fig. 10.

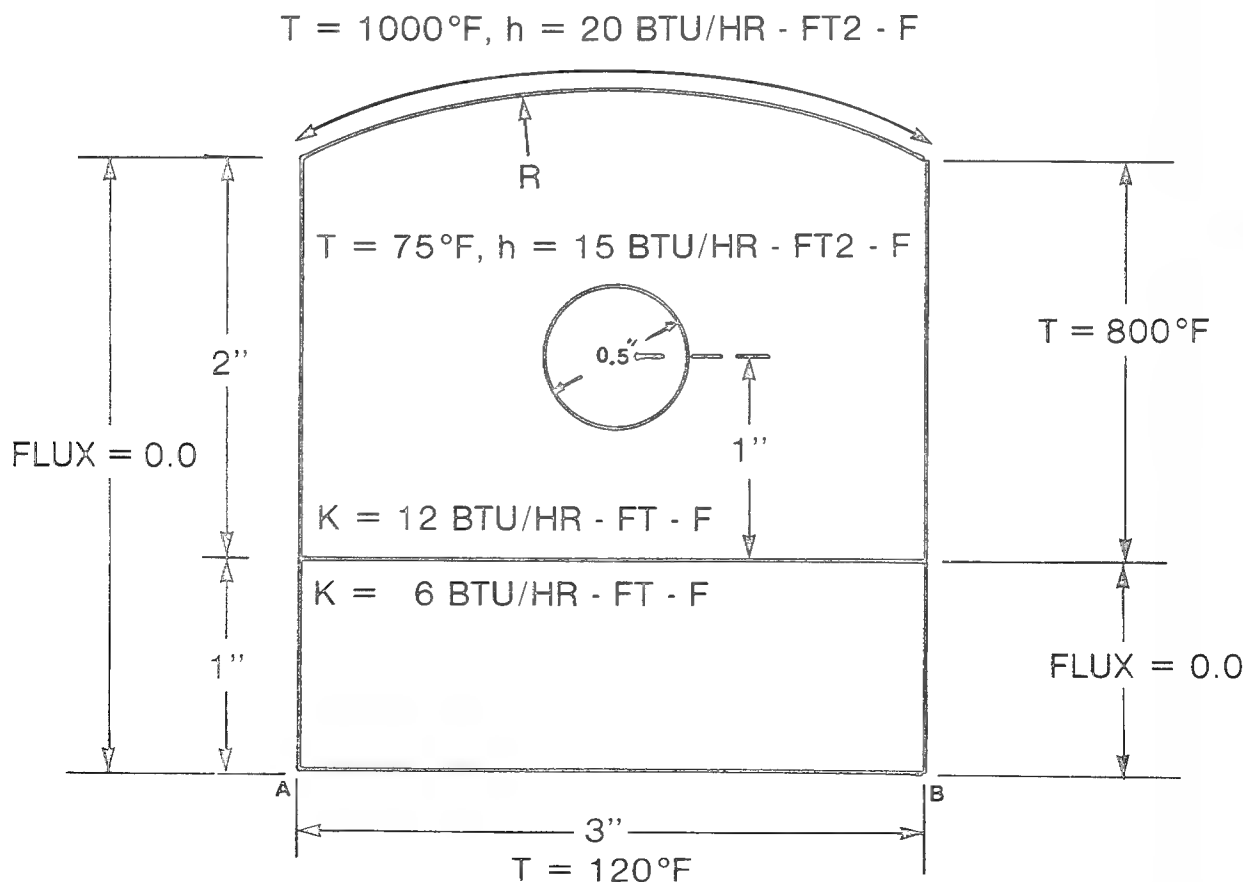


Fig. 9. Example Problem

### RESULTS:

The temperature distribution in the structure was plotted as shown in Fig. 11. The cooling hole was interactively moved and its diameter reduced for the second analysis. The new results were plotted as shown in Fig. 12.

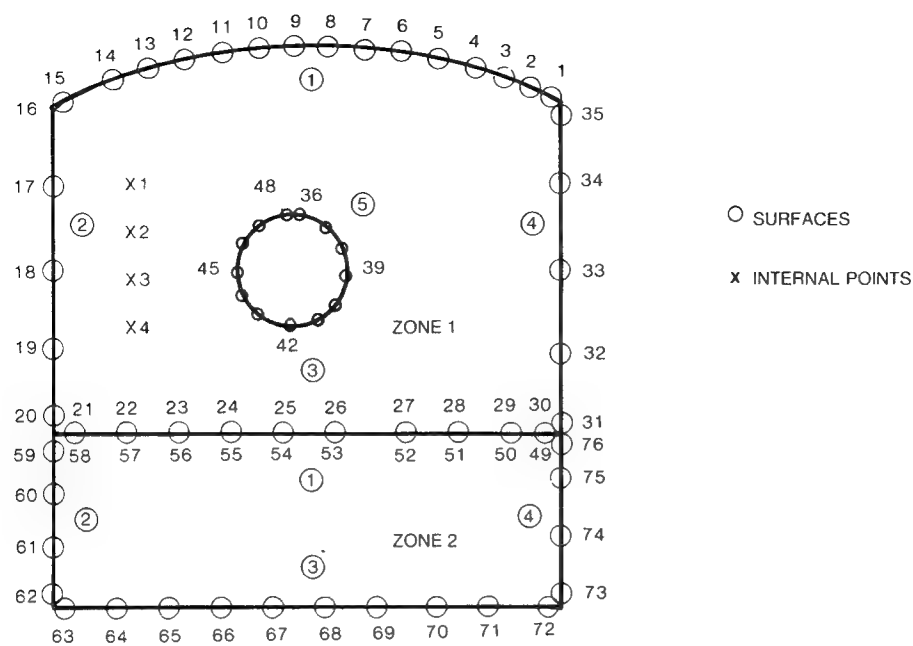


Fig. 10. Discretization of Boundary

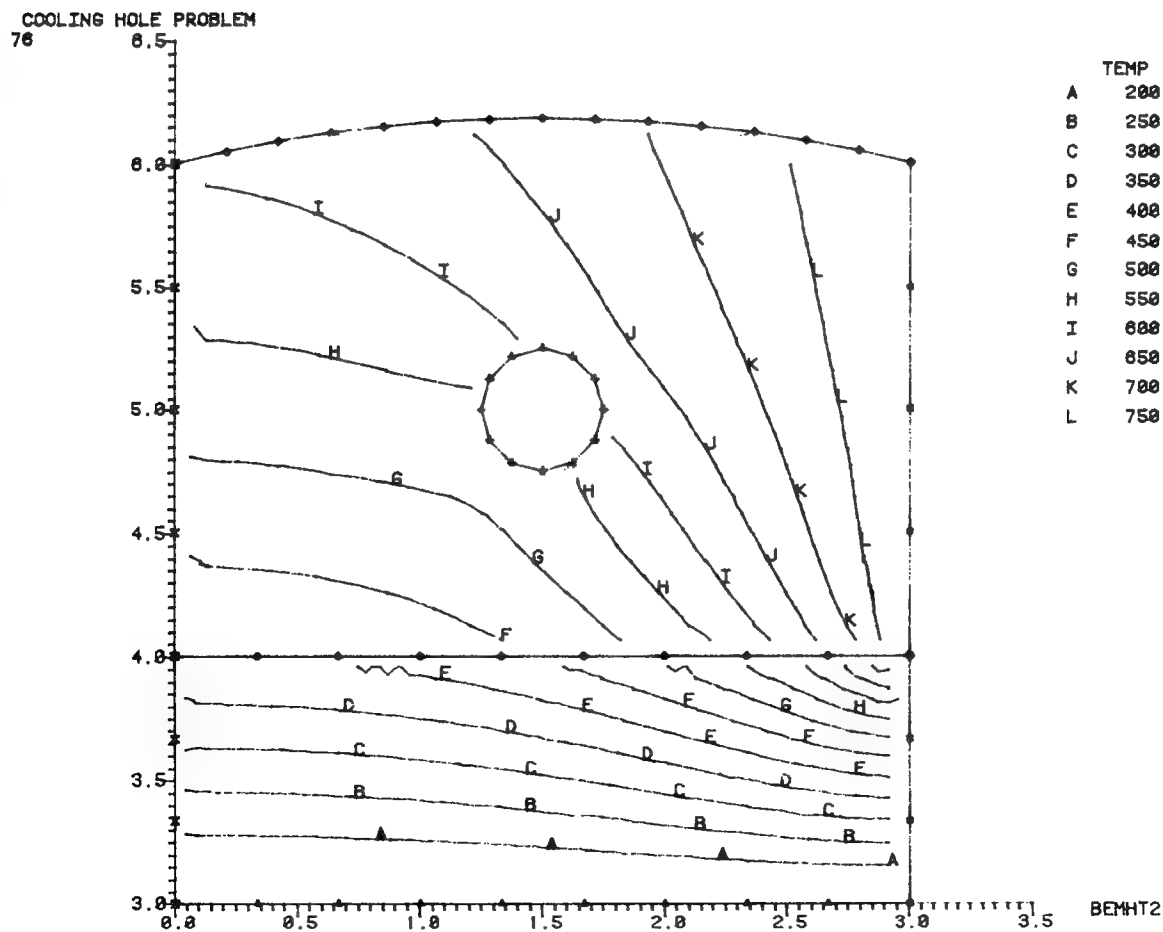


Fig. 11. Temperature Distribution for Case 1

COOLING HOLE PROBLEM  
76

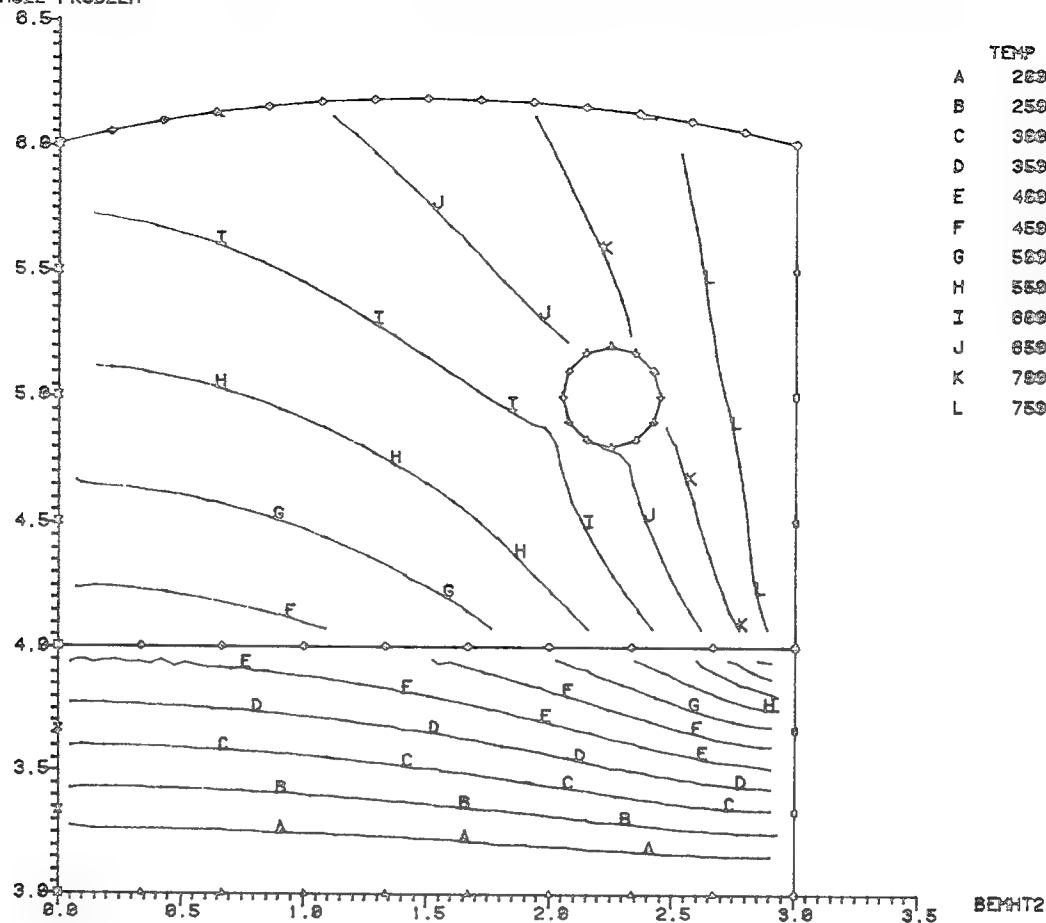


Fig. 12. Temperature Distribution for Case 2

## REFERENCES

1. Rizzo, F.J., "An Integral Equation Approach to Boundary Value Problems of Classical Elastostatics," Q. Appl. Math., Vol. 25, No. 83, 1967.
2. Cruse, T.A., and Rizzo, F.J., "A Direct Formulation and Numerical Solution of the General Transient Elastodynamic Problem," Part I, J. Math. Anal. Appl. 22, 1968.
3. Cruse, T.A., "A Direct Formulation and Numerical Solution of General Transient Elastodynamic Problem," Part II, J. Math. Anal. Appl. 22, 1968.
4. Cruse, T.A., "Application of Boundary Integral Equation Solution Method in Solid Mechanics," Variational Methods in Engineering, Edited by C.A. Brebbia and H. Tottenham, Southampton University Press, 1973.

# IMPLEMENTATION OF A $C^1$ TRIANGULAR ELEMENT

BASED ON THE P-VERSION OF THE FINITE ELEMENT METHOD<sup>†</sup>

D. W. Wang<sup>\*</sup>, I. N. Katz<sup>\*\*</sup>, and B. A. Szabo<sup>\*\*\*</sup>

School of Engineering and Applied Science  
Washington University  
St. Louis, Missouri 63130

## SUMMARY

The implementation of a computer code CONE (for  $C^1$  continuity) based on the p-version of the finite element method is described. A hierarchic family of triangular finite elements of degree  $p \geq 5$  is used. This family enforces  $C^1$ -continuity across inter-element boundaries, and the code is applicable to fourth-order partial differential equations in two independent variables, in particular to the biharmonic equation. Applications to several benchmark problems in plate bending are presented. Sample results are examined and compared with theoretical predictions. In particular the analysis of the bending of a rhombic plate shows a significant improvement over other published results.

## INTRODUCTION

One of the most widely used numerical techniques for the solution of partial differential equations (PDEs), is the finite element method. This method is based on the minimization of the functional corresponding to the PDE by piecewise smooth functions on convex subdomains such as triangles. The conventional approach termed the h-version, keeps the degrees of the polynomials of the approximation functions fixed and makes the diameters of the element subdomains approach zero. Accuracy is attained by increasing the number of elements which represent the process being modeled. Although theoretical asymptotic estimates are available for the error in energy when using the h-version, it has been observed in practice that the sizes of elements which must be used are often so large that they lie outside of the range of asymptotic behavior (ref. 1).

In a new approach, called the p-version, the subdomains are kept constant but the degrees of approximating polynomials are increased. Both numerical experiments and theoretical results show that the convergence rate of the p-version is no worse than that of the h-version; moreover in problems where convergence is limited by

<sup>†</sup> Research sponsored by the Air Force Office of Scientific Research, Air Force Systems Command, USAF, under grant Number AFOS 81-0252.

<sup>\*</sup> Department of Systems Science and Mathematics. The work presented here is part of the doctoral research of this author.

<sup>\*\*</sup> Department of Systems Science and Mathematics.

<sup>\*\*\*</sup> Department of Civil Engineering.



singularities due to corners in the domain, the rate of convergence of the p-version is twice that of the h-version (ref. 2 and 3).

In this paper, we describe the implementation of a p-version finite element program which solves fourth-order partial differential equations. More specifically, we consider plate-bending problems and we use the displacement method under the usual Kirchhoff-Love assumptions: that is, we solve the Dirichlet problem for the biharmonic operator  $\Delta^2$ :

$$\Delta^2 u = f \quad \text{in } \Omega \subset \mathbb{R}^2, \text{ a bounded polygonal domain} \quad (1a)$$

$$u = \partial_\nu u = 0 \quad \text{on } \Gamma \quad (\text{clamped edges}) \quad (1b)$$

where  $\partial_\nu$  is the first derivative normal to the boundary  $\Gamma$ . A solution to (1) is sought in the weak sense, i.e. let  $H^2_0(\Omega)$  be the Sobolev space of functions with square integrable second derivatives which satisfy (1b). We seek  $v \in H^2_0(\Omega)$ , which minimizes the functional

$$J(v) = \frac{1}{2} \int_{\Omega} \left\{ |\Delta v|^2 + 2(1-\sigma) \left( \left( \frac{\partial^2 v}{\partial x \partial y} \right)^2 - \frac{\partial^2 v}{\partial x^2} \frac{\partial^2 v}{\partial y^2} \right) \right\} dA - \int_{\Omega} f v dA \quad (2)$$

where  $\sigma$  is Poisson's ratio.

Since second derivatives are present in the variational formulation, the conforming finite element method requires  $C^1$  continuity; that is, both displacements and the normal derivatives must be continuous across the boundary of each element.

It is well known that in the case of  $C^1$  continuity, conformity is not enforced as easily as in the case of  $C^0$  continuity where only displacements need to be continuous (ref. 4). Various approaches have been proposed for enforcing  $C^1$  continuity while at the same time not enforcing continuity higher than  $C^1$ . These include: a) satisfying certain constraint equations at the vertices of each element, b) use of macroelements, c) use of penalty functions, and d) adding corrective rational functions to the polynomial basis. We have chosen the last approach because it leads to a standard procedure for assembling the elements.

We describe here the computer implementation of a  $C^1$  triangular element with the following salient features:

1. The pth degree approximation contains a complete polynomial of degree  $p \geq 5$ .
2. The element is conforming because of the corrective rational functions.
3. The element is hierarchic in the sense that the elemental stiffness matrix of degree  $p+1$  contains as a submatrix the elemental stiffness matrix of degree  $p$ .
4. Precomputed arrays based on closed-form integration formulas for the corrective rational functions are used to compute elemental stiffness matrices.

In the last section, computational results for several sample problems are presented. These results confirm the faster convergence rate of the p-version for the singularity problem, especially in the case of the difficult problem of a rhombic plate under uniform loading.

# THE p-VERSION FINITE ELEMENT FOR $C^1$ -PROBLEMS

## The Convergence Rate for $C^1$ -Problems

In finite element computations, a determining factor in meeting prescribed relative error tolerances is the number of degrees of freedom. This number, however, is strongly dependent on the asymptotic rate of convergence.

Suppose the variational problem (2) has a solution in the form: (ref. 5)

$$u_o = w + \sum_{i=1}^n a_i v_i \quad \text{with } w \in H^k(\Omega) \cap H_o^2(\Omega) \quad (3)$$

and 
$$v_i = r^{\gamma_i} g_i(|\ln r|) \theta_i(\phi_i) \quad \text{for each corner } i$$

where  $g_i, \theta_i$  are functions with continuous and bounded derivatives of all orders, and  $\gamma_i$  is a constant dependent on the vertex angle  $\alpha_i$  at corner  $A_i$  and the boundary conditions at the corner.  $\gamma_i$  is obtained as the root of a nonlinear equation. Then we have the following theorem for the p-version finite element:

### THEOREM

Let  $u_o$  be the exact solution of the variational problem (2), and let  $u_p$  be the p-version finite element solution. Then for  $k > 2$ ,

$$\|u_o - u_p\|_{2,\Omega} \leq C(\epsilon) p^{-\mu+\epsilon} \|u\|_{k,\Omega} \quad (4)$$

where  $\mu = \min [k-2, 2(\gamma_i-1)]$ , if  $u \in H^k(\Omega)$ , and  $\epsilon > 0$  is arbitrarily small.

In the singularity problem the rate of convergence is always dominated by the factor  $2(\gamma_i-1)$ . Since  $p^2 \approx N$  in the p-version of the finite element, we have:

$$\|u_o - u_p\|_{2,\Omega} \leq kN^{-(\gamma-1)} \quad \text{where } \gamma = \min \gamma_i. \quad (5)$$

In the h-version finite element method, it is clear that

$$h^2 \approx 1/N \quad \text{and it is known that}$$

$$\|u_o - u_h\|_{2,\Omega} \leq Ch^{\gamma-1} \approx CN^{-\frac{\gamma-1}{2}} \quad (6)$$

Comparing (5) with (6), we conclude that the p-version of the finite element method has twice the rate of convergence of the h-version for singularity problems.

## A p-Version, Hierarchic $C^1$ -Triangular Element

The hierarchic property of the finite element family is particularly important for the p-version. To obtain a refined solution, the polynomial degree of the approximation functions is increased without modification of the topology of the mesh. For the hierarchic element, only the portion of the stiffness matrix related

to the new higher order polynomials needs to be calculated, hence significant computation time is saved in obtaining a more accurate solution.

When increasing the polynomial degree from a starting value  $p-1$  to  $p$ ,  $p+1$  new independent functions are added and therefore  $p+1$  nodal variables have to be introduced. The hierarchical structure arises if and only if the new nodal variables correspond to new shape functions, i.e. none of the previously used shape functions is changed. This can be achieved if we choose as nodal variables  $p+1$ ,  $p$ th order derivatives.

Another goal in constructing a family of finite elements for the  $p$ -version is to have interpolation functions of arbitrary polynomial degrees which are exactly and minimally  $C^1$ -continuous.

However, it is easy to prove (ref. 6) that no set of nodal variables exists which satisfies the following two requirements if the continuity of the slopes is required:

1. There is a 1-1 transformation between the polynomial coefficients  $\{a^e\}$  and the corresponding subset of nodal variables  $\{\delta^e\}$ .
2. The  $\{\delta^e\}$ 's completely enforce the appropriate continuity requirements.

In fact, at the corner of a triangular element, since  $\partial^2 w / \partial s_2 \partial s_1 = \partial^2 w / \partial s_1 \partial s_2$ , the second derivatives are linearly dependent

$$\frac{\partial^2 w}{\partial s_1^2} \cos \phi + \frac{\partial^2 w}{\partial s_1 \partial n_1} \sin \phi - \frac{\partial^2 w}{\partial s_2^2} \cos \phi + \frac{\partial^2 w}{\partial s_2 \partial n_2} \sin \phi = 0 \quad (7)$$

where  $\phi$  is the angle at the corner,  $\partial^2 w / \partial s_2 \partial s_1$  is the mixed tangential derivative.

To destroy the analyticity of the polynomial approximation at the vertices, a set of rational functions are introduced.

### Nodal Variables and Shape Functions

#### Fifth-Order Finite Element ( $p=5$ )

In Fig. 1 we define the nodal variables for the fifth-order hierarchic finite element. It can be represented as the set

$$\{w(a_i), \partial_x w(a_i), \partial_y w(a_i), \partial_{\tau_{i-1}}^2 w(a_i), \partial_{\tau_{i+1}}^2 w(a_i), \partial_{\tau_{i-1} \nu_{i-1}} w(a_i), \\ -\partial_{\tau_{i+1} \nu_{i+1}} w(a_i), \partial_{\tau_{i+2} \nu_{i+2}}^4 w(a_{i,i+1}), i=1,2,3\}$$

where  $\partial_{\tau_i}$ ,  $\partial_{\nu_i}$  are tangential and normal derivatives respectively along the edge  $i$ , and  $a_{i,i+1}$  is the midpoint of  $a_i$  and  $a_{i+1}$ .

The shape functions corresponding to the six nodal variables of mixed derivatives at the vertices are rational functions of the form:

$$\eta_1 = \frac{L_1^2 L_2^2 L_3}{L_2 + L_3}, \quad \eta_2 = \frac{L_1^2 L_2 L_3^2}{L_2 + L_3}, \quad \text{etc.}$$

Since sums of pairs of the rational functions are polynomials (e.g.  $\eta_1 + \eta_2 = L_1^2 L_2 L_3$ ), it is possible to express the fifth-order approximation function in terms of six rational functions and 18 polynomial shape functions which correspond to the remaining 18 nodal variables.

The simplest polynomial shape functions are of the form  $N_{19} = L_1 L_2^2 L_3^2$  which have zeroth order contact with one side and first-order contact with the other two, hence are shape functions corresponding to  $\partial_{\tau_3}^4 v_3^w(a_{12})$ .

The shape functions corresponding to the nodal variables of the second derivatives  $\partial_{\tau_1}^2 w(a_1)$  are the form  $L_1^2 L_2^2 (L_2 - 1)$  which has first-order contact with sides 1 and 2 and the factor  $(L_2 - 1)$  assures that the second derivative along side 3 at vertex 2 is also zero. However, the mixed fifth derivative of this function at the midpoint  $a_{12}$  is not zero. We must correct for these shape functions and hence obtain:

$$N_4 = \frac{1}{2} L_1^2 L_2^2 (1 - L_2) - \frac{1}{4} (1 + 5\mu_3) \frac{1}{|M|} N_{21} + \frac{1}{2} (1 + \mu_3) \frac{1}{|M|} \eta_1 \quad (8)$$

where  $|M|$  is twice the area of the triangle, and  $\mu_3$  is defined in Table 1.

Similar procedures are applied to construct shape functions corresponding to the nodal variables of first derivatives and the displacements (ref. 6). These shape functions, however, are just linear combinations of polynomials and rational functions described before. Some of the coefficients depend on the geometry of the element. See Table 1 for a list of the shape functions for the Quintic  $C^1$  triangle.

### Higher Order Finite Element ( $p \geq 6$ )

Higher order shape functions do not correspond to simple nodal variables but they do enforce  $C^1$  continuity. In this sense they are nodeless shape functions. Side modes assure conformity and internal modes are used to obtain a complete  $p$ th order polynomial.

One of the shape functions for side modes represents rotation, and for side 1 is of the form:

$$N_{\text{rot},1}^p = L_1 L_2^2 L_3^2 [L_2^{p-5} + (-L_3)^{p-5}] \quad (9)$$

The shape function corresponding to the deflection on side 1 is represented as:

$$N_{\text{def},1}^p = L_2^3 L_3^3 [(L_2)^{p-6} + (-L_3)^{p-6}] + L_1 L_2^2 L_3^2 F(L_2, L_3) \quad (10)$$

where the polynomial  $F(L_2, L_3)$  can be determined in such a way that the normal slope of  $N_{\text{def},1}^p$  is zero along side 1. A straightforward computation shows that

$$\begin{aligned} N_{\text{def},1}^p &= L_2^3 L_3^3 [L_2^{p-6} + (-L_3)^{p-6}] + L_1 L_2^2 L_3^2 \left\{ \frac{3}{2} [L_2^{p-5} - (-L_3)^{p-5}] \right. \\ &\quad + \frac{p-3}{2} [L_3 L_2^{p-6} + L_2 (-L_3)^{p-6}] + \frac{3\mu_1}{2} [L_2^{p-5} + (-L_3)^{p-5}] \\ &\quad \left. - \mu_1 \frac{p-3}{2} [L_3 L_2^{p-6} - L_2 (-L_3)^{p-6}] \right\} \quad (11) \end{aligned}$$

The  $p$ th-order internal modes are a set of polynomial terms which make the set of shape functions complete:

$$\begin{aligned}
 & L_1^{\frac{p}{3}} L_2^{\frac{p}{3}} L_3^{\frac{p}{3}} \quad \text{if } p=3n \\
 & L_1^{[\frac{p}{3}]+1} L_2^{[\frac{p}{3}]} L_3^{[\frac{p}{3}]} , L_1^{[\frac{p}{3}]} L_2^{[\frac{p}{3}]+1} L_3^{[\frac{p}{3}]} \quad \text{if } p=3n+1 \\
 & L_1^{[\frac{p}{3}]+1} L_2^{[\frac{p}{3}]+1} L_3^{[\frac{p}{3}]} , L_1^{[\frac{p}{3}]} L_2^{[\frac{p}{3}]+1} L_3^{[\frac{p}{3}]+1} , L_1^{[\frac{p}{3}]+1} L_2^{[\frac{p}{3}]} L_3^{[\frac{p}{3}]+1} \quad \text{if } p=3n+2
 \end{aligned}$$

and for  $n \geq 3$

$$\begin{aligned}
 & L_1^{p-5} L_2^3 L_3^2, L_1^2 L_2^{p-5} L_3^3, L_1^3 L_2^2 L_3^{p-5}, \dots \\
 & L_1^{[\frac{p}{3}]+1} L_2^{[\frac{p}{3}]} L_3^{[\frac{p}{3}]-1} , L_1^{[\frac{p}{3}]-1} L_2^{[\frac{p}{3}]+1} L_3^{[\frac{p}{3}]} , L_1^{[\frac{p}{3}]} L_2^{[\frac{p}{3}]-1} L_3^{[\frac{p}{3}]+1}
 \end{aligned}$$

where  $[x] =$  the greatest integer  $\leq x$ .

This gives a total of  $p+1$  shape functions of  $p$ th order, and  $\frac{1}{2}(p+1)(p+2)+3$  shape functions in all. The number of monomials in a complete polynomial of degree  $p$  is  $\frac{1}{2}(p+1)(p+2)$ . The additional 3 functions correspond to 3 linearly independent rotational corrective functions.

## COMPUTER IMPLEMENTATION

### Computation of the Stiffness Matrix and the Load Vector

The elemental potential energy of the variational problem (2) is:

$$\pi^e = \frac{D}{2} \iint_e [w_{xx} w_{xy} w_{yy}] [S^e] \begin{Bmatrix} w_{xx} \\ w_{xy} \\ w_{yy} \end{Bmatrix} dx dy - \iint_e \begin{Bmatrix} w_x \\ \vdots \\ w_{yy} \end{Bmatrix} dA \quad (12)$$

$$\text{where } [S^e] = \begin{bmatrix} 1 & 0 & \sigma \\ 0 & 2(1-\sigma) & 0 \\ \sigma & 0 & 1 \end{bmatrix} \quad \text{where } D = \text{thickness of the plate} \\
 \text{and } \sigma \text{ is Poisson's ratio.}$$

Transferring to global coordinates from triangular coordinates, we have

$$\begin{Bmatrix} x \\ y \\ 1 \end{Bmatrix} = \begin{bmatrix} x_1 & x_2 & x_3 \\ y_1 & y_2 & y_3 \\ 1 & 1 & 1 \end{bmatrix} \begin{Bmatrix} L_1 \\ L_2 \\ L_3 \end{Bmatrix} \quad (13)$$

it is easy to obtain:

$$\begin{Bmatrix} w_{xx} \\ w_{xy} \\ w_{yy} \end{Bmatrix} = \begin{bmatrix} a_1^2 & a_2^2 & a_3^2 & 2a_1a_2 & 2a_1a_3 & 2a_2a_3 \\ a_1b_1 & a_2b_2 & a_3b_3 & (a_1b_2 + b_1a_2) & (a_1b_3 + b_1a_3) & (a_2b_3 + b_2a_3) \\ b_1^2 & b_2^2 & b_3^2 & 2b_1b_2 & 2b_1b_3 & 2b_2b_3 \end{bmatrix} \begin{Bmatrix} w_{L_1^2} \\ w_{L_2^2} \\ w_{L_3^2} \\ w_{L_1L_2} \\ w_{L_1L_3} \\ w_{L_2L_3} \end{Bmatrix}$$

$$= [G^e] \{w\}$$

where  $a_1 = \frac{y_2 - y_1}{|M|}$   $a_2 = \frac{y_3 - y_1}{|M|}$   $a_3 = \frac{y_1 - y_2}{|M|}$

$b_1 = \frac{x_3 - x_2}{|M|}$   $b_2 = \frac{x_1 - x_3}{|M|}$   $b_3 = \frac{x_2 - x_1}{|M|}$

Representing  $\{w\}$  in terms of nodal variables and shape functions, we have  $\{w\} = [N] \{a^e\}$

$$\pi^e = \frac{D}{2} [a^e] \iint_e [N]^T [G^e]^T [S^e] [G^e] [N] dA \{a^e\} - \iint_e [Z^e] [G^e] [N] dA \{a^e\} \quad (15)$$

Therefore, the elemental stiffness matrix is:

$$[K^e] = \iint_e [N]^T [\tilde{S}^e] [N] dA \quad (16)$$

where  $[\tilde{S}^e] = [G^e]^T [S^e] [G^e]$

In order to make the computation faster, we choose a set of primitive functions which are independent of the geometrical properties of each element, namely,

$$[N] = [P][Q]^T \quad (17)$$

where all the geometric information is contained in  $[Q]^T$ . Now we have

$$[K^e] = [Q] \iint_e [P]^T [\tilde{S}^e] [P] dA [Q]^T \quad (18)$$

The primitive functions for the cases  $p=6,7$  are given in Table 2. (The case  $p=5$  has been omitted from the Table, for brevity.) At this point, the integral still contains the matrix  $[\tilde{S}^e]_{6 \times 6}$ , which is element-dependent. To decompose it, (ref. 7) let

$$[\tilde{S}^e] = \sum_{j=1}^6 \sum_{i=1}^6 \tilde{s}_{ij}^e [E_{ij}^-] \quad (19)$$

$$\text{where } [E_{ij}]_{kl} = \begin{cases} 1 & k=i, l=j \\ 0 & \text{otherwise} \end{cases}$$

$$[K^e] = [Q] \left( \sum_{j=1}^6 \sum_{i=1}^6 \tilde{s}_{ij}^e \iint_e [P]^T [E_{ij}] [P] dA \right) [Q]^T \quad (20)$$

Now the matrices inside the integral are all independent of the element, so we can precompute:

$$\iint_e [P]^T [E_{ij}] [P] dA \quad i=1,2,\dots,6, j=1,\dots,6 \quad (21)$$

and save them in a disk file for future use. For the computation of the load vector, another set of precomputed arrays is also saved in the disk.

The other computations involving stiffness matrices and load vectors for each element consist only of linear combinations of matrices. These are much faster than numerical integration of functions.

#### Integration of Rational Functions

Since the primitive functions are just polynomials and rational functions of a specific form, the integrals of precomputed arrays fall into two classes: (ref. 8)

Class I:

$$J = \iint_e L_1^a L_2^b L_3^c \frac{L_1^i L_2^j L_3^k}{(1-L_1)^n} dA = 2A \frac{(a+i)!(b+c+j+k+1-n)!(b+j)!(c+k)!}{(a+b+c+i+j+k+2-n)!(b+c+j+k+1)!} \quad (22)$$

$a, b, c, i, j, k \geq 0, 1 \leq n \leq 3$

Class II:

$$J = \iint_e \frac{L_1^a L_2^b L_3^c}{(1-L_1)^n (1-L_2)^m} dA$$

$$= \frac{2Aa!c!}{(m-1)!} \sum_{k=m-1}^{\infty} \frac{k(k-1)\dots(k-m+2)}{(b+k-m+2)\dots(b+k-m+2+c)(b+c+3-m-n+k)\dots(b+c+3-m-n+k+a)}$$

where A is the area of the triangle.

(23)

The integral in (23) exists provided that  $b+c+1 \geq n$ . This condition is satisfied by all rational shape functions in Class II so that (23) is always valid. The series are also convergent if  $d=a+c+2-(m-1) \geq 2$ . (Actually, the series converge at least as rapidly as  $\Sigma 1/k^5$ .)

## Program Structure

For practical applications, the  $C^1$ -triangular element was implemented with polynomial degree  $p$  up to 8. The program was coded in FORTRAN and was tested on a VAX-11/780 super-mini computer with 1 megabyte core memory.

The program has two major parts as shown in Fig. 2:

1. Off-line computation for the precomputed arrays. INTA and INTB compute type I and type II integrals for all possible combinations of rational functions and polynomials; PRE1, PRE2 and PRE3 calculate the integrals of the primitive functions, and save results in a disk file as precomputed arrays for both the stiffness matrices and load vectors.
2. On-line computation for the plate bending analysis. MULT prepares the elemental stiffness matrix and load vector using the input data and the precomputed arrays in the disk. ASMBL works with SOLV to do the assembly of stiffness matrices and to solve the global system of equations by using a frontal-solver technique (ref. 9). The solution of the nodal variables is manipulated by the postprocessor POST in order to compute displacement, moments, strain energy and other quantities of engineering interest.

## COMPUTATIONAL RESULTS AND DISCUSSION

Several benchmark problems were tested with CONE, the  $p$ -version  $C^1$ -triangular finite element program, to examine the performance of the code.

### Uniform Load on a Simply Supported Equilateral Triangle

In this case, the analytic solution of the displacement is a fifth-order polynomial (ref. 10). Using  $p=5$  and a single element for the whole triangular plate, we can easily obtain the exact solution with only three degrees of freedom:

At the center point,

$$\text{Deflection} = 5.787037 \times 10^{-3} D/q_0 L^4$$

$$\text{Moment} = 1.805556 \times 10^{-2} / q_0 L^2$$

### Square Plate Problems

Tests were made on the square plate with simply supported edges or clamped edges, under uniform load or concentrated load at the center point. Since all the four corners are 90 degrees, the roots  $\gamma_i$  are 2 and 3.75 for simply supported edges and clamped edges respectively. Hence the solutions are quite smooth.



By symmetry of the geometry, we can use either 1/2 or 1/8 of the plate as a single element to do the computation. As shown in Table 3, with  $p=5$ , CONE obtains at least 4-digits accuracy using very few degrees of freedom (DOF). The convergence rate, however, is dependent on the smoothness of the solution. For clamped edges, only 10 DOF's are needed, for simply supported edges, 18 DOF's are needed. Nevertheless, the  $p$ -version requires significantly fewer degrees of freedom than other finite element programs based on the  $h$ -version (ref. 11 and 12).

#### Simply Supported Equilateral Triangular Plate Under a Concentrated Load

Since the radial shearing force at distance  $r$  from the concentrated load  $p$  is:

$$Q_r = -\frac{p}{2\pi r}, \text{ where } Q_r = -D \frac{\partial}{\partial r} (\Delta w) \quad (24)$$

it follows that the solution in the neighborhood of the point load is of the form:

$$w = \frac{p}{8\pi D} r^2 \ln \frac{r}{a} \quad (25)$$

Since

$$\frac{\partial^3 w}{\partial r^3} = \frac{p}{4\pi D} \frac{1}{r} \quad (26)$$

and

$$\int_0^C \left( \frac{\partial^3 w}{\partial r^3} \right)^2 r dr = \left( \frac{p}{4\pi D} \right)^2 \int_0^C \frac{1}{r} dr,$$

which is not integrable, we know that the solution is in the space  $H^{3-\epsilon}$ , where  $H^{3-\epsilon}$  is a Sobolev space and  $\epsilon$  is a positive number. Based on the theorem which gives the rate of convergence, we expect an asymptotic rate of  $N^{-0.5}$ , which is better than the  $N^{-0.25}$  predicted for the  $h$ -version. The computational result (Fig. 3) shows a still better convergence rate in the non-asymptotic range. With  $p=8$ , a 2-element mesh, and 39 degrees of freedom, the energy error reduces to only 0.3%. The presence of rational functions which is not accounted for in the theoretical estimation of the rate of convergence in a polynomial function space, may be responsible for the improved-convergence rate.

#### Simply Supported Rhombic Plate Under Uniform Load

The simply supported rhombic plate with an angle of  $150^\circ$  at the obtuse vertex is a more difficult problem which has received a great deal of attention (ref. 13 and 14). Based on William's paper (ref. 5), for a corner simply supported on both sides, the roots are:

$$\gamma_{150^\circ} = 1.2, \quad \gamma_{30^\circ} = 6$$

By the theorem,  $\|u_o - u_p\|_{2,\Omega} \leq C(\epsilon) p^{-\mu+\epsilon} \|u\|_{k,\Omega}$  where  $\mu = \min [k-2, 2(\gamma_i-1)] = 0.4$ .

So we expect that in the p-version of the finite element method,

$$\|u_o - u_p\|_{2,\Omega} \leq C_h/p^{0.4} = C_h/N^{0.2}, \quad \text{where } C_h \text{ is independent of } p,$$

and in the h-version of the finite element method,

$$\|u_o - u_h\|_{2,\Omega} \leq C_p/N^{0.1}, \quad \text{where } C_p \text{ is independent of } h.$$

The computational results of the p-version and h-version for a quasi-uniform mesh (Fig.4(a)) are shown in Fig. 5; both the convergence rates of the p-version and h-version are quite close to the theoretical predictions (0.232 and 0.118, respectively).

Since there is a very strong singularity at the obtuse corner, it is of interest to examine the computational performance when using a strongly graded mesh as shown in Fig. 4(b) (ref. 15). By using this non-quasi-uniform mesh, with  $p=5$ ,  $p=6$ , a very fast convergence rate is obtained as shown in Fig. 5. Table 4 shows that at least 3 digits of accuracy (ref. 16) are obtained with only 60 degrees of freedom. The solutions presented here are the most efficient of the solutions published to date for this sample problem. Development of a combined h-version and p-version of the finite element method, in which the mesh is graded and at the same time  $p$  is changed, is a very promising approach for future research.

# REFERENCES

1. Babuska, I. and Szabo, B.A.: On the Rates of Convergence of the Finite Element Method. Int. J. Num. Meth. Engng., Vol. 18, pp. 323-341, 1982.
2. Babuska, I.; Szabo, B.A.; and Katz, I.N.: The p-Version of the Finite Element Method. SIAM J. Numer. Anal., Vol. 18, pp. 515-545, 1981.
3. Wang, D.W. and Katz, I.N.: The Rate of Convergence of the p-Version of the Finite Element Method for Plate-Bending Problems. SIAM 1981 Fall Meeting, Cincinnati, Ohio.
4. Peano, A.G.: Conforming Approximations for Kirchhoff Plates and Shells. Int. J. Num. Meth. Engng., Vol. 14, pp. 1273-1291, 1979.
5. Williams, M.L.: Surface Stress Singularities Resulting from Various Boundary Conditions in Angular Corners of Plates Under Bending. U.S. National Congress of Applied Mechanics, Illinois Institute of Technology, Chicago, Ill., June 1951.
6. Peano, A.G.: Hierarchies of Conforming Finite Elements for Plane Elasticity and Plate Bending. Comp. & Maths. with Appls., Vol. 2, pp. 211-224, 1976.
7. Kratochvil, J.; Zenisek, A.; and Zlamal, M.: A Simple Algorithm for the Stiffness Matrix of Triangular Plate-Bending Elements. Int. J. Num. Meth. Engng., Vol. 3, pp. 553-563, 1971.
8. Katz, I.N.: Integration of Triangular Finite Elements Containing Corrective Rational Functions. Int. J. Num. Meth. Engng., Vol. 11, pp. 107-114, 1977.
9. Irons, B.M.: A Frontal Solution Program for Finite Element Analysis. Int. J. Num. Meth. Engng., Vol. 2, pp. 5-32, 1970.
10. Timoshenko, S. and Woinowsky-Krieger, S.: Theory of Plates and Shells, 2nd ed., NY, McGraw-Hill, 1959.
11. Cowper, G.R.; Kosko, E.; Lindberg, G.M.; and Olsen, M.D.: A High Precision Plate-Bending Element. NRC NAE, Aero Report LR 514, National Research Council of Canada, 1968.
12. Caramanlian, C.; Selby, K.A.; and Hill, G.T.: A Quintic-Conforming Plate-Bending Triangle. Int. J. Num. Meth. Engng., Vol. 12, pp. 1109-1130, 1978.
13. Sander, G.: Application of the Dual Analysis Principle. Proc. Symp. on High Speed Computing of Elastic Structures, Universite de Liege, pp. 167-207, 1971.
14. Argyris, J.H., et. al.: On the Application of the SHEBA Shell Element. Comp. Meth. Appl. Mech. Engng., Vol. 1, pp. 317-347, 1972.
15. Szabo, B.A.; Basu, P.K.; Dunavant, D.A.; and Vasilopoulos, D.: Adaptive Finite Element Technology in Integrated Design and Analysis. Report WU/CCM-81/1, Washington University, St. Louis, MO, Jan. 1981.
16. Morley, L.S.D.: Skew Plates and Structures, MacMillan, NY, 1963.

TABLE 1. - LIST OF SHAPE FUNCTIONS (HIERARCHIC QUINTIC C<sup>1</sup> TRIANGLE)

p=5

$$\eta_1 = \frac{L_1^2 L_2 L_3}{L_2 + L_3} |M|$$

$$\eta_2 = \frac{L_1^2 L_2 L_3}{L_2 + L_3} |M|$$

$$\eta_3 = \frac{L_1^2 L_2 L_3}{L_1 + L_3} |M|$$

$$\eta_4 = \frac{L_1^2 L_2 L_3}{L_1 + L_3} |M|$$

$$\eta_5 = \frac{L_1^2 L_2 L_3}{L_1 + L_2} |M|$$

$$\eta_6 = \frac{L_1^2 L_2 L_3}{L_1 + L_2} |M|$$

$$N_1 = L_1^3 + 3(\hat{N}_2 + \hat{N}_3) - 6(\hat{N}_4 + \hat{N}_5 + \hat{N}_6)$$

$$N_2 = (X_2 - X_1)\hat{N}_2 + (X_3 - X_1)\hat{N}_3$$

$$N_3 = (Y_2 - Y_1)\hat{N}_2 + (Y_3 - Y_1)\hat{N}_3$$

$$N_4 = \frac{1}{2}L_1^2 L_2^2 (1 - L_2) - \frac{1}{4}(1 + 5\mu_3)N_{21}^* + \frac{1}{2}(1 + \mu_3)\eta_1^*$$

$$N_6 = \frac{1}{2}L_1^2 L_3^2 (1 - L_3) - \frac{1}{4}(1 - 5\mu_2)N_{20}^* + \frac{1}{2}(1 - \mu_2)\eta_2^*$$

$$N_7 = L_2^3 + 3(\hat{N}_8 + \hat{N}_9) - 6(\hat{N}_{10} + \hat{N}_{11} + \hat{N}_{12})$$

$$N_8 = (X_3 - X_2)\hat{N}_8 + (X_1 - X_2)\hat{N}_9$$

$$N_9 = (Y_3 - Y_2)\hat{N}_8 + (Y_1 - Y_2)\hat{N}_9$$

$$N_{10} = \frac{1}{2}L_2^2 L_3^2 (1 - L_3) - \frac{1}{4}(1 + 5\mu_1)N_{19}^* + \frac{1}{2}(1 + \mu_1)\eta_3^*$$

$$N_{12} = \frac{1}{2}L_1^2 L_2^2 (1 - L_1) - \frac{1}{4}(1 - 5\mu_3)N_{21}^* + \frac{1}{2}(1 - \mu_3)\eta_4^*$$

$$N_{13} = L_3^3 + 3(\hat{N}_{14} + \hat{N}_{15}) - 6(\hat{N}_{16} + \hat{N}_{17} + \hat{N}_{18})$$

$$N_{14} = (X_1 - X_3)\hat{N}_{14} + (X_2 - X_3)\hat{N}_{15}$$

$$N_{15} = (Y_1 - Y_3)\hat{N}_{14} + (Y_2 - Y_3)\hat{N}_{15}$$

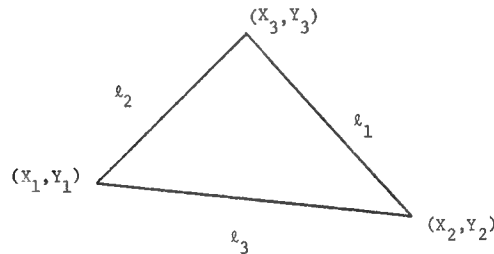
$$N_{16} = \frac{1}{2}L_1^2 L_3^2 (1 - L_1) - \frac{1}{4}(1 + 5\mu_2)N_{20}^* + \frac{1}{2}(1 + \mu_2)\eta_5^*$$

$$N_{18} = \frac{1}{2}L_2^2 L_3^2 (1 - L_2) - \frac{1}{4}(1 - 5\mu_1)N_{19}^* + \frac{1}{2}(1 - \mu_1)\eta_6^*$$

$$N_{19} = L_1 L_2 L_3 |M|$$

$$N_{20} = L_1^2 L_2 L_3 |M|$$

$$N_{21} = L_1^2 L_2 L_3 |M|$$



$$\text{where } \mu_1 = \frac{l_3^2 - l_2^2}{l_1^2}, \mu_2 = \frac{l_1^2 - l_3^2}{l_2^2}, \mu_3 = \frac{l_2^2 - l_1^2}{l_3^2}$$

$$|M| = 2 \cdot (\text{Area of element})$$

$$\hat{N}_5 = L_1^2 L_2 L_3$$

$$\hat{N}_{11} = L_1 L_2^2 L_3$$

$$\hat{N}_{17} = L_1 L_2 L_3^2$$

$$\hat{N}_2 = L_1^2 L_2 (1 - L_2) + 2\hat{N}_5 + 6\hat{N}_4$$

$$\hat{N}_3 = L_1^2 L_3 (1 - L_3) + 2\hat{N}_5 + 6\hat{N}_6$$

$$\hat{N}_8 = L_2^2 L_3 (1 - L_3) + 2\hat{N}_{11} + 6\hat{N}_{10}$$

$$\hat{N}_9 = L_2^2 L_1 (1 - L_1) + 2\hat{N}_{11} + 6\hat{N}_{12}$$

$$\hat{N}_{14} = L_3^2 L_1 (1 - L_1) + 2\hat{N}_{17} + 6\hat{N}_{16}$$

$$\hat{N}_{15} = L_3^2 L_2 (1 - L_2) + 2\hat{N}_{17} + 6\hat{N}_{18}$$

$$\hat{N}_4 = \frac{1}{2}L_1^2 L_2^2 (1 - L_2) - \frac{1}{4}(1 + 5\mu_3)N_{21}^*$$

$$\hat{N}_6 = \frac{1}{2}L_1^2 L_3^2 (1 - L_3) - \frac{1}{4}(1 - 5\mu_2)N_{20}^*$$

$$\hat{N}_{10} = \frac{1}{2}L_2^2 L_3^2 (1 - L_3) - \frac{1}{4}(1 + 5\mu_1)N_{19}^*$$

$$\hat{N}_{12} = \frac{1}{2}L_1^2 L_2^2 (1 - L_1) - \frac{1}{4}(1 - 5\mu_3)N_{21}^*$$

$$\hat{N}_{16} = \frac{1}{2}L_1^2 L_3^2 (1 - L_1) - \frac{1}{4}(1 + 5\mu_2)N_{20}^*$$

$$\hat{N}_{18} = \frac{1}{2}L_2^2 L_3^2 (1 - L_2) - \frac{1}{4}(1 - 5\mu_1)N_{19}^*$$

$$N_i^* = \frac{1}{|M|} N_i, \quad i=19, 20, 21$$

$$\eta_i^* = \frac{1}{|M|} \eta_i, \quad i=1, 2, \dots, 6$$

TABLE 2. - LIST OF SHAPE FUNCTIONS IN TERMS OF PRIMITIVE FUNCTIONS (p=6 and 7)

p=6

$$\left\{ \begin{matrix} N_{25} \\ N_{26} \\ N_{27} \\ N_{28} \\ N_{29} \\ N_{30} \\ N_{31} \end{matrix} \right\}$$

=

$$\begin{bmatrix} 2 & 0 & 0 & 3+3\mu_1 & 3-3\mu_1 & 0 & 0 & 0 & 0 & 0 \\ 0 & 0 & 0 & 1 & -1 & 0 & 0 & 0 & 0 & 0 \\ 0 & 2 & 0 & 0 & 0 & 3+3\mu_2 & 3-3\mu_2 & 0 & 0 & 0 \\ 0 & 0 & 0 & 0 & 0 & 1 & -1 & 0 & 0 & 0 \\ 0 & 0 & 2 & 0 & 0 & 0 & 0 & 3+3\mu_3 & 3-3\mu_3 & 0 \\ 0 & 0 & 0 & 0 & 0 & 0 & 0 & 1 & -1 & 0 \\ 0 & 0 & 0 & 0 & 0 & 0 & 0 & 0 & 0 & 1 \end{bmatrix}$$

$$\left\{ \begin{matrix} {}^3L_2^3 \\ {}^3L_3^3 \\ {}^3L_1^3 \\ {}^3L_2^2 \\ {}^3L_1^2 \\ {}^3L_2^3 \\ {}^3L_$$

TABLE 4. - DISPLACEMENT OF THE CENTER OF A RHOMBIC PLATE UNDER NON-QUASI-UNIFORM  
MESH REFINEMENT

	<u>Polynomial Degree</u>	<u>Degrees of Freedom</u>	<u>Central Point Deflection</u>	<u>% error</u>
Sander (ref. 13)	5	>1000		24.
Argyris (ref. 14)	5	≈1300		2.
COMET-X (ref. 15)	5 in 3 fields	180		1.
CONE	5	8	2.8938	29.2
		16	3.1520	22.8
		25	3.4651	14.9
		33	3.8217	6.4
		42	4.0049	1.8
		51	4.0217	1.4
	6	60	4.0824	0.
		12	3.0375	25.6
		24	3.4081	16.5
		37	3.6708	9.9
		49	3.9198	3.9
		62	4.0471	0.8
		76	4.0660	0.3
		Analytic Value (ref. 16)		

FIG.1 HIERARCHIC QUINTIC C' ELEMENT

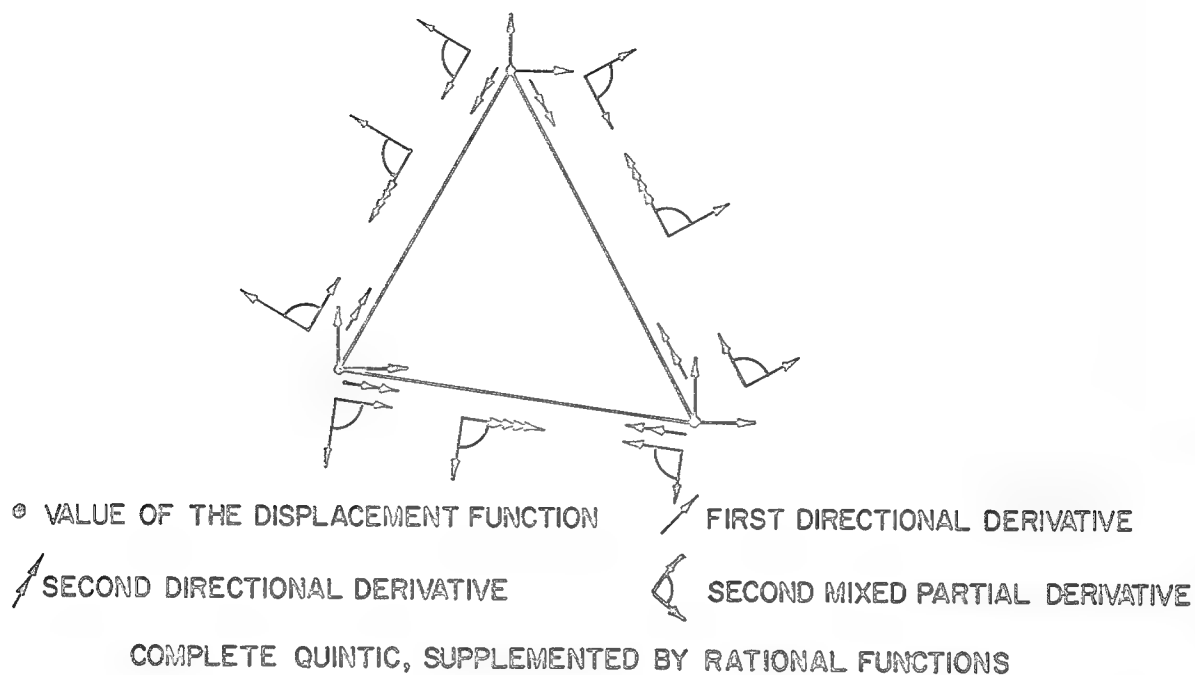


FIG.2 MACRO FLOW CHART OF CONE (C' TRIANGULAR ELEMENT)

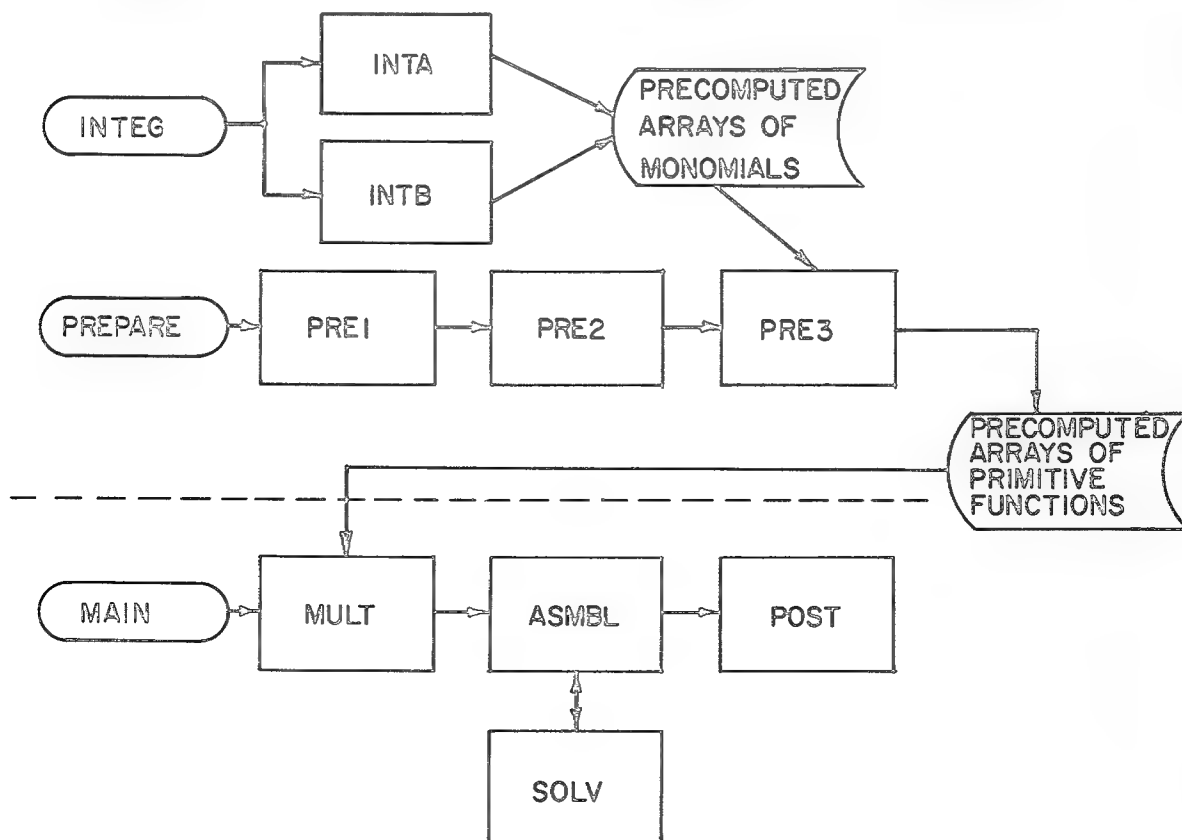
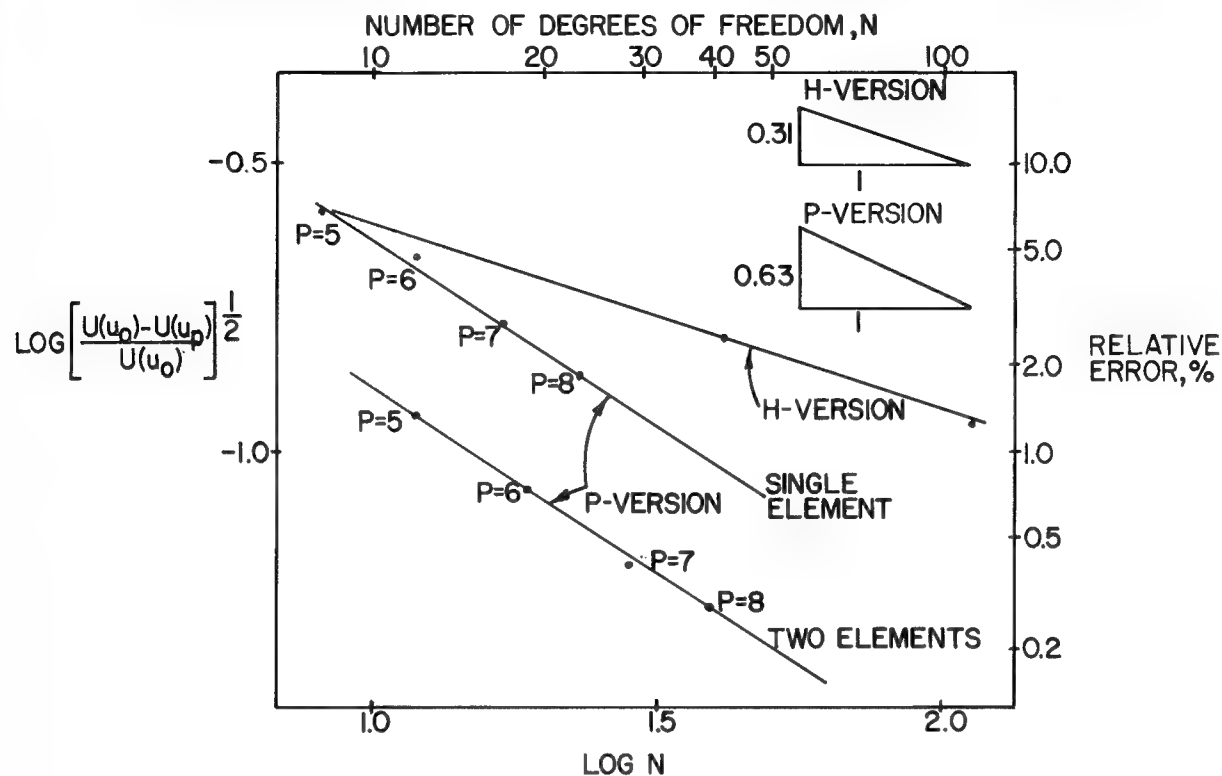


FIG.3 RELATIVE ERROR IN ENERGY NORM vs. NUMBER OF DEGREES OF FREEDOM -SIMPLY SUPPORTED EQUILATERAL TRIANGULAR PLATE WITH CONCENTRATED LOAD AT CENTER POINT



$U(u_0)$ =STRAIN ENERGY, EXACT SOLUTION  $U(u_p)$ =STRAIN ENERGY, COMPUTED

FIG.4 MESHES FOR THE ANALYSIS OF A RHOMBIC PLATE  
(A) QUASI - UNIFORM (B) NON -QUASI-UNIFORM

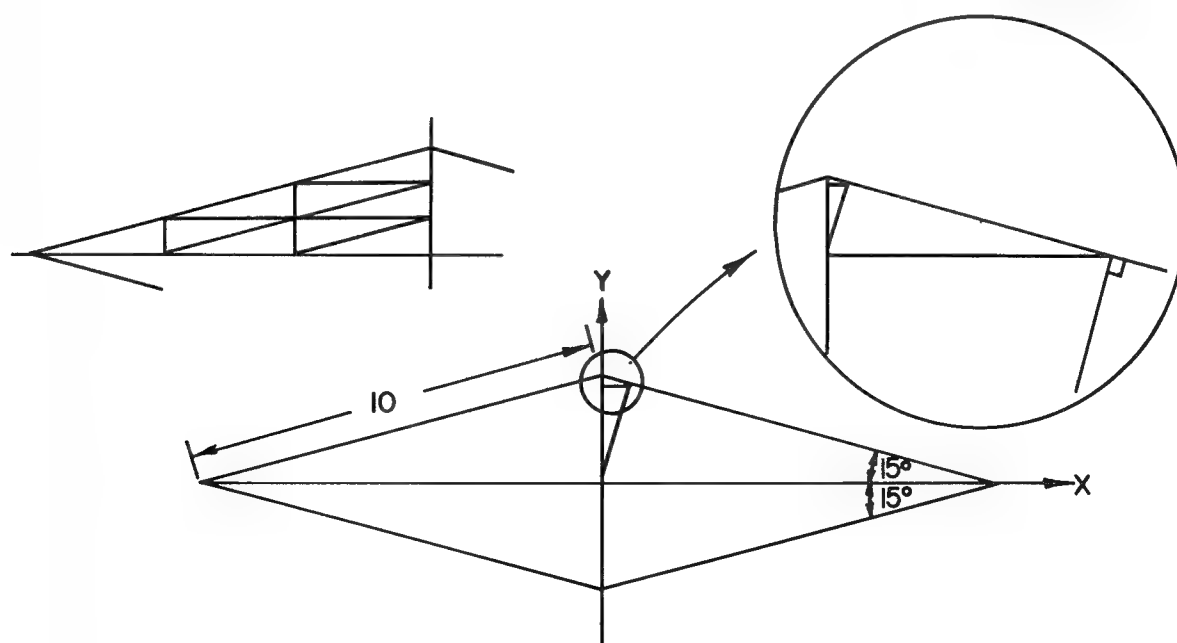
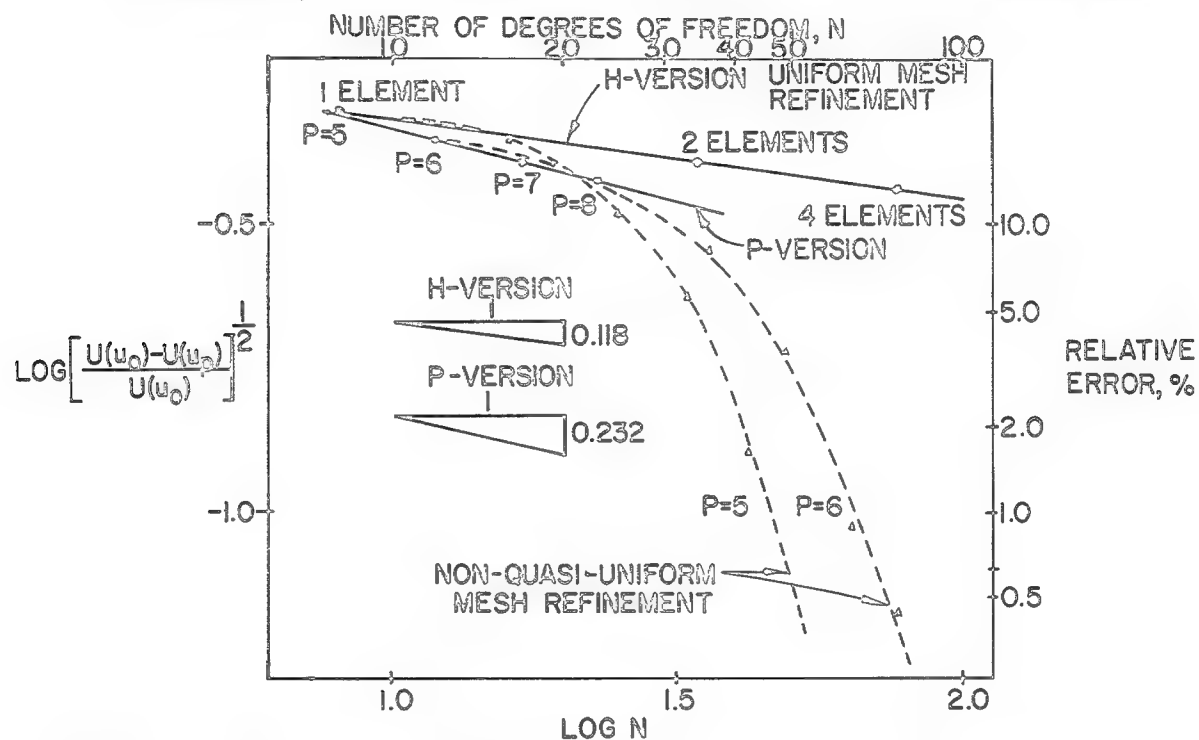




FIG.5 RELATIVE ERROR IN ENERGY NORM vs. NUMBER OF DEGREES OF FREEDOM; SIMPLY SUPPORTED RHOMBIC PLATE UNDER UNIFORM LOAD



$U(u_0)$  = STRAIN ENERGY, EXACT SOLUTION     $U(u_p)$  = STRAIN ENERGY, COMPUTED

# INTEGRATION OF MULTIDIMENSIONAL REGIONS WITH APPLICATIONS TO FINITE ELEMENT ANALYSIS

Robert L. Mullen  
Department of Civil Engineering  
Case Institute of Technology

## SUMMARY

Alternatives to Gaussian integration methods for multidimensional regions are presented. These rules preserve the convergence behavior of the exact integrated element but require less evaluation points than the Gauss methods. Numerical examples are given to verify the behavior of the new integration rules.

## INTRODUCTION

A considerable portion of the computational effort involved in the solution of problems by the finite element method is consumed by the numerical integration necessary to compute the element stiffness matrices and/or the element internal forces. Therefore, a reduction in the number of integration points will reduce the overall time required to solve a problem. This reduction will be most notable when the problem being considered involves a complex constitutive relationship. A reduction in the number of integration points will also reduce the storage required for state variables associated with the material law which, in explicit transient analysis, is often the largest component of the total storage required.

In one-dimensional problems, it is well known that the quadrature method with the least number of evaluation points for a given truncation error is Gaussian quadrature. For integration in multidimensional regions, most finite element texts recommend quadrature rules based on Cartesian products of the one-dimensional Gauss rules. These product rules have been shown to retain the same order of truncation error as their one-dimensional counterparts, but they may use more than the minimum number of evaluation points. Irons [1] has presented some more efficient quadrature rules for brick based elements.

In this paper, the integration of polynomials over rectangular regions will be considered. In particular, the number of evaluation points necessary to compute the element stiffness of the linear displacement quadrilateral is examined.

In the following section, a three point rule which is exact for quadratic polynomials over rectangular regions will be presented. In the third section, an alternating two point rule is presented. This two point rule does not integrate the quadratic polynomials that make up the stiffness of the bilinear quadrilateral exactly but will preserve the rank of the element stiffness matrix; this method will also preserve the convergence behavior of the exactly integrated element stiffness. The fourth section contains numerical results in order to compare the various integration methods.

## THREE POINT INTEGRATION METHOD

The general formula for numerical integration over a rectangular region is [2]

$$\int_{-1}^1 \int_{-1}^1 f(\xi, \eta) d\xi d\eta = \sum_{i=1}^n w_i f(\xi_i, \eta_i) + E \quad (2.1)$$

where  $w_i$  are the weight factors,  $(\xi_i, \eta_i)$  define the evaluation point, and  $E$  is the truncation error. Similar expressions exist for other dimensions. The evaluation points, weight factors, and truncation error for several quadrature methods in one and two dimensions are given in Table 1. In order to develop specific integration methods for a given element, the order of the polynomials that make up the unintegrated stiffness must be known. For the rectangular bilinear element, shown in figure 1, when used for plane stress or plane strain analysis, the product of the first partial derivatives of the shape functions are either constant in one direction and quadratic in the other or linear in both directions. If the constitutive law is assumed constant within an element, the terms that make up the unintegrated stiffness are

$$f(\xi, \eta) = a_1 + a_2\xi + a_3\eta + a_4\xi\eta + a_5\xi^2 + a_6\eta^2 \quad (2.2)$$

The presence of the quadratic terms indicates the well-known result that the lowest order Gauss integration rule applicable to this element is the four point rule. Due to the linear form of the shape functions, some researchers have recommended the use of one point Gauss integration for this element [3,4,5,6]. The use of one point integration, which reportedly results in a 1/3 to 1/4 reduction in the computational effort, also results in the existence of an "hourglass mode". In general, the rank of the element stiffness is reduced when the order of Gauss integration is reduced. This reduction of rank has been noted by several authors and is essential in the formulation of the penalty method for incompressible problems [7].

In order to construct a three point integration rule which will exactly integrate the stiffness of a rectangular bilinear element, equation (2.2) is substituted into equation (2.1) with  $n = 3$  and  $E = 0$ .

$$\begin{aligned} 4 a_1 &= a_1(w_1 + w_2 + w_3) \\ + (0) a_2 & a_2(w_1\xi_1 + w_2\xi_2 + w_3\xi_3) \\ + (0) a_3 & a_3(w_1\eta_1 + w_2\eta_2 + w_3\eta_3) \\ + (0) a_4 & a_4(w_1\xi_1\eta_1 + w_2\xi_2\eta_2 + w_3\xi_3\eta_3) \\ + 4/3 a_5 & a_5(w_1\xi_1^2 + w_2\xi_2^2 + w_3\xi_3^2) \\ + 4/3 a_6 & a_6(w_1\eta_1^2 + w_2\eta_2^2 + w_3\eta_3^2) \end{aligned} \quad (2.3)$$

Since the  $a_i$  are arbitrary constants, equation (2.3) becomes the six equations

$$\begin{aligned}
w_1 + w_2 + w_3 &= 4 \\
w_1 \xi_1 \eta_1 &= w_2 \xi_2 \eta_2 + w_3 \xi_3 \eta_3 = 0 \\
w_1 \xi_1^2 + w_2 \xi_2^2 + w_3 \xi_3^2 &= 4/3 \\
w_1 \xi_1 + w_2 \xi_2 + w_3 \xi_3 &= 0 \\
w_1 \eta_1^2 + w_2 \eta_2^2 + w_3 \eta_3^2 &= 4/3 \\
w_1 \eta_1 + w_2 \eta_2 + w_3 \eta_3 &= 0
\end{aligned} \tag{2.4}$$

with 9 unknowns.

In order to have a reasonable integration rule, the following constraints will be added to equation (2.4)

$$\begin{aligned}
w_1, w_2, w_3 &\geq 0 \\
\xi_i, \eta_i &\in [-1, 1]
\end{aligned} \tag{2.5}$$

There are several solutions to (2.4) subject to the constraints (2.5); each solution represents an acceptable three point integration rule for the bilinear element. Since a number of acceptable rules are available, the incorporation of some additional properties will be attempted.

One possible goal is to have one of the integration points in the center of the element. This would permit the reduction in the total number of integration points required to compute the stiffness matrix of an incompressible element based on the penalty method from five points to three. This would also allow the stresses to be computed at a super convergent point within an element [8].

Unfortunately, there exists no real solutions to equation (2.4) when

$$\xi_3 = \eta_3 = 0 \tag{2.6}$$

An alternate goal would be to have the evaluation points as uniformly distributed within the element as possible, which may provide an advantage if any nonlinear material behavior occurs within an element. To find the evaluation point and weights for an integral method with the above properties, the following nonlinear programming problem was solved.

Find minimum  $x$ , where  $x$  is the maximum distance between any point in the element and the nearest integration point subject to the constraint Eqs. (2.4) and (2.5). The solution to this problem is given in Table 1 as method 3c. Three point integration rules with other properties can be constructed in a similar manner.

## TWO POINT INTEGRATION METHOD

It can be shown that no two point method based on eq. (2.1) that satisfies equation (2.2) exists. However, there exists a two point method that preserves the rank of the stiffness matrix. The two point method results in a small integration error for smooth finite element solutions. First, an estimate of the order of each term in the stiffness is made based on the material constant associated with that term. This estimate indicates that the  $\xi\eta$  term is Poisson's ratio,  $\nu$ , times the other term in plane stress and  $\frac{\nu}{(1-\nu)}$  times the other tension plane strain. For physically relevant values of  $\nu$ , the  $\xi\eta$  term is smaller than other terms in the stiffness and is a good term to eliminate the exact integration requirement.

This reduces the number of equations to five

$$\begin{aligned} w_1 + w_2 &= 4 \\ w_1 \xi_1 + w_2 \xi_2 &= 0 \\ w_1 \eta_1 + w_2 \eta_2 &= 0 \\ w_1 \xi_1^2 + w_2 \xi_2^2 &= 4/3 \\ w_1 \eta_1^2 + w_2 \eta_2^2 &= 4/3 \end{aligned} \tag{3.1}$$

These five equations subject to the constraint Eq. (2.4) yield the integration rules 2a and 2b in Table 1 as solutions. Since the truncation errors of the two methods are the same magnitude, but opposite in sign, alternating between method 2a and method 2b on diagonally adjacent elements, as shown in figure 2, could result in compensatory errors.

## NUMERICAL RESULTS

In order to compare the integration rules presented, several problems were solved using the 1, 2, 3, and 4 point integration rules given in Table 1.

The first problem considered is a cantilever beam whose geometry and material constants are given in figure 3. Several different meshes were run in order to determine the effect of the integration rule on the convergence behavior of the element. The error in energy is given in Table 2 and plotted versus element size in figure 4. The two, three and four point rules compare favorably, each exhibiting the expected second order convergence in element size,  $h$ . The one point method, on the other hand, converges from the opposite side.

The second problem considered is that of a circular hole in a rectangular plate. This problem was chosen in order to see if non-vector isometric elements behave when the integration rules are employed. The mesh used is shown in figure 5. The results given in Table 3 show little difference in the two, three and four point rules.

The last problem consists of a square block with an initial rotation at time zero. The formulation used to solve this dynamic large displacement problem is the velocity strain-Cauchy stress formulation described in [9], using central difference time integration. The displacement of a corner of the unit square is plotted as a function of time in figure 6. There is again only a small variation between the two and four point rules and no difference between the three and four point rules while the one point rule was unstable due to hourglass deformation.

#### CONCLUSION

Several integration methods with fewer evaluation points than product Gauss rules have been examined. The efficiency of these methods over Gauss integration in two dimensions has been shown. These rules involve a change in weight factors and evaluation points. The incorporation of these methods into existing finite element programs is very simple. Integration rules can be developed for higher order elements [10] and higher dimensions [11], that require fewer evaluation points than the Gauss method.

While the smallest number of evaluation points does not always result in the most efficient finite element formulation [12] in nonlinear problems, the use of the least number of points required to retain the expected accuracy should result in an economical numerical formulation.

# REFERENCES

- [1] B.M. Irons, "Quadrature Rules for Brick Based Elements," International Journal for Numerical Methods in Engineering, 3, 1971.
- [2] Philip J. Davis and Philip Rabinowitz, Numerical Integration, Blaisdell Publishing, Waltham, Massachusetts, 1967.
- [3] T. Belytschko and J.M. Kennedy, "A Fluid Structure Finite Element Method for the Analysis of Reactor Safety Problems," Nuclear Engineering and Design, 38, 71-81, 1976.
- [4] S.W. Key, Z. E. Beisinger, and R.D. Kuiey, Hondo II - A Finite Element Computer Program for the Large Deformation Dynamic Response of Axisymmetric Solids, Sandia Laboratories, Albuquerque, 1978.
- [5] G. Maenchen and S. Sack, "The TENSOR Code," Methods in Computational Physics, 3, Academic Press, 181-210, 1964.
- [6] D.P. Flanagan and T. Belytschko, "A Uniform Strain Hexahedron and Quadrilateral with Orthogonal Hourglass Control," International Journal for Numerical Methods in Engineering, 17, 679-706, 1981.
- [7] D.J. Naylor, "Stress in Nearly Incompressible Materials by Finite Element with Application to the Calculation of Excess Pore Pressures," International Journal for Numerical Methods in Engineering, 8, 443-460, 1974.
- [8] Miloš Zlámal, "Super Convergence and Reduced Integration in the Finite Element Method," Mathematics of Computation, 32, 663-687, 1978.
- [9] T. Belytschko and R. Mullen, "WHAMS - A Program for Transient Analysis of Structures and Continua," Structural Mechanics Software Series, 2, University Press of Virginia, 1978.
- [10] H.J. Schmid, "On Cubature Formulae with a Minimal Number of Knots," Numerische Mathematik, 31, 281-297, 1978.
- [11] A.H. Stroud, "Numerical Integration Formulas of Degree Two," Mathematics of Computation, 14, 21, 1960.
- [12] William G. Gray and Martinus Th. Van Genuchten, "Economical Alternatives to Gaussian Quadrature Over Isoparametric Quadrilaterals," International Journal for Numerical Methods in Engineering, 12, 1478-1484, 1978.

TABLE 1  
Numerical Integration Rules

Dimension	Rule	Weights	Evaluation Points	Error
1	1	2	0	$\frac{1}{3} \frac{\partial^2 f}{\partial \xi^2}$
1	2	1,1	$+\frac{1}{\sqrt{3}}, -\frac{1}{\sqrt{3}}$	$\frac{1}{135} \frac{\partial^2 f}{\partial \xi^4}$
2	1	4	(0,0)	$\frac{2}{3} (\frac{\partial^2 f}{\partial \xi^2} + \frac{\partial^2 f}{\partial \eta^2})$
2	2a	2,2	$(\frac{1}{\sqrt{3}}, \frac{1}{\sqrt{3}}), (\frac{-1}{\sqrt{3}}, \frac{-1}{\sqrt{3}})$	$\frac{4}{3} \frac{\partial^2 f}{\partial \xi \partial \eta}$
2	2b	2,2	$(\frac{1}{\sqrt{3}}, \frac{-1}{\sqrt{3}}), (\frac{-1}{\sqrt{3}}, \frac{1}{\sqrt{3}})$	$\frac{4}{3} \frac{\partial^2 f}{\partial \xi \partial \eta}$
3	3a	$\frac{8}{7}, \frac{8}{7}, \frac{12}{7}$	$(\frac{7}{12}, \frac{-1}{2}), (-\frac{7}{12}, \frac{-1}{2}) (0, 2/3)$	$+\frac{1}{3} \frac{\partial^3 f}{\partial \xi^2 \partial \eta} - \frac{14}{315} \frac{\partial^3 f}{\partial \eta^3}$
2	3b	$\frac{8}{7}, \frac{8}{7}, \frac{12}{7}$	$(\frac{7}{12}, \frac{1}{2}), (-\frac{7}{12}, \frac{1}{2}) (0, -2/3)$	$-\frac{1}{3} \frac{\partial^3 f}{\partial \xi^2 \partial \eta} + \frac{14}{315} \frac{\partial^3 f}{\partial \eta^3}$
2	4	1.	$(\frac{1}{\sqrt{3}}, \frac{1}{\sqrt{3}})$	$\frac{2}{135} \frac{\partial^4 f}{\partial \xi^4} + \frac{\partial^4 f}{\partial \eta^4}$
		1.	$(\frac{1}{\sqrt{3}}, \frac{-1}{\sqrt{3}})$	
		1.	$(\frac{-1}{\sqrt{3}}, \frac{1}{\sqrt{3}})$	
		1.	$(\frac{-1}{\sqrt{3}}, \frac{-1}{\sqrt{3}})$	
2	3c	1.2578343	(.85220159, .021027579)	$-.10398 \frac{\partial^3 f}{\partial \xi^3} + .26811 \frac{\partial^3 f}{\partial \xi^2 \partial \eta}$
		18315722	(-.37877782, -.50116473)	$-.0206 \frac{\partial^3 f}{\partial \xi \partial \eta^2} + .10229 \frac{\partial^3 f}{\partial \eta^3}$
		0.91059353	(-.4153000, -.97899901)	



TABLE 2

## Error in Energy for Various Integration Methods

<u>Element Size</u>	<u>Integration Rule</u>	<u>Energy</u>	<u>Energy Error</u>
6	1	10.885	-2.785
4	1	9.3325	-1.2325
3	1	8.7292	-0.6292
1.5	1	8.3915	-0.215
6	2 alternate	7.3743	.7257
4	2 alternate	7.7039	.3961
3	2 alternate	7.8515	.2485
1.5	2 alternate	8.0498	.0502
6	2b	7.0222	1.0778
4	2b	7.5740	.5260
3	2b	7.7928	.3072
1.5	2b	8.0423	.0577
6	3a	7.0071	1.0929
4	3a	7.5674	.5326
3	3a	7.7880	.3120
1.5	3a	8.0398	.0602
6	4	7.0071	1.0929
4	4	7.5674	.5326
3	4	7.7880	.3120
1.5	4	8.0398	.0602

TABLE 3

## Hole in Plate Results

<u>Integration Rule</u>	<u>Energy</u>
1	.012487
2a & 2b	.012146
3a	.012028
4	.012030

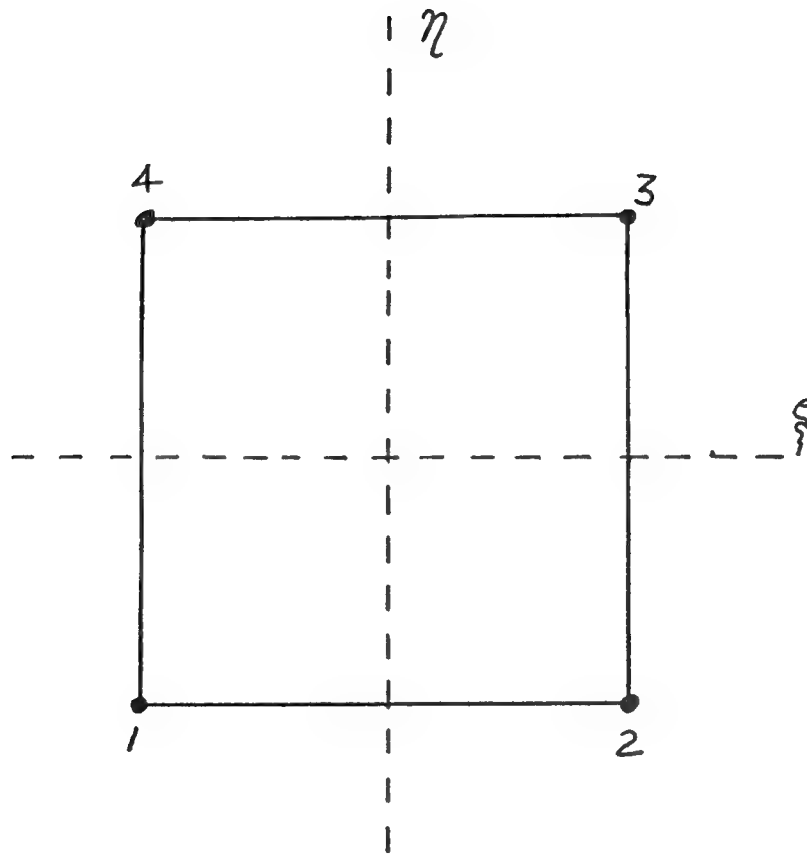
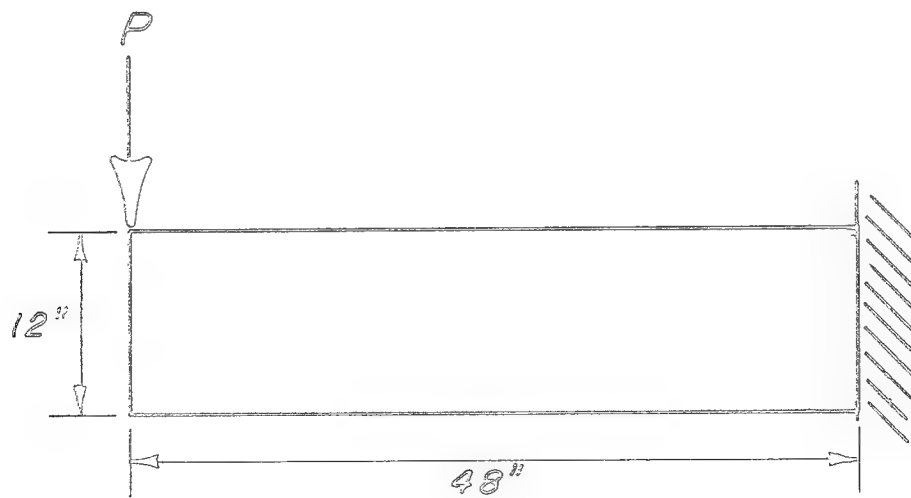


Figure 1.- Generic finite element.



Figure 2.- Evaluation points for alternate two-point integration.



Young's Modulus =  $3.0 \times 10^7$  PSI

Poisson's Ratio = 0.3

P = 1000 lb

Plane strain

Figure 3.- Geometry of beam model problem.

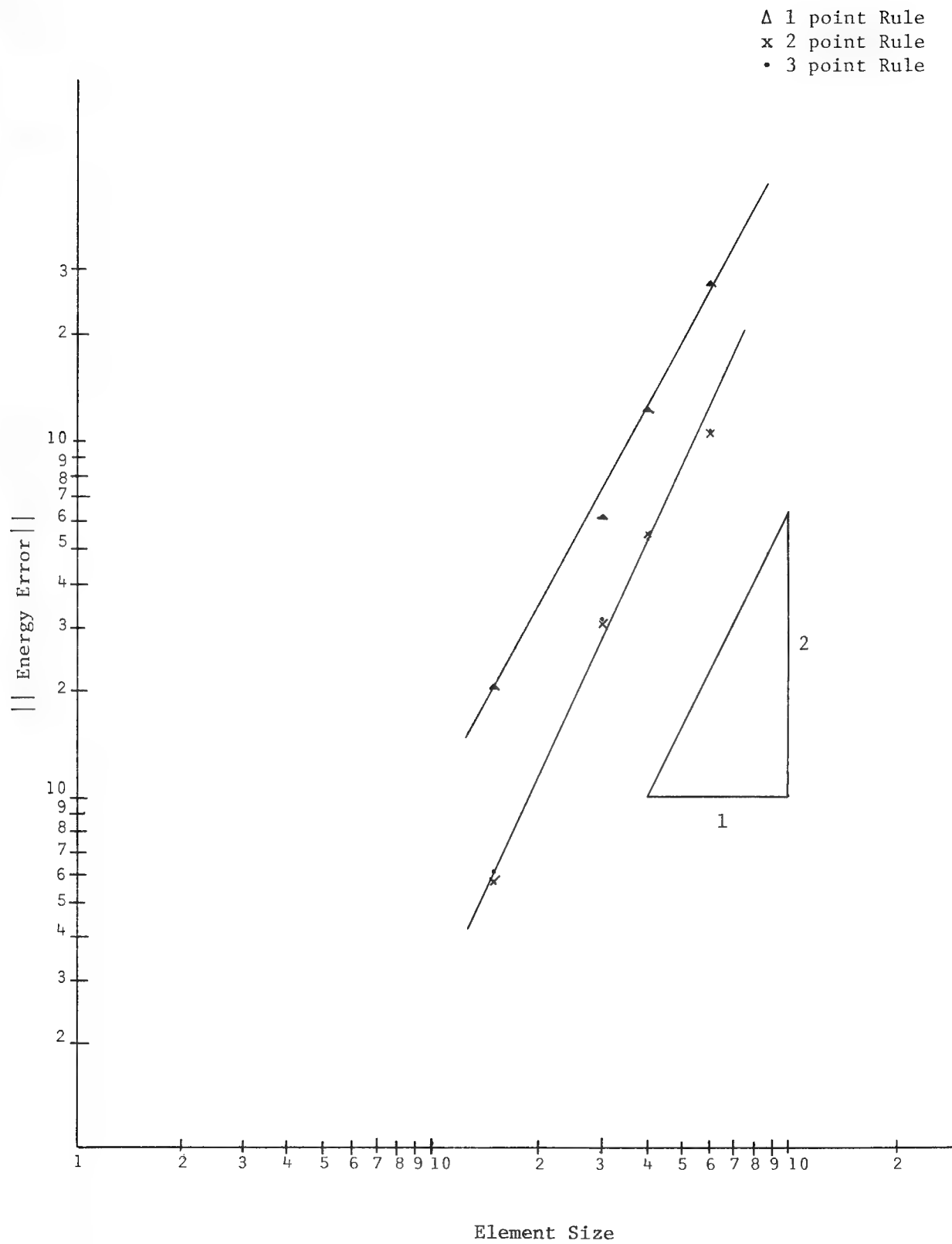


Figure 4.- Error in energy for various integration methods.

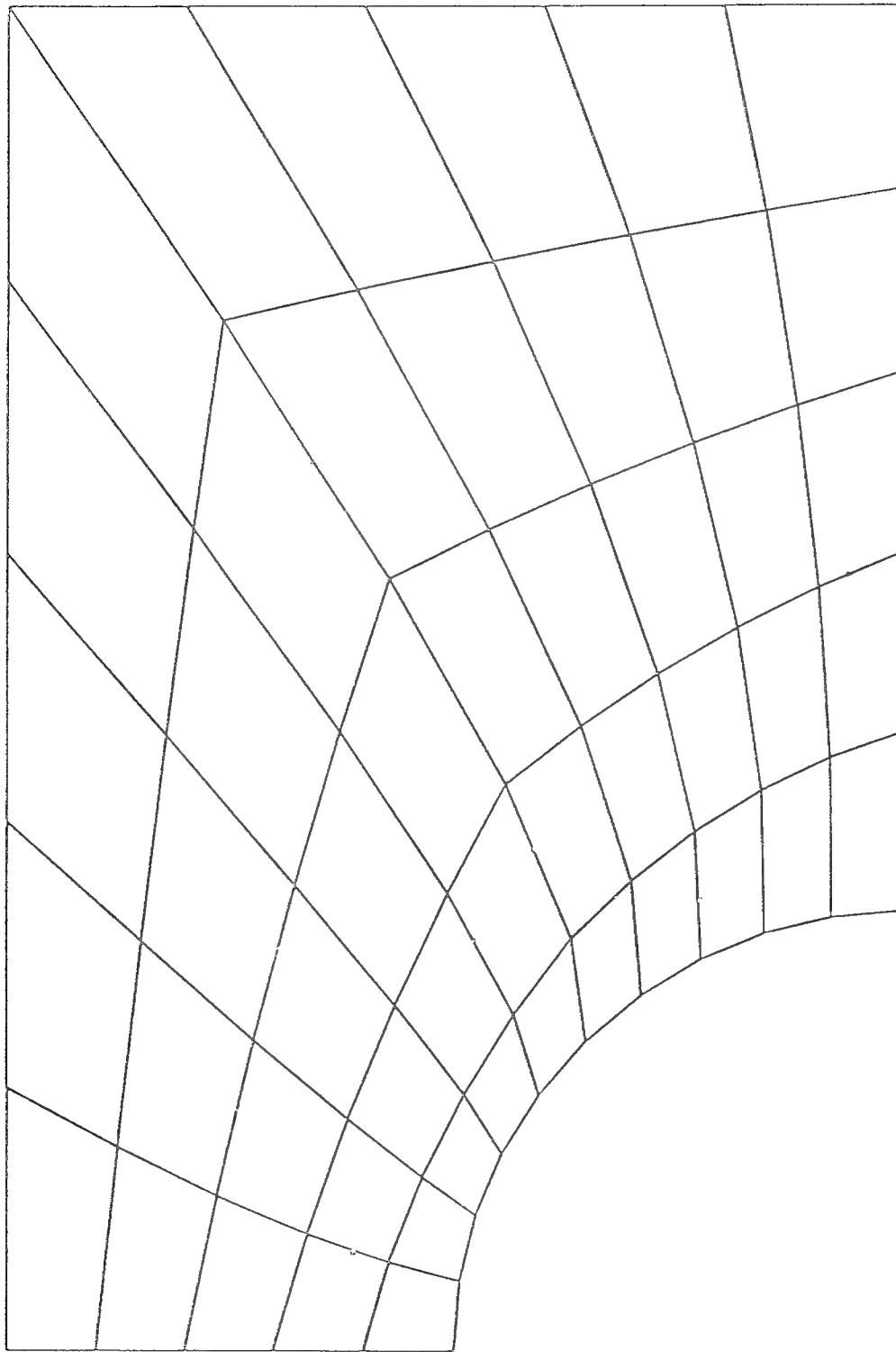


Figure 5.- Mesh for hole in plate problem.

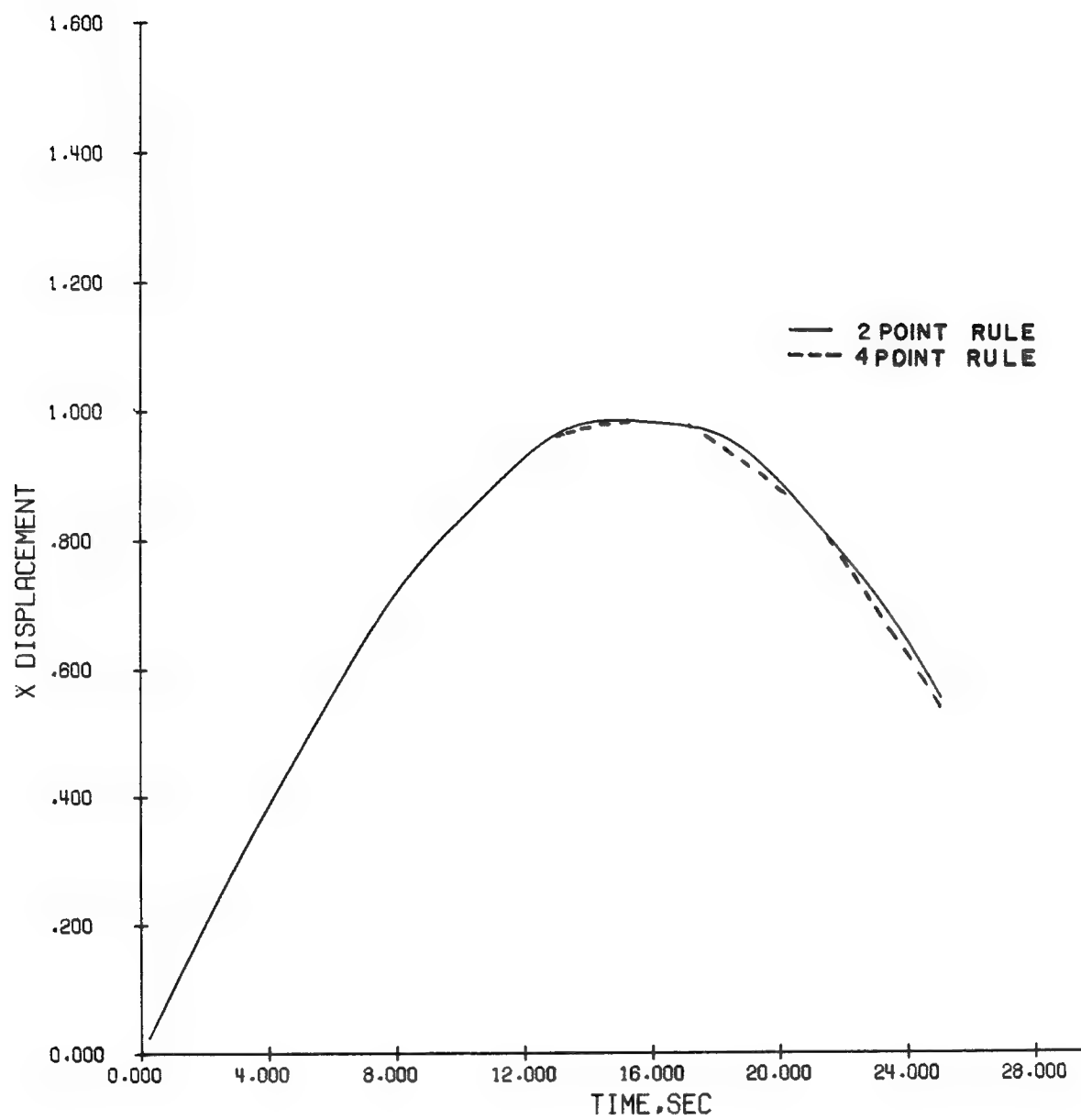


Figure 6.- Large rotation of an element.

AN EMULATOR FOR MINIMIZING FINITE ELEMENT  
ANALYSIS IMPLEMENTATION RESOURCES

Robert J. Melosh and Senol Utku  
Duke University

Moktar Salama  
Jet Propulsion Laboratory

Munir Islam  
NuTech Corporation

SUMMARY

When many calculations will be involved, a finite element analysis emulator provides a basis for efficiently establishing an optimum computer implementation strategy.

SCOPE is such an emulator. It determines computer resources required as a function of the structural model, structural load-deflection equation characteristics, storage allocation plan, and computer hardware capabilities. Thereby, it provides data for trading analysis implementation options to arrive at a best strategy. The models contained in SCOPE lead to micro-operation computer counts of each finite element operation as well as overall computer resource cost estimates.

Application of SCOPE to the Memphis-Arkansas bridge analysis provides measures of the accuracy of resource assessments. Data indicate that predictions are within 17.3 percent for calculation times and within 3.2 percent for peripheral storage resources for the ELAS code.

INTRODUCTION

Yearly structural analysis applications of finite element modeling in the United States incur over one billion dollars of computer expense. Thus, since run time for any particular large problem can be changed by a factor of two to five depending on the analysis strategy, considerable care is justified in selecting a near-optimum implementation approach.

There are two types of decisions which affect run time: problem model and the solution implementation decisions. Decisions bearing on the problem model (number and type of finite element modes, number and allocation of nodal points and nodal lines) determine analysis accuracy and can have an important impact on analysis cost (ref. 1-4).

The focus of this paper, however, is the implementation decisions. Thus, the decisions of interest here are which computer code, computer hardware configuration, primary storage allocations, and data management plan should be used for a given structural analysis problem.

The usual approach to making these decisions is to base them on data collected on benchmark problems. Then run times for the problem of interest are extrapolated from small problem tests or calculation counts for equation solving.

The authors' experiments indicate that neither of these approaches leads to accurate resource assessments - probably because neither reflects the variety of influential data management strategies or accommodates large changes of the structural model or nonlinear analysis complications. Accordingly, the SCOPE code was developed.

This paper describes the capabilities and basis for estimating SCOPE computer resource needs. It reports on calibration and test of SCOPE on an existing structure using the Amdahl computer.

The authors acknowledge the financial support of Duke University and the Jet Propulsion Laboratory for the developments herein.

## SCOPE CHARACTERISTICS

### SCOPE Output

Table 1 lists output produced by a SCOPE run. In general, this output completely particularizes the structural geometry, loading and boundary conditions, and the computer hardware and software. As a result of an emulation of the analysis, it produces partitioned data in the computer time needed for calculations and data management.

Reference 5 provides an illustration of SCOPE output.

### SCOPE Capabilities

Table 2 defines the abilities of the emulator to represent structural finite element analyses. The capabilities encompass the vast majority of production finite element analyses. Studies suggest that with minor modifications SCOPE can be extended to parallel processors (ref. 6).

## SCOPE OPERATION

SCOPE operates interactively on a microprocessor. It consists of about 6000 BASIC instructions organized into 23 subprograms. Because subprograms are chained, only 32K bytes of storage are required for execution.



SCOPE execution is divided into three phases. In phase 1, file data defining the structural model is created and assessed. This phase provides for accumulating a number of structural files before performing an emulation. In phase 2, a "run file" is created and assessed. This file contains all the computer implementation parameters for an emulation. In phase 3, the emulation is performed.

Reference 7 documents subprogram functions and data interfaces in more detail.

## EMULATOR MODELS

This section describes SCOPE's models of the computer, generation of equation coefficients, equation solution, and stress-recovery.

### Computer Model

SCOPE models the computer as a machine capable of performing micro-operations. These include integer arithmetic, floating point arithmetic, and fetch and store in primary and secondary memory. Finite element operations are synthesized from the number of micro-operations required for their implementation. Micro-operations are converted to machine cycles based on hardware capabilities. Sums of machine cycles are converted to run requirements using the cost algorithm of the computer installation of interest.

### Generation of Equation Coefficients

Finite element matrices are assumed to be generated by performing sparse matrix arithmetic. Thus, multiplications by zero in obtaining stress-displacement and local coordinate stiffness matrices are ignored. Similarly calculations for transforming to global coordinates are ignored.

### Equation Solving

The SCOPE code finds the optimal solution stratagem, with respect to substructuring, by using the actual data about the computer resources and the problem, and interacting with its user iteratively.

In any one iterative step, the user of the SCOPE code inputs the size data as follows: the maximum size of a substructure stiffness matrix and size of the primary memory which should accommodate, at least, all the data needed for structuring. The data needed for substructuring includes data obtained from the problem file: the maximum size of an elemental stiffness matrix and the size of the constraint data. With these, SCOPE determines the stratagem which is the most cost effective for a nonlinear analysis step (ref. 8) and outputs the details of this stratagem. Included in the output also are the

primary memory size used,  
secondary memory size used,  
number of unformatted reads,  
number of unformatted writes,  
total number of words read,  
total number of words written,  
primary memory occupancy time, and  
central processing unit usage time

for a nonlinear analysis step with one or more substeps.

Following the output, the SCOPE code provides an opportunity to alter the size data for a new stratagem. Thus the user may try various size data in an interactive mode to find the optimum stratagem for the problem and the computer resources at hand.

Given a consistent set of size data, SCOPE first tries the standard stratagem which assumes the following:

1. Nodal data is N logical records [N is the total number of nodes, and the nodal data for a node consists of the nodal coordinates (updated, and slopes and curvatures are included, if necessary), current nodal deflections (and as many of its spatial derivatives as necessary), and nodal loads].
2. Elemental data is M logical records [M is the total number of elements, and the elemental data of an element consists of the node labels of its vertices, geometric data (such as thicknesses, cross-sectional area, area moments), and, for each Gaussian point, the current stress tensor, the current strain tensor, the current strain rate tensor, and the current material data].
3. Constraint data is 1 logical record (data defining supports, symmetries, etc.).
4. Elemental stiffness matrices are generated as M logical records (each contains not only the stiffness due to material but also stiffness due to initial stresses, and other pertinent information).
5. Elemental load vectors are generated as M logical records (each contains the free-free load vectors, and other pertinent information).
6. Substructure stiffness matrices are generated as  $n_s$  number of logical records ( $n_s$  is the total number of substructures; both  $n_s$  and substructure definition data are automatically computed by the SCOPE code, using the size data, labels of element vertices, and connectivity due to constraints as described in reference 6).
7. Substructure load vectors are generated as  $n_s$  logical records.

8. Triangular factor matrix partitions are generated as  $n_s$  logical records during Cholesky factorization.
9. Substructure forward-pass results are generated as  $n_s$  logical records.
10. Substructure backward-pass results are generated as  $n_s$  logical records.
11. Elemental residual force vectors are generated as  $n_s$  logical records.
12. All logical records are on disk files, and at a given time, not more than one logical record from the 11 different types listed above can stay in the primary memory (excluding the first type).

A logical record is a data unit which requires one access time (assumed constant), and one transfer time (assumed proportional to the record length) for its transfer between primary and secondary storages. In the standard stratagem, the logical records are generated one at a time (save type 1). For example, a substructure stiffness matrix is generated by bringing from the secondary storage one elemental matrix at a time, keeping the constraint data continuously in the primary storage. If there is space in the primary memory, the SCOPE code tries other stratagems, called fitted stratagems. The fitted stratagems are created by trying the feasibility of

- .keeping all nodal data as 1 logical record,
- .keeping all elemental data as 1 logical record and
- .computing residual force vector norms directly without substructures.

The output tables contain data for both the standard stratagem, and the fitted stratagem.

### Stress-Recovery Model

The primary task in the SCOPE stress recovery link is to estimate the computer resources required during computation of the stress components at one or more Gaussian integration points within each element, the equivalent element stress resultants at the nodes, and the Euclidian norm of the nodal unbalanced forces.

The total Lagrangian formulation for large deformation is implied, wherein all quantities such as deformations, strains, and stresses, as well as their increments, are associated with the current configuration relative to the original undeformed state.

Given the results of the equation solution phase at the current configuration, the computational resources associated with the following basic steps are simulated during the stress recovery:

1. From the full set of incremental deformation, extract a subset pertaining to the element in question by making use of the element connectivity data.
2. Transform the incremental deformation from the global coordinates to the element local coordinates.
3. For each Gaussian integration point in the element,
  - a. Generate the strain-displacement matrices of the zero and first order if these were not saved during the element generation link. The latter involves the current deformation state.
  - b. The incremental strains are computed.
  - c. Compute the total Green-Lagrange strains.
  - d. Generate the elastic stress-strain material matrix from input material property data, if not already saved from the element generation link.
  - e. Compute each component of second Piola-Kirchhoff stress and its increment.
  - f. If the material nonlinearity option is selected, the current stress state is checked against yielding. If yielding has occurred, compute the incremental plastic strains, the elastic-plastic material matrix, the corrected second Piola-Kirchhoff stresses and its increment.
  - g. If updating the stiffness matrix is desired for the next loading increment, compute the tangent material matrix from the current incremental stresses and strains.
  - h. If the stresses are requested for output for the current configuration, the Cauchy stress tensor is computed for this configuration.
4. Using consistent lumping of the stresses at the element nodes, the stress resultants are computed in the element local coordinates.
5. Transform the stress resultants from the local element coordinates to the global coordinates to obtain the global equivalent stress resultants.

6. Again, using the element connectivity data, expand the subset of nodal stress resultants to the full set and form the residual unbalanced forces.

In Step 3-f, only one material nonlinearity model is included in the program. This material model employs von Mises yield condition, and assumes the classical isotropic hardening which includes elastic perfectly plastic conditions. It is further assumed that all elastic-plastic material relations used above along with the second Piola-Kirchhoff stresses and the Green-Lagrange strains are valid extensions of the usual infinitesimal strains and engineering stress relations associated with the small deformation theory.

### SCOPE CALIBRATION AND TEST

SCOPE has been calibrated for the Amdahl computer and the ELAS code (ref. 9). Tests on a bridge analysis suggest some analysis policies for small problems. This section describes these developments (ref. 7).

#### Calibration

The SCOPE code has been calibrated on two levels: the micro-operation and the finite element analysis phase levels.

For the micro-operations level, pairs of tests of each operation were performed on the Amdahl computer to deduce the number of machine cycles per operation.

Results of these tests are summarized in Table 3. These data show large factors of up to three between machine specifications and measured calculation times. Average times were developed, based on multiple experiments, because computer times varied  $\pm 50$  percent from the average depending on the computer load.

For the phase level, CPU and PPU factors were determined for each finite element phase (generation, equation solution, stress recovery) to scale the SCOPE results to the ELAS code phase results. By changing the problem from a truss analysis to a frame analysis, a check on the validity of the phase calibration was developed.

Tables 4 and 5 show results of these tests. These data suggest high fidelity in PPU and CPU calibration. The total error in PPU is less than four percent - all phases showing small errors. The total CPU error is about 17 percent - with big variations between phases. In view of the  $\pm 50\%$  range in CPU tests, these results are very good.

#### Tests

Phase and strategy tests were based on the bridge structure of figure 1 (ref. 10). This steel bridge spans the Mississippi river at Memphis.

Quarter- and half-span models of the bridge were represented for SCOPE analyses. The quarter-span model involves 68 nodes, 120 elements, and about 200 degrees of freedom. The half-span involves about twice as many nodes, elements, and degrees of freedom (ref. 11).

Linear and nonlinear SCOPE emulations were executed. For each analysis, the primary memory allocation was established to minimize computer run costs for various numbers of substructures.

Table 5 provides a sampling of results.

These and similar data suggest the following:

1. The benefit of optimum substructuring for small problems (less than 500 D.O.F.) does not justify their emulation.
2. The SCOPE code reflects the advantage of avoiding substructuring when the problem is small and substructuring for larger problems to balance total primary memory costs.
3. Considering 15 load steps and averaging three iteration substeps to simulate nonlinear material effects increased computer time to about 16 times that of a linear analysis suggesting the desirability of minimizing load steps and the small penalty of substep iterations.

#### SUMMARY AND CONCLUSIONS

These pages describe the characteristics and models of SCOPE, a finite element analysis emulator. They present an approach to calibration to a particular computer and finite element analysis code. They describe results of emulating small problems.

Development, calibration, and use of SCOPE lead to the following conclusions:

1. SCOPE'S accuracy in predicting CPU and PPU time depends intrinsically on the accuracy of calibration data developed using a particular computer and finite element code. (SCOPE tests on an Amdahl and ELAS basis indicate negligible PPU error, but CPU errors of about 18 percent.)
2. Calibration requires actual tests of the hardware - the manufacturer's performance specifications were not sufficient. (SCOPE tests indicated that actual performance of micro-operators took as much as three times the manufacturer's times.)
3. For small problems (less than 500 degrees of freedom, 500 elements) substructuring is undesirable because

idle core storage prevents optimum use of memory.

4. For small problems, the penalty for nonlinear analysis is nearly proportional to the number of load steps.

The SCOPE code fidelity is established for small problems.

# REFERENCES

1. Utku, Senol; Melosh, R. J., "Solution Errors in Finite Element Analysis," ASCE Vol. 1, State-of-the-Art of Computational Methods, edited by Pilkey, W. D.; Noor, A. K., fall 1982.
2. Melosh, R. J.; Utku, Senol, "Principles for Design of Finite Element Meshes," ASCE Vol. 1, State-of-the-Art of Computational Methods, edited by Pilkey, W. D.; Noor, A. K., fall 1982.
3. Melosh, R. J., "Finite Element Approximations in Transient Analysis," Cheng Kung/IAS symposium, Tainan, Taiwan, Dec. 1981.
4. Melosh, R. J., "Computer Solution of Crash Equations of Motion," Crashworthiness Workshop, Duke University, Nov. 1981.
5. Melosh, R. J.; Utku, S.; Salama, M. S.; Islam, M., "An Emulator of Finite Element Analysis," Proc. 12th Modeling and Simulation Conf., Vol. 12, Pittsburg, 1981, p. 697.
6. Utku, S.; Melosh, R. J.; Salama, M. S.; Islam, M., "On Nonlinear FEM Analysis in Parallel Processing," ASCE Annual Meeting, Hollywood, Florida, Oct., 1980 (also Computers and Structures, Vol. 15, pp. 39-47, 1982).
7. Islam, Humirul, "Simulation of Nonlinear Finite Element Analysis," Duke University Master's thesis, Dec., 1981.
8. Kluttz, B. E.; Utku, S., "Best Partitions of a Structure in a Given Computing Environment," Computers and Structures, Vol. 7, 1977, pp. 35-43.
9. Utku, Senol, "ELLAS - A General Purpose Computer Program for the Equilibrium Problems of Linear Structures," Vol. 11, Documentation of the Program, Jet Propulsion Laboratory, Pasadena, 1969.
10. Modjeski and Masters, "Memphis and Arkansas Highway Bridge," final report to Arkansas Highway Commission and Dept. of Highways and Public Works, Tennessee, Dec. 1950.
11. Robert, Catherine, "Finite Element Modeling of the Memphis and Arkansas Highway Bridge," Master's thesis, Duke University, Dec. 1981.



Table 1  
SCOPE OUTPUT

<u>Data Type</u>	<u>Tabular Printouts</u>
Structural Configuration	<ul style="list-style-type: none"> <li>• Finite element type data</li> <li>• Element connectivity data</li> <li>• Linear constraints data</li> </ul>
Structural Behavior Characteristics	<ul style="list-style-type: none"> <li>• Characteristics of structural equations</li> <li>• Characteristics of structural materials</li> <li>• Characteristics of loadings</li> </ul>
Computer Configurations	<ul style="list-style-type: none"> <li>• Micro operation timing</li> <li>• Secondary storage timing</li> <li>• Arithmetic/storage relative costs</li> </ul>
Computer Storage Plan	<ul style="list-style-type: none"> <li>• Total primary storage available</li> <li>• Words reserved for program logic</li> <li>• Words reserved for substructure data</li> </ul>
Solution Strategy	<ul style="list-style-type: none"> <li>• Generate/assembly mode</li> <li>• Stress recovery mode</li> <li>• Data to be plotted</li> <li>• Data to be printed</li> </ul>
Required Computer Resources	<ul style="list-style-type: none"> <li>• Micro-operation counts for each F.E.A. step</li> <li>• Storage requirements for each F.E.A. step</li> <li>• Computer costs for each and all F.E.A. steps</li> </ul>

Table 2

SCOPE CAPABILITIES

<u>Capability Class</u>	<u>Specifications</u>
Structural Configuration	<ul style="list-style-type: none"> <li>• Up to 1200 nodes; 14,000 degrees of freedom</li> <li>• Rod, beam, membrane, plate, shell and globe elements</li> <li>• Analytical, reduced integration, complete integration, over-integration elements</li> <li>• Up to 64 nodes/element</li> <li>• Any number of element types/model</li> <li>• Isotropic, orthotropic, and anisotropic materials</li> <li>• One, two or three dimensional geometry</li> <li>• Any number of linear constraints; up to six nodes per constraint</li> <li>• Element and nodal loads</li> </ul>
Structural Behavior Characteristics	<ul style="list-style-type: none"> <li>• Linear or nonlinear material</li> <li>• Linear or nonlinear geometry changes</li> <li>• Temperature varying or isothermal</li> <li>• Static, rate, or acceleration dependent</li> </ul>
Computer Configuration	<ul style="list-style-type: none"> <li>• Uniprocessor</li> <li>• Random and/or sequential secondary storage</li> <li>• Serial execution of micro-operations (add, subtract,...)</li> <li>• Off line, printing and plotting</li> <li>• Any fixed number of words of primary memory</li> <li>• Unlimited secondary memory</li> <li>• In-core or chained finite element code</li> </ul>

Table 3

TIMING FOR MICRO-OPERATIONS ON THE  
AMDAHL 470 V/8 COMPUTER

MACHINE CYCLE TIME = 26 nano-seconds

ITEM	MICRO-OPERATION	MANUFACTURER'S TIMING IN NANO-SECS	AVERAGE TIMING IN NANO-SECS	NUMBER OF COMPUTER CYCLES
1.	INTEGER ADD OR SUB	32	47	1.81
2.	INTEGER MULTIPLY	112	165	6.35
3.	INTEGER DIVISION	812	752	28.92
4.	INTEGER FETCH	32	100	3.85
5.	INTEGER STORE	32	100	3.85
6.	COMPARE	244	760	29.23
7.	FLOATING POINT ADD OR SUB.	96	168	6.46
8.	FLOATING POINT MULTIPLY	132	336	12.92
9.	FLOATING POINT DIVISION	440	685	26.35
10.	FLOATING POINT FETCH	---	100	3.85
11.	FLOATING POINT STORE	---	100	3.85
12.	SIN FUNCTION	---	5620	216.15
13.	COS FUNCTION	---	5650	217.31
14.	TAN FUNCTION	---	7360	283.08
15.	SQUARE-ROOT FUNCTION	---	6470	248.85
16.	DISK ACCESS	25,000,000	---	961,538.46
17.	DISK WORD TRANSFER	3340	---	128.46

Table 4

COMPUTER RESOURCE NEEDS FOR ONE-FOURTH  
SPAN BRIDGE ANALYSIS

NUMBER OF SUBSTRUCTURE	PRIMARY MEMORY SIZE (in kilowords)	PRIMARY MEMORY USE TIME (in megacycles)	ANALYSIS COST (in megacycles)
1	35.00	1210	1350
1	25.00	1210	1310
1	22.10	1210	1300
1	10.22	1210	1250
2	8.22	1220	1260
3	7.52	1230	1270
6	7.02	1270	1300
9	6.75	1300	1333

Table 5

COMPUTER RESOURCE NEEDS FOR ONE-HALF  
SPAN BRIDGE ANALYSIS

NUMBER OF SUB- STRUCTURE	PRIMARY MEMORY SIZE (in Kilo- words)	PRIMARY MEM. USE TIME (in mega- cycles)	LINEAR ANALYSIS COST (in megacycles)	NONLINEAR ANALYSIS COST (in megacycles)	NON- LINEAR COST FACTOR
1	14.32	2350	2460	38500	15.7
2	10.32	2360	2440	38200	15.7
3	10.22	2370	2450	38400	15.7



Figure 1.- Memphis Arkansas Bridge - foreground.

## THE FINITE ELEMENT MACHINE: An Experiment in Parallel Processing

O. O. Storaasli and S. W. Peebles  
NASA Langley Research Center  
Hampton, Virginia

T. W. Crockett and J. D. Knott  
Kentron Technical Center  
Hampton, Virginia

L. Adams  
University of Virginia  
Charlottesville, Virginia

### SUMMARY

The Finite Element Machine at the NASA Langley Research Center is a prototype computer designed to support parallel solutions to structural analysis problems. This paper describes the hardware architecture and support software for the machine, initial solution algorithms and test applications, preliminary results, and directions for future work.

### INTRODUCTION

A large class of structural analysis problems is solved by computer using finite element and finite difference approximation techniques. Although these problems have traditionally been solved on conventional sequential computers, an analysis of these methods shows that they contain many calculations which could be performed simultaneously, thereby reducing the time required for a solution (ref. 1). To support this concurrency, special computers are needed which can perform many operations in parallel. One option is to construct vector computers which operate on large arrays of data, but this approach is only effective when the data can be structured appropriately. A different approach is to construct a machine which consists of a large number of general-purpose processing elements coupled together in a parallel architecture. Advances in microcomputer technology during the last decade have reduced the size and cost of computing elements, making construction of this type of parallel processor increasingly practical. Such processors are being actively investigated for their potential uses. Examples include CM\* and C.mmp at Carnegie-Mellon University (ref. 2), ZMOB at the University of Maryland (ref. 3), and the New York University Ultracomputer (ref. 4).

Work is currently underway at NASA Langley Research Center to investigate solutions of structural analysis problems using parallel microprocessor

systems. Research topics include hardware configurations, software design, problem partitioning, and numerical algorithms. As part of this effort, a prototype parallel processor designated the Finite Element Machine (FEM) is being built and evaluated. This paper describes the Finite Element Machine, its support software, current applications and algorithms, and preliminary results.

## FEM DESCRIPTION

To support parallel processing, an appropriate combination of hardware features and system software is needed. This section first outlines the FEM hardware organization, and then describes two packages of system software developed to provide control and run-time support.

### Hardware Architecture

The architecture of the Finite Element Machine was specifically designed to support a parallel decomposition of structural problems by assigning nodes in the structural model to processors in the machine (refs. 1, 5, and 6). This approach is illustrated in figure 1 with an idealized wing model. The calculations to be performed at nodes in the model are mapped onto the array of microprocessors. The lines drawn between microprocessors indicate dependencies between nodes which lie on the same finite element, but have been mapped into different processors. Because of these dependencies, data transfer is required between these processors. The number of structural nodes is not limited to the number of processors, since multiple nodes may be assigned to a single processor (see, for example, ref. 7). The mapping of nodes onto processors is discussed in more detail in later sections.

The Finite Element Machine is a multiple-instruction multiple-data (MIMD) parallel processor consisting of an asynchronous array of interconnected microcomputers (the Array) linked to a minicomputer front end (the Controller). A block diagram of the architecture is shown in figure 2. Unlike many multiprocessor designs which use large shared memories, the FEM architecture provides each processor with its own local memory, and no sharing is possible. Instead, special communication hardware (described below) allows the processors to communicate with each other. The current prototype machine (figure 3) is being built in stages of 4, 16, and 36 processors. In principle, however, the architecture could be expanded to accommodate large numbers of processors (perhaps hundreds or thousands). At this writing, a four-processor Array is operational and the hardware for the 16- and 36-processor stages is nearly complete.

All processors in the Array are identical and consist of a 16-bit microprocessor, an attached floating-point unit, 32K bytes of random access memory (RAM), and 16K bytes of read-only memory (ROM). Serial I/O ports called "local links" provide data communication paths between a processor and up to twelve of its neighbors. The local links are reconfigurable and can support a variety of interconnection topologies. A time-multiplexed parallel "global

bus" connects all processors to each other and to the controller, and provides a general-purpose secondary communications path. A network of binary flags spans the Array and is used for processor synchronization and other signaling needs. A distributed "sum/maximum" network computes the sum and maximum of the inputs from all of the processors. This can be used for global calculations (ref. 8), cooperative sorting, and processor sequencing. For more details on the Array hardware, see reference 9.

The Controller is a small minicomputer which initiates and monitors activity on the Array and provides mass storage for programs and data on attached peripherals. It also hosts the user interface to the system, including interactive graphics.

### Controller Support Software

The Controller provides the user with program development tools and the ability to define problems, activate and monitor the Array, and obtain and process results. The Controller runs a general-purpose disk-based operating system accessed by a menu-driven command interpreter. Commands on the Controller are implemented as control language procedures. All FEM commands are constructed in this manner. This approach presents the user with a consistent interface which is a natural extension of the Controller operating system. The system software provided on the Controller can be divided into four functional areas of support: program development, problem description, program execution on the Array, and post-processing or analysis.

Program development on the Controller is supported primarily by the vendor's standard software. A screen editor, an assembler, a reverse assembler, a Pascal compiler, and a link editor are available. Parallel application programs for the Array are written in Pascal; support for the FEM architecture is provided by a library of special routines. Users ordinarily select a program from a package of solution algorithms available for general use. Should a user prefer to write his own solution code or require special post-processing of data, he has access to all the necessary tools on the Controller.

Before executing the parallel solution program, the user must model his problem and provide data in accordance with the protocols of the intended solution algorithm. An interactive graphics interface allows the user to model structures and generate nodal coordinates, element connectivity, material properties, and constraints. As an alternative, the user may choose to create or modify data files using the text editor or his own utility program.

Normally, the program execution environment is established by entering a single Controller command. One command can be structured to call all necessary sub-commands via the command interpreter. Typically, the execution session involves Array initialization, selection of the Array configuration desired, downloading the selected algorithm and any necessary data, and entering an interactive execute mode. During program execution on the Array, all messages from a preselected reference processor and errors from all



processors are displayed on the user's CRT. Processors can send messages, make interactive queries, and report error conditions at any time during the execute sequence.

Three files are maintained for the user during execution on FEM. A "FEMDATA" file records all data transferred to the Controller, formatted in accordance with its type, and identified by source processor number. A "FEMLOG" file is used to record events over the course of an entire FEM session. This file is initialized when the Array is reset, and thereafter records each command invocation along with its associated data. For example, the command to download a program writes entry and exit messages, the name of the file downloaded, status information, and the load and entry addresses of the object code for each of the affected processors. The FEMLOG also records the source and error number for all errors as they occur. This process provides the user with a session record for later reference or analysis. A "FEMERROR" file is initialized at the beginning of each command. This file is used to record errors detected within the scope of a single command. It contains the error number, severity, source, processor status information, and an expanded error message for each error detected. If an error is detected during execution of any command, the FEMERROR file is displayed upon exit.

Additional user support is provided in the form of interactive debug commands. Debugging commands allow the user to dump memory and set breakpoints, to single step, halt, kill, and resume tasks, and to inspect and change status, registers, and memory. In addition, the Array keeps execution statistics and can be directed to trace execution and check in with the Controller at regular intervals to maintain confidence during long computations.

Software support on the Controller for post-processing and analysis of data consists of a set of utility programs. Commands are provided to sort the data file to provide a listing of communications by processor, analyze the trace information to determine where each processor spent its time during execution, and upload and format the results of computations on the Array. In addition, information such as nodal displacements can be displayed in graphic form (see figure 4).

#### System Software for the Array

System software for the array of microprocessors consists of an operating system, a subroutine library, and a set of diagnostics. The relationships of these components to each other and to the applications software are shown in figure 5. Although diagnostics are vitally important for the validation and maintenance of a computer system, they are beyond the scope of this paper.

A complete copy of the operating system, called Nodal Exec, is stored in ROM on each of the microcomputers in the Array. Nodal Exec is divided into two major sections, a nucleus and a package of command routines. The nucleus (the innermost portion of the operating system) provides such functions as interrupt handling, basic I/O, timing, memory allocation, task management, and a command monitor.

Command routines are used to implement all functions which the Controller may direct the microcomputers to perform. Such functions include downloading object code and data, establishing processor connectivity, executing programs, and uploading results. Several debug commands are also available to read and modify memory locations, inspect registers, set breakpoints, and step through instruction execution. The philosophy of Nodal Exec is to provide sufficient functionality with a set of relatively simple commands so that the Controller software can combine them into a sophisticated user interface.

A library of Pascal-callable subroutines, PASLIB, provides support facilities for application programs. The PASLIB routines are essentially an extension to Nodal Exec, serving as high-level supervisor calls or, in some cases, interfacing directly to hardware functions. They allow user programs to communicate with other processors and with the Controller, to use the flag and sum/max networks, to access data areas, and to perform arithmetic using the floating-point processor. Frequently used mathematical subroutines (e.g., vector dot product) are also available which use the stack architecture of the floating-point unit to optimize performance. The most commonly used PASLIB routines are stored in ROM on the processors. The remaining routines reside in a library file on the Controller where they can be linked to user programs and downloaded with the object code.

Nodal Exec and PASLIB support three major concepts which are important in understanding the flow of data on FEM: data areas, connectivity, and inter-processor communication. Explanations of each of these concepts are presented in the subsequent paragraphs.

Data areas are the primary mechanism for transferring data between the Controller and the application programs running on the processors in the Array. Data areas required by an application are allocated in each processor's memory prior to program execution. They contain space for a specified number of data items of a particular type. Allowable data types are integer, long integer, real, double precision, or user-defined records. Once allocated, a data area can be filled with data from the Controller, initialized to some value, or left empty. Application programs reference data areas via pointer variables. Data areas can provide input to the program, receive output, or both. Since data areas exist independently of the programs which access them, they can be used to pass information between separate programs which execute in a series. When a program (or series of programs) is finished, results stored in data areas are uploaded to the Controller for file storage or post-processing.

Connectivity is the concept of establishing communication paths between programs executing on different processors. Connectivity may be viewed at two levels, the logical problem level and the physical processor level. Logical connectivity refers to the interconnections between nodes in a structure by virtue of the fact that the nodes lie on the same finite element. Physical connectivity refers to the physical I/O interconnections between processors. For simple or regular structures, mapping the logical interconnection pattern onto the planar mesh of physical processors may be straightforward. In general, however, the mapping problem is difficult and the local neighbor

connections are insufficient; therefore, the global bus must be used. Bokhari has addressed this problem and developed an algorithm which attempts to maximize the use of the local links (ref. 10). This algorithm is implemented on the Controller by an auxiliary program whose output is the logical-to-physical mapping of node numbers to processor numbers.

Interprocessor communication takes place via the local and global I/O paths which were enabled during the connectivity process. Communication is based on the transmission of records which contain from one to 255 data words. An associated tag word in the record header is used to distinguish the information content when multiple records are sent to the same processor. Interprocessor communication is handled either synchronously or asynchronously by the system software. If synchronous mode is used, input from a neighboring processor is queued in the order in which it is received, and it must all be read and processed by the receiver. In the asynchronous case, only the most recently received record (for each different tag) is saved. An algorithm which uses this asynchronous or "chaotic" communication technique is discussed in the next section.

#### CURRENT ALGORITHMS AND APPLICATIONS

To solve structural problems in parallel requires the development of algorithms to support parallel computations and a scheme to partition the structural model for distribution among the processors. The following section discusses the assignment of problems to the Array, and gives results from several applications run on the four-processor version of FEM.

##### Problem Partitioning

Factors that influence the design of an appropriate algorithm for solving problems on FEM include the structural region discretization, the number of processors available, and the amount of communication required between processors. The following example illustrates these considerations.

Figure 6a shows a cantilevered rectangular plate in plane stress constrained on one edge and loaded on the opposite edge. If the plate is discretized by linear triangular finite elements, a structural node is common to at most six elements, and is connected to at most six other nodes (see figure 6b). This is significant because it implies that in the system of equations for the vector of displacements,  $u$ , the stiffness matrix,  $K$ , is a sparse matrix containing at most 14 nonzero entries in each row:

$$K u = f \quad (1)$$

Twelve of these entries represent contributions of the six neighboring nodes (two per node) to the solution at a given node while two additional entries are contributions from the given node itself.

The sparsity of the stiffness matrix,  $K$ , suggests that an iterative algorithm could be used to solve equation (1) by assigning one processor to calculate displacements at each node in the plate. For maximum efficiency, an algorithm should be developed such that each processor would only need to communicate information to its six neighbors via the dedicated local links, as shown in figure 6c. This scheme is feasible only if the number of processors is not less than the number of structural nodes and if a suitable iterative algorithm can be found to take advantage of the connectivity shown in figure 6c. Furthermore, such an algorithm is efficient only if the overhead due to communication between processors is not prohibitive.

In most instances, the number of structural nodes exceeds the number of available processors. For these cases, it is necessary to assign multiple nodes to a processor and to develop algorithms to solve for the displacements at these nodes. Figures 6d and 6e show, respectively, how nodes of the plate can be assigned to a 4- or 16-processor Array. The local links that are used by the processors in figures 6d and 6e are illustrated in figures 6f and 6g.

Even though FEM was designed with finite element discretizations in mind, the architecture also supports the solution of problems that are discretized by finite difference techniques. Two such problems and their associated discretizations are given in figure 7. The five star discretization of the membrane equation is shown in figure 7a and the discretization for the plate equation is given in figure 7b. For a one node per processor assignment, the iterative solution of the membrane equations using the discretization of figure 7a requires four local links of each processor while the iterative solution of the plate equation using the discretization of figure 7b requires all twelve of the local links. In the case of multiple nodes per processor, the solution algorithm determines the proper assignment of nodes to processors. In the following, algorithms that have been run on FEM for both finite element and finite difference discretizations are discussed.

### FEM Applications

Solution algorithms for the first applications run on FEM used three standard iterative methods: Jacobi, conjugate gradient, and successive over-relaxation (SOR). These methods contain suitable parallelism and were used to solve sparse symmetric positive definite systems of linear structural equations resulting from finite element or finite difference discretizations.

Smith and Loendorf (ref. 11) solved a cantilevered wing box finite element model using the basic Jacobi iterative method. This small problem provided a useful benchmark for assessing a number of performance issues. Their results for one, two, and four processors show that the increased overhead for interprocessor communication largely offset the improvements gained by distributing the computation, thereby resulting in only modest reductions in the solution time. Their analysis suggests that there is a break-even point beyond which additional partitioning of a problem is ineffective. The results from this problem have also prompted a re-thinking of processor communication strategies and several modifications have been proposed to reduce overhead.

The same problem was also solved using an asynchronous Jacobi iterative method (see Baudet, ref. 12) in which each processor performs its calculations independently with no synchronization among processors. Intermediate results were passed between processors using the asynchronous communication mode discussed previously. The asynchronous Jacobi algorithm was run using two and four processors, and the results were inconclusive. In both cases, the asynchronous method required less time per iteration than the standard Jacobi technique, and the program converged to results which were similar to those of the standard Jacobi. However, the number of iterations required for convergence differed, with the two-processor case using about the same number as the standard Jacobi, and the four-processor case using more. The result was that for two processors, the asynchronous method slightly outperformed the standard Jacobi, but with four processors, the reverse was true. Further experimentation with modified communication procedures and other application problems is needed to better assess the asynchronous approach.

While the Jacobi iteration can be easily adapted as a parallel technique, it is not guaranteed to converge for general symmetric positive definite systems. The SOR method is guaranteed to converge for these systems, but is sequential in nature. To parallelize the successive overrelaxation method for FEM, the problem must be partitioned in such a way that the system is decoupled. A classical method of decoupling is the Red/Black ordering (ref. 13) for Laplace's equation. This procedure colors the discretization grid in a checkerboard fashion. Then an SOR sweep can be carried out by two Jacobi iterations, one on the equations corresponding to the red points, and one on the equations corresponding to the black points. This strategy does not work for higher order finite difference or finite element discretizations, however, because two colors are insufficient to decouple the system. Adams and Ortega (ref. 7) have developed a new iterative method that they call "Multi-Color" SOR which is a generalization of the Red/Black ordering. In Multi-Color SOR, an ordering is imposed on the sequence in which the displacements at the nodes are calculated, based on the number of colors required for decoupling. For example, if three colors (red, black, green) are used, the displacements for each color can be calculated by the processors in parallel. Each iteration of the algorithm first computes all red values, then all black values, and finally all green values. This scheme allows SOR to be implemented as a multiple sweep (one for each color) Jacobi-type method on FEM.

To test this method, Laplace's equation was solved on a square region discretized by quadratic triangular finite elements for which six colors are necessary and sufficient to color the discretization. This six-color SOR algorithm was programmed on a minicomputer to test its convergence properties and on the four-processor FEM to test its suitability for parallel implementation. A comparison showed that the problem converged with identical results on both machines.

A plane stress analysis of a plate was used to compare the Multi-Color SOR algorithm to the standard conjugate gradient method. The computer program for this procedure can be used to solve large plate problems by assigning three structural nodes to each processor or by assigning any multiple of three nodes to each processor if the number of processors is limited. The components of the program include the following:

1. Parallel assembly of stiffness matrix  $K$
2. Three-color SOR solution of  $K u = f$   
or alternatively,  
Conjugate gradient solution of  $K u = f$
3. Parallel stress calculation

The Array can be used to assemble, in parallel, the stiffness matrix from the problem data without any communication between processors. Linear triangular finite elements are used to discretize the plate so that three colors are necessary and sufficient to implement SOR (see ref. 7). The calculation of the stresses can also be done in parallel without any processor communication. A more detailed description of the matrix assembly and the stress calculation processes is given in reference 14.

A comparison of the performance of four processors to one processor on a plane stress problem with 60 degrees of freedom is given in table 1. These speedups reflect the execution times of both the solution algorithms and the underlying system software. The maximum theoretical speedup for a four-processor system is 4.00. The processor efficiency values given are a measure of the overhead required for synchronization and communication in the multi-processor case. Improved interprocessor communication times should increase the efficiency of these algorithms on FEM.

#### FUTURE DIRECTIONS

The solution of the plane stress analysis of a plate on FEM was felt to be a good starting place to address the issues of parallel matrix assembly, parallel displacement calculation, and parallel stress calculation. The experience gained by solving this problem provides a basis for the solution of more complex structural problems.

Although the initial applications of FEM have been based on iterative solution approaches, Gannon (ref. 15) has demonstrated that the architecture is sufficiently flexible to permit direct solution techniques. The study of such techniques on FEM is a major research area currently being investigated.

In conjunction with algorithm development, alternative processor interconnection strategies may also be investigated. To date, the local links have only been configured in an eight-nearest-neighbor planar mesh topology with toroidal wrap-around at the edges. This scheme leaves four of the links unused. Since the local links can be reconfigured by merely unplugging and rearranging the interconnecting cables, other topologies such as trees, rings, perfect shuffles (ref. 16), or cube-connected cycles (ref. 17) are possible. Because of the relatively large number of links per processor, it would even be possible to implement multiple interconnection patterns simultaneously (e.g., eight-neighbor mesh plus shuffle-exchange). The development of algorithms to make efficient use of alternate topologies is another topic for research.

The current FEM hardware is viewed as an experimental device rather than as a production machine. Data management considerations and an analysis of hardware and software performance are expected to point to changes in the architecture which could be incorporated in a second generation FEM. Such a machine would undoubtedly benefit from continuing advances in VLSI circuit technology which would improve performance and reduce the size and cost of components.

The potential range of FEM applications is not limited to structural analysis problems, although they provided the original motivation. By designing a parallel architecture thought to be suitable for finite element analysis, a flexible, reconfigurable machine has resulted which can emulate several distinct computer architectures. FEM could therefore be useful for parallel algorithms research in a number of disciplines.

#### CONCLUDING REMARKS

The Finite Element Machine is providing the impetus for development of new parallel techniques for the solution of structural analysis problems. Several of these techniques have been implemented and evaluated on the FEM hardware, thereby demonstrating that parallel solution of structural problems is a feasible approach. Initial results show that there can be a significant execution time advantage to be gained by using multiple cooperating processors. The degree of speedup is dependent on the number of processors, the algorithms used, and the extent to which the ratio of computation to inter-processor communication is maximized.

The work done so far has just begun to address the algorithms and applications suitable for investigation on FEM. Expansion of the machine to 16 and 36 processors will provide a research testbed for the exploration of many issues relating to parallel processing. It is hoped that the results of this research can be applied to future production computers which will benefit not only structural engineers, but other users as well.

#### REFERENCES

1. Loendorf, David D.: Advanced Computer Concepts for Engineering Analysis and Design. Ph.D. thesis (in progress), University of Michigan, Ann Arbor.
2. Jones, A. K.; and Schwarz, P.: Experience Using Multiprocessor Systems---A Status Report. Computing Surveys, Vol. 12, No. 2, June 1980, pp. 121-165.
3. Rieger, C.; Trigg, R.; and Bane, B.: ZMOB: A New Computing Engine for AI. University of Maryland, TR-1028, March 1981.
4. Gottlieb, Allan; et al.: The NYU Ultracomputer---Designing a MIMD, Shared-Memory Parallel Machine. Proceedings of the Ninth Annual Symposium on Computer Architecture, April 1982, pp. 27-42.



5. Jordan, Harry F.: A Special Purpose Architecture for Finite Element Analysis. Proceedings of the 1978 International Conference on Parallel Processing, August 1978, pp. 263-266.
6. Jordan, Harry F.; and Sawyer, Patricia L.: A Multi-Microprocessor System for Finite Element Structural Analysis. Trends in Computerized Structural Analysis and Synthesis, A. K. Noor and H. G. McComb, Jr., Editors, Pergamon Press, Oxford, 1978, pp. 21-29.
7. Adams, L.; and Ortega, J.: A Multi-Color SOR Method for Parallel Computation. Accepted for presentation at the 1982 International Conference on Parallel Processing, August 1982.
8. Jordan, Harry F.; Scalabrin, M.; and Calvert, W.: A Comparison of Three Types of Multiprocessor Algorithms. Proceedings of the 1979 International Conference on Parallel Processing, August 1979, pp. 231-238.
9. Jordan, Harry F., Ed.: The Finite Element Machine Programmer's Reference Manual. Computer Systems Design Group, University of Colorado, Boulder, 1979.
10. Bokhari, Shahid H.: On the Mapping Problem for the Finite Element Machine. Proceedings of the 1979 International Conference on Parallel Processing, August 1979, pp. 239-248.
11. Smith, Connie U.; and Loendorf, David D.: Performance Analysis of Software for an MIMD Computer. Report CS-1982-7, Department of Computer Science, Duke University, 1982.
12. Baudet, G.: Asynchronous Iterative Methods for Multiprocessors. Journal of the ACM, Vol. 25, April 1978.
13. Young, D.: Iterative Solution of Large Linear Systems, Academic Press, 1971.
14. Adams, L.: Iterative Algorithms for Parallel Computers. Ph.D. Dissertation (in progress), University of Virginia.
15. Gannon, Dennis: A Note on Pipelining a Mesh Connected Multiprocessor for Finite Element Problems by Nested Dissection. Proceedings of the 1980 International Conference on Parallel Processing, August 1980, pp. 197-204.
16. Stone, H. S.: Parallel Processing with the Perfect Shuffle. IEEE Transactions on Computers, Vol. C-20, No. 2, Feb. 1971, pp. 153-161.
17. Preparata, F. P.; and Vuillemin, J.: The Cube-Connected Cycles: A Versatile Network for Parallel Computation. Communications of the ACM, Vol. 4, No. 5, May 1981, pp. 300-309.



Table 1. Speedup Ratios for the Plane Stress Problem  
on Four Processors vs. One Processor

<u>Algorithm</u>	<u>Speedup</u>	<u>Processor Efficiency</u>
Stiffness Matrix Assembly	3.20	80%
3-Color SOR ( $K u = f$ )	2.84	71%
Conjugate Gradient ( $K u = f$ )	2.82	71%
Stress Calculation	4.00	100%

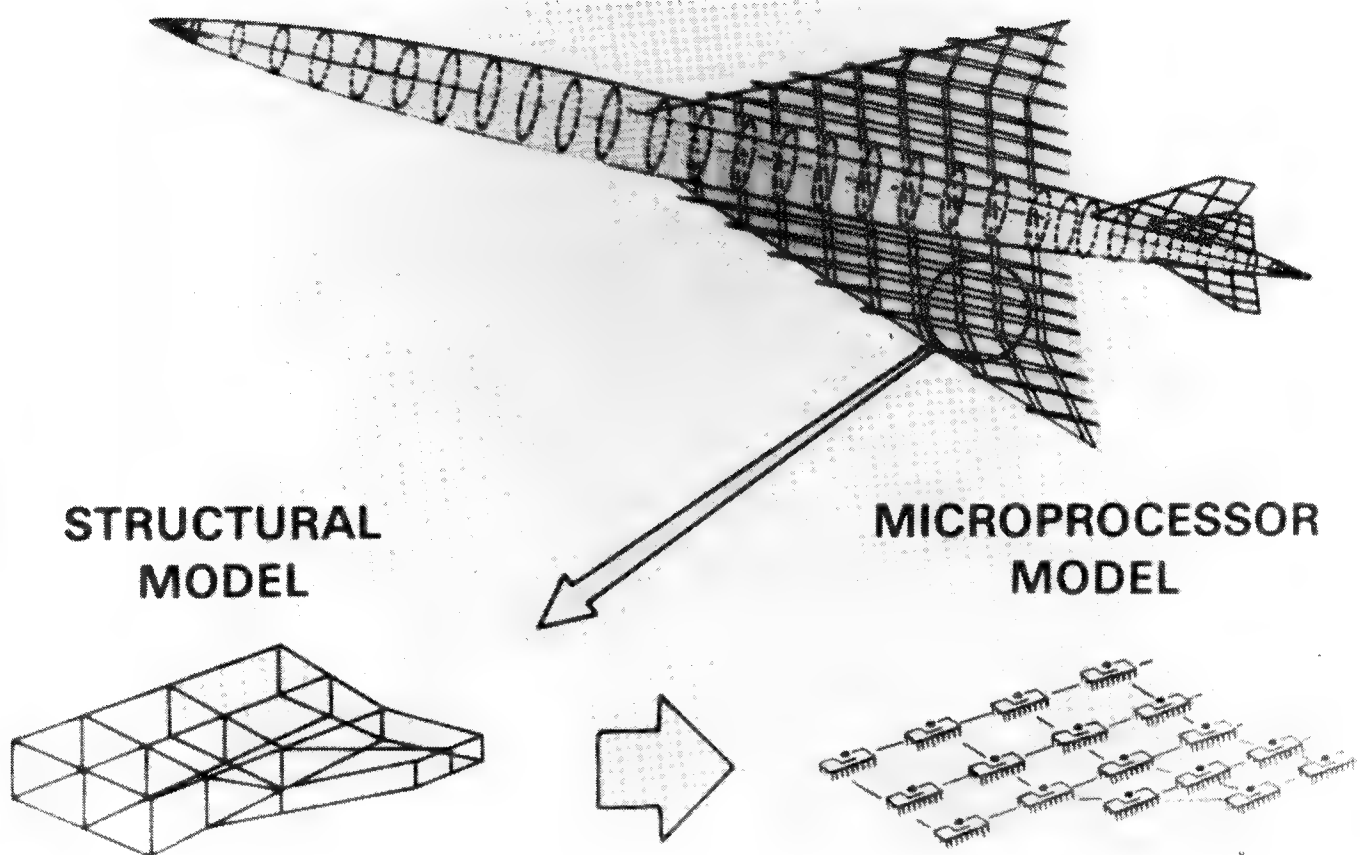


Figure 1.- A concept for parallel computation.

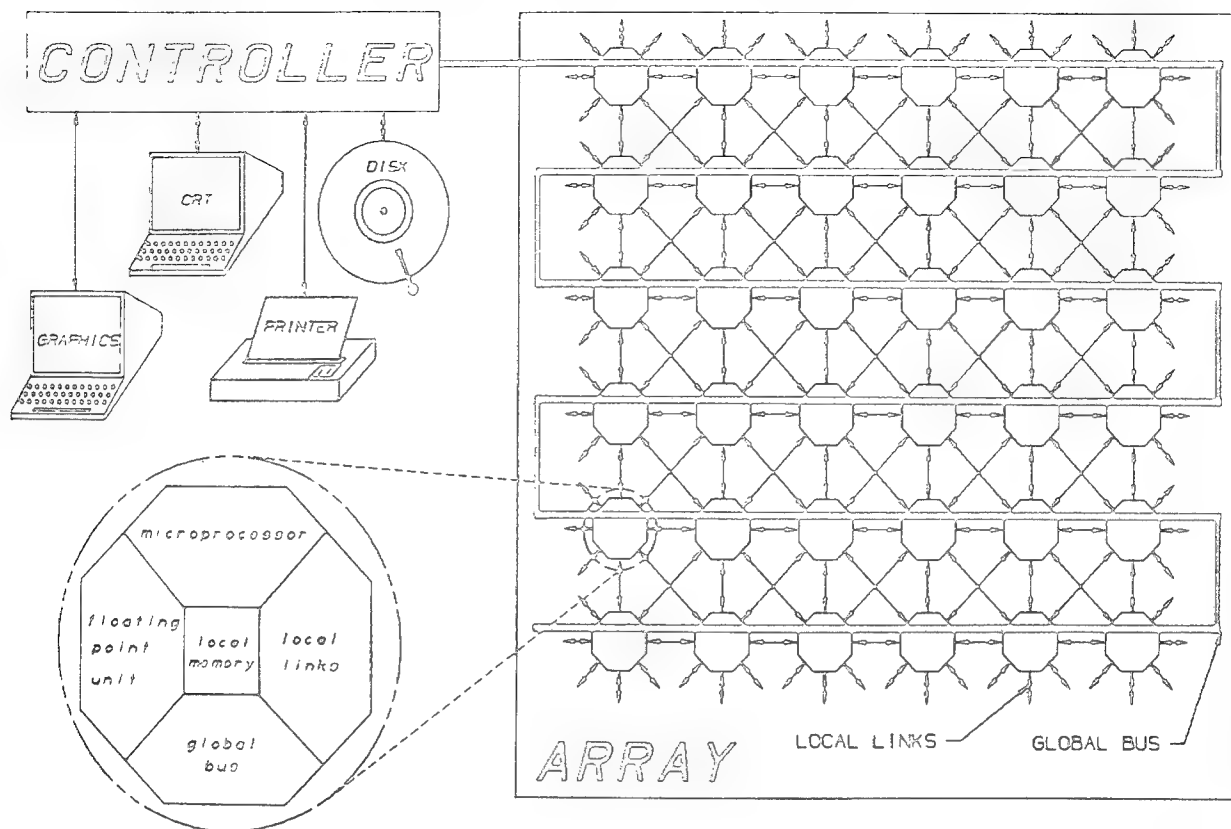


Figure 2.- Finite element machine block diagram.

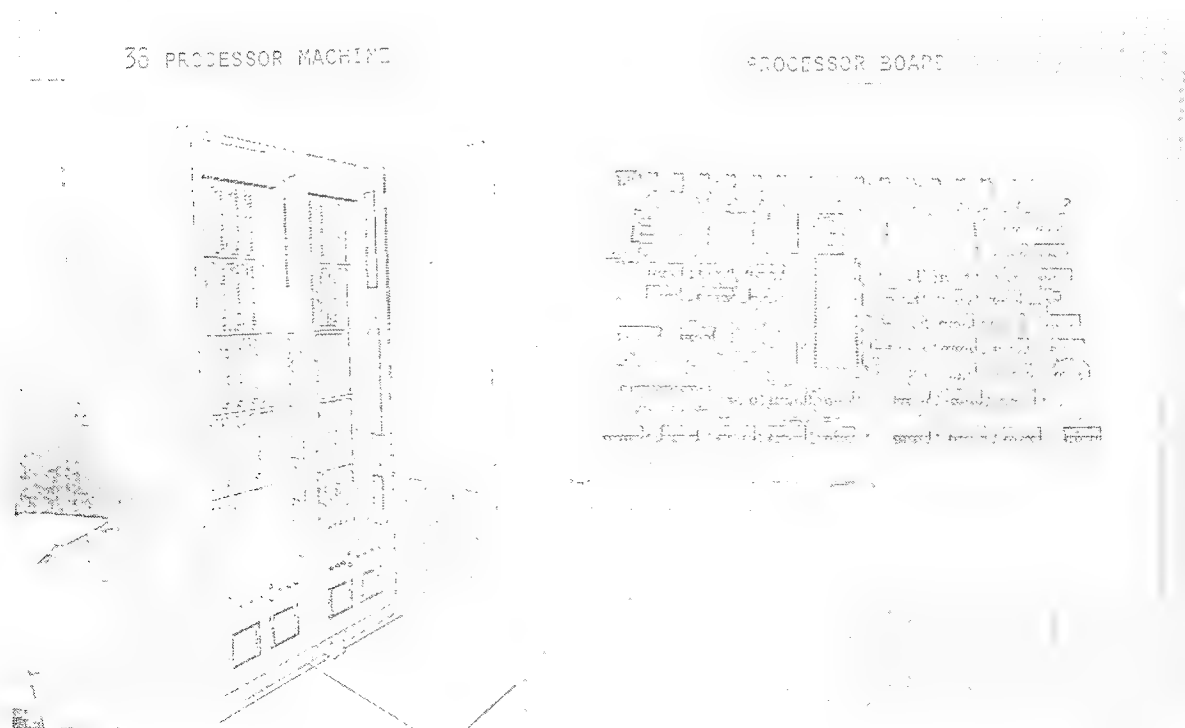


Figure 3.- Prototype finite element machine hardware.

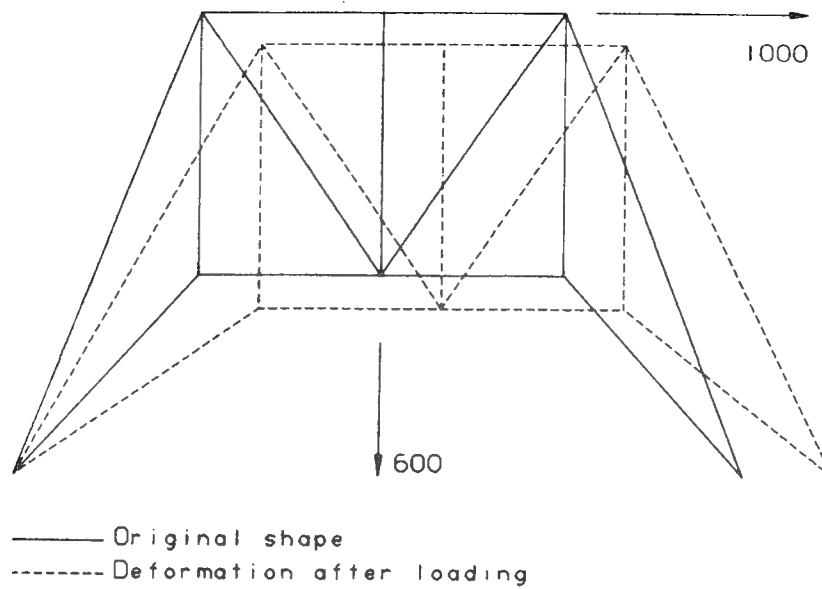


Figure 4.- Graphic display of nodal displacement.

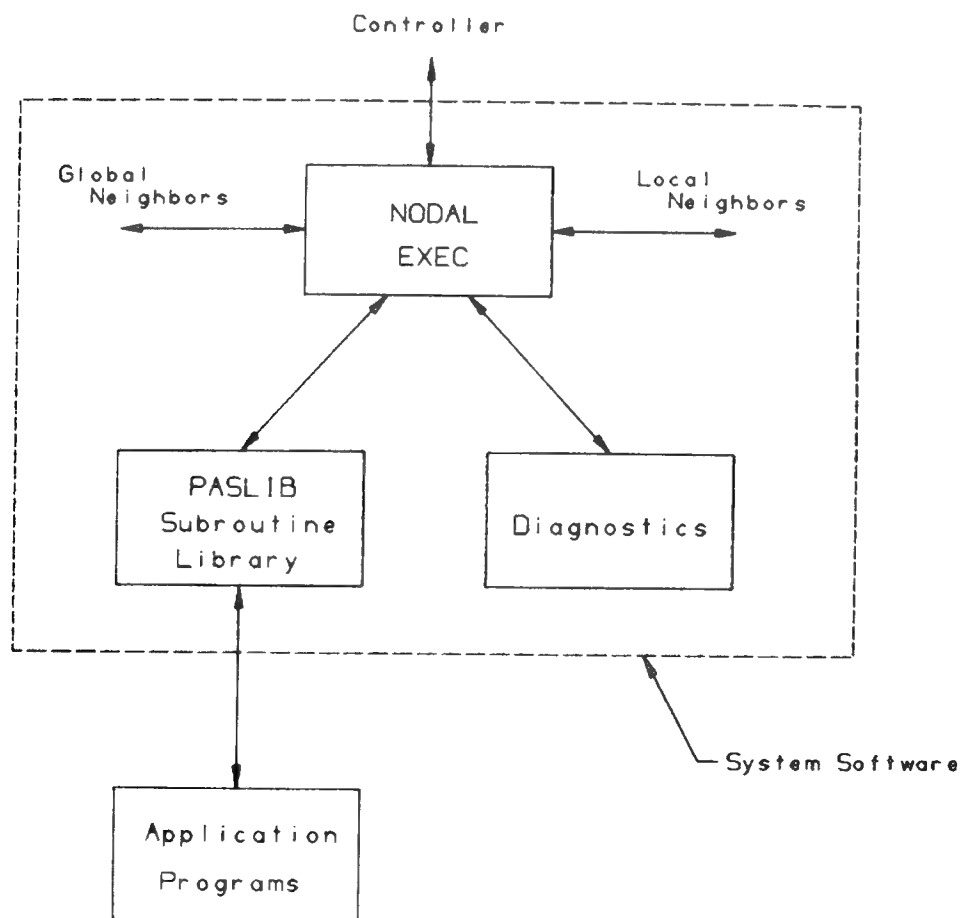
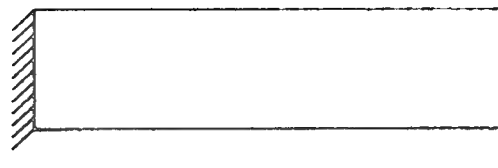
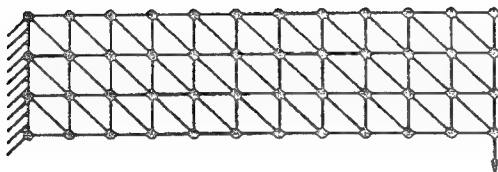


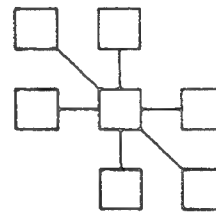
Figure 5.- Processor software configuration.



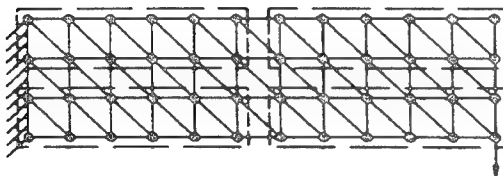
a). Plate under load.



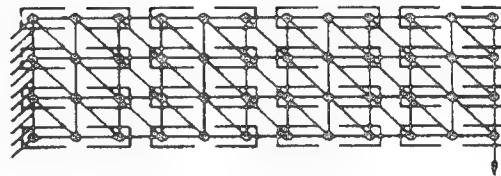
b). Finite element discretization.



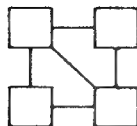
c). Six neighboring nodes.



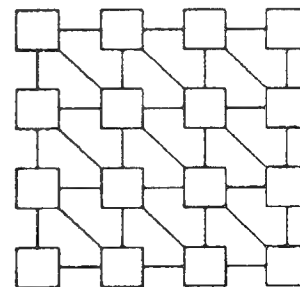
d). Four processor assignment.



e). Sixteen processor assignment

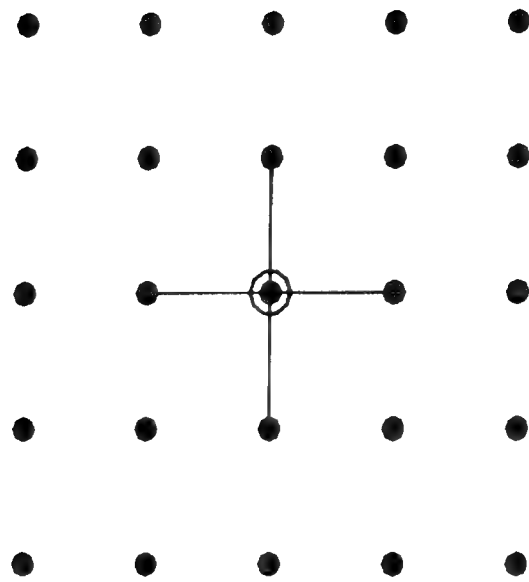


f). Connectivity for four processors.



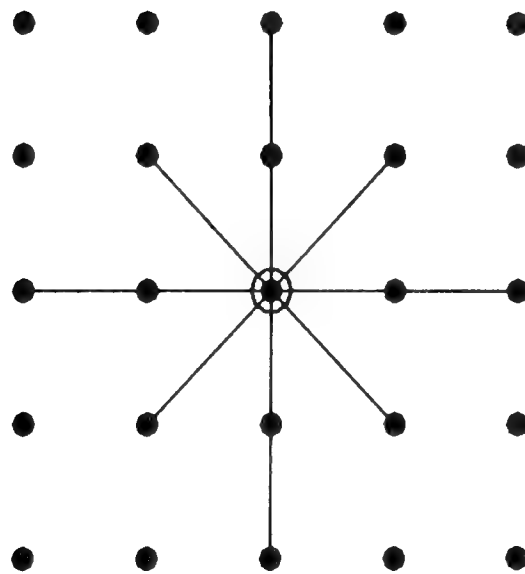
g). Connectivity for sixteen processors.

Figure 6.- Plane stress analysis of a plate.



a). Membrane Problem

$$(\nabla^2 u = 0)$$



b). Plate Bending Problem

$$(\nabla^4 u = 0)$$

Figure 7.- Finite difference discretizations.

# A MIXED FORMULATION FINITE ELEMENT

## FOR LINEAR THIN SHELL ANALYSIS

S.W. Lee and S.C. Wong  
Department of Aerospace Engineering  
University of Maryland, College Park, Maryland

### SUMMARY

An eight node curved thin shell element has been developed and tested. The element is based on the degenerate solid concept and the mixed formulation with the independent inplane and transverse shear strains. The number of unknown parameters in the assumed strains is chosen to alleviate the spurious constraining or locking effect. Numerical results for a pinched cylindrical shell with diaphragmed ends and fixed ends indicate reasonably good performance of the present element.

### INTRODUCTION

The degenerate solid approach (ref. 1) has been the subject of considerable research interest since it does away with the need for more complicated shell theories and can be used to model arbitrary shell geometries. In addition, the interelement compatibility requirement is easily satisfied. The degenerate solid approach can also be quite readily extended to problems involving geometrical and material nonlinearities. For plate bending, the degenerate solid approach reduces to the Mindlin theory with the effect of transverse shear deformation included. Unfortunately, however, for thin plates and shells the inclusion of the transverse shear strain effect in the finite element modeling introduces an undesirable locking or overconstraining effect when exact integration is used for the generation of element stiffness matrices. For thin curved shells, an additional locking effect associated with inplane deformation and rigid body modes has been identified. Left uncured, the locking phenomenon imposes severe limitations on the deformation behavior of a finite element model.

In an effort to alleviate locking, the reduced and/or selective integration schemes have been used (ref. 2-6). In another development, Lee and Pian (ref. 7) showed that the locking or spurious overconstraining effect can be alleviated by using the mixed formulation based on the Hellinger-Reissner principle or a modified Hellinger-Reissner principle. In special cases, the mixed formulation is equivalent to the reduced and/or selective integration scheme (ref. 8 and 9). In reference 10, two plate bending elements, designated as PLAT8 and PLAT8H, have been developed following the mixed formulation. In these elements, proper sets of assumed independent transverse shear strains were used to eliminate spurious constraint. Good modeling characteristics of these elements were demonstrated by solving various example problems which cover wide ranges of length to thickness ratios.

Encouraged by the result of ref. 10, in this paper an eight node finite element with 40 degrees of freedom has been developed for analysis of thin shell structures. The element is based on the Ahmad's degenerate solid concept and the mixed

formulation with the assumed independent inplane strains and transverse shear strains. The formulation and some numerical results for a pinched cylindrical shell are given in subsequent sections.

## FINITE ELEMENT FORMULATION

The degenerate solid concept (ref. 1) is well described in existing textbooks on the finite element method. See, for example, Zienkiewicz (ref. 11) and Cook (ref. 12). In this approach, we need basically two coordinate systems. A global coordinate system with Cartesian coordinates  $X, Y, Z$  and local coordinate systems located at the shell midsurface (fig. 1). The local coordinates with orthogonal unit vectors  $a_1, a_2$  and  $a_3$  are defined at the element nodes and at the Gaussian integration points. The local coordinate system at the nodes is prescribed as an input to the element subroutine. For the local orthogonal coordinate system located at an integration point, the  $x$  and  $y$  axes are tangential to the midsurface with the  $x$  axis parallel to the  $\xi$  coordinate. The  $z$  coordinate is normal to the midsurface. The geometry of a shell element is defined by expressing the global coordinates of a point in the shell as follows:

$$\begin{Bmatrix} X \\ Y \\ Z \end{Bmatrix} = \sum_{i=1}^8 N_i(\xi, \eta) \begin{Bmatrix} X_i \\ Y_i \\ Z_i \end{Bmatrix} + \frac{\zeta}{2} \sum_{i=1}^8 N_i(\xi, \eta) t_i \begin{Bmatrix} a_{31}^i \\ a_{32}^i \\ a_{33}^i \end{Bmatrix} \quad (1)$$

where  $X_i, Y_i, Z_i$  = global coordinates at node  $i$

$t_i$  = shell thickness at node  $i$

$a_{3j}^i$  =  $j$  component of the unit vector  $\vec{a}_3$  normal to the midsurface at node  $i$

$N_i$  = shape function

$\xi, \eta, \zeta$  = parent coordinates

The three displacement components  $U, V$  and  $W$  with respect to the global coordinate system are assumed as follows:

$$\begin{Bmatrix} U \\ V \\ W \end{Bmatrix} = \sum_{i=1}^8 N_i \begin{bmatrix} a_{11}^i & a_{21}^i & a_{31}^i \\ a_{12}^i & a_{22}^i & a_{32}^i \\ a_{13}^i & a_{23}^i & a_{33}^i \end{bmatrix} \begin{Bmatrix} u_i \\ v_i \\ w_i \end{Bmatrix} + \frac{\zeta}{2} \sum_{i=1}^8 N_i t_i \begin{bmatrix} a_{11}^i & a_{21}^i \\ a_{12}^i & a_{22}^i \\ a_{13}^i & a_{23}^i \end{bmatrix} \begin{Bmatrix} \phi_1^i \\ \phi_2^i \end{Bmatrix} \quad (2)$$

where  $u_i, v_i, w_i$  are nodal displacements at node  $i$  defined with respect to the nodal local coordinate system. The nodal rotation angles  $\phi_1^i$  and  $\phi_2^i$  are defined such



that  $\phi_1^i$  represents the rotation around the  $\vec{a}_2$  axis while  $\phi_2^i$  is the rotation around the  $\vec{a}_1$  axis. Each node has five degrees of freedom.

With the description of geometry and displacement given above, it is easy to establish a relationship between the strain components in the global coordinate system and the nodal degrees of freedom. For a degenerate solid shell, it is necessary to express the strain—nodal-degrees-of-freedom relationship for the local coordinate system located at an integration point. Therefore a strain transformation is required at each integration point.

In the mixed formulation, based on the modified Hellinger-Reissner principle, it is necessary to introduce the assumed independent inplane strains and transverse shear strains. With a proper set of assumed strains, it is possible to avoid locking or overconstraint without triggering unstable spurious kinematic modes. Therefore maximum care must be exercised in the choice of assumed strains. For the present eight node element, the following two sets of assumed inplane strains were tested:

(1) 12 $\alpha$  version with

$$\begin{aligned}\epsilon_{xx} &= \alpha_1 + \alpha_2 \xi + \alpha_3 \eta + \alpha_4 \xi \eta \\ \epsilon_{yy} &= \alpha_5 + \alpha_6 \xi + \alpha_7 \eta + \alpha_8 \xi \eta \\ \epsilon_{xy} &= \alpha_9 + \alpha_{10} \xi + \alpha_{11} \eta + \alpha_{12} \xi \eta\end{aligned}\tag{3}$$

(2) 11 $\alpha$  version with

$$\begin{aligned}\epsilon_{xx} &= \alpha_1 + \alpha_2 \xi + \alpha_3 \eta + \alpha_4 \xi \eta \\ \epsilon_{yy} &= \alpha_5 + \alpha_6 \xi + \alpha_7 \eta + \alpha_8 \xi \eta \\ \epsilon_{xy} &= \alpha_9 + \alpha_{10} \xi + \alpha_{11} \eta\end{aligned}\tag{4}$$

In general, the 11 $\alpha$  version should be less susceptible to overconstraint than the 12 $\alpha$  version. The following two sets of the assumed independent transverse shear strains were tested:

(1) 6 $\beta$  version with

$$\begin{aligned}\epsilon_{xz} &= \beta_1 + \beta_2 \xi + \beta_3 \eta \\ \epsilon_{yz} &= \beta_4 + \beta_5 \xi + \beta_6 \eta\end{aligned}\tag{5}$$

(2) 5 $\beta$  version with

$$\begin{aligned}\epsilon_{xz} &= \beta_1 + \beta_2 \xi + \beta_3 \eta \\ \epsilon_{yz} &= \beta_4 + \beta_5 \xi + \beta_6 \eta\end{aligned}\tag{6}$$

In reference 10, it was shown that the 5 $\beta$  version is less susceptible than the 6 $\beta$  version to locking especially when the element geometry is non-rectangular. Note that the above independent inplane and transverse shear strains are defined with respect to the local coordinate systems defined at integration points.

For the numerical integration, the 2 x 2 point rule is used. A higher order 3 x 3 point integration could be used. However it will result in more computing time.

### NUMERICAL EXAMPLE

A pinched thin cylindrical shell (fig. 2) was chosen as an example to investigate the performance of the present shell element with different combinations of the assumed independent inplane and transverse shear strains. Two boundary conditions, one with diaphragmed ends and the other with fixed ends, were considered. Due to symmetry, only 1/8 of the shell was modeled by uniform 4 x 2, 5 x 3, 6 x 4 and 7 x 5 meshes. The first integer in each mesh indicates the number of element divisions in the circumferential direction. Two different radius-to-thickness (R/t) ratios were considered.

#### (a) Diaphragmed Ends

In figures 3 and 4, the computed nondimensional deflection  $\bar{w} = \frac{Etw}{P}$  at the load point is given for  $\frac{R}{t} = 100$  and  $\frac{R}{t} = 500$  respectively. The solutions for different assumed strains seem to converge as the size of mesh increases. The number of degrees of freedom shown in the figure are those after applying the boundary conditions. For  $\frac{R}{t} = 100$ , the computed nondimensional axial inplane force  $\bar{N}_{ax} = \frac{N_{ax}R}{P}$  and circumferential inplane force  $\bar{N}_{cir} = \frac{N_{cir}R}{P}$  are given along the line B-C in figures 5 and 6.

#### (b) Fixed Ends

Computed nondimensional deflection  $\bar{w} = \frac{Etw}{P}$  at the load point is given in figures 7 and 8 for the fixed ends. Again the solutions for different combinations of assumed strains seem to converge as the number of elements increases. The 11 $\alpha$  - 5 $\beta$  combination seems to perform slightly better than other combinations. However, the differences are small.

### DISCUSSION AND CONCLUSION

Numerical results indicate that the present eight node element performs reasonably well for both diaphragmed and fixed ends. Solutions with different combinations of assumed strains seem to converge. Although the 11 $\alpha$  - 5 $\beta$  combination seems to be the best, other combinations also look good. However, it should be pointed out that in the present calculation, only regular meshes were used. That is, no distorted element meshes were considered. As demonstrated in reference 10 for the plate bending problem, the performance of a particular choice of assumed strains can be degraded appreciably when the element geometry is distorted. Therefore further investigation is needed to clarify the effect of element geometry. In addition, the present

element possesses spurious kinematic modes. For the present example problem with diaphragmed and fixed ends, these kinematic modes are suppressed and do not cause any problem. However, research is needed to find a means of controlling spurious kinematic modes for all boundary conditions.

# REFERENCES

1. Ahmad, S., Irons, B.M. and Zienkiewicz, O.C.: Analysis of Thick and Thin Shell Structures by Curved Elements. Int. J. Num. Meth. Engng., Vol. 2, 1970, pp 419-451.
2. Zienkiewicz, O.C., Too, J. and Taylor, R.L.: Reduced Integration Technique in General Analysis of Plates and Shells. Int. J. Num. Meth. Engng., Vol. 3, 1971, pp 275-290.
3. Pugh, E.P.L., Hinton, E. and Zienkiewicz, O.C.: A Study of Quadrilateral Plate Bending Elements with Reduced Integration. Int. J. Num. Meth. Engng., Vol. 12, 1978, pp 1059-1079.
4. Pawsey, S.F. and Clough, R.W.: Improved Numerical Integration of Thick Shell Finite Elements. Int. J. Num. Meth. Engng., Vol. 3, 1971, pp 545-586.
5. Hughes, R.J.R., Cohen, M. and Haroun, M.: Reduced and Selective Integration Techniques in the Finite Element Analysis of Plates. Nuclear Engng. Design, Vol. 46, 1978, pp 203-222.
6. Hughes, T.J.R. and Cohen, M.: The Heterosis Finite Element for Plate Bending. Computers and Structures, Vol. 9, 1978, pp 445-450.
7. Lee, S.W. and Pian, T.H.H.: Improvement of Plate and Shell Finite Element by Mixed Formulation. AIAA J., Vol. 16, 1978, pp 29-34.
8. Malkus, D.S. and Hughes, T.J.R.: Mixed Finite Element Methods--Reduced and Selective Integration Techniques: A Unification of Concepts. Comp. Meth. Appl. Mech. Engng., Vol. 15, 1978, pp 63-81.
9. Lee, S.W.: Finite Element Methods for Reduction of Constraints and Creep Analysis. Ph.D. Dissertation, Dept. of Aeronautics and Astronautics, M.I.T., February 1978.
10. Lee, S.W. and Wong, S.C.: Mixed Formulation Finite Elements for Mindlin Theory Plate Bending. To appear in Int. J. Num. Meth. Engng., 1982.
11. Zienkiewicz, O.C.: The Finite Element Method. 3rd Edition, McGraw-Hill, New York, 1977.
12. Cook, R.D.: Concepts and Applications of Finite Element Analysis. John Wiley & Sons, Inc., New York, 1974.
13. Lindberg, G.M., Olsen, M.D. and Coweper, G.R.: New Developments in the Finite Element Analysis of Shells. NRC Canada DM/NAE Quarterly Bulletin, No. 1969(4).

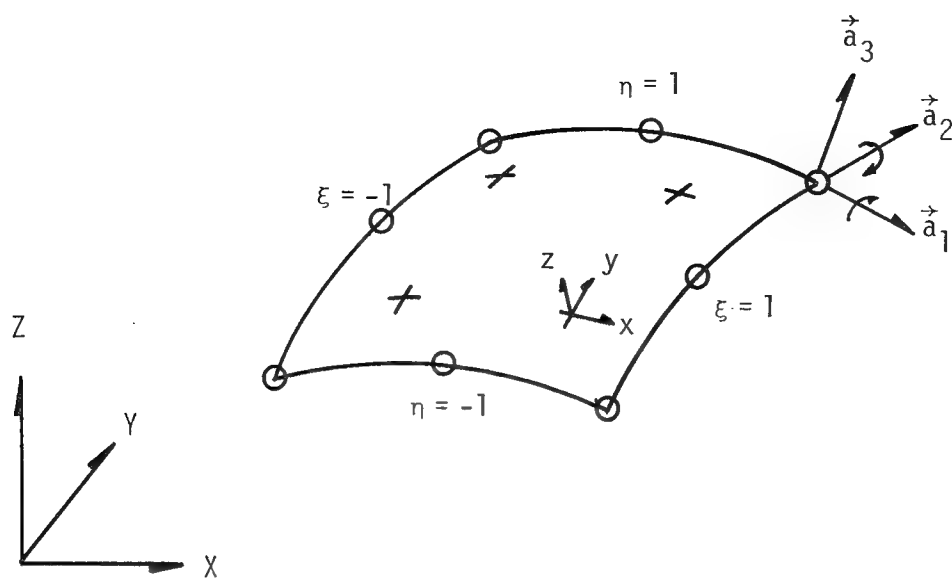


Figure 1. Coordinate Systems for Shell Element

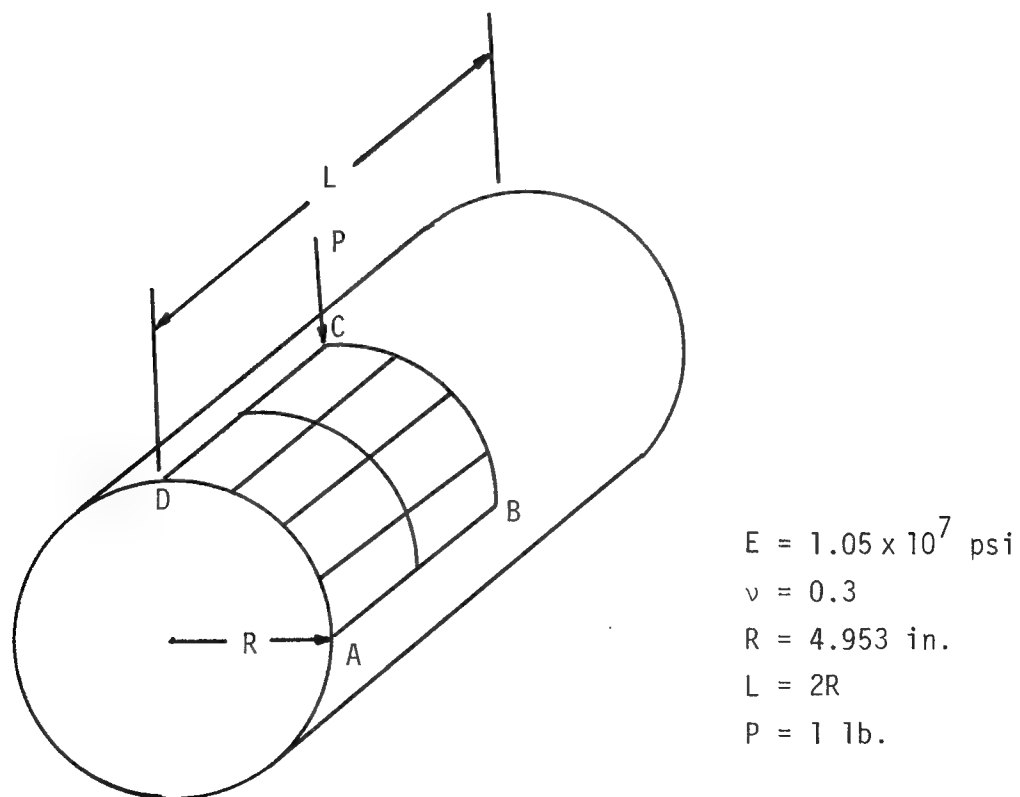


Figure 2. A Pinched Cylinder (4 x 2 mesh)

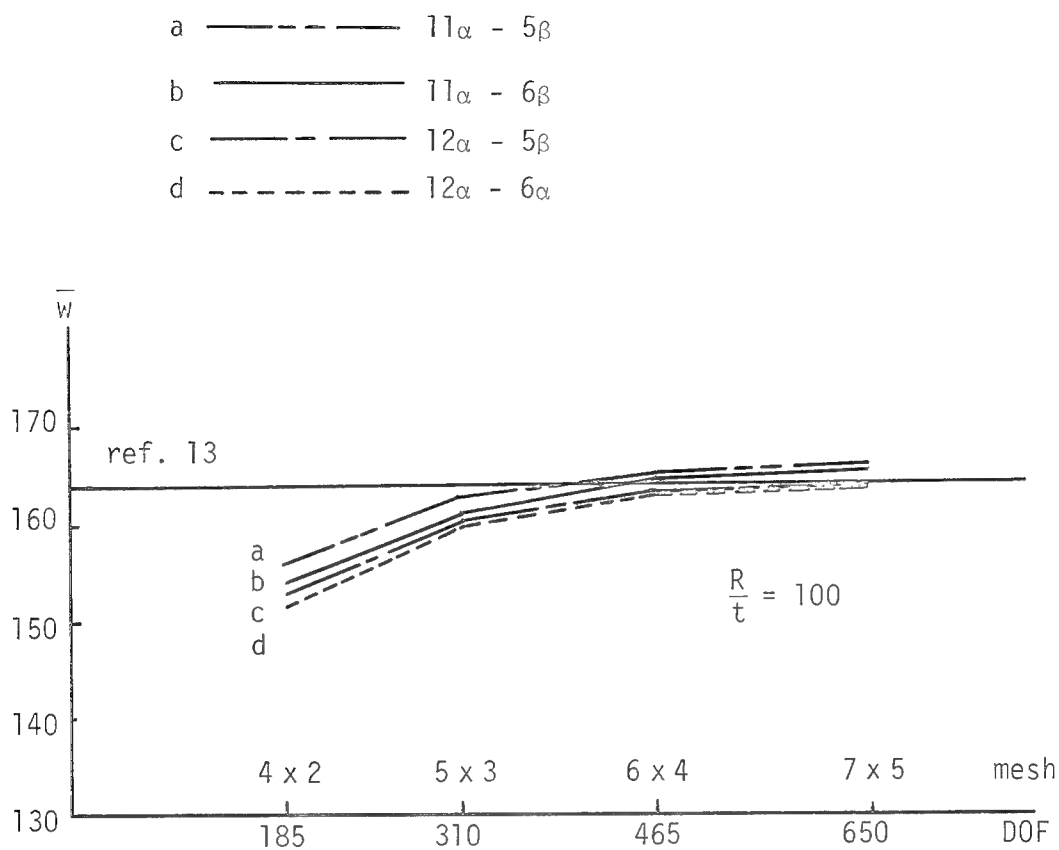


Figure 3.  $\bar{w}$  at the Load Point - Diaphragmed End

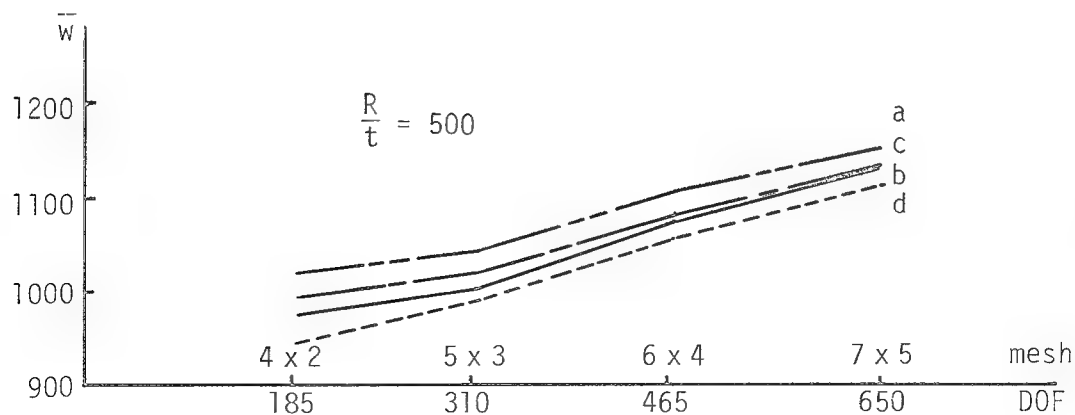


Figure 4.  $\bar{w}$  at the Load Point - Diaphragmed End

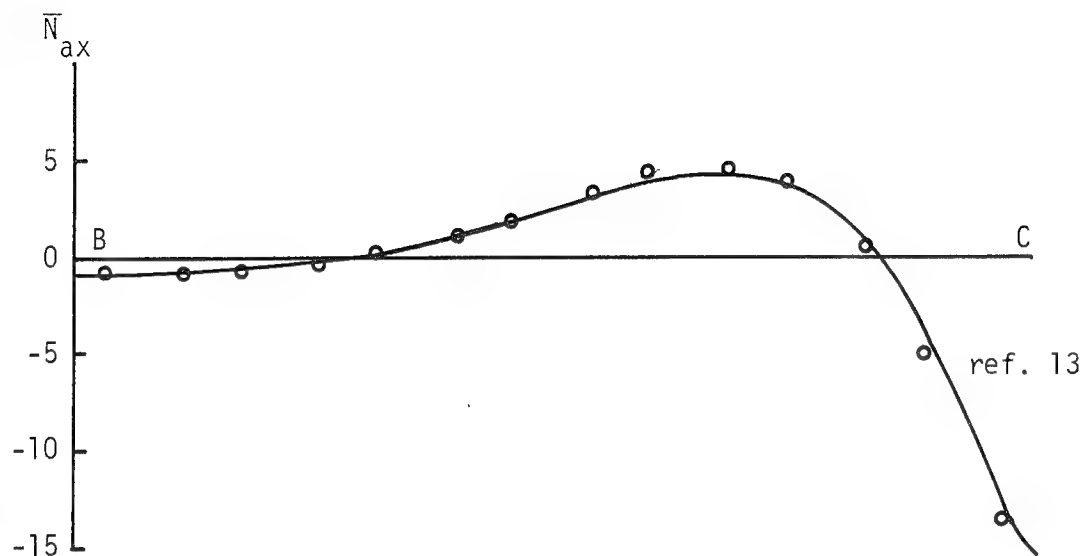


Figure 5. Axial Inplane Force  $\bar{N}_{ax}$  Along B-C - Diaphragmed End

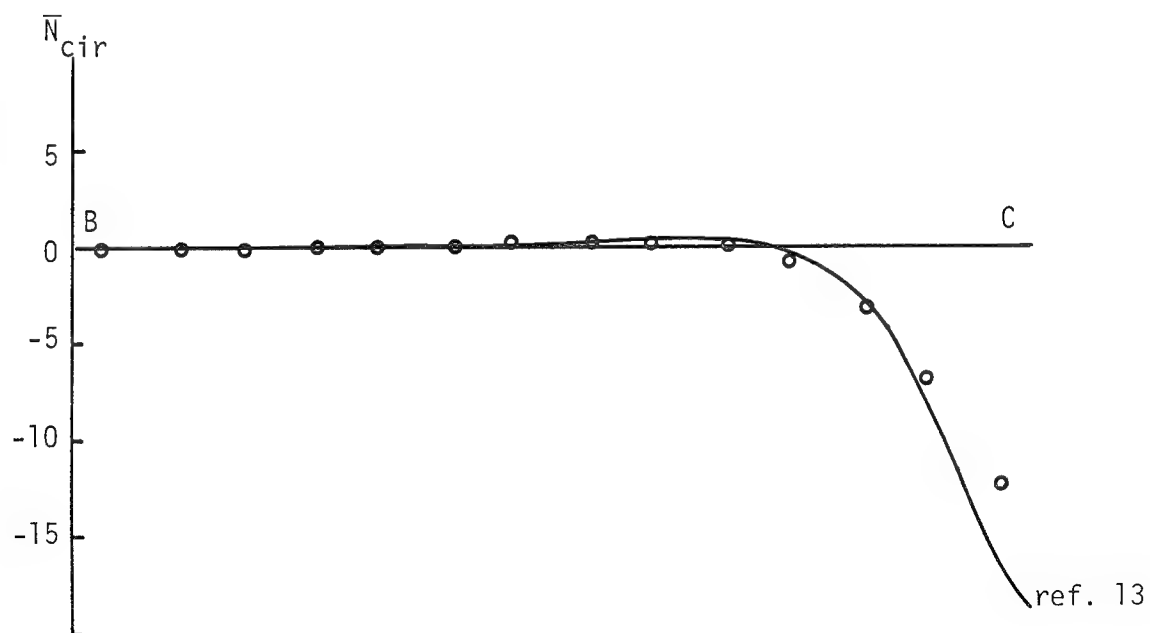


Figure 6. Circumferential Inplane Force  $\bar{N}_{cir}$  Along B-C - Diaphragmed End

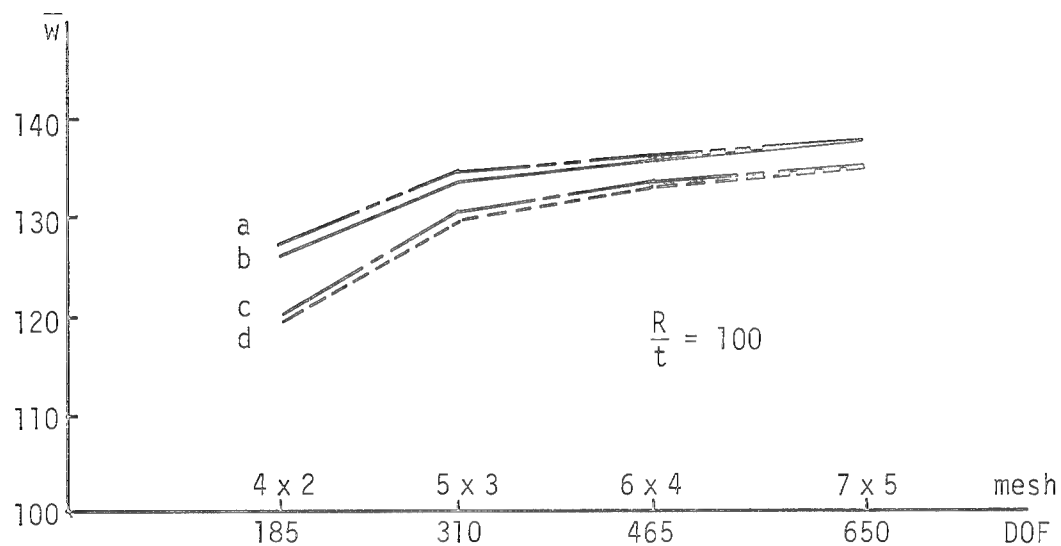


Figure 7.  $\bar{w}$  at the Load Point - Fixed End

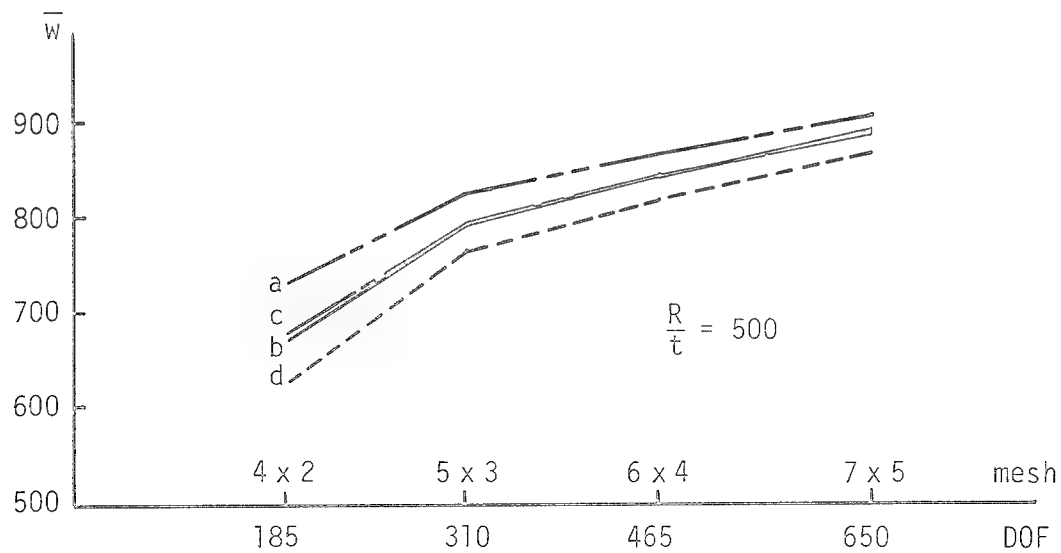


Figure 8.  $\bar{w}$  at the Load Point - Fixed End



# AN EXACT ZOOMING METHOD FOR FINITE ELEMENT ANALYSES

Itio Hirai  
Kumamoto University, Japan

Bo Ping Wang and Walter D. Pilkey  
University of Virginia

## SUMMARY

In this paper, an exact zooming technique is developed which employs static condensation and exact structural reanalysis methods. For a multiple level of zooming such that the successive level of zooming is contained within the prior levels of zoom, successive application of static condensation will reduce the system to one that is only associated with the degrees of freedom (dof) of the original model. Then, application of an exact static reanalysis technique permits the displacements at the dof of the original model that are contained in the zoomed portion of the structure to be obtained first. Next, the response external to the zoom, as well as the response of additional dof within various levels of zooming, can be computed. With the triangular factor of the stiffness matrix of the original system available, this approach involves only the solution of a system of equations of small order. The proposed method is demonstrated by a numerical example.

## INTRODUCTION

In stress analyses using finite element methods, the mesh of the model is often non-uniform. In general, finer meshes are required in locations where rapid changes of stress may occur. To investigate the convergence of the solution, several different mesh configurations may be utilized. A conventional finite element analysis requires a complete assembly of system matrices and a new solution for each mesh used. In many analyses, the changed mesh may be limited to a small "local" portion of the system. Then, the mesh refinements constitute an attempt to "zoom" into the local area to study the detailed stress distribution. In this paper, an exact zooming technique is developed. This method permits the stress distribution in the zoomed area to be investigated with the same accuracy as the direct, brute-force approach, yet with reduced computational requirements.

The exact zooming method presented here employs static condensation (ref. 1) and exact structural reanalysis methods (refs. 2,3). For multiple levels of zooming such that each successive level of zooming is contained within the prior levels of zoom (figure 1), successive application of static condensation will reduce the system to one that involves only the dof of the original model within the zoomed portion of the structure. Then, application of an exact static reanalysis technique permits the displacements at these dof to be obtained. All other responses of interest can then be calculated. This approach involves only the solution of a system of equations of small order if the triangular factor of the original stiffness matrix has been computed.

This method is demonstrated by solving the classical problem of finding the stress concentration factor of a rectangular plate in plane stress with a center hole.

# DEVELOPMENT OF THE METHOD

Let  $\{u_o\}$ ,  $[K_o]$ , and  $\{F_o\}$  be the displacement vector, stiffness matrix, and loading matrix of the original system before zooming. The system is of order  $n_o$ . Partition the dof into two sets,  $\{u_a\}$  representing the  $n_a$  dof which are outside the zoomed area and  $\{u_b\}$  representing the  $n_b$  dof that are contained in the zoomed area. Note that  $n_o = n_a + n_b$ .

The displacement equation for system 0 is

$$[K_o]\{u_o\} = \{F_o\} \quad (1)$$

or

$$\begin{bmatrix} K_{aa} & K_{ab} \\ K_{ba} & K_{bb} \end{bmatrix} \begin{bmatrix} u_a^{(o)} \\ u_b^{(o)} \end{bmatrix} = \begin{bmatrix} F_a \\ F_b \end{bmatrix} \quad (2)$$

Assume equation (1) has been solved for  $\{u_o\}$ , which has decomposed  $[K_o]$

$$[K_o] = [L][D][L^T] \quad (3)$$

For the purposes of discussion, assume  $[K_o]^{-1}$  is known.

## First Level Zooming

Suppose one level of zooming is imposed on system 0. For example, see system 1 of figure 1b. Let  $\{u_1\}$  be the  $n_1$  new dof introduced by the first level zooming. Then, the total number of dof of system 1 is  $t_1 = n_o + n_1$ . The governing equation of system 1 can be written as

$$[K^{(1)}]\{u^{(1)}\} = \{F^{(1)}\} \quad (4)$$

where

$$\{u^{(1)}\} = \begin{bmatrix} u_o^{(1)} \\ u_1^{(1)} \end{bmatrix} = \begin{bmatrix} u_{oa}^{(1)} \\ u_{ob}^{(1)} \\ u_1^{(1)} \end{bmatrix} \quad (5)$$

$$\{F^{(1)}\} = \begin{Bmatrix} F_o \\ 0 \end{Bmatrix} = \begin{Bmatrix} F_{oa} \\ F_{ob} \\ 0 \end{Bmatrix} \quad (6)$$

Here the superscript (1) is used to indicate that this is first level zooming. The stiffness matrix  $[K^{(1)}]$  in partitioned form is

$$\begin{bmatrix} K_{aa}^{(1)} & K_{ab}^{(1)} & K_{al}^{(1)} \\ K_{ba}^{(1)} & K_{bb}^{(1)} & K_{bl}^{(1)} \\ K_{la}^{(1)} & K_{lb}^{(1)} & K_{ll}^{(1)} \end{bmatrix} \quad (7)$$

By definition of the  $\{u_a\}$  and  $\{u_b\}$  dof

$$\begin{aligned} [K_{aa}^{(1)}] &= [K_{aa}] \\ [K_{ab}^{(1)}] &= [K_{ab}] \\ [K_{ba}^{(1)}] &= [K_{ba}] \\ [K_{al}^{(1)}] &= [K_{la}] = 0 \end{aligned} \quad (8)$$

Thus, the partitioned matrix in (7) becomes

$$[K^{(1)}] = \begin{bmatrix} K_{aa} & K_{ab} & 0 \\ K_{ba} & K_{bb}^{(1)} & K_{bl}^{(1)} \\ 0 & K_{lb}^{(1)} & K_{ll}^{(1)} \end{bmatrix} \quad (9)$$

Substitute equation (5) and (9) into equation (4):

$$[K_o^{(n)}] \{u_o^{(n)}\} + \begin{bmatrix} 0 \\ K_{bl}^{(n)} \end{bmatrix} \{u_l^{(n)}\} = \{F_o\} \quad (10a)$$

$$\begin{bmatrix} 0 & K_{ib}^{(1)} \end{bmatrix} \{u_o^{(1)}\} + \begin{bmatrix} K_{11}^{(1)} \end{bmatrix} \{u_i^{(1)}\} = \{0\} \quad (10b)$$

where

$$\begin{bmatrix} K_o^{(1)} \end{bmatrix} = \begin{bmatrix} K_{aa} & K_{ab} \\ K_{ba} & K_{bb}^{(1)} \end{bmatrix}$$

From equation (10b)

$$\{u_i^{(1)}\} = -\begin{bmatrix} K_{11}^{(1)} \end{bmatrix}^{-1} \begin{bmatrix} 0 & K_{ib}^{(1)} \end{bmatrix} \{u_o^{(1)}\} \quad (11)$$

Substitute equation (11) into equation (10a):

$$\begin{bmatrix} \bar{K}_o^{(1)} \end{bmatrix} \{u_o^{(1)}\} = \{F_o\} \quad (12)$$

where

$$\begin{bmatrix} \bar{K}_o^{(1)} \end{bmatrix} = \begin{bmatrix} K_o^{(1)} \end{bmatrix} - \begin{bmatrix} 0 \\ K_{bi}^{(1)} \end{bmatrix} \begin{bmatrix} K_{11}^{(1)} \end{bmatrix}^{-1} \begin{bmatrix} 0 & K_{ib}^{(1)} \end{bmatrix}$$

or

$$\begin{bmatrix} \bar{K}_o^{(1)} \end{bmatrix} = \begin{bmatrix} K_{aa} & K_{ab} \\ K_{ba} & K_{bb}^{(1)} - K_{bi}^{(1)} K_{11}^{(1)-1} K_{ib}^{(1)} \end{bmatrix} \quad (13)$$

We choose to redefine equation (12) as

$$\begin{bmatrix} K_o^{(0)} - \Delta K \end{bmatrix} \{u_o^{(1)}\} = \{F_o\} \quad (14)$$

where

$$\begin{bmatrix} \Delta K \end{bmatrix} = \begin{bmatrix} 0 & 0 \\ 0 & \hat{\Delta K} \end{bmatrix} = \begin{bmatrix} 0 & 0 \\ 0 & K_{bb}^{(0)} - K_{bb}^{(1)} + K_{bi}^{(1)} K_{11}^{(1)-1} K_{ib}^{(1)} \end{bmatrix} \quad (15)$$

Rewrite equation (14) as

$$\begin{bmatrix} K_o^{(0)} \end{bmatrix} \begin{Bmatrix} u_{oa}^{(1)} \\ u_{ob}^{(1)} \end{Bmatrix} = \begin{Bmatrix} F_{oa} \\ F_{ob} \end{Bmatrix} + \begin{bmatrix} 0 \\ \hat{\Delta K} \end{bmatrix} \{u_{ob}^{(1)}\} \quad (16)$$

Define

$$[Y] = \begin{bmatrix} Y_a \\ Y_b \end{bmatrix} = [K_o]^{-1} \begin{bmatrix} 0 \\ \Delta K \end{bmatrix} \quad (17)$$

Then equation (16) becomes

$$\begin{Bmatrix} U_{oa}^{(1)} \\ U_{ob}^{(1)} \end{Bmatrix} = \begin{Bmatrix} U_{oa}^{(0)} \\ U_{ob}^{(0)} \end{Bmatrix} + \begin{bmatrix} Y_a \\ Y_b \end{bmatrix} \{U_{ob}^{(1)}\} \quad (18)$$

Thus

$$\{U_{ob}^{(1)}\} = (I - [Y_b])^{-1} \{U_{ob}^{(0)}\} \quad (19)$$

Once  $\{u_b^{(1)}\}_1$  is found, we can use the upper portion of equations (18) and (11) to compute  $\{u_a^{(1)}\}$  and  $\{u_1^{(1)}\}$ . That is,

$$\{U_{oa}^{(1)}\} = \{U_{oa}^{(0)}\} + [Y_a] \{U_{ob}^{(1)}\} \quad (20)$$

and

$$\{U_1^{(1)}\} = -[K_{11}^{(1)}]^{-1} [K_{1b}^{(1)}] \{U_{ob}^{(1)}\} \quad (21)$$

Equations (19) - (21) complete the displacement solution of system 1. Other response variables can be computed readily.

This procedure requires the decomposition of an  $n_6 \times n_6$  matrix  $([I] - [Y_b])$  and an  $n_1 \times n_1$  matrix  $[K_{11}]$ , together with the computation of the response of the original model due to  $n_b$  additional load cases (equation (17)). A direct solution would require solution of a system of  $(n_1 + n_o)$  equations. For  $(n_1 + n_o) \gg n_b$  and  $(n_1 + n_o) \gg n_1$ , the present method is definitely more efficient.

#### Multi-level Zooming

Consider system 2 of figure 1c, which has two levels of zooming. Let  $\{u_2\}$  be the  $n_2$  additional dof created due to the second level zooming. Then system 2 has  $t_2 = n_o + n_1 + n_2$  dof and

$$\{U^{(2)}\} = \begin{Bmatrix} U_o^{(2)} \\ U_1^{(1)} \\ U_2^{(2)} \end{Bmatrix} \quad (22)$$

The system equation becomes

$$[K^{(2)}] \{U^{(2)}\} = \{F^{(2)}\} \quad (23)$$

where

$$[K^{(2)}] = \begin{bmatrix} K_{00}^{(2)} & K_{01}^{(2)} & K_{02}^{(2)} \\ K_{10}^{(2)} & K_{11}^{(2)} & K_{12}^{(2)} \\ K_{20}^{(2)} & K_{21}^{(2)} & K_{22}^{(2)} \end{bmatrix} \quad \{F^{(2)}\} = \begin{Bmatrix} F_0 \\ 0 \\ 0 \end{Bmatrix} \quad (24)$$

Substitute equations (22) and (24) into equation (23) and expand as

$$\begin{aligned} K_{00}^{(2)} U_0^{(2)} + K_{01}^{(2)} U_1^{(2)} + K_{02}^{(2)} U_2^{(2)} &= F_0 \\ K_{10}^{(2)} U_0^{(2)} + K_{11}^{(2)} U_1^{(2)} + K_{12}^{(2)} U_2^{(2)} &= 0 \\ K_{20}^{(2)} U_0^{(2)} + K_{21}^{(2)} U_1^{(2)} + K_{22}^{(2)} U_2^{(2)} &= 0 \end{aligned} \quad (25)$$

Now, in expanded form for  $\{U_0^{(2)}\}$ , i.e.,

$$\{U_0^{(2)}\} = \begin{Bmatrix} U_a^{(2)} \\ U_b^{(2)} \end{Bmatrix}$$

we have

$$\begin{aligned} [K_{01}^{(2)}] &= \begin{bmatrix} 0 \\ K_{b1}^{(2)} \end{bmatrix} & [K_{02}^{(2)}] &= \begin{bmatrix} 0 \\ K_{b2}^{(2)} \end{bmatrix} \\ [K_{10}^{(2)}] &= \begin{bmatrix} 0 & K_{1b}^{(2)} \end{bmatrix} & [K_{20}^{(2)}] &= \begin{bmatrix} 0 & K_{2b}^{(2)} \end{bmatrix} \end{aligned} \quad (26)$$

From equations (25b) and (25c) solve for

$$\begin{aligned} \{U_1^{(2)}\} &= [A_1] \{U_b^{(2)}\} \\ \{U_2^{(2)}\} &= [A_2] \{U_b^{(2)}\} \end{aligned} \quad (27)$$

where

$$\begin{aligned} [A_1] &= (K_{11}^{(2)} - K_{12}^{(2)} K_{22}^{(2)-1} K_{21}^{(2)})^{-1} (K_{12}^{(2)} K_{22}^{(2)-1} K_{2b}^{(2)} - K_{1b}^{(2)}) \\ [A_2] &= -[K_{22}^{(2)}]^{-1} \{K_{2b}^{(2)} + K_{21}^{(2)} A_1\} \end{aligned} \quad (28)$$

Substitute equations (26) and (27) into equation (25a):

$$[K_{00}^{(2)}] \{U_0^{(2)}\} + \begin{bmatrix} 0 \\ K_{b1}^{(2)} \end{bmatrix} [A_1] \{U_b^{(2)}\} + \begin{bmatrix} 0 \\ K_{b2}^{(2)} \end{bmatrix} [A_2] \{U_b^{(2)}\} = \{F_0\}$$

or

$$[\bar{K}_o^{(2)}] \{U_o^{(2)}\} = \{F_o\} \quad (29)$$

where

$$\begin{aligned} [\bar{K}_o^{(2)}] &= [K_o^{(2)}] + \begin{bmatrix} 0 & 0 \\ 0 & K_{b1}^{(2)}A_1 + K_{b2}^{(2)}A_2 \end{bmatrix} \\ &= \begin{bmatrix} K_{aa} & K_{ab} \\ K_{ba} & K_{bb}^{(2)} + K_{b1}^{(2)}A_1 + K_{b2}^{(2)}A_2 \end{bmatrix} \end{aligned} \quad (30)$$

Substitute equation (30) into (29):

$$[K_o^{(0)} - \Delta K] \{U_o^{(2)}\} = \{F_o\} \quad (31)$$

where

$$\begin{aligned} [\Delta K] &= \begin{bmatrix} 0 & 0 \\ 0 & \Delta \hat{K} \end{bmatrix} \\ \Delta \hat{K} &= [K_{bb}^{(0)}] - [K_{bb}^{(2)} + K_{b1}^{(2)}A_1 + K_{b2}^{(2)}A_2] \end{aligned} \quad (32)$$

Note the similarity between equation (31) and (14). Following similar procedures, we can solve for

$$\{U_b^{(2)}\}, \{U_a^{(2)}\}, \{U_1^{(2)}\}, \{U_2^{(2)}\}$$

The above procedure can be extended to systems 3,4,..., with 3,4,... levels of zooming.

#### NUMERICAL EXAMPLE

The proposed zooming procedure is applied to the problem of figure 2. The 400 mm x 200 mm plate has a center hole of 50 mm diameter. The plate is 1 mm thick and is made of steel with a Young's modulus of  $2.059 \times 10^6$  N/mm<sup>2</sup> and a Poisson ratio of 0.3. The uniform loading is 9.806 N/mm<sup>2</sup>. It is desired to compute the stress concentration factor  $\alpha$ . Since the plate is symmetric about the x and y axes, a quarter (hatched) part of the plate is taken as the finite element calculation model.

The stress concentration factor  $\alpha$  is defined by

$$\alpha = \sigma_{\max y} / \sigma_o \quad (33)$$

where

$\sigma_{\max y}$  = the maximum stress in the y-direction

$$\begin{aligned}\sigma_o &= \text{average stress in the y-direction at the} \\ &\quad \text{narrower cross section}_2 \text{ of } y = 0 \\ &= 980.6/75 = 13.075 \text{ N/mm}^2\end{aligned}$$

The stress concentration factor  $\alpha_o$  is found from elastic theory to be theoretically  $\alpha_o = 2.43$ , which is used for comparison purposes as the exact solution.

The analysis begins with the two relatively crude finite element meshes of figures 3 and 4, respectively. Since the maximum stress occurs near the hole, the region abcd of figure 4 is chosen for the first level zoom and region aghi within abcd is selected as the area for the second level zoom.

The zooming approach proceeds using the finite element meshes shown in figures 3 to 10. The names of the meshes in the figures represent the zooming zone and the mesh types. The subscript numbers indicate the zooming levels. If the subscript is zero, no zooming operation has been performed and the mesh represents the mesh of the original system. The numbers in the mesh indicate the element numbers.

The final finite element mesh produced by the several levels of zooming is indicated by the mesh names. For example, the zooming process  $a_o - a_1$  produces a mesh which is composed of mesh  $a_o$ , a portion of which is zoomed to mesh  $a_1$ . The second level zoom process designated as  $a_o - a_1 - a_2$  means that after the mesh of  $a_o - a_1$  is completed, a portion of this mesh is zoomed to the mesh  $a_2$ .

#### Numerical Results

Starting with mesh  $a_o$ , the stress concentration factor is computed using four levels of zooming. The results are summarized in figure 11. Also shown in figure 11 are some direct finite element solutions. As expected, the direct solution and the zooming method yield the same results for the same mesh. Table 1 summarizes the detailed distribution of the stress concentration factor for 3 different 4-level zooming solutions.

The results of figure 11 show that the solution converges to the theoretically correct result monotonically from the no-zoom solution to the 3-level zooming solution. But the level 4 solution shows disappointing results. We suspect this is due to the numerical difficulty of using very small elements. Judging from the irregular distribution of the stress concentration factors near the corner having the maximum stress (per Table 1), it can be concluded that the type of mesh affects the stress distribution.

#### CONCLUDING REMARKS

An exact zooming method for finite element analyses using the displacement formulation is presented in this paper. A numerical example demonstrates the efficiency and accuracy of the method. This sort of zooming technique can be quite useful in stress analysis situations where many different meshes of a model are to be employed. This method may also be useful in adaptive mesh generation in analyses involving material nonlinearities where remeshing may be required due to high stress in some area of the model.

At first glance, the proposed method may appear to be quite similar to substructuring techniques. We feel that this is not the case, since with the proposed method the analysis leads to new nodes and elements in the original system, whereas substructuring techniques connect several subsystems to make a total system.

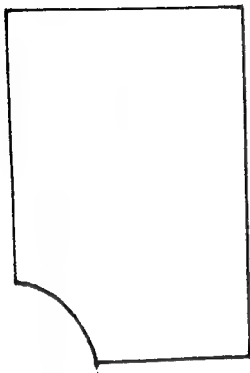


#### REFERENCES

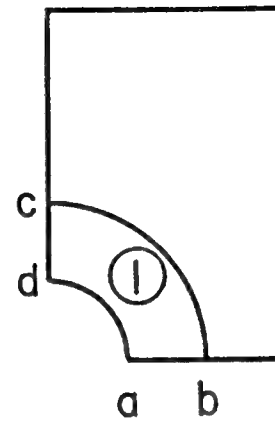
1. Bathe, K.-J.; E.L. Wilson: Numerical Methods in Finite Element Analysis. Prentice-Hall, Inc., Englewood Cliffs, New Jersey, 1976, pp. 259-253.
2. Wang, B.P.; Palazzolo, A.B.; and Pilkey, W.D.: Reanalysis, Modal Synthesis, and Dynamic Design. Chapter 8 of Special AMD Publication on State of the Art Survey of Finite Element Technology, edited by A. Noor and W. Pilkey, ASME, 1982.
3. Wang, B.P.; and Pilkey, W.D.: Efficient Reanalysis of Locally Modified Structures. Proceeding of First Chautauqua on Finite Element Modeling, Schaeffer Analysis, 1980.

TABLE I DISTRIBUTION OF STRESS CONCENTRATION FACTORS

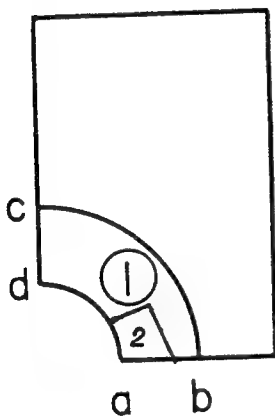
Element No.	Stress Concentration $\alpha$ for the Zooming Process		
	$a_0 - a_1 - a_2 - a_3 - a_4$	$a_0 - c_1 - a_2 - a_3 - a_4$	$a_0 - d_1 - a_2 - a_3 - a_4$
1	2.39	2.40	2.42
2	2.32	2.33	2.34
3	2.32	2.33	2.35
4	2.40	2.41	2.42
5	2.40	2.40	2.42
6	2.32	2.32	2.34
17	2.33	2.34	2.35
18	2.25	2.26	2.27
19	2.26	2.26	2.28
20	2.33	2.34	2.35
21	2.33	2.33	2.35
22	2.25	2.26	2.27
32	2.27	2.27	2.29
33	2.19	2.19	2.20
34	2.20	2.20	2.22
35	2.26	2.27	2.28
36	2.26	2.27	2.28
37	2.19	2.19	2.21



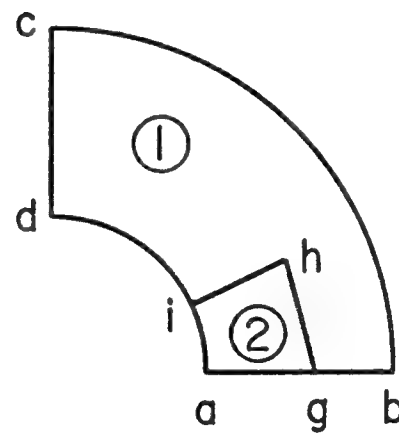
(a) System 0: Original Model



(b) System 1: First Level Zoom



(c) System 2: Second Level Zoom



(d) Details of the Second Level Zoom

Figure 1 Model for Zooming

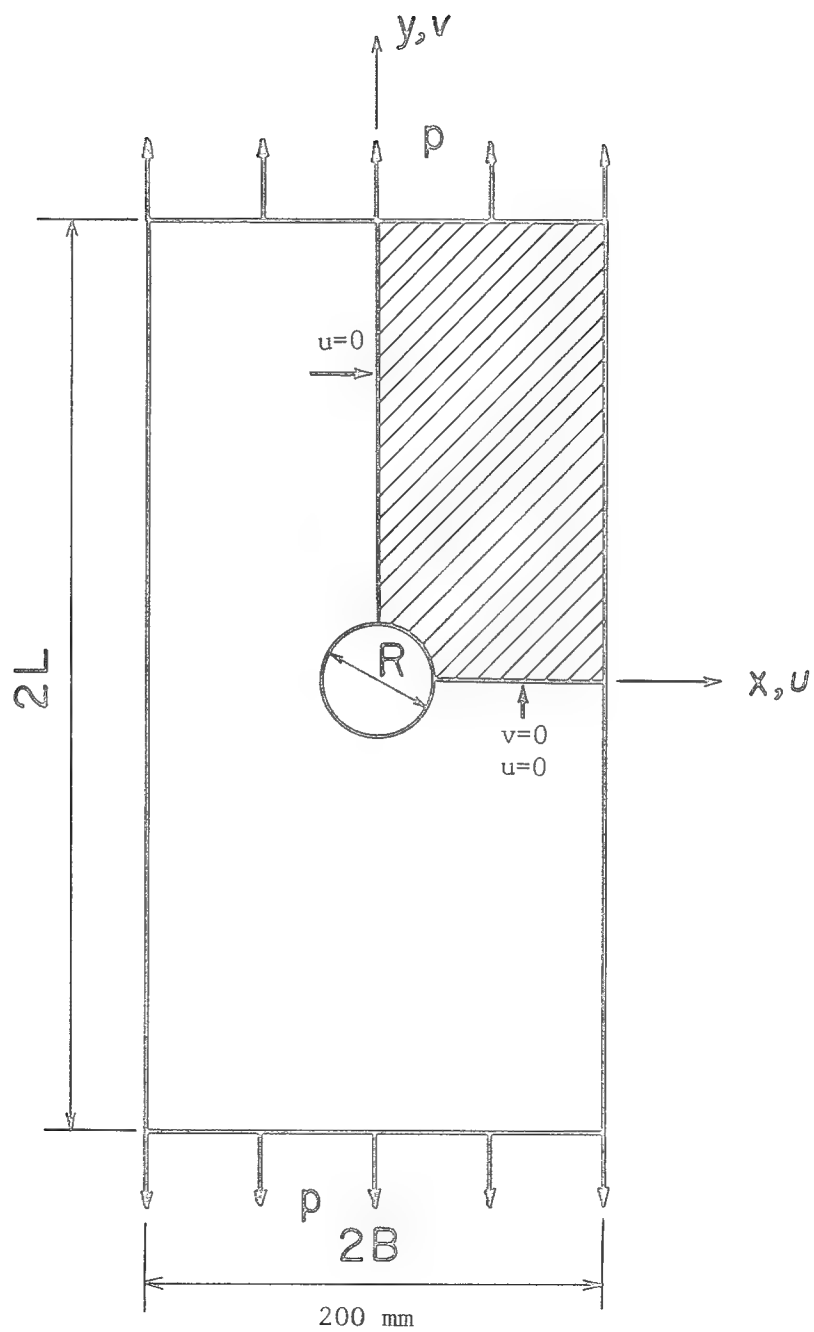


Figure 2 Model for the Sample Problem

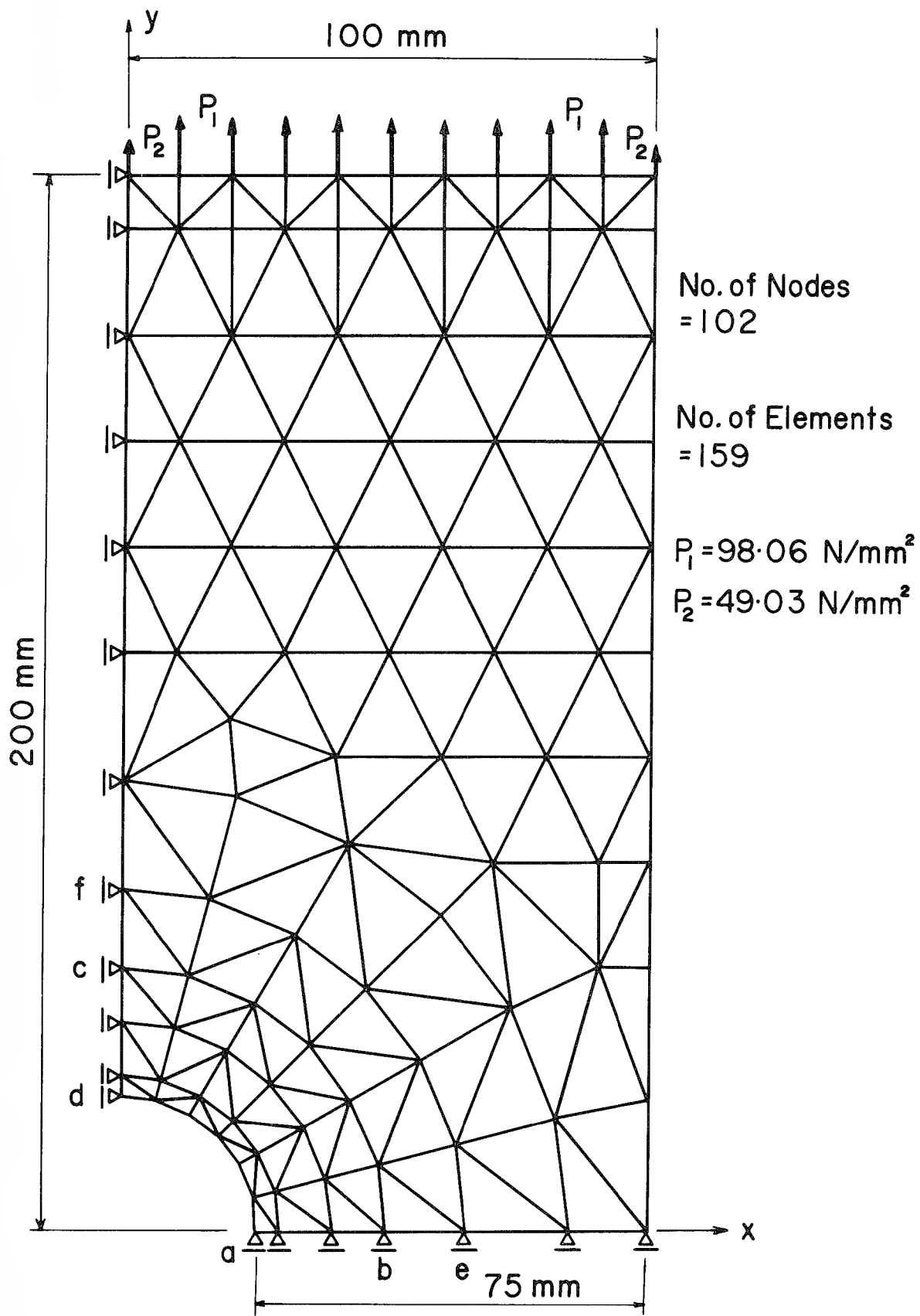


Figure 3 Mesh  $a_o$

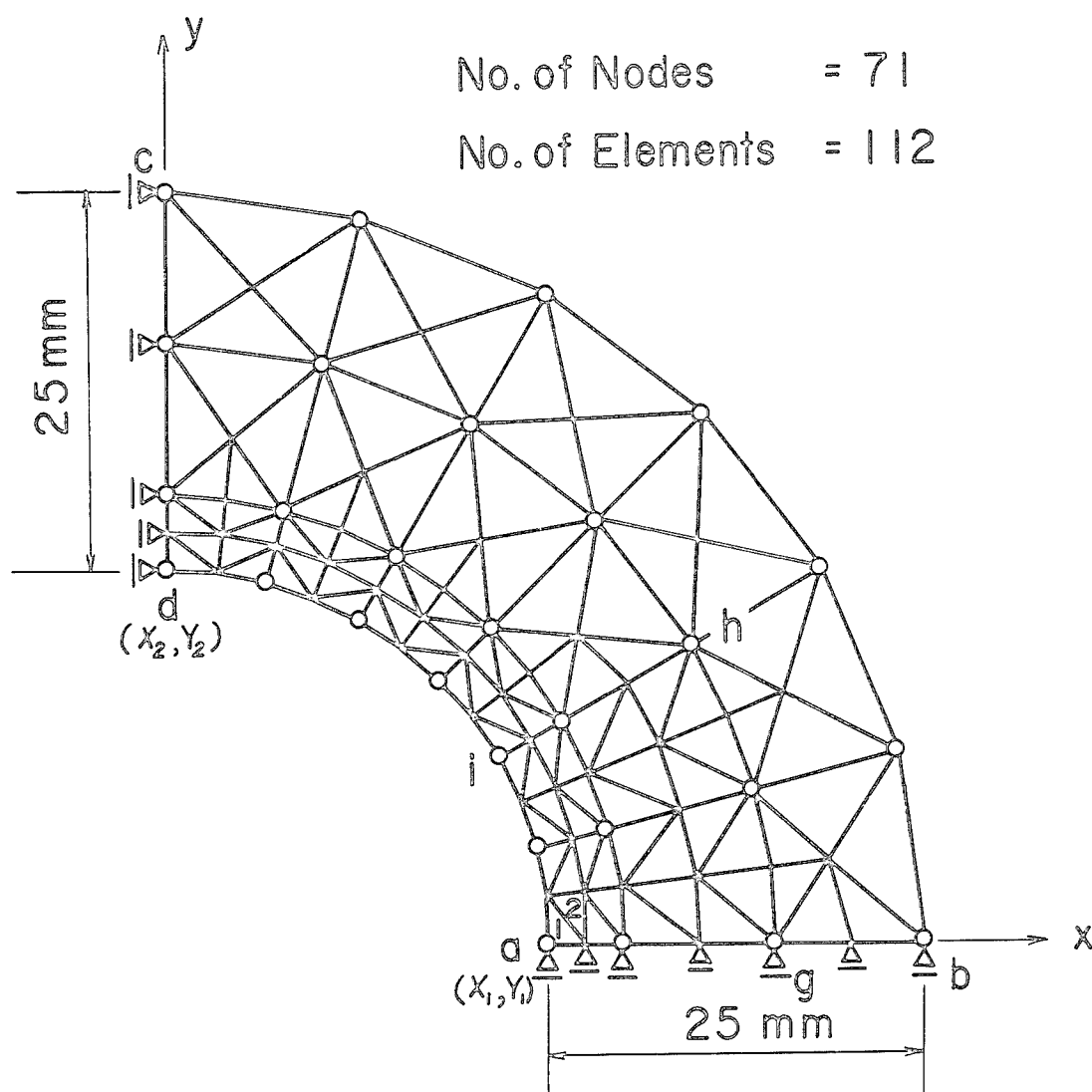


Figure 4 Mesh  $a_1$ . Nodes from the former mesh are represented by open circles.

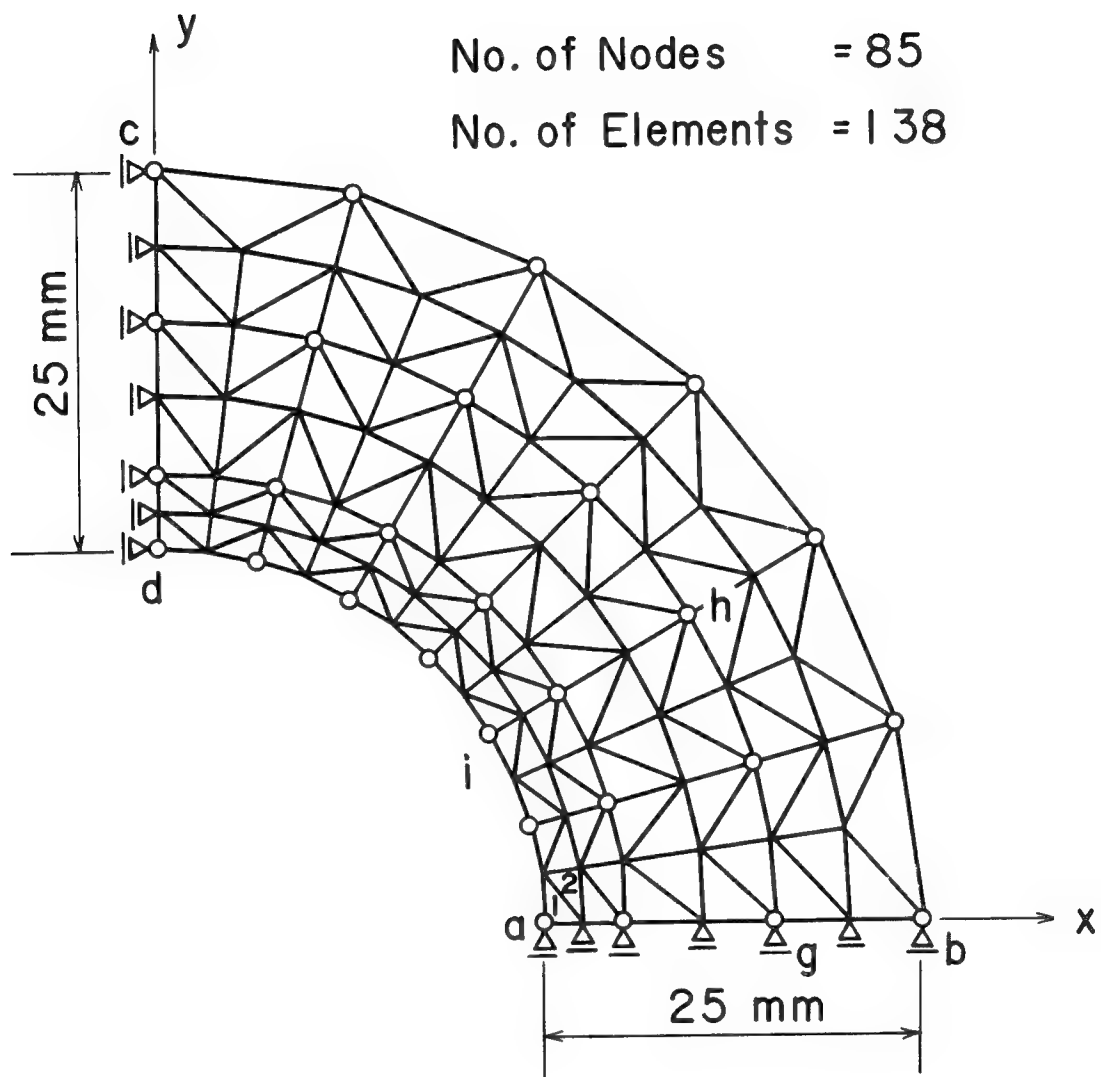


Figure 5 Mesh  $C_1$

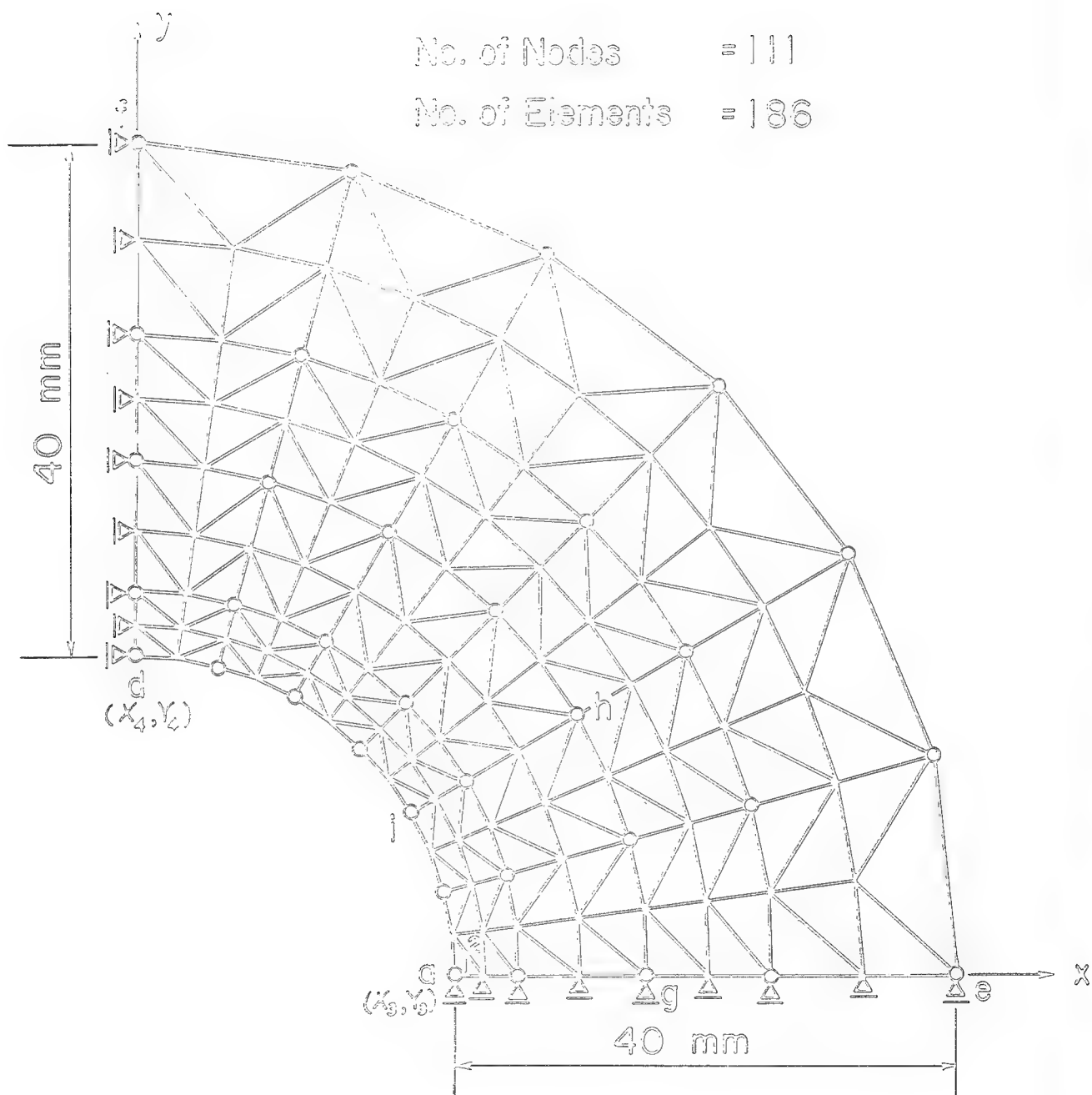


Figure 6 Mesh  $d_1$



No. of Nodes = 73

No. of Elements = 120

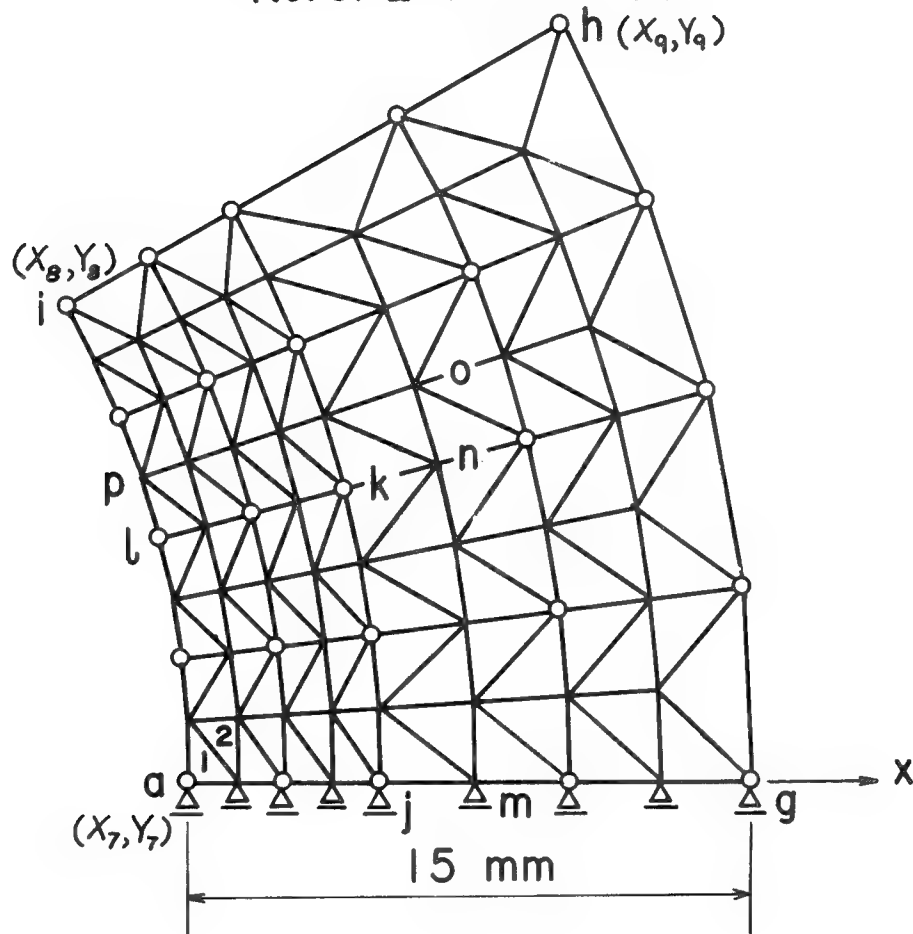


Figure 7 Mesh  $a_2$

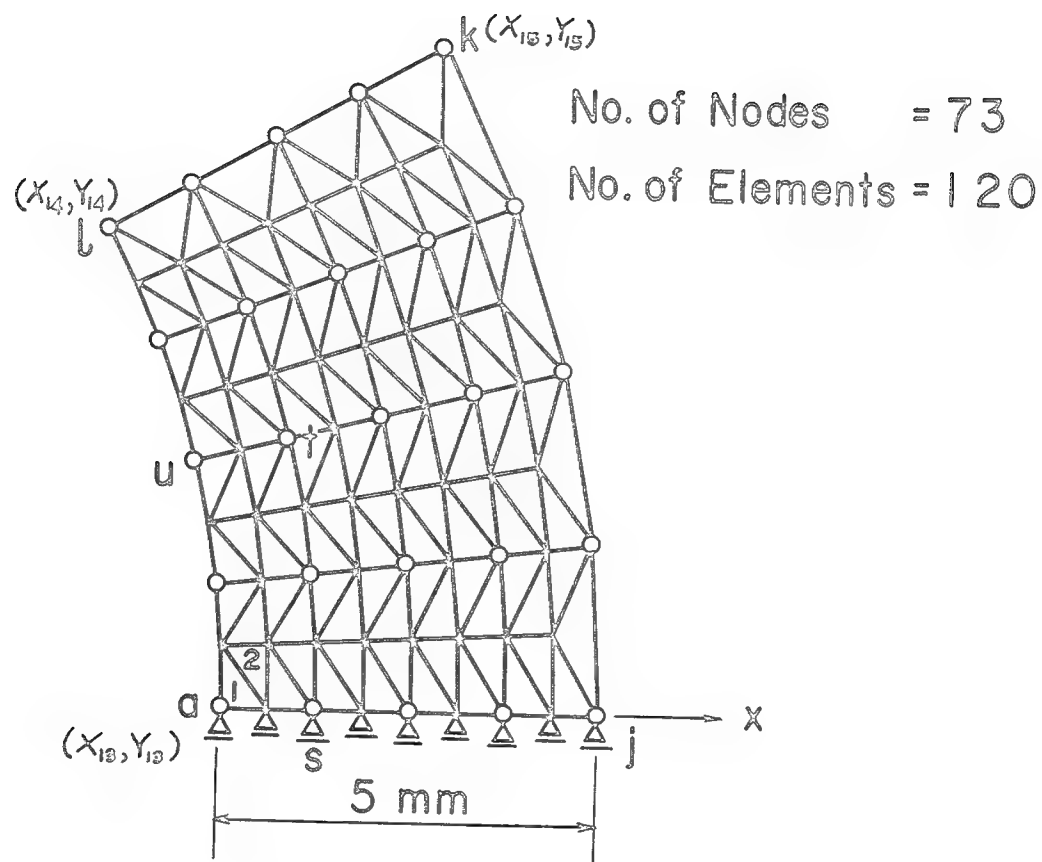


Figure 8 Mesh  $a_3$

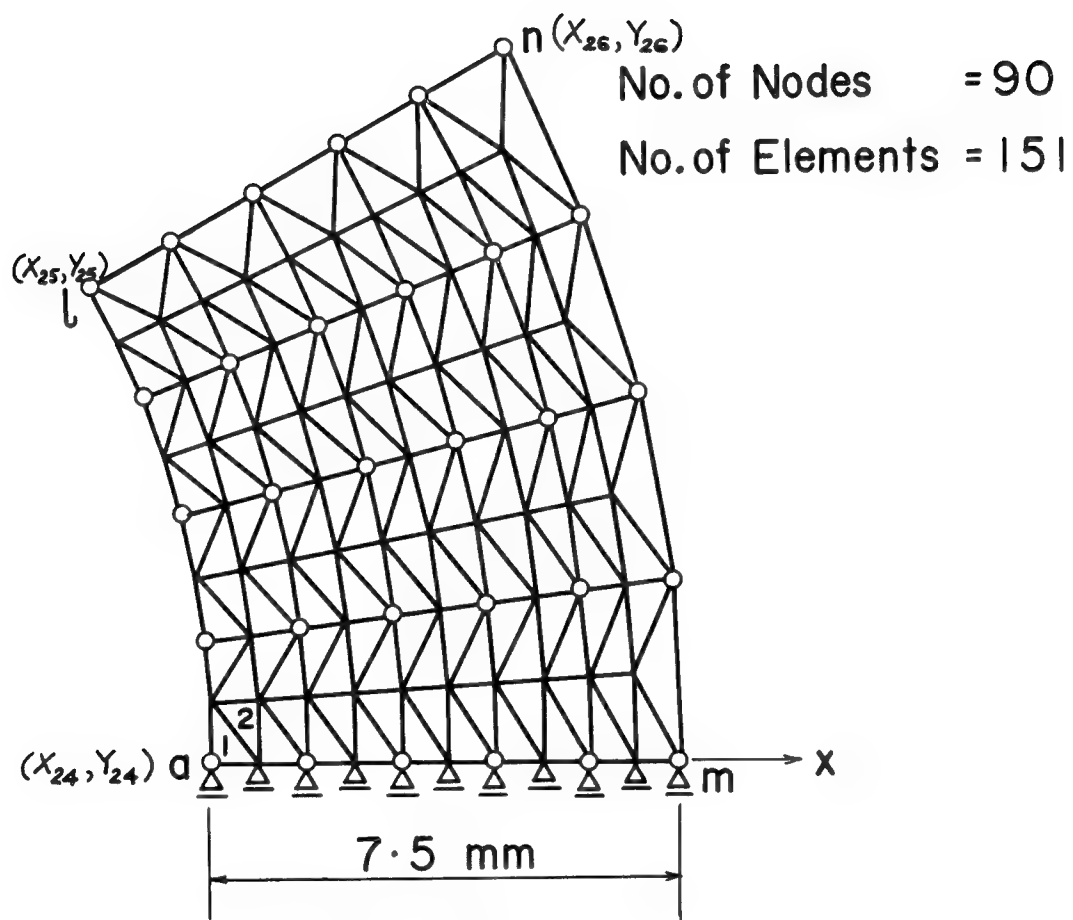


Figure 9 Mesh  $h_3$



248

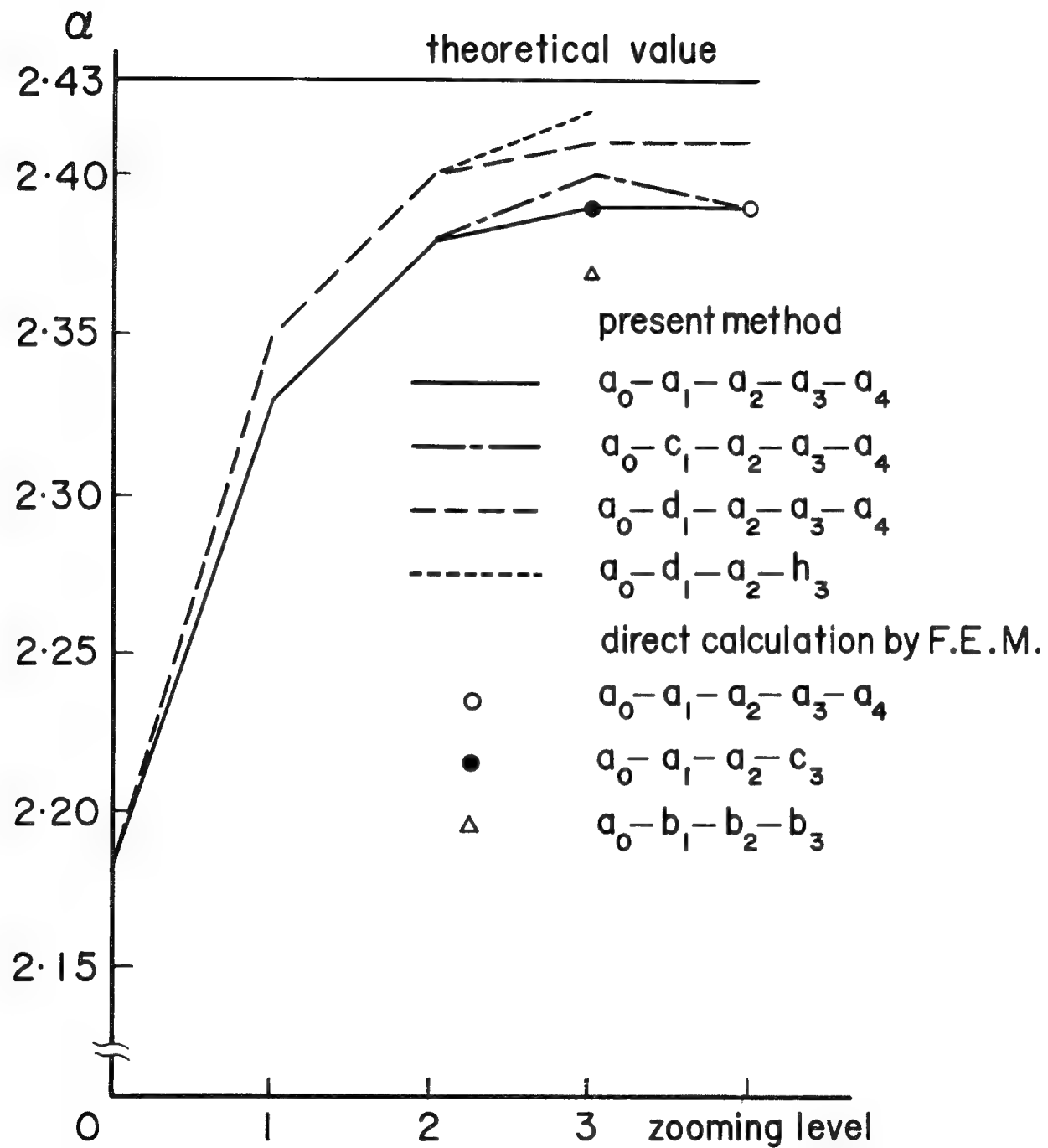


Figure 11 Stress Concentration Factor

## DYNAMIC RESPONSE OF LINED TUNNELS BY BOUNDARY ELEMENTS

G.D. Manolis

Assistant Professor, Department of Civil Engineering, State  
University of New York at Buffalo, Buffalo, New York, 14260

### SUMMARY

In this work, the dynamic stress concentration phenomenon manifested around a lined cylindrical tunnel buried in an infinitely extending linear elastic or visco-elastic medium due to the passage of transient disturbances is investigated. Conditions of plane strain are assumed to hold and the transient disturbances can be of any arbitrary time variation. The numerical method employed is the Boundary Element Method formulated in the Laplace transform domain. Isoparametric boundary elements are used in the discretization of the liner and tunnel surfaces. Visco-elastic material behavior can be readily obtained from the linear elastic case in the Laplace transform domain through the use of the correspondence principle. Finally, the transient solution is recovered by numerical inversion of the solution obtained in the transformed domain.

### INTRODUCTION

The use of underground space is presently attracting attention as one possible factor that will aid the realization of national goals such as energy conservation, improved environment, power generation and efficient transportation [1]. Furthermore, the earth surrounding a buried structure ameliorates the effects of surface loads, and the amplitude of seismic disturbances decreases with increased depth of embedment [2].

The analysis of two-dimensional buried structures under dynamic loads commenced in the early sixties by first considering the case of a circular cylindrical cavity in an infinitely extending linear elastic medium [3,4]. Subsequently, the harmonic [5] and transient [6,7] responses of a lined circular cylindrical cavity were obtained. Analytic methods of solution, however, are difficult for arbitrary structure geometries and for material behavior other than linear elastic. Therefore, resort to numerical methods of solution must be made. In recent years, the Finite Element Method (FEM) and Finite Difference Method (FDM) have been employed, but they do not provide an entirely satisfactory solution because of the fact that an infinite medium is represented by a finite size model. The proposed Boundary Element Method (BEM) is a numerical technique well suited for problems of this kind because Sommerfeld's radiation condition for an infinitely extending medium is automatically accounted for [8]. Although integral equation formulations for the analysis of transient phenomena in solids as well as in fluids have a long history, their adaption for constructing numerical algorithms to be used in the solution of boundary value problems is recent [9,10,11 and 12].

In this work, the Laplace transform with respect to time is applied to the hyperbolic partial differential equations of motion, which become elliptic (in the Laplace transform parameter  $s$ ) and as such are more amenable to numerical treatment. By using the appropriate Green's functions (fundamental solutions) that satisfy the

transformed governing equations of motion in conjunction with Betti's reciprocal theorem, the transformed dynamic equivalent to Somigliana's identity is obtained [11]. Taking the field point to lie on the boundary of the problem results in a set of constraint singular integral equations on the transformed displacement and traction vectors. For specified boundary data, these constraint equations, which are parametric in  $s$ , become a system of algebraic equations that are used to numerically solve for the unknown boundary quantities in terms of the known ones. For the purposes of this work, the boundary of the problem is discretized into a number of isoparametric elements employing quadratic shape functions, and Gaussian quadrature is used for the numerical integration of the fundamental solution times the shape function products. The contributions of the singularities, which occur when the field point coincides with the source point, are evaluated analytically. Finally, the time domain solution is obtained by a numerical Laplace inverse transformation [13] of the solution obtained by the BEM in the transformed domain. Two examples are considered in order to illustrate the methodology presented in this work. In reference to Figure 1, the first example considers a liner that is stiffer than the surrounding medium and the second example considers a liner that is softer.

#### FORMULATION OF THE PROBLEM

The equations of motion for a body of volume  $V$  with bounding surface  $S$  and under the assumptions of small displacement theory and linear elastic, isotropic, and homogeneous material behavior, are

$$(c_1^2 - c_2^2) u_{i,ij} + c_2^2 u_{j,ii} + f_j = \ddot{u}_j \quad (1)$$

In the above equation, a coordinate system  $(\underline{x}, t)$  is employed, where  $\underline{x}$  denotes the Cartesian spatial coordinates and  $t$  is the time. Furthermore,  $u_i(\underline{x}, t)$  is the displacement vector and  $f_j$  is the body force per unit mass. Commas indicate differentiation with respect to space, dots indicate differentiation with respect to time, and the summation convention for repeated indices is implied. Indices  $i$  and  $j$  range from 1 to 2. The propagation velocities of the pressure (P) and shear (S) waves in the body are given, respectively, as

$$c_1^2 = (\lambda + 2\mu)/\rho \quad ; \quad c_2^2 = \mu/\rho \quad (2)$$

where  $\lambda$  and  $\mu$  are the Lamé constants and  $\rho$  is the mass density.

The displacements  $u_i(\underline{x}, t)$  and the tractions  $t_i(\underline{x}, t)$  satisfy the boundary conditions

$$\begin{aligned} t_i &= \sigma_{ij} n_j = p_i(\underline{x}, t) \quad , \quad \underline{x} \in S_t \\ u_i &= q_i(\underline{x}, t) \quad , \quad \underline{x} \in S_u \end{aligned} \quad (3)$$

where  $\sigma_{ij}$  is the stress tensor,  $n_i$  the outward pointing normal, and  $S = S_t \cup S_u$ . In addition, the displacements and velocities satisfy the initial conditions

$$\begin{aligned} u_i(\underline{x}, 0^+) &= u_{i0} \quad , \quad \underline{x} \in V \cup S \\ \dot{u}_i(\underline{x}, 0^+) &= \dot{u}_{i0} \quad , \quad \underline{x} \in V \cup S \end{aligned} \quad (4)$$

and the Sommerfeld radiation condition at infinity. Finally, the constitutive equations are of the form

$$\sigma_{ij} = \rho [(c_1^2 - 2c_2^2) u_{m,m} \delta_{ij} + c_2^2 (u_{i,j} + u_{j,i})] \quad (5)$$

where  $\delta_{ij}$  is the Kronecker delta.

The equations of motion, along with equations (3) - (5), state a well-posed problem in the time domain. This system of equations will be transformed to the Laplace domain. The definition of the Laplace transform of a function  $f(x,t)$  is

$$\bar{f}(\underline{x}, s) = L\{f(\underline{x}, t)\} = \int_0^\infty f(\underline{x}, t) e^{-st} dt \quad (6)$$

where  $s$  is the Laplace transform parameter and  $f(\underline{x}, t)$  must be at least piecewise continuous in time. With the aid of (6), the Laplace transform of the equations of motion becomes

$$(c_1^2 - c_2^2) \bar{u}_{i,ij} + c_2^2 \bar{u}_{j,ii} + \bar{f}_j - s^2 \bar{u}_j + \dot{u}_{j0} + s u_{j0} = 0 \quad (7)$$

The boundary conditions and the constitutive equations do not involve time derivatives so their Laplace transforms simply are

$$\bar{t}_i = \bar{p}_i(\underline{x}, s), \quad \underline{x} \in S_t \quad (8)$$

$$\bar{u}_i = \bar{q}_i(\underline{x}, s), \quad \underline{x} \in S_u$$

and

$$\bar{\sigma}_{ij} = \rho [(c_1^2 - 2c_2^2) \bar{u}_{m,m} \delta_{ij} + c_2^2 (\bar{u}_{i,j} + \bar{u}_{j,i})]$$

The additional assumptions that are made for the sake of convenience are (a) a quiescent state exists before  $t = 0^+$ , which implies that the initial conditions are zero and (b) the body force is zero.

As discussed earlier, equations (7) and (8) may be recast in the following integral equation form

$$\varepsilon(\underline{\xi}) \bar{u}_i(\underline{\xi}, s) = \int_S \{ \bar{G}_{ji}(\underline{x}, \underline{\xi}, s) \bar{t}_i(\underline{x}, s) - \bar{F}_{ji}(\underline{x}, \underline{\xi}, s) \bar{u}_i(\underline{x}, s) \} dS(\underline{x}) \quad (9)$$

where  $\underline{\xi}$  is a source point,  $\underline{x}$  is a receiver point and  $\bar{G}_{ij}$  and  $\bar{F}_{ij}$  are the Green's function and its derivative, respectively. The physical meaning of  $\bar{G}_{ij}$  is that it represents the displacement vector at  $\underline{x}$  in direction  $i$  due to a unit impulse at  $\underline{\xi}$  in direction  $j$ . The kernels  $\bar{G}_{ij}$  and  $\bar{F}_{ij}$  may be found in Reference 11. The factor  $\varepsilon(\underline{\xi})$  is equal to  $0.5 \delta_{ij}$ , provided that the surface is smooth at  $\underline{\xi}$ . Once the boundary problem is solved, then the transformed displacements at any interior point can be found via (9) with  $\varepsilon(\underline{\xi}) = \delta_{ij}$  (the Somigliana identity). The BEM described herein is based on the numerical solution of equation 9.

Finally, the inverse transformation to the time domain of the results obtained by the BEM is accomplished through the inversion integral



$$f(\underline{x}, t) = (1/2\pi i) \int_{\beta-i\infty}^{\beta+i\infty} \bar{f}(\underline{x}, s) e^{st} ds \quad (10)$$

where  $i = \sqrt{-1}$  and  $\beta > 0$  is arbitrary but greater than the real part of all the singularities of  $\bar{f}(\underline{x}, s)$ . The integration over the complex plane in (10) is performed numerically through the use of the algorithm described in Durbin [13]. The transform parameter is a complex number of the form

$$s = \beta + i (2\pi/T)n \quad (11)$$

where  $T$  is the total time interval of interest and  $n$  ranges from 1 to  $N$ , the total number of steps used in the algorithm.

#### NUMERICAL IMPLEMENTATION

It is obvious that equation 9 cannot, in general, yield a closed form solution for the unknown displacements and tractions on the boundary  $S$  in terms of the prescribed boundary conditions. Therefore, resort has to be made to numerical methods of solution. To that purpose, the boundary of the two-dimensional body is discretized into  $N$  isoparametric curvilinear segments. Each isoparametric segment is defined by  $K$  nodes. Therefore, the discretized version of (9) becomes

$$0.5 \bar{u}_j(\xi^p) = \sum_{n=1}^N \left[ \int_{\Delta S_n} \bar{G}_{ji}(\underline{x}, \xi^p) \bar{t}_i(\underline{x}) dS(\underline{x}) \right. \quad (12)$$

$$\left. - \int_{\Delta S_n} \bar{F}_{ji}(\underline{x}, \xi^p) \bar{u}_i(\underline{x}) dS(\underline{x}) \right]$$

where  $p$  ranges from 1 to  $N(K-1)$  and  $\Delta S_n$  is the length of the  $n$ th isoparametric element. It should be remembered that in (12) parametric dependence on the complex transform parameter  $s$  is implied.

Assume that the variation of the displacements over an isoparametric element is of the general form

$$\bar{u}_i(\underline{x}) = \sum_{k=1}^K N^k(\eta) \bar{u}_i^k \quad (13)$$

where  $N^k(\eta)$  are shape functions,  $\eta$  is a dimensionless length parameter ranging from -1 to +1, and  $\bar{u}_i^k$  is the value of the displacement vector at node  $k$ . In this work, a quadratic variation of the boundary quantities is adopted and, therefore,  $K = 3$  and

$$\begin{aligned} N^1(\eta) &= -\eta/2 + \eta^2/2 \\ N^2(\eta) &= 1 - \eta^2 \\ N^3(\eta) &= \eta/2 + \eta^2/2 \end{aligned} \quad (14)$$

The same isoparametric representation is also used for the tractions. All that remains now is to express  $dS(\underline{x})$  in terms of  $\eta$ . This is accomplished in terms of the Jacobian  $J(\eta)$  of the transformation so that

$$\int_{\Delta S_n} f(\underline{x}) dS(\underline{x}) = \int_{-1}^1 f(\underline{x}(\eta)) J(\eta) d\eta \quad (15)$$

Therefore, in view of the above, the final form of equation (12) is

$$0.5 \bar{u}_j(\xi^P) = \sum_{n=1}^N \left\{ \sum_{k=1}^K \bar{t}_i^k \int_{-1}^1 \bar{G}_{ji}(\underline{x}(\eta), \xi^P) N^k(\eta) J(\eta) d\eta \right. \quad (16)$$

$$\left. - \sum_{k=1}^K \bar{u}_i^k \int_{-1}^1 \bar{F}_{ji}(\underline{x}(\eta), \xi^P) N^k(\eta) J(\eta) d\eta \right\}$$

For more details on the numerical evaluation of (16), reference should be made elsewhere [14]. The matrix form of equation 16 is

$$[\bar{Q}] \{\bar{u}\} = [\bar{P}] \{\bar{t}\} \quad (17)$$

where the column matrices contain the transformed displacement and traction vectors defined at the boundary of the problem, while matrices  $[\bar{Q}]$  and  $[\bar{P}]$  contain the values resulting from the numerical integration of the product of the tensors  $\bar{F}_{ij}$  and  $\bar{G}_{ij}$ , respectively, times the shape functions and the Jacobian. Note that equation 17 requires complex arithmetic formalism in view of the form of the Laplace transform parameter  $s$  (11).

Since the case of a liner reinforcing a tunnel opening is a problem involving multiple connected domains, the final part of this section develops the superposition procedure necessary for solving problems of this kind. In reference to Figure 2, let  $\underline{u}_L(Q)$  and  $\underline{t}_L(Q)$  be the displacement and traction vectors at the inner surface of the liner,  $\underline{u}_L(P)$  and  $\underline{t}_L(P)$  be the respective quantities at the outer surface of the liner, and  $\underline{u}_M(P)$  and  $\underline{t}_M(P)$  be the displacements and tractions at the surface of the medium. Note that the outer surface of the liner and the surface of the medium are the same surface. The total field is decomposed into the incident field (superscript  $i$ ) and scattered field (superscript  $s$ ) so that the following equations hold true:

$$\begin{aligned} \underline{u}_M(P) &= \underline{u}_M^i(P) + \underline{u}_M^s(P) \quad ; \quad \underline{t}_M(P) = \underline{t}_M^i(P) + \underline{t}_M^s(P) \\ \underline{u}_L(P) &= \underline{u}_L^i(P) + \underline{u}_L^s(P) \quad ; \quad \underline{t}_L(P) = \underline{t}_L^i(P) + \underline{t}_L^s(P) \\ \underline{u}_L(Q) &= \underline{u}_L^i(Q) + \underline{u}_L^s(Q) \quad ; \quad \underline{t}_L(Q) = \underline{t}_L^i(Q) + \underline{t}_L^s(Q) \end{aligned} \quad (18)$$

Note that in (18) the bars over the vectors denoting Laplace transform quantities are omitted for convenience. The boundary conditions for this problem are that (a)  $\underline{u}_L(P) = \underline{u}_M(P)$  because of compatibility, (b)  $\underline{t}_L(P) = -\underline{t}_M(P)$  because of equilibrium, and (c)  $\underline{t}_L(Q) = 0$ .

Applying equation (17) to the liner alone for the scattered field gives

$$\begin{bmatrix} Q_A & Q_B \\ Q_C & Q_D \end{bmatrix} \begin{Bmatrix} \underline{u}_L^s(P) \\ \underline{u}_L^s(Q) \end{Bmatrix} = \begin{bmatrix} P_A & P_B \\ P_C & P_D \end{bmatrix} \begin{Bmatrix} \underline{t}_L^s(P) \\ \underline{t}_L^s(Q) \end{Bmatrix} \quad (19)$$

where the matrices  $[Q]$  and  $[P]$  have been appropriately partitioned. Application of the BEM to the medium alone for the scattered field results in a system of equations which reads as

$$[Q] \{ \underline{u}_M^s(P) \} = [P] \{ \underline{t}_M^s(P) \} \quad (20)$$

Thus, equations (19) and (20), in addition to conditions (a)-(c) result in a system of six equations in the six unknowns, which are  $\underline{u}_M^s(P)$ ,  $\underline{u}_L^s(P)$ ,  $\underline{u}_L^s(Q)$ ,  $\underline{t}_M^s(P)$ ,  $\underline{t}_L^s(P)$ ,  $\underline{t}_L^s(Q)$ . The incident field is known and the total field can be recovered from equation (18).

Alternatively, the BEM can be formulated for the total field as shown below:

$$[Q] \{ \underline{u}_M(P) \} = [P] \{ \underline{t}_M(P) \} + \{ \underline{u}_M^i(P) \}$$

$$\begin{bmatrix} Q_A & Q_B \\ Q_C & Q_D \end{bmatrix} \begin{Bmatrix} \underline{u}_L(P) \\ \underline{u}_L(Q) \end{Bmatrix} = \begin{bmatrix} P_A & P_B \\ P_C & P_D \end{bmatrix} \begin{Bmatrix} \underline{t}_L(P) \\ \underline{t}_L(Q) \end{Bmatrix} + \begin{Bmatrix} 0 \\ 0 \end{Bmatrix} \quad (21)$$

The first of the above two matrix equations pertains to the medium, and the incident displacement field appears in the formulation because the radiation condition cannot be satisfied by the total field in an exterior domain. The second matrix equation pertains to the liner, for which the radiation condition does not apply since it is an interior domain. Finally, equation (21) along with conditions (a)-(c) are sufficient to solve for the six unknown quantities of the total field.

## EXAMPLES

This section describes in detail the numerical solution of two examples that serve to illustrate the method as well as the dynamic behavior of a lined circular cylindrical cavity in an infinite plane.

### Example 1

Consider an infinitely extending linear elastic medium with a circular cylindrical cavity of radius  $r_0$  and of infinite length reinforced by a linear elastic liner under the influence of a compressional plane shock wave whose front is parallel to the axis of the cavity, as shown in Figure 1. The following numerical values are assigned to the constants describing the medium:

$$\begin{aligned}\mu &= \lambda = 3,597,000 \text{ lb/in}^2 \\ \rho &= 0.00025 \text{ lb-sec}^2/\text{in}^4\end{aligned}\tag{22}$$

The above material properties correspond physically to granite. The liner material properties are

$$\begin{aligned}\mu_L &= \lambda_L = 12,000,000 \text{ lb/in}^2 \\ \rho_L &= 0.00073 \text{ lb-sec}^2/\text{in}^4\end{aligned}\tag{23}$$

corresponding physically to steel. The liner inner and outer radii are

$$\begin{aligned}r_i &= 204 \text{ in} \\ r_o &= 212 \text{ in}\end{aligned}\tag{24}$$

respectively, which result in a liner radial thickness of 8 inches. The characteristic time  $2\tau$  for this problem, namely the time required for the pressure wave to travel the diameter of the hole, is about 0.002 seconds. The dynamic load is the step pressure wave front carrying the stress components  $\sigma_x = s_0$  and  $\sigma_y = (\nu/(1-\nu))s_0$ , where  $\nu$  is Poisson's ratio and  $s_0$  is conveniently taken as  $-1.0 \text{ lb/in}^2$ . The point with polar coordinates  $(r_o, 0^\circ)$  is the first point of the liner to experience the arrival of the P-wave.

The liner is divided into 40 equal curvilinear segments, 20 on each surface. The medium surface is also divided into 20 equal curvilinear segments so as to match the discretization of the outer surface of the liner. The time interval considered is  $T = 0.009$  seconds divided into  $N = 10$  intervals of 0.001 seconds each. In addition, the finite element program SAP IV of Bathe et al [15] is employed to solve this problem. The finite element mesh used is shown in Figure 3 and it is observed that advantage is taken of the symmetry of the problem about the Y-axis. Seventeen time increments of 0.001 seconds each are assigned, and the results are shifted by the amount of time it takes for the wave originating at the far right-hand side of mesh to reach the liner before they are plotted. It should be mentioned at this point that the SAP IV program used numerical integration to solve the equations of motion.

Figures 4 and 5 are plots of the stress concentration factor (SCF), defined as the ratio of the circumferential stress  $\sigma_{\theta\theta}$  to the applied stress  $s_0$ , versus the dimensionless time  $t/\tau$  at the polar location  $\theta = 90^\circ$ . In particular, in Figure 4 the results obtained by the BEM and the SAP IV program for the liner at  $r = r_i$  (the inner surface I.S.), are concurrently plotted with the analytic-numerical results of Baron and Parnes [7] and of Garnet and Pascal [6] pertaining to the middle surface (M.S.) of the liner. There is a small difference (about 7%) between the results obtained by References 6 and 7, probably attributable to the inescapable errors (series truncations, etc.) associated with the numerical implementation of their analytic solutions. The difference between the middle and the inner surface dynamic stresses, which reaches a maximum value of about 10%, is due to the additional effect of bending present in the latter surface. It should be mentioned at this point that Reference 7 employs a thin shell analysis and does not incorporate the bending stresses because they are regarded as negligible for the present case. The results obtained by the BEM (Case 1) are in good agreement with the results obtained by Garnet and Pascal [6] at the inner surface. All of the aforementioned solutions approach the exact static

value of -7.59 that can be computed from Savin [16]. The results obtained from SAP IV underestimate the maximum SCF of -8.43 occurring around  $t/\tau = 6.0$  by about 11%. Cases 1 and 2 associated with the BEM refer to formulations using the total field and the scattered field, respectively, as mentioned in the previous section. It is observed that the former case yields better answers than the latter one, in addition to being more efficient. One possible reason is that the formulation for the total field basically involves one large operation (a matrix inversion), while the other formulation involves a number of smaller operations (matrix inversions and multiplications) that accumulate errors. Another possible reason for this discrepancy is that the matrix inverted in the total field formulation is strongly diagonal, while some of the submatrices inverted in the scattered field formulation lack this characteristic. This last fact, coupled with the occasional ill-conditioning of the original matrices, may be an important source of error.

Figure 5 depicts the SCF history in the medium at  $r = r_0$  obtained by the BEM (Case 1) and by the FEM program SAP IV. Here the results from the two numerical methods are in reasonable agreement and predict a maximum SCF of -2.1 at the time point  $t/\tau = 4.0$  and -2.5 at  $t/\tau = 6.0$ , respectively, well below the corresponding SCF of -3.0 at  $t/\tau = 4.0$  obtained in Baron and Matthews [3] for the case of the unlined cavity. The static solution for the unlined cavity [16] predicts a SCF of -2.67. It should be mentioned that Mow and McCabe [5], who solved for the harmonic (steady state) equivalent of this transient problem for material properties and a geometric configuration very similar to the ones used in this example, predict a maximum absolute value for the SCF of 8.3 for the liner and 2.2 for the medium. Finally, Table I presents the amounts of memory and time the dynamic BEM program and the finite element SAP IV program required for compilation and execution, where it appears that the former method is less efficient than the latter.

## Example 2

In this example, a liner that is softer than the surrounding medium is considered, and the following numerical values are assigned to its material properties:

$$\begin{aligned}\mu_L &= 695,000 \text{ lb/in}^2 ; \quad \lambda_L = 1,042,000 \text{ lb/in}^2 \\ \rho_L &= 0.00022 \text{ lb-sec}^2/\text{in}^4\end{aligned}\tag{25}$$

The geometry of the problem remains the same as the one in Example 1. Two cases are considered for the medium. In the first case, the material properties assigned to the medium are listed in equation (22). In the second case, the medium is represented by a linear viscoelastic Maxwell model with a coefficient of viscosity  $\eta$  equal to  $f\mu$ , where  $f$  is assigned the value of 0.5%. Linear viscoelastic material behavior can easily be accounted for in the dynamic BEM in conjunction with the Laplace transform by replacing the elastic coefficients of the medium by expressions derived from application of the correspondence principle. For the Maxwell model, these expressions are:

$$\begin{aligned}\mu_v &= \mu s / (s + \mu/\eta) \\ \lambda_v &= (\lambda s + (\mu/\eta) (\lambda + 2\mu/3)) / (s + \mu/\eta)\end{aligned}\tag{26}$$

The values for  $\mu$  and  $\lambda$  in (26) are taken the same as the ones used for the medium in Example 1.

Figure 6 is a plot of the time history of the SCF obtained by the BEM at the polar location  $\theta = 90^\circ$  in both the soft liner at  $r = r_i$  and the medium at  $r = r_o$ . Concurrently plotted are analytic-numerical results of Garnet and Pascal [6] pertaining to the soft liner embedded in the linear elastic medium. It is observed that the difference between the maximum SCF in the liner predicted by the BEM (1.02 at  $t/\tau = 6.0$ ) is about 17% over the maximum SCF predicted in Reference 6 (.85 at  $t/\tau = 5.5$ ). The maximum SCF in the medium for this case is almost identical to the maximum SCF obtained for the unlined cavity case (see Figure 5), which indicates that the presence of the soft liner does not help in decreasing the peak stress in the medium. The results of assuming linear viscoelastic material behavior for the medium are that on the one hand the peak SCF in the medium decreases by 15%, while on the other hand the liner experiences a maximum increase in stress of about 84%. The computer time and memory requirements for the BEM applied to the two cases of elastic and viscoelastic media are listed in Table I, where it is observed that there is very little difference between the two. It should finally be mentioned that the BEM is formulated for the total field, in view of the comments made in Example 1.

#### CONCLUDING REMARKS AND FUTURE WORK

A general numerical method for solving for the dynamic response of underground structures under conditions of plane strain or stress is presented. In particular, the structure may be of arbitrary shape embedded in a linear elastic or viscoelastic medium and under the action of general transient disturbances. The method consists of solving the dynamic problem in the Laplace transform domain by the BEM and numerically inverting the transformed solution to obtain the time domain behavior.

The use of curvilinear elements incorporating a quadratic representation for both the geometry of the problem and for the variation of the boundary quantities is a good improvement in terms of accuracy and flexibility over earlier formulations that employed straight line boundary elements and constant values of the boundary quantities over those segments. Also, better agreement of the BEM results with solutions obtained by analytic formulations can be achieved by merely increasing the number of sampling points  $N$  for the Laplace transform parameter  $s$ , but this will increase the cost of the BEM program proportionally.

The method is quite general and can be extended to propagation and diffraction problems in three-dimensional elastodynamics. Such an extension would necessitate the construction of curved isoparametric "patch" elements in order to appropriately discretize the two-dimensional surfaces of such problems. Also, Green's functions defined for the infinite space would have to be used instead of the ones defined for the infinite plane. Furthermore, the use of specialized Green's functions in conjunction with the methodology presented herein will allow for the efficient solution of structures embedded in a half plane or in a half space that exhibit linear elastic isotropic or anisotropic material behavior. Finally, the addition of volume integrals in the BEM formulation will allow for the incorporation of non-zero initial conditions as well as the incorporation of body forces such as the weight of the material.

# REFERENCES

1. Baker, C.F., Chairman, "The Use of Underground Space to Achieve National Goals," Underground Construction Research Council, ASCE, New York, 1972.
2. Duke, C.M. and Leeds, D.J., "Effects of Earthquakes on Tunnels," in J.J. O'Sullivan, Ed., Protective Construction in a Nuclear Age, 303-328, McMillan, New York, 1961.
3. Baron, M.L. and Matthews, A.T., "Diffraction of a Pressure Wave by a Cylindrical Cavity in an Elastic Medium," J. Appl. Mech., 28, 347-354, 1961.
4. Pao, Y.H., "Dynamic Stress Concentration in an Elastic Plate," J. Appl. Mech., 29, 299-305, 1962.
5. Mow, C.C. and McCabe, W.L., "Dynamic Stresses in an Elastic Cylinder," Proc. ASCE, EM3, 89, 21-40, 1963.
6. Garnet, H. and Pascal, J.C., "Transient Response of a Circular Cylinder of Arbitrary Thickness in an Elastic Medium to a Plane Dilatational Wave," J. App. Mech., 33, 521-531, 1966.
7. Baron, M.L. and Parnes, R., "Diffraction of a Pressure Wave by a Cylindrical Shell in an Elastic Medium," Proc. 4th U.S. Nat. Congress Applied Mech., ASME, 63-70, 1962.
8. Banerjee, P.K. and Butterfield, R., Boundary Element Methods in Engineering Science, McGraw-Hill, New York, 1981.
9. Friedman, M.B. and Shaw, R.P., "Diffraction of Pulses by Cylindrical Objects of Arbitrary Cross-Section," J. Appl. Mech., 29, 40-46 (1962).
10. Banaugh, R.P. and Goldsmith, W., "Diffraction of Steady Elastic Waves by Surfaces of Arbitrary Shape," J. Appl. Mech., 30, 589-597 (1963).
11. Cruse, T.A. and Rizzo, F.J., "A Direct Formulation and Numerical Solution of the General Transient Elastodynamic Problem, I," J. Math. Anal. Appl., 22, 341-355, 1968.
12. Niwa, Y., Kobayashi, S. and Fukui, T., "Applications of Integral Equation Methods to some Geomechanical Problems," 120-131 in C.S. Desai, Editor, Numerical Methods in Geomechanics, ASCE, New York, 1976.
13. Durbin, F., "Numerical Inversion of Laplace Transforms: An Efficient Improvement to Dubner and Abate's Method," Comp. J., 17, 297-301, 1974.
14. Manolis, G.D. and Beskos, D.E., "Dynamic Response of Lined Tunnels by an Isoparametric Boundary Element Method," Comp. Meth. Applied Mech. Engng. (To be published.)
15. Bathe, K.J., Wilson, E.L. and Peterson, F.E., "SAP IV: A Structural Analysis Program for Static and Dynamic Response of Linear Systems," Rept. No. EERC 73-11, Univ. of California, Berkeley, 1973.
16. Savin, G.N., Stress Concentration around Holes, Pergamon Press, New York, 1961.

TABLE I  
COMPUTER TIME AND MEMORY REQUIREMENTS

	CPU* execution time (sec)	Total CPU* time (sec)	Field length** (octal words)	Cost (\$)
BEM, strong liner, case 1.	726.1	762.9	133400	43.3
BEM, strong liner, case 2.	738.2	775.4	151400	45.5
SAP IV.	28.4	28.8	140000	10.4
BEM, soft liner, elastic solution.	624.2	661.0	133400	37.8
BEM, soft liner, viscoelastic soln.	625.4	662.3	133400	37.9

\*Central Processing Unit

\*\*During execution



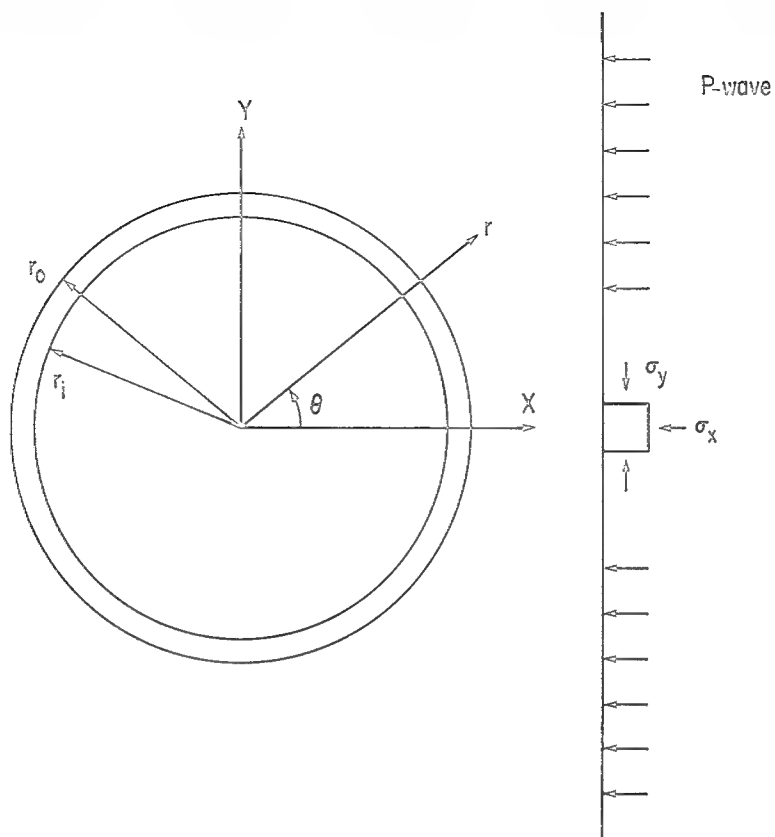


Figure 1.- Lined tunnel in an infinite medium under the action of a suddenly applied P-wave.

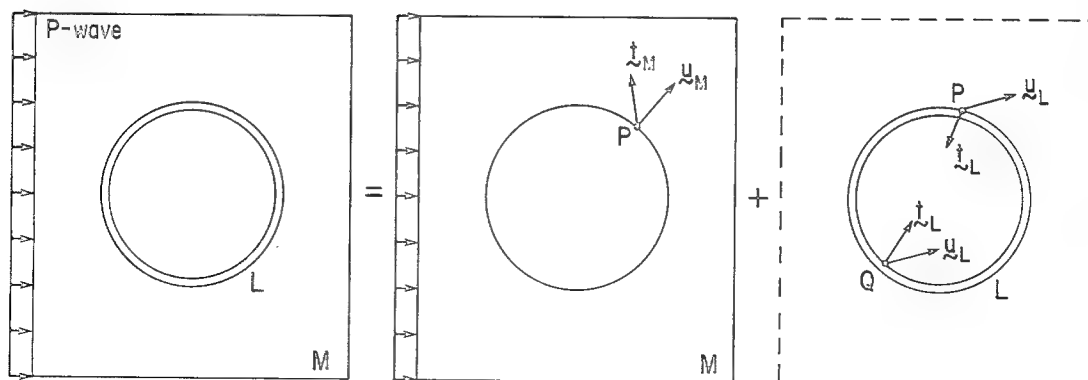


Figure 2.- Superposition concept for the lined tunnel.

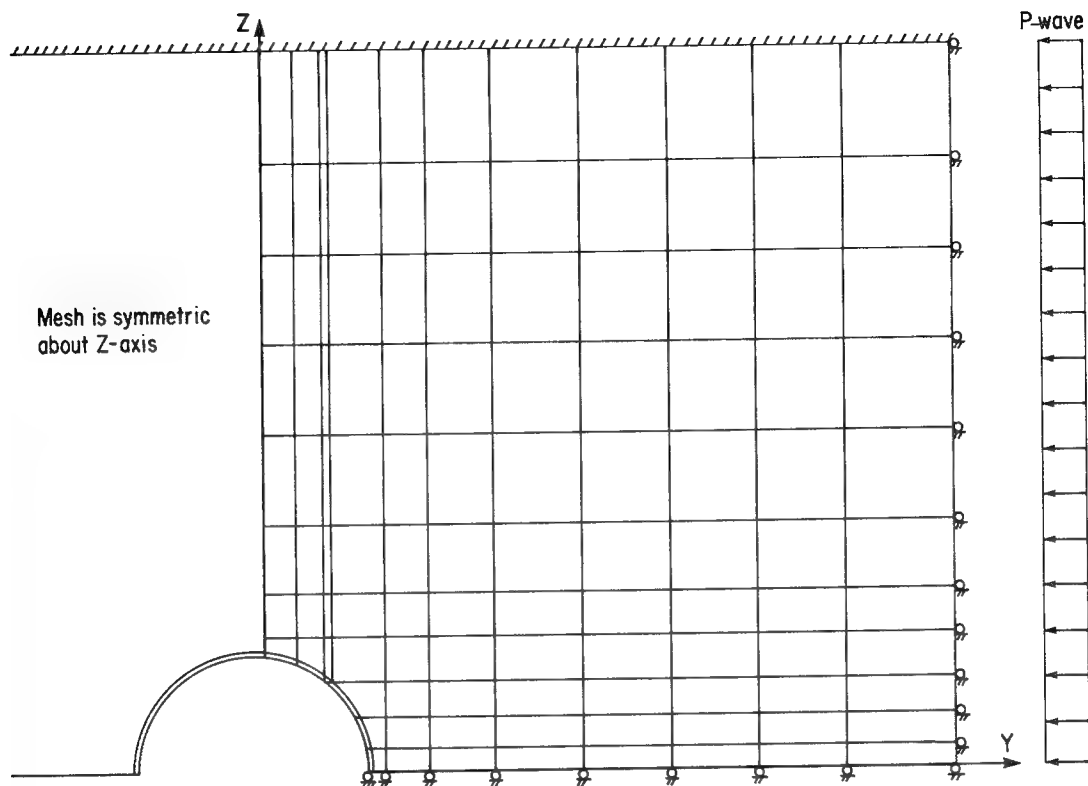


Figure 3.- Finite element mesh used in the program SAP IV.

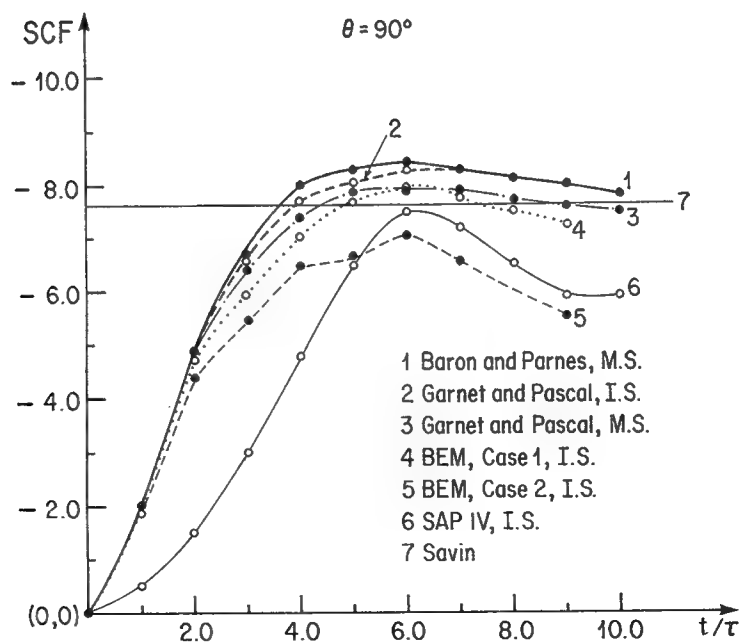


Figure 4.- Stress concentration history of the strong liner at  $\theta = 90^\circ$ .

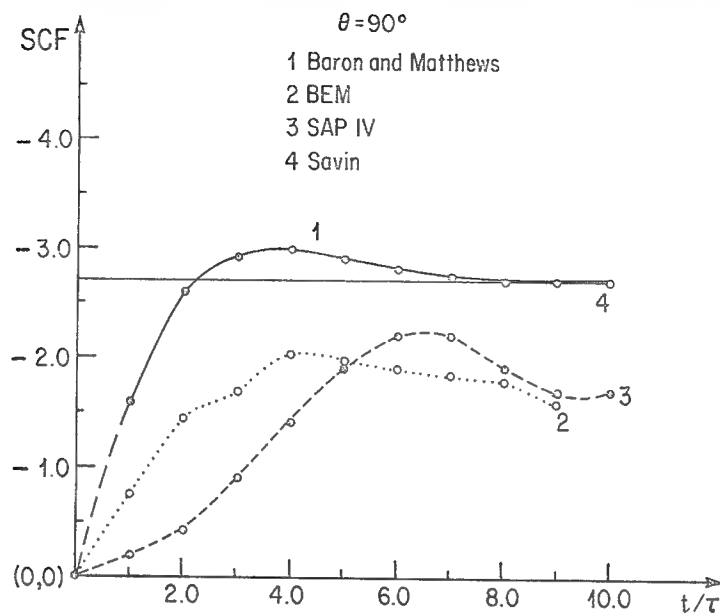


Figure 5.- Stress concentration history of the medium reinforced by the strong liner at  $\theta = 90^\circ$ .

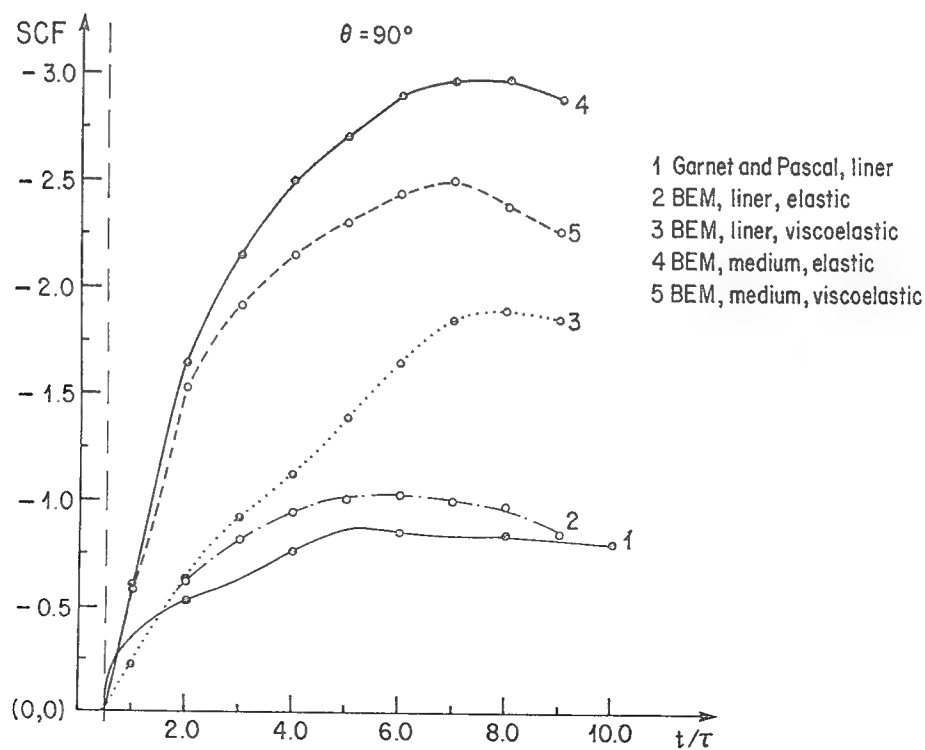


Figure 6.- Stress concentration history of the soft liner and the surrounding medium (both elastic and viscoelastic cases) at  $\theta = 90^\circ$ .

A FINITE ELEMENT APPROACH  
FOR SHELLS OF REVOLUTION WITH A LOCAL DEVIATION \*

by

Prof. Kye J. Han, D.Sc.  
Department of Civil Engineering  
Universtiy of Houston

and

Prof. Phillip L. Gould, Ph.D.  
Department of Civil Engineering  
Washington University

SUMMARY

A finite element model that is suitable for the static analysis of shells of revolution with arbitrary local deviations is presented. The model employs three types of elements: rotational, general, and transitional shell elements. The rotational shell elements, which are most efficient, are used in the region where the shell is axisymmetric. The general shell elements, which can simulate almost any shell geometry, are used in the local region of the deviation. The transitional shell elements connect these two distinctively different types of elements and make it possible to combine them in a single analysis.

The form of the global stiffness matrix resulting when different forms of nodal degrees of freedom are combined is illustrated. Also studied is the coupling of harmonic degrees of freedom due to the locally non-axisymmetric geometry. An efficient solution procedure which takes advantage of many scattered zero terms in the stiffness matrix is suggested. These steps include the use of a substructuring technique and separate partial harmonic analysis. A numerical example is presented and compared with existing solutions to demonstrate the capability and efficiency of the new model.

INTRODUCTION

Many shells of revolution encountered in industrial applications have local irregularities which deviate from the basic axisymmetry of the shells. Examples are cut-outs, pipe connections, and constructional imperfections. From the design engineers' point of view, axisymmetry is a desired feature since it facilitates stress analysis, both theoretically and numerically. Once a deviation is created on a rotational shell, however, the structure is no longer a shell of revolution, at least in the region of the deviation. Thus, the usual techniques for the analysis of shells of revolution are no longer valid. In practice, these irregularities are frequently ignored, or are considered only approximately while the whole structure

\*This work was supported by the U.S. National Science Foundation under Grant No. CEE-8111797.

is treated as axisymmetric. In the case of constructional imperfections, many researchers have studied so-called 'axisymmetric imperfections' which have little resemblance to the actual case.

In this paper an efficient finite element model is developed which is suitable for the static analysis of shells of revolution with arbitrary local deviations, both geometric and material. This model combines, in a single analysis, three different shell elements: rotational, general, and transitional. The rotational elements are used where the shell is axisymmetric, while the general elements are specified over a limited region of the irregularity (Figure 1a). The transitional elements facilitate a smooth transition between the two domains. Since the rotational shell element is computationally more efficient than the general shell element, this approach takes advantage of the prevailing axisymmetry, and at the same time provides the required generality for the non-axisymmetric portion.

The use of transitional elements is necessary to achieve continuity of displacement fields. The rotational element [1,2] has nodal circles (Figure 1b) and uses trigonometric Fourier series' to express displacement fields in the circumferential direction, whereas the general element [3] has nodal points (Figure 1c) and uses polynomial shape functions between the nodes. Since the two are not compatible, the displacement fields will be discontinuous if the elements are adjacent. The transitional element [4] provides the required continuity between the two elements by employing a line node and point nodes within a single element (Figure 2). All three types of elements utilized in the new model will be examined in this paper. However, these elements have already been derived by the authors and their colleagues elsewhere [1-4]. Therefore, details of the formulation will not be repeated; only the basic definitions of geometry and displacements, which are essential for the consideration of compatibility, will be discussed.

The form of the global stiffness matrix is somewhat unique in the new model. Non-zero terms are not limited to a narrow band along the diagonal, but are spread all over the matrix. This is due to the following: (1) two different types of nodes, ring nodes and point nodes, are combined in a single analysis; and (2) a locally non-axisymmetric geometry creates a coupling of the Fourier harmonic coefficients of the rotational elements. Yet, the matrix still contains many zero terms that are scattered and that must be considered for numerical efficiency. In this paper a solution algorithm that is effective in this situation is suggested. Also, some numerical examples are presented to demonstrate the usage and the capability of the new model. Examples which show the accuracy of the new model have been presented in reference 4.

#### ROTATIONAL SHELL ELEMENT

The geometry of this element is described by the middle-surface configuration and the corresponding thickness of the shell. The middle surface is described by the specification of the meridional curve in a cylindrical coordinate system ( $r$ ,  $\theta$ , and  $z$ ), and the thickness is a function of a meridional parameter since the element is axisymmetric by definition (Figure 3a). Thus, the geometric data for a nodal circle, which is on the middle surface, are the two coordinates ( $r$  and  $z$ ) and the thickness of the shell at the nodal circle. As long as an adjacent element has a rotational boundary with the same coordinates,  $r$  and  $z$ , the two elements are geometrically compatible.

Being based on a thin shell theory, this element ignores normal strains acting on planes parallel to the middle surface. Transverse shear strains, on the other

hand, are included by the use of independent rotational degrees of freedom, i.e., rotations of a normal to the undeformed middle surface about the two tangent lines along the principal directions of the surface. Therefore, this element requires only  $C^0$  continuity. Since the displacements of any point on the shell can be uniquely defined by the corresponding middle surface translations and the rotations of the normal (Figure 3b), a displacement vector on a nodal circle has five components: three curvilinear components of the translation ( $u_\phi$ ,  $u_\theta$ ,  $u_n$ ) and two rotational components of the normal ( $\beta_\phi$  and  $\beta_\theta$ ) about the circumferential and the meridional directions, respectively. The variation of each of the five displacement components along the nodal circle is expressed by

$$\begin{Bmatrix} u_\phi \\ u_\theta \\ u_n \\ \beta_\phi \\ \beta_\theta \end{Bmatrix} = \sum_{j \geq 0} \begin{Bmatrix} u_\phi^j \cos j\theta \\ u_\theta^j \sin j\theta \\ u_n^j \cos j\theta \\ \beta_\phi^j \cos j\theta \\ \beta_\theta^j \sin j\theta \end{Bmatrix} + \sum_{j < 0} \begin{Bmatrix} -u_\phi^j \sin j\theta \\ -u_\theta^j \cos j\theta \\ -u_n^j \sin j\theta \\ -\beta_\phi^j \sin j\theta \\ -\beta_\theta^j \cos j\theta \end{Bmatrix} \quad (1)$$

where  $u_\phi^j$ ,  $u_\theta^j$ , etc. are the unknown,  $j^{\text{th}}$  harmonic coefficients for the node.

#### GENERAL SHELL ELEMENT

This element is patterned after the super-parametric element developed by Ahmad et al. [5] with the reduced integration technique by Zienkiewicz et al. [6]. The only difference is the use of *cylindrical* coordinates ( $r$ ,  $\theta$ , and  $z$ ) for the description of the geometry, instead of *rectangular* cartesian coordinates ( $x$ ,  $y$ , and  $z$ ) which are employed by the 'Ahmad' element. The adaptation of the cylindrical coordinates has twofold advantages: (1) it allows a better representation of the basically axisymmetric geometry of the shell; and (2) it facilitates a simpler formulation when this element is combined with the rotational element in a single analysis.

To define the geometry, two vectors must be specified at each node which is located only on the middle surface (Figure 4a). One is the position vector of the node with three components  $r_i$ ,  $\theta_i$ , and  $z_i$ , where the subscript  $i$  designates the node  $i$ . The other is the normal vector,  $\vec{v}_{3i}$ , which is directed toward the positive normal direction of the shell, and whose magnitude represents the thickness of the shell at the point. Establishing local curvilinear coordinates  $\xi$ ,  $\eta$ , and  $\zeta$  for each element, the geometry of the element is equated as

$$\begin{Bmatrix} r \\ \theta \\ z \end{Bmatrix} = \sum_i N_i(\xi, \eta) \begin{Bmatrix} r_i \\ \theta_i \\ z_i \end{Bmatrix} + \sum_i N_i(\xi, \eta) \frac{\xi}{2} \tilde{V}_{3i} \quad (2)$$

where  $N_i(\xi, \eta)$  is the shape function for the node  $i$ .

Strains and stresses are defined with the same assumptions as those for the rotational shell element, i.e., the normal stresses are neglected and the transverse shear strains are included. Thus, this element also has five degrees of freedom at each node (Figure 4b). They are the three cartesian components of the translation ( $u_i$ ,  $v_i$  and  $w_i$ ) and two rotational components of the vector  $\tilde{V}_{3i}$  ( $\alpha_i$  and  $\beta_i$ ) about the positive circumferential and the negative meridional directions of the shell, respectively. Erecting two unit vectors,  $V_{1i}$  and  $V_{2i}$ , such that they are parallel to the positive meridional and the positive circumferential directions, respectively, displacements are expressed in the global cartesian coordinates as

$$\begin{Bmatrix} u \\ v \\ w \end{Bmatrix} = \sum_i N_i \begin{Bmatrix} u_i \\ v_i \\ w_i \end{Bmatrix} + \sum_i N_i \xi \frac{t_i}{2} [\hat{V}_{1i} \hat{V}_{2i}] \begin{Bmatrix} \alpha_i \\ \beta_i \end{Bmatrix} \quad (3)$$

where  $t_i$  is the thickness of the shell at the node  $i$ .

#### TRANSITIONAL ELEMENT

This element borders on a rotational element on one side, on a general element on the opposite side, and joins with other transitional elements on the remaining two sides. In this mesh arrangement, the transitional element must provide continuity of displacement fields as well as geometry with adjoining elements. Suppose that a general shell element were used in place of the transitional shell element. Then, the compatibility is automatically achieved on three sides of the element, but is not satisfied on the remaining boundary with the rotational element. If a modification is made such that the element is also compatible with the rotational element on the remaining boundary, all of the continuity requirements are fulfilled. The transitional element achieves this by adapting a line node which extends all along the common boundary with the rotational element and which can accommodate any function along the line. The line node possesses three subnodes, one at each end of the line and a moving node which may be located anywhere on the line (Figure 5). As a set, these three nodes can represent any function that the adjoining element may impose on the common boundary. Details of the development of the line node as well as its shape function are given in reference 4. On the remaining three sides, the transitional element has the same point nodes, with the identical shape functions, as those of the general element.

Once the shape functions are developed, the remaining formulation follows similar steps as those of the general shell element. Thus, the position and the normal vectors are specified at each nodal point, including the moving node; the geometry is defined by equation (2); and displacements are expressed by equation (3). There are, however, some differences in applying these equations. First, it should be noted that  $\theta_i$  for the moving node in equation (2) is a function of the coordinates, instead of a constant, since the node itself can move along the boundary. Therefore, the nodal value of the moving node must also be differentiated when the Jacobian matrix is computed from the equation. Second, cartesian displacement components ( $u$ ,  $v$ , and  $w$ ) are used for the transitional and general element, while curvilinear displacement components ( $u_\phi$ ,  $u_\theta$  and  $u_n$ ) are used for the rotational element. Thus, a coordinate transformation is necessary along the line node. Furthermore, the generalized coordinates for the transitional element are physical displacement components at each node while those for the rotational element are Fourier harmonic coefficients along each nodal circle. (See equations (1) and (3).) Thus, at each subnode, the nodal degrees of freedom must be related to the harmonic degrees of freedom by

$$\begin{Bmatrix} u_i \\ v_i \\ w_i \end{Bmatrix} = [T_i] \sum_j \begin{bmatrix} \cos j\theta_i & 0 & 0 \\ 0 & \sin j\theta_i & 0 \\ 0 & 0 & \cos j\theta_i \end{bmatrix} \begin{Bmatrix} u_\phi^j \\ u_\theta^j \\ u_n^j \end{Bmatrix} \quad (4)$$

and

$$\begin{Bmatrix} \alpha_i \\ \beta_i \end{Bmatrix} = \sum_j \begin{bmatrix} \cos j\theta_i & 0 \\ 0 & \sin j\theta_i \end{bmatrix} \begin{Bmatrix} \beta_\phi^j \\ \beta_\theta^j \end{Bmatrix} \quad (5)$$

where  $\theta_i$  is the  $\theta$  coordinate of the node  $i$  and  $[T_i]$  is the matrix of coordinate transformation at the node  $i$  as defined in reference 4. In equations (4) and (5), only the first terms of equation (1) are included for simplicity. If the second terms of equation (1) are used as harmonic degrees of freedom, they can be included in equation (4) and (5) in a similar form.

#### GLOBAL SYSTEM

The global stiffness matrix of a linear shell of revolution analyzed only with rotational elements has two distinctive characteristics: (1) all off-diagonal terms that relate one harmonic to the others are zeros; and (2) the bandwidth is very small in comparison to the total number of degrees of freedom of the structure. As an example, if three harmonics are considered in an analysis of a cylindrical shell with eight nodes (seven elements), the stiffness matrix is in the banded form shown in figure 6. In the figure, each box is also a sub-matrix whose side dimension is the number of degrees of freedom per node per harmonic, i.e., five or



three depending on the harmonic. A shaded box contains non-zero values, and an unshaded box, zeros. The first characteristic is due to the fact that a shell of revolution with a loading whose circumferential distribution can be expressed in terms of a Fourier harmonic deforms such that the displacement fields can be completely described in terms of the same Fourier harmonic. If the global stiffness matrix in figure 6 is subdivided for each harmonic in each direction to form nine submatrices, all off-diagonal submatrices that couple one harmonic with the others are null matrices. This contracts the global stiffness matrix into three independent matrices, one for each harmonic. Thus, instead of considering all harmonics simultaneously, each is solved separately, involving only a small number of unknowns at one time. Superposition is then used to combine the harmonic analyses for a general loading case. The second characteristic is due to the fact that a rotational element has nodal circles, instead of nodal points. Since any internal node has only two neighboring nodes (except in the case of a branched shell), the semi-bandwidth includes the nodal degrees of freedom of only two nodes (Figure 6).

The small bandwidth property is destroyed when general as well as transitional shell elements are combined with rotational shell elements. Since there would be several transitional elements along the circumference of a shell, a nodal circle would have many neighboring point nodes. Consequently, all off-diagonal terms in the stiffness matrix that relate the nodal circle with adjacent point nodes would have non-zero values. As an example, if the general and the transitional elements are introduced between the fourth and the fifth nodal circles of the example of figure 6, the global stiffness matrix assumes the form of figure 7. In the figure, all point nodes are shown to be coupled with each other as well as with the fourth and the fifth nodal circles in each harmonic. These newly shaded areas may not be completely populated with non-zero values, because actual coupling of one node with the other depends on the mesh arrangement. However, it is immaterial in this context.

When a shell is geometrically non-axisymmetric, the off-diagonal terms that relate one harmonic with the others in the global stiffness matrix may no longer be zeros. For example, if the shell in figure 7 has a non-axisymmetric geometry between the fourth and the fifth nodal circles, the form of the resulting stiffness matrix is as shown in figure 8. In this example, all harmonics are coupled through the fourth and the fifth nodal circles. If the deviation is not confined within the bounds of these two nodal circles, more coupling terms would appear in the stiffness matrix. In this finite element model, however, any deviation is described by the general and the transitional shell elements that are confined by two nodal circles. Therefore, the stiffness matrix would be similar to the one shown in figure 8. Since this matrix does not possess the two desirable characteristics of rotational elements previously cited, a solution method that is efficient for the analysis of shells of revolution may not be applicable. Yet, there are definite similarities between the two matrices in figures 6 and 8, i.e., the two matrices are in the same form except for the degrees of freedom in the region of the deviation. Taking advantage of this similarity, the solution is carried out in three steps:

- (1) Substructuring of the region of the general and the transitional shell elements and subsequent condensation of the degrees of freedom of point nodes, marked "P" in figure 8.
- (2) Condensation of uncoupled harmonic degrees of freedom for each harmonic, marked "UH."
- (3) Simultaneous solution of coupled harmonic degrees of freedom for all harmonics, marked "CH."

In the above procedure, the first and the second steps are interchangeable.

Although the presence of the point nodes creates, in the global stiffness matrix, several off-diagonal blocks that are filled with non-zero values, these blocks tie the point nodes with only two nodal circles. Any remaining off-diagonal blocks that connect the point nodes with any other nodal circles are still null. In order to avoid unnecessary numerical effort in dealing with many zero terms in the global stiffness matrix, the region between the two nodal circles is taken as a substructure. The stiffness matrix of the substructure consists of the portions of the global stiffness matrix that are marked "P" and "CH" in figure 8. Since all of the point nodes are internal nodes of the substructure, their degrees of freedom, marked "P" in the figure, may be eliminated by kinematic condensation at the substructure level. The stiffness matrix of the substructure after condensation contains only the harmonic degrees of freedom of the two external nodal circles, marked "CH" in the figure. Thus, the global stiffness matrix that is assembled with this reduced matrix for the substructure assumes a much simpler form, containing only harmonic degrees of freedom (Figure 9).

The stiffness matrix in the form of figure 9 must now be considered. While the matrix is narrowly banded along the diagonal, it also has non-zero terms scattered off the diagonal due to the geometric non-axisymmetry. Since these off-diagonal terms couple all harmonics, separate harmonic analyses are not possible. However, the couplings are effected only through the two nodal circles that bound the region of the deviation. This property may be advantageously exploited if the uncoupled harmonic degrees of freedom, marked "UH" in figure 9, are eliminated first. In other words, separate harmonic analyses are partially carried out, so that the global stiffness matrix as shown in figure 9 is never assembled in the actual calculation. Instead, the stiffness matrix for each harmonic, i.e., the submatrices along the diagonal of figure 9, is computed. Since the uncoupled harmonic degrees of freedom are eligible to be eliminated without considering any other harmonics, they are eliminated at each harmonic level. This leaves only the degrees of freedom of the two nodal circles, marked "CH" in the figure, for each harmonic. When all harmonics are assembled after this partial harmonic condensation, the global stiffness matrix contains only the coupled harmonic degrees of freedom (Figure 10).

The stiffness matrix of figure 10 is densely populated with non-zero terms even off the diagonal. Any standard solution method of simultaneous linear equations will yield all the harmonic degrees of freedom of the two nodal circles, i.e., the Fourier coefficients of the displacements along the nodal circles. Once the harmonic degrees of freedom of the two nodal circles are found, the uncoupled harmonic degrees of freedom may be computed by back-substitution which may be carried out individually for each harmonic. Likewise, the back-substitution to find the displacements of the point nodes is carried out at the substructure level. This is a standard procedure that is well explained in many texts [7,8], and will not be repeated here.

#### NUMERICAL EXAMPLE

An infinitely long cylinder with a circular cutout has been analyzed by Van Dyke [9] using a shallow shell theory. Key [10] studied a long cylinder with a circular cutout (Figure 11) under axial tension and compared the results with those of Van Dyke to demonstrate the capability of his newly developed quadrilateral finite element. In this paper, the same shell used by Key is treated using the mesh shown in figures 11 and 12. Taking advantage of the symmetry about  $Z = 0$ , only one-half of the length of the shell is considered (Figure 11), while the symmetry about  $\theta = 0$  is utilized in the mesh of the substructure (Figure 12).

Since a local deviation from the axisymmetry couples all Fourier harmonics, an infinite number of harmonic terms must theoretically be included as degrees of freedom of rotational elements. In other words, an infinite series is necessary to express the displacements of the rotational elements. However, a good approximation can be obtained with only a limited number of Fourier harmonics. Figure 13 shows stresses at a few key points on the shell as the number of harmonic terms included in the analysis is increased. The harmonic terms included in each analysis are the smallest numbers possible, i.e.,  $j = 0$  through  $n-1$ , where  $j$  is the Fourier harmonic used and  $n$  is the truncation limit for the harmonics included in the analysis. Though the stresses change initially as the number  $n$  is increased (Figure 13), values stabilize fairly rapidly, i.e., when  $n = 12$  in this example. It should be noted at this time that a larger value of  $n$  would be required to represent the displacements of rotational elements as the length of the substructure is decreased, and vice versa. This is due to the fact that the effect of the geometric deviation is most severe in the immediate vicinity of the deviation.

The results of the analysis when 12 harmonics are included ( $n = 12$ ) are shown in Table 1 along with those of Van Dyke [9] and Key [10]. In Table 1,  $\sigma$  is the membrane stress,  $\sigma_b$  is the bending part, and  $\sigma_\infty$  is the membrane stress at infinity. It should be noted that the new finite element model requires only approximately one-quarter the number of degrees of freedom of the conventional finite element model to obtain comparable results. This translates into an enormous savings in computing time when one considers that the CPU time required to solve simultaneous equations is nominally a cubic function of the number of equations.

### CONCLUSIONS

A finite element model that is suitable for analyzing shells of revolution with arbitrary local deviations was developed. The model combines rotational shell elements and general shell elements in a single analysis by the use of transitional elements. The coupling of Fourier harmonics due to the loss of geometric symmetry is treated efficiently by the substructuring technique and by partially separate harmonic analyses. The rather complicated solution procedure of the new model is justified by the efficiency demonstrated.

The technique may be used in the analysis of pressure vessels with cutouts or pipe connections, or for shells with construction or manufacturing imperfections. Shells with locally defective material may also be analyzed with the same model. In addition to the geometric and/or material non-axisymmetry of the shells, the model can be used for the analysis of perfectly axisymmetric shells, but with concentrated loads. The representation of concentrated loads by Fourier harmonic series generally requires so many terms that precise analysis of such a loading by rotational elements only is often not economical.

### REFERENCES

1. P. K. Basu and P. L. Gould, "SHORE-III, Shell of Revolution Finite Element Program - User's Manual," Research Report No. 49, Structural Division, Washington University, St. Louis, MO, September 1977.
2. P. K. Basu and P. L. Gould, "SHORE-III, Shell of Revolution Finite Element Program - Theoretical Manual," Research Report No. 48, Structural Division, Washington University, St. Louis, MO, September, 1977.

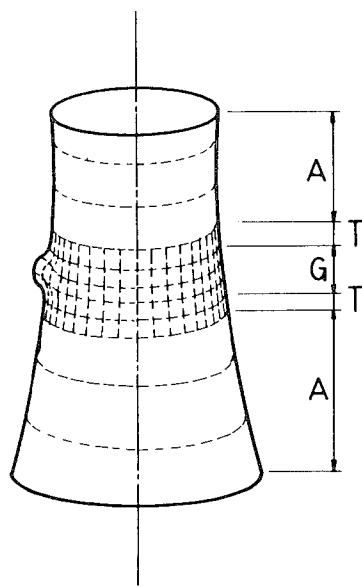
3. K. J. Han and P. L. Gould, "Quadrilateral Shell Element for Rotational Shells," Engineering Structures, Vol. 4, pp. 129-131, April 1982.
4. K. J. Han and P. L. Gould, "Line Node and Transitional Shell Element for Rotational Shells," International Journal for Numerical Methods in Engineering, accepted for publication.
5. S. Ahmad, B. M. Irons and O. C. Zienkiewicz, "Analysis of Thick and Thin Shell Structures by Curved Finite Elements," International Journal for Numerical Methods in Engineering, Vol. 2, pp. 419-451, 1970.
6. O. C. Zienkiewicz, R. L. Taylor and J. M. Too, "Reduced Integration Technique in General Analysis of Plates and Shells," International Journal for Numerical Methods in Engineering, Vol. 3, pp. 275-290, 1971.
7. O. C. Zienkiewicz, "The Finite Element Method," 3rd Edition, McGraw-Hill, New York, 1977.
8. R. D. Cook, "Concepts and Applications of Finite Element Analysis," 2nd Edition, John Wiley and Sons, Inc., New York, 1981.
9. P. Van Dyke, "Stresses about a Circular Hole in a Cylindrical Shell," AIAA Journal, Vol. 3, No. 9, pp. 1733-1742, September 1965.
10. S. W. Key, "The Analysis of Thin Shells with a Doubly Curved Arbitrary Quadrilateral Finite Element," Computers and Structures, Vol. 2, pp. 637-673, 1972.

TABLE 1. STRESSES FOR A CYLINDER UNDER AXIAL TENSION  
WITH A CIRCULAR CUTOUT

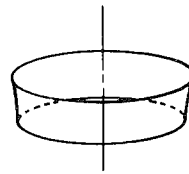
	Van Dyke [9]	Key [10] Coarse mesh (1534 d.o.f.)	Key [10] fine mesh (5301 d.o.f.)	New Model (1447 d.o.f.)
$\sigma_m/\sigma_\infty$ @A	3.60	3.44 (4.6%)	3.59 (0.3%)	3.66 (1.60%)
$\sigma_b/\sigma_\infty$ @A	$\pm 0.59$	$\pm 0.55$ (7.4%)	$\pm 0.55$ (7.4%)	$\pm 0.554$ (6.06%)
$\sigma_m/\sigma_\infty$ @B	-1.25	-1.08 (15.7%)	-1.18 (5.4%)	-1.20 (3.87%)
$\sigma_b/\sigma_\infty$ @B	$\pm 0.809$	$\pm 0.806$ (0.4%)	$\pm 0.812$ (0.4%)	$\pm 0.795$ (1.71%)

A is at the side of the hole at  $r\theta = 25.4$ ,  $z = 0.0$

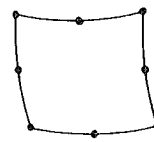
B is at the top of the hole at  $r\theta = 0.0$ ,  $z = 25.4$



(a) Combined mesh.



(b) Rotational shell element.



(c) General shell element.

Figure 1.- Finite element mesh using different elements.

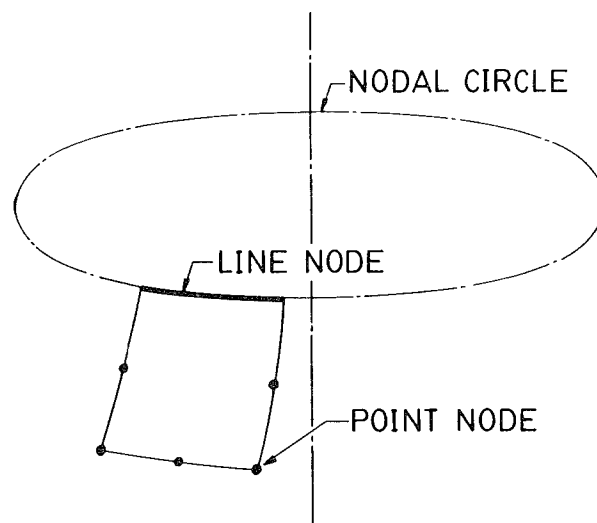
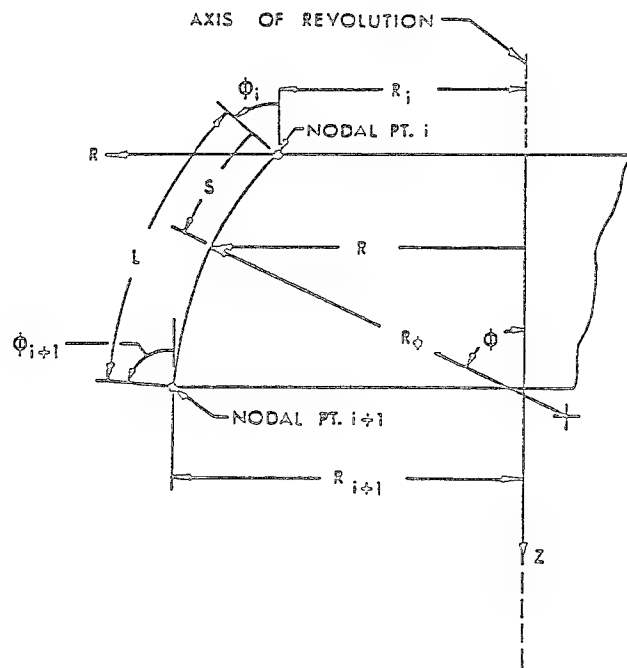
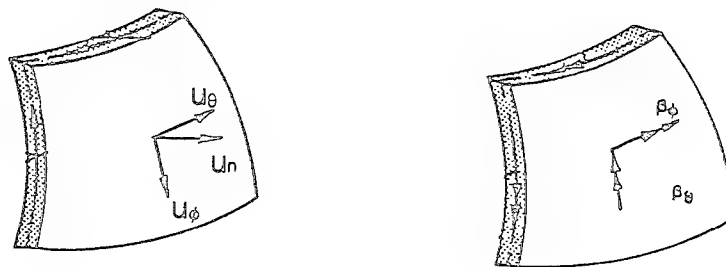


Figure 2.- Transitional shell element.

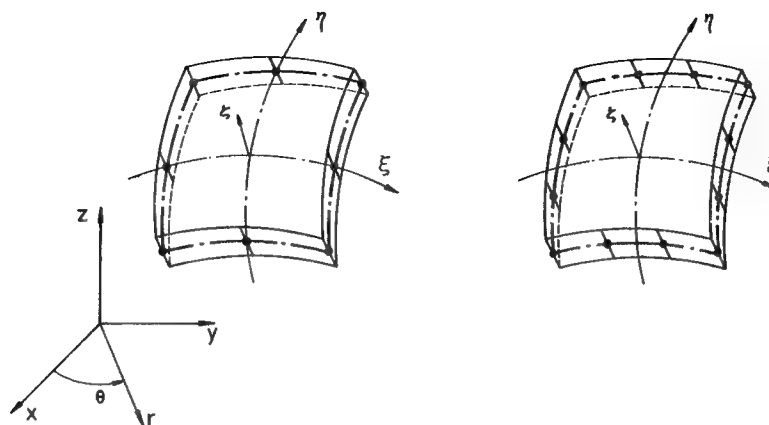


(a) Geometry.

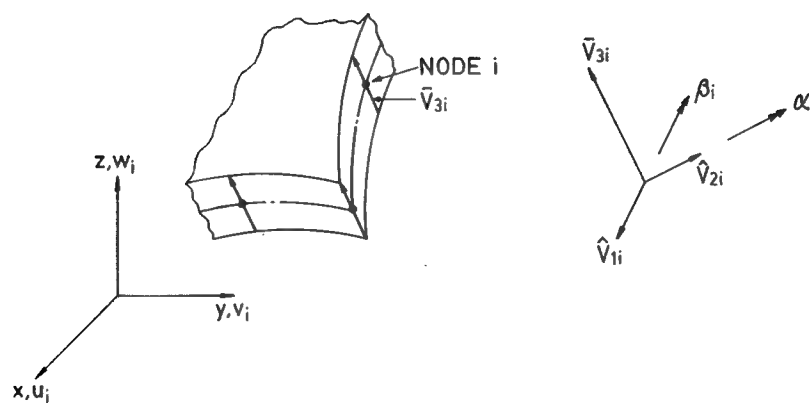


(b) Displacement components.

Figure 3.- Rotational shell element.



(a) Geometry.



(b) Displacement components.

Figure 4.- General shell element.



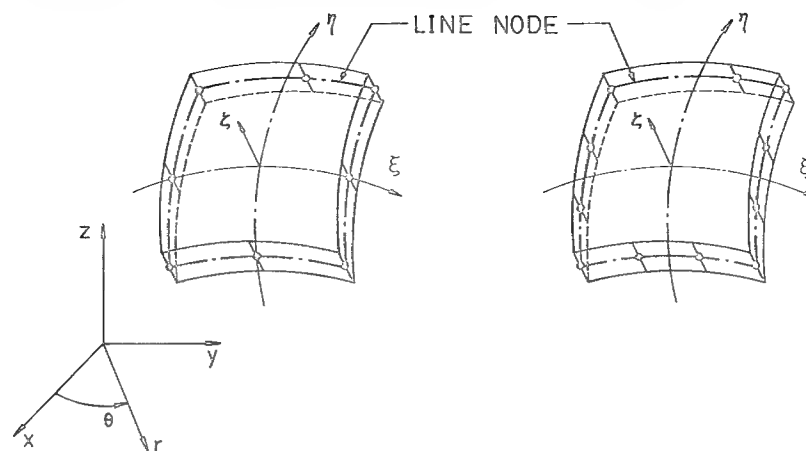


Figure 5.- Transitional shell element.

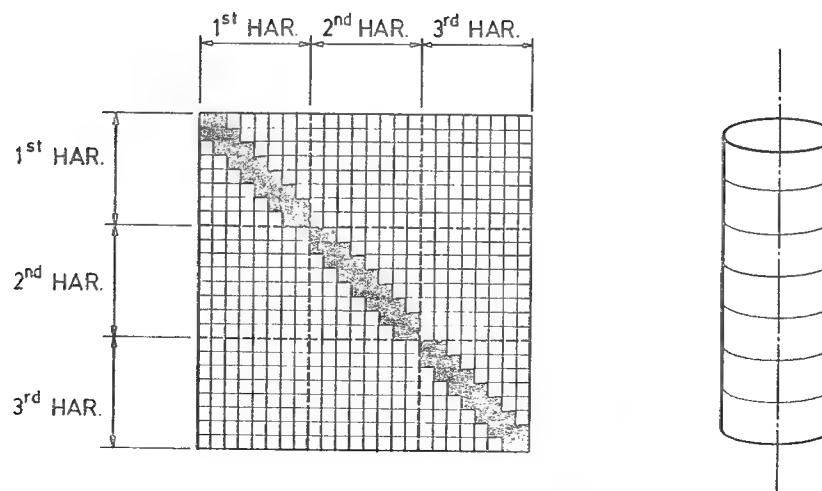


Figure 6.- Stiffness matrix using rotational shell elements only.

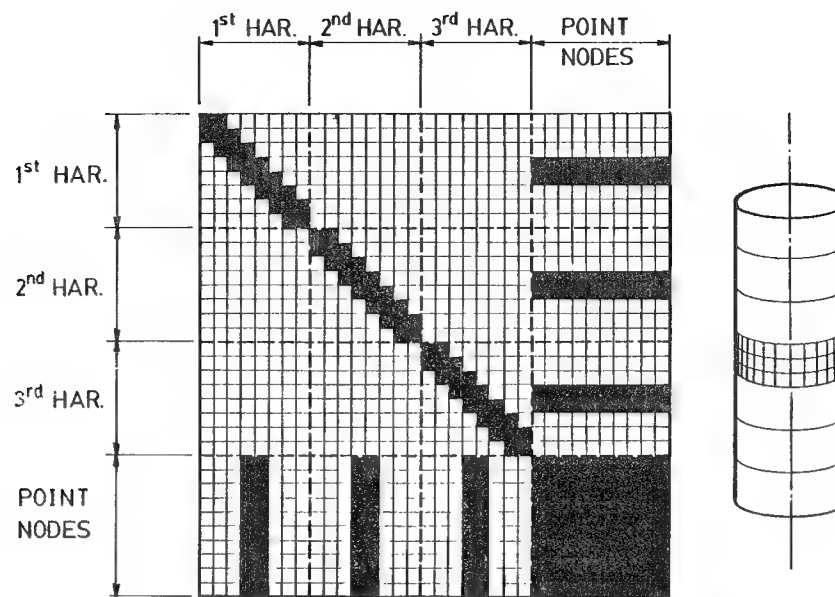


Figure 7.- Stiffness matrix using rotational, general, and transitional shell elements.

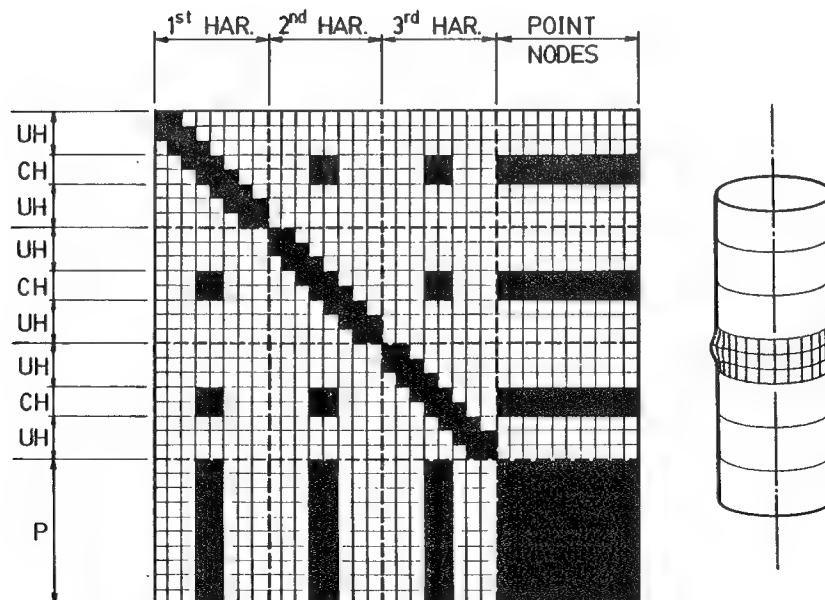


Figure 8.- Stiffness matrix of shell of revolution with a local deviation.

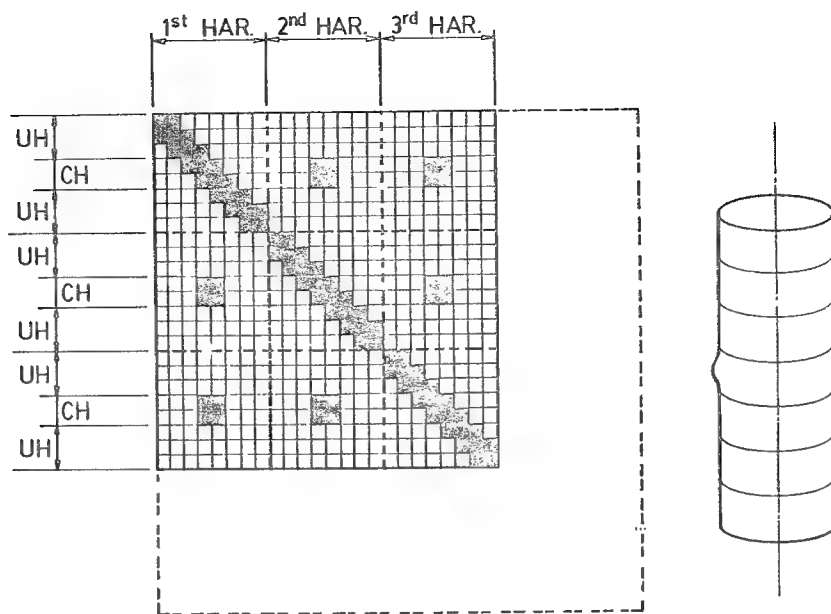


Figure 9.- Stiffness matrix after substructuring.

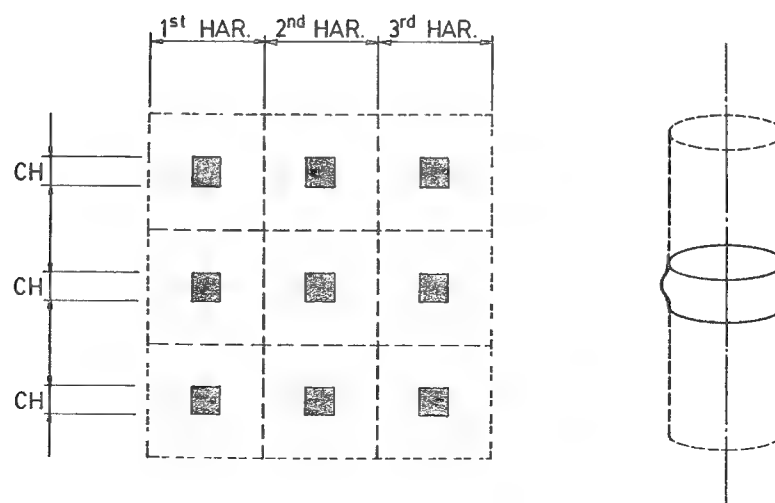


Figure 10.- Stiffness matrix after separate harmonic analysis.

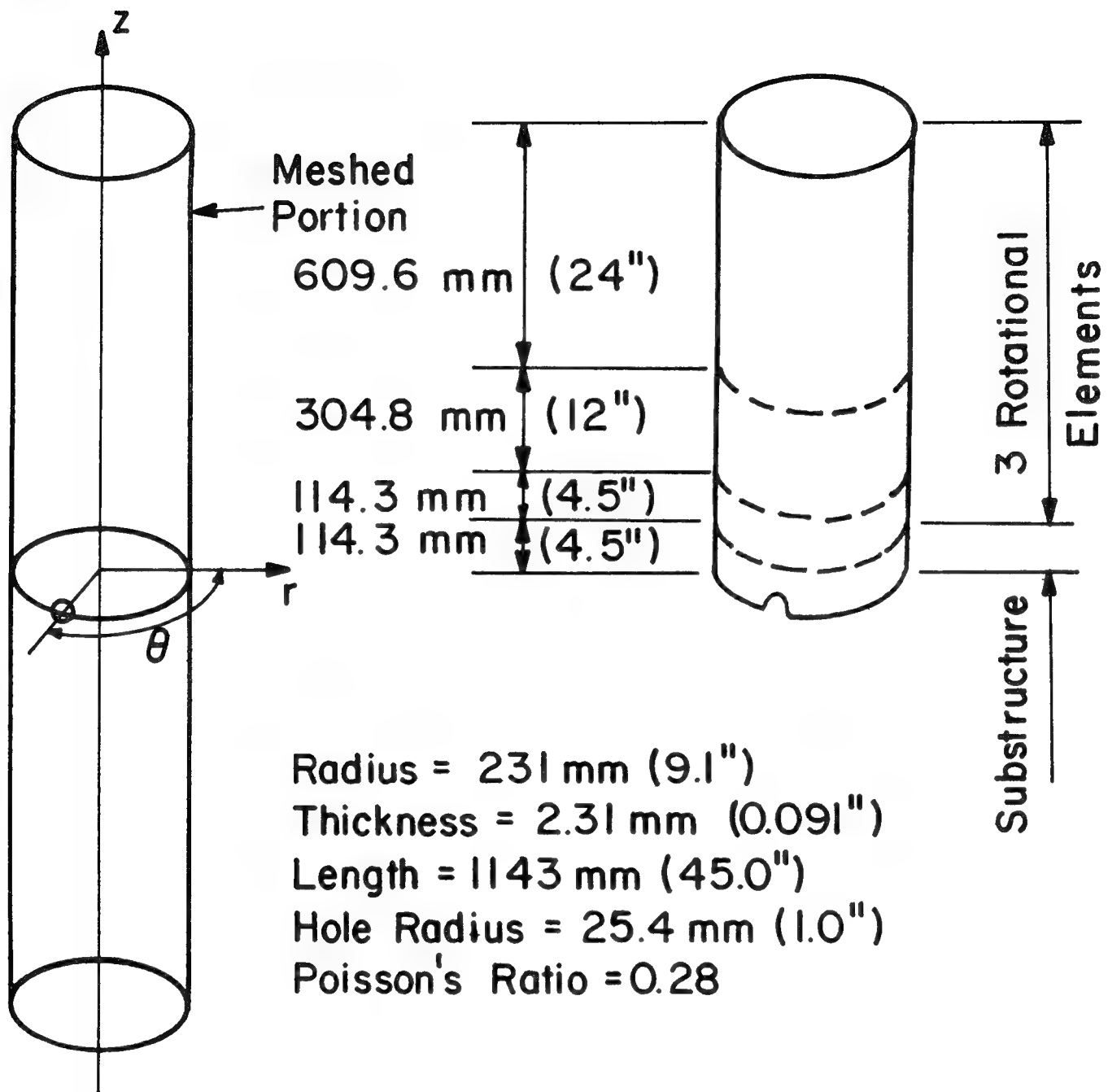


Figure 11.- Cylinder with circular cutout and finite element mesh.

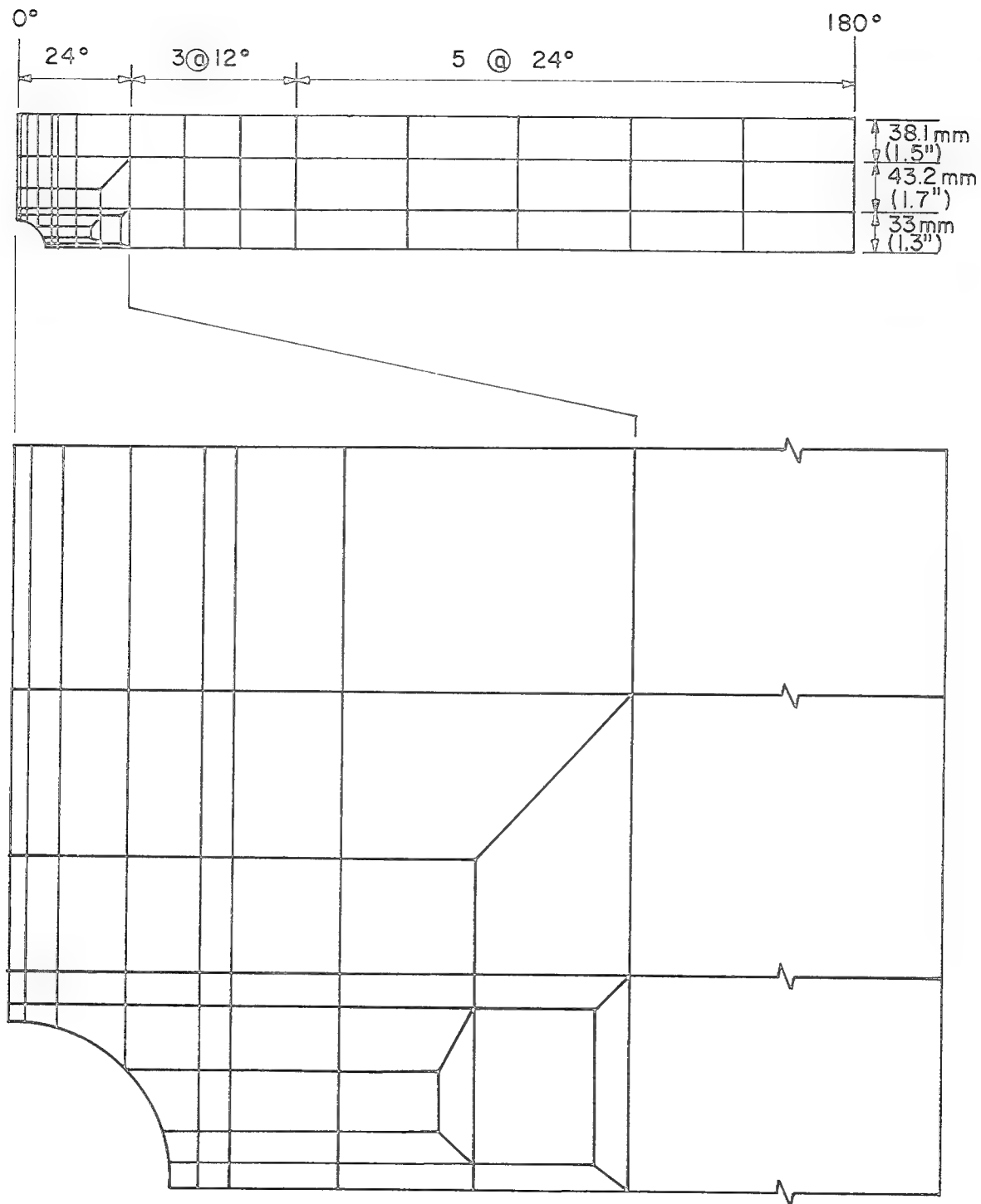
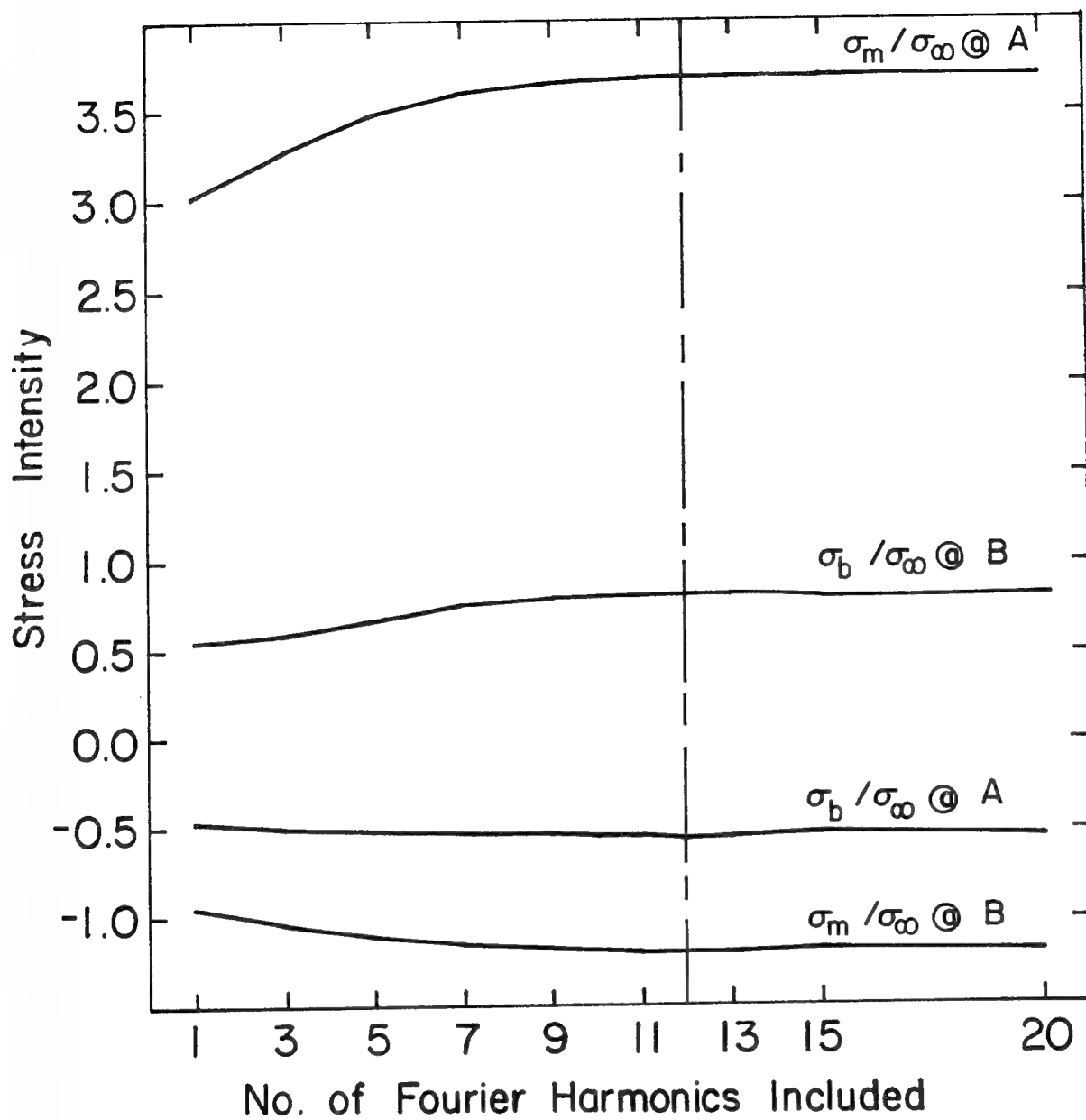


Figure 12.- Finite element mesh of substructure.



A is at the side of the hole at  $r\theta = 25.4$ ,  $z = 0.0$   
 B is at the top of the hole at  $r\theta = 0.0$ ,  $z = 25.4$

Figure 13.- Stress intensity around hole.

# SYNTHESIS OF FRAMEWORKS UNDER MULTILEVEL PERFORMANCE CONSTRAINTS<sup>1</sup>

Donald E. Grierson and Thomas C.W. Chiu  
Solid Mechanics Division  
University of Waterloo, Waterloo, Ontario, Canada

## SUMMARY

A method is presented for the minimum weight design of practical planar frameworks under both service and ultimate-loading conditions. Acceptable elastic stresses and displacements are ensured at the service-load level while, simultaneously, adequate safety against plastic collapse is ensured at the ultimate-load level. The features of the design method are illustrated for an industrial steel-mill building.

## INTRODUCTION

This study addresses the problem of efficiently designing practical engineering frameworks for proper performance at a number of distinctly different loading levels. A conventional approach to design in this regard has been to separately proportion the structure for proper performance at one loading level, and to then modify the resulting design to satisfy requirements at one or more other loading levels of concern. For multistory steel frames, for example, several procedures have been developed whereby a plastic design is initially conducted to ensure adequate safety against plastic collapse under specified ultimate loads, and then the member proportions are modified to satisfy elastic stress and displacement limitations under specified service loads (e.g., ref. 1). A major drawback to such an approach, however, is that design decisions at one loading level must be made in the absence of explicit information as to their consequences at the other loading levels of concern. As such, previous design gains are very often unnecessarily negated and, at best, a cumbersome iterative procedure is required to achieve a reasonably efficient design.

A recent study considered thin-wall structures composed of bar, membrane and/or shear-panel elements and developed a minimum weight design method whereby performance constraints are satisfied *simultaneously* at both a specified service-load level and at a specified ultimate-load level (ref. 2). Specifically, for proportional static loading, the design method ensures acceptable elastic stresses and displacements under specified service loads while, at the same time, ensuring adequate post-elastic strength reserve of the structure under specified ultimate loads. In other words, a serviceable design is found cognizant of the margin of safety against failure in a plastic mechanism mode. The method represents an extension to the conventional 'limit states design' philosophy that essentially defines 'failure' as being the onset of 'first-yielding' anywhere in the structure (e.g., ref. 3). This latter failure definition is somewhat artificial for hyperstatic structures and, in contrast to that considered in ref. 2 and herein, provides little information as to what the real margin of safety is against actual catastrophic failure.

<sup>1</sup>Research sponsored by the Natural Sciences and Engineering Research Council (Canada) under Grant No. A5306.

The minimum weight design method developed in ref. 2 involves an iterative process having the following essential features: 1) for a given design (e.g., the initial 'trial' design), sensitivity analysis techniques are employed to approximate the performance constraints as linear functions of the design variables; 2) optimization techniques are applied to find an improved (lower weight) design; 3) the constraints are updated for the next weight optimization, and the process is repeated until weight convergence occurs after a number of design stages.

The present study extends the described design method to planar frameworks composed of beam and column elements under combined axial and bending stresses. It is shown that the iterative (re)analysis/(re)design scheme developed for thin-wall structures (ref. 2) is directly applicable for this type of structure as well. It is shown specifically that the stiffness and strength properties of the elements may be approximated as linear functions of the sizing variables so as to permit each weight optimization to be conducted using a 'generalized optimality criteria' technique (refs. 2,4). And, it is also shown that consistent updating procedures may be applied so as to ensure a monotonically converging iteration history through to the final minimum weight design.

The notation used in the paper is as follows: an underscored 'bar' ( $\_$ ) denotes a matrix or vector; a superimposed 'tilde' ( $\sim$ ) denotes the transpose of a matrix or vector; a superimposed 'dot' ( $\dot{\phantom{x}}$ ) denotes rate quantities.

#### THE DESIGN PROBLEM

All loads are taken to be static, and the specified service loads are proportionally related to the specified ultimate loads. The framework is discretized into an assemblage of  $n$  prismatic elements, which may be of a variety of member types (e.g., HSS columns, WF beams, open-channel bracing struts, etc.). The design variable for each element  $i$  is taken to be its cross-section area  $a_i$ . In its general form, the minimum weight design problem is expressed as

$$\text{Minimize: } \sum_{i=1}^n w_i a_i \quad (1a)$$

$$\text{Subject to: } \delta_j \leq \delta_j \leq \hat{\delta}_j \quad (j = 1, 2, \dots, d) \quad (1b)$$

$$\sigma_k \leq \sigma_k \leq \hat{\sigma}_k \quad (k = 1, 2, \dots, s) \quad (1c)$$

$$\alpha_m \leq \alpha_m \leq \hat{\alpha}_m \quad (m = 1, 2, \dots, p) \quad (1d)$$

$$a_i \leq a_i \leq \hat{a}_i \quad (i = 1, 2, \dots, n) \quad (1e)$$

where: Eq. (1a) defines the weight of the structure ( $w_i$  is the weight coefficient for element  $i$ ); Eqs. (1b) define the  $d$  service-load constraints on displacements  $\delta_j$ ; Eqs. (1c) define the  $s$  service-load constraints on stresses  $\sigma_k$ ; Eqs. (1d) define the  $p$  ultimate-load constraints on plastic collapse-load factors  $\alpha_m$ ; and Eqs. (1e) are side-constraints on element sizes  $a_i$  to satisfy fabrication and technological requirements. (Quantities with under- and super-imposed 'hat'  $\wedge$  denote specified lower- and upper-bounds, respectively.)



In their present form, the performance constraints Eqs. (1b)-(1d) are 'implicit' functions of the design variables  $a_i$ . To facilitate implementation of the design method these constraints are reformulated as 'explicit' functions of the variables  $a_i$ . To this end, the stiffness-size and strength-size relationships for the elements are first established.

### STIFFNESS-SIZE RELATIONSHIP

For the case of combined axial and bending stresses, the (global) stiffness matrix for a planar element  $i$  can be expressed as

$$\underline{K}_i = \underline{K}_i^A a_i + \underline{K}_i^B I_i \quad (2)$$

where  $\underline{K}_i^A$  and  $\underline{K}_i^B$  are constant matrices that correspond to the axial and bending stiffness properties of the element, respectively, and  $I_i$  is the cross-section moment of inertia.

In general, the relationship between the moment of inertia  $I_i$  and the cross-section area  $a_i$  for element  $i$  can be expressed as

$$I_i = k_i a_i^x \quad (3)$$

where the constant  $k_i$  depends on the shape of the element cross-section (e.g., hollow-box, wide-flange, etc.), and the exponent  $x$ , often an integer, depends on the way the cross-section shape varies as the size varies. When  $x = 1$ , Eq. (3) refers to thin-walled elements of fixed overall cross section dimension (e.g., hollow tubes of fixed outside radius, open channels of fixed height and width, etc.). For  $x = 2$ , the cross section *uniformly* varies in size (i.e., maintains a constant shape). When  $x = 3$ , Eq. (3) refers to an element cross section for which the height varies while all other dimensions remain fixed. Other values for the exponent  $x$  are also possible (ref. 6). However, for the reason that is noted in the following section concerning the strength-size relationship for an element, the 'constant-shape' case is adopted herein (i.e.,  $x = 2$ ). As such, Eq. (3) becomes

$$I_i = k_i a_i^2 \quad (4)$$

(Formulae for the constant  $k_i$  in Eq. (4) are given in ref. 5 for a range of cross sections; e.g., see figure 1).

To facilitate the application of an efficient 'generalized optimality criteria' technique to conduct the weight optimization for each design stage (refs. 2,4), Eq. (4) is approximated as a *linear* function of the design variable  $a_i$ . Suppose that the cross-section area  $a_i$  has the known value  $a_i^0$  for a given design stage (e.g., the initial 'trial' design). Eq. (4) can then be expressed as the linear function

$$I_i = k_i (a_i^0) a_i = k_i^* a_i \quad (5)$$

where the constant  $k_i^*$  is such that Eq. (5) gives precisely the same value for the moment of inertia  $I_i$  as Eq. (4) when  $a_i = a_i^0$ .

From Eqs. (2) and (5), the stiffness matrix for element  $i$  can be expressed as the linear function

$$\underline{K}_i = \underline{K}_i^A a_i + \underline{K}_i^B k_i^* a_i = \underline{K}_i^* a_i \quad (6)$$

where  $\underline{K}_i^* = \underline{K}_i^A + \underline{K}_i^B k_i^*$  is a constant matrix (note that  $\underline{K}_i^* = \underline{K}_i^A$  for a bar element under axial stress alone, while  $\underline{K}_i^* = \underline{K}_i^B k_i^*$  for a flexural element under bending stress alone). Eq. (6) defines the 'stiffness-size' relationship prevailing for element  $i$  at the beginning of the design stage when  $a_i = a_i^0$ . The matrix  $\underline{K}_i^*$  is taken to prevail constant during the next weight optimization and, then, it is updated through Eq. (5) for the new cross-section area of element  $i$  found for the next design stage.

### STRENGTH-SIZE RELATIONSHIP

To facilitate the application of an efficient 'finite-incremental' plastic analysis technique to determine the 'critical' collapse mechanism for each design stage (refs. 5,7), a conservative (inscribed) piecewise-linear (PWL) yield criterion is adopted to govern the plastic behavior of each element under combined axial and bending stresses. For example, adopting intermediate yield-point vertices ( $\pm v_1, \pm v_2$ ) on the bisector axes of the four quadrants of the 'normalized' (non-dimensionalized) stress space, the 8-sided yield surface in figure 1 defines the 'normalized' PWL yield condition for a WF cross section under combined axial force  $N$  and bending moment  $M$ ; where  $N_p$  and  $M_p$  are the 'principal' plastic axial and bending capacities of the cross section, respectively, and the  $\underline{r}^N = [r_1^N, r_2^N, \dots, r_8^N]$  are the 'normalized' plastic capacities corresponding to the linear yield modes (orthogonal distances from the origin of the 'normalized' stress space for the cross section).

It is of interest to note that a 'normalized' yield condition (e.g., fig. 1a) has exactly the same form for all similar-shape cross sections (i.e., regardless of cross-section size). On the other hand, the form of the PWL yield condition in the 'actual' stress space for an element cross section depends on both the shape and the size of the cross section. If, however, the shape of the cross section is maintained constant as the size varies, the form of the yield condition is then only a function of the magnitudes of the 'principal' plastic capacities for the element. Exploitation of this fact significantly improves the computational efficiency of the design process (refs. 5,8), which is the fundamental reason for adopting the 'constant-shape' assumption noted in the preceding section. (While resulting in less computational efficiency, other 'shape' assumptions can be readily adopted).

Adopting similar PWL yield conditions to govern plastic behavior at the two end-sections  $j$  and  $k$  of element  $i$ , the vector of plastic capacities corresponding to all linear yield modes in the 'actual' stress space for the element is

$$\underline{\tilde{R}}_i = [\underline{\tilde{R}}_j, \underline{\tilde{R}}_k] \quad (7)$$

where, for a 'constant-shape' cross section, the components of the subvectors  $\underline{R}_j = \underline{R}_k$  are fixed functions of the 'principal' plastic capacities for the element. For example, for the WF cross-section shape and 8-sided yield surface in figure 1,  $\underline{R}_j = \underline{R}_k = [r_1, r_2, \dots, r_8]$ , where

$$r_1 = r_4 = r_5 = r_8 = 0.545 N_{pi} M_{pi} / (0.2079 N_{pi}^2 + 0.2970 M_{pi}^2)^{0.5} \quad (8a)$$

$$r_2 = r_3 = r_6 = r_7 = 0.545 N_{pi} M_{pi} / (0.2970 N_{pi}^2 + 0.2079 M_{pi}^2)^{0.5} \quad (8b)$$

(Similar relationships as Eqs. (8) are given in ref. 5 for a number of other cross sections under combined axial force and bending moment).

The 'principal' plastic axial capacity  $N_{pi}$  of element  $i$  is a linear function of the cross-section area  $a_i$ , i.e.,

$$N_{pi} = \sigma_y a_i \quad (9)$$

where  $\sigma_y$  is the material yield stress. On the other hand, for a 'constant-shape' cross section, the 'principal' plastic bending capacity  $M_{pi}$  is related to  $a_i$  as

$$M_{pi} = m_i a_i^{1.5} \quad (10)$$

where the constant  $m_i$  depends on the shape of the cross section. (Formulae for the constant  $m_i$  in Eq. (10) are given in ref. 5 for a range of cross sections; e.g., see fig. 1). For the cross-section area  $a_i$  having a known value  $a_i^0$  at the beginning of any given design stage, Eq. (10) can be expressed as the linear function

$$M_{pi} = m_i (a_i^0)^{0.5} a_i = m_i^* a_i \quad (11)$$

where the constant  $m_i^*$  is such that Eq. (11) gives precisely the same value for  $M_{pi}$  as Eq. (10) when  $a_i = a_i^0$ .

Having Eqs. (9) and (11), the vector of plastic capacities  $\underline{R}_i$  can be expressed as a linear function of the design variable  $a_i$  for element  $i$  as

$$\underline{R}_i = \underline{R}_i^* a_i \quad (12)$$

where  $\underline{R}_i^*$  is a constant vector. For example, Eqs. (8) become from Eqs. (9) and (11),

$$r_1 = r_4 = r_5 = r_8 = 0.545 \sigma_y m_i^* a_i / (0.2079 \sigma_y^2 + 0.2970 m_i^{*2})^{0.5}$$

$$r_2 = r_3 = r_6 = r_7 = 0.545 \sigma_y m_i^* a_i / (0.2970 \sigma_y^2 + 0.2079 m_i^{*2})^{0.5}$$

(Note that  $\tilde{\underline{R}}_i^* = [\sigma_y, \sigma_y]$  for a bar element under axial stress alone, while  $\underline{R}_i^* = [m_i^*, m_i^*, m_i^*, m_i^*]$  for a flexural element under bending stress alone). Eq. (12) defines the 'strength-size' relationship prevailing for element  $i$  at the beginning of the design stage when  $a_i = a_i^0$ . The vector  $\underline{R}_i^*$  is taken to prevail constant during the next weight optimization and, then, it is updated through Eq. (11) for the new cross-section area of element  $i$  found for the next design stage.

## EXPLICIT SERVICE-LOAD CONSTRAINTS

Having the linear 'stiffness-size' relationship Eq. (6) for each element  $i$  ( $i=1,2,\dots,n$ ), the formulation of the explicit service-load constraints for each design stage can proceed exactly as for thin-walled structures (refs. 2,4). First, since displacements and stresses vary inversely with the sizing variables  $a_i$ , it is recognized that 'good' quality constraints are achieved by formulating them as explicit functions of the 'reciprocal' variables

$$x_i = \frac{1}{a_i} \quad (i = 1,2,\dots,n) \quad (13)$$

Then, first-order Taylor's series expansions and elastic sensitivity analysis based on 'virtual-load' or 'pseudo-load' techniques are employed to formulate each of the displacement and stress constraints Eqs. (1b) and (1c) as the 'explicit-linear' constraints

$$\hat{\delta}_j \leq \sum_{i=1}^n d_{ij}^{\circ} x_i \leq \hat{\delta}_j \quad \hat{\sigma}_k \leq \sum_{i=1}^n s_{ik}^{\circ} x_i \leq \hat{\sigma}_k \quad (14a,b)$$

where the superscript  $^{\circ}$  denotes quantities evaluated for the current design stage.

Based on, say, 'virtual-load' techniques, the displacement and stress sensitivity coefficients (gradients)  $d_{ij}^{\circ}$  and  $s_{ik}^{\circ}$  in Eqs. (14) are evaluated as

$$d_{ij}^{\circ} = \frac{1}{x_i^{\circ}} (\tilde{u}_j K_i u)^{\circ} \quad s_{ik}^{\circ} = \frac{1}{x_i^{\circ}} (\tilde{u}_k K_i u)^{\circ} \quad (15a,b)$$

where the (global) element stiffness matrix  $K_i^{\circ} = K_i^* a_i^{\circ}$  from Eq. (6) for  $a_i = a_i^{\circ}$ , and the various vectors of nodal displacements for the structure are found from elastic analyses as

$$\underline{u} = \underline{K}^{-1} \underline{P} \quad \underline{u}_j = \underline{K}^{-1} \underline{b}_j \quad \underline{u}_k = \underline{K}^{-1} \underline{t}_k, \quad (16a,b,c)$$

in which  $\underline{K} = \sum_{i=1}^n K_i$  is the structure stiffness matrix,  $\underline{u}$  is the vector of nodal displacements due to (each) applied load vector  $\underline{P}$ , and  $\underline{u}_j$  and  $\underline{u}_k$  are 'virtual' displacement vectors associated with 'virtual-load' vectors  $\underline{b}_j$  and  $\underline{t}_k$ , respectively.

The 'virtual-load' vectors in Eqs. (16b,c) are identified from

$$\delta_j = \tilde{b}_j u \quad \sigma_k = \tilde{t}_k U \quad (17a,b)$$

where  $\underline{b}_j$  is a specified vector that identifies the nodal displacement  $\delta_j$  of concern to the design, and  $\underline{t}_k$  is the row of the particular element stress matrix that is associated with the stress  $\sigma_k$  of concern to the design. Regardless of the type of structure, the vector  $\underline{b}_j$  remains constant throughout the iterative design process. As well, the vector  $\underline{t}_k$  is invariant for thin-walled structures (for a truss, e.g.,  $\underline{t}_k$  is row  $k$  of the structure topological matrix multiplied by Young's modulus and divided by the length of bar element  $k$ ). For a flexural structure, however, the vector  $\underline{t}_k$  is a function of the neutral-axis position for the element cross section associated with the

stress  $\sigma_k$ , and therefore it varies as the design changes over the iteration history. For a 'constant-shape' cross section, the position of the neutral axis  $y_i$  (the 'maximum' distance to the extreme fibers of the cross section) is related to the cross section  $a_i$  for flexural element  $i$  as

$$y_i = n_i a_i^{0.5} \quad (18)$$

(Formulae for the constant  $n_i$  in Eq. (18) are given in ref. 5 for a range of cross sections; e.g., see figure 1). Having Eq. (18), the vector  $\underline{t}_k$  is readily updated at the end of each design stage to account for the change in the neutral axis position for element  $i$ .

### EXPLICIT ULTIMATE-LOAD CONSTRAINTS

Having the linear 'strength-size' relationship Eq. (12) for each element  $i$  ( $i = 1, 2, \dots, n$ ), the formulation of the explicit ultimate-load constraints for each design stage also can proceed exactly as for thin-walled structures (ref. 2). To be consistent with the service-load constraints, the 'reciprocal' variables  $x_i$  are adopted here as well. Then, first-order Taylor's series expansions and sensitivity analysis are employed to formulate each of the load-factor constraints Eqs. (1d) as the 'explicit-linear' constraint

$$\alpha_m^\circ - 2\alpha_m^\circ \leq \sum_{i=1}^n p_{im}^\circ x_i \leq \hat{\alpha}_m - 2\alpha_m^\circ \quad (19)$$

The load factor  $\alpha_m^\circ$  in Eq. (19), which defines the load level at which plastic collapse mechanism  $m$  forms for the current design stage, is evaluated from plastic analysis as

$$\alpha_m^\circ = (\tilde{\underline{R}} \dot{\underline{\lambda}}_m)^\circ = \sum_{i=1}^n (\tilde{\underline{R}}_i \dot{\underline{\lambda}}_{im})^\circ \quad (20)$$

where  $\underline{R}^\circ$  is the vector of plastic capacities for all elements of the structure (for element  $i$ , the subvector  $\underline{R}_i^\circ = \underline{R}_i^* a_i^\circ$  from Eq. (12) for  $a_i = a_i^\circ$ ), and  $\dot{\underline{\lambda}}_m^\circ$  is the vector of element plastic deformation rates associated with collapse mechanism  $m$  ( $\dot{\underline{\lambda}}_{im}$  is the subvector associated with element  $i$ ). Each of the load-factor sensitivity coefficients (gradients)  $p_{im}^\circ$  in Eq. (18) is evaluated as

$$p_{im}^\circ = -\frac{1}{x^\circ} (\tilde{\underline{R}}_i \dot{\underline{\lambda}}_{im})^\circ \quad (21)$$

Note that, for fixed structure topology, the vector  $\dot{\underline{\lambda}}_m^\circ$  (hence  $\dot{\underline{\lambda}}_{im}^\circ$ ) is invariant with changes in the design. (An efficient 'finite-incremental' plastic analysis technique to find  $\alpha_m^\circ$  and  $\dot{\underline{\lambda}}_m^\circ$  is presented in refs. 5, 7 ).

The ultimate-load constraint Eq. (19) is of poorer quality than the service-load constraints Eqs. (14a,b). This is because collapse load factors vary directly rather than inversely with the sizing variables  $a_i$  (whereas the latter is the case for displacements and stresses). However, Eq. (19) is always a 'conservative' (safe) constraint for any intermediate design stage and, like Eqs. (14), is an 'exact' constraint for the final stage that determines the minimum weight design (ref. 2).

## THE EXPLICIT DESIGN PROBLEM

From Eqs. (1a), (1e), (13), (14) and (19), the minimum weight design problem Eqs. (1) expressed explicitly in terms of 'reciprocal' sizing variables  $x_i$  is

$$\text{Minimize: } \sum_{i=1}^n w_i / x_i \quad (22a)$$

Subject to:

$$\hat{\delta}_j \leq \sum_{i=1}^n d_{ij}^{\circ} x_i \leq \hat{\delta}_j \quad (j = 1, 2, \dots, d) \quad (22b)$$

$$\hat{\sigma}_k \leq \sum_{i=1}^n s_{ik}^{\circ} x_i \leq \hat{\sigma}_k \quad (k = 1, 2, \dots, s) \quad (22c)$$

$$\hat{\alpha}_m - 2\alpha_m^{\circ} \leq \sum_{i=1}^n p_{im}^{\circ} x_i \leq \hat{\alpha}_m - 2\alpha_m^{\circ} \quad (m = 1, 2, \dots, p) \quad (22d)$$

$$\hat{x}_i \leq x_i \leq \hat{x}_i \quad (i = 1, 2, \dots, n) \quad (22e)$$

where, from Eqs. (1e) and (13),  $x_i = 1/\hat{a}_i$  and  $\hat{x}_i = 1/a_i$ .

Eqs. (22) define the weight optimization problem for each design stage. After each weight optimization, the sensitivity coefficients  $d_{ij}^{\circ}$ ,  $s_{ik}^{\circ}$  and  $p_{im}^{\circ}$  are updated, if necessary the design is scaled to restore feasibility, and the weight optimization is repeated. The numbers  $d$  and  $s$  of service-load displacement and stress constraints are the same for all design stages. However, the number  $p$  of ultimate-load constraints progressively increases to account for new 'critical' plastic collapse modes as the design changes over the iteration history. Initially, for each load case, there is one such constraint corresponding to the 'critical' collapse mechanism for the given 'trial' design. For each design stage thereafter, one new ultimate-load constraint may or may not be added depending on whether or not the load factor for the 'critical' mechanism is strictly less than that for all mechanisms accounted for in the previous weight optimization. For each load case, the maximum possible number of ultimate-load constraints at the final design stage is equal to the number of degrees of freedom for the structure (the number is usually much less due to the service-load and sizing constraints).

The iterative process converges to the final minimum weight design when there is no change in the design weight from one design stage to the next. (A full exposition of the iterative design process, as well as of an efficient 'generalized optimality criteria' technique to solve Eqs. (21), is provided in refs. 2,4,5).

## EXAMPLE APPLICATION

A computer program named STRUSY (STRUctural SYnthesis) has been developed in ref. 5 to implement the described design method. For each design stage, the program employs a finite-element elastic analysis technique to establish the service-

load constraints, a 'finite-incremental' plastic analysis technique (refs. 5,7) to establish the ultimate-load constraints and a 'generalized optimality criteria' technique (refs. 2,4) to conduct the weight optimization. With a view to improving the computational efficiency, enhancing the convergence properties and meeting special design requirements, the program also incorporates the following special features: 1) a 'constraint-deletion technique' is employed to retain only those constraints that are critical or potentially critical for each design stage (ref. 9); 2) an 'area-averaging technique' is employed to stabilize the convergence history and reduce the number of iterations required to achieve the minimum weight design (ref. 8); 3) a 'design-variable linking technique' is employed to group elements together so as to meet special fabrication requirements concerning relative element sizes (ref. 9). The STRUSY program was used to conduct the example design presented in the following (ref. 5).

### Industrial Steel-Mill Building

The industrial steel-mill building in fig. 2 is composed of 7 roof-truss web elements (of any cross-section shape) and 26 beam, column and chord elements having the 'constant-shape' WF cross section shown in fig. 2. (Note that the formulae given in fig. 1 for the constants  $k$ ,  $m$  and  $n$  apply as well for the WF shape in fig. 2). Axial stresses alone are of concern for the web elements, while combined axial and bending stresses are of concern for the WF elements. A PWL yield condition similar to that in fig. 1 (but for the WF shape in fig. 2) is adopted to govern the plastic behavior of the WF elements. The frame is subject to the three independent load cases indicated in fig. 2 (the load parameter  $P = 44.4$  KN defines the service-load level).

Material properties and constraint bounds are given in table 1 ( $\rho$  = material density;  $E$  = Young's modulus). Note that the compressive yield stress  $\hat{\sigma}_y$  has been (artificially) taken to be less than the tensile yield stress  $\hat{\sigma}_y$  so as to indirectly account for compression buckling of the elements. For all elements, the elastic stresses in tension and compression are limited to 66.67% of the yield stresses  $\hat{\sigma}_y$  and  $\hat{\sigma}_y$ , respectively. The lower-bound value of 1.8 on collapse-load factors requires the frame to withstand a 80% overload beyond the service-load level without failing in any plastic mechanism mode. The size of each element cross section is bounded from below by an arbitrarily small value (see table 1), and is unbounded from above.

Since the structure and the loads are symmetrical, 'design-variable linking' is employed to reduce the number of independent design variables from 33 to 17. For each of the 3 load cases: 1) one (tension/compression) stress constraint is imposed for each of the 4 groups of web elements; 2) two constraints are imposed on the 'maximum' extreme-fiber stresses for each of the 13 groups of WF elements (i.e., one constraint at each of the two element ends). The total number of stress constraints is 90. Six horizontal displacement constraints are imposed (at nodes 2, 3, 7, 9, 11, 13) for load case 2 alone. Ultimate-load constraints on plastic-collapse load factors are imposed for load cases 1 and 2 alone.

An arbitrary 'trial' design corresponding to a structure weight of 5256.75 kg. is selected to commence the design process. The 'final' design corresponding to the 'minimum' structure weight of 4150.43 kg. is found after six iterations of the design process. The 'optimum' cross-section areas for the 13 groups of WF elements (numbered 1 to 13 in fig. 2) are 26.77, 137.56, 32.15, 51.44, 51.44, 36.53, 36.53, 65.77,

111.59, 8.94, 9.51, 6.93 and 6.93 cm<sup>2</sup>, while those for the 4 groups of web elements (numbered 14 to 17 in fig. 2) are 7.26, 4.21, 2.75 and 0.79 cm<sup>2</sup>.

The history of the iterative design process is shown in fig. 3 (note that monotonic convergence is exhibited through to the final minimum weight design). Three 'critical' plastic collapse modes (numbered 1,2,3 in fig. 3) become active at various design stages of the iterative process. The three collapse mechanisms are shown in fig. 4 along with the values of their load factors  $\alpha$  at the final design stage (the parameters  $\delta$  and  $\theta$  refer to axial and flexural plastic deformation rates, respectively). Note that collapse mode 1 occurs under load case 1, while modes 2 and 3 occur under load case 2. The 'active' or 'potentially active' constraint conditions at the final design stage are: 1) horizontal displacements at nodes 3 and 11 under load case 2; 2) stresses in the elements of groups 2,3,6,7 and 8 under one or more of three load cases; 3) plastic-collapse modes 2 and 3 under load case 2; 4) lower-bound sizes of the elements of groups 12, 13 and 17.

#### CONCLUDING REMARKS

Through the coordinated use of approximation concepts, finite-element elastic analysis, incremental plastic-collapse analysis and generalized optimality criteria techniques, the described design method (and associated computer program STRUSY) can provide the designer with an efficient and effective tool to conduct the design of practical engineering frameworks under multiple performance constraints.

Some important features of the design method are: 1) the number of iterations required to achieve the minimum weight design is generally quite small, and is almost totally independent of the complexity of the structure (as demonstrated in ref. 5 for a range of example structures, including the example presented herein, six to seven iterations are required on average to achieve 1% weight convergence); 2) for collapse-load factors that are consistent with the ultimate load levels specified by current design practice, a mix of both service-load and ultimate-load constraints will often control the design (in fact, as demonstrated by the example herein, a number of independent collapse modes may be critical for a design); 3) whenever both types of constraints are active for a design, the required structure weight will be greater than that determined by a minimum weight design that accounts for service-load constraints alone.

The computer implementation of the design method is quite efficient. For example, the steel-mill building design involved 90 stress constraints, 6 displacement constraints, 17 sizing constraints and, at the final design stage, 3 plastic-collapse constraints, and required only 2 minutes to complete using the STRUSY program on an IBM 4341 computer (University of Waterloo).

#### REFERENCES

1. Emkin, L.Z.; and Litle, W.A.: Storywise Plastic Design for Multi-Story Steel Frames. ASCE, J. of Str. Div., Vol. 98, No. ST1, Jan. 1972.
2. Grierson, D.E.; and Schmit, L.A., Jr.: Synthesis Under Service and Ultimate Performance Constraints. J. of Comp. and Struct., Vol. 15, No. 4, 1982, pp. 405-417.
3. CAN 3-316.1-M78: Steel Structures for Buildings - Limit States Design. Canadian Standards Association, 1978.



4. Fleury, C.; and Sander, G.: Structural Optimization by Finite Elements. LTAS Rep. SA-58, U. of Liege, Belgium, 1978.
5. Chiu, T.C.W.: Structural Synthesis of Skeletal Frameworks Under Service and Ultimate Performance Constraints. M.A.Sc. Thesis, U. of Waterloo, Canada, April 1982.
6. Fleury, C.; and Sander G.: Generalized Optimality Criteria for Frequence Constraints, Buckling Constraints and Bending Elements. LTAS Rep. SA-78, U. of Liege, Belgium, 1979.
7. Franchi, A.; Grierson, D.E.; and Cohn, M.Z.: A Computer System for the Elastic-Plastic Analysis of Large-Scale Structures. J. of Struct. Mech., Vol. 9, No. 3, 1981, pp. 295-324.
8. Grierson, D.E.; and Aly, A.A.: Plastic Design Under Combined Stresses. ASCE, J. of EM Div., Vol. 106, No. EM4, Aug. 1980, pp. 585-607.
9. Schmit, L.A., Jr.; and Miura, H.: An Advanced Structural Analysis/Synthesis Capability - ACCESS 2. Int. J. for Num. Meth. in Engng., Vol. 12, 1978.

TABLE 1 - DATA FOR INDUSTRIAL STEEL-MILL BUILDING

Material Properties	Steel, $\rho = 0.00849 \text{ Kg/cm}^3$ ( $0.283 \text{ lb/in}^3$ ) $E = 2.0685 \times 10^8 \text{ KN/m}^2$ ( $30 \times 10^6 \text{ lb/in}^2$ ) $\hat{\sigma}_y = +248,220 \text{ KN/m}^2$ ( $36,000 \text{ lb/in}^2$ ) $\sigma_{\hat{y}} = -165,480 \text{ KN/m}^2$ ( $24,000 \text{ lb/in}^2$ )
Size Limits	Lower Bounds: $6.4516 \text{ cm}^2$ ( $1.0 \text{ in}^2$ ) for WF elements $0.6452 \text{ cm}^2$ ( $0.1 \text{ in}^2$ ) for web elements Upper Bounds: none
Displacement Limits	Nodes 2, 3, 7, 9, 11, 13; $\delta = \pm 3.81 \text{ cm}$ ( $1.5 \text{ in}$ ) in horizontal direction
Stress Limits	$\hat{\sigma}_i = +165,480 \text{ KN/m}^2$ ( $24,000 \text{ lb/in}^2$ ) $\sigma_{\hat{i}} = -110,320 \text{ KN/m}^2$ ( $16,000 \text{ lb/in}^2$ )
Load Factor Limits	$\alpha_{\hat{m}} = 1.8$ for all critical modes. No upper bounds

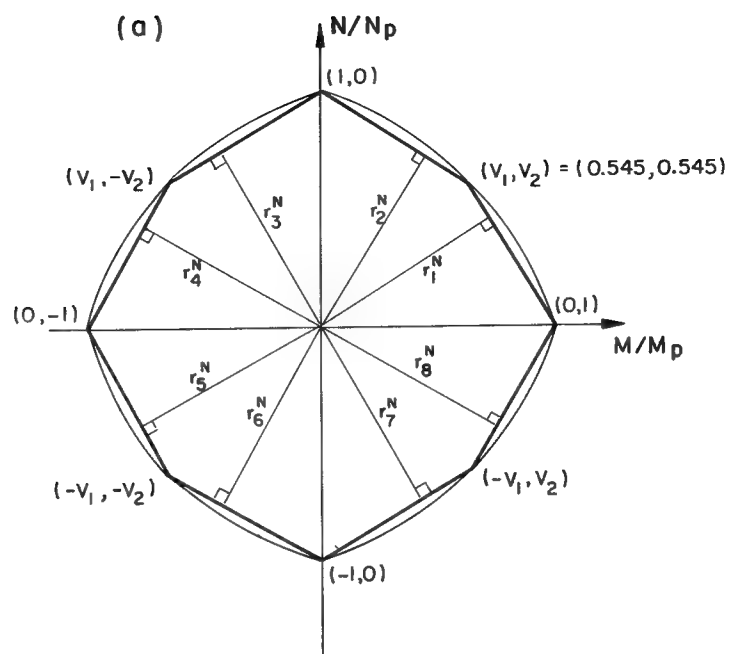
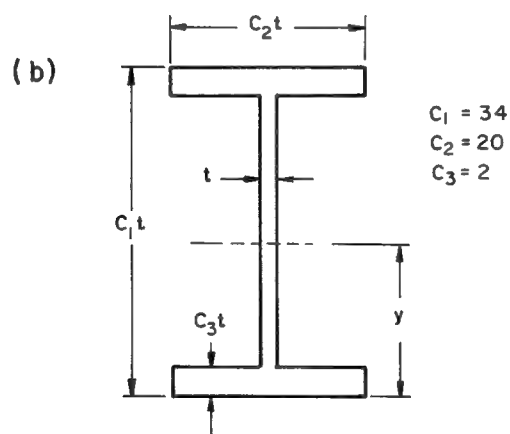


Figure 1 (a) - Normalized Piecewise-Linear Yield Condition for Figure 1 (b)



$$I = k a^2 ; M_p = m a^{1.5} ; y = n a^{0.5}$$

$$k = \frac{(C_1 - 2C_3)^3 + 2C_2C_3 + 6C_2C_3(C_1 - C_3)^2}{12(C_1 + 2C_2C_3 - 2C_3)^2}$$

$$m = \frac{\sigma_y [C_2C_3 - C_3^2](C_1 - C_3) + C_1^2/2}{(C_1 + 2C_2C_3 - 2C_3)^{1.5}}$$

$$n = \frac{C_1}{2(C_1 + 2C_2C_3 - 2C_3)^{0.5}}$$

Figure 1 (b) - Constant-Shape Wide-Flange Cross Section

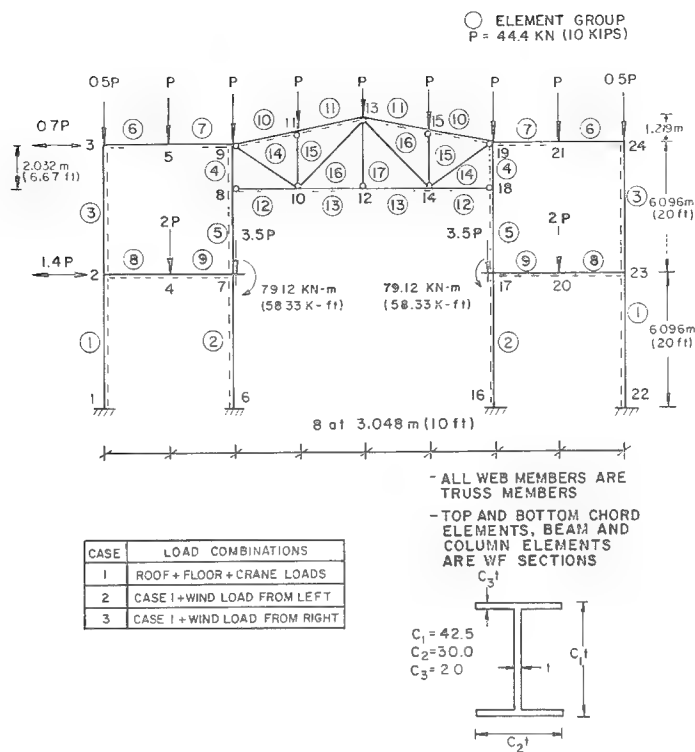


Figure 2 - Industrial Steel-Mill Building

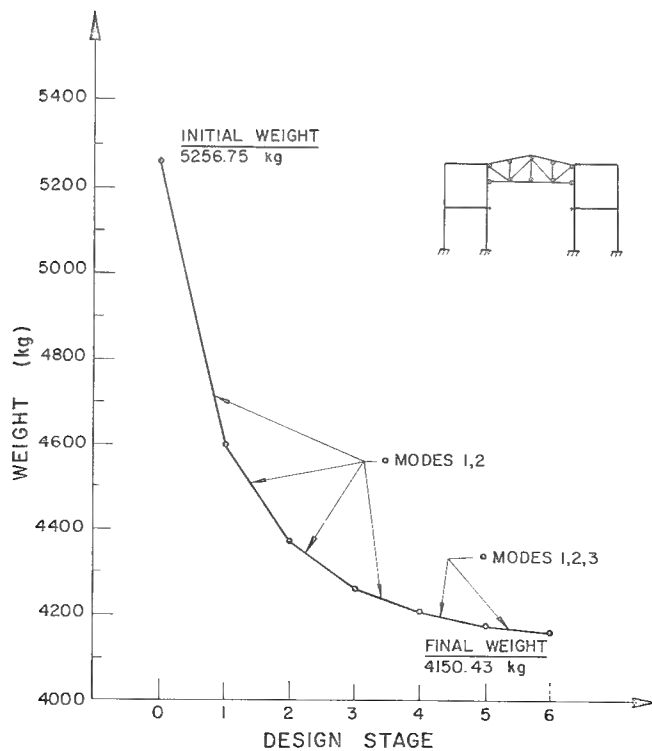


Figure 3 - Iteration History for Industrial Steel-Mill Building Design

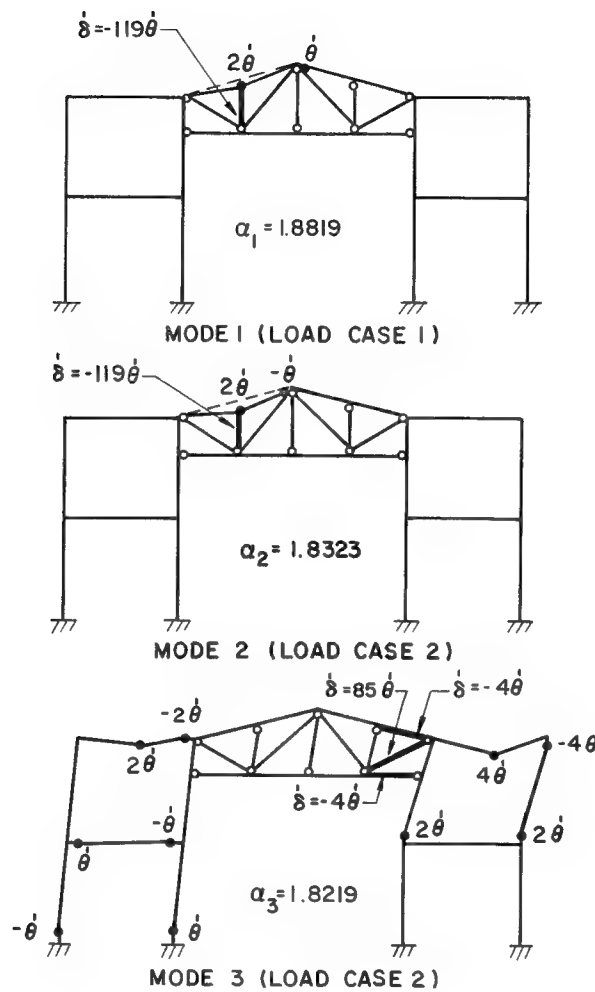


Figure 4 - Critical Collapse Modes for Industrial Steel-Mill Building Design

## A SIMULATION LANGUAGE APPROACH TO STRUCTURAL

### INTERACTION PROBLEMS<sup>†</sup>

Malcolm A. Cutchins  
Auburn University, Alabama 36849

James W. Purvis  
Sandia Laboratories  
Albuquerque, New Mexico 87185

### SUMMARY

Advantages and disadvantages of using simulation languages in solving structural problems are given. Emphasis is placed on those structural and solid mechanics problems which have strong interactions with other disciplines. An aeroservoelastic illustration is described with significant interactions between the dynamics of a flexible flight vehicle structure, the aerodynamics to which it is subjected, the dynamic flight equations, and the vehicle's servo-control system.

### INTRODUCTION

More and more in the fields of structural and solid mechanics, interaction with other disciplines is on the increase in the successful solution to "real world" problems. For instance, sharp increases in fuel costs have sped the trend toward more fuel efficient vehicles (land, air, and sea). This, in turn, has led to more flexible flight vehicles which require more in-depth aeroelastic analysis, for example. And land vehicles, while more fuel efficient, are less tolerant of vehicle crashes and more apt to become unstable. Numerous other examples exist including off-shore structures, long flight space vehicles, zero-gravity orbiting structures, and new structure-material concepts like those in the forward swept wing concept. To the structural and solid mechanics analyst, such interactions usually increase the complexity of the simulations considerably. Such complexity may force research into a field new to the analyst, or they may force heavy involvement with an engineer in one or more of the related fields. That such intra-field cooperation cannot be ignored is well documented in well publicized failures such as the Tacoma-Narrows suspension bridge (which failed in aeroelastic flutter), or the Electra aircraft (which failed in propeller-induced gyroscopic oscillations following hard landings which "softened" the propulsion plant suspension system). The reader is referred to reference 1 for an unprecedented presentation of many up to date examples of other flow-induced oscillations/instabilities.

The point is, very often the structures/solid mechanics researcher/engineer must involve either the simulation of these non-structural aspects in his own simulation, or he must deal very closely with a companion specialist in a non-structural field. While most of us might belittle the difficulties of the latter, there do exist some documentations of the shortcomings of such interfacing between specialists (refs. 2

<sup>†</sup>Supported by Contract AF F08635-78-C-0027, Eglin AFB, FL, and AU Engr. Exp. Sta.

and 3). Such shortcomings are rarely documented, but anyone with significant engineering experience knows of similar instances.

## SIMULATION LANGUAGES

The authors are not so brazen as to suggest a solution to these engineer-interface problems in one paper. But a part of the solution to problems that usually exist in structural interaction problems is the use of advanced simulation languages. Much of this paper will explore further the advantages, disadvantages, and an illustrative example of such use. Certainly there is no intent to demean other techniques by which the engineer A/engineer B and discipline P/discipline Q interfacing is enhanced.

What features would such an advanced simulation language have? What trends for future modification should it incorporate? What appealing characteristics should it possess to woo the engineer already deeply ingrained in a solution language and technique pattern? Table I summarizes some of the answers to these questions. The table is ordered with those features easiest to achieve listed first; those most difficult to achieve towards the end. Obviously the last three features in the table are probably not achieved very well to date except in very specialized simulation problems. But as storage capacities of large digital systems increase, as more software research is successful, and as man/machine interaction arrangements improve, even these three should fall within the achievable. (The authors suspect the last feature will always escape solution, however!)

## STRUCTURAL SIMULATION WITH ACSL

Figure 1 indicates the typical interrelationships involved in many simulations of structural systems. As mentioned previously, the "structure" may be an actual flight vehicle or automobile, a hydraulic gate, or a space platform. In some cases any particular element of figure 1 may dominate the simulation in terms of the simulation software effort, but in general, it is the structure itself and how it responds that play a major role in the interaction, both physically and simulation-wise. And often it is the structure itself which catches the brunt of any real failure which might occur, even if the root cause of the failure is not really primarily a structural shortcoming.

One excellent simulation language which incorporates many of the ideas previously mentioned is ACSL - Advanced Continuous Simulation Language. The language, developed by Mitchell and Gauthier, Associates, is well documented in reference 4. It has been used extensively by the authors in research efforts and extensively by the first author in a teaching environment. While its capabilities are primarily geared to solving systems which are described by time dependent, non-linear differential equations, the language is extremely versatile and has many of the table I features.

To give some introduction to the types of simulation capabilities, consider figure 2. First, note the one-to-one relationship for each statement and each block, or event, to be simulated. The first three shown are typical control system blocks, a second-order transfer function (a complex pole), followed by a real pole and a

lead-lag simulation. Shown fourth on the figure is a typical integrator simulation (simulations involving dozens of integrators are common). Last on figure 1 is a vector integration. In this instance, the three variables BX (for  $\beta_x$ ), BXDOT, and BXIC are vectors of direction cosines, their time rates of change, and their initial conditions, respectively. One advantage of using the latter in simulations is that the nine direction cosines may be "kept up with" using only three statements, for  $\beta_x$ ,  $\beta_y$ , and  $\beta_z$ . Such use has certain advantages over the use of Euler angles with their often different definitions as illustrated by references 5, 6 and 7.

A very important structural-related use of the ACSL vector integrating capability is illustrated in figure 3. Starting at the top center of the figure, all time zero initializations in a structural time domain simulation are accomplished. From a separate structural finite element model (FEM) it is assumed that a digital model of the elastic structure is available. This would include the stiffness matrix  $[K]$ , the mass matrix  $[M]$ , a modal matrix  $[\phi]$ , and a set of natural frequencies  $[\omega]$ . From this information, one may form a set of  $n$  normal coordinate equations for  $\ddot{q}$  as shown in figure 3. The right-hand side of these equations, of course, involves the normal coordinates  $q$  and a generalized force vector. A simple vector integrator of the form

$$QD = \text{INTVC}(QDD, QD0), \text{ i.e., } \{\dot{q}\} = \int \{\ddot{q}\} dt + \{\dot{q}_0\}$$

yields the lower order of the normal coordinates. Here conversational names for the variables have been used. These variables are easily dimensioned in an ARRAY statement which plays the same role in ACSL as the DIMENSION statement does in FORTRAN. There follows a move of the  $\dot{q}$  vector to dummy storage with a standard call followed by another vector integrator of the form

$$Q = \text{INTVC}(QD, Q0), \text{ i.e., } \{q\} = \int \{\dot{q}\} dt + \{q_0\}$$

The elastic motions of the structure can now be formed from FORTRAN statements within ACSL which accomplish the following:

$$\{x\} = [\phi]\{q\} \text{ and } \{\dot{x}\} = [\phi]\{\dot{q}\}$$

Here  $[\phi]$  is the modal matrix. The structural grid point coordinates  $\{x\}$  and their derivatives can now be used in forming the load vector,  $\{P\}$ , and then completing the loop by forming the generalized force vector,  $[\phi]^T\{P\}$ . Recall that this force vector was required to form the  $\ddot{q}$  equations to start with. Often an algebraic loop is formed by this loop as described, however; this is easily handled by the use of an ACSL IMPLICIT statement which incorporates mathematically efficient iterative techniques. Concluding our consideration of figure 3, the illustration is used here of a structure which has its motions governed by a control system as shown on the right-hand side of the figure. Various kinds of disturbance(s) can be introduced from the ACSL collection of forcing functions. The analyst can then examine a critical coordinate's rate with time, for instance, and assess the structure's stability as indicated in the center of figure 3. Of course, other structural calculations of interest may be made using the structural grid point coordinates  $\{x\}$ .



Before proceeding further with a specific illustration of simulation language use as described, it seems appropriate to consider typical disadvantages which face the structures/solid mechanics analyst in such use. Table II summarizes these. The most significant in structural interaction problems are the third (because often the digital structural model has to be handled by overriding the normal ACSL sorting algorithm), and the last (in cases where changes to the FEM may still be occurring such as in design or optimization problems).

It should be pointed out that, while oversimplified, ACSL essentially has five "sections." The first can be thought of as a preface to the simulation; next are all those instructions done at time = 0 in an INITIAL section. The "meat" of the simulation occurs next in DYNAMIC and DERIVATIVE sections (for  $0 < t < t_{\max}$ ). A TERMINAL section (for  $t = t_{\max}$  instructions) completes the model definition. A RUN-TIME control section is then used similar to a Case Control Deck of NASTRAN.

#### A FLIGHT STABILITY STUDY ILLUSTRATION

An early version of the F-16 experienced some in-flight instabilities which proved to be rather difficult to simulate with traditional approaches. One reason was that one of the instabilities involved an interaction between the elastic structure, especially as it affected the aerodynamic loading on a tip-mounted missile. Also involved was the aircraft's complicated control system, the first fly-by-wire system. And, of course, the flight dynamic equations in their less restrictive forms are quite extensive by themselves. The latter are given in table III, primarily to indicate the level of complexity of equations which are easily handled by an ACSL simulation in addition to a structural simulation. In table III, the large brackets set off the Euler angle form of some of the equations on the left, and those of the direction cosine form on the right. Note the twelve integrations involved (or nine plus three vector integrators for the direction cosine form).

Figure 4 indicates the various modules of this aeroservoelastic simulation. All elements of the simulation within the bold lines are performed in a "built-in" and extremely versatile time stepping loop within ACSL. The blocks above and below the bold lines are performed at time equal zero. The right-most block is performed by the analyst in this stability assessment study after the run.

A thorough description of the results from a flight dynamics perspective is given in reference 8 while the emphasis herein is on the structural interaction and simulation aspects. One should recognize that all of the elements of figure 4 are present in the stability assessment simulation whether a full flight dynamic simulation is performed, or whether any one of the several typical flight dynamic simplifications is used such as lateral-directional, longitudinal, etc.

In this particular study, flight tests yielded a fairly good definition of the boundary between stable and unstable flight (ref. 9). This boundary location varied with Mach number and altitude, of course. It was also heavily dependent on whether or not the tip missile was on, or off.

A roll-only ACSL simulation (without elastic effects) was sufficient to simulate the missile-off instability. It was dominated by an aircraft roll oscillation with few structural flexibility effects. The frequency of the instability simulation

matched extremely well with that recorded in-flight. Also, the instability seemed to be limited in its buildup with time.

The missile-on instability proved much more elusive, not predictable at all without the inclusion of elastic effects in the ACSL simulation as described in figures 3 and 4. And even with an almost exact simulation of the in-flight frequency of the instability (almost twice that of the missiles-off case), the simulated instability boundary turned out to be unconservative, yielding unstable speeds approximately 10% above the observed flight Mach number instabilities up to an altitude of 12,000 feet, matching the observed boundary at 15,000 feet, and predicting no instability at 20,000 feet and above. (Flight results indicated greater stability with increases in altitude as well.) Figure 5 indicates a typical, diverging with time instability for the missiles-on case.

While a number of avenues were explored to explain this discrepancy, most were of an aerodynamic or stability and control nature and are discussed in Ref. 8. The only one of a structural nature was to vary the number of free vibration modes used in the simulation. It made little difference: both five-mode and ten-mode simulations yielded practically the same results. With the frequency of the instability so well predicted, areas other than those of a structural nature were more highly suspect. It should also be mentioned that the time-domain results of this effort yielded much better results than some of the non-time-domain efforts. This was probably due to the more capable simulation in ACSL of non-linear effects.

## CONCLUSION

Present-day structures tend to be more interactive with nonstructural parts of a system. For these types of structures, advanced simulation languages offer significant capabilities to the structural and solid mechanics engineer. Some of these capabilities have been explored in this paper, especially as they relate to incorporating the influence of flexible structures into an overall simulation.

A flight stability and control investigation is used to illustrate the concepts described herein and the use of the ACSL language. Results of this study were slightly unconservative with in-flight results. Frequencies of the instabilities were very accurately modeled only when elastic effects were considered in the simulation.

#### REFERENCES

1. Naudascher, E., and Rockwell, D. (Editors): Practical Experiences with Flow-Induced Vibrations, Springer-Verlag, 1980.
2. Schwanz, R. C.: Formulations of the Equations of Motion of an Elastic Aircraft for Stability and Flight Control Applications, AFFDL/FCG-TM-72-14, August 1972, pp. 4, 5, 30, 37.
3. McRuer, D. T., and Johnston, D. E.: Flight Control Systems: Properties and Problems, Vol. I, NASA CR-2500, February 1975, pp. 1-5.
4. Advanced Continuous Simulation Language (ACSL), User Guide/Reference Manual, 2nd Ed., Mitchell and Gauthier Assoc., Inc., P.O. Box 685, Concord, Mass., 01742, 1975.
5. Tischler, M. B., and Barlow, J. B.: Determination of the Spin and Recovery Characteristics of a General Aviation Design, Journal of Aircraft, Vol. 18, No. 4, April 1981, pp. 238-244.
6. Roskam, J.: Airplane Flight Dynamics and Automatic Flight Controls - Part I, Roskam Aviation and Engineering Corporation, 1979, pp. 23-25.
7. Meriam, J. L.: Dynamics (2nd Ed.), John Wiley & Sons, Inc., 1975, p. 303.
8. Cutchins, M. A., Purvis, J. W., and Bunton, R. W.: "Aeroservoelasticity in the Time Domain," presented at the AIAA Dynamics Specialists Conference, April 1981, Atlanta, Georgia (to be published in the Journal of Aircraft).
9. Peloubet, R. P., et al.: Application of Three Aeroservoelastic Stability Analysis Techniques, AFFDL-TR-76-89, September 1976, pp. 25-104.

TABLE I. DESIRABLE FEATURES OF LANGUAGES FOR  
STRUCTURAL INTERACTION SIMULATIONS

*FORTRAN-like* in its makeup (realizing the almost universal appeal of FORTRAN among engineers for what is now approaching 25 years).

*Conversational* in its use for almost any discipline.<sup>†</sup>

Widely *versatile* with features that incorporate ease of integration, ease of incorporation of arrays, ease of relating time-domain and frequency-domain analyses and others.

*Easily modularized* (with the ability to have mini-simulations within simulations or easily invoked mini-simulations).

Possessing a trend to *uncomplicate* difficult simulations (at least compared to typical host-language simulations). Tends to "compress" a simulation to fewer instructions. "Flow" of program closer to physical problem.

*Simplified input/output* arrangements with versatile plotting schemes and arrangements.

The ability to *generate a model*, then *run variations* of cases with the model - much like the Bulk Data and Case Control Decks of NASTRAN.

Machine times which *tend to approach* real time.

*Diagnostics which really communicate* to the user.

*Protection* against erroneous simulations.

---

<sup>†</sup>A major advantage in interdisciplinary problems, and when returning to a simulation when it is cold.

TABLE II. DISADVANTAGES OF ADVANCED SIMULATION LANGUAGE USE

Diagnostics less extensive than typical host languages;  
often very misleading to the novice.

Large storage required.

Sorting of statements, normally done internally, often has  
to be overridden by the user.

Tailored output form, instead of standard output form, slightly  
more involved to obtain if desired.

All variables and constants are REAL unless specified otherwise  
(no real disadvantage).

Run times are increased.

Some limitations exist re use of variable names for certain  
arguments which ought to be totally general.

Bulky output; some of it rather automatically generated and of  
little real use to the engineer.

While excellent for studying interaction of a specific model  
(garnered from a FEM), it is not always very convenient  
to change the FEM itself without linking ACSL with other  
programs.

TABLE III. FLIGHT DYNAMIC EQUATIONS

Body Forces and Moments

$$L_B = \bar{q} S b C_L$$

$$M_B = \bar{q} S \bar{c} C_m$$

$$N_B = \bar{q} S b C_n$$

$$\left. \begin{aligned} X_B &= T - \bar{q} S C_A - mg \sin \theta \\ Y_B &= \bar{q} S C_Y + mg \cos \theta \sin \phi \\ Z_B &= -\bar{q} S C_N + mg \cos \theta \cos \phi \end{aligned} \right\} \text{ or } \left\{ \begin{aligned} X_B &= T - \bar{q} S C_A + mg \cdot B_{x_3} \\ Y_B &= \bar{q} S C_Y + mg \cdot B_{y_3} \\ Z_B &= -\bar{q} S C_N + mg \cdot B_{z_3} \end{aligned} \right.$$

Force Resolution to Wind Axes

$$X_s = X_B \cos \alpha + Z_B \sin \alpha$$

$$X_w = X_s \cos \beta + Y_B \sin \beta$$

$$Y_w = -X_s \sin \beta + Y_B \cos \beta$$

$$Z_w = -X_B \sin \alpha + Z_B \cos \alpha$$

Acceleration Equations

$$\dot{V}_p = X_w / m$$

$$\dot{\alpha} = q_B - (p_B \cos \alpha + r_B \sin \alpha) \tan \beta + Z_w / (m V_p \cos \beta)$$

$$\dot{\beta} = Y_w / (m V_p) - r_B \cos \alpha + p_B \sin \alpha$$

$$\dot{p}_B = (L_B - q_B r_B (I_{zz} - I_{yy}) / I_{xx}}$$

$$q_B = (M_B - p_B r_B (I_{xx} - I_{zz})) / I_{yy}$$

$$r_B = (N_B - p_B q_B (I_{yy} - I_{xx})) / I_{zz}$$

$$\left\{ \begin{aligned} \dot{\psi} &= (r_B \cos \phi + q_B \sin \phi) / \cos \theta \\ \dot{\theta} &= q_B \cos \phi - r_B \sin \phi \\ \dot{\phi} &= p_B + \dot{\psi} \sin \theta \end{aligned} \right\} \text{ or } \left\{ \begin{aligned} \dot{B}_{x_1} &= r_B B_{y_1} - q_B B_{z_1} \\ \dot{B}_{y_1} &= p_B B_{z_1} - r_B B_{x_1} \\ \dot{B}_{z_1} &= q_B B_{x_1} - p_B B_{y_1} \end{aligned} \right.$$

Velocity Resolution (to Inertial Axes)

$$u_B = V_p \cos \alpha \cos \beta$$

$$v_B = V_p \sin \beta$$

$$w_B = V_p \sin \alpha \cos \beta$$

$$\left\{ \begin{aligned} w' &= v_B \sin \phi + w_B \cos \phi \\ v' &= v_B \cos \phi - w_B \sin \phi \\ u' &= u_B \cos \theta + w' \sin \theta \\ u_E &= u' \cos \psi - v' \sin \psi \\ v_E &= u' \sin \psi + v' \cos \psi \\ \dot{h} &= u_B \sin \theta - w' \cos \theta \end{aligned} \right\} \text{ or } \left\{ \begin{aligned} u_E &= u_B x_1 + v_B y_1 + w_B z_1 \\ v_E &= u_B x_2 + v_B y_2 + w_B z_2 \\ \dot{h} &= -(u_B x_3 + v_B y_3 + w_B z_3) \end{aligned} \right.$$

Integrals

$$V_p = V_o + \int \dot{V}_p dt$$

$$\alpha = \alpha_o + \int \dot{\alpha} dt$$

$$\beta = \beta_o + \int \dot{\beta} dt$$

$$p_B = p_{o_B} + \int \dot{p}_B dt$$

$$q_B = q_{o_B} + \int \dot{q}_B dt$$

$$r_B = r_{o_B} + \int \dot{r}_B dt$$

$$x_E = x_{o_E} + \int u_E dt$$

$$y_E = y_{o_E} + \int v_E dt$$

$$h = h_o + \int \dot{h} dt$$

$$\bar{M} = V_p / a$$

$$\left\{ \begin{aligned} \psi &= \psi_o + \int \dot{\psi} dt \\ \theta &= \theta_o + \int \dot{\theta} dt \\ \phi &= \phi_o + \int \dot{\phi} dt \end{aligned} \right\} \text{ or } \left\{ \begin{aligned} B_{x_1} &= \int \dot{B}_{x_1} dt + B_{x_1}(0) \\ B_{y_1} &= \int \dot{B}_{y_1} dt + B_{y_1}(0) \\ B_{z_1} &= \int \dot{B}_{z_1} dt + B_{z_1}(0) \end{aligned} \right.$$

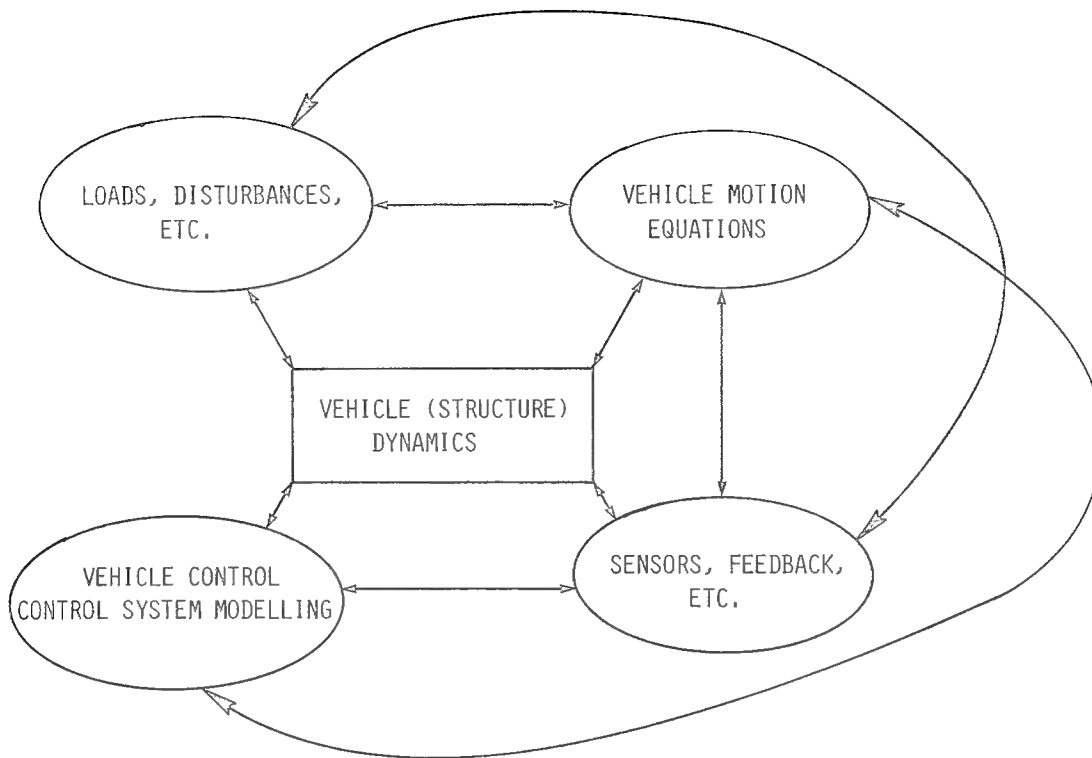


Figure 1.- Interrelationships involved in simulation of elastic structures

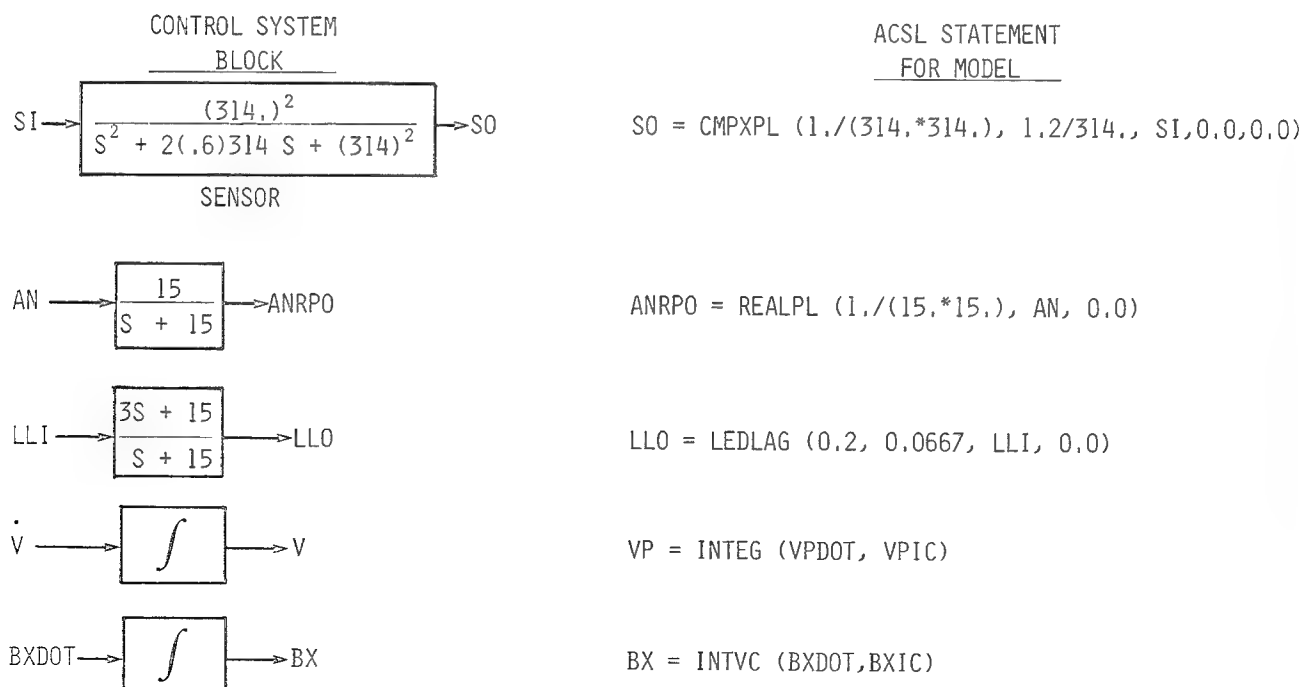


Figure 2.- Typical ACSL modeling features.

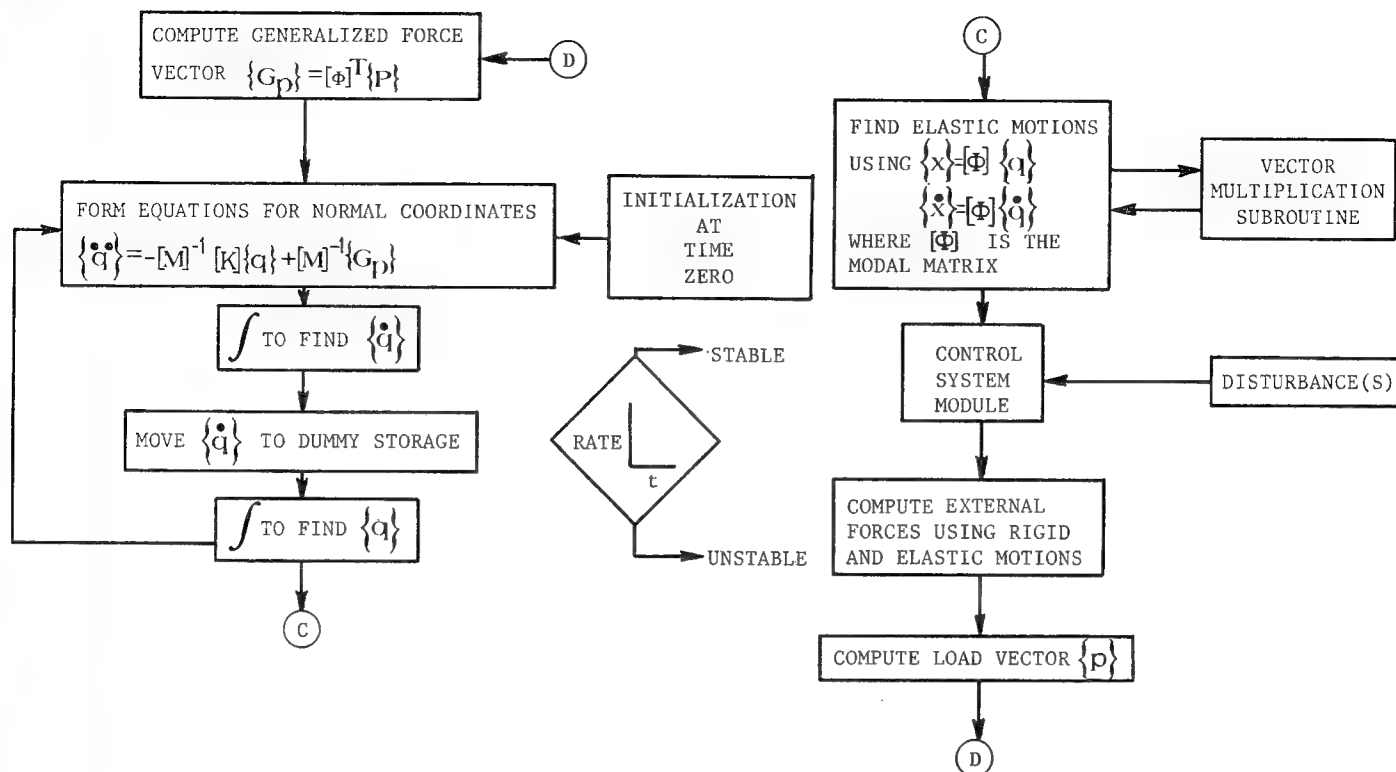


Figure 3.- Time loop sequence for structural interaction simulations.

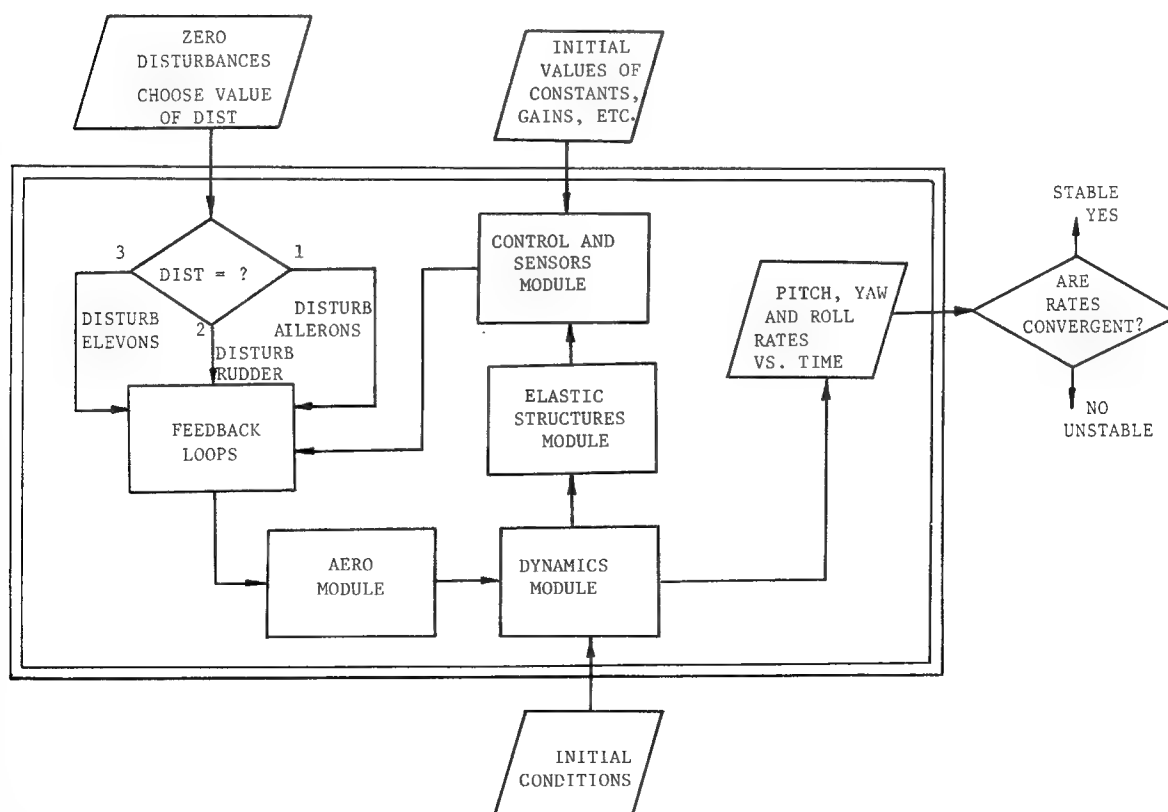


Figure 4.- Flow chart of aeroservoelastic time domain simulation



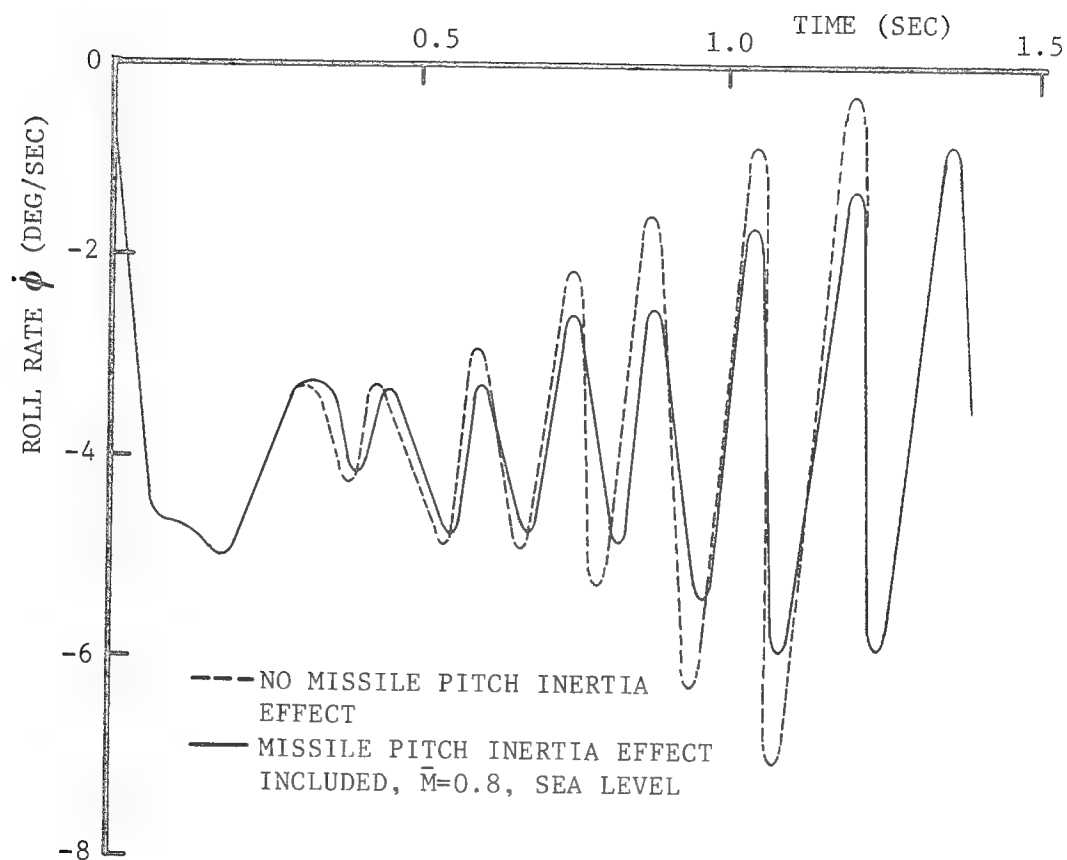


Figure 5.- Typical response of  $\dot{\phi}$  during missiles-on instability.

## SUSCEPTIBILITY OF SYMMETRIC STRUCTURES

### TO NONLINEAR TORSIONAL COUPLING

O.A. Pekau and Pradip K. Syamal

Department of Civil Engineering, Concordia University  
Montreal, Canada

#### SUMMARY

This paper presents the results of an investigation of the susceptibility to induced torsional response of symmetric building structures with nonlinear resisting elements. Results are presented in the form of stability curves showing the effect of the arrangement of the load resisting elements on induced torsional coupling in these nonlinear but otherwise symmetric structures. Universal upper and lower bound instability curves are also derived; these identify the susceptibility to torsional coupling of symmetric structures having different stiffness arrangements but which have equal mass and total lateral stiffness, and which are intended to model alternative structural strategies for lateral load resistance.

#### INTRODUCTION

In recent years numerous studies concerned with the response of both symmetric and unsymmetric structures subjected to earthquake excitation have emphasized the importance of dynamically induced torsion. Torsional motion is usually the result of a lack of symmetry (refs. 1-4), although nonlinearity of resisting elements (refs. 5-8) as well as rotational ground motion (refs. 9-10) are equally capable of inducing torsion. Kan and Chopra (ref. 2) demonstrated that torsion in elastic multi-story buildings can be modelled by analogy to torsion in single-story structures. Thus, torsional coupling in symmetric and unsymmetric single-story building models has been the subject of many studies in recent years (refs. 3-9). Even code provisions for torsion are, to a large extent, based on the results of the analysis of partially symmetric single-story building models. A recent evaluation of code requirements (ref. 11) for earthquake resistant design of torsionally coupled buildings concluded that for small eccentricities and particular building configurations current seismic codes fail to predict correctly the effects of torsion.

Several previous studies of linear structures (refs. 1, 4 and 10) have indicated that the susceptibility of symmetric buildings to induced torsional response is influenced to a significant degree by the distribution of the resisting elements within the plan area of the building.

Thus, this paper presents the results of an investigation of the susceptibility to induced torsional response of symmetric structures with nonlinear resisting elements. Attention is directed toward parameters such as the influence of the distribution and geometric arrangement of the lateral load-resisting elements (see figure 1). Results are presented in the form of stability curves showing the effects of the arrangement of the load-resisting elements on the induced torsional coupling in these nonlinear but otherwise symmetric structures.

## METHOD OF ANALYSIS

A simplified single-story system with rigid diaphragm and coincident centers of mass and resistance is considered in the present study (figures 1 and 2). Letting  $k_{ix}$  and  $k_{iy}$  represent the translational stiffnesses of the  $i^{\text{th}}$  resisting element in the x- and y-directions respectively, the total translational stiffnesses  $K_x$  and  $K_y$  and the torsional stiffness of the structure  $K_\theta$  are given by

$$K_x = \sum k_{ix} \quad (1)$$

$$K_y = \sum k_{iy} \quad (2)$$

$$K_\theta = \sum k_{ix} y_i^2 + \sum k_{iy} x_i^2 \quad (3)$$

The load-displacement relationship of resisting elements is taken to be weakly nonlinear and of the elastic softening type, with cubic nonlinearity expressed as

$$R_x(\delta_j) = k_x \delta_j \left[ 1 - \lambda \left( \frac{\delta_j}{\delta_o} \right)^2 \right] \quad (4)$$

$$R_y(\delta_j) = k_y \delta_j \left[ 1 - \lambda \left( \frac{\delta_j}{\delta_o} \right)^2 \right] \quad (5)$$

in which  $k_x$ ,  $k_y$  are the linear stiffnesses of the resisting elements in the x- and y-directions respectively;  $\delta_o$  is some convenient reference displacement;  $\lambda$  is a measure of the nonlinearity of the force displacement relation;  $\delta_j$  are the displacements of the lateral resisting elements, and  $R_x(\delta_j)$  and  $R_y(\delta_j)$  represent the restoring forces in the x- and y-directions of element 'j'.

The necessity of using nonlinear resisting elements with cubic nonlinearity can readily be visualized as follows. The corner displacements  $\delta_j$  (figure 2) may be expressed in terms of mass center lateral displacements  $u$  and  $v$  and rotational displacement  $\theta$  by the following relations

$$\delta_1 = u - b\theta \quad (6)$$

$$\delta_2 = u + b\theta \quad (7)$$

$$\delta_3 = v - a\theta \quad (8)$$

$$\delta_4 = v + a\theta \quad (9)$$

It is now assumed that restoring forces  $R_x(\delta_j)$  and  $R_y(\delta_j)$  are antisymmetric functions about the origin. Expanding one of the restoring functions, say  $R_x(\delta_1)$ , in the form of Taylor's series (ref. 7) about equilibrium position  $R_x(o)$  for element 1 yields

$$\begin{aligned}
 R_x(\delta_1) &= R_x(u - b\theta) \\
 &= R'_x(0) (u - b\theta) + \frac{R'''_x(0)}{3!} (u - b\theta)^3 + \dots
 \end{aligned}
 \quad (10)$$

For a linear load-displacement relationship  $R'_x(0)$  represents the linear stiffness of the resisting element and the motions  $u$  and  $\theta$  are uncoupled. However, if resisting elements are nonlinear it can be seen that the lateral motion becomes coupled to the torsional motion.

To approximate earthquake effects, the structure is subjected to sinusoidal ground acceleration in the  $x$ -direction of magnitude

$$\ddot{U}_g = U \cos \omega t \quad (11)$$

The nonlinear system initially had three degrees of freedom ( $u$ ,  $v$  and  $\theta$  in  $x$ -,  $y$ -, and  $\theta$ -directions, respectively). Since ground excitation exists only in the  $x$ -direction,  $v$  is assumed zero, and the system is governed by the following two nondimensionalized coupled equations of motion

$$\ddot{\Lambda}_x + f_1 \dot{\Lambda}_x + f_2 \Lambda_x - (f_3 \Lambda_x^3 + f_5 \Lambda_x \Lambda_\theta^2) = -\cos \Omega \tau \quad (12)$$

$$\ddot{\Lambda}_\theta + h_1 \dot{\Lambda}_\theta + h_2 \Lambda_\theta - [h_3 \Lambda_\theta \Lambda_x^2 + (h_4 + h_6) \Lambda_\theta^3] = 0 \quad (13)$$

in which

$$f_1 = 2\zeta_x \quad f_2 = 1.0 \quad f_3 = \lambda \quad (14a)$$

$$f_5 = 3\lambda \gamma_1^2 / \Omega_\theta^4 \quad h_1 = 2\zeta_\theta \Omega_\theta \quad h_2 = \Omega_\theta^2 \quad (14b)$$

$$h_3 = 3\lambda \gamma_1^2 E^2 \quad h_4 = \lambda \gamma_1^4 E^2 / \Omega_\theta^4 \quad h_6 = \lambda \beta_1^4 \Omega_y^2 F^2 / \Omega_\theta^4 \quad (14c)$$

$$\beta_1 = \frac{a}{l} = \sqrt{\frac{3r^2}{1+r^2}} \quad \gamma_1 = \frac{b}{l} = \sqrt{\frac{3}{1+r^2}} \quad r = a/b \quad (14d)$$

$$\Omega_y = \omega_y / \omega_x \quad \Omega_\theta = \omega_\theta / \omega_x \quad \Omega = \omega / \omega_x \quad (14e)$$

$$\omega_x^2 = K_x / M \quad \omega_y^2 = K_y / M \quad \omega_\theta^2 = K_\theta / M l^2 \quad (14f)$$

$$\tau = \omega_x t \quad E^2 = (\sum k_{ix} y_i^2) / (b^2 \sum k_{ix}) \quad F^2 = (\sum k_{iy} x_i^2) / (a^2 \sum k_{iy}) \quad (14g)$$

$$\Lambda_x(\tau) = u(t) / \delta_x \quad \Lambda_\theta(\tau) = \theta(t) / \delta_\theta \quad (14h)$$

$$\delta_x = U / \omega_x^2 \quad \delta_\theta = U / \Gamma \omega_\theta^2 \quad (14i)$$

where  $\zeta_x$ ,  $\zeta_\theta$  are translational and torsional damping coefficients;  $\omega_x$ ,  $\omega_\theta$  are fundamental uncoupled frequencies of the system;  $r$  is the building plan aspect ratio;  $\Gamma$  is the mass radius of gyration about the vertical axis through the center of mass;  $\tau$  represents nondimensional time;  $\Lambda_x$ ,  $\Lambda_\theta$  represent nondimensional response of the system. Also,  $E$  and  $F$  are coefficients representing the stiffness distribution over the plan area of the building;  $M$  denotes mass of the rigid diaphragm, and  $2a$  and  $2b$  are the building plan dimensions in  $x$ - and  $y$ -directions, respectively.

To investigate torsional stability of the system, equations (12) and (13) are cast into the form of damped coupled Mathieu-Hill variational equations (refs. 8 and 12).

Neglecting torsional damping, the region of instability is defined by the following upper and lower bound equations (ref. 12), respectively

$$\Omega_\theta^2 = \Omega^2 + \frac{27\lambda D E^2}{4(1+r^2)} \quad (15)$$

$$\Omega_\theta^2 = \Omega^2 + \frac{9\lambda D E^2}{4(1+r^2)} \quad (16)$$

where

$$D = [(1 - \Omega^2)^2 + (2\zeta_x \Omega)^2]^{-1} \quad (17)$$

It should be noted that stiffness distribution coefficient  $E$  appears in equations (15) and (16) above. Thus, the torsional stability of a particular system is dependent upon the location of resisting elements within the plan area of the building.

However, to validate these instability equations for a general system, equations (15) and (16) may be normalized by dividing by  $E^2$ , yielding the following upper and lower bound equations, respectively

$$\hat{\Omega}_\theta^2 = \hat{\Omega}^2 + \frac{27\lambda D}{4(1+r^2)} \quad (18)$$

$$\hat{\Omega}_{\theta}^2 = \hat{\Omega}^2 + \frac{9\lambda D}{4(1+r^2)} \quad (19)$$

In the above,

$$\hat{\Omega}_{\theta} = \Omega_{\theta}/E \quad (20)$$

$$\hat{\Omega} = \Omega/E \quad (21)$$

In deriving the above instability equations the magnitude of reference displacement  $\delta_0$  (in equations (4) and (5)) was chosen as

$$\delta_0 = \frac{U}{\omega_x^2} \quad (22)$$

which represents static displacement or the steady-state elastic displacement when forcing frequency approaches zero. However, one can choose an alternative definition of  $\delta_0$  given by the following expression

$$\delta_0 = \frac{UD}{\omega_x^2} \quad (23)$$

which indicates that the magnitude of the reference displacement is nonstationary and dependent upon the steady-state amplitude of vibration.

Using this definition of  $\delta_0$  the upper and lower instability bounds (equations (15) and (16)) become

$$\left(1 - \frac{9\lambda}{4}\right) \Omega_{\theta}^2 = \Omega^2 - \frac{27\lambda\kappa r^2 E^2}{4(1+r^2)} \quad (24)$$

$$\left(1 - \frac{3\lambda}{4}\right) \Omega_{\theta}^2 = \Omega^2 - \frac{9\lambda\kappa r^2 E^2}{4(1+r^2)} \quad (25)$$

in which  $\kappa$  represents the ratio between total translational stiffnesses in y- and x-directions of the system, given by

$$\kappa = \frac{K_y}{K_x} \quad (26)$$

The corresponding universal upper and lower bound expressions of equations (18) and (19) can be reformulated as

$$\left(1 - \frac{9\lambda}{4}\right) \hat{\Omega}_{\theta}^2 = \hat{\Omega}^2 - \frac{27\lambda\kappa r^2}{4(1+r^2)} \quad (27)$$

$$(1 - \frac{3\lambda}{4}) \hat{\Omega}_{\theta}^2 = \hat{\Omega}^2 - \frac{9\lambda\kappa r^2}{4(1+r^2)} \quad (28)$$

These bounds are now applicable for any distribution of lateral resistance within the plan area of the building.

## RESULTS AND DISCUSSION

To investigate the influence of the distribution of resisting elements, a variety of structural strategies have been examined. Figure 1 shows typical examples, namely, systems with periphery resistance, uniformly distributed resistance, central-core resistance, and 9- and 4-column resistance. The plan dimensions are selectively constant ( $2a \times 2b$ ) for all systems. To obtain a meaningful comparison, total translational stiffnesses  $K_x$  and  $K_y$  and mass  $M$  are also assumed equal for all systems. With equal translational stiffnesses, the torsional frequencies of these systems are related as follows

$$\omega_{p\theta}^2 = 3\omega_{d\theta}^2 = \omega_{c\theta}^2/s^2 = 1.5\omega_{n\theta}^2 = \omega_{f\theta}^2 \quad (29)$$

where subscripts p, d, c, n, and f denote periphery, distributed, core, 9-column and 4-column systems, respectively. The magnitudes of  $E^2$  for these systems are 1.0,  $1/3$ ,  $s^2$ ,  $2/3$ , and 1.0 for periphery, distributed, core, 9-column and 4-column cases, respectively.

The following relationships between torsional frequency  $\omega_{\theta}$  and stiffness distribution parameter  $E$  result for the various systems

$$\frac{\omega_{p\theta}}{E_p} = \frac{\omega_{d\theta}}{E_d} = \frac{\omega_{c\theta}}{E_c} = \frac{\omega_{n\theta}}{E_n} = \frac{\omega_{f\theta}}{E_f} = \text{constant} \quad (30)$$

The above equation indicates that, for a particular aspect ratio and equal mass and total translational stiffness, the parameter  $\left(\frac{\omega_{\theta}}{E}\right)$  remains constant regardless of the distribution of stiffness.

To demonstrate the application of the results equations (15) and (16) are plotted. Typical curves for the instability regions in  $\Omega_{\theta} - \Omega$  parameter space of the aforementioned systems and an example set of values for parameters  $r$ ,  $\lambda$  and  $\zeta_x$  are shown in figures 3-6. Assuming a distributed resistance system to lie within the unstable region of figure 5, the corresponding periphery system (figure 3) will fall outside the stability curves, thus indicating that the distributed system is more susceptible to torsional response than the companion periphery system having equal mass and total lateral stiffnesses.

Figure 7 presents the universal upper and lower bound stability curves drawn for equations (18) and (19). For any plan layout of the structural system, knowing properties such as frequencies and aspect ratios, the stability of the system can easily be determined. If the values of  $\hat{\Omega}_{\theta}$  and  $\hat{\Omega}$  are such that they fall within the instability boundaries the system is unstable, whereas falling outside the curves means the structure is torsionally stable.

In figures 3-7 it may be observed that the stability curves for all systems do not include any point on the equal frequency line  $\Omega_\theta = \Omega$ ; all the lower bound curves are asymptotic to this line. While it is known that coincident lateral input and translational frequencies result in translational resonance,  $\Omega_\theta = \Omega$  (i.e., coincident torsional and input translational frequencies) does not induce torsional coupling. Parametric excitation is thus possible only when the torsional frequency of the system is slightly higher than the translational exciting frequency.

Equations (24) and (25) are plotted in figures 8-10 for periphery, distributed and core systems, respectively. In these diagrams the peaks of figures 3-7 do not exist and the upper and lower bound curves are almost straight lines. The magnitude of static torsional buckling is also shown. Static torsional buckling corresponds to zero magnitude for the "apparent" torsional frequency (ref. 7). In terms of real frequency  $\Omega_\theta$  this condition yields

$$\Omega_\theta^2 = \frac{9\lambda E^2}{2(1 + r^2)} \quad (31)$$

for which further normalization gives

$$\hat{\Omega}_\theta^2 = \frac{9\lambda}{2(1 + r^2)} \quad (32)$$

Equation (31) is represented by the dashed lines in figures 8-10. In these figures, some overlapping of the static buckling regions with the dynamic coupling regions is noticed. The overlapping zones do not have any physical meaning in the sense of instability since, for this condition, the Mathieu-Hill equation does not exist. This situation only arises in the neighborhood of zero  $\Omega$  values.

The corresponding universal upper and lower bound instability curves defining the zone of induced torsional coupling, following equations (27) and (28) and again without resonance-resembling peaks, are identical to those of the periphery system shown in figure 8.

## CONCLUSIONS

Within the scope of the present investigation, the following conclusions are noted.

1. Torsional motion in a symmetric structure can be induced due to nonlinearity of the resisting elements.
2. The distribution of the resisting elements influences stability against induced torsion; selectively rearranging the resisting elements can eliminate torsional coupling for given excitation frequency.
3. Universal upper and lower bound instability curves have been presented to



identify the susceptibility of symmetric structures with different stiffness distributions and equal mass and total lateral stiffness to torsional coupling.

4. It has been shown that torsional oscillations are induced only when  $\Omega_0$  is greater than input frequency ratio  $\Omega$ .

Thus, in summary, the results obtained in this study can usefully be employed in evaluating the susceptibility to nonlinear torsional coupling of a proposed or existing building structure, even though the structure is symmetric and the expected ground excitation is purely translational.

#### SYMBOLS

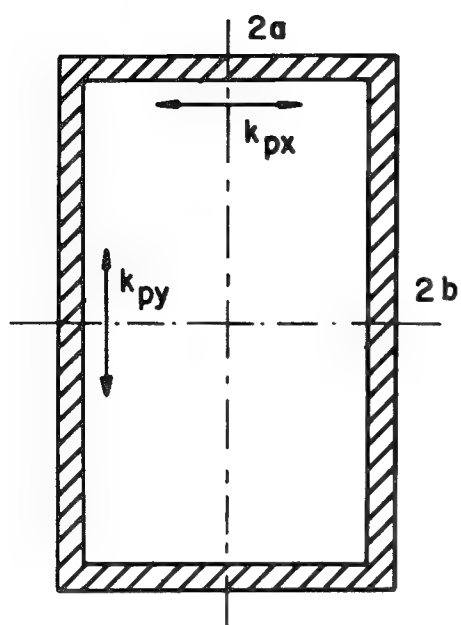
$a, b$	plan dimensions of building
$D$	square of nondimensional amplitude of single degree of freedom system
$E, F$	stiffness distribution parameters in x- and y-directions, respectively
$\kappa$	ratio of total translational stiffnesses ( $K_x/K_y$ )
$K_x, K_y$	total translational stiffnesses in x- and y-directions, respectively
$K_\theta$	torsional stiffness of the system about vertical axis
$r$	building plan aspect ratio ( $a/b$ )
$R_x(\delta_j), R_y(\delta_j)$	resisting forces in element 'j'
$s$	ratio of length of core with respect to lateral dimension of building
$t$	time
$u(t), v(t)$	lateral displacements of mass center
$U$	amplitude of sinusoidal ground excitation
$x, y$	principal coordinates
$\bar{r}$	mass radius of gyration
$\delta_0$	reference displacement
$\delta_j$	displacements of resisting elements
$\zeta_x, \zeta_\theta$	critical damping ratios
$\theta(t)$	rotational displacement

$\lambda$	coefficient of nonlinearity
$\Lambda_x(\tau), \Lambda_\theta(\tau)$	nondimensional response
$\tau$	nondimensional time
$\omega$	frequency of sinusoidal ground excitation
$\omega_x, \omega_\theta$	uncoupled frequencies
$\Omega$	ground excitation frequency ratio ( $\omega/\omega_x$ )
$\Omega_y$	translational frequency ratio ( $\omega_y/\omega_x$ )
$\Omega_\theta$	torsional frequency ratio ( $\omega_\theta/\omega_x$ )
$\hat{\Omega}$	normalized frequency ratio ( $\Omega/E$ )
$\hat{\Omega}_\theta$	universal torsional frequency ratio ( $\Omega_\theta/E$ )

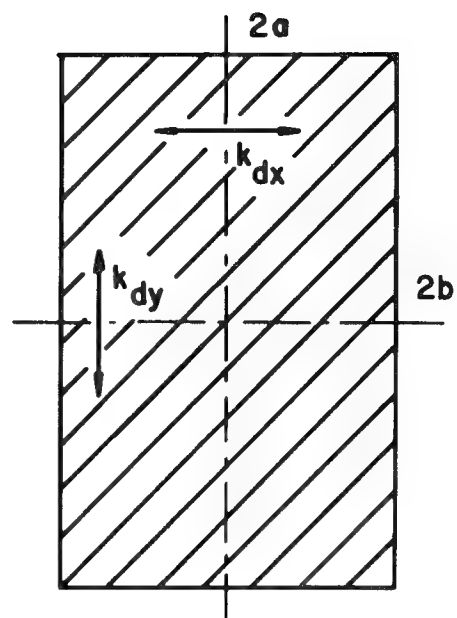
#### REFERENCES

1. Hoerner, J.B.: Modal Coupling and Earthquake Response of Tall Buildings. Ph.D. Thesis, California Institute of Technology, Pasadena, California, 1971.
2. Kan, C.L., and Chopra, A.K.: Coupled Lateral Torsional Response of Buildings to Ground Shaking. Report No. EERC 76-13, University of California, Berkeley, California, May 1976.
3. Dempsey, K.M., and Irvine, H.M.: Envelopes of Maximum Seismic Response for a Partially Symmetric Single Story Building Model. Earthquake Engineering and Structural Dynamics, Vol. 7, 1979, pp. 161-180.
4. Pekau, O.A., and Gordon, H.A.: Coupling of Torsional-Translational Response of Buildings During Earthquakes. Canadian Journal of Civil Engineering, Vol. 7, No. 2, 1980, pp. 282-293.
5. Pekau, O.A., and Syamal, P.K.: Coupling in Dynamic Response of Nonlinear Unsymmetric Structures. Computers and Structures, Vol. 13, No. 1-3, 1981, pp. 197-204.
6. Tso, W.K., and Asmis, K.G.: Torsional Vibrations of Symmetrical Structures. Proceedings of the First Canadian Conference on Earthquake Engineering, Vancouver, Canada, 1971, pp. 178-186.
7. Tso, W.K.: Induced Torsional Oscillations in Symmetrical Structures. Earthquake Engineering and Structural Dynamics, Vol. 3, No. 4, April-June 1975, pp. 337-346.
8. Syamal, P.K., and Pekau, O.A.: Dynamic Torsional Response of Symmetric Structures. Proceedings of the ASCE/EMD Specialty Conference on Dynamic Response of Structures, Atlanta, 1981, pp. 902-916.

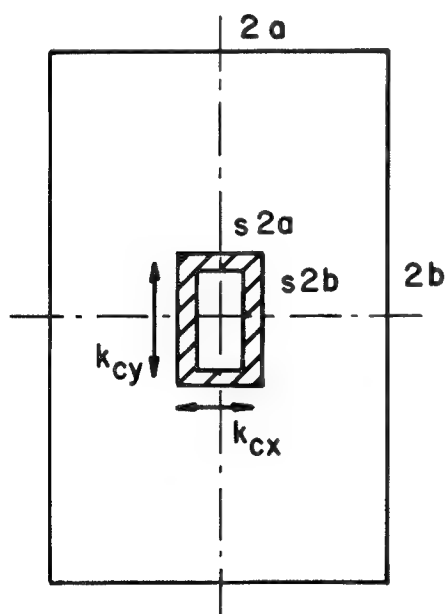
9. Morgan, J.R.: Response of Simple Structural Systems to Travelling Seismic Waves. Ph.D. Thesis, University of Illinois at Urbana-Champaign, 1979.
10. Newmark, N.M: Torsion in Symmetrical Buildings. Proceedings of the Fourth World Conference on Earthquake Engineering, Vol. 2, Santiago, Chile, 1969, pp. A3.19-A3.32.
11. Tsicnias, T.G., and Hutchinson, G.L.: Evaluation of Code Requirements for the Earthquake Resistant Design of Torsionally Coupled Buildings. Proceedings of the Institution of Civil Engineers, Part 2, Vol. 71, September 1981, pp. 821-843.
12. Bolotin, V.V.: The Dynamic Stability of Elastic Systems. Holden-Day Inc., San Francisco, 1964.



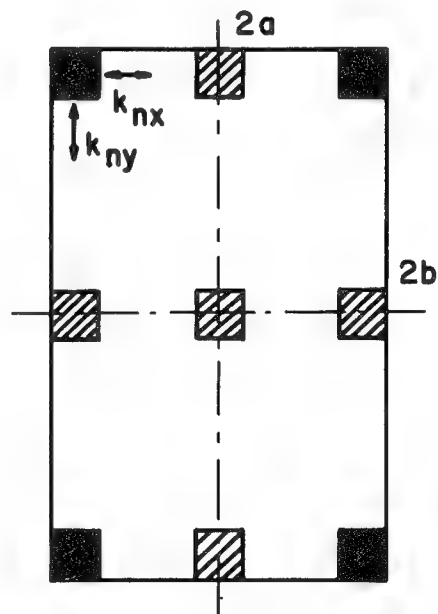
(a) Periphery resistance



(b) Uniformly distributed resistance



(c) Central-core resistance



(d) 9- and 4-column resistance

Figure 1 - Arrangement of structural systems

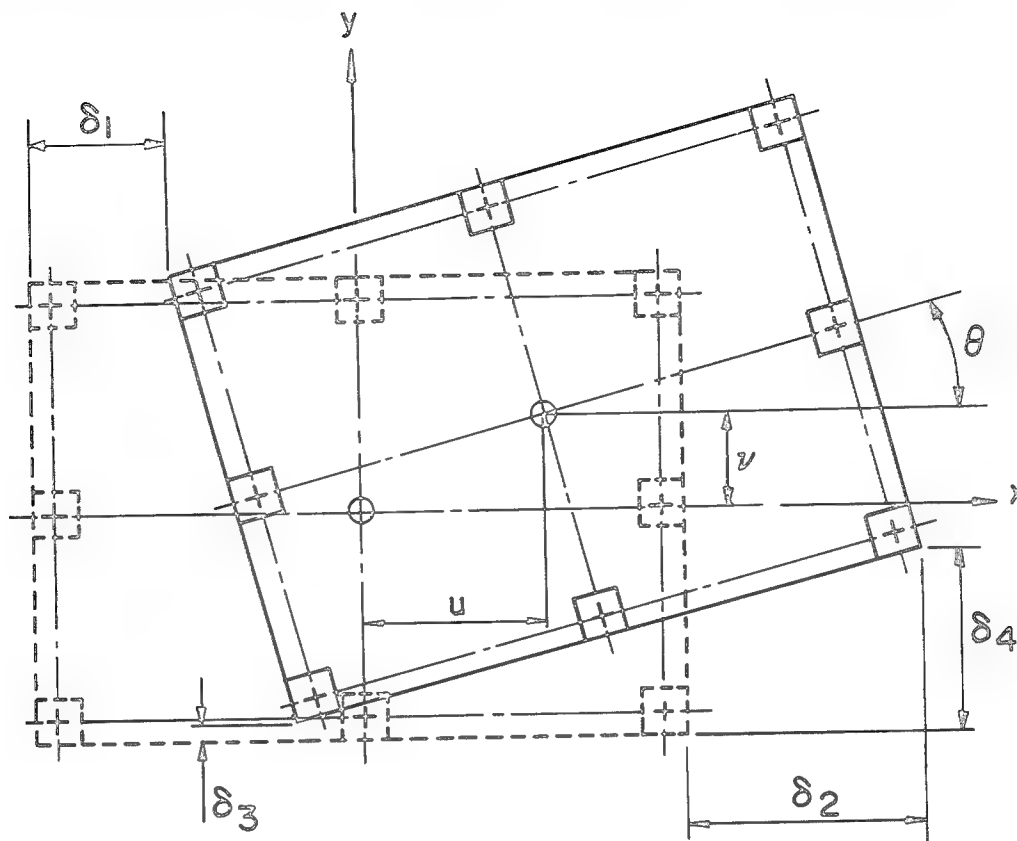


Figure 2 - Displaced position of building.

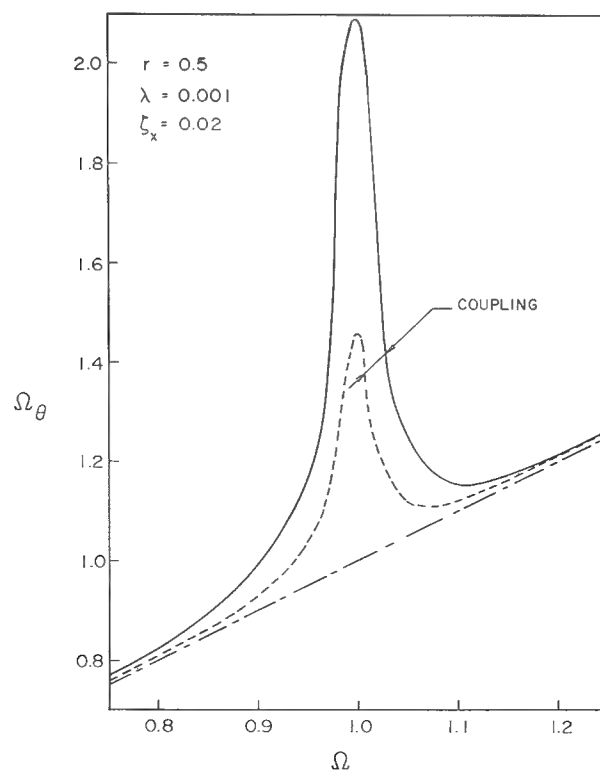


Figure 3 - Region of induced torsional coupling - periphery and 4-column systems.

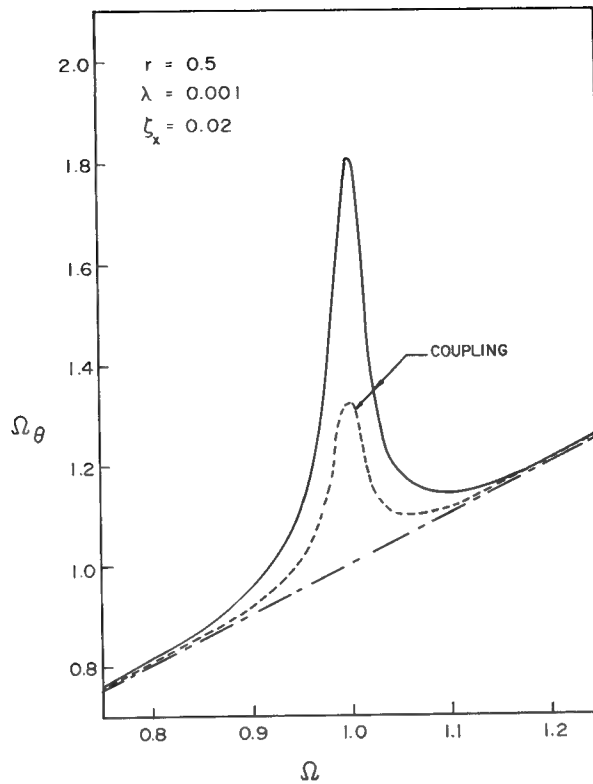


Figure 4 - Region of induced torsional coupling - 9-column system.

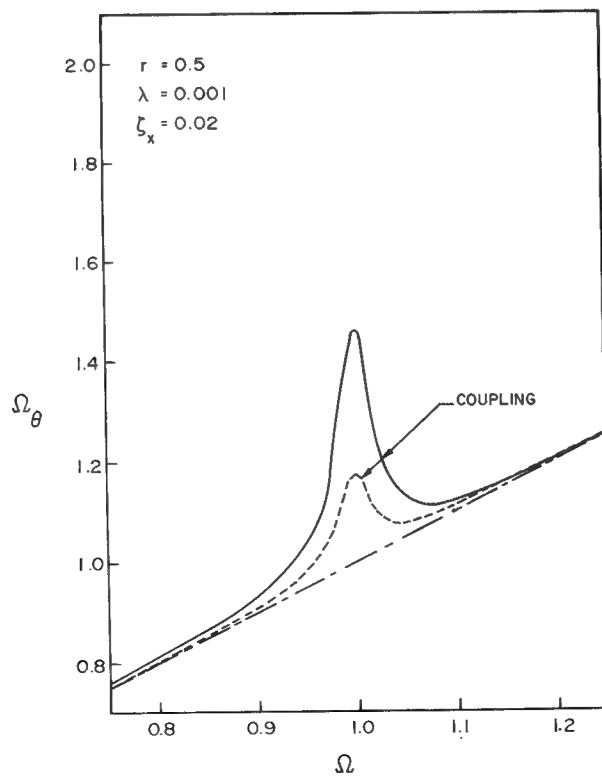


Figure 5 - Region of induced torsional coupling - distributed system.

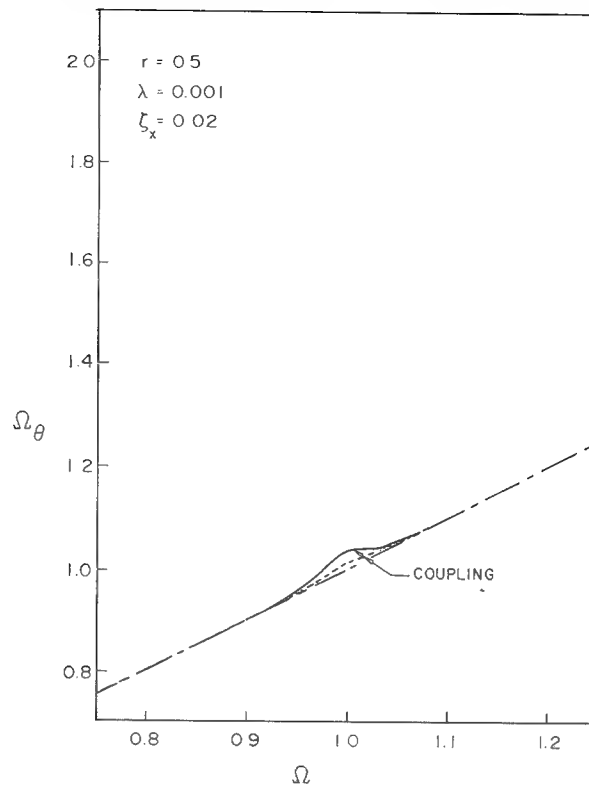


Figure 6 - Region of induced torsional coupling - core system.

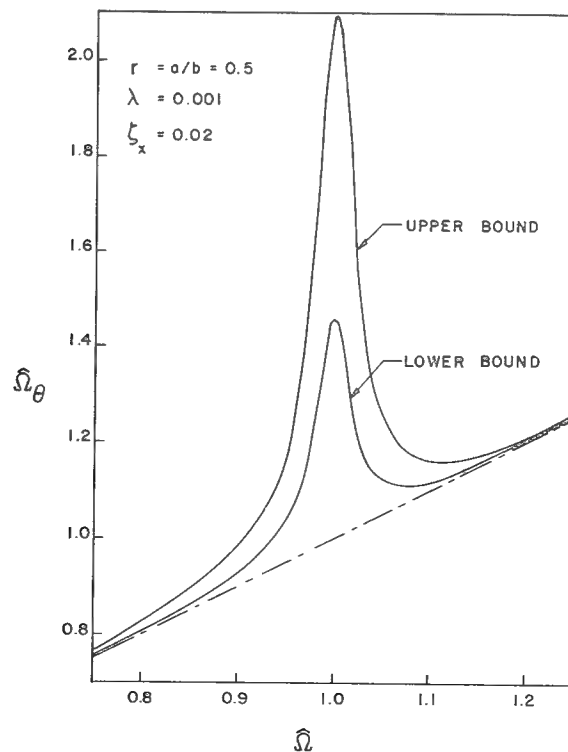


Figure 7 - Normalized region of torsional coupling (applicable for all systems).

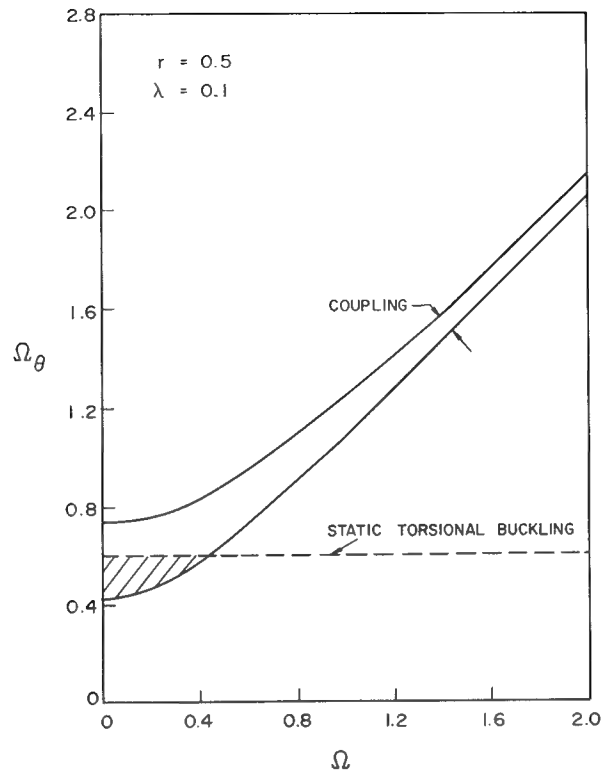


Figure 8 - Region of induced torsional coupling - periphery system with  $\delta_o = UD/\omega_x^2$ .

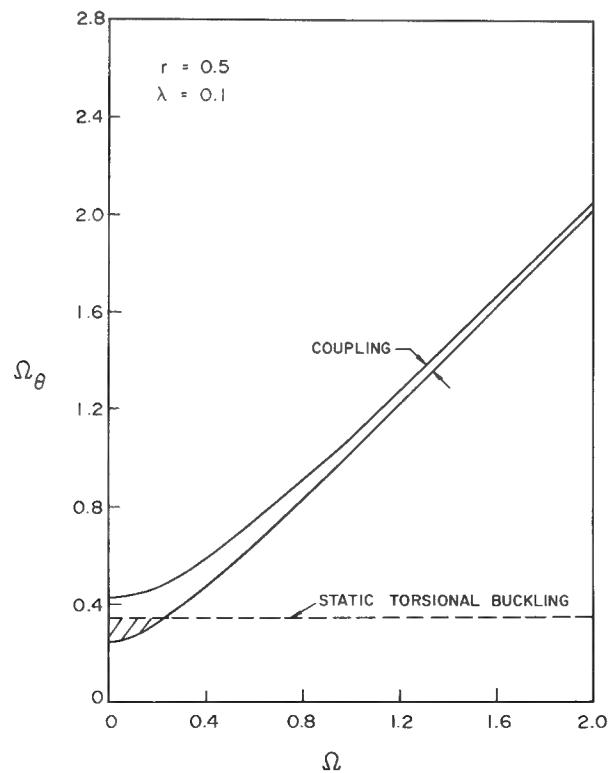


Figure 9 - Region of induced torsional coupling - distributed system with  $\delta_o = UD/\omega_x^2$ .



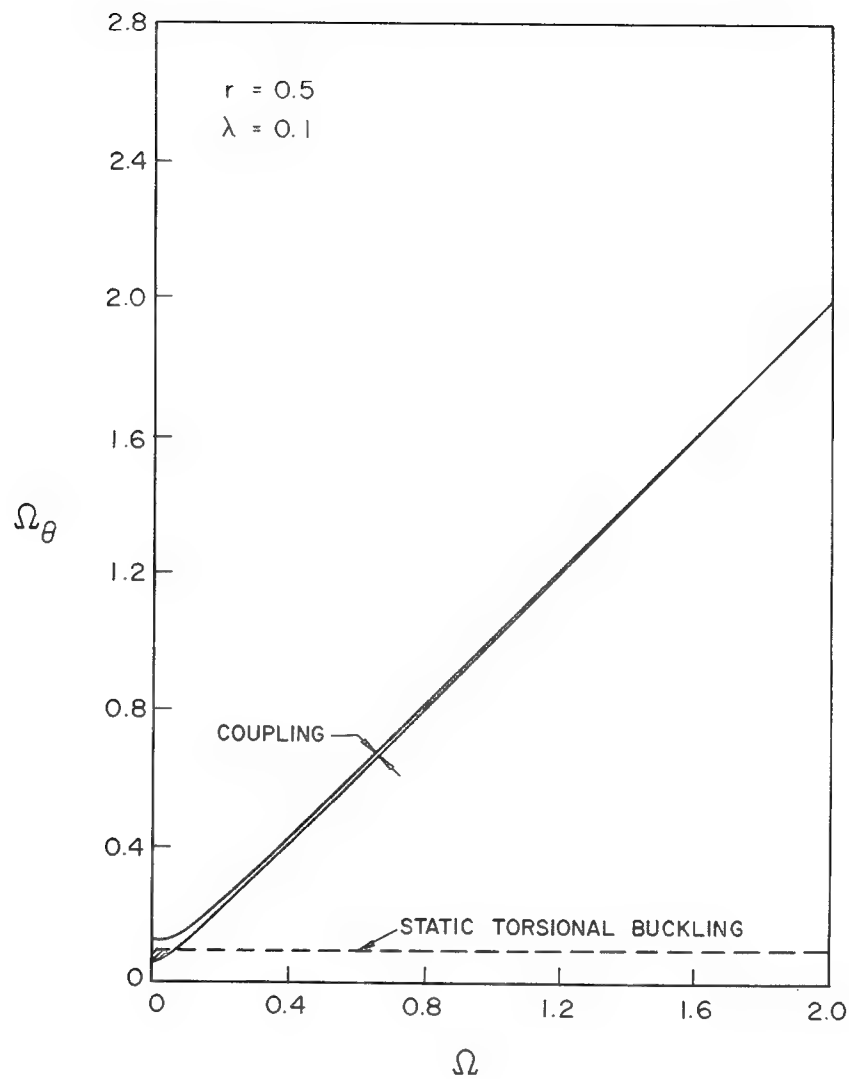


Figure 10 - Region of induced torsional coupling - core system with  $\delta_o = UD/\omega_x^2$ .

# ADVANCES AND TRENDS IN PLATE BUCKLING RESEARCH\*

Arthur Leissa  
Department of Engineering Mechanics  
Ohio State University

## SUMMARY

Recent advances and current trends in plate buckling research are summarized. The field is divided into three parts: (1) classical buckling studies, including plates of rectangular, circular and other shapes; (2) classical complicating effects, including elastic foundation, anisotropic material, variable thickness, shear deformation and nonhomogeneous material and; (3) nonclassical considerations, including postbuckling, imperfections, parametric excitation, follower forces, magnetoelastic buckling and inelastic buckling. Approximately 100 references for the period 1978-present are cited.

## INTRODUCTION

The buckling of plates is a vast, complicated and somewhat disordered subject. Analytical solutions to problems began ninety years ago with the classical paper of Bryan (ref. 1) and have continued at a rapid rate since that time, yielding on the order of 2000 publications in the technical literature. Part of the achievement of earlier decades was summarized in the well known works by Timoshenko and Gere (ref. 2), Gerard and Becker (ref. 3) and Bulson (ref. 4). The writer is currently engaged in a research project attempting to organize, clarify and summarize this vast body of knowledge dealing with plate buckling by means of a comprehensive monograph. The intent of the present paper is to identify recent advances and current trends in plate buckling research from the relatively recent literature (i.e., 1978 - present).

## CLASSICAL BUCKLING STUDIES

Classical buckling theory is based upon the assumptions of small deflections and a linearly elastic material, and yields the bifurcation behavior depicted in figure 1. That is, the well-known plot of transverse plate displacement versus inplane loading follows the ordinate (I) upwards, showing no displacement with increased load until a critical force ( $P_{cr}$ ) is reached. At this bifurcation point the curve theoretically may continue up the ordinate (II) or, more realistically, may follow a buckling path (III), which is horizontal for the linear idealization.

The classical plate buckling problem is governed by the universally accepted differential equation of equilibrium:

\* This work was supported by the Office of Naval Research and the Air Force Office of Scientific Research under Contract No. N00014-80-K-0281.

$$D\nabla^4 w + P_x \frac{\partial^2 w}{\partial x^2} + 2 P_{xy} \frac{\partial^2 w}{\partial x \partial y} + P_y \frac{\partial^2 w}{\partial y^2} = 0 \quad (1)$$

in rectangular coordinates, where  $w$  is the transverse displacement,  $D$  is the flexural rigidity,  $\nabla^4$  is the biharmonic differential operator,  $P_x$  and  $P_y$  are compressive inplane forces (per unit length) and  $P_{xy}$  is inplane shearing force, along with appropriate linear equations representing the boundary conditions. This set of homogeneous equations defines a linear eigenvalue problem for which the eigenvalues are nondimensional buckling parameters, and the eigenfunctions describe the corresponding buckled mode shapes.

On the order of 1000 references can be found dealing with classical plate buckling. These treat a variety of shapes (e.g., rectangular, circular, triangular, parallelogram, sectorial), edge constraints (clamped, simply supported, free, elastically supported, intermittently supported, point supported), loading conditions (e.g., uniform and variable edge loads, body forces) and interior complications (e.g., holes, cracks, point supports). Exact solutions exist only for a very few problems involving rectangular and circular plates subjected to uniform normal edge loading. For all others solutions are necessarily obtained by approximate methods (e.g., Rayleigh-Ritz-Galerkin, finite elements, finite differences, collocation) the exact solution ultimately requiring the formulation of an infinite eigenvalue determinant. Approximate solutions are then obtained to any desired degree of accuracy by successive truncation of the determinant (and/or generating mesh size).

### Rectangular Plates

Although hundreds of references are available for classical, bifurcation buckling problems for rectangular plates, the subject is far from exhausted (cf., refs. 5-17) and, indeed, quite a bit of useful information still needs to be found. The design considerations entering the problem include: (a) edge conditions (b) loading conditions (c) aspect ratio and (d) Poisson's ratio. For any arbitrary loading, there exist 108 combinations of classical boundary conditions (i.e., clamped, simply supported or free). Typically, one can find a significant amount of results in the literature for relatively few of these combinations (e.g., all sides simply supported, all sides clamped), and mostly for constant uniaxial or biaxial loading (i.e.,  $P_x$  and  $P_y$  constant, and  $P_{xy} = 0$  in eq. (1)).

The thorough development and widespread understanding of approximate analytical methods, along with the continued increase in digital computer speed and storage capabilities, have made it possible to obtain numerical results straightforwardly and cheaply which, not too long ago, were out of the question. Efficacy of this type was notably shown by Bassily and Dickinson (ref. 5) who used the Ritz method with beam functions to determine first the nonuniform inplane stresses present under certain loading conditions, and once again to calculate critical values of the loading parameters for buckling. The procedure was demonstrated with a cantilevered plate subjected to inplane acceleration loads (fig. 2). Kielb and Han (ref. 11) gave comprehensive results for hydrostatically loaded (i.e.,  $P_x = P_y = \text{constant}$ ,  $P_{xy} = 0$  in eq. (1)) plates having all six possible combinations of clamped and simply supported edges.

The most extensive results to date for rectangular plates were obtained recently by Kalro (ref. 10) using the Ritz method with algebraic polynomial trial functions. Complete sets of critical buckling loads were presented for rectangular plates having

three aspect ratios ( $a/b = 0.5, 1, 2$ ) and the following loading conditions:

- (1) uniaxial compression (36 cases)
- (2) hydrostatic compression (21 cases)
- (3) constant shear stress (21 cases)
- (4) inplane bonding (54 cases; e.g., fig. 3)

The results for shear loading may be seen in Table 1, arranged in order of descending buckling loads for square ( $a/b=1$ ) plates.

Considerably more research has recently taken place on the buckling of rectangular plates having internal holes (refs. 18, 19) and cracks (refs. 20-22) than for the corresponding free vibration problems (ref. 23). Buckling mode shapes have also been determined experimentally by means of moire fringes (ref. 24).

### Circular and Other Shapes

Not a great deal has been done recently to determine buckling loads and mode shapes for plates having non-rectangular shape. Circular plates have received some attention (refs. 25-28). Ku (ref. 27) developed a method for obtaining lower bounds for buckling loads, and used it on clamped and simply supported plates loaded in hydrostatic compression. Pardoen (ref. 28) demonstrated the finite element method on the same two problems, as well as on a clamped-free annular plate. Sato (ref. 29) analyzed elliptical plates utilizing the solution of equation (1) in elliptical coordinates in terms of Mathieu functions to solve problems for simply supported boundaries having elastic moment constraint.

Plates of parallelogram shape were analyzed by a number of researchers (refs. 30-36). Edwardes and Kabaila (ref. 30) discussed a method for dealing with the stress singularity that exists at the obtuse corners of simply supported plates by means of finite elements. The buckling of simply supported, isotropic plates was also studied by Kennedy and Prabhakara (refs. 31, 32) using a form of the series method; by Mizusawa, Kajita and Naruoka (refs. 33, 34) using the Ritz method with B-spline functions as trial functions; and by Thangam Babu and Reddy (ref. 36) using a finite strip method. Numerical results for the buckling parameters of regular polygonal, isotropic plates having 5, 6, 7 and 8 sides all clamped, subjected to hydrostatic compressive stress, were obtained by Laura, Luisoni and Sarmiento (ref. 37), using the Ritz method and algebraic polynomial trial functions.

### CLASSICAL COMPLICATING EFFECTS

In this section a number of phenomena will be considered which serve to complicate the classical differential equation of the buckling problem (eq. (1)) and make it more difficult to solve. These complicating effects include:

- (1) elastic foundation
- (2) anisotropic material
- (3) variable thickness
- (4) shear deformation
- (5) nonhomogeneous material, including laminated fibrous composites.

In each case, however, the resulting formulation typically still yields eigenvalue problems, and they are linear. The aforementioned phenomena arise quite commonly in practical design situations and their effects in buckling problems have all been studied for decades. Advances in understanding in each of these areas have been made during the past several years.

### Elastic Foundation

In the case of a plate having its transverse displacement ( $w$ ) resisted in both directions by a force supplied by an elastic foundation (or surrounding medium), the governing differential equation of equilibrium (1) is traditionally modified by adding a linear term,  $k w$  (where  $k$  is the stiffness of the foundation) to its left-hand side. The eigenvalue problem of free vibration is essentially unaffected by this added term, yielding frequencies whose squares are shifted upward linearly by the foundation stiffness (cf., ref. 38, p. 1). However, the plate buckling problem is typically a different one, requiring a more complicated solution of the governing differential equation.

Several recent works have appeared dealing with the effects of elastic foundations (refs. 39-43). Cimetiere (refs. 39, 40) examined the problem of the plate having unilateral constraints. Wang (ref. 43) used finite difference and finite elements to analyze the elastic buckling of an ice sheet, which is modeled as a semi-infinite plate on an elastic foundation with a semicircular cutout at the edge.

### Anisotropic Material

For a plate composed of material which is generally anisotropic the first term ( $D \nabla^4 w$ ) of the governing equation (1) is replaced by

$$D_1 \frac{\partial^4 w}{\partial x^4} + D_2 \frac{\partial^4 w}{\partial x^3 \partial y} + D_3 \frac{\partial^4 w}{\partial x^2 \partial y^2} + D_4 \frac{\partial^4 w}{\partial x \partial y^3} + D_5 \frac{\partial^4 w}{\partial y^4} \quad (2)$$

where  $D_1, \dots, D_5$  are constant coefficients depending upon the material properties. However, the second and fourth terms of expression (2) prohibit separation of variables and exact solution of the resulting differential equation. For plates of orthotropic material, with directions of rectangular orthotropy parallel to the edges, these terms vanish, and exact solutions are possible which are algebraic generalizations of the well-known ones for isotropic plates (i.e., plates having two opposite sides simply supported).

Considerable research has been reported in recent publications for the buckling of orthotropic plates (refs. 31, 32, 36, 37, 44-50). Of particular interest are the results for plates of non-rectangular shape, viz:

- (1) parallelograms (refs. 31, 32, 36)
- (2) regular polygons having 5, 6, 7 or 8 sides (ref. 37)
- (3) polar-orthotropic annular plates (ref. 50)
- (4) circular sectors having polar orthotropy (ref. 51)

### Variable Thickness

Plates of variable thickness introduce considerable complication into the mathematical eigenvalue problem. In particular, the governing equation (1) must be generalized so that its first term ( $D \nabla^4 w$ ) is replaced by a more general set of terms having variable coefficients, viz:

$$\nabla^2(D\nabla^2 w) - (1-\nu) \frac{\partial^2 D}{\partial y^2} \frac{\partial^2 w}{\partial x^2} - 2 \frac{\partial^2 D}{\partial x \partial y} \frac{\partial^2 w}{\partial x \partial y} + \frac{\partial^2 D}{\partial x^2} \frac{\partial^2 w}{\partial y^2} \quad (3)$$

in rectangular coordinates (with similar complications in other coordinate systems, such as polar), where  $\nabla^2$  is the Laplacian operator and  $\nu$  is Poisson's ratio. The flexural rigidity is defined, as in equation (1), by

$$D = \frac{Eh^3}{12(1-\nu^2)} \quad (4)$$

but now the thickness,  $h$ , is a variable. The resulting differential equation although linear has, in general, been incapable of exact solution.

However, if an energy approach is used, such as the Ritz method, no major complication is added by the presence of variable thickness. This method was recently used by Laura, Ficcadenti and Valerga de Greco to analyze the buckling of circular plates having a quadratic (ref. 52) and a piecewise linear (ref. 53) thickness variation. Gupta and Lal (ref. 54) were able to obtain solutions to the differential equation in polar coordinates by the method of Frobenius and used them to determine the critical buckling parameters for hydrostatically loaded, clamped and simply supported circular plates of linear thickness variation.

#### Shear Deformation

Consideration of shear deformation, in addition to the usual bending deformation, adds to the flexibility of a system, thereby decreasing the buckling loads and becoming of increased importance as the thickness-to-length (or width) of a plate increases. Mathematically, the theory is typically generalized to include three dependent variables, transverse total displacement ( $w$ ) and orthogonal bending slope changes ( $\psi_x$  and  $\psi_y$ ), yielding a governing set of differential equations of the sixth order (compared with the fourth order eq. (1)), and requiring three independent boundary conditions per edge. An application of a typical shear deformation theory to rectangular plates having two opposite sides simply supported was made by Hinton (ref. 55).

Ziegler (ref. 56) recently made a significant further development of thick plate theory including the effects of inplane (i.e., extensional) deformation together with shear deformation. He further showed that the inplane deformation effects can be more important than the shear deformation effects in the same problem.

#### Nonhomogeneous Material

Nonhomogeneous material may involve either continuous or discontinuous nonhomogeneity. The first case may readily arise, for example, for certain non-metallic materials such as rubber or styrofoam, or because of nonuniform thermal or other environmental effects upon the material properties, and includes material property variation through the thickness and/or in the other two directions. The second case includes layered, sandwich and fibrous composite plates. A number of references dealing with layered and sandwich plates have recently appeared (refs. 57-63).

Laminated fibrous composite plates have received a particularly large amount of interest in recent years. Here the geometry of the laminate (e.g., elastic modulus ratios of individual plies, angle-ply or cross-ply layups, number of plies, symmetry with respect to the midplane) is exceedingly important in determining stiffness properties of the plate and, hence, its buckling characteristics. For example, a cross-ply plate symmetrically laminated with respect to its midplane may be treated as an orthotropic plate. Similarly, a symmetric angle-ply plate may be accommodated by homogeneous, anisotropic plate theory. However, antisymmetric or asymmetric laminates result in bending-stretching coupling, resulting in an eighth order set of governing equations (as for a shell). For such plates it has been shown that buckling loads are significantly reduced from those predicted by homogeneous plate theory when only a small number of layers is used. A summary of research in the buckling of composite plates has recently appeared (ref. 64).

### NONCLASSICAL CONSIDERATIONS

In this part considerations relevant to buckling will be treated, which are not dealt with by the foregoing linear, eigenvalue problems. These include

- (1) postbuckling
- (2) geometric imperfections
- (3) parametric excitation
- (4) follower forces
- (5) magnetoelastic buckling
- (6) inelastic material

#### Postbuckling

It is well known that, if a plate should reach its critical loading condition and buckle, under usual conditions it will deflect into a shape having finite amplitude which will be able to support the buckling load. This postbuckling configuration will correspond to another equilibrium state, and will typically require utilizing nonlinear, large amplitude plate equations in order to be determined analytically. Indeed, the plate will typically be able to withstand still larger loads by suffering larger displacements (curve IV in fig. 1) until it fails due to another reason, such as plastic collapse.

The subject of postbuckling has received significant consideration during the past four years (refs. 65-77). Numerical results for rectangular (refs. 66, 68, 69, 70, 72, 73, 75, 76), circular (refs. 66, 71, 77), annular (ref. 74) and parallelogram (ref. 67) plates have appeared.

Another phenomenon that may occur in the postbuckling range is called "secondary buckling". It has been shown both theoretically and experimentally that for loads sufficiently greater than the critical buckling value, and after significant postbuckling displacement has occurred, the plate may jump from one postbuckled configuration into another, having a different number of waves. Thus, curve IV of figure 1 may have a "secondary" bifurcation point. Indeed, still more bifurcation points may be reached as the load is increased further. This topic has received recent attention (refs. 68, 69, 72, 73, 75).

#### Geometric Imperfections

If a plate is not perfectly flat, then the application of small inplane forces

at its edges or its interior will cause finite transverse displacements. This deviation from flatness (called an "imperfection") may be present in the unloaded state due to, for example, manufacturing or previous loading conditions, or it may be due to the presence of initial transverse loading or edge moments. The resulting inplane load-transverse displacement curve, is a nonlinear one. A representative plot is depicted by curve V in figure 1. That is, the curve deviates from the first part of the linear bifurcation path (I) as the load is increased, and then typically adapts itself to become asymptotic with the bifurcation postbuckling curve (IV) for large inplane loads. No bifurcation exists. As the imperfection amplitude approaches zero, curve V smoothly approaches the kinked bifurcation path I-IV with sharply increasing curvature at the bifurcation point.

Recent studies of the effects of imperfections have included rectangular (refs. 78-80) and circular plates (refs. 81-84). Hui and Hansen (ref. 79) studied the infinite plate on an elastic foundation. Turvey (ref. 84) examined simply supported and clamped circular plates having linear thickness variation.

#### Parametric Excitation

In the case of "parametric excitation" part of the inplane forces are caused to vary periodically (usually sinusoidally) with time. Under some circumstances the forced vibration response will become dynamically unstable at smaller critical loads.

There has been a small amount of recent work on this subject (refs. 85-87). For example, Datta (ref. 85) made an experimental study on a thin rectangular plate having an internal slot with straight sides and circular ends, subjected to initial static tension in addition to the sinusoidal end force. As in the purely static case, local instability was observed in the vicinity of the slot. Tani and Nakamura (ref. 86) examined clamped annular plates having both edges subjected to the same static plus periodic radial loads.

#### Follower Forces

In classical plate buckling problems the inplane loads are prescribed to remain acting in the same plane while the plate deforms. If one prescribes that the direction of the force must follow the rotation of the plate at the point of force application, about an axis perpendicular to the force, then one has what is termed a "follower force". If the force only rotates some fraction of the total plate slope, then the fraction is called the "tangency coefficient". The resulting system is non-conservative with respect to energy and the analysis is a dynamic one.

Celep (ref. 88) recently studied the axisymmetric instability of a completely free circular plate having edge loads of arbitrary tangency angle. Farshad (ref. 89) examined the square cantilever plate and obtained results for the case of uniform compressive loads upon the two opposite free edges. Leipholz (ref. 90) treated the rectangular simply supported plate having tangential body forces of the follower type.

#### Magnetoelastic Buckling

A plate of magnetically soft material oriented so that its face is normal to a magnetic field may buckle as the field intensity is increased to a critical value. The destabilizing load may be a magnetic body torque which is proportional to the rotation of the plate at each point.



Miya, Hara and Someya (ref. 91) obtained experimental results for a cantilevered rectangular plate, and numerical results for solid and annular circular plates. Numerical results for the first problem were subsequently achieved (ref. 92). Van de Ven (ref. 93) examined circular plates having clamped, simply supported or free edges.

### Inelastic Material

In this section we will consider plates made of material which, under the given loading conditions, violates the classical assumption of a linear elastic stress-strain curve. A typical and important case is that of elastic-plastic material behavior. In this case the inplane load-transverse displacement curves IV or V of figure 1 would begin to fall away from the curves shown when the load corresponding to the yield point is reached at any point in the plate. Another important case is that of creep buckling. Here the material undergoes time-dependent deformations. This case is not a stability problem of the classical type, but rather a matter of determining the length of time before failure.

Inelastic plate buckling problems have received considerable attention in the past four years (refs. 66, 94-114). A sample of the problems considered follows below. Dietrich et al. (ref. 96) made experimental, plastic buckling studies for simply supported rectangular plates subjected to biaxial compression. Gupta (ref. 100) developed a numerical procedure for the solution of plastic buckling problems, and demonstrated it for simply supported and clamped plates subjected to uniaxial compression. Popov and Hjelmstad (ref. 106) made tests of plate girder webs (which may be considered as plates) subjected to cyclic loading in the inelastic range. Needleman and Tvergaard (ref. 105) made analyses of the imperfection sensitivity of simply supported square plates exhibiting elastic-plastic behavior. Tvergaard (ref. 113) also considered creep buckling. Shrivastava (ref. 109) included transverse shear deformation effects in a plastic analysis of various uniaxially loaded rectangular plate configurations.

### CONCLUSIONS

The field of plate buckling research is a reasonably active one, with more than 100 technical references having appeared in the past four years.

However, it seems that the rate of research using classical plate theory has ebbed somewhat in recent years, compared with the activity of previous decades. Certainly the 30 references found in the present search are far less than the 100 found for classical plate vibrations over a similar period (ref. 23). A similar disparity exists for classical complicating effects - less than 30 in the present work covering buckling, and about 200 for plate vibrations (ref. 116). Furthermore, the literature search for the present plate buckling paper was more complete than for the vibration ones (refs. 23, 116).

The number of classical buckling problems yet unsolved is still great. And because of their practical importance it is hoped that researchers will return to them in the coming decade and provide accurate and comprehensive results useful for design and to serve as a solid foundation upon which further nonclassical studies may be based. The analytical methods and computational capability used for plate vibration problems are equally useable for buckling solutions.

## REFERENCES

1. Bryan, G. H.: On the Stability of a Plane Plate under Thrusts in its own Plane with Applications to the "Buckling" of the Sides of a Ship. Proc. London Math. Soc., vol. 22, 1891, pp. 54-67.
2. Timoshenko, S. P.; and Gere, J. G.: Theory of Elastic Stability, 2nd ed., McGraw-Hill Book Co., 1961, 541 pp.
3. Gerard, G.; and Becker, H.: Handbook of Structural Stability. Part I. Buckling of Flat Plates. NACA TN 3781, 1957, 102 pp. Part VII. Strength of Thin-Wing Construction. NACA TN D-162, 1959, 83 pp.
4. Bulson, P. S.: The Stability of Flat Plates. Chatto and Windus, London, 1970, 470 pp.
5. Bassily, S. F.; and Dickinson, S. M.: Buckling and Vibration of In-Plane Loaded Plates Treated by a Unified Ritz Approach. J. Sound Vib., vol. 59, 1978, pp. 1-14.
6. Datta, P. K.: Static Stability Behavior of Plate Elements with Nonuniform, In-Plane Stress-Distribution. J. Mech. Engrg. Sci., vol. 21, no. 5, 1979, pp. 363-365.
7. Dickinson, S. M.: The Buckling and Frequency of Flexural Vibration of Rectangular Isotropic and Orthotropic Plates Using Rayleigh's Method. J. Sound Vib., vol. 1, 1978, pp. 1-8.
8. Garashchuk, I. N.; Zamula, G. N.; and Prikazchikov, V. G.: Numerical Solution of Plate-Stability Problems. Soviet Appl. Mech., vol. 14, no. 5, 1978, pp. 509-512.
9. Graves Smith, T. R.; and Sridharan, S.: A Finite Strip Method for the Buckling of Plate Structures under Arbitrary Loading. Intl. J. Mech. Sci., vol. 20, no. 10, 1978, pp. 685-693.
10. Kalro, C. M.: Vibration and Buckling of Rectangular Plates under Non-Uniform Inplane Loading, with Classical Edge Conditions. M.S. Thesis, Ohio State Univ., 1982, 52 pp.
11. Kielb, R. E.; and Han, L. S.: Vibration and Buckling of Rectangular Plates under In-Plane Hydrostatic Loading. J. Sound Vib., vol. 70, no. 4, 1980, pp. 543-555.
12. Lind, N. C.: Numerical Buckling Analysis of Plate Assemblies. ASCE J. Struc. Div., vol. 104, ST 2, 1978, pp. 329-339.
13. Shih, P.-Y.; and Schreyer, H. L.: Lower Bounds to Fundamental Frequencies and Buckling Loads of Columns and Plates. Intl. J. Solids Struc., vol. 14, no. 12, 1978, pp. 1013-1026.
14. Sundararajan, C.: Stability Analysis of Plates by a Complementary Energy Method. Intl. J. Numer. Methods Engrg., vol. 15, no. 3, 1980, pp. 343-349.

15. Tabarrok, B.; and Gass, N.: A Variational Formulation for Plate Buckling Problems by the Hybrid Finite Element Method. Intl. J. Solids Struc., vol. 14, no. 1, 1978, pp. 67-80.
16. Vielsack, P.: Das Beulen von Platten infolge annähernd homogener Spannungszustände. Ing. Arch., vol. 48, no. 3, 1979, pp. 205-211.
17. Wong, P. M.; and Bettess, P.: Elastic Buckling of Rectangular Clamped Plates. Intl. J. Solids Struc., vol. 15, no. 6, 1979, pp. 457-466.
18. Guz, A. N.; Kuliev, G. G.; Zeinalov, N. K.; and Dyshel, M. S.: Theoretical and Experimental Study of Stability for a Stretched Plate with a Noncircular Hole. Akademiia Nauk URSR, Kiev., Dopovidi, Seriia A, no. 2, 1980, p.37. (In Ukrainian).
19. Zeinalov, N. K.: Buckling of an Unbounded Thin Plate with a Circular Hole under Biaxial Extension. Soviet Appl. Mech., vol. 13, no. 12, 1978, pp.1272-1274.
20. Dyshel, M. Sh.: Failure in a Thin Plate with a Slit. Soviet Appl. Mech., vol. 14, no. 9, 1979, pp.1010-1012.
21. Markstrom, K.; and Storakers, B.: Buckling of Cracked Members under Tension. Intl. J. Solids Struc., vol. 16, no. 3, 1980, pp 217-229.
22. Milovanova, O. B.; and Dyshel, M. Sh.: Experimental Investigation of the Buckling Form of Tensioned Plates with a Slit. Soviet Appl. Mech., vol. 14, no. 1, 1978, pp. 101-104.
23. Leissa, A. W.: Plate Vibration Research, 1976-1980: Classical Theory. Shock Vib. Dig., vol. 13, no. 9, 1981, pp. 11-22.
24. Kucheryuk, V. I.; Lobanok, I. V.; et al.: Stability of Plates by the Method of Moiré Fringes. Soviet Appl. Mech., vol. 14, no. 9, 1979, pp. 956-961.
25. Guz, A. N.: Stability of Round Compressible Plate under All-Round Compression. Akademiia Nauk URSR, Kiev., Dopovidi. Seriia A, no. 9, 1978, p. 801. (In Ukrainian).
26. Guz, A. N.: Stability of Round Incompressible Plate with All-Round Compression. Akademiia Nauk URSR, Kiev., Dopovidi. Seriia A, no. 11, 1978, p. 983. (In Ukrainian).
27. Ku, A. B.: The Elastic Buckling of Circular Plates. Intl. J. Mech. Sci., vol. 20, 1978, pp 593-597.
28. Pardoen, G. C.: Axisymmetric Vibration and Stability of Circular Plates. Computers Struc., vol. 9, 1978, pp. 89-95,
29. Sato, K.: Buckling of an Elastically Restrained Elliptical Plate under Uniform Compression. Bull. JSME, vol. 23, no. 180, 1980, pp. 874-879.

30. Edwardes, R. J.; and Kabaila, A. P.: Buckling of Simply-Supported Skew Plates. *Intl. J. Numer. Methods Engrg.*, vol. 12, no. 5, 1978, pp. 779-785.
31. Kennedy, J. B.; and Prabhakara, M. K.: Buckling of Simply Supported Orthotropic Skew Plates. *Aeronaut. Quart.*, vol. 29, no. 3, 1978, pp 161-174.
32. Kennedy, J. B.; and Prabhakara, M. K.: Combined-Load Buckling of Orthotropic Skew Plates. *ASCE J. Engrg. Mechanics Div.*, vol. 105, no. 1, 1979, pp. 71-79.
33. Mizusawa, T.; Kajita, T.; and Naruoka, M.: Buckling of Skew Plate Structures Using B-Spline Functions. *Intl. J. Numer. Methods Engrg.*, vol. 15, no. 1, 1980, p. 87.
34. Mizusawa, T.; Kajita, T.; and Naruoka, M.: Vibration and Buckling Analysis of Plates of Abruptly Varying Stiffness. *Computers Struc.*, vol. 12, no. 5, 1980, pp. 689-693.
35. Sekiya, T.; and Katayama, T.: Analysis of Buckling Using Influence Function. *Proc. 29th Japan Natl. Cong. for Appl. Mech.*, 1979, pp. 25-31.
36. Thangam Babu, P. V.; and Reddy, D. V.: Stability Analysis of Skew Orthotropic Plates by the Finite Strip Method. *Computers Struc.*, vol. 8, no. 5, 1978, pp. 599-607.
37. Laura, P. A. A.; Luisoni, L. E.; and Sarmiento, G. S.: Buckling of Orthotropic Plates of Complicated Boundary Shape Subjected to a Hydrostatic State of In-Plane Stress. *Instituto de Mecanica Aplicada No. 79-21* (Puerto Belgrano, Argentina), June 1979, 10 pp. (to be published).
38. Leissa, A. W.: *Vibration of Plates*. NASA SP-160, U. S. Govt. Printing Office, 1969, 353 pp.
39. Cimetière, A.: *Mecanique des Solides Elastiques. - Flambement unilatéral d'une plaque reposant sans frottement sur un support élastique tridimensionnel.* *Comptes Rendus Acad. Sc. Paris, Série B*, vol. 290, 1980, pp. 337-340.
40. Cimetière, A.: *Un problème de flambement unilatéral en théorie des plaques.* *J. de Mécanique*, vol. 19, no. 1, 1980, pp. 183-202. (In French).
41. Petrenko, M. P.: Special characteristics of the vibrations and the loss of Stability of a Compressed Round Plate on an Elastic Base. *Soviet Appl. Mech.*, vol. 14, no. 5, 1978, pp. 541-543.
42. Simmons, L. D.: Harmonic Buckling of a Thin Plate Due to Constrained Thermal Expansion. *J. Appl. Mechanics, Trans. ASME*, vol. 46, no. 2, 1979, pp. 456-457.
43. Wang, Y.-S.: Buckling of a Half Ice Sheet Against a Cylinder. *ASCE J. Engrg. Mechanics Div.*, vol. 104, EM 5, 1978, pp 1131-1145.
44. Crouzet-Pascal, J.: Comment on "Buckling of Rotationally Restrained Orthotropic Plates under Uniaxial Compression". *J. Composite Materials*, vol. 12, 1978, pp 215-219.

45. Garashchuk, I. N.; Zamula, G. N.; and Prikazchikov, V. G.: Numerical Solution of Plate-Stability Problems. Soviet Appl. Mech., vol. 14, no. 5, 1978, pp. 509-513.
46. Guz, A. N.; and Kokhanenko, Yu. V.: Solution of Plane Problems of the Three Dimensional Theory of Elastic Stability of Plates for Inhomogeneous Subcritical States. Soviet Appl. Mech., vol. 13, no. 12, 1978, pp. 1227-1234.
47. Johnston, G. S.: Buckling of Orthotropic Plates Due to Biaxial In-Plane Loads Taking Rotational Restraints Into Account. Fibre Science Tech., vol. 12, no. 6, 1979, p. 435.
48. Lee, D. J.: Some Observations on the Local Instability of Orthotropic Structural Sections. Aeronaut. J., vol. 83, no. 819, 1979, pp. 110-114.
49. Libove, C.: Buckling of Orthotropic Plates. Section 4.5, Structural Stability Res. Council, Guide to Stability Design Criteria for Metal Structures. (To be published).
50. Durban, D.; and Stavsky, Y.: Elastic Buckling of Polar-Orthotropic Plates in Shear. Intl. J. Solids Struc., vol. 18, no. 1, 1982, pp. 51-58.
51. Rubin, C.: Stability of Polar-Orthotropic Sector Plates. J. Appl. Mechanics, Trans. ASME, vol. 45, no. 2, 1978, pp. 448-450.
52. Ficcadenti, G. M.; and Laura, P. A. A.: Fundamental Frequency and Buckling Load of Circular Plates with Variable Profile and Non-Uniform Boundary Conditions. J. Sound Vib., vol. 78, 1981, pp. 147-153.
53. Valerga de Greco, B.; and Laura, P. A. A.: A Note on Vibrations and Elastic Stability of Circular Plates With Thickness Varying in a Bilinear Fashion. Instituto de Mecanica Aplicada No. 81-23 (Puerto Belgrano, Argentina), 1981.
54. Gupta, U. S.; and Lal, R.: Buckling and Vibrations of Circular Plates of Variable Thickness. J. Sound Vib., vol. 58, no. 4, 1978, pp. 501-507.
55. Hinton, E.: Buckling of Initially Stressed Mindlin Plates Using a Finite Strip Method. Computers Struc., vol. 8, no. 1, 1978, pp. 99-105.
56. Ziegler, H.: The Influence of Inplane Deformation on the Buckling Loads of Isotropic Elastic Plates. Ing. Arch. (to be published).
57. Getman, I. P.; and Ustinov, Y. A.: Stability and Supercritical Behavior of a Layered Plate. Soviet Appl. Mech., vol. 15, no. 10, 1979, p. 971.
58. Goldenshtein, A. M.: An Approximate Method for Solving Flexure and Stability Problems of Three-Layer Plates of Variable Thickness. Soviet Appl. Mechanics, vol. 14, no. 3, 1978, pp. 290-295.
59. Kaplevatsky, I. D.; and Shestopal, V. O.: Bending and Buckling of Multilayer Thin Plates. Material Mechanics Lab., Faculty of Mech. Engrg., Technion - Israel Inst. of Tech., Jan. 1980, 16 pp.

60. Miller, C. J.; and Springer, D. R.: Buckling of Plates Composed of Discretely Fastened Sheets. In "Finite Element Methods in Engineering", Proc. of the 3rd Intl. Conf. on Finite Elem. Methods, Univ. of NSW, Sydney, Aust., Jul. 2-6, 1979, Unisearch Ltd., Kensington, NSW, Aust., 1979, pp. 455-466.
61. Perel, D.; and Libove, C.: Elastic Buckling of Infinitely Long Trapezoidally Corrugated Plates in Shear. J. Appl. Mechanics, Trans. ASME, vol. 45, no. 3, 1978, pp. 579-582.
62. Romanow, F.: Critical Stresses of Simply Supported Sandwich Plates in Shear. Mech. Teor. Stos., vol. 16, no. 2, 1978, pp. 199-213. (In Polish).
63. Wrzecioniarz, P. A.: Local Stability of Sandwich Plates with a Variable Strength Characteristic of the Core. Forsch. Ingenieurwesen, vol. 45, no. 6, 1979, pp. 178-182. (In German).
64. Leissa, A. W.: Advances in Vibration, Buckling and Postbuckling Studies on Composite Plates. In Composite Structures, I.H. Marshall, Ed., Appl. Sci. Publishers, 1981, pp. 312-334.
65. Grisham, A. F.: Method for Including Post-Buckling of Plate Elements in the Internal Loads Analysis of any Complex Structure Idealized Using Finite Element Analysis Methods. Collect. Tech. Pap. AIAA, ASME, 19th Conf. on Struct. Struct. Dyn. Mater., Bethesda, Md., April 3-5, 1978, pp. 359-369.
66. Jones, R.; Mazumdar, J.; and Cheung, Y. K.: Vibration and Buckling of Plates at Elevated Temperatures. Intl. J. Solids Struc., vol. 16, 1980, pp. 61-70.
67. Kennedy, J. B.; and Prabhakara, M. K.: Postbuckling of Orthotropic Skew Plate Structures. ASCE J. Struc. Div., vol. 106, no. 7, 1980, pp. 1497-1513.
68. Matkowski, B. J.; Putnick, L. J.; and Reiss, E. L.: Secondary States of Rectangular Plates. SIAM J. Appl. Math., vol. 38, no. 1, 1980, pp. 38-51.
69. Nakamura, T.; and Uetani, K.: The Secondary Buckling and Post-Secondary-Buckling Behaviours of Rectangular Plates. Intl. J. Mech. Sci., vol. 21, no. 5, 1979, pp. 265-286.
70. Pomazi, L.: On Post-Buckling Behaviour of Regularly Multilayered Rectangular Elastic Plates. Acta Technica Acad. Sci. Hung. (Budapest), vol. 87, no. 1-2, 1978, pp. 111-120.
71. Rao, G. V.; and Raju, K. K.: Post-Buckling Behavior of Elastic Circular Plates Using a Simple Finite-Element Formulation. Computers Struc., vol. 10, no. 6, 1979, p. 911.
72. Schaeffer, D.; and Golubitsky, M.: Boundary Conditions and Mode Jumping in the Buckling of a Rectangular Plate. Communications in Math. Physics, vol. 69, no. 3, 1979, pp. 209-236.

73. Shye, K.-Y.; and Colville, J.: Post-Buckling Finite Element Analysis of Flat Plates. ASCE J. Struc. Div., vol. 105, no. 2, 1979, pp. 297-311.
74. Strzelczyk, A.: General Nonsymmetric Postbuckling of Orthotropic Annular Plates. J. Struc. Mech., vol. 6, no. 1, 1978, pp. 107-132.
75. Uemura, M.; and Byon, O.-I.: Secondary Buckling of a Flat Plate under Uniaxial Compression: Part 2, Analysis of Clamped Plate by F.E.M. and Comparison with Experiments. Int. J. Nonlin. Mechanics, vol. 13, no. 1, 1978, pp. 1-14.
76. Vanderbauwhede, A.: Generic and Nongeneric Bifurcation for the von Kármán Equations. J. Math. Analysis and Applications, vol. 66, no. 3, 1978, pp. 550-573.
77. Venkateswara Rao, G.; and Kanaka Raju, K.: Post-Buckling Behaviour of Elastic Circular Plates Using a Simple Finite Element Formulation. Computers Struc., vol. 10, no. 6, 1979, pp. 911-913.
78. Carlsen, C. A.; and Czujko, J.: The Specification of Postwelding Distortion Tolerances for Stiffened Plates in Compression. Structural Engineer, vol. 56A, no. 5, 1978, pp. 133-141.
79. Hui, D.; and Hansen, J. S.: Two-Mode Buckling of an Elastically Supported Plate and Its Relation to Catastrophe Theory. J. Appl. Mechanics, Trans. ASME, vol. 47, 1980, pp. 607-612.
80. Kalyanaraman, V.; and Peköz, T.: Analytical Study of Unstiffened Elements. ASCE J. Struc. Div., vol. 104, ST 9, 1978, pp. 1507-1524.
81. Tani, J.: Thermal Buckling of an Annular Plate with Axisymmetric Initial Deflection. J. Appl. Mechanics, Trans. ASME, vol. 45, no. 3, 1978, pp. 693-695.
82. Tani, J.: Elastic Instability of an Annular Plate under Uniform Compression and Lateral Pressure. J. Appl. Mechanics, Trans. ASME, vol. 47, no. 3, 1980, pp. 591-594.
83. Tani, J.; and Yamaki, N.: Elastic Instability of a Uniformly Compressed Annular Plate with Axisymmetric Initial Deflection. Intl. J. Nonlin. Mechanics, vol. 16, no. 2, 1981, pp. 213-220.
84. Turvey, G. J.: Axisymmetric Snap Buckling of Imperfect Tapered Circular Plates. Computers Struc., vol. 9, 1978, pp. 551-558.
85. Datta, P.K.: An Investigation of the Buckling Behaviour and Parametric Resonance Phenomenon of a Tensioned Sheet with a Central Opening. J. Sound Vib., vol. 58, no. 4, 1978, pp. 527-534.
86. Tani, J.; and Nakamura, T.: Dynamic Stability of Annular Plates under Periodic Radial Loads. J. Acoust. Soc. Amer., vol. 64, no. 3, 1978, pp. 827-831.

87. Tylikowski, A.: Stability of a Nonlinear Rectangular Plate. J. Appl. Mechanics, Trans. ASME, vol. 45, no. 3, 1978, pp. 583-585.
88. Celep, Z.: Axially-Symmetric Stability of a Completely Free Circular Plate Subjected to a Non-Conservative Edge Load. J. Sound Vib., vol. 65, no. 4, 1979, p. 549.
89. Farshad, M.: Stability of Cantilever Plates Subjected to Biaxial Subtangential Loading. J. Sound Vib., vol. 58, no. 4, 1978, pp. 555-561.
90. Leipholz, H. H. E.: Stability of a Rectangular Simply Supported Plate Subjected to Nonincreasing Tangential Follower Forces. J. Appl. Mechanics, Trans. ASME, vol. 45, no. 1, 1978, pp. 223-224.
91. Miya, K.; Hara, K.; and Someya, K.: Experimental and Theoretical Study on Magnetoelastic Buckling of a Ferromagnetic Cantilevered Beam-Plate. J. Appl. Mechanics, Trans. ASME, vol. 45, no. 5, 1978, pp. 355-360.
92. Miya, K.; Takagi, T.; and Ando, Y.: Finite-Element Analysis of Magnetoelastic Buckling of Ferromagnetic Beam Plate. J. Appl. Mechanics, Trans. ASME, vol. 47, 1980, pp. 377-382.
93. Van de Ven, A. A. F.: Magnetoelastic Buckling of Thin Plates in a Uniform Transverse Magnetic Field. J. Elasticity, vol. 8, no. 3, 1978, pp. 297-312.
94. Antman, S. S.: Buckled States of Nonlinearly Elastic Plates. Arch. Rational Mechanics and Analysis, vol. 67, no. 2, 1978, pp. 11-149.
95. Besseling, J. F.; Ernst, L. J.; Van der Werff, K.; de Koning, A. U.; and Riks, E.: Geometrical and Physical Nonlinearities. Some Developments in the Netherlands. Comput. Meth. Appl. Mech. Eng., vol. 17/18, pt. 1, 1979.
96. Dietrich, L.; Kawahara, W.; and Phillips, A.: An Experimental Study of Plastic Buckling of a Simply Supported Plate under Edge Thrusts. Acta Mech., vol. 29, no. 1-4, 1978, pp. 257-267.
97. Do, C.: Elastic-Plastic Buckling of a Thin Plate. Comptes Rendus, Acad. des Sciences, Paris, Series A-B, vol. 290, no. 7, 1980, p. 143. (In French).
98. Gadjieyev, V. D.; Isayev, F. K.; and Shamiyev, T. M.: Stability of Elastic-Plastic Plates and Shells with Mechanical Properties Depending on Hydrostatic Pressure. Izv. Akad. Nauk Azerbaidzhanskoi SSR, Seriya Iziko-Tekhnicheskikh i Matematik., no. 3, 1979, p. 58. (In Russian).
99. Gadjiev, V. D.; and Shamiev, T. M.: Stability of a Rectangular Plate with Mechanical Properties Depending on Kind of a Strained Condition. Izv. Akad. Nauk Azerbaidzhanskoi SSR Seriya Iziko-Tekhnicheskikh i Matematik., no. 2, 1978, p. 49. (In Russian).
100. Gupta, K. K.: On a Numerical Solution of the Plastic Buckling Problem of Structures. Intl. J. Numer. Methods Engrg., vol. 12, no. 6, 1978, pp. 941-947.



101. Jones, R.; Mazumdar, J.; and Cheung, Y. K.: Vibration and Buckling of Plates at Elevated Temperatures. *Intl. J. Solids Struc.*, vol. 16, 1980, pp. 61-70.
102. Kurshin, L. M.: Creep Stability: A Survey. *Mech. of Solids*, vol. 13, no. 3, 1978, pp. 111-146.
103. Markenscoff, X.; and Triantafyllidis, N.: Effects of Third-Order Elastic Constants on the Buckling of Thin Plates. *Intl. J. Solids Struc.*, vol. 15, no. 12, 1979, pp. 987-992.
104. Mignot, F.; and Puel, J. P.: A Buckling Model for a Thin Elastoplastic Plate. *Comptes Rendus, Acad. des Sciences, Paris, Séries A-B*, vol. 290, no. 11, 1980, p. 519. (In French).
105. Needleman, A.; and Tvergaard, V.: An Analysis of the Imperfection Sensitivity of Square Elastic-Plastic Plates under Axial Compression. *Intl. J. Solids Struc.*, vol. 12, 1978, pp. 185-201.
106. Popov, E. P.; and Hjelmstad, K. D.: Web Buckling under Cyclic Loading. Pres. at the Structural Stability Research Council Meeting, Chicago, Ill., April 8, 1981, 2 pp.
107. Sherbourne, A. N.; and Haydl, H.-M.: Ultimate Web Shear Capacity in Large Rectangular Ducts. *Canadian J. Civil Engrg.*, vol. 7, no. 1, 1980, pp. 125-132.
108. Sherbourne, A. N.; and Haydl, H.-M.: Carrying Capacity of Edge-Compressed Rectangular Plates. *Canadian J. Civil Engrg.*, vol. 7, no. 1, 1980, pp. 19-26.
109. Shrivastava, S. C.: Inelastic Buckling of Plates Including Shear Effects. *Intl. J. Solids Struc.*, vol. 15, no. 7, 1979, pp. 567-575.
110. Sorokin, V. I.; and Shvaiko, N. Y.: Bifurcation of the Elastic-Plastic Deformation Process and Post-Critical Behavior of the Plate Model. *Akad. Nauk URSR, Kiev, Dopovidi, Seriya A*, no. 1, 1979, p. 43. (In Ukrainian).
111. Taylor, J. W.; Harlow, F. H.; and Amsden, A. A.: Dynamic Plastic Instabilities in Stretching Plates and Shells. *J. Appl. Mechanics, Trans. ASME*, vol. 45, no. 1, 1978, pp. 105-110.
112. Tvergaard, V.; and Needleman, A.: On the Localization of Buckling Patterns. *J. Appl. Mechanics, Trans. ASME*, vol. 47, no. 3, 1980, pp. 613-619.
113. Tvergaard, V.: Creep Buckling of Rectangular Plates under Axial Compression. *Intl. J. Solids Struc.*, vol. 15, no. 6, 1979, pp. 441-456.
114. Tvergaard, V.; and Needleman, A.: On the Foundations of Plastic Buckling. *Developments in Thin-Walled Structures*, Eds. J. Rhodes and A. C. Walker, Appl. Sci. Publishers, 1981.
115. Uenoya, M.; and Redwood, R. G.: Elasto-Plastic Shear Buckling of Square Plates with Circular Holes. *Computers Struc.*, vol. 8, no. 2, 1978, pp. 291-300.

116. Leissa, A. W.: Plate Vibration Research, 1976-1980; Complicating Effects.  
Shock Vib. Dig., vol. 13, no. 10, 1981, pp. 19-36.

TABLE I.-CRITICAL VALUES OF  $P_{xy} b^2/D$  FOR INPLANE SHEAR LOADING

Edge Conditions	a/b		
	0.5	1	2
CCCC	404.89	144.50	101.20
CCCS	399.69	132.08	84.278
CSCS	397.48	124.06	66.232
CCSS	326.29	115.69	81.573
CSSS	319.83	105.69	65.285
SSSS	258.78	92.064	64.692
CCCF	323.66	83.997	27.260
CSCF	326.87	83.406	23.213
CFCF	319.10	74.175	17.509
CCSF	246.41	64.180	24.048
CSSF	247.54	63.665	19.146
CFSF	247.14	57.394	12.206
CSFS	90.308	49.027	45.605
SSSF	182.16	47.097	16.123
SFSF	174.60	41.823	8.0238
SFFF	38.452*	17.745*	5.0360*
FFFF	11.977*	9.9489*	2.9942*
CCFF	18.047	6.2201	4.5118
CSFF	17.896	4.8615	1.7462
CFFF	17.724	3.8833	.82613
SSFF	5.3476	2.6476	1.3369

\*-First nontrivial eigenvalue (i.e., not a rigid body mode)

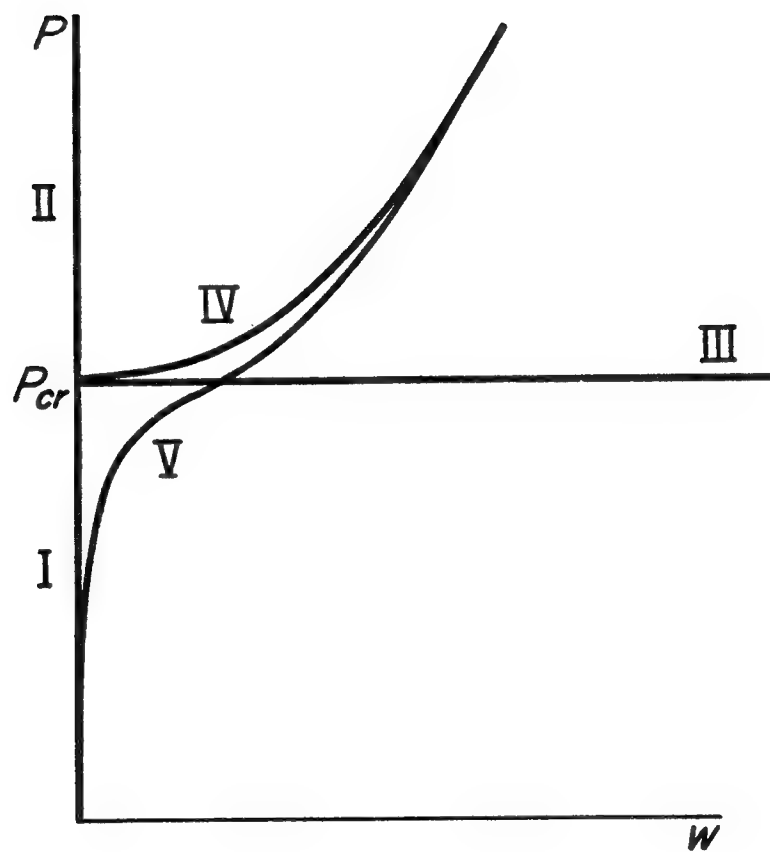


Figure 1.- Representative curves of load versus transverse displacement.

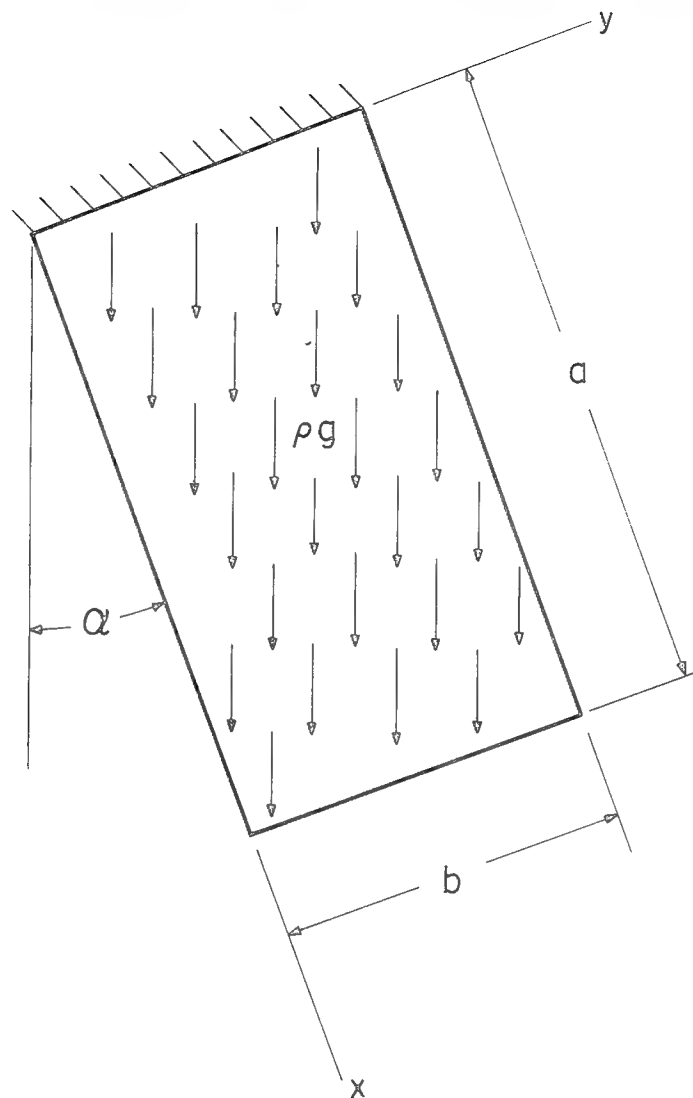


Figure 2.- Cantilever plate with inplane acceleration body forces.

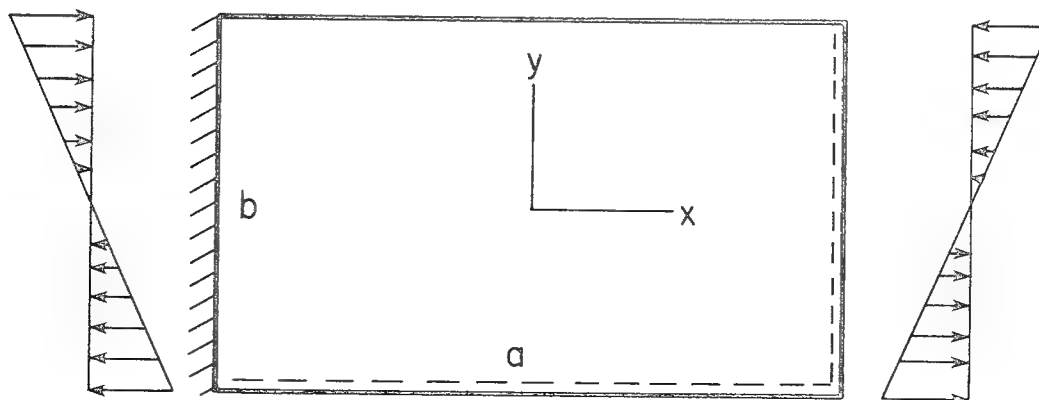


Figure 3.- Clamped, simply supported, simply supported, free (CSSF) rectangular plate with inplane bending stresses.

# SOLUTION OF VON KÁRMÁN'S PLATE EQUATIONS

## WITH PERTURBATION AND SERIES SUMMATION

L. Glen Watson

Transportation Centre, University of Saskatchewan

Joseph M. Chudobiak

Department of Mechanical Engineering, University of Saskatchewan

### SUMMARY

Problems involving finite deflections of plates with simply supported or free edges have, in the past, been regarded as almost intractable. In this paper a nonlinear-series summation technique has been combined with Chien's small-parameter perturbation technique to solve the problem of the finite deflection of a simply supported circular plate subjected to a uniform transverse load. The results demonstrate the great advantage of incorporating the summation method into the solution procedure and are in excellent agreement with previous results.

### INTRODUCTION

Many investigators have found ways of obtaining approximate solutions to Von Kármán's plate equations [1]. In particular, they have produced load versus central-deflection curves for circular plates with geometric boundary conditions. When one attempts to extend these methods to obtain better approximations for the inplane "membrane" loads or for cases with one or more "natural" boundary conditions, one usually encounters almost insurmountable difficulties. These difficulties take several forms. Often the cases treated in the literature have degenerate boundary conditions and while generalizations may not be impossible, the labor involved in "solving" Von Kármán's equations for a different set of boundary conditions is prohibitive. Other methods, particularly the well-known Berger's method [2] can lead to incorrect and, in some cases, nonsensical answers [3]. A similar method due to Goldberg [4] appears to yield incorrect solutions when applied to a transversely loaded annular disc with a free outer edge [5].

Chien's method [6] has been used by numerous investigators to obtain solutions to the Von Kármán plate equations [7], [8], [9] but with few exceptions these investigators terminated the asymptotic series after obtaining two non-zero terms. Those who invested the effort to obtain further terms encountered difficulties with series divergence [10].

Workers in fluid dynamics have long encountered such divergence problems when trying to extend the range of their solutions. Many have treated or advocated the treatment of their series with various summation and transformation procedures [11]. However, workers in solid mechanics do not appear to have utilized this technique. In this paper the authors combine the nonlinear  $e_1$  transform of Shanks [12] with Chien's [6] small-parameter perturbation method to obtain a solution to the problem

of a simply supported circular plate subjected to a transverse load.

This set of boundary conditions was chosen for a test problem since Berger's method had been found to fail for this problem and in addition Bromberg [13] had solved the problem using a combination of a power-series method, a perturbation method, and an asymptotic boundary layer method. These methods were matched to provide solutions over a wide range of transverse loads.

#### SYMBOLS

$b$	Plate boundary radius
$f_i$	Coefficients in the asymptotic expansion of $S_r$
$g_i$	Coefficients in the asymptotic expansion of $S_t$
$h$	Plate thickness
$q$	Uniform transverse loading
$r$	Radius
$D$	Flexural rigidity of a plate
$E$	Modulus of elasticity
$P$	Dimensionless loading intensity
$S_r, S_t$	Dimensionless radial and tangential average stresses (i.e., $S_r = N_r/h$ , $S_t = N_t/h$ )
$W$	Dimensionless plate deflection
$W_i$	Coefficients of the asymptotic solution of dimensionless plate deflection
$\alpha_i$	Coefficients in the asymptotic expansion of $P$
$\delta$	Dimensionless central deflection of a circular plate
$\eta$	$1 - r^2/b^2$
$\nu$	Poisson's ratio
$N_r$	Normal force per unit length (radial direction)
$N_t$	Normal force per unit length (tangential direction)
$M_r, M_t$	Radial and tangential moments per unit length
$Q_r, Q_t$	Radial and tangential shearing forces

# VON KÁRMÁN'S FINITE DEFLECTION PLATE EQUATIONS

Von Karman's equations are usually given as:

$$\nabla^4 w = \frac{1}{D} \left[ q + \frac{\partial^2 F}{\partial y^2} \frac{\partial^2 w}{\partial x^2} - \frac{2\partial^2 F}{\partial x \partial y} \frac{\partial^2 w}{\partial x \partial y} + \frac{\partial^2 F}{\partial x^2} \frac{\partial^2 w}{\partial y^2} \right] \quad (1)$$

and

$$\nabla^4 F = Eh \left[ \left( \frac{\partial^2 w}{\partial x \partial y} \right)^2 - \frac{\partial^2 w}{\partial x^2} \frac{\partial^2 w}{\partial x^2 \partial y^2} \right] \quad (2)$$

where F is a stress function, such that

$$N_x = \frac{\partial^2 F}{\partial y^2} \quad N_y = \frac{\partial^2 F}{\partial x^2} \quad N_{xy} = - \frac{\partial^2 F}{\partial x \partial y}$$

and

$$D = \frac{Eh^3}{12(1-\nu^2)}$$

Chien [6] expressed the axisymmetric form of Von Kármán's equations in terms of the dimensionless radius  $\eta$ . Thus

$$- \frac{1}{4} \frac{d^2}{d\eta^2} \left[ (1-\eta) \frac{dW}{d\eta} \right] = \frac{3P}{16} - \frac{3}{4} (1-\nu^2) S_r \frac{dW}{d\eta} \quad (3)$$

$$\frac{d^2}{d\eta^2} \left[ (1-\eta) S_r \right] + \frac{1}{2} \left( \frac{dW}{d\eta} \right)^2 = 0 \quad (4)$$

and

$$S_t = S_r - 2(1-\eta) \frac{dS_r}{d\eta} \quad (5)$$

where

$$W = \frac{w}{h} \quad N_r = \frac{Eh^2}{b^2} S_r \quad N_t = \frac{Eh^2}{b^2} S_t$$

$$P = \frac{b^4 q}{h^4 E} (1-\nu^2) \quad \text{and} \quad \eta = 1 - \frac{r^2}{b^2}$$



Chien [6] expanded "P", "W", "S<sub>r</sub>", and "S<sub>t</sub>" in power series of  $\delta$ , the dimensionless central deflection, as

$$\frac{3P}{16} = \alpha_1 \delta + \alpha_3 \delta^3 + \alpha_5 \delta^5 + \quad (6)$$

$$W = W_1(\eta) \delta + W_3(\eta) \delta^3 + W_5(\eta) \delta^5 + \quad (7)$$

$$S_r = f_2(\eta) \delta^2 + f_4(\eta) \delta^4 + f_6(\eta) \delta^6 + \quad (8)$$

and

$$S_t = g_2(\eta) \delta^2 + g_4(\eta) \delta^4 + g_6(\eta) \delta^6 + \quad (9)$$

Equations (6), (7), (8), and (9) were then substituted into equations (3), (4), and (5) and the coefficients of each power of  $\delta$  were collected to form families of governing equations.

The family of differential equations governing the transverse deflections is to the seventh order in  $\delta$ .

$$-\frac{d^2}{4d\eta^2} [(1-\eta) \frac{dW_1}{d\eta}] = \alpha_1 \quad (10)$$

$$-\frac{d^2}{4d\eta^2} [(1-\eta) \frac{dW_3}{d\eta}] = \alpha_3 - \frac{3}{4} (1-\nu^2) (f_2 \frac{dW_1}{d\eta}) \quad (11)$$

$$-\frac{d^2}{4d\eta^2} [(1-\eta) \frac{dW_5}{d\eta}] = \alpha_5 - \frac{3}{4} (1-\nu^2) [f_4 \frac{dW_1}{d\eta} + f_2 \frac{dW_3}{d\eta}] \quad (12)$$

$$-\frac{d^2}{4d\eta^2} [(1-\eta) \frac{dW_7}{d\eta}] = \alpha_7 - \frac{3}{4} (1-\nu^2) [f_6 \frac{dW_1}{d\eta} + f_4 \frac{dW_3}{d\eta} + f_2 \frac{dW_5}{d\eta}] \quad (13)$$

and the radial stresses are governed by the series,

$$\frac{d^2}{d\eta^2} [(1-\eta)f_2] + \frac{1}{2} \left( \frac{dW_1}{d\eta} \right)^2 = 0 \quad (14)$$

$$\frac{d^2}{d\eta^2} [(1 - \eta)f_4] + \frac{dW_1}{d\eta} \frac{dW_3}{d\eta} = 0 \quad (15)$$

$$\frac{d^2}{d\eta^2} [(1 - \eta)f_6] + \frac{dW_1}{d\eta} \frac{dW_5}{d\eta} + \frac{1}{2} \left( \frac{dW_3}{d\eta} \right)^2 = 0 \quad (16)$$

$$\frac{d^2}{d\eta^2} [(1 - \eta)f_8] + \frac{dW_1}{d\eta} \frac{dW_7}{d\eta} + \frac{dW_3}{d\eta} \frac{dW_5}{d\eta} = 0 \quad (17)$$

Finally, the circumferential stresses are given by;

$$g_i = f_i - 2(1 - \eta) \frac{df_i}{d\eta} \quad i = 2, 4, 6 \dots \quad (18)$$

For a simply supported circular plate subjected to a uniform transverse load the governing boundary conditions for the transverse deflections are:

$$W_1(1) = 1 \quad (19)$$

$$W_3(1) = W_5(1) = W_7(1) = 0 \quad (20)$$

and

$$\left. \frac{dW_1}{d\eta} \right|_{\eta=1} \quad \left. \frac{dW_3}{d\eta} \right|_{\eta=1} \quad \left. \frac{dW_5}{d\eta} \right|_{\eta=1} \quad \left. \frac{dW_7}{d\eta} \right|_{\eta=1} \quad (21)$$

are finite.

$$W_1(0) = W_3(0) = W_5(0) = W_7(0) = 0 \quad (22)$$

$$- (1 + \nu) \left. \frac{dW_i}{d\eta} \right|_{\eta=0} + \left. \frac{2d^2W_i}{d\eta^2} \right|_{\eta=0} = 0 \quad i = 1, 3, 5, 7 \dots \quad (23)$$

The radial stresses must satisfy the conditions

$$f_i(0) = 0 \quad i = 2, 4, 6, 8 \dots \quad (24)$$

and

$$f_i(1) \text{ should remain finite for } i = 2, 4, 6, 8 \dots \quad (25)$$

The equations (10) to (18) were then solved sequentially in the order: (10), (14), (18) with  $i = 2$ , (11), (15), (18) with  $i = 4$ , (12), (16), and (18) with  $i = 6$ . At this point the unknown functions in equations (7) to (9) were known up to the sixth order in  $\delta$ . The boundary conditions (19) - (24) were then invoked to evaluate the constants of integration. Table I gives the values for  $W_i$ ,  $f_i$ ,  $g_i$  and  $\alpha_i$  for the case  $\nu = 0.3$ .

Figure 1 shows plots of the approximate relationships between the central deflection  $\delta$  and the dimensionless loading parameter  $\frac{qb^4}{Dh}$ . The approximations were obtained by retaining 1, 3 and 5 terms of equation 6. Figure 2 shows the stress for  $\nu = 0.25$  and  $\delta = 3.78$  (this was chosen because Bromberg [13] had studied it). These curves were produced by retaining 1, 2 and 3 terms of equation (9). In both figures the problems caused by retaining the highest order terms are illustrated.

From Figure 1 it can be seen that the inclusion of the fifth order term causes the solution to become meaningless at central deflections of about nine plate thicknesses. Figure 2 illustrates the divergent behavior of equation (9) with the sixth order term dominating the second and fourth order terms with a central deflection of only 3.78 plate thicknesses. The sixth order solution would be rejected because the sixth order term dominates near  $r = 0$ . However, it would be difficult to decide whether or not to retain the fourth-order term. Thus, for deflections of only 3.78 plate thicknesses the membrane stress solutions are of little value.

The divergence of the series was not completely unexpected since other investigators had noted the same phenomena [10].

#### SERIES TRANSFORMATION

Van Dyke [11] notes that many asymptotic series appear to initially converge and then diverge. He illustrates such behavior for asymptotic series and notes that one gets the best answer by retaining the initial decreasing terms but discarding the later divergent terms. However, the rate of convergence of many series can be improved.

Many authors, among them [12], [14], [15], [16], [17], and [18] have presented methods for improving such series but Shanks'  $e_1$  transform [12] appears to be the most appropriate when only 3 terms of the series are known.

Using this transform, the partial series of the form

$$f(\delta) = a_1\delta_1 + a_3\delta^3 + a_5\delta^5 \dots\dots$$

are summed with the relation,

$$f(\delta) = \frac{a_1a_3\delta + \delta^2(a_3^2 - a_1a_5)}{a_3 - a_5\delta^2} \quad (26)$$

If the  $e_1$  transform is applied to Equations (6), (8) and (9), the following expressions are obtained.

(a) To relate the intensity of transverse loading and deflection;

$$\frac{qb^4}{Dh} = 64\delta \left[ \frac{-\alpha_1\alpha_3 + \delta^2(\alpha_1\alpha_5 - \alpha_3^2)}{-\alpha_3 + \alpha_5\delta^2} \right] \quad (27)$$

(b) The radial and circumferential stresses at any radius are given by Equations (28) and (29) respectively;

$$\sigma_r(n) = \frac{Eh^2}{b^2} \delta^2 \left\{ \frac{-f_2(n)f_4(n) + \delta^2[f_2(n)f_6(n) - f_4(n)f_4(n)]}{-f_4(n) + f_6(n)\delta^2} \right\} \quad (28)$$

$$\sigma_t(n) = \frac{Eh^2}{b^2} \delta^2 \left\{ \frac{-g_2(n)g_4(n) + \delta^2[g_2(n)g_6(n) - g_4(n)g_4(n)]}{-g_4(n) + g_6(n)\delta^2} \right\} \quad (29)$$

## RESULTS

Figures 1 and 3 demonstrate the efficacy of Shanks'  $e_1$  transform in improving the behavior of asymptotic series for deflection and membrane stresses. Figure 1 shows that equation (27) is in extremely close agreement with Bromberg's solution for deflection versus transverse load intensity. Figure 3 indicates how the  $e_1$  transform rectifies the divergent and oscillatory series (9) and how closely the values of equations (28) and (29) follow Bromberg's values for membrane stresses at a central transverse deflection of 5.61 plate thicknesses.

## DISCUSSION

A comparison between the asymptotic series and Bromberg's solutions shows that the two-term asymptotic series is a good approximation for the relationship between the central plate deflection and the intensity of the transverse load. However, for deflections greater than 4 plate thicknesses, it would appear to overestimate the nonlinear effects. The transformed solution appears very reasonable and is in good agreement with Bromberg's work. However, at this point it is not obvious how to estimate the upper limit of the validity of this solution.

The two-term solutions for membrane stresses are found to be unreliable at very low transverse deflections, certainly by deflections of 4 plate thicknesses. The transformed solution was, again, in excellent agreement with Bromberg's work, even at 5.6 plate thicknesses of deflection.

## DIRECTIONS OF FUTURE WORK

The authors have already used Chien's method for a variety of axisymmetric plate problems with excellent results. These include large deflections of circular plates with transverse loads of varying intensity, and annular plates with various edge conditions under transverse loads. In two of the cases investigated it appears necessary to extend the asymptotic series to three terms in order to get any meaningful results. The first is for an annular plate held on the inner radius, subjected to a transverse load and held in such a manner that the inplane displacement boundary must remain zero. The second case was for a study of annular plates being pressed into elastic foundations. In order for these solutions to be useful it appears to be imperative to use the transform technique. The authors are anticipative of further work on each case.

It appears that with the  $e_1$  transform, Chien's method is a viable method of investigating finite deflection plate problems where "boundary layer" effects are significant. The results presented in this paper indicate that in order to investigate the membrane stresses in the boundary layer at least three terms of the asymptotic series are required and in order to get useful numerical results a series summation procedure must be used.

The Shanks'  $e_1$  transform also appears to be useful in other areas in solid mechanics, for example, in predicting the limit of sequences generated by finite element solutions with progressively smaller elements.

The utility of Chien's method may also be extended by using approximate solutions to the families of differential equations and then evaluating higher order coefficients for the asymptotic series and finally, summing the series with a higher order transform.

## CONCLUSION

Using Shanks'  $e_1$  transform to sum the asymptotic series generated by Chien's small-parameter perturbation method greatly increases the range and usefulness of the perturbation solutions.

# REFERENCES

1. VON KARMAN, T., "Festigkeitsproblem in Maschinbau." Encyl. der Math. Wissenschaften: Vol. IV-4 Leipzig, 1907-1914, pp 348-352.
2. BERGER, H.M., "A New Approach to the Analysis of Large Deflections of Plates". Journal of Applied Mechanics, December, 1955. pp 465-472.
3. NOWINSKI, J.L., and OHNABE, H., "On Certain Inconsistencies in Berger Equations for Large Deflections of Elastic Plates". International Journal of Mechanical Sciences, Vol. 14, No. 3, March, 1973, pp 165-170.
4. GOLDBERG, M.A., "A Modified Large Deflection Theory of Plates". Proceedings of the Fourth U.S. National Conference of Applied Mechanics, 1962, pp 611-618.
5. WATSON, L.G., "Non-linear Bending of Axi-symmetric Plates". Ph.D. Thesis, University of Saskatchewan, 1979.
6. CHIEN, W.Z., "Large Deflection of a Circular Clamped Plate Under Uniform Pressure". Chinese Journal of Physics, Vol. 7, 1947, pp 102-113.
7. CHIEN, W.Z., and YEH, K.Y., "Large Deflection of Rectangular Plates". Proceedings of the Ninth International Congress for Applied Mechanics, 1959, pp 403-407.
8. NASH, W.A., and COOLEY, I.D., "Large Deflections of a Clamped Elliptical Plate Subjected to Uniform Pressure". Journal of Applied Mechanics, Vol. 81, Series E., 1959, pp 291-293.
9. CHIA, C.Y., "Large Deflection of Rectangular Orthotropic Plates". Journal of the Engineering Mechanics Division Proceedings of the ASCE, October, 1972, pp 1285-1297.
10. NG, S.F., and KENNEDY, J.B., "Linear and Nonlinear Analyses of Skewed Plates". Journal of Applied Mechanics, June, 1967, pp 271-277.
11. VAN DYKE, M., "Perturbation Methods in Fluid Mechanics", Academic Press, 1964.
12. SHANKS, D., "Nonlinear Transformations of Divergent and Slowly Convergent Sequence". Journal of Math and Physics, Vol. 34, 1955, pp 1-42.
13. BROMBERG, E., "Nonlinear Bending of a Circular Plate Under Normal Pressure". Communications on Pure and Applied Mathematics, Vol. IX, 633-659 (1956).
14. LUBKIN, S., "A Method of Summing Infinite Series". Journal of Research of the National Bureau of Standards, Vol. 48, #3, March, 1952, pp 228-254.
15. GRAY, H.L., and CLARK, W.D., "On a Class of Nonlinear Transformations and Their Applications to the Evaluation of Infinite Series". Journal of Research of National Bureau of Standards - B. Mathematical Science, Vol. 73B, #3, pp 251-274.

16. VAN DYKE, M., "Analysis and Improvement of Perturbation Series". Quarterly Journal of Mechanics and Applied Mathematics, Vol. XXVII, P.T. 4, 1974.
17. FROST, P.A., and HARPER, E.Y., "An Extended Pade Procedure for Constructing Global Approximations from Asymptotic Expansions: An Explication with Examples". SIAM Review, Vol. 18 #1, January, 1976, pp 62-91.
18. WIMP, J., "New Methods for Accelerating the Convergence of Sequences Arising in Laplace Transform Theory". SIAM J. Numer. Anal. Vol. 14, #2, 1977.

TABLE I - CONSTANTS FOR ASYMPTOTIC EVALUATION OF DEFLECTION AND STRESS FOR  $\nu = 0.3$

Coefficients For Asymptotic Equation (3)

$$\alpha_1 = 0.245283D \ 00 \quad \alpha_3 = 0.704351D \ -01 \quad \alpha_5 = -0.504526D \ -03$$

Coefficients For Asymptotic Equations (7), (8) and (9)

$r/b = 0.00$	0.295894D 00	-0.145090D -01	0.182860D -02	$f_2, f_4, f_6$
	0.295894D 00	-0.145090D -01	0.182860D -02	$g_2, g_4, g_6$
	0.100000D 01	0.000000D 00	0.000000D 00	$w_1, w_3, w_5$
$r/b = 0.20$	0.280549D 00	-0.120942D -01	0.145080D -02	$f_2, f_4, f_6$
	0.250182D 00	-0.752062D -02	0.755947D -03	$g_2, g_4, g_6$
	0.950581D 00	0.380473D -02	-0.440150D -03	$w_1, w_3, w_5$
$r/b = 0.40$	0.236430D 00	-0.628974D -02	0.639145D -03	$f_2, f_4, f_6$
	0.122551D 00	0.655742D -02	-0.987341D -03	$g_2, g_4, g_6$
	0.807034D 00	0.120971D -01	-0.126014D -02	$w_1, w_3, w_5$
$r/b = 0.60$	0.169056D 00	-0.531546D -03	0.952714D -05	$f_2, f_4, f_6$
	-0.601012D -01	0.129866D -01	-0.117427D -02	$g_2, g_4, g_6$
	0.583487D 00	0.174822D -01	-0.153774D -02	$w_1, w_3, w_5$
$r/b = 0.80$	0.868525D -01	0.189606D -02	-0.145700D -03	$f_2, f_4, f_6$
	-0.258338D 00	0.257408D -02	0.384606D -04	$g_2, g_4, g_6$
	0.303487D 00	0.133758D -01	-0.957788D -03	$w_1, w_3, w_4$
$r/b = 1.00$	0.138778D -16	-0.138778D -16	-0.975782D -18	$f_2, f_4, f_6$
	-0.428266D 00	-0.179975D -01	0.101237D -02	$g_2, g_4, g_6$
	-0.104738D -16	-0.416334D -16	-0.867362D -18	$w_1, w_3, w_5$



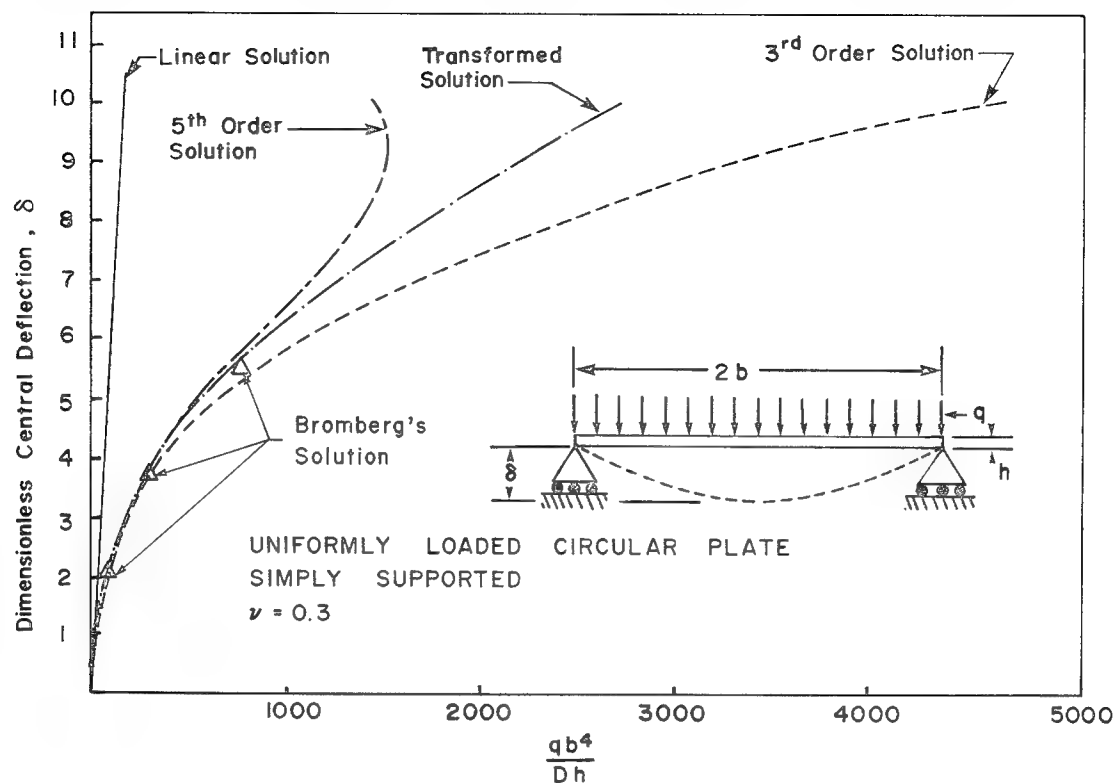


Figure 1. - Calculated central deflection.

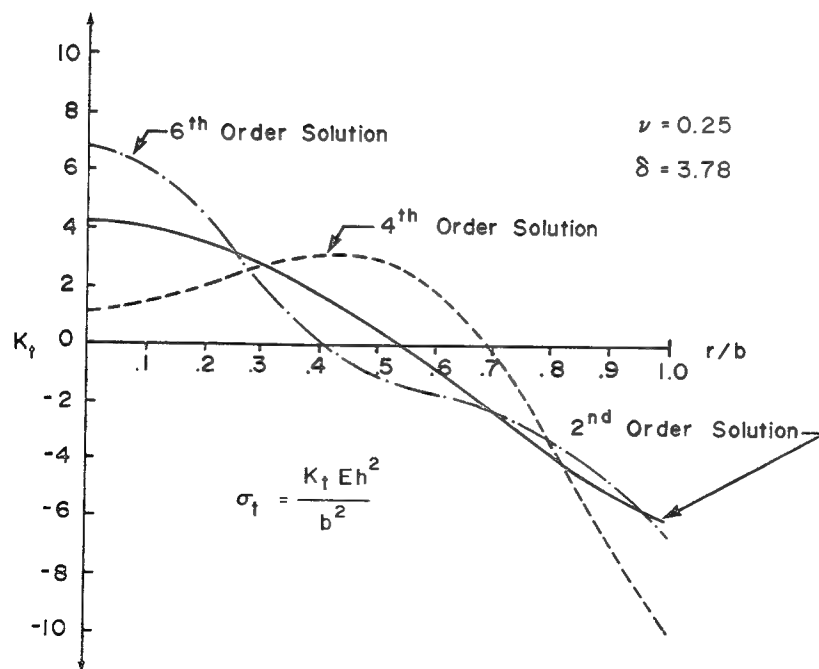


Figure 2. - Circumferential membrane stress in a uniformly loaded, simply supported circular plate. Central deflection 3.78 plate thickness.

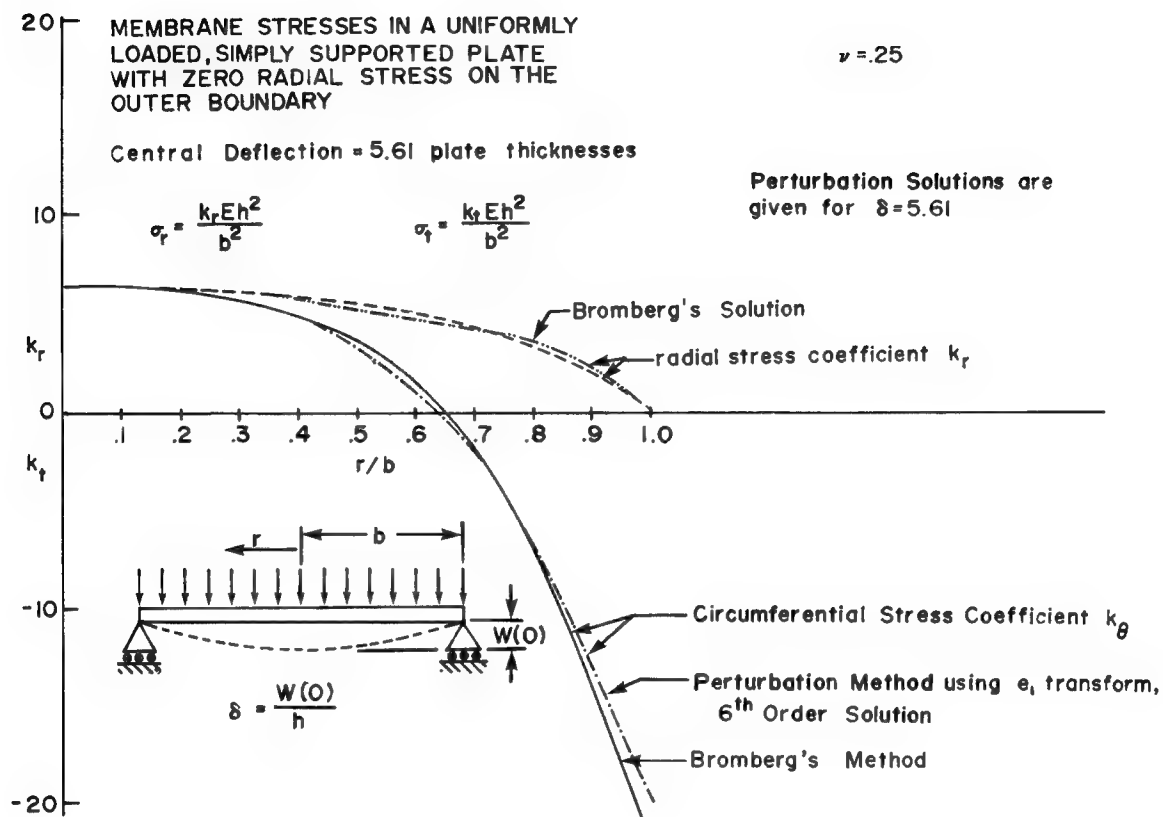


Figure 3. - Comparison of predicted membrane stresses for a central deflection of 5.61 plate thickness.

# CONSTRAINED MULTIBODY SYSTEM DYNAMICS

## - AN AUTOMATED APPROACH\*

James W. Kamman and Ronald L. Huston  
University of Cincinnati

### SUMMARY

The governing equations for constrained multibody systems are formulated in a manner suitable for their automated, numerical development and solution. Specifically, the "closed loop" problem of multibody chain systems is addressed.

The governing equations are developed by modifying dynamical equations obtained from Lagrange's form of d'Alembert's principle. This modification, which is based upon a solution of the constraint equations obtained through a "zero eigenvalues theorem," is, in effect, a contraction of the dynamical equations.

It is observed that, for a system with  $n$  generalized coordinates and  $m$  constraint equations, the coefficients in the constraint equations may be viewed as "constraint vectors" in  $n$ -dimensional space. Then, in this setting the system itself is free to move in the  $n-m$  directions which are "orthogonal" to the constraint vectors.

### INTRODUCTION

This paper presents a formulation of the governing equations of constrained multibody systems. The objective is the establishment of procedures for the automated generation of the equations.

Recently there has been an increasing interest in the efficient development of governing dynamical equations of multibody systems. This interest is stimulated by the fact that many physical systems can be modelled by systems of connected rigid bodies. Foremost among these physical systems of interest are robots, manipulators, human body models and biodynamic systems, and flexible cables or chains.

There have been a number of formulations of the equations of motion of multibody systems (refs. 1-19). The majority of these have been restricted to "open tree" systems: that is, systems of rigid bodies such that adjacent bodies have at least one common point and such that no closed loops are formed. Figure 1 illustrates such a system. The formulation of the governing equations of motion of such systems has advanced to the point where the coefficients of the governing differential equations can be formed automatically (numerically) by simply knowing the connection configuration (refs. 10-12).

However, during recent years, there has also been interest in the dynamics of systems possessing closed loops, where some of the branches of the tree or chain are connected. Figure 2 illustrates such a system. These systems are useful in

---

\* Partial support for this research was obtained from the Office of Naval Research under Contract N00014-76C-0139

modelling such physical systems as: closed mechanisms, "docking" manipulators of spacecraft, ship cranes, restrained human body models, and cables anchored at both ends.

As noted above, this paper presents a procedure for the automatic formulation of the governing equations of such closed-loop multibody systems. The procedure is based upon Lagrange's form of d'Alembert's principle as exposited by Kane et al. (refs. 14, 20-22) and as used in refs. 9-12 to develop the dynamical equations of motion. It is also based upon a "zero eigenvalues theorem" as exposited by Walton and Steeves (ref. 23) to provide an automatic inclusion in the analysis of the constraint equations. The balance of the paper itself is divided into four parts, with the following part providing some preliminary information useful in the sequel. This includes a review of dynamical formulations of multibody systems and a statement of the "zero eigenvalues theorem." This is followed in the next part by the governing equation formulation for constrained or closed-loop multibody systems. The final two parts discuss generalizations and other features of the formulation.

## PRELIMINARY CONSIDERATIONS

### Coordinates and Kinematics

Consider again the multibody system of figure 1. This system will have, in general,  $3N+3$  degrees of freedom where  $N$  is the number of bodies of the system. These degrees of freedom might be delineated as follows: Arbitrarily select a body of the system as a reference body. Call this body  $B_1$ . Next, label or number the remaining bodies of the system in ascending progression away from  $B_1$  through the branches of the tree structure, moving from branch to branch. Then the orientation of  $B_1$  relative to a fixed (inertial) reference frame  $R$  together with the orientation of the remaining bodies of the system relative to their adjacent lower-numbered bodies defines  $3N$  degrees of freedom. Finally, the location of an arbitrary reference point in  $B_1$  relative to  $R$  defines an additional 3 degrees of freedom.

The position and configuration of the system can thus be described by  $3N+3$  generalized coordinates  $x_\ell$ . Let  $y_\ell$  ( $\ell=1, \dots, 3N+3$ ) represent their time derivatives.\* Next, let  $\tilde{n}_i$  ( $i=1,2,3$ ) represent a mutually perpendicular unit vector set fixed in  $R$ . Let  $G_k$  represent the mass center of body  $B_k$  ( $k=1, \dots, N$ ). Then, it has been shown (refs. 20,21) that the velocity of  $G_k$  in  $R$  and the angular velocity of  $B_k$  in  $R$  may be expressed in the form:

$$\tilde{v}_k = v_{k\ell m} y_\ell \tilde{n}_m \quad \text{and} \quad \tilde{\omega}_k = \omega_{k\ell m} y_\ell \tilde{n}_m \quad (1)$$

(Regarding notation, a repeated index, such as  $\ell$  or  $m$  in Equation (1) represents a

\* The reason for using the symbol  $y_\ell$  instead of  $\dot{x}_\ell$  is that there are instances when it is convenient to select the  $y_\ell$  prior to the selection of the  $x_\ell$ . This often results in functions  $y_\ell$  (called "generalized speeds") which cannot be integrated to obtain the coordinate  $x_\ell$ . In such cases, the  $x_\ell$  do not, in general, exist (and are sometimes called "quasi-coordinates"). This occurs, for example, when the  $y_\ell$  are selected as angular velocity components. (See ref. 24.)

sum over the range of that index, unless otherwise stated.) The coefficients  $v_{k\ell m}$  and  $\omega_{k\ell m}$  in equation (1), and their derivatives, play a central role in the analysis of the sequel. They are components of the so-called "partial velocity" and "partial angular velocity" vectors:  $\partial v_k / \partial y_\ell$  and  $\partial \omega_k / \partial y_\ell$ . These vectors are useful in forming the generalized active and inertia forces of the system. The coefficients  $v_{k\ell m}$  and  $\omega_{k\ell m}$  and their derivatives may be formed by simple multiplication algorithms as developed in refs. 9-12. Hence, by differentiating in equation (1), the acceleration of  $G_k$  in  $R$  and the angular acceleration of  $B_k$  in  $R$  may be expressed as:

$$\ddot{a}_k = (\dot{v}_{k\ell m} y_\ell + v_{k\ell m} \dot{y}_\ell) \underline{n}_m \quad \text{and} \quad \ddot{\alpha}_k = (\dot{\omega}_{k\ell m} y_\ell + \omega_{k\ell m} \dot{y}_\ell) \underline{n}_m \quad (2)$$

### Equations of Motion

Consider the system in figure 1 to be subjected to an externally applied force field which may be represented on a typical body  $B_k$  by a single force  $\underline{F}_k$  passing through  $G_k$  together with a couple with torque  $\underline{M}_k$ . Similarly, let the inertia force system on  $B_k$  be represented by a single force  $\underline{F}_k^*$  passing through  $G_k$  together with a couple with torque  $\underline{M}_k^*$ . Then  $\underline{F}_k^*$  and  $\underline{M}_k^*$  may be expressed as (ref. 21):

$$\underline{F}_k^* = -m_k \ddot{a}_k \quad (\text{no sum}) \quad (3)$$

and

$$\underline{M}_k^* = -\underline{I}_k \cdot \ddot{\alpha}_k - \underline{\omega}_k \times (\underline{I}_k \cdot \underline{\omega}_k) \quad (\text{no sum}) \quad (4)$$

where  $m_k$  is the mass of  $B_k$  and  $\underline{I}_k$  is the inertia dyadic of  $B_k$  relative to  $G_k$ . Through use of orthogonal transformation matrices (ref. 10),  $\underline{I}_k$  may be expressed in the form:

$$\underline{I}_k = I_{kmn} \underline{n}_m \underline{n}_n \quad (5)$$

Lagrange's form of d'Alembert's principle then leads to governing dynamical equations of motion of the form (ref. 21):

$$\underline{F}_\ell + \underline{F}_\ell^* = 0 \quad \ell = 1, \dots, 3N+3 \quad (6)$$

where  $\underline{F}_\ell$  is called the "generalized active force" and may be expressed as:

$$\underline{F}_\ell = v_{k\ell m} \underline{F}_{km} + \omega_{k\ell m} \underline{M}_{km} \quad (7)$$

where there is a sum from 1 to  $N$  on  $k$  and from 1 to 3 on  $m$ , and where  $\underline{F}_{km}$  and  $\underline{M}_{km}$  are the  $\underline{n}_m$  components of  $\underline{F}_k$  and  $\underline{M}_k$ . Similarly,  $\underline{F}_\ell^*$ , in equation (6), is called the "generalized inertia force" and may be expressed as:

$$\underline{F}_\ell^* = v_{k\ell m} \underline{F}_{km}^* + \omega_{k\ell m} \underline{M}_{km}^* \quad (8)$$

where there is a sum from 1 to  $N$  on  $k$  and from 1 to 3 on  $m$ , and where  $\underline{F}_{km}^*$  and  $\underline{M}_{km}^*$  are the  $\underline{n}_m$  components of  $\underline{F}_k^*$  and  $\underline{M}_k^*$ .

Substituting from equations (1) to (5) into (7) and (8) and finally into (6) leads to the equations of motion which may be written in the form (ref. 10):

$$a_{\ell q} \ddot{y}_q = f_\ell \quad \ell = 1, \dots, 3N+3 \quad (9)$$

where there is a sum from 1 to  $3N+3$  on  $q$  and where  $a_{\ell q}$  and  $f_\ell$  are given by:

$$a_{\ell q} = m_k v_{k\ell m} v_{kqm} + I_{kmn} \omega_{k\ell m} \omega_{kqn} \quad (10)$$

and

$$f_\ell = F_\ell - (m_k v_{k\ell m} \dot{v}_{kum} y_u + I_{kmn} \omega_{k\ell m} \dot{\omega}_{kun} y_u + e_{nmh} I_{kmr} \omega_{kun} \omega_{ksr} \omega_{k\ell h} y_u y_s) \quad (11)$$

where there is a sum from 1 to  $N$  on  $k$ , from 1 to  $3N+3$  on  $u$  and  $s$  and from 1 to 3 on the other repeated indices and where  $e_{nmh}$  is the standard permutation symbol (ref. 25).

### Constraint Equations

Equations (9) represent the governing dynamical equations for open chain or open tree systems. However, if the system has one or more closed loops, as illustrated in figure 2, there are additional equations which need to be satisfied to insure that the closed loops are maintained throughout the motion of the system. These equations are holonomic constraint equations (ref. 21) and they may be written in the form:

$$g_i(x_\ell) = 0 \quad i = 1, \dots, m; \quad m < 3N+3 \quad (12)$$

(These equations may be obtained by simply adding to zero the relative position vectors of the connecting joints around the respective loops.) It should be noted that constraint equations of the form of equation (12) can arise in ways different than that of the closed loops mentioned above. This can occur, for example, with restrictions on the motion at a joint or with the anchoring of one or several of the bodies to a fixed frame  $R$ . Finally, by differentiating, equation (12) becomes a linear relation in the  $y_\ell$  and may be expressed in the form:

$$b_{i\ell} \dot{y}_\ell = 0 \quad i = 1, \dots, m; \quad \ell = 1, \dots, 3N+3 \quad (13)$$

where the  $b_{i\ell}$  are, in general, functions of  $x_\ell$  and  $t$ . Equations (9) and (13) thus constitute the governing equations for a "closed-loop" system. These are to be cast into a solvable form in the sequel.

### Zero Eigenvalues Theorem

For a constrained  $N$  body chain system, the  $n$  dynamical equations (9) together with the  $m$  constraint equations (13) constitute  $n+m$  equations for the unknown  $y_\ell$ , where  $n$  is  $3N+3$ . Hence, the system is overdetermined. One approach to overcoming this difficulty is to solve equations (13) for  $m$ , say the last  $m$ , of the  $y_\ell$  in terms of the first  $n-m$   $y_\ell$  as "independent" generalized coordinate derivatives. The

velocities and angular velocities can then be expressed exclusively in terms of these  $y_\ell$  (ref. 21). Finally, by following the procedure suggested by equations (6), (7), and (8),  $n-m$  governing dynamical equations are obtained for the  $y_\ell$  ( $\ell=1, \dots, n-m$ ).

Although this approach is suitable for relatively small systems, there are difficulties encountered in attempting to automate it for large systems. Among these difficulties is the development of an automated procedure for obtaining a consistent solution of equations (13) for  $m$  of the  $y_\ell$  in terms of the remaining  $n-m$   $y_\ell$ . Another difficulty is the problem of automatically eliminating these  $m$   $y_\ell$  from the velocities and the angular velocities. However, in 1966, while working on a constraint problem of a different context, Walton and Steeves (ref. 23) developed an automated procedure for solving equations such as equations (13), for the  $y_\ell$  ( $\ell=1, \dots, n$ ) in terms of  $p \geq n-m$  new independent coordinates  $z_r$  ( $r=1, \dots, p$ ). Moreover, an extension of their procedure can be developed to automatically eliminate  $m$  of the  $y_\ell$  from the velocity and angular velocity vectors. Their procedure and its extension are based on a "zero eigenvalues theorem" as outlined in the following paragraphs:

Consider equations (13) to be written in the matrix form as:

$$By = 0 \quad (14)$$

where  $B$  is an  $m \times n$  rectangular matrix with elements  $b_{i\ell}$  and  $y$  is an  $n$  element column matrix with elements  $y_\ell$ . From  $B$ , form the  $n \times n$  symmetric matrix  $S$ , defined as:

$$S = B^T B \quad (15)$$

where  $B^T$  is the transpose of  $B$ . Since  $S$  is symmetric, there exists an orthogonal matrix  $T$  such that:

$$T^T S T = \Lambda \quad (16)$$

where  $\Lambda$  is an  $n \times n$  diagonal matrix with real elements or "eigenvalues"  $\lambda_i$  ( $i=1, \dots, n$ ) (ref. 26). These eigenvalues are readily seen to be non-negative as follows: Let  $v$  be a typical column of  $T$  and let  $w$  be  $Bv$ . Then  $w^T w = v^T B^T B v = v^T S v$ . But  $w^T w \geq 0$ , and by equation (16),  $v^T S v$  is seen to be an element of  $\Lambda$ , say  $\lambda_i$ . Hence,  $\lambda_i \geq 0$ . It is also readily seen that there exist zero eigenvalues: Since  $B$  is an  $m \times n$  matrix, its rank is less than or equal to  $m$  (ref. 26). Then, by equation (15), the rank of  $S$  is also less than or equal to  $m$ . But since  $m < n$  the rank of the  $n \times n$  matrix  $S$  is less than  $n$ .

Let the columns of  $T$  in equation (16) be arranged so that the eigenvalues of  $S$ , or the diagonal elements of  $\Lambda$ , are ordered. That is, arrange  $T$  such that  $\lambda_1 \geq \lambda_2 \geq \dots \geq \lambda_n$ . (From the preceding argument, the last  $p$  of these will be zero, where  $p \geq n-m$ .) Next, let the  $m \times n$  matrix  $D$  be defined as:

$$D = B T \quad (17)$$

Then, from equations (15) and (16) it is seen that:

$$D^T D = \Lambda \quad (18)$$

Hence, since the last  $p$  rows (and columns) of  $\Lambda$  are zero,  $D$  may be written in the partitioned form:

$$D = [\hat{D}|0] \quad (19)$$

where  $\hat{D}$  is an  $(n-p) \times (n-p)$  matrix with mutually orthogonal columns, and where  $n-m \leq p < n$ . By noting that  $TT^T$  is the  $n \times n$  identity matrix, the constraint equation (14) may be written as:

$$By = BTT^T y \stackrel{D}{=} Dz = 0 \quad (20)$$

where  $z$  is the  $n$  element column matrix defined at  $T^T y$ . In view of equation (19), the final equality in equation (20) is satisfied if the first  $n-p$  elements of  $z$  are zero, irrespective of the values of the last  $p$  elements of  $z$ .

Since  $T$  is orthogonal, the definition in equation (20) may be "inverted" leading to the expression:

$$y = Tz \quad z \text{ is } n \times 1 \text{ vector} \quad (21)$$

However, since the first  $n-p$  elements of  $z$  are zero,  $y$  may be rewritten as:

$$y = \hat{T}\hat{z} \quad \hat{z} \text{ is } p \times 1 \text{ vector} \quad (22)$$

where  $\hat{T}$  is the  $n \times p$  matrix whose columns are the last  $p$  columns of  $T$ . (In view of the ordering defined above, these columns are the columns of  $T$  associated with the zero eigenvalues of  $S$ .) Thus, equation (22) provides a solution to equation (14) for the  $y_\ell$  in terms of the  $p$  independent (the last  $p$ ) elements of  $z$ . Moreover, equation (22) is an "algorithmic" expression in that standard numerical procedures exist for matrix diagonalization, eigenvalue determination, and hence, for the numerical evaluation of the  $n \times p$  matrix  $\hat{T}$ .

In index notation, equation (22) may be written as:

$$y_\ell = t_{\ell r} z_r \quad \ell = 1, \dots, n; \quad r = 1, \dots, p \quad (23)$$

where the  $t_{\ell r}$  may be thought of as components of the column eigenvectors  $\underline{t}_r$  in  $n$  dimensional space.

Finally, the formal statement of equation (22) constitutes the "zero eigenvalues theorem" (ref. 23).

#### GOVERNING EQUATIONS

The procedures outlined above can be used to systematically formulate governing equations of the multibody system which will automatically satisfy the constraint equations (13). To develop this formulation, consider again the partial velocity and partial angular velocity vectors discussed above. From equations (1) and (23) the velocity of  $G_k$  in  $R$  and the angular velocity of  $B_k$  in  $R$  may be expressed in the form:

$$\underline{v}_k = v_{k\ell m} t_{\ell r} z_r \underline{n}_m \quad \text{and} \quad \underline{\omega}_k = \omega_{k\ell m} t_{\ell r} z_r \underline{n}_m \quad (24)$$



where the  $z_r$  ( $r=1, \dots, p$ ) may be viewed as new generalized coordinate derivatives. The partial velocity of  $G_k$  in  $R$  and the partial angular velocity of  $B_k$  in  $R$ , with respect to  $z_r$ , then become:

$$\partial v_k / \partial z_r = v_{k\ell m} t_{\ell r} \dot{z}_m \quad \text{and} \quad \partial \omega_k / \partial z_r = \omega_{k\ell m} t_{\ell r} \dot{z}_m \quad (25)$$

Hence, the generalized active and inertia forces of equations (7) and (8) become:

$$F_r = v_{k\ell m} t_{\ell r} F_{km} + \omega_{k\ell m} t_{\ell r} M_{km} \quad (26)$$

and

$$F_r^* = v_{k\ell m} t_{\ell r} F_{km}^* + \omega_{k\ell m} t_{\ell r} M_{km}^* \quad (27)$$

Then, from Lagrange's form of d'Alembert's principle, the governing equations (6) become:

$$F_r + F_r^* = 0 \quad r = 1, \dots, p \quad (28)$$

or, more specifically:

$$a_{\ell q} t_{\ell r} \dot{y}_q = f_{\ell} t_{\ell r} \quad r = 1, \dots, p \quad (29)$$

where  $a_{\ell q}$  and  $f_{\ell}$  are given by equations (10) and (11).

Equations (29) together with the constraint equations (13) constitute the system of equations to be solved. A numerical procedure for their solution can be formulated as follows: Consider the general case where  $p=n-m$ . Then, by differentiating, the constraint equations (13) become:

$$b_{i\ell} \dot{y}_{\ell} = -\dot{b}_{i\ell} y_{\ell} \quad i = 1, \dots, m \quad (30)$$

Equations (29) and (30) form a total of  $n$  equations for the  $2n$  unknowns  $y_{\ell}$  and  $x_{\ell}$ . Hence, there needs to be annexed to these equations the expressions:

$$\dot{x}_{\ell} = y_{\ell} \quad \ell = 1, \dots, n \quad (31)$$

for the consistent numerical formulation of the governing equations. If the  $y_{\ell}$  are chosen such that the  $x_{\ell}$  do not exist, as mentioned earlier, then equations (11) must be replaced by analogous expressions relating  $y_{\ell}$  to other variables (such as Euler parameters (ref. 10) which define the relative orientations of the bodies).

The balance of the numerical formulation of the solution of equations (29), (30), and (31) is now routine: It is perhaps most conveniently expressed in matrix notation. To this end, let  $C$  be the  $n \times n$  matrix containing the coefficients of  $\dot{y}_{\ell}$  in equations (29) and (30). Then, in partitioned form  $C$  is:

$$C = \begin{bmatrix} a_{\ell q} t_{\ell r} \\ b_{i\ell} \end{bmatrix} \quad \begin{matrix} r = 1, \dots, n-m \\ i = 1, \dots, m \\ q, \ell = 1, \dots, n \end{matrix} \quad (32)$$

Similarly, let the right sides of equations (29) and (30) be combined into the column matrix  $f$ , which in partitioned form is:

$$f = \begin{bmatrix} f_{\ell r} \\ -b_{i\ell} y_{\ell} \end{bmatrix} \quad \begin{array}{l} r = 1, \dots, n-m \\ i = 1, \dots, m \\ \ell = 1, \dots, n \end{array} \quad (33)$$

Then the governing equations to be solved may be expressed in the relatively compact matrix form:

$$\dot{y} = C^{-1} f \quad \text{and} \quad \dot{x} = y \quad (34)$$

where  $x$  and  $y$  are the column matrices with elements  $x_{\ell}$  and  $y_{\ell}$  ( $\ell = 1, \dots, n$ ), respectively.

#### DISCUSSION

At this point there are several comments and observations which might be helpful. First, in the procedure of the zero eigenvalues theorem, the  $m$  constraint equations are solved for the  $n$   $y_{\ell}$  in terms of  $n-m$  new variables  $z_r$ . Interestingly, in the subsequent formulation of governing equations, these new variables  $z_r$  do not appear. Indeed, it is only the coefficients  $t_{\ell r}$  of the  $z_r$  which are used. As noted earlier, these coefficients are the components in  $n$ -dimensional space of the eigenvectors  $\underline{t}_r$  associated with the zero eigenvalues of  $S$ . However, in this context, since the corresponding eigenvalues are zero,  $S \underline{t}_r$  is zero and the eigenvectors  $\underline{t}_r$  are thus "orthogonal" to the rows of  $S$ . This in turn means that these eigenvectors are orthogonal to the rows of the constraint matrix  $B$ . (This conclusion was also reached in an earlier analysis of constraint equations in  $n$ -dimensional space (ref. 27).) Hence, let the rows of  $B$  be thought of as "constraint vectors" in  $n$ -dimensional space. Then, since the  $t_{\ell r}$  are used to form the new partial velocity and partial angular velocity vectors, the physical system can be considered to be constrained to move, in  $n$ -dimensional space, in directions orthogonal to these constraint vectors — that is, in directions defined by the eigenvectors  $\underline{t}_r$ .

Next, Lagrange's form of d'Alembert's principle is an ideally suited method for formulating the dynamical equations when there are accompanying constraint equations. Indeed, the governing differential equations may be developed by simply contracting the dynamical equations obtained, via the principle, by using the  $t_{\ell r}$  array obtained from the zero eigenvalues theorem. This procedure is seen to be successful since the generalized forces are linear, homogeneous functions of the partial velocity and angular velocity vectors, which in turn, are coefficients of the generalized coordinate derivatives (in the velocity and angular velocity vectors). Therefore, a modification of these derivatives directly changes these vectors and hence, also the generalized forces. This means that the modification procedure for the generalized coordinate derivatives, as developed by the zero eigenvalues theorem, may be directly applied to the dynamical equations themselves. Also, due to these arguments, it is seen that this procedure would not necessarily be successful if the dynamical equations were obtained by some other method. (Additional discussion of the merits of Lagrange's form of d'Alembert's principle may be found in refs. 10, 14, 20, 21, and 22.)

Finally, the procedure developed herein is deemed to be well suited for the automated development of the governing equations. Numerical algorithms are

currently being prepared to be incorporated into the computer codes discussed in refs. 10, 11, and 12. Additional information on this may be obtained from the authors.

#### REFERENCES

1. Bayazitoglu, Y. A.; and Chace, M. A.: Methods of Automated Dynamic Analysis of Discrete Mechanical Systems. ASME Journal of Applied Mechanics, vol. 40, 1973, pp. 809-819.
2. Chace, M. A.: Analysis of the Time Dependence of Multifreedom Mechanical Systems in Relative Coordinates. ASME Journal of Engineering for Industry, vol. 89, 1967, pp. 119-125.
3. Chace, M. A.; and Bayazitoglu, Y. A.: Development and Application of a Generalized d'Alembert Force for Multifreedom Mechanical Systems. ASME Journal of Engineering for Industry, vol. 93, 1971, pp. 317-327.
4. Gupta, V. K.: Dynamic Analysis of Multirigid-Body Systems. ASME Journal of Engineering for Industry, vol. 96, 1974, pp. 886-892.
5. Hollerback, J. M.: A Recursive Lagrangian Formulation of Manipulator Dynamics and a Comparative Study of Dynamics Formulation Complexity. IEEE Transactions, Systems, Man, and Cybernetics, vol. SMC-10, 1980, pp. 730-736.
6. Hooker, W. W.; and Margulies, G.: The Dynamical Attitude Equations for an n-Body Satellite. Journal of the Astronautical Sciences, vol. 12, 1965, pp. 123-128.
7. Hooker, W. W.: A Set of r Dynamical Attitude Equations for an Arbitrary n-Body Satellite Having r Rotational Degrees of Freedom. AIAA Journal, vol. 8, 1970, pp. 1205-1207.
8. Hooker, W. W.: Equations of Motion for Interconnected Rigid and Elastic Bodies. Celestial Mechanics, vol. 11, 1975, pp. 337-359.
9. Huston, R. L.; and Passerello, C. E.: On the Dynamics of Chain Systems. ASME Paper No. 74-WA/Aug 11, 1974.
10. Huston, R. L.; Passerello, C. E.; and Harlow, M. W.: Dynamics of Multi-Rigid-Body Systems. ASME Journal of Applied Mechanics, vol. 45, 1978, pp. 889-894.
11. Huston, R. L.; and Passerello, C. E.: On Multi-Rigid-Body System Dynamics. Computers and Structures, vol. 10, 1979, pp. 439-446.
12. Huston, R. L.; and Passerello, C. E.: Multibody Structural Dynamics Including Translation Between the Bodies. Computers and Structures, vol. 12, 1980, pp. 713-720.
13. Jerkovsky, W.: The Transformation Operator Approach to Multisystems Dynamics, Part I: The General Approach. Matrix and Tensor Quarterly, vol. 27, 1976, pp. 48-59.

14. Kane, T. R.; and Levinson, D. A.: Formulation of Equations of Motion for Complex Spacecraft. *Journal of Guidance and Control*, vol. 3, 1980, pp. 99-112.
15. Orin, D. E.; McGhee, R. B.; Vukobratovic, M.; and Hartoch, G.: Kinematic and Kinetic Analysis of Open-Chain Linkages Utilizing Newton-Euler Methods. *Mathematical Biosciences*, vol. 43, 1979, pp. 107-130.
16. Stepanenko, Y.; and Vukobratovic, M.: Dynamics of Articulated Open Chain Active Mechanisms. *Mathematical Biosciences*, vol. 28, 1976, pp. 137-170.
17. Uicker, J. J., Jr.: Dynamical Behavior of Spatial Linkages. *ASME Journal of Engineering for Industry*, vol. 91, 1969, pp. 251-265.
18. Vukobratovic, M.: Computer Method for Dynamic Model Construction of Active Articulated Mechanisms Using Kinetostatic Approach. *Mechanism and Machine Theory*, vol. 13, 1978, pp. 19-39.
19. Wittenburg, J.: Dynamics of Systems of Rigid Bodies. B. G. Teubner, Stuttgart, 1977.
20. Kane, T. R.: Dynamics of Nonholonomic Systems. *ASME Journal of Applied Mechanics*, vol. 28, 1961, pp. 574-578.
21. Kane, T. R.: Dynamics. Holt, Rinehart, and Winston, New York, 1968.
22. Huston, R. L.; and Passerello, C. E.: On Lagrange's Form of d'Alembert's Principle. *Matrix and Tensor Quarterly*, vol. 23, 1973, pp. 109-112.
23. Walton, W. C., Jr.; and Steeves, E. C.: A New Matrix Theorem and Its Application for Establishing Independent Coordinates for Complex Dynamical Systems with Constraints. NASA Technical Report TR R-326, October 1969.
24. Kane, T. R.; and Wang, C. F.: On the Derivation of Equations of Motion. *Journal of the Society for Industrial and Applied Mathematics*, vol. 13, 1965, pp. 487-492.
25. Brand, L.: Vector and Tensor Analysis. Wiley, 1947.
26. Ayres, F., Jr.: Matrices. Schaum's Outline Series, McGraw Hill, 1962.
27. Huston, R. L.; and Passerello, C. E.: On Constraint Equations - A New Approach. *ASME Journal of Applied Mechanics*, vol. 41, 1974, pp. 1130-1131.

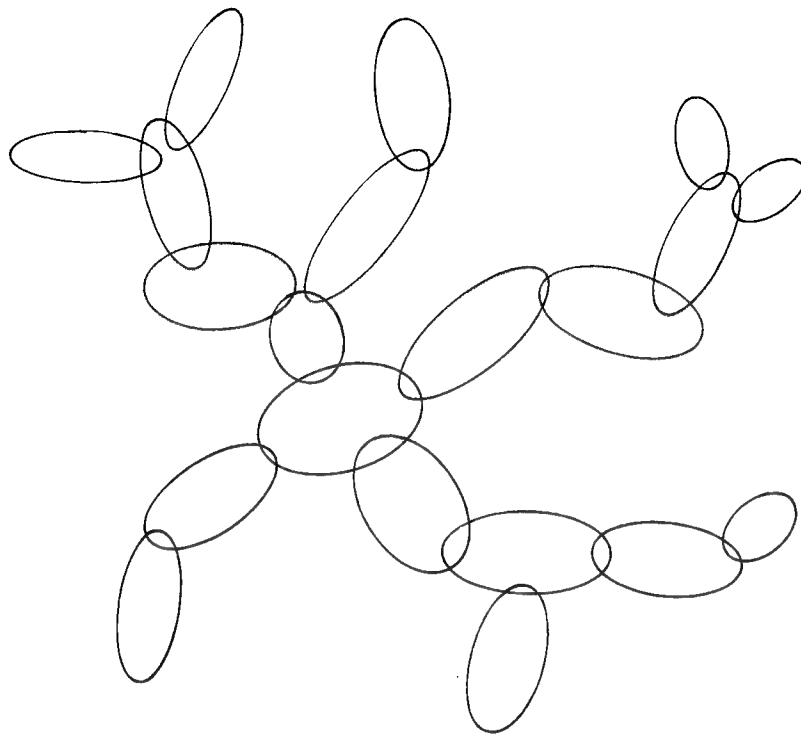


Figure 1.- An open-chain multibody system.

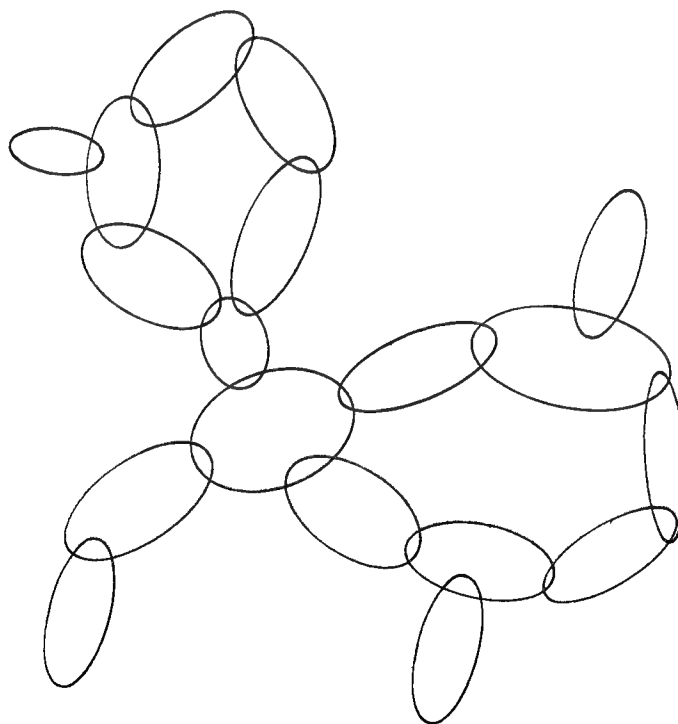


Figure 2.- A multibody chain system with closed loops.

SYSTEM IDENTIFICATION: A QUESTION OF  
UNIQUENESS, REVISITED\*

Joseph E. Hardee and Vernon C. Matzen  
North Carolina State University  
Raleigh, North Carolina

SUMMARY

Questions of uniqueness of parameters obtained from a system identification algorithm were investigated by using the local properties of the surface defined by the error function. Static and dynamic numerical experiments on determinate and indeterminate trusses and on shear buildings were used to illustrate the procedure. Examples are given of loading and sensor configurations which will ordinarily produce unique parameters.

INTRODUCTION

System identification as a method of forming or improving mathematical models using measured data is becoming more widely used in structural and solid mechanics. Conceptually, the method is very simple. As described for parametric models\*\* by Bekey (ref. 1), the method involves the following steps:

1. Select the form of the model and the parameters which are to be determined.
2. Select an error function to quantify the difference between the measured and predicted responses.
3. Minimize this error function using a parameter adjustment algorithm.

Unfortunately, the simplicity of the concept does not always lead to simplicity in the application. Complications can and often do arise which prevent the process from producing useful results. Three types of problems commonly encountered are

1. The parameter adjustment algorithm fails to converge.
2. Even if it does converge, the resulting parameters are not unique.
3. Even if the parameters are unique, they have little physical significance.

---

\*This work was performed under NSF Contract Number PFR-8007389.

\*\*Mathematical models for which terms and parameters have some physical significance, as opposed to nonparametric models in which they do not have any physical significance.

The primary purpose of this paper is to discuss the second of these problems in light of several static and dynamic numerical experiments conducted on trusses and shear buildings. In particular, we sought to find a method which would enable us to determine a) whether or not the parameters are unique, b) how many sensors are needed and where to place them, and c) the practical implication of parameters not being unique. We also touch briefly on the other two problems mentioned.

In this paper, we will describe our implementation of the three steps of system identification, the numerical experiments on trusses and shear buildings, our conclusions based on these experiments, and finally some recommendations for future research. It is perhaps worth repeating here that this work is based on numerical and limited physical experiments, and not on mathematical proofs. There have been several papers on the mathematical side of this uniqueness question (see refs. 2 and 3 for example), but they provide no direct help in obtaining parameters in time-domain models.

## SYSTEM IDENTIFICATION

The choice of the model and the parameters to be found depends not only on the structure, but also on the reasons for constructing the model. Because our interest was in the use of mathematical models to locate damaged members in structures, we chose a time-domain model with individual member properties as parameters. Two methods of excitation\* were used for the dynamic tests. The first was ground acceleration. The second was a pull-back-and-quick-release test. This second method is commonly used for testing structures, but it presents a problem in system identification. The pull-back load produces an initial set of displacements (with zero initial velocities) but, since displacements are not usually measured at every degree of freedom, the initial condition is not completely known. The solution we found most satisfactory was to use the current set of parameters in a static analysis to compute an initial condition.

Our error function was the integral of the weighted squared errors between the measured and computed accelerations (displacements for the static tests) at those degrees of freedom having sensors. As alluded to earlier, the number and placement of sensors affect the uniqueness of the results. This point will be discussed later along with the results of the numerical experiments. Another interesting point is how much time to use in the error integral. Using different amounts of time did not have the effect we expected of merely scaling up or down the ordinates of the error surface, but in some cases radically changed the surface configuration. This point, too, will be discussed later.

The parameter adjustment algorithms we used were the Conjugate Gradient and the modified Gauss-Newton. In most cases, the Gauss-Newton method worked very well, but in the more difficult situations, it was necessary to use the slower but more robust Conjugate-Gradient method.

---

\*Not all methods of system identification require that the excitation be known, but ours does.

## TRUSSES

### Static Loading

#### Numerical Experiments

The early stages of our work dealt with statically loaded, planar trusses. (See refs. 4 and 5.) A truss configuration typical of those we considered is shown in figure 1. The mathematical model was of the form

$$[K] \{X^j\} = \{P^j\} \quad (1)$$

where  $[K]$  is the stiffness matrix,  $\{X^j\}$  is the displacement vector, and  $\{P^j\}$  is the load vector, both for the  $j^{\text{th}}$  loading condition. The error function had the form

$$E^2(K) = \sum_{j=1}^{NLC} \sum_{i=1}^{NS} [X_c(K)_i^j - X_{m_i}^j]^2 \quad (2)$$

where the subscripts  $c$  and  $m$  refer to the computed and measured quantities,  $NLC$  is the number of loading conditions,  $NS$  is the number of sensors, and  $(K)$  indicates dependence on the member axial stiffnesses. The modified Gauss-Newton method was used for this part of the work.

After verifying that the procedure would locate the correct set of parameters if the displacements were known at every degree of freedom (DOF), we proceeded to the more realistic (and more interesting) case in which displacements were not known at every DOF. Our approach to investigating this question was to see how various changes in the given information affected the configuration of the error surface. The first truss considered had only two bars, with the obvious advantage that the error surface could be plotted. As a reference, figure 2 shows the surface for the case of a single load and displacements measured at both DOFs. The circled point has a zero error and corresponds to the correct values of the member stiffnesses. We might ask, if the figure were drawn using a wider range of values for  $K_1$  and  $K_2$ , would we encounter other points having exactly the same displacements as  $X_1$  and  $X_2$  and hence a zero error? No. In fact, physical insight leads us to the conclusion that the minimum shown is the only strict local minimum in the entire space of positive stiffnesses and is therefore a strict global minimum (i.e. the parameters are unique). Physical insight can be used here to make this determination about the global property of the minimum, but, unfortunately, it is not possible to use this approach on structures much more complex than this two-bar truss.

If displacements are known at every DOF, as they were in the example just given, then we say that the displacements are complete. It is possible to have incomplete displacement information and still have the parameters be unique. For example, if the two-bar truss shown in figure 2 had had only one sensor, but there had been two independent loading conditions, the surface would be similar to the one shown in figure 1 and the parameters could still be found uniquely. It is instructive here to consider other configurations of a single-node truss. If there are three members connected to the node, the truss becomes statically indeterminate, but this is of no consequence as long as there are at least as many measurements as



there are members. Complete displacement information and two independent loading conditions (producing four measurements) will work. If there are four members connected to the node, it may seem as though we could use the same loading and sensor configuration to obtain the four member stiffnesses. We cannot though because of another limitation which has to do with the number of independent terms in a symmetric stiffness matrix. A two-DOF structure has only three independent terms ( $N(N+1)/2$  independent terms for an  $N$  DOF structure), and there are an infinite number of combinations of member stiffnesses in a four-bar truss that will give the same stiffness matrix. Thus, it is impossible to obtain unique values for the four member stiffnesses using only displacement information.

The investigation of the two-bar truss described above was made easier by plotting the error surface as a function of the member stiffnesses, and noting the characteristics of the surface. When there are more than two parameters, this visual approach can no longer be used, but the characteristics of the surface can still be obtained mathematically. In particular, the eigenvalues of the Hessian matrix are the principal curvatures of the surface at the point where the Hessian is evaluated. For example, in figure 2 the eigenvalues at the minimum are both positive, indicating a strict local minimum. The surface for the three-bar truss would have the same characteristics. The error surface for the four-bar truss, on the other hand, although it cannot be plotted, would have an infinitely long valley of zero error. The correct set of stiffnesses would lie somewhere at the bottom of this valley, but, without more information, there would be no way of knowing where. The parameter adjustment algorithm would converge to different zero-error points along the valley for different sets of initial parameters. At each of these minima, the error and the gradient would both be zero, and the Hessian would have one zero eigenvalue. Based on these (and other) examples, we see that, as a general rule, the way to determine whether a minimum is strict, or whether it is merely one of the points along the bottom of the valley, is to do one or both of the following:

1. Compute the eigenvalues of the Hessian at the minimum to see if any are zero, and/or
2. Perturb the final set of parameters and restart the minimization algorithm to see if it converges to another set of parameters

This rule can be used for trusses of any complexity.

Returning to the two-bar truss, we consider two cases in which the parameters are not unique. The first of these, shown in figure 3, has a zero-force member. The displacements,  $X_1$  and  $X_2$ , are independent of  $K_2$ , and hence  $K_2$  cannot be found uniquely. The Hessian at every point along the bottom of the valley has a zero eigenvalue, and starting from different sets of initial parameters will give different values for  $K_2$  but not, of course,  $K_1$ . The second of these cases, shown in figure 4, is a truss having a single loading condition and a single sensor. Since this sensor provides only one piece of information, and since there are two parameters, the information is clearly insufficient. Again for this case, the algorithm would converge to some point along the bottom of the valley, and this point would have a zero eigenvalue associated with it.

In addition to the two-DOF truss, we also worked with the ten-bar, eight-DOF truss shown in figure 1. Since there can be at most eight independent loading

conditions, there must be at least two sensors\* in order to have at least ten measurements. We used five independent loading conditions and sensors at degrees of freedom one and three, and the algorithm converged easily to the correct set of stiffnesses.

### Physical Experiments

We report here briefly on a set of static experiments performed in our laboratory on a small truss model. The results turned out to be rather poor, but the experiment is a good example of one of the problems that can arise when using real as opposed to simulated measured data.

The structure tested was not actually a planar ideal truss, but rather a symmetric rectangular space frame. It was fabricated of 1/4" square aluminum bars bolted to double 1/8" steel gussett plates. Loads were applied symmetrically at nodes, and displacements were measured on both sides of the structure to ensure that the response was symmetric. Displacements were measured with 0.0001" dial gauges. Mathematical analyses of the structure, considering it to be first a truss and then a frame, demonstrated that the dominate effect was truss action.

Several loading conditions were applied in order to obtain a sufficient number of measurements. The minimization algorithm converged easily and the eigenvalue of the Hessian\*\* at the minimum were all positive. To give the resulting parameters some physical significance, we used the known cross-sectional area and elastic modulus for each member, and computed an effective member length. Results from one of the truss configurations used are shown in figure 5. (The measured lengths are clear lengths between the gussett plates.) The measured and computed lengths are clearly not in good agreement.

Our appraisal of this result is that the minimum found is indeed the global minimum, but that the mathematical model does not represent well the physical model (perhaps because of slipping at the joints). The solution is to change the mathematical model so that it better represents the truss model; system identification can do no more for this mathematical model since it has already found the best possible set of parameters and hence the best possible equivalent "planar, ideal truss" model.

From this example, we conclude that if the terms in the model are to represent specific structural characteristics (and not all researchers require this) then the resulting parameters must be treated with caution unless some independent verification is available. For this reason, we recommend including one or more parameters which can be determined by other means as a check on the work.

---

\*We reported in reference 5 that there must be a sensor at every node. We have since learned that this is not necessary.

\*\*We do not actually compute the Hessian, but rather an approximation to it. The two matrices are identical when the error is zero. At the minimum in this example, the error was not zero, and so the eigenvalues of the approximate Hessian were not exactly the principal curvatures. However, the error was small enough that we still considered the eigenvalues to contain curvature information.

## Dynamic Loading

The second stage of our work involved dynamic numerical experiments on the truss shown in figure 1. The mathematical model given in equation (1) was modified to include lumped masses at each joint. Using a pull-back-and-quick-release test, we found that the program converged easily to the correct set of parameters using accelerations at every DOF. We systematically reduced the number of accelerometers until we were using data from only one accelerometer. In all cases, the algorithm converged to the correct set of parameters.

Except for the case of complete data, it is not possible to determine whether or not the parameters are unique. It seems possible that, when the data are incomplete, there might be other combinations of stiffnesses that would also give zero error, although we did not find any such points.

It is interesting to note that the number of sensors required for static and dynamic loadings are different. The truss shown in figure 1 required two sensors for static loading and only one for dynamic loading. The reason for this difference is not yet understood.

## SHEAR BUILDINGS

The only experiments performed on shear buildings were for dynamic loading and numerically simulated data. The first was a two-story structure subjected to ground acceleration. This structure and type of loading have been discussed by Udwadia and Sharma in reference 6. The following summarizes two pertinent points from their paper:

1. If the accelerations are known at the base and at the first floor, then all of the parameters (stiffnesses and/or damping coefficients) can be found uniquely.
2. If the accelerations are known at the base and at the top floor, then there are at most  $n!$  different sets of parameters that give a zero error. ( $n$  is the number of floors.)

Our work supports these findings. We considered three different placements of sensors in this investigation and obtained the following results:

1. When the accelerations were known at the base and at both floors, our program (using only the modified Gauss-Newton algorithm) converged easily to the correct set of parameters, regardless of the initial set used.
2. If the accelerations at the base and at the first floor were used, the program covered as above; again regardless of the initial set of parameters.
3. When the accelerations at the base and at the top floor were used, the results were more interesting. Our program located two different sets of parameters, each of which gave a zero error. Udwadia and Sharma gave, and we verified, the following relationship between the correct and alternate set of parameters:

$$\tilde{K}_1 = K_2 m_r$$

$$\tilde{K}_2 = K_1 / m_r$$

where  $m_r = m_1 / (m_1 + m_2)$ , and the tilde indicates the alternate set. Each point is a strict relative minimum, as shown by the fact that the eigenvalues of the approximate Hessian at both points are greater than zero.

The second case we investigated was the pull-back-and-quick-release test. We pulled the structure back in two different configurations. The structure was first pulled from the top floor, and then from the bottom floor. In each case, we used the same three sensor configurations that were used in the previous set of tests. However, unlike the previous results, the algorithm converged to the correct set of parameters for each of the three sensor configurations, regardless of the initial values used. This result suggests to us that the restrictions needed to ensure uniqueness when ground accelerations are used, are probably not applicable to the pull-back-and-quick-release test. In this case, a single sensor placed at any floor is sufficient to ensure uniqueness.

An unexpected result, and one that has practical implications, was obtained in this set of tests. In one test, the minimization became more difficult as more time was used in the error function. This was contrary to our understanding of how system identification ought to work for linear\* structures. To investigate this behavior, we plotted the error surface for four different amounts of time in the error integral. Figure 6 shows the result. These data were generated using sensors at each floor, that is, using complete information. This figure illustrates that, even though there may be only one point with zero error, there may be many points that have zero gradient and positive eigenvalues. Thus, if a very poor choice is made for the initial set of parameters, the algorithm may converge to one of these spurious local minima. This problem can be avoided by adding to the error function the weighted squared difference between the current and initial set of parameters. The term can then be taken out as the algorithm begins to converge to the correct minimum. On the other hand, if one or more of the natural frequencies have been measured, then the weighted squared difference between these quantities and their computed counterparts could be added to the error function. Both of these terms have the effect of modifying the surface so that the spurious minima become less significant.

The next structure considered was a three-story shear building. The test program for this structure was conducted in the same manner as before, with base excitation as the first loading. Again, three different sensor configurations were investigated. The results are

1. When the accelerations were known at the base and all three floors, our program converged with no difficulty to the correct set of parameters.
2. When the accelerations at the base and at the first floor were used, the program again converges with no difficulty.

---

\*See reference 7 for an example of this behavior for nonlinear structural response.

3. When the accelerations at the base and at the top floor were used, however, the results were less straightforward. Six sets of initial parameters were tried, with the following results:
  - a. From three of the sets of initial parameters, the program did converge to the correct set, although the Conjugate-Gradient method was needed in the first few iterations before the modified Gauss-Newton method would work well.
  - b. One initial set was at a minimum identified by Udwadia and Sharma. In that case, the convergence criterion was satisfied at this first point, and no further iterations were required. It is perhaps worth noting here that our algorithm failed to converge to any of the other five minima indicated by Udwadia and Sharma to exist (but not given).
  - c. From the two other sets of initial parameters, the program failed to converge after a reasonable number of iterations. Our assessment was that, whereas this difficulty was directly linked to having the sensor at a poor location, the real problem was an algorithm that was not robust enough.

The second series of tests with this structure were conducted using the pull-back-and-quick-release loading. We pulled the structure in three different configurations.

1. In the first configuration, the structure was pulled from the top floor.
  - a. Using accelerations at all floors, the algorithm converged easily to the correct set of parameters.
  - b. Using only the acceleration at the top floor, the program still converged to the correct set of parameters from every initial set we tried.
  - c. Using the acceleration at the bottom floor only, the program still usually converged to the correct set. However, three of the initial sets led to what we thought at first might be a second minimum which was very close (5-7% difference in each parameter) to the correct set. However, by using more time in the error function and restarting the minimization at this point, the algorithm converged to the correct set. Thus it seems that using more time in the error function has two effects. It may add spurious minima to the error surface, while at the same time improving the surface in the neighborhood of the true minimum.
2. The second configuration was pulling the structure from the bottom floor. In the only experiment conducted with the load in this position, the acceleration from the top floor was used. The algorithm converged, but with some difficulty. This difficulty is thought to be similar to the problem discussed above in 1c.

3. In the third configuration, the loads were applied such that the deflected shape was exactly the same as the first mode shape. The algorithm converged with no difficulty. This result is in contrast to a statement by Ibanez (ref. 8) in which he lists as one of the limitations of this type of testing the possibility of exciting certain modes and not others. In our example, it seemed to make no difference that only one mode was excited.

These results on the three-story shear building seem to reinforce the tentative conclusion given for the two-story shear building. We can now restate the conclusion as follows: For a pull-back-and-quick-release test, a single sensor placed at any floor is sufficient to ensure uniqueness, as long as an appropriate amount of time is used in the error function.

### CONCLUSIONS AND RECOMMENDATIONS

The conclusions given here are based on numerical experiments with two types of structures (planar ideal trusses and shear buildings) subjected to two types of loading (ground acceleration and pull-back-and-quick-release type loading). Whether or not these conclusions will turn out to be valid under all conditions and whether or not they might be applicable to other types of structures and loading, we do not yet know. Answers to these questions must await further research.

Based on our numerical static experiments with planar ideal trusses, we conclude that all member stiffnesses can be found uniquely if the number of independent measurements is greater than or equal to the number of stiffnesses. If the condition on the number of independent measurements is not met, the error surface will have at least one valley of zero error going through the correct set of stiffnesses, and there will be an infinite number of sets of parameters satisfying the measured information. Parameters for zero-force members can, of course, never be found uniquely.

Based on our numerical dynamic experiments with pull-back-and-quick-release tests on trusses and shear buildings, we conclude that all member stiffnesses can be found uniquely using accelerations measured at any one of the degrees of freedom.

Numerical dynamic experiments with shear buildings subjected to ground acceleration lead us to the same conclusion Udawadia and Sharma (ref. 6) arrive at--that, for almost all cases except for sensors placed at the base and at the first floor, parameters cannot be found uniquely. Our experience, however, was that all sets of parameters other than the correct set were very difficult to locate; and, once found, were different enough from the correct set that, under normal circumstances, there would be no difficulty in determining whether or not a set is correct.

Further research is needed in the following areas:

1. Determine the validity of the conclusion given above using additional numerical experiments and, if possible, theoretical mathematical methods.
2. Extend the application of this work to include more complex and realistic structures.

3. Investigate the effect of imperfect models and noisy data, and
4. Obtain and use high-quality data from well-controlled static and dynamic experiments on trusses, shear buildings, and other structures of interest. Benchmark data such as this, in my opinion, would be a valuable asset to all researchers involved in system identification research.

#### REFERENCES

1. Bekey, G. A., "System Identification - An Introduction and a Survey," Simulation, Vol. 5, No. 4, October 1970, pp. 151-166.
2. Beck, J. L., "Determining Models of Structures from Earthquake Records," Earthquake Engineering Research Laboratory, EERL 78-01, California Institute of Technology, Pasadena, California, June 1978.
3. Udwadia, F. E., Sharma, D. K., and Shah, P. C., "Uniqueness of Damping and Stiffness Distributions in the Identification of Soil and Structural Systems," Jour. Appl. Mech. Vol. 45, No. 1, March 1978, pp. 181-187.
4. Hardee, J. E., Jr., "On the Development of Two System Identification Techniques for the Formulation of Mathematical Models of Statically Loaded Linear Elastic Planar Trusses," MS Thesis, North Carolina State University, Raleigh, 1980.
5. Matzen, V. C., and Hardee, J. E., "Mathematical Modelling of Indeterminate Trusses," Proceedings of the Second ASCE/EMD Specialty Conference on the Dynamic Response of Structures, January 1981, Atlanta, Georgia.
6. Udwadia, F. E., and Sharma, D. K., "Some Uniqueness Results Related to Building Structural Identification," SIAM Journal of Applied Mathematics, Vol. 34, No. 1, Jan. 1978, pp. 104-118.
7. Matzen, V. C., and McNiven, H. D., "Investigation of the Inelastic Characteristics of a Single Story Steel Structure Using System Identification and Shaking Table Experiments," Report No. EERC 76-20, Earthquake Engineering Research Center, University of California, Berkeley, August 1976.
8. Ibanez, P., "Review of Analytical and Experimental Structural Techniques for Improving Structural Dynamic Models," Welding Research Bulletin No. 249, June 1979.

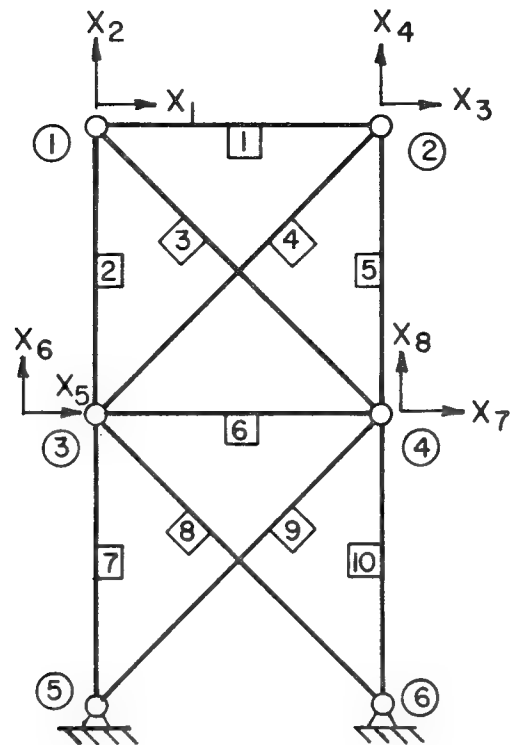


FIGURE 1. TYPICAL TRUSS CONFIGURATION

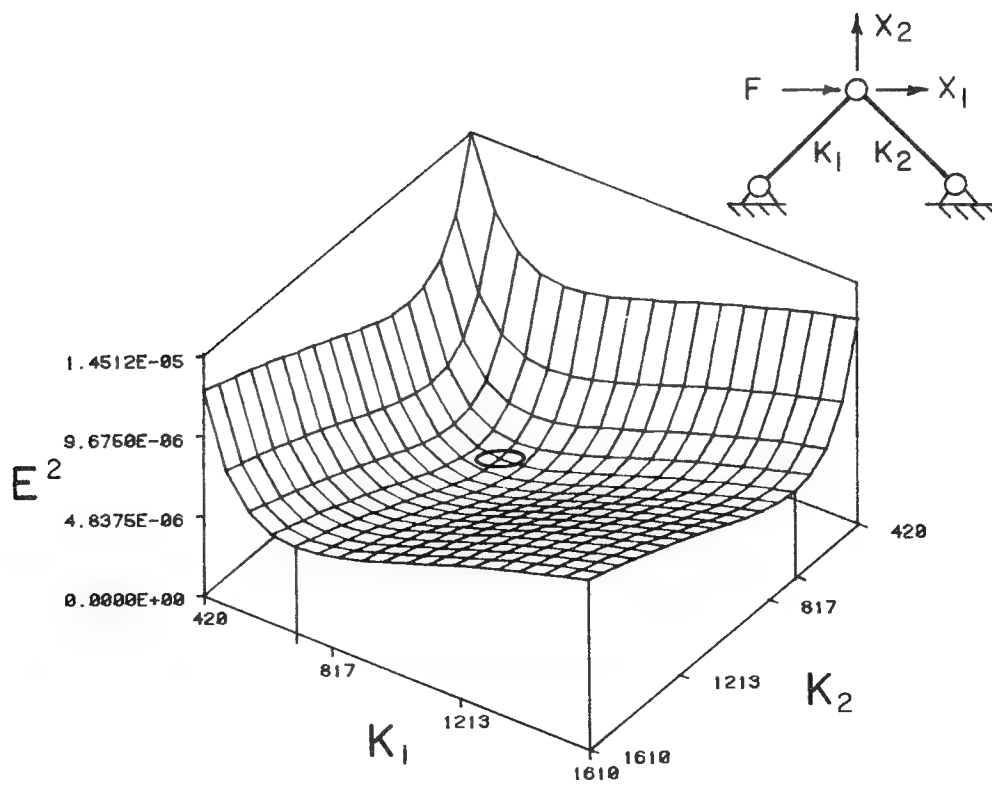


FIGURE 2. ERROR SURFACE FOR TRUSS WITH SUFFICIENT INFORMATION



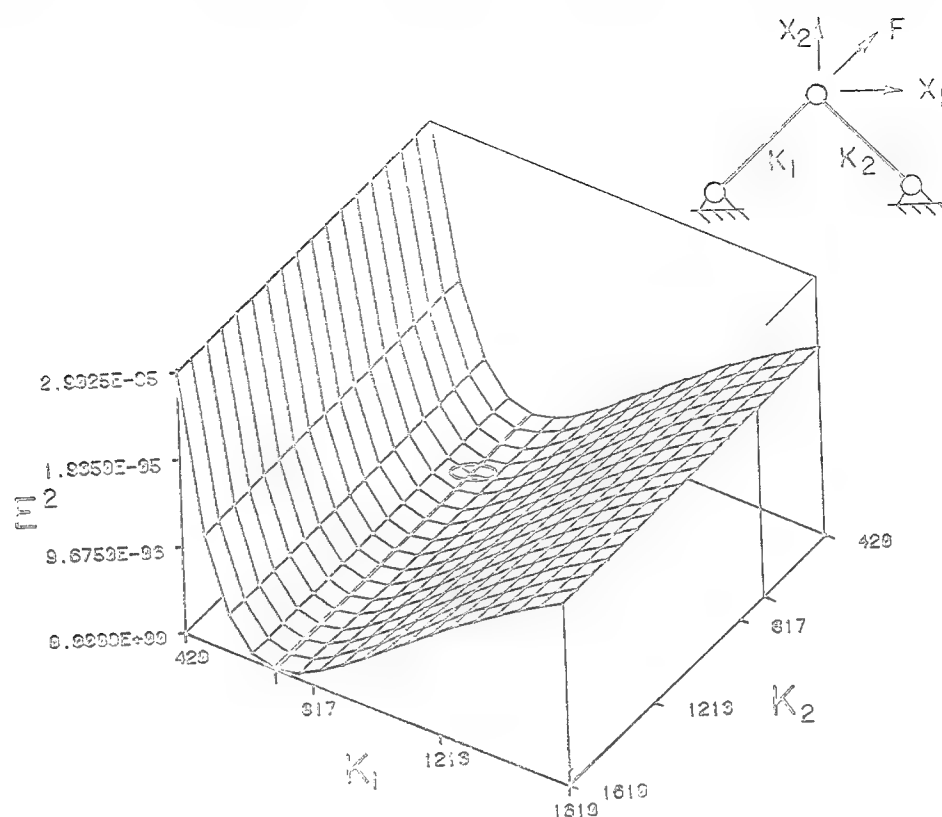


FIGURE 3. ERROR SURFACE FOR TRUSS WITH A ZERO FORCE MEMBER

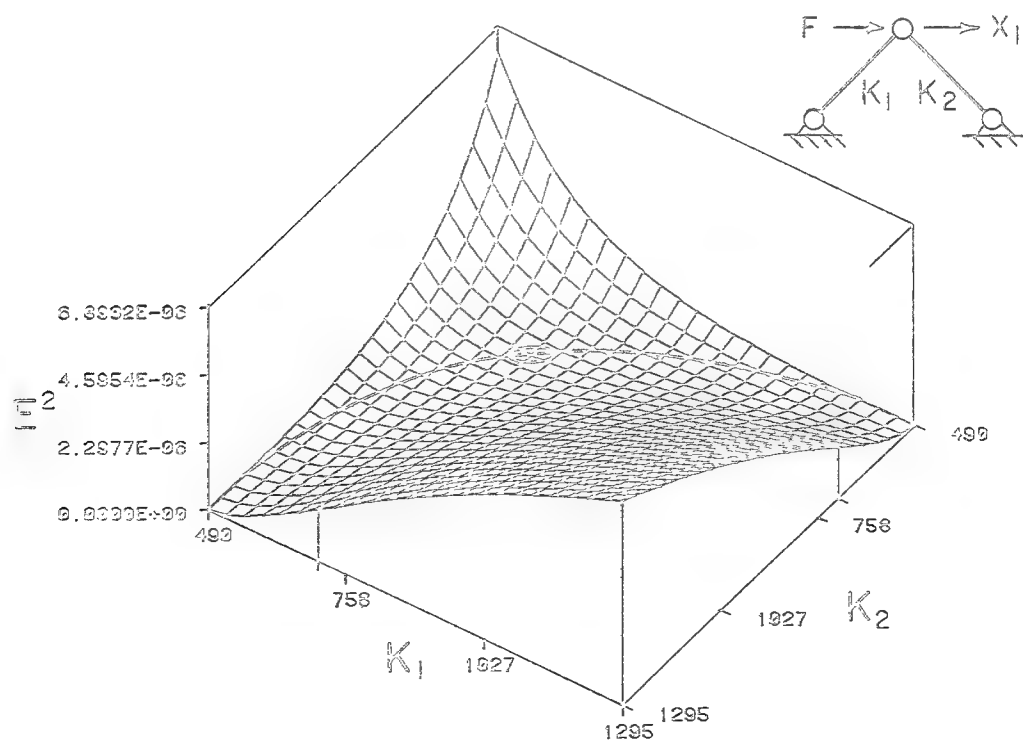
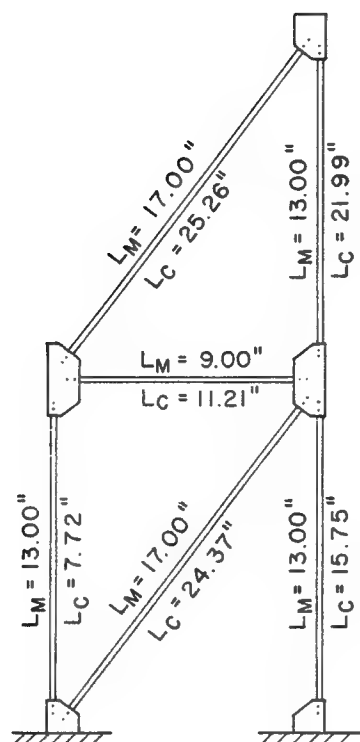


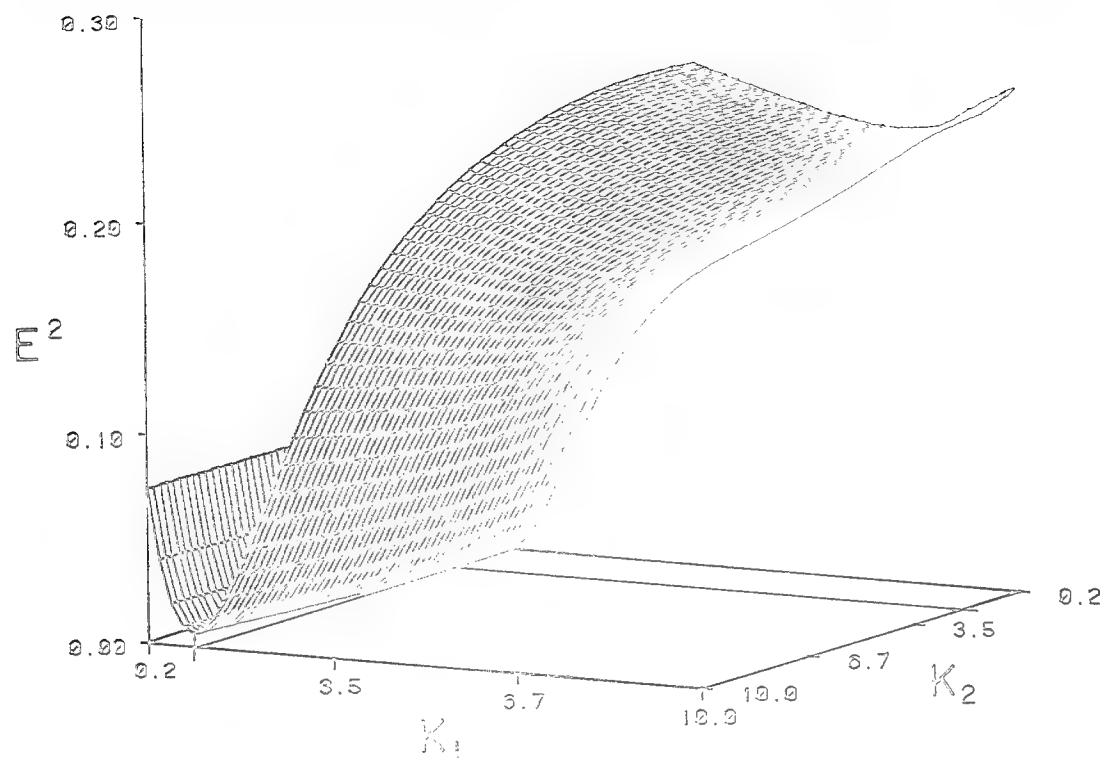
FIGURE 4. ERROR SURFACE FOR TRUSS WITH INSUFFICIENT INFORMATION



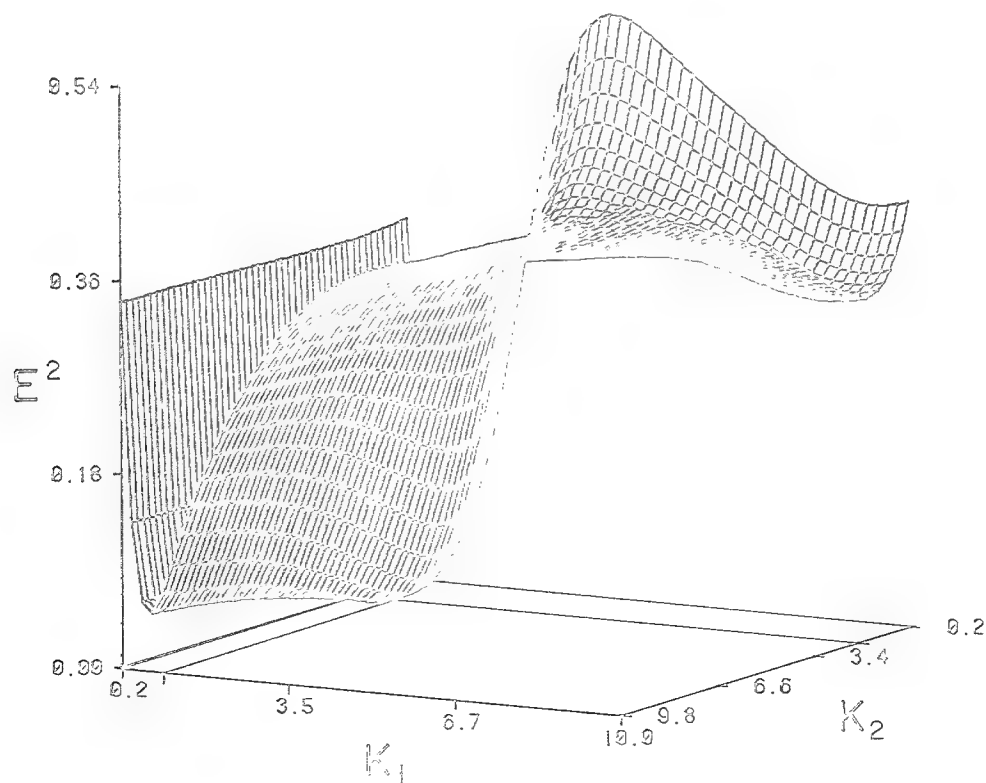
$L_M$  - MEASURED LENGTHS

$L_C$  - COMPUTED LENGTHS

FIGURE 5. LABORATORY TRUSS MODEL

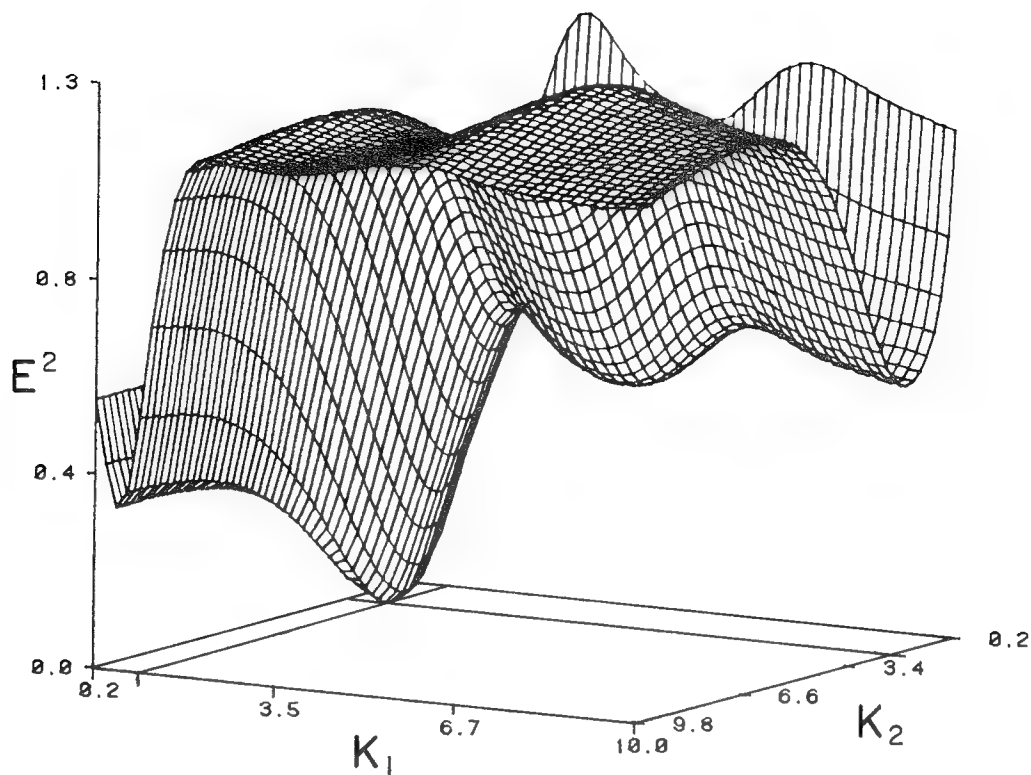


A)  $T = 1.5$  SECONDS

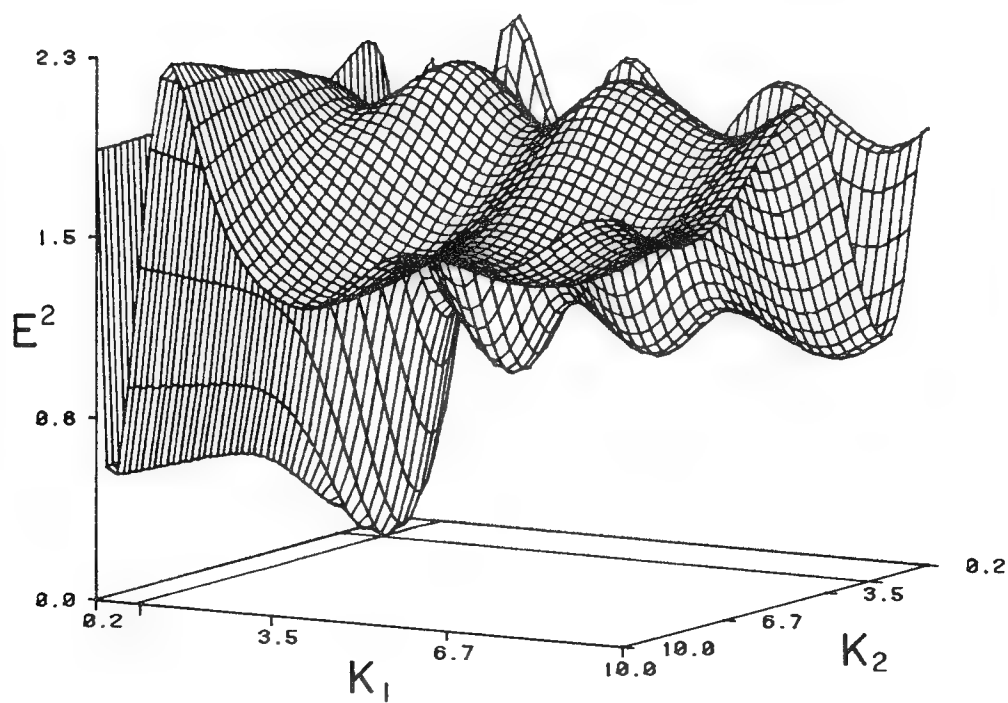


B)  $T = 3$  SECONDS

FIGURE 6. ERROR SURFACES FOR A DYNAMICALLY LOADED SHEAR BUILDING USING DIFFERENT AMOUNTS OF TIME IN THE ERROR FUNCTION



C)  $T = 6$  SECONDS



D)  $T = 9$  SECONDS

FIGURE 6. (CONCLUDED)

A COMPUTER PACKAGE FOR THE DESIGN AND EIGENPROBLEM  
SOLUTION OF DAMPED LINEAR MULTIDEGREE OF FREEDOM SYSTEMS\*

Mehdi Ahmadian and Daniel J. Inman  
Department of Mechanical and Aerospace Engineering  
State University of New York at Buffalo

SUMMARY

Systems described by the matrix differential equation of the form  $[M]\ddot{\underline{x}}(t) + [C]\dot{\underline{x}}(t) + [K]\underline{x}(t) = 0$  are considered. For the case of positive definite mass, damping, and stiffness matrices an interactive design routine is presented. Designing is accomplished by adjusting the mass, damping, and stiffness matrices to obtain a desired oscillation behavior (overdamping, underdamping, critically damping, or mixed damping). The algorithm also features interactively modifying the physical structure of the system, obtaining the matrix structure and a number of other system properties. In case of a general system, where the  $[M]$ ,  $[C]$ , and  $[K]$  matrices lack any special properties (i.e., symmetry, positive definiteness, ...), a routine for the eigenproblem solution (latent roots and latent vectors) of the system is developed. The latent roots are obtained by computing the characteristic polynomial of the system and solving for its roots. The latent vectors are computed by substituting the latent roots in the equation  $D_2(\lambda_i)\underline{z}_i$   $i=1,2,\dots,n$  and solving for the  $\underline{z}_i$ . The above routines are prepared in FORTRAN IV and prove to be usable for the machines with low core memory.

INTRODUCTION

Many linear damped multidegree of freedom systems can be described by using the matrix differential equation:

$$[M]\ddot{\underline{x}}(t) + [C]\dot{\underline{x}}(t) + [K]\underline{x}(t) = 0 \quad (1)$$

where  $\underline{x}(t)$  is an  $n$ -dimensional vector representing the displacement and  $[M],[C],[K]$  are  $n \times n$  mass, damping and stiffness matrices. A computer package based on equation (1) has been developed for designing and obtaining the eigenproblem solution of linear damped systems. The package consists of two programs; i) an interactive design routine based on the adjustment of mass, damping and stiffness matrices, ii) a batch routine for solving the eigenproblem of a general damped system, regardless of any property of the matrices.

Assuming positive definite mass, damping, and stiffness matrices, the properties of such systems have been studied in previous works (ref. 1). It has been shown that a great deal of information regarding the oscillatory behavior and stability of a damped linear system can be obtained by studying the properties of these matrices.

---

\* This work was performed under National Science Foundation Grant Number MEA 8112826.

It also has been shown in the above references that overdamping, underdamping, or critically damping can be obtained in each mode by adjusting the  $[M]$ ,  $[C]$ , and  $[K]$  matrices in a prescribed fashion. Based on these principles an interactive procedure has been developed. This procedure allows the user to design a system of given structure so that each mode of the free response will oscillate (underdamped) or not oscillate (overdamped or critically damped) as required by the user. In addition to the above, the program also calculates the eigenproblem solution of the designed system, plots the mode shapes, and indicates whether or not the system possesses classical normal modes (i.e., if  $[C][M]^{-1}[K] = [K][M]^{-1}[C]$ ) (ref. 2). This information is useful for comparison, as well as for indicating the success of the design routine.

In most classical approaches and even in a large number of recent publications, damping has been either ignored or assumed as a linear combination of the mass and stiffness matrices (Rayleigh damping). The above assumptions cannot be made for every practical system and such assumptions may result in intolerable errors. Even the restriction of symmetric damping and stiffness matrices are sometimes not reasonable. For instance, many systems contain gyroscopic forces and/or constraint damping which produce an asymmetric matrix equation. As a result a more versatile routine, capable of solving the eigenproblem for any mass, damping, and stiffness matrix is also provided. The program provides the definiteness of the matrices, characteristic equation, latent roots, latent vectors (ref. 3), and a plot of modes.

Two examples, a clamped-end flexible beam with internal and external damping and a simply supported rotatory shaft with an axial load, are used to illustrate the utility of the package.

#### INTERACTIVE DESIGN ROUTINE

First equation (1) is transformed into a more tractable form. Assuming  $\underline{x}(t) = [M]^{-1/2} \underline{y}(t)$  and premultiplying by  $[M]^{-1/2}$  results in:

$$\ddot{\underline{y}}(t) + [\tilde{C}]\dot{\underline{y}}(t) + [\tilde{K}]\underline{y}(t) = 0 \quad (2)$$

where

$$[\tilde{C}] = [M]^{-1/2}[C][M]^{-1/2}$$

and

$$[\tilde{K}] = [M]^{-1/2}[K][M]^{-1/2}$$

Note that in the above transformation,  $[M]^{-1/2}$  denotes the inverse of the unique square root of the mass matrix. Since  $[M]$  is assumed to be positive definite (denoted  $[M] > 0$ ), the matrix  $[M]^{1/2} > 0$  exists and is unique (ref. 4).

Inman and Andry (ref. 1) have shown that the oscillation behavior of the system is determined by the definiteness of the matrix  $[\tilde{C} - 2\tilde{K}^{1/2}]$ . These concepts can be used to develop a design routine. But it is observed that the computation of the matrix  $[K]^{1/2}$  is a lengthy process. Thus a more efficient routine is desired. According to Bellman (ref. 5), if  $[A] > 0$  and  $[B] > 0$ , then  $[A]^{1/2}$  and  $[B]^{1/2}$  are also positive definite matrices. And, if  $[A-B] > 0$ , then  $[A^{1/2} - B^{1/2}]$  is also positive definite. This theorem can be used to rewrite the results in reference 1 in a more

efficient fashion which does not involve  $[K]^{1/2}$  as follows:

If  $[\tilde{C}^2 - 4\tilde{K}] > 0$ , then the system is overdamped in each mode. This case results in negative real latent roots.

If  $[4\tilde{K} - \tilde{C}^2] > 0$ , then the system is underdamped in each mode. In this case all the latent roots are complex numbers with negative real parts.

If  $[\tilde{C}^2 - 4\tilde{K}] = 0$ , then each mode is critically damped. In this case all the latent roots are pairs of negative real numbers.

If  $[\tilde{C}^2 - 4\tilde{K}]$  is indefinite and if  $\tilde{C}$  and  $\tilde{K}$  commute (i.e.,  $\tilde{C}\tilde{K} = \tilde{K}\tilde{C}$ ), then the system has mixed damping. In this case some of the modes are overdamped, which results in negative real latent roots, and some are underdamped resulting in complex latent roots with negative real parts.

Before discussing the design strategy for each case, the following theorem is required:

**THEOREM 1:** If  $[A]$  is not a positive definite matrix, then there exists a diagonal positive definite matrix  $[\Delta]$  such that  $[A] + [\Delta]$  is positive definite (ref. 6).

#### OVERDAMPED SYSTEM

As mentioned above, if the matrix  $[\tilde{C}^2 - 4\tilde{K}]$  is positive definite we have an overdamped system. Performing an orthogonal transformation on this matrix by using the modal matrix of  $[\tilde{C}]$  (denoted  $[S]$ ) results in:

$$[S]^T[\tilde{C}^2 - 4\tilde{K}][S] = [\lambda_{\tilde{C}^2}] - 4[S]^T[\tilde{K}][S] \quad (3)$$

where  $[\lambda_{\tilde{C}^2}]$  presents a diagonal matrix whose elements are the eigenvalues of the matrix  $[\tilde{C}]^2$ . According to theorem 1 if (3) is not positive definite, it is possible to find a positive definite diagonal matrix  $[\Delta]$  such that:

$$[\Delta] + [\lambda_{\tilde{C}^2}] - 4[S]^T[\tilde{K}][S] > 0 \quad (4)$$

Assume  $[\Delta]$  is chosen such that:

$$[\Delta] = \alpha[\lambda_{\tilde{C}^2}] \quad (5)$$

where  $\alpha$  is a scalar. Replacing  $[\Delta]$  by  $\alpha[\lambda_{\tilde{C}^2}]$  in (4) and performing the inverse orthogonal transformation results in:

$$(\alpha+1)[\lambda_{\tilde{C}^2}] + 4[S]^T[\tilde{K}][S] = [(\alpha+1)\tilde{C}^2 - 4\tilde{K}] > 0 \quad (6)$$

Thus, we have succeeded in constructing a damping matrix,  $[\tilde{C}]'^2 = (\alpha+1)[\tilde{C}]^2$ , which makes the original system overdamped. Note that the matrix  $[\Delta]$  has been chosen in a special form, shown in (5), in an attempt to keep the physical structure of the original system unchanged (i.e., so that no extra dampers or springs must be added to, or eliminated from, the system).

The above concept is programmed through an interactive routine. In each iteration a value of  $\alpha$  is chosen,  $[(\alpha+1)\tilde{C}^2 - 4\tilde{K}]$  is calculated and tested for its

definiteness. If the matrix is positive definite the iteration is stopped, otherwise  $\alpha$  is increased and replaced by  $\alpha + s$  and the process is repeated.

#### UNDERDAMPED SYSTEM

Considering the underdamped case, combined with theorem (1) it is possible to find a scalar multiple for  $[\tilde{K}]$  such that

$$[4(\alpha+1)\tilde{K}-\tilde{C}^2] > 0 \quad (7)$$

Again the above equation is programmed through an iterative routine similar to the previous case.

#### MIXED DAMPED SYSTEM

The system exhibits mixed damping if  $[\tilde{C}^2-4\tilde{K}]$  is indefinite. The previous concepts can be used to alter  $[\tilde{C}^2-4\tilde{K}]$  by forming the matrix

$$[(1+\alpha)\tilde{C}^2 - 4(1+\beta)\tilde{K}] \quad (8)$$

where  $\alpha$  and  $\beta$  are two scalars. If the above is positive definite,  $\beta$  is increased and if it is negative definite  $\alpha$  is increased. The process of changing these two variables is continued until the matrix shown in (8) becomes indefinite.

#### CRITICALLY DAMPED SYSTEM

For a critically damped system, we must have

$$[\tilde{C}^2-4\tilde{K}] = 0$$

which also implies commutivity between the  $[\tilde{C}]$  and  $[\tilde{K}]$  matrices (i.e.,  $[\tilde{C}][\tilde{K}] = [\tilde{K}][\tilde{C}]$ ). Applying an orthogonal transformation to the above equation results in:

$$[S]^T[\tilde{C}]^2[S] - 4[S]^T[\tilde{K}][S] = 0 \quad (9)$$

where  $[S]$  is the modal matrix of  $[\tilde{K}]$ . Because of commutivity between  $[\tilde{C}]$  and  $[\tilde{K}]$ , both  $[\tilde{C}]^2$  and  $[\tilde{K}]$  matrices are simultaneously diagonalized by the orthogonal transformation and (9) can be written as

$$[\Lambda_{\tilde{C}}^2] - 4[\Lambda_{\tilde{K}}] = 0$$

This implies

$$\Delta_{i\tilde{C}}^2 - 4\Delta_{i\tilde{K}} = 0 \quad (10)$$

where  $\Delta_{i\tilde{C}}$  and  $\Delta_{i\tilde{K}}$  are the  $i$ th eigenvalues of the  $[\tilde{C}]$  and  $[\tilde{K}]$  matrices. Then, to make a system critically damped, we proceed as follows:

- i - find the eigenvalues and modal matrix of  $[\tilde{K}]$
- ii - use the eigenvalues and (10) to find eigenvalues of  $[\tilde{C}]$  (i.e.,  $\Delta_{i\tilde{C}} = 2\Delta_{i\tilde{K}}^{1/2}$ )



iii - use the modal matrix  $[S]$ , obtained in step i, to calculate the matrix  $[\tilde{C}]$  according to the following transformation

$$[\tilde{C}] = [S][\Delta\tilde{C}][S]^T$$

Note that in this case there is no guarantee that the physical structure of the system remains unchanged. This means that we may have to add (eliminate) a number of dampers or springs to (from) the system.

#### EIGENPROBLEM SOLUTION OF GENERAL DAMPED SYSTEMS

It was mentioned previously that the dynamic behavior of a linear damped multidegree of freedom system can be described by equation (1). The characteristic equation associated with this equation is:

$$|[M]\lambda^2 + [C]\lambda + [K]| = 0 \quad (11)$$

where  $|\cdot|$  denotes the determinant of the matrix. The determinant of a matrix is defined as:

$$|A| = \sum_{j=1}^n a_{ij} A_{ij} \quad i=1,2,3,\dots,n$$

where  $A_{ij}$  is the  $(i,j)$ th cofactor and  $a_{ij}$  is the  $(i,j)$ th element. In our case  $a_{ij}$  and also each element of  $A_{ij}$  are quadratic elements in  $\lambda$ . Carrying out the above operation will result in the characteristic polynomial of the system which can be solved for the latent roots.

To find the product of two polynomial elements, each element is stored in two string storages  $B$  ( $B(N)$ ,  $N=1,2,3,\dots,I$ ) and  $C$  ( $C(N)$ ,  $N=1,2,3,\dots,J$ ). Their product is stored in another string storage  $D$  ( $D(N)$ ,  $N=1,2,3,\dots,(I+J-1)$ ) according to:

$$D(N) = \sum_{K=1}^I C(N+1-I) * B(K) \quad (12)$$

where

$$C(N+1-I) = 0 \quad \text{if} \quad I \leq N+1 < J+I$$

Each element (i.e., element  $m$ ) of the above arrays represents the coefficient of the  $(m-1)$ th power of  $\lambda$  (i.e.,  $\lambda^{m-1}$ ).

After finding the characteristic polynomial of the system, it is desired to compute its roots. Although many classical methods are available, most of them suffer from complications resulting from dealing with complex roots. One of the most suitable and efficient methods for dealing with complex roots is Lin-Baristow's method (refs. 7,8). This method works by extracting quadratic factors from the polynomial and solving each factor individually for its roots. The concepts presented in references 7 and 8 have been modified to handle zero roots and is used in this package.

The next step in the eigensolution of the system is to find the latent vectors. A non-zero vector  $\underline{z}_i$  is called an eigenvector corresponding to the eigenvalue  $\lambda_i$  if

$$[M]\lambda_i^2 + [C]\lambda_i + [K]z_i = 0 \quad \forall z_i \neq 0$$

or

$$[A]z_i = 0 \quad (13)$$

where  $[A]$  is in general a complex matrix. The above implies that the matrix  $[A]$  has a null space of at least rank 1. Equation (13) can be written as:

$$\begin{bmatrix} a_{11} & a_{12} & \dots & a_{1n} \\ a_{21} & a_{22} & \dots & a_{2n} \\ \vdots & \vdots & & \vdots \\ \vdots & \vdots & & \vdots \\ a_{1n} & a_{2n} & \dots & a_{nn} \end{bmatrix} \begin{bmatrix} z_1 \\ z_2 \\ \vdots \\ \vdots \\ z_n \end{bmatrix} = 0 \quad (14)$$

Because of the non-trivial null space, at least one of the rows of the above matrix is linearly dependent on the others. For the sake of discussion let's assume the last row is the dependent row. Using Gauss elimination method, the matrix  $[A]$  can be transformed into an upper triangle form and be written as:

$$\begin{bmatrix} b_{11} & b_{12} & \dots & b_{1n} \\ 0 & b_{22} & \dots & b_{2n} \\ 0 & 0 & & \vdots \\ \vdots & \vdots & & \vdots \\ \vdots & \vdots & & \vdots \\ 0 & 0 & \dots & 0 \end{bmatrix} \begin{bmatrix} z_1 \\ z_2 \\ \vdots \\ \vdots \\ z_n \end{bmatrix} = 0 \quad (15)$$

Assuming a known value for  $z_n$  and using the backward substitution method, equation (15) can be solved for the vector  $z_i$ . In general if the  $j$ th row is the dependent row, the matrix  $[A]$  is transformed into:

$$\begin{bmatrix} b_{11} & b_{12} & \dots & \dots & b_{1n} \\ 0 & b_{22} & \dots & \dots & b_{2n} \\ \vdots & \vdots & \dots & \dots & \vdots \\ \vdots & \vdots & & 0 & \vdots \\ 0 & 0 & & 0 & b_{1n} \\ \vdots & \vdots & & b_{(j+1)j} & \vdots \\ \vdots & \vdots & & \vdots & \vdots \\ 0 & 0 & & b_{nj} & b_{nn} \end{bmatrix} \begin{bmatrix} z_1 \\ z_2 \\ \vdots \\ \vdots \\ z_j \\ \vdots \\ \vdots \\ z_n \end{bmatrix} \quad (16)$$

Again, by assuming  $z_j$  to be known, the backward substitution method can be used to compute the vector  $z_i$ .

The above concept is generalized for a null space of any rank, in order to compute the latent roots of a system with multiple latent roots.

## FEATURES OF THE PACKAGE

The package consists of two programs for interactively designing a symmetric linear damped system (INTSYD) and eigenproblem solution of a general damped system (MUDSYS).

INTSYD is an interactive design routine which enables the user to interactively design a system by taking advantage of a large number of options provided in a MENU. The user is capable of obtaining all the important information regarding the system (i.e., the matrices, latent roots, latent vectors, characteristic polynomial, ...). It is also possible to change the structure of the system (by adding or eliminating mass, damper or spring), or to ask the program to design a system with a desired oscillation behavior. Loading the program, the user is provided with an introduction presenting the main functions of the program. Next the program requires the necessary data which include the degree of freedom of the system, mass, damping, and stiffness matrices. To simplify the inputting process, all the required data are free-formatted. Completing this step, the program informs the user of the status of the system (i.e., overdamped, underdamped, ...) and starts the interactive routine by providing the user with the list of the available options. Completing each inputted option, the interactive process is resumed and the user is provided with a chance to exercise another option.

MUDSYS is a routine for computing the eigenproblem solution, and other necessary information, of a general linear damped system. This routine computes the latent roots, latent vectors, a plot of mode shapes, and the characteristic polynomial of the system. It also provides the user with the definiteness of the mass, damping, and stiffness matrices as well as the commutivity of [C] and [K]. The required inputs to the program are the degree of freedom, printing code, [M], [C], and [K] matrices. These are all inputted in free-format form. Three different sets of information can be printed out by using the following printing codes:

IPRINT=1: Only the final results which are the latent roots and latent vectors are printed out.

IPRINT=2: This results in printing [M], [C], and [K] matrices along with the latent roots and vectors.

IPRINT=3: All the computed information which includes latent roots, latent vectors, characteristic polynomial, definiteness of mass, damping, and stiffness matrices are printed out.

### EXAMPLE 1:

Consider a clamped-end flexible beam with internal damping. It has been shown in reference 9 that the beam can be discretized as  $n$  equal masses connected in a continuous chain by springs (with the same spring constant) and by dashpots (with equal damping). If no external damping is considered, the equation of motion for the  $i^{\text{th}}$  mass is:

$$\ddot{x}_i(t) = \frac{c}{m} (\dot{x}_{i+1}(t) - 2\dot{x}_i(t) + \dot{x}_{i-1}(t)) + \frac{k}{m} (x_{i+1}(t) - 2x_i(t) + x_{i-1}(t))$$

Assuming four masses along the beam and using the above equation, the matrix equation of motion is

$$\begin{bmatrix} 1 & 0 & 0 & 0 \\ 0 & 1 & 0 & 0 \\ 0 & 0 & 1 & 0 \\ 0 & 0 & 0 & 1 \end{bmatrix} \ddot{\underline{x}}(t) + \frac{g}{m} \begin{bmatrix} 2 & -1 & 0 & 0 \\ -1 & 2 & -1 & 0 \\ 0 & -1 & 2 & -1 \\ 0 & 0 & -1 & 2 \end{bmatrix} \dot{\underline{x}}(t) + \frac{g}{m} \begin{bmatrix} 2 & -1 & 0 & 0 \\ -1 & 2 & -1 & 0 \\ 0 & -1 & 2 & -1 \\ 0 & 0 & -1 & 2 \end{bmatrix} \underline{x}(t) = 0$$

It is desired to find the characteristic polynomial and eigenvalues of the model based on the above matrices. It is also desired to modify the model by adding external damping to the beam (modeled as a dashpot connected to each mass and ground) and find the damping matrix for which the structure becomes overdamped. INTSYD is used for this purpose and the actual listing of the output for this example is as follows:

THIS IS AN INTERACTIVE PROGRAM FOR DESIGNING A LINEARLY DAMPED MULTIDEGREE OF FREEDOM SYSTEM .  
PROGRAM PROVIDES USER WITH NATURAL FREQUENCIES(EIGENVALUES),  
NATURAL MODES (EIGENVECTORS), CHARACTERISTIC POLYNOMIAL,  
STATUS OF SYSTEM AND A PLOT OF MODES .

REQUIRED INPUTS TO THE PROGRAM ARE :

1-DEGREE OF FREEDOM

2-MASS MATRIX

3-DAMPING MATRIX

4-STIFFNESS MATRIX

PLEASE NOTICE THAT ALL THE INPUTS(I.E.MATRICES),MUST ONLY BE SEPERATED WITH A COMMA .

INPUT DEGREE OF FREEDOM (N < 11)

? 4

READ IN MASS MATRIX (SEPERATE SS WITH A COMMA)

? 1,0,0,0,0,1,0,0,0,0,1,0,0,0,0,1

READ IN DAMPING MATRIX

? 2,-1,0,0,-1,2,-1,0,0,-1,2,-1,0,0,-1,2

READ IN STIFFNESS MATRIX

? 2,-1,0,0,-1,2,-1,0,0,-1,2,-1,0,0,-1,2

STATUS OF SYSTEM :

UNDERDAMPED

ENTER M,C,K,CH,EV,EE,POL,CK,R,H,P,TP,AUTO,Q,...OR MENU FOR EXPLANATION

? MENU

\*\* EXPLANATION OF MENU :

CH----GIVES OPTION OF CHANGING [M],[C],[K]

POL----PRINT OUT CHARACTERISTIC POLYNOMIAL

EV----PRINT OUT NATURAL FREQUENCIES(EIGENVALUES)

EE----PRINT OUT NATURAL FREQ. AND NATURAL MODES

CK----DO [C] AND [K] COMMUTE ?

H----WRITE CURRENT INFOR. TO LOCAL FILE "HRDCPY"

M----PRINT OUT MASS MATRIX

C----PRINT OUT DAMPING MATRIX

K----PRINT OUT STIFFNESS MATRIX

R----RETRIVE THE ORIGINAL DATA FROM THE BEGINING OF SESSION

P----PLOT OF MODES

TP----PLOT OF MODES ON TEXTRONIX GRAPHICAL TERMINAL

AUTO--[M],[C],[K] ARE FOUND AUTOMATICALLY FOR DESIRED  
 TYPE OF SYSTEM  
 Q-----QUIT,TERMINATE PROGRAM

ENTER M,C,K,CH,EV,EE,POL,CK,R,H,P,TP,AUTO,Q....OR MENU FOR EXPLANATION  
 ? POL

CHARACTRISTIC POLYNOMIAL OF SYSTEM IS :

.1000000E+01 X\*\* 8+  
 .8000000E+01 X\*\* 7+  
 .2900000E+02 X\*\* 6+  
 .6200000E+02 X\*\* 5+  
 .8600000E+02 X\*\* 4+  
 .8000000E+02 X\*\* 3+  
 .5000000E+02 X\*\* 2+  
 .2000000E+02 X\*\* 1+  
 .5000000E+01

ENTER M,C,K,CH,EV,EE,POL,CK,R,H,P,TP,AUTO,Q....OR MENU FOR EXPLANATION  
 ? EV

\*\*\*\* EIGENVALUES :

REAL	IMAG
-.190983E+00	.587785E+00
-.190983E+00	-.587785E+00
-.690983E+00	.951057E+00
-.690983E+00	-.951057E+00
-.130902E+01	.951057E+00
-.130902E+01	-.951057E+00
-.180902E+01	.587785E+00
-.180902E+01	-.587785E+00

ENTER M,C,K,CH,EV,EE,POL,CK,R,H,P,TP,AUTO,Q....OR MENU FOR EXPLANATION  
 DO YOU WANT TO CHANGE [M] ?Y/N

? N

DO YOU WANT TO CHANGE [C] ?Y/N

? Y

READ IN NEW VALUES OF [C]

? 2.5,-1,0,0,-1,2.5,-1,0,0,-1,2.5,-1,0,0-1,2.5

DO YOU WANT TO CHANGE [K] ?Y/N

? N

STATUS OF SYSTEM :

MIXED DAMPED

ENTER M,C,K,CH,EV,EE,POL,CK,R,H,P,TP,AUTO,Q....OR MENU FOR EXPLANATION

? AUTO

ENTER DESIRED TYPE OF SYSTEM (OVDA,UNDA,CRDA,MXDA)

? OVDA

STATUS OF SYSTEM :

OVERDAMPED

ENTER M,C,K,CH,EV,EE,POL,CK,R,H,P,TP,AUTO,Q....OR MENU FOR EXPLANATION

? C

\*\* DAMPING MATRIX :

5.00	-2.00	0.00	0.00
-2.00	5.00	-2.00	0.00
0.00	-2.00	5.00	-2.00
0.00	0.00	-2.00	5.00

ENTER M,C,K,CH,EV,EE,POL,CK,R,H,P,TP,AUTO,Q....OR MENU FOR EXPLANATION

? Q

.352 CP SECONDS EXECUTION TIME.

## EXAMPLE 2:

Consider an elastic, simply supported, rotatory shaft. The shaft is rotating with a constant angular velocity  $\bar{\xi}$  and is loaded with a constant axial force  $\bar{\eta}$ . The axial coordinate is indicated by  $x$  and  $y_i(x,t)$  ( $i=1,2$ ) denotes the transverse displacements in the principle directions.  $\mu$  denotes the mass per unit length,  $\ell$  the length, and  $s_i=EI_i$  ( $i=1,2$ ) the flexural rigidities in the principle directions.

Assuming both internal ( $\bar{d}_i$ ) and external ( $\bar{d}_e$ ) damping for the shaft, the matrix equation of the motion corresponding to the first two modes is given as:

$$\begin{bmatrix} M & 0 \\ 0 & M \end{bmatrix} \ddot{z} + (d_i + d_e) \begin{bmatrix} M & 0 \\ 0 & M \end{bmatrix} \dot{z} + 2\xi \begin{bmatrix} 0 & -M \\ M & 0 \end{bmatrix} z + \begin{bmatrix} U - \eta E - \xi^2 M & 0 \\ 0 & V - \eta E - \xi^2 M \end{bmatrix} z + d_e \xi \begin{bmatrix} 0 & -M \\ M & 0 \end{bmatrix} z = 0 \quad (17)$$

where

$$M = \frac{1}{\ell^2} \begin{bmatrix} .5 & 0 \\ 0 & .5 \end{bmatrix}$$

$$U = \frac{1}{\ell^2} \begin{bmatrix} .5 & 0 \\ 0 & 8 \end{bmatrix}$$

$$V = \frac{s_1}{s_2 \ell^2} \begin{bmatrix} .5 & 0 \\ 0 & 8 \end{bmatrix}$$

$$E = \frac{1}{\ell^2} \begin{bmatrix} .5 & 0 \\ 0 & 2 \end{bmatrix}$$

$$z = \{z_{11}, z_{12}, z_{21}, z_{22}\}^T$$

$$\xi = \frac{\bar{\xi} \ell^2}{\pi^2} (\mu/s_1)^{1/2}$$

$$\eta = \frac{\bar{\eta} \ell^2}{\pi^2 s_1}$$

$$d_i = \bar{d}_i \frac{\ell^2}{\pi^2} (\mu/s_1)^{1/2}$$

$$d_e = \bar{d}_e \frac{\ell^2}{\pi^2} (\mu/s_1)^{1/2}$$

$z_{ik}$  represents the displacement at mode  $k$  with respect to  $y_i$ . The derivation of the above equation is presented in detail in reference 10.

Assuming  $d_i=.5$ ,  $d_e=.4$ ,  $\eta=.6$ ,  $\xi=.3$ ,  $\ell=1$ , and  $S_1=S_2$  equation (17) can be written as:

$$\begin{bmatrix} .5 & 0 & 0 & 0 \\ 0 & .5 & 0 & 0 \\ 0 & 0 & .5 & 0 \\ 0 & 0 & 0 & .5 \end{bmatrix} \ddot{z} + \begin{bmatrix} .45 & 0 & -.3 & 0 \\ 0 & .45 & 0 & -.3 \\ .3 & 0 & .45 & 0 \\ 0 & .3 & 0 & .45 \end{bmatrix} \dot{z} + \begin{bmatrix} .155 & 0 & -.06 & 0 \\ 0 & 6.755 & 0 & -.06 \\ .06 & 0 & .155 & 0 \\ 0 & .06 & 0 & 6.755 \end{bmatrix} z = 0$$

MUDSYS is used to compute the latent roots, latent vectors, and the characteristic polynomial of the above asymmetric equation. The actual listing of the output is as follows:

**\*\* MASS MATRIX :**

```
.50000E+00  0.          0.          0.
0.          .50000E+00  0.          0.
0.          0.          .50000E+00  0.
0.          0.          0.          .50000E+00
```

**\*\* DAMPING MATRIX :**

```
.45000E+00  0.          -.30000E+00  0.
0.          .45000E+00  0.          -.30000E+00
.30000E+00  0.          .45000E+00  0.
0.          .30000E+00  0.          .45000E+00
```

**\*\* STIFFNESS MATRIX :**

```
.15500E+00  0.          -.60000E-01  0.
0.          .67550E+01  0.          -.60000E-01
.60000E-01  0.          .15500E+00  0.
0.          .60000E-01  0.          .67550E+01
```

CHARACTERISTIC POLYNOMIAL OF SYSTEM IS :

.6250000E-01 X\*\* 8+  
.2250000E+00 X\*\* 7+  
.2076250E+01 X\*\* 6+  
.4945300E+01 X\*\* 5+  
.1740002E+02 X\*\* 4+  
.2452109E+02 X\*\* 3+  
.2168900E+02 X\*\* 2+  
.8177642E+01 X\*\* 1+  
.1260629E+01

---

LATENT ROOTS :

REAL	IMAG
-.291090E+00	.171966E+00
-.291090E+00	-.171966E+00
-.608910E+00	.771966E+00
-.608910E+00	-.771966E+00
-.429510E+00	.336032E+01
-.429510E+00	-.336032E+01
-.470490E+00	.396032E+01
-.470490E+00	-.396032E+01

NOTE: Because of the lengthy output, the latent vectors are not presented here.



## CONCLUSION

Linear damped multidegree of freedom systems were studied by using the matrix differential equation. For systems with symmetric positive definite matrices, previously developed theorems were used to develop an interactive designing routine to design and obtain the important information regarding the system. A second routine for the eigenproblem solution of a general system, where the matrices lack any special properties (i.e., symmetry, positive definiteness, ...), was presented. A clamped-end flexible beam with internal and external damping and an elastic, simply-supported rotatory shaft were used to illustrate the utility of both routines.

## REFERENCES

1. Inman, D.J. and A.N., Jr. Andry, "Some Results on the Nature of Eigenvalues of Discrete Damped Linear Systems", ASME Journal of Applied Mechanics, Vol. 47, 1980, pp. 927-930.
2. Caughey, T.K. and O'Kelly, M.F.J., "Classical Normal Modes in Damped Linear Dynamic Systems", ASME Journal of Applied Mechanics, Vol. 32, 1965, pp. 583-588.
3. Lancaster, P., Lambda-Matrices and Vibrating Systems, 1st Edn., Pergamon Press, 1966, pp. 11-13.
4. Bellman, R., Introduction to Matrix Analysis, 2nd Edn., McGraw Hill, New York, 1970.
5. Bellman, R., "Some Inequalities for the Square Root of a Positive Definite Matrix", Linear Algebra and its Applications, Vol. 1, 1968, pp. 321-324.
6. Ahmadian, M., "A Computer Design Package for Damped Linear Dynamic Systems", Masters Thesis, State University of New York at Buffalo, 1982.
7. Havanessian, S.A. and Pipes, L.A., Digital Computer Methods in Engineering, 1st Edn., McGraw Hill, New York, 1969, pp. 134-140.
8. Shoup, T.E., A Practical Guide to Computer Methods for Engineers, 1st Edn., Prentice-Hall, Inc., New York, 1979, pp. 24-25.
9. Stakgold, I., Boundary Value Problems of Mathematical Physics, Vol. 2, 1st Edn., Macmillan Company, 1967, pp. 264-265.
10. Huseyin, K., Vibrations and Stability of Multiple Parameter Systems, 1st Edn., Noordhoff International Publishing, 1978, pp. 165-168.

## EXTENSIONAL COLLAPSE MODES OF STRUCTURAL MEMBERS

Robert J. Hayduk  
NASA Langley Research Center  
Hampton, Virginia

Tomasz Wierzbicki  
Massachusetts Institute of Technology  
Cambridge, Massachusetts

### SUMMARY

In recent years considerable crash-dynamics research has been devoted to improving passenger survivability in transportation vehicles of all types. One of the objectives of this research is to attenuate the load transmitted to an occupant by the structure, either by modifying structural assembly, changing geometry of its elements, or adding specific load-limiting devices to help dissipate kinetic energy.

General aviation aircraft (both rotary and fixed wing) have fuselage subfloors of a built-up structure which are generally very stiff perpendicular to the floor of the cabin. The subfloor structure, designed to crush at an appropriate force level, can be used to advantage in a crash by dissipating energy through plastic buckling of the floor beams and frames. Simple closed-form solutions to predict the mean crushing-force levels of subfloor designs would be useful in engineering practice. With that objective in mind, the complicated problem of analyzing the crushing process of thin-walled, plate-formed, open structures with particular emphasis on "L" and cruciform shapes has been successfully attacked by using a simple type of analysis.

Lower- and upper-bound solutions for the mean crushing strength of cruciforms have been obtained by considering modes of deformation which account for both bending and extensional deformation. The analysis and experimental data show the importance of extensional deformation to the energy absorption process, representing at least one-third of the dissipated energy.

### INTRODUCTION

In recent years considerable crash-dynamics research has been devoted to transportation vehicles of all types with the objective of improving passenger survivability. It is generally understood that in a crash environment an occupant should be maintained in a livable, unintruding volume, be well restrained, and not be subjected to intolerable acceleration levels. The vehicle structure, seat, and restraint system should act together as a protective system for the occupants.

Crash-dynamics research at the NASA Langley Research Center (ref. 1) focused on general aviation aircraft during the period from 1973 to 1982. This effort has been concerned primarily with determining vehicle crash loads, identifying structural failure modes during crashes, evaluating restraint system/seat performance, and assessing loads imposed on anthropomorphic dummy passengers for potentially

survivable crashes. The development of structural concepts to reduce the load transmitted to the occupant in a crash is an important aspect of this research program. (See ref. 2.) The objective of the research program is to attenuate the load transmitted by a structure by modifying structural assembly, changing geometry of its elements, or adding specific load-limiting devices to help dissipate kinetic energy.

General aviation aircraft (both rotary and fixed-wing) have fuselage subfloors of built-up structure which are generally very stiff perpendicular to the floor of the cabin. A typical subfloor has intersecting floor beams and frames which form cruciform elements. The "L", "T", and "Z" structural elements are also common in aircraft construction. These elements are not simple structures because there is generally reinforcement at joint intersections, as well as discontinuous connections, that is, rivets. The subfloor structure, designed to crush at an appropriate force level, can be used to advantage in a crash by dissipating energy through plastic buckling of the floor beams (frames) through local bending and extensional deformation.

The objective of the present work is to describe the crushing process of a class of thin-walled open structures, with particular emphasis on angle shapes ("L") and cruciforms. Simple expressions will be derived for the mean crushing force and for the local buckling wavelength; and comparisons will be made with experiments on thin copper specimens of various flange widths and heights. The problem of local plastic collapse of angle elements will first be reexamined in this paper. A cruciform may be regarded as two angles joined together along the vertical edge. Because of additional geometrical constraints on the deformation field imposed by the joint, the collapse mechanisms of a cruciform differ substantially from that observed in angles. It necessarily involves much more in-plane extension leading to increased strength and energy dissipation.

The problem of elastic buckling of short angles and cruciforms is extensively covered in the classical treatise by Timoshenko and Gere in reference 3. The bifurcation and maximum loads of cruciform columns undergoing torsional buckling in the plastic range were determined by Hutchinson and Budiansky in reference 4. The same problem was discussed more recently by Needleman and Tvergaard in references 5 and 6. Their solutions apply to slender columns for which the reciprocal of the square of the slenderness ratio is small compared to unity. The cruciforms studied here have slenderness ratios that are not small, and the higher-order slenderness-ratio terms cannot be neglected.

An exhaustive theoretical study of the maximum strength of cruciform columns, in which shear, compression, and bending deformations of flanges were taken into account, was conducted by Stowell in reference 7. Good correlation of the theoretical predictions with experimental data for 24S-T4 aluminum alloy cruciforms and "H" section columns was reported. Empirical formulas for the maximum strength of flanges with various end conditions were developed independently by Gerard in reference 8. The maximum strength of thin plates in compression can also be predicted in an approximate way by the so-called "effective width" theory of Von Kármán, et al., in reference 9.

The problem of crushing of metal columns with closed cross sections of rectangular, square, or hat-shaped configurations has received considerable attention. The progressive crushing of "L" shapes and cruciforms appears not to have been studied in the literature except for reference 10 in which some aspects of the optimum design of progressively crushing angle elements were discussed. Most authors have used an empirical or semiempirical approach for the determination of the maximum strength and

mean crushing force (refs. 10, 11, and 12) of thin-walled columns. In a recent paper Wierzbicki and Abramowicz (ref. 13) developed a self-consistent theory describing the local crush response of thin-walled structures. In the present paper this theory is further extended to include additional in-plane deformation in the localized zones of plastic deformations.

#### SYMBOLS

$A_1, A_2, A_3, A_4$	constant coefficients
$C$	flange width
$E_1$	energy dissipation of a continuous deformation field in the section of a toroidal shell
$E_2$	energy dissipation of the discontinuous velocity field in the horizontal hinge line
$E_3$	work done by an inclined hinge line through the deformation process
$E_4$	energy dissipation of extensional deformation in the trapezoidal region
$E_5$	energy dissipation along a stationary horizontal hinge line (same as $E_2$ )
$E_6$	plastic work in the inclined stationary plastic hinge
$H$	mode half-wavelength
$h$	flange thickness
$j, k, l$	extensional deformation region end-point identifiers
$L$	length of the thin-walled structure
"L", "H", "T", "Z"	cross-sectional shapes of structural members
$\ell$	length of the inclined stationary plastic hinge
$M_0 = \sigma_0 h^2 / 4$	fully plastic yield moment
$P$	load
$P_c$	critical load
$P_m$	mean crushing load
$P_{max}$	maximum load
$R_1, R_2$	principal curvatures of a shell
$r$	radius of the toroidal surface
$u_y$	displacement component in y-coordinate direction

$v_y$	velocity component in y-coordinate direction
$V$	magnitude of the velocity field in the deforming region
$x, y, z$	right-handed Cartesian coordinate system
$\alpha$	angle defining current mode geometry
$\beta$	angle formed by intersecting plates
$\gamma$	angle defining deformation process
$\delta$	end displacement
$\dot{\epsilon}_y, \dot{\epsilon}_{yz}$	nonvanishing components of the strain-rate tensor
$\sigma_0$	flow stress; taken as $0.7\sigma_u$
$\sigma_u$	ultimate strength
$\psi$	angle formed by intersection plates

#### COLLAPSE MODES

The present paper is concerned with the deformation process of thin-walled structures in which deflections exceed 100 to 1000 times the wall thickness and become comparable to the linear dimension of the structure. A typical load-deflection curve for a thin-walled structure in compression is shown in figure 1. The thin-gage compression member loses stability in the elastic or plastic range at a critical load  $P_c$ . In the post-buckling stage the flanges can usually carry additional loads until the maximum strength is reached at a load  $P_{max}$ . Then, the resistance of the member diminishes rapidly as the local collapse mode develops. An interaction between this local mode and an Euler (global) buckling mode accelerates the failure of the structure. However, for short structures, which are of interest here, the member often regains its strength after an initial dramatic drop in the resisting force. Additional load peaks signal the formation of the second and subsequent folds. (See fig. 1.) On continuing the crushing process, a quite complicated pattern is formed as the member is fully compressed. (See fig. 2.) The mean crushing force  $P_m$  is also shown in figure 1. This mean force is determined by measuring the area under the load-deflection curve and dividing by the maximum displacement considered.

#### Isometric Transformation Modes

A distinctive feature of isometric transformation modes (inextensional deformation) is that the strain energy function (in the case of elastic shells) or the dissipation function (in the case of plastic shells) is concentrated over narrow zones called fold lines or hinge lines while the remainder of the structure undergoes a rigid body motion. The area of these zones is small compared with the total area of the structure. It can be shown that a sheet of paper or thin metal foil can be easily bent, but not so easily stretched, in either direction. To activate extensional deformations a considerable amount of energy and a sufficiently high force

level are required. Thus, it would be expected that the folds and wrinkles in a crushing structure be formed predominantly by bending with as little extension as necessary to ensure material continuity. Physically, this means that the structure tends to assume an inextensible deformation mode. Mathematically, the transformation of two surfaces, which preserves the lengths of corresponding arc elements (inextensional deformation), is called an isometric transformation. Most crushing deformations are quasi-isometric since some extension is always inevitable.

A necessary condition for a transformation to be isometric is that the Gaussian curvatures of both surfaces be the same. The Gaussian curvature  $K$  is a product of two principal curvatures of the shell,  $1/R_1$  and  $1/R_2$ , at any point. Thus,

$$K = \frac{1}{R_1} \frac{1}{R_2} \quad (1)$$

An example of an isometric transformation is a cylinder transformed into another cylinder (with a smaller, larger, negative radius) or into a flat plate. Another example is that a transformation which interchanges curvatures as seen in equation (1) (the first nonvanishing principal curvature becomes the second  $\frac{1}{R_1} = 0$ ,  $\frac{1}{R_2} \neq 0$ ) is isometric. (See fig. 3.) The foundations of the mathematical theory of isometric transformations were laid by Pogorelov in reference 14. His work was recently followed by Lukasiewicz and Szyszkowski in reference 15. A parallel but independent study of the compression of thin elastic shells was made by Foster in reference 16.

The isometric transformation is a local property of the surface and does not impose boundary conditions. However, the mathematical theory does not state how one surface transforms into the other; it simply states conditions about the initial and final states. In mechanics, however, the energy dissipated is a function of the deformation path between the initial and final states. There may be many alternative paths to reach the same final state, some isometric, others not.

Illustrations are provided in figure 4 of inextensional and extensional deformation paths from an initial to a final state. In figure 4(a) the initially flat element is folded inextensionally along the stationary hinge line AB to arrive at a final state. The same final state is achieved in figure 4(b) by first folding along hinge line AB and then simultaneously folding about hinge lines AB and AC. Again, the deformations are inextensional. In general, the inextensional collapse mode of thin-walled flat plates or panels involving folding along stationary hinge lines can be formed only if the boundaries have sufficient freedom to deform. An illustration of an extensible deformation path is shown in figure 4(c) where the element is first folded inextensionally along the stationary hinge line AB and then the panels are rotated extensibly to obtain the final state.

Isometric failure modes of thin-walled structures formed by folding along stationary straight hinge lines were studied in references 17 and 18. These modes can be easily visualized by means of models made of construction paper. Certain constraints imposed in the deformation process, for example, by restricting the motion of a part of the boundary, preclude in general the existence of these simple collapse modes. Because of limited applicability, these simple collapse modes will not be considered in this paper.

## Hinge Collapse Modes

Consider a system of two plates joined at a vertical edge and forming a short angle column. The column is placed between two rigid plattens and is subjected to compressive loading. The geometrical constraints are imposed by the condition of continuity of displacements at the joint and the requirements that the horizontal edges remain in contact with the plattens and that the angle between edges is kept constant.

With increasing end shortening, the initially vertical flange intersection becomes more and more inclined until it assumes a horizontal position and the angle element is completely flattened out. (See fig. 2(c).) The deformation of the flange may follow different paths depending upon whether the line of slope discontinuity is a material line or a propagating plastic hinge.

Propagating hinge line (Mode I).— If the hinge line is allowed to move with respect to material points, then effectively a part of the material from one flange continuously passes to the adjacent flange and a shape distortion is produced which apparently does not require any in-plane extension in the flanges. However, the condition of kinematical continuity in the propagating hinge line requires that some form of extensional deformation be produced in the vicinity of the hinge line, as discussed in reference 13. This mode of deformation, where extension is limited to the neighborhood of the hinge line, will be referred to as Mode I. This mode is observed in all crushed thin-walled structures consisting of two intersecting plates, such as box beams and columns, and channel and "L" sections subjected to bending or compression.

Stationary hinge line (Mode II).— Suppose now that the hinge line is fixed in the material. Then, both side flanges of an initially rectangular shape are transformed into trapezoidal elements. Evidently, there must be considerable in-plane extension in one flange and likewise in-plane compression in the other flange to accommodate such large shape distortion. This mode of deformation in which extension occurs over an entire flange will be called Mode II. A modification of this mode, shown in figure 4(c), involves extension in both flanges.

## Assembled Collapse Modes

A method of assembling the folding patterns shown in figure 4 into more complicated symmetric, asymmetric, and mixed collapse modes is shown in figure 5. A question arises into which of the modes the compressed shell will actually collapse. This depends to a large extent on the boundary and symmetry conditions of a given structure and on additional geometric constraints, if any. A triggering of a particular mode in the structure may also depend on the shape of an initial elastic buckling mode and on initial imperfection. In the later stages of the crushing process, the modes are more likely to persist which minimize the plastic energy dissipation. This problem has been extensively discussed in reference 19. Of particular interest here are the modes shown in figures 5(a) and 5(b), because they are observed in many crushed thin-walled structures. The definition of geometrical parameters involved in these modes is given in figure 6. The initial geometry of either of the modes is defined by the half-wavelength  $H$ , width of each flange  $C$ , and an angle  $\psi$  formed by intersecting plates. The current geometry is described either by the angle  $\alpha$  or the end displacement

$$\delta = 2H(1 - \cos \alpha) \quad (2)$$

## ANALYSIS

### Theoretical Crushing Strength of Angle Elements

Extensional collapse mode with a propagating hinge line (Mode I).— Consider an idealized structure made of a rigid perfectly plastic material collapsing in Mode I. The theory of perfectly plastic solids states that there may be a jump in the displacement gradients only across stationary hinge lines. Such discontinuities are inadmissible across propagating hinge lines. Consequently, the displacement field should be described by a continuous and smooth function. When referring to figure 6 this means that a straight hinge line should be replaced by a single curvature surface. At the same time a double-curvature surface should be introduced in the small neighborhood of the corner point. (See point B in fig. 6.) It is this small area where all extensional deformations are now concentrated. (See fig. 7.) This approach has been extensively discussed in reference 13 where the concept of a basic folding mechanism was first introduced.

The collapse mode (fig. 7), which is consistent geometrically (displacement field) and kinematically (velocity field), consists of the following:

- (I) Four plane trapezoidal elements moving as rigid bodies
- (II) Two sections of cylindrical surfaces at which continuous bending takes place without any extension
- (III) Two sections of conical surfaces in which material is bent and rebent again as the material moves from one flange to the other
- (IV) A section of a toroidal surface which produces extension in a circumferential direction and continuously changes principal curvature in the other direction (from positive to a larger negative curvature)

Calculations based on an energy-balance postulate, presented in reference 13, show that the zones of extensional deformations are, indeed, restricted to a small fraction of the total area of the structure but dissipate as much as one-third of the total work done by the applied load during the crushing deformation mode. The remaining two-thirds of the energy dissipation is concentrated in equal proportions in inextensional deformations at stationary and moving hinge lines.

Experiments show that short angle elements subjected to compressive loading usually collapse in an asymmetric mode. Therefore, the foregoing analysis of Mode I deformation can be directly applied to find a mean crushing strength  $P_m$  of "L"-shaped angle elements. By omitting the details of the calculations, which are presented in reference 13, only the final results are presented here.

The energy of a continuous deformation field in the section of a toroidal shell, which is dissipated on complete folding of the wall through the angle  $\pi/2$ , is given as

$$E_1 = 9.28 M_o \frac{Hr}{h} \quad (3a)$$



The internal energy dissipated by the discontinuous velocity field in the horizontal hinge line of length  $C$  is

$$E_2 = \frac{\pi}{2} M_O C \quad (3b)$$

where  $r$  is the small radius of the toroidal surface and  $M_O = \sigma_O h^2/4$  is the fully plastic yield moment.

The work done by an inclined hinge line through the deformation process is

$$E_3 = 2.22 M_O \frac{H^2}{r} \quad (3c)$$

In the basic folding mechanism there are eight horizontal hinge lines, two inclined hinge lines, and one toroidal shell section. The mean crushing strength of the member is, therefore, defined by the energy balance equation

$$2HP_m = E_1 + 8E_2 + 2E_3 \quad (4)$$

The deformation  $\delta$  from equation (2) is taken to be the complete folding of a local collapse mode of wavelength  $2H$ . By using equation (3), equation (4) becomes

$$\frac{P_m}{M_O} = A_1 \frac{r}{h} + A_2 \frac{C}{H} + A_3 \frac{H}{r} \quad (5)$$

where the numerical values for the coefficients are

$$A_1 = 4.64$$

$$A_2 = 2\pi$$

$$A_3 = 2.22$$

The first term in equation (5) represents the contribution of extensional deformation, in the section of a toroidal shell. The second term results from the bending about horizontal hinge lines, whereas the last term describes the energy of bending and rebending along the inclined plastic hinges of region III. (See fig. 7.)

Equation (5) can be optimized with respect to the unknown local radius  $r$  and the half-wavelength  $H$ . Thus,

$$\frac{\partial P_m}{\partial r} = \frac{\partial P_m}{\partial H} = 0 \quad (6)$$

The optimized values of  $H$  and  $r$  are

$$r = \sqrt[3]{A_2 A_3 / A_1^2} \sqrt[3]{C h^2} \quad (7a)$$

$$H = \sqrt[3]{A_2^2 / A_1 A_3} \sqrt[3]{C^2 h} \quad (7b)$$

Substituting equations (7a) and (7b) back into equation (5) gives the general expression for the mean crushing force:

$$\frac{P_m}{M_0} = 3 \sqrt[3]{A_1 A_2 A_3} \sqrt[3]{C/h} \quad (8)$$

Regardless of the numerical values of the coefficients  $A_1, A_2, A_3$ , the three basic mechanisms of energy dissipation appear equally weighted in the final equation for the mean crushing force. Introducing the numerical values of  $A_1, A_2$ , and  $A_3$  for an "L"-shaped column into equation (8) yields the theoretical crushing strength given by the simple formula

$$\frac{P_m}{M_0} = 12.04 \sqrt[3]{C/h} \quad (9)$$

Short-angle columns fold up and fail almost always in an antisymmetric mode unless very large initial imperfections are introduced in the shape of the symmetric modes. As shown in reference 20, the symmetric mode leads to an instantaneous and mean crushing force which is two to three times greater than the asymmetric mean crushing force. The structure assumes the configuration with the least resistance, and an asymmetric mode constitutes such a configuration.

Extensional collapse mode with a stationary hinge line (Mode II).— Consider next the Mode II (fig. 6) deformation discussed previously. The energy is dissipated through plastic bending of adjacent panels about horizontal hinge lines and through the shape distortion of each of four panels. (See fig. 6.)

Consider a current deformation state of a single trapezoidal element which originally was of a rectangular shape. (See fig. 8.) Assume that there is only one component of the displacement vector  $(0, u_y, 0)$  and that the plastic deformations are confined to the curvilinear triangle denoted by  $jkl$ . The shape of the boundary between the deforming and rigid region is an arbitrary function of the  $z$ -coordinate. By assuming a linear variation of the velocity field in the  $y$ -direction,

$$v_y(y, z) = -v \frac{z}{H} \left[ 1 - \frac{y}{g(z)} \right] \quad (10)$$

The nonvanishing components of the strain-rate tensor are

$$\left. \begin{aligned} \dot{\epsilon}_y &= \frac{V}{H} \frac{z}{g(z)} \\ \dot{\epsilon}_{yz} &= V \frac{y}{H} \frac{d}{dz} \left[ \frac{z}{g(z)} \right] - \frac{V}{H} \end{aligned} \right\} \quad (11)$$

where

$$V = \frac{H}{\sin^2 \gamma} \dot{\gamma}$$

The rate of energy dissipation can be expressed as

$$\dot{E}_4 = h \int_0^H \left[ \int_0^{g(z)} (\dot{\epsilon}_y \sigma_y + \dot{\epsilon}_{yz} \sigma_{yz}) dy \right] dz \quad (12)$$

By neglecting the energy dissipation due to the shear strain rate  $\dot{\epsilon}_{yz}$ , equation (12) reduces to

$$\dot{E}_4 = \sigma_o h \int_0^H \left( \int_0^{g(z)} \dot{\epsilon}_y dy \right) dz \quad (13)$$

Substituting equation (11) into equation (13) and performing the integration gives

$$\dot{E}_4 = \frac{1}{2} \sigma_o V H h = 2M_o V \frac{H}{h} \quad (14)$$

The result is seen to be independent of the extent of plastic zones since the function  $g(z)$  drops out during the integration.

The angle  $\gamma$  in the expression for velocities varies from  $\pi/2$  at the beginning of the deformation process to  $\pi/4$  at the end. Substituting for  $V$  from equation (11) into equation (14) and integrating with respect to  $\gamma$  from  $\pi/2$  to  $\pi/4$  yields the final expression for the plastic work on the continuous deformation field

$$E_4 = 2M_o \frac{H^2}{h} \int_{\pi/2}^{\pi/4} \frac{d\gamma}{\sin^2 \gamma} = 2M_o \frac{H^2}{h} \quad (15)$$

The rate of energy dissipation along the stationary horizontal hinge line of length  $C$  is calculated as before to give

$$\left. \begin{aligned} \dot{E}_5 &= M_O C \dot{\alpha} \\ E_5 &= M_O C \int_0^{\pi/2} d\alpha = \frac{\pi}{2} M_O C \end{aligned} \right\} \quad (16)$$

Finally, the rate of plastic work in the inclined stationary plastic hinge is

$$\dot{E}_6 = M_O \ell \dot{\beta} \quad (17)$$

where  $\ell$  is the length of the hinge and is given as

$$\ell = \frac{H}{\sin \gamma} \quad (18)$$

and  $\beta$  denotes the angle formed by the intersecting plates and is related to  $\alpha$  by

$$\cos \beta = -\sin^2 \alpha \quad (19)$$

The exact integration of equation (17) can be performed over the whole deformation process ( $0 \leq \alpha \leq \pi/2$  in fig. 6) and the result is

$$E_6 = 2M_O H \quad (20)$$

#### Theoretical Crushing Strength of a Cruciform

Consider a cruciform in which four flanges are rigidly joined along the initially vertical edge. It has been demonstrated by tests that the local kinematics of the crushing process is quite complicated. However, a few relatively simple mechanisms can be identified, which incorporate basic deformation modes, as discussed earlier.

Mode II/Mode II.— It is advantageous to think of a cruciform as being made of two angle elements. These elements should deform in such a way that the joint line is not separated. This can be accomplished by assuming that the two angles deform in the Mode II pattern. The joint line, which is an inclined hinge line fixed in the material, stays in the plane of symmetry and is inclined by  $45^\circ$  to the neighboring flanges. It is postulated that the rate of external work is equal to the total energy required to make a complete single fold of length  $2H$ . That is,

$$2HP_m = 8E_4 + 16E_5 + 4E_6 \quad (21)$$

Substituting equations (15) to (20) into equation (21) produces

$$\frac{P_m}{M_o} = 8 \frac{H}{h} + 4\pi \frac{C}{H} + 4 \quad (22)$$

The right-hand side of equation (22) can be optimized with respect to the wavelength  $H$ . The minimum exists at

$$H = \sqrt{\frac{\pi}{2}} Ch \quad (23)$$

and equation (22) becomes

$$\frac{P_m}{M_o} = 8\sqrt{2\pi} \sqrt{\frac{C}{h}} + 4 \quad (24)$$

The constant term in equation (22) is small compared with the leading term and can be neglected without loss of accuracy. The crushing strength of a cruciform column then becomes

$$\frac{P_m}{M_o} = 20.05 \sqrt{\frac{C}{h}} \quad (\text{Upper bound}) \quad (25)$$

Note that the contributions of in-plane deformations and discontinuous bending along horizontal hinge lines are the same. (See eqs. (22) and (24).) Also, the energy dissipated at the inclined hinge lines is negligible for sufficiently large  $C/h$ . In most of the experiments on cruciforms the ratio  $C/h$  was 143.

The present solution has been obtained on the assumption that the material in four trapezoidal panels was subjected to the uniaxial extensions, whereas in the remaining four panels a state of uniaxial compression prevailed.

The width-to-thickness ratio of the small trapezoidal panels, calculated from equation (23), is of the order of  $H/h = 15$ . It is very likely that such moderately thin plates will lose stability prior to developing their full compressive strength with uniform compressive stress. Consequently, the prediction of the formula in equation (25) should be regarded as an upper bound in the compressive strength of cruciforms.

Mode I/Mode I.— A lower bound on  $P_m/M_o$  can also be given by noting that a continuous joint along the vertical edge of a cruciform increases the column strength as compared to a column composed of two unjoined angles. The crushing strength of the cruciform can, thus, be bounded from below by doubling the result of equation (9) for an assemblage of two single "L"-shaped columns

$$\frac{P_m}{M_o} = 24.08 \sqrt[3]{C/h} \quad (\text{Lower bound}) \quad (26)$$

Mode I/Mode II.— A careful inspection of several crushed cruciforms revealed that the actual collapse mechanism is a combination of the two basic deformation modes, Mode I and Mode II. However, a modified Mode II shown in figure 5(b) should now be used. This would involve extensional deformation only. A model of such a combined mode made of the construction paper is shown in figure 9. The mean crushing force is defined, as before, by the energy balance postulate

$$2HP_m = E_1 + 8E_2 + 2E_3 + 4E_4 + 8E_5 + 2E_6 \quad (27)$$

where the first three terms represent the energies dissipated in the Mode I and the last three terms represent the energies dissipated in Mode II. A substitution of the previously derived expressions for energies  $E_1$  through  $E_6$  into equation (27) yields

$$\frac{P_m}{M_O} = A_1 \frac{r}{h} + A_2 \frac{C}{H} + A_3 \frac{H}{r} + A_4 \frac{H}{h} + 2 \quad (28)$$

where

$$\left. \begin{aligned} A_1 &= 4.64 \\ A_2 &= 12.56 \\ A_3 &= 2.22 \\ A_4 &= 4 \end{aligned} \right\} \quad (29)$$

The right-hand side of equation (28) is subjected to the optimization with respect to two free parameters  $r$  and  $H$ . The condition for a minimum gives rise to the following fourth-order algebraic equations for the nondimensional wavelength  $H/h$  and radius  $r/h$ :

$$\frac{H}{h} = \frac{A_1}{A_3} \left( \frac{r}{h} \right)^2 \quad (30)$$

$$\left( \frac{r}{h} \right)^3 \left[ 1 + \left( \frac{r}{h} \right) \frac{A_4}{A_3} \right] = \frac{A_2 A_3}{A_1^2} \left( \frac{C}{h} \right) \quad (31)$$

A numerical solution for  $r/h$  as a function of  $C/h$  is shown in figure 10 by the dashed line. In particular, for  $C/h = 143$ ,  $X_O = r/h = 3.06$ . The objective is to find a closed-form solution for  $r/h$ ,  $H/h$ , and  $P_m/M_O$ . Note that equation (31) can be solved by means of the method of successive approximation:

$$\left(\frac{r}{h}\right)_n = \left(\frac{A_2 A_3}{A_1^2} \frac{C}{h}\right)^{1/3} \left[1 + \left(\frac{r}{h}\right)_{n-1} \frac{A_4}{A_3}\right]^{-1/3} \quad (32)$$

A sufficient accuracy is obtained by taking just the first iteration, i.e., by substituting  $\frac{r}{h} = x_0$  into equation (32). (See the solid line in fig. 10.) By substituting the approximate solution for the free parameters into equation (28), a general solution for the dimensionless crushing force is

$$\frac{P_m}{M_0} = 3 \sqrt[3]{\frac{A_2 A_3}{A_1 A_2 A_3}} \sqrt[3]{\frac{C}{h}} \frac{1 + \frac{x_0}{3} \frac{A_4}{A_3}}{\sqrt[3]{1 + x_0 \frac{A_4}{A_3}}} + \sqrt[3]{\frac{A_2^2}{A_1 A_3}} \sqrt[3]{\left(\frac{C}{h}\right)^2} \frac{A_4}{\sqrt[3]{\left(1 + x_0 \frac{A_4}{A_3}\right)^2}} + 2 \quad (33)$$

Except for the small constant last term, the above expression reduces to equation (8) in the limiting case of  $A_4 \rightarrow 0$ . By using equation (29) and neglecting the constant term in equation (33), the final formula for the crushing strength of a cruciform becomes

$$\frac{P_m}{M_0} = 22.96 \sqrt[3]{\frac{C}{h}} + 2.88 \sqrt[3]{\left(\frac{C}{h}\right)^2} \quad (34)$$

#### DESCRIPTION OF TESTS AND ANALYSIS OF DATA

Aluminum was the preferred specimen material, because an aircraft structure is usually made of that material. However, cruciforms with continuous joints were desired as well for simplification of analysis. To produce continuous joints on aluminum specimens, a number of bonding materials were tried unsuccessfully, as well as continuous spot welding. However, thin copper sheet joined by soldering satisfactorily met the requirements.

A copper sheet of 0.014-in. thickness was first fully annealed and cut in strips of width  $L$  plus 0.5 in., such that the grain would be parallel to the direction of loading in the finished specimen. Strips of length  $2C$  were next bent to form  $90^\circ$  equal-leg "L"s. To form a cruciform two "L"s were butted along the bend line and soldered with common 60-40 lead-tin solder. An uncrushed cruciform specimen is shown in figure 2 along with a crushed specimen and the test clamping fixture.

The 4-in.-square fixtures were designed to provide clamping of 1/4-in. of the flanges on both ends. This is the reason for the additional 1/2-in. of strip width. The clamping fixtures were aligned parallel prior to testing. The test specimens with parallel clamping fixtures were placed between the table and head of the Baldwin Southwark Tate-Emery Testing Machine. Double-backed tape was used between the clamping fixtures and the testing machine to reduce the tendency of the specimen to twist during loading. The Baldwin Testing Machine has loading ranges of 120,000 lb,

24,000 lb, and 6000 lb. A loading rate of approximately 1/2-in. per minute of head movement was used. This was slow enough to be considered quasi-static for all practical purposes. These data are shown in table I. For the majority of the specimens the maximum displacement considered in computing the mean crush force represents 40 to 60 percent crushing of the original length. Several of the test specimens of table I were crushed to only 30 to 35 percent of the original length. There are several reasons for the variation in degree of specimen crushing. When joint separation was judged to be excessive and/or the flanges began to pull out of the fixtures, the test was terminated. These occurrences varied from specimen to specimen, giving rise to a range of acceptable maximum crushing displacements.

Specimen length  $L$  varied from 2.0 to 4.0 in. with the preponderance of specimens being 4.0 in. Flange widths of 1.0, 1.25, 1.5, and 2.0 in. were tried. For the series of tests reported here the ratio  $L/C$  of specimen length to flange width varied from 1.0 to 4.0, and the ratio  $C/h$  of flange width to thickness varied from 71 to 143.

For the simplified analysis of these cruciform specimens, only the value of the fully plastic yield moment,  $M_O = \sigma_O h^2/4$ , is needed with the flow stress  $\sigma_O$  taken to be 0.7 times the ultimate stress  $\sigma_u$  of the material. For the fully annealed copper used to make these specimens,

$$\left. \begin{aligned} \sigma_u &= 27,400 \text{ lb/in.}^2 \\ \sigma_O &= 0.7\sigma_u \\ &= 19,180 \text{ lb/in.}^2 \\ M_O &= \frac{1}{4} \sigma_O h^2 \\ &= 0.940 \text{ lb} \end{aligned} \right\} \quad (35)$$

for  $h = 0.014$  in. Thus, the nondimensional mean crushing force  $P_m/M_O$  is given in table I.

#### DISCUSSION

The lower- and upper-bound solution for the mean crushing strength of cruciforms is plotted against the width-to-thickness ratio of a flange in figure 11. The experimental points for joined cruciforms are shown by circles. A considerable scatter of experimental points indicates that there are many collapse mechanisms in which the cruciforms fail and that the collapse is imperfection sensitive. This is in sharp contrast with the crushing behavior of rectangular box column and hexagonal cell structures where the magnitude of the crushing strength was well reproducible for all values of  $C/h$ .

However, all joined-cruciform test points fell within the region bounded from above by equation (25) and from below by equation (26). The curve representing the mixed-mode formula (eq. (34)) passes between the two bounding curves and approximates



the trend of experimental points better. This solution seems to lead to the best prediction of the strength of cruciforms with the present understanding of the crushing phenomenon and with the simple energy approach to the problem.

The quantitative correlation between the theory and experiments is not good because of several difficulties encountered in trying to satisfy experimentally all of the assumptions used in the theoretical analysis. The main difficulties are as follows:

(1) The force deflection of the 2-in.-high cruciform columns used in the experiments exhibited only two to three peaks. The first peak, corresponding to the initial strength of the member, is much higher than the following ones. The presence of this peak increases the experimental mean crushing force. This effect is not taken into account by the theory.

(2) In most test specimens the joint failed locally at some stage of the crushing process. Clearly, this weakens the cruciform and diminishes the average crushing strength measured in experiments. Thinner gage sheets could be used to eliminate this problem.

(3) The free edges of the flanges do not deform in a plane of symmetry, as assumed in the theory. Instead, noticeable in-plane displacements  $u_y$  were found in all tested cruciforms which clearly reduces the energy  $E_4$  of extensional deformation. The displacements  $u_y$  in the plane of symmetry vanish only for cruciforms arranged in a cellular structure. Besides, there are certain members of "T" and "L"-shaped columns in the boundary cells. Consequently, it is not possible to determine the strength of a single cruciform in the experiment performed on the cellular structure. Also, the structure manages somehow to minimize the amount of in-plane extensions by breaking the joint and by pulling the material from the edges.

(4) It was observed that the local folding modes interact with the "global" mode with fewer waves seen in the free edge. The lines of interaction between these "local" and "global" modes form the stationary or moving plastic hinges which contribute to the overall energy dissipation. No consideration to this complicated interaction was given in the present theory.

(5) The work-hardening properties of the material are accounted for in our calculation by raising the average flow stress to the value  $\sigma_0 = 0.7\sigma_u$ . However, the work hardening also changes the details of the kinematics of the problem. For example, the slope discontinuities at stationary plastic hinges are rounded to a finite radius so that a double-curvature shell is formed locally around the corner point B. (See fig. 6.) Consequently, some additional extensional deformation must be produced and the crushing force may increase even slightly above that predicted by equation (25).

The experimental points for "L" columns, denoted by triangles, are seen to fall considerably below the curve representing the theoretical solution. This discrepancy is largely due to the interaction of the global elastic buckling mode with the local plastic failure mode which eventually changes the plastic collapse mode to the one giving a lower crushing force. Several experiments were performed with cruciforms consisting of unjoined angle elements. When loaded in the testing machine, there was little interaction between the angles (separation occurred almost immediately) and the mean crushing force was simply the same as doubling that of a single angle element.

## CONCLUDING REMARKS

The subfloor structure of general aviation aircraft can be used to advantage in a crash by absorbing energy through local plastic buckling with bending and extensional deformation. In order to use this advantage the structural designer must design the subfloor to crush at an appropriate force level. Simple closed-form solutions to predict the mean crushing force levels of subfloor designs would be useful in engineering practice. To this end, the very complicated problem in mechanics of analyzing the crushing process of a class of thin-walled open structures with particular emphasis on "L"-shaped and cruciform cross sections has been successfully studied by using a simple type of analysis.

Lower- and upper-bound solutions for the mean crushing strength of cruciforms have been obtained by considering modes of deformation which account for both bending and extensional deformation. The analyses and experimental data show the importance of extensional deformations to the energy-absorption process, representing at least one-third of the dissipated energy.

Experimental data for joined cruciforms reveal considerable scatter, indicating that there are many collapse mechanisms in which the cruciforms fail and that the collapse is imperfection sensitive. However, all joined-cruciform data points fell within the region bounded by the analytical solutions. A mixed-mode solution, which falls between the bounding solutions, yields the best prediction to the strength of cruciforms with the present understanding of the crushing phenomenon and with the simple energy approach used.

These results represent a starting point in the analysis and optimum design of riveted cruciforms and other more complicated structural elements.

## ACKNOWLEDGEMENT

The present work was completed while Tomasz Wierzbicki was a Visiting Professor in the Department of Civil Engineering at Duke University (Fall 1981) and in the Department of Ocean Engineering of the Massachusetts Institute of Technology (Spring 1982). The financial support of both Departments is gratefully acknowledged.

# REFERENCES

1. Hayduk, Robert J.; Thomson, Robert G.; and Carden, Huey D.: "NASA/FAA General Aviation Crash Dynamics Program - An Update," Forum, Vol. 12, No. 3, Winter 1979, pp. 147-156.
2. Carden, Huey D.; and Hayduk, Robert J.: Aircraft Subfloor Response to Crash Loadings. Business Aircraft Meeting and Exposition, Wichita, Kansas, April 7-10, 1981, SAE Paper 810614.
3. Timoshenko, S. P.; and Gere, J. M.: Theory of Elastic Stability, McGraw-Hill Book Company, 1961.
4. Hutchinson, J. W.; and Budiansky, B.: Analytical and Numerical Study of the Effects of Initial Imperfections on the Inelastic Buckling of a Cruciform Column, Buckling of Structures (Editor B. Budiansky), Springer-Verlag, Berlin, 1976, pp. 98-105.
5. Needleman, A.; and Tvergaard, V.: Aspects of Plastic Postbuckling Behavior. Mechanics of Solids, The Rodney Hill 60th Anniversary Volume (Edited by H. G. Hopkins and M. J. Sewell), Pergamon Press, Oxford, 1981.
6. Tvergaard, V.; and Needleman, A.: On the Foundation of Plastic Buckling. Developments in Thin-Walled Structures (Edited by J. Rhodes and A. C. Walker), Applied Science Publishers, 1981.
7. Stowell, E. Z.: Compressive Strength of Flanges. NACA Rep. 1029, 1951.
8. Gerard, G.: The Crippling Strength of Compression Elements. J. Aeronautical Sciences, Vol. 25, January 1958, No. 1, pp. 37-52.
9. Von Kármán, Theodor; Sechler, Ernest E.; and Donnell, L. H.: The Strength of Thin Plates in Compression. Trans. ASME, vol. 54, no. 5, Jan. 1932, pp. 53-57.
10. Magee, C. L.; and Thornton, P. H.: Design Consideration in Energy Absorption by Structural Collapse. SAE Paper No. 780434, Proc. Congress and Exposition, Cobo Hall, Detroit, Feb 27-March 3, 1978.
11. Aya, N.; and Takahashi, K.: Energy Absorption Characteristics of Vehicle Body Structure. Transactions of the Society of Automotive Engineers of Japan, No. 7, May 1974.
12. Mahmood, H. F.; and Paluszny, A.: Design of Thin Walled Columns for Crash Energy Management - Their Strength and Mode of Collapse. Proc. 4th Instructional Conference on Vehicle Structural Mechanics, November 18-20, 1981, Detroit, pp. 7-18.
13. Wierzbicki, T.; and Abramowicz, W.: On the Crushing Mechanics of Thin-Walled Structures. Department of Ocean Engineering, MIT, Technical Report No. 82-4, April 1982.
14. Pogorelov, A. B.: Geometrical Methods in Nonlinear Theory of Elastic Shells (in Russian), Izd, Nauka, Moscow, 1967.

15. Lukasiewicz, S.; and Szyszkowski, W.: Geometrical Analysis of Large Elastic Deflections of Axially Compressed Cylindrical and Conical Shells. *Int. J. Non-Linear Mechanics*, 14, 1979, pp. 273-284.
16. Foster, C. G.: Some Observations on the Yoshimura Buckle Pattern for Thin-Walled Cylinders (Part I), and Estimation of the Collapse Loads of Thin-Walled Cylinders in Axial Compression (Part II). *J. Applied Mechanics*, 46, 1979, pp. 377-385.
17. Johnson, W.; Soden, P. D.; and Al-Hassani, S. T. S.: Inextensional Collapse of Thin-Walled Tubes Under Axial Compression. *J. Strain Analysis*, 12, 1977, pp. 317-330.
18. Soden, P. P.; Al-Hassani, S. T. S.; and Johnson, W.: The Crumpling of Polyvinylchloride Tubes Under Static and Dynamic Axial Loads. *Proc. Mech. Prop. of Mater. at High Rates of Strain 1974, Instn. P.A.Y.S., Conf. 21*, 327-338.
19. Wierzbicki, T.: On the Formation and Growth of Folding Modes. To be published in "The Buckling of Structure in Theory and Practice" (Edited by J. M. T. Thompson and G. W. Hunt), Cambridge University Press, 1983.
20. Wierzbicki, T.; and Akerstrom, T.: Dynamic Crushing of Strain Rate Sensitive Box Columns. SAE Paper No. 770592, *Proc. 2nd Int. Conf. Vehicle Struct. Mech.*, Southfield, Michigan, April 18-20, 1977.

TABLE I  
EXPERIMENTAL DATA FOR COPPER CRUCIFORM AND "L" ELEMENTS

Test	$P_{max}$ , lb	$P_m$ , lb	L, in.	C, in.	L/C	C/h	$P_m/M_o$
4	277	156.4	3.5	2.0	1.75	143	166.4
5	277	138.5	3.5	2.0	1.75	143	147.3
a8	121	38.1	3.0	2.0	1.50	143	81.1
a11	98	35.3	4.0	1.0	4.00	71.4	75.1
a12	90	31.8	4.0	1.0	4.00	71.4	67.7
16	370	174.7	2.0	2.0	1.00	143	185.9
18	331	173.4	3.0	2.0	1.50	143	184.5
19	257	150.4	4.0	1.0	4.0	71.4	160.0
21	286	119.1	4.0	1.5	2.67	107	126.7
22	273	154.1	4.0	1.5	2.67	107	163.9
23	357	224.6	3.5	2.0	1.75	143	238.9
24	337	153.8	3.5	2.0	1.75	143	163.6
25	323	164.0	3.5	2.0	1.75	143	174.5
27	305	168.8	4.0	2.0	2.00	143	179.6
29	393	168.8	4.0	2.0	2.00	143	179.6
b37	216	84.4	4.0	2.0	2.00	143	89.8
b38	196	90.1	4.0	2.0	2.00	143	95.9
39	225	138.4	4.0	1.0	4.00	71.4	147.2
40	220	117.9	4.0	1.0	4.00	71.4	125.4
42	233	140.3	4.0	1.0	4.00	71.4	149.3
44	245	155.6	4.0	1.5	2.67	107	165.5
45	238	132.2	4.0	1.25	3.20	89.3	140.6
46	270	162.3	4.0	1.25	3.20	89.3	172.7
48	283	171.0	4.0	1.50	2.67	107	181.9

<sup>a</sup>Single "L" test specimen;  $P_m/M_o$  value doubled.

<sup>b</sup>Cruciform specimen consisting of two unjoined "L"s.

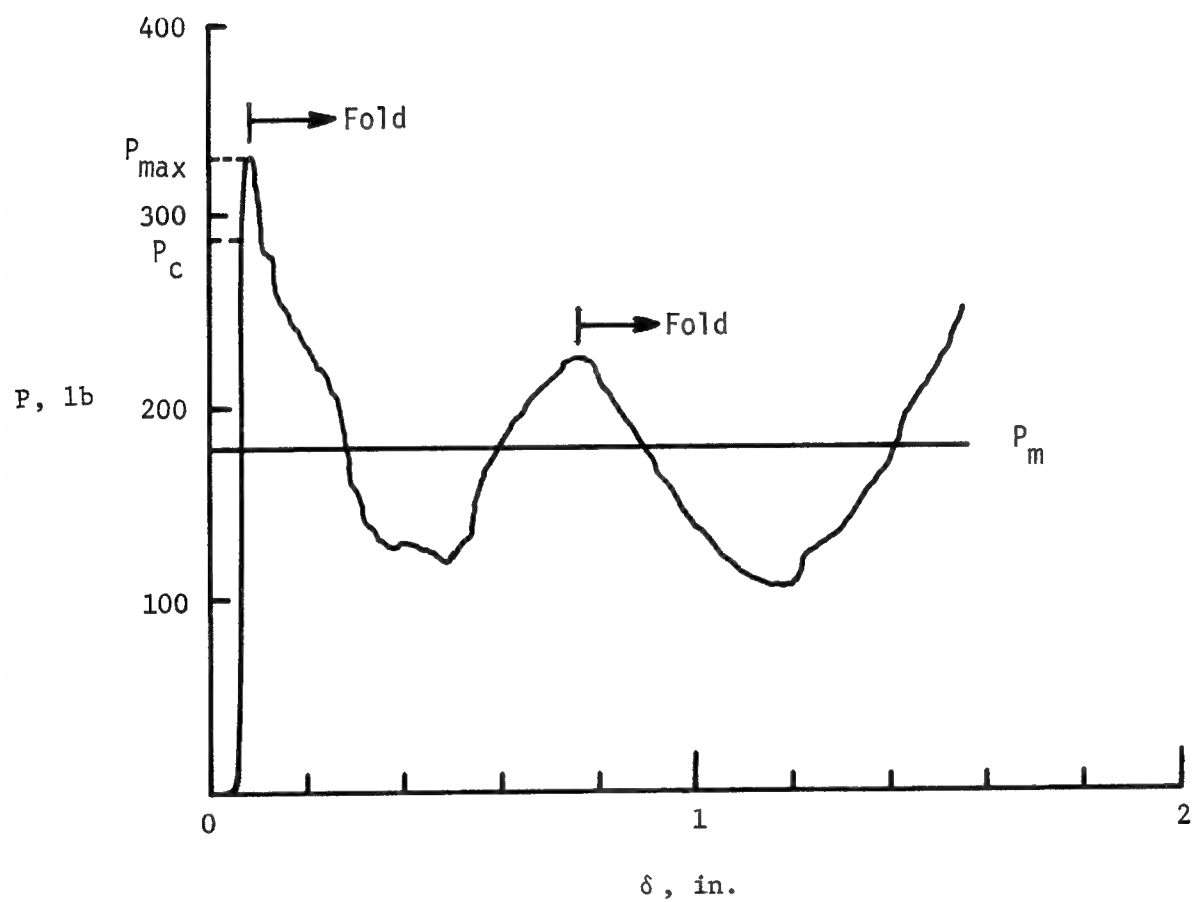





Figure 1.- Typical load-deflection characteristics of a crushed cruciform.



(a) Before testing with clamping fixture.

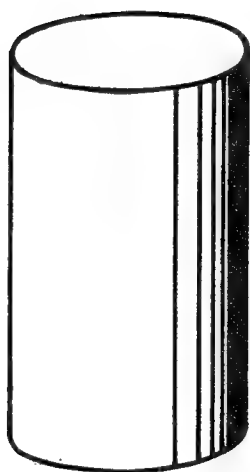


(b) Partially crushed.

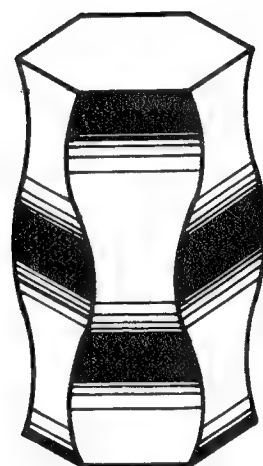


(c) Fully crushed.

Figure 2.- Thin-gage cruciform compression specimen.



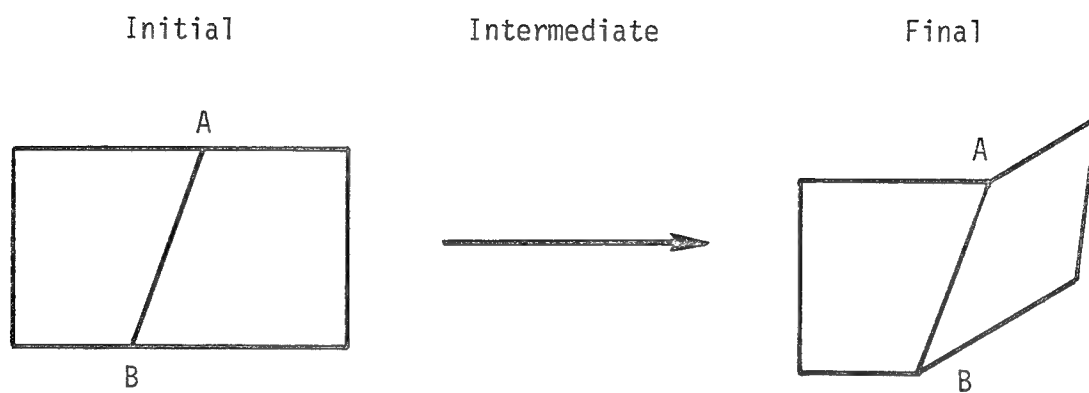
$$\left[ \frac{1}{R_1} \neq 0 ; \frac{1}{R_2} = 0 \right]$$



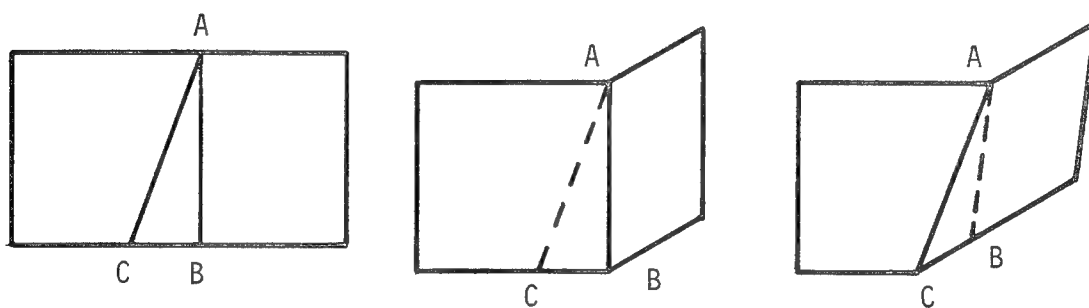
$$\left[ \frac{1}{R_1} = 0 ; \frac{1}{R_2} \neq 0 \right]$$

Figure 3.- Isometric transformation of a cylinder.

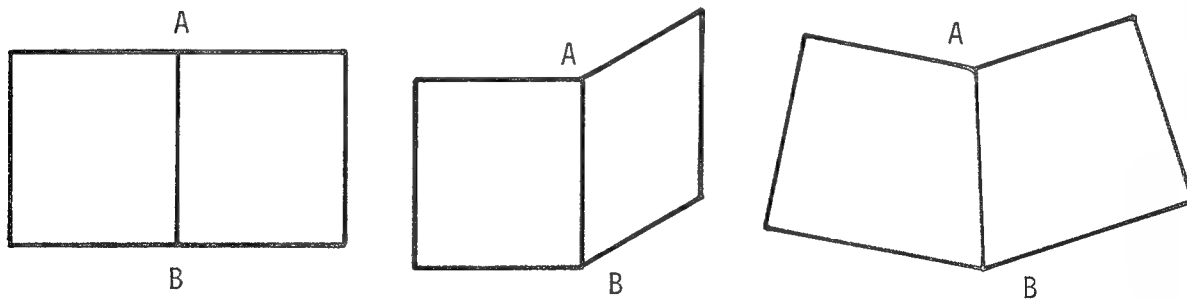




(a) Inextensional deformation path.

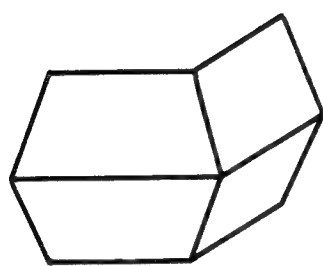


(b) Inextensional deformation path.

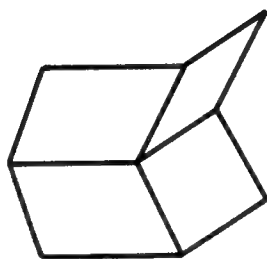


(c) Extensional deformation path.

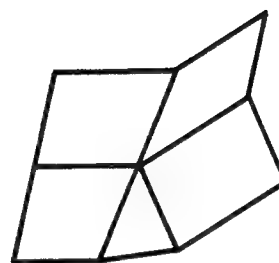
Figure 4.- Illustrations of inextensional and extensional deformation paths.



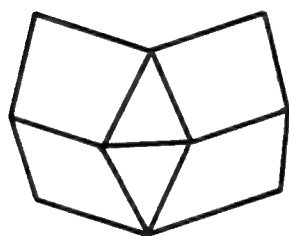
(a)



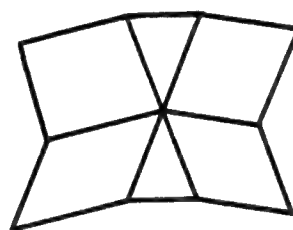
(b)



(c)

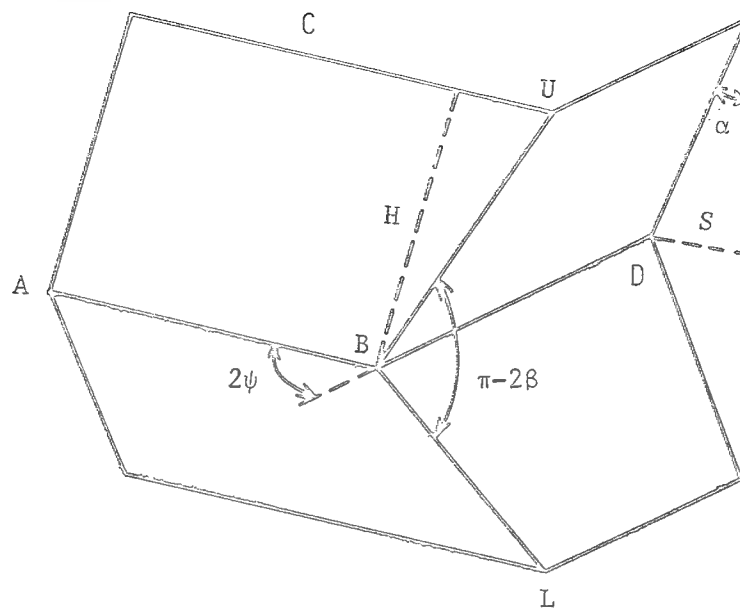


(d)

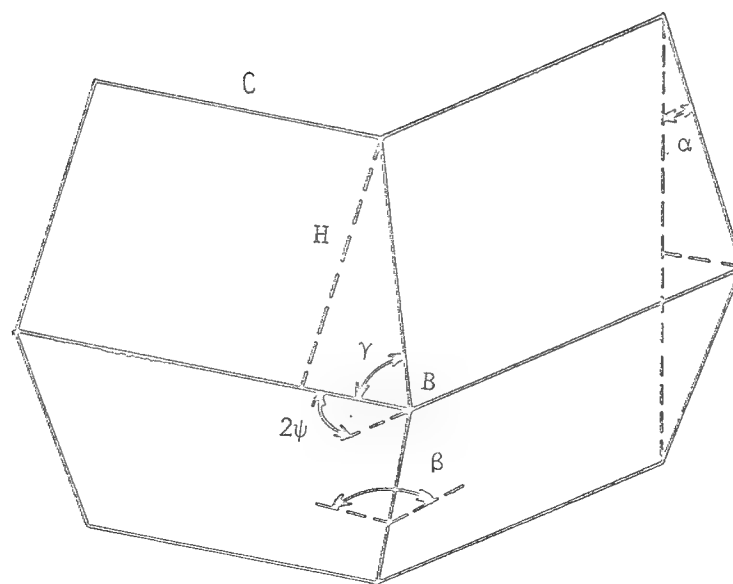


(e)

Figure 5.- Assembling folding modes into more complicated patterns.



Mode I



Mode II

Figure 6.- Extensional collapse modes; definition of geometrical parameters.

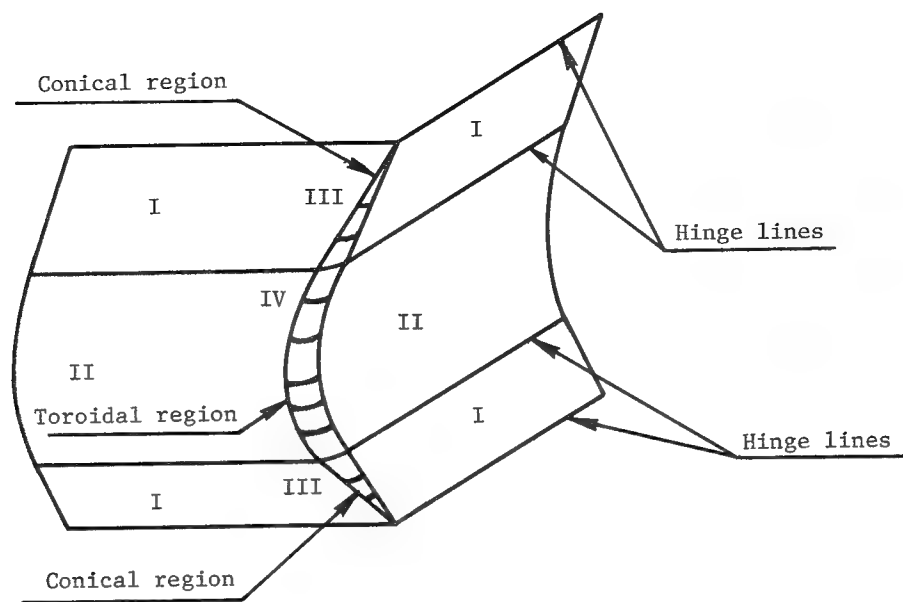


Figure 7.- Basic folding mode with continuous and smooth displacement field.

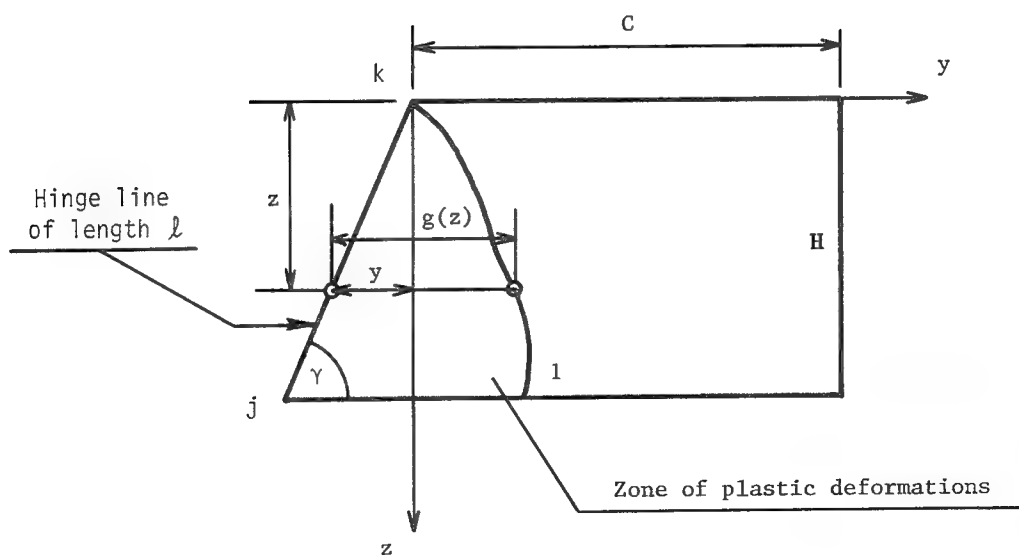
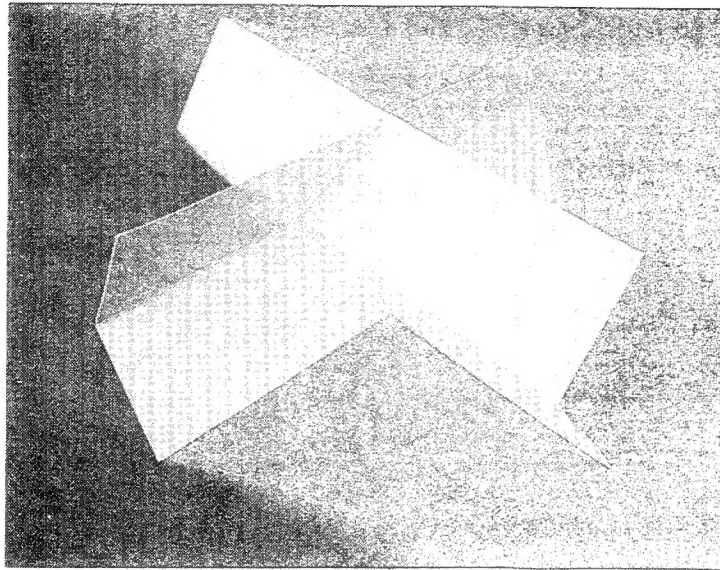
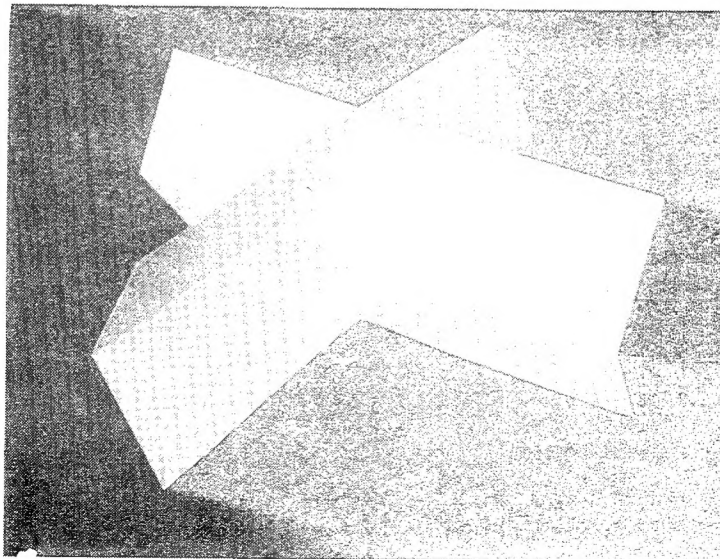


Figure 8.- Plastic distortion of a rectangle into a trapezoid.



Mode I/Mode I



Mode I/Mode II

Figure 9.- Two computational models of a crushed cruciform.

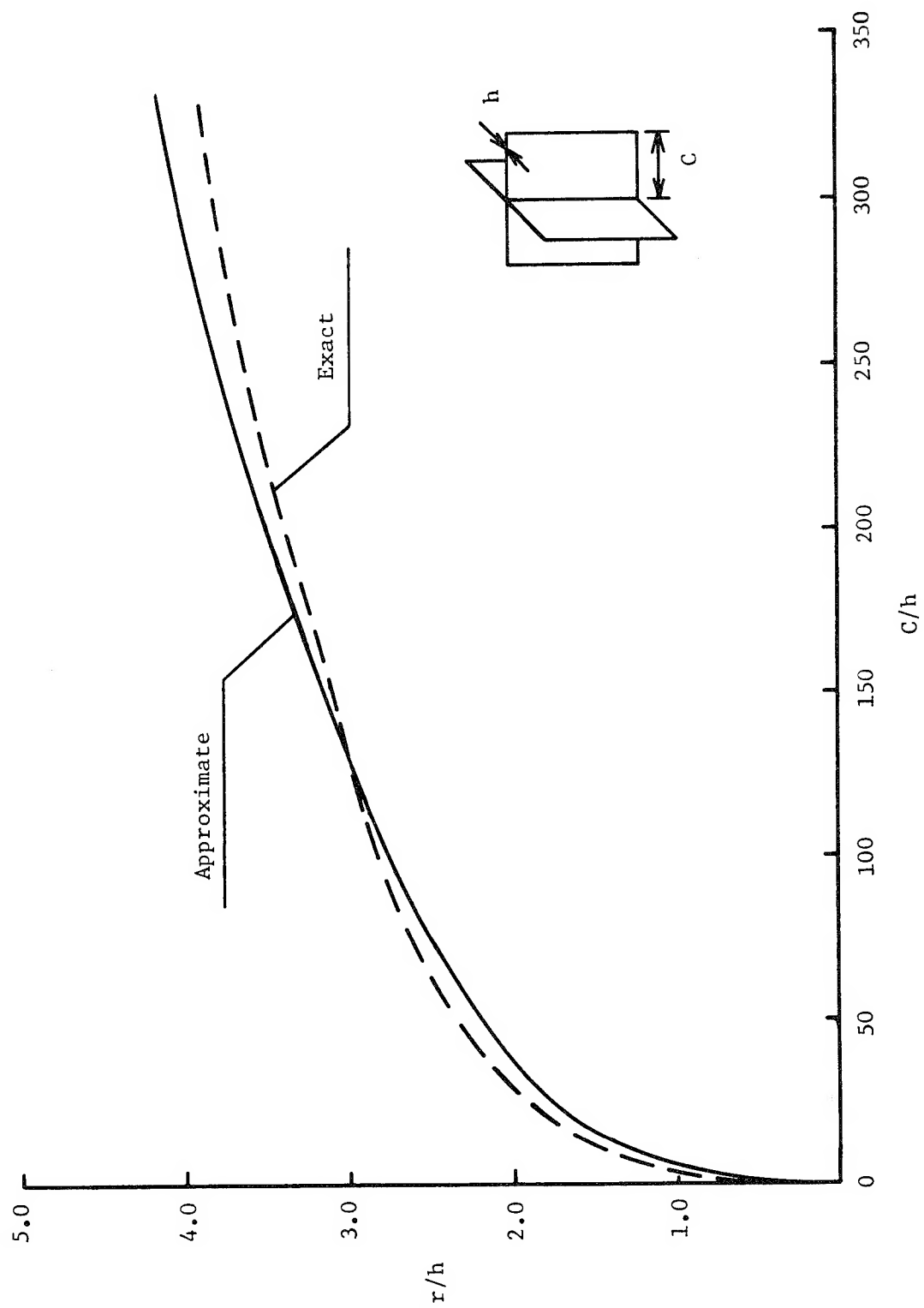


Figure 10.- The dimensionless radius of the folding mode as a function of  $C/h$ .

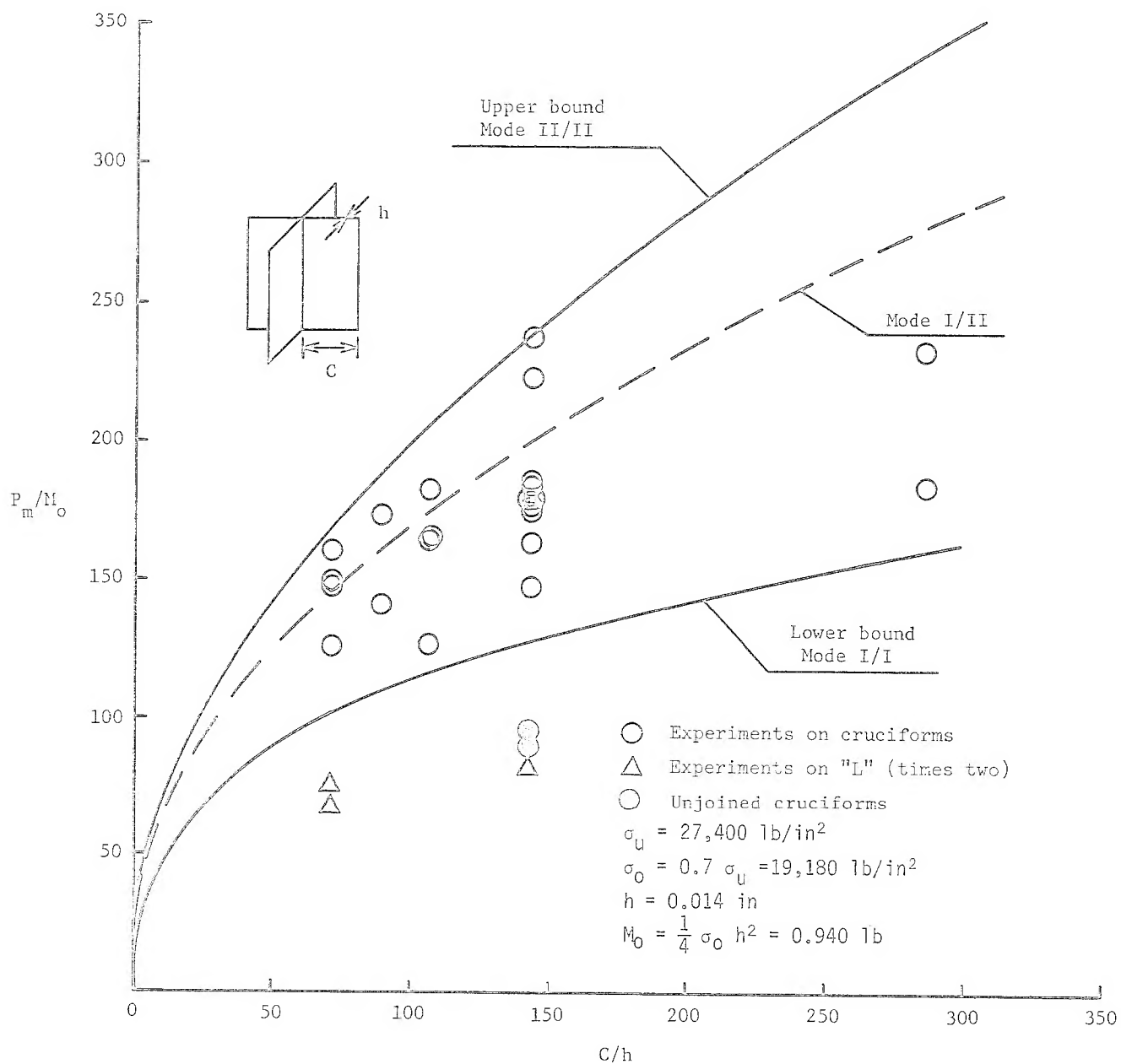


Figure 11.- Mean crushing strength of a cruciform versus  $C/h$ .

1. Report No. NASA CP-2245		2. Government Accession No.		3. Recipient's Catalog No.	
4. Title and Subtitle  RESEARCH IN STRUCTURAL AND SOLID MECHANICS - 1982				5. Report Date October 1982	
				6. Performing Organization Code 506-53-43-04	
7. Author(s) Jerrold M. Housner and Ahmed K. Noor, compilers				8. Performing Organization Report No. L-15506	
9. Performing Organization Name and Address  NASA Langley Research Center Hampton, VA 23665				10. Work Unit No.	
				11. Contract or Grant No.	
12. Sponsoring Agency Name and Address  National Aeronautics and Space Administration Washington, DC 20546				13. Type of Report and Period Covered  Conference Publication	
				14. Sponsoring Agency Code	
15. Supplementary Notes  Jerrold M. Housner: NASA Langley Research Center. Ahmed K. Noor: The George Washington University, Joint Institute for Advancement of Flight Sciences, NASA Langley Research Center.  Most of the papers presented at the symposium are contained in Noor, Ahmed K.; and Housner, J. M., eds.: Advances and Trends in Structural and Solid Mechanics. Pergamon Press Ltd., 1982.					
16. Abstract  A Symposium on Advances and Trends in Structural and Solid Mechanics was held in Washington, D.C., on October 4-7, 1982. NASA Langley Research Center and George Washington University sponsored the symposium in cooperation with the National Science Foundation, the Office of Naval Research, the Air Force Office of Scientific Research, the American Society of Civil Engineers, and the American Society of Mechanical Engineers. The objectives of the symposium were to communicate recent advances and new insights into physical behavior and to identify the trends in the solution procedures for structural and solid mechanics problems. This conference publication includes 26 papers; 19 were presented at research-in-progress sessions and 7 at other sessions. The papers deal with (1) computational strategies for nonlinear problems, (2) material characterization, (3) advances in boundary elements and finite element technology, (4) advanced structural applications, (5) structural stability and analytical techniques, and (6) structural dynamics and vehicle crashworthiness.					
17. Key Words (Suggested by Author(s)) Structural mechanics Solid mechanics Computational methods				18. Distribution Statement  Unclassified - Unlimited	
19. Security Classif. (of this report)  Unclassified		20. Security Classif. (of this page)  Unclassified		21. No. of Pages  441	
				22. Price  A19	